No !

PROGRAMME FOR ATMOSPHERIC WATER SUPPLY (PAWS)

PHASE 1
1983 - 1986 FINAL REPORT

VOLUME 4
Instruments, Techniques & Studies

Report to the
Water Research Commission
Pretoria, South Africa

by

Simpson Weather Associates, Inc
Charlottesville Va., USA

Cansas International Corp. (Pty) Ltd
Nelspruit, South Africa

DECEMBER 1986

133/4/88

ISBN : 0 947447 07 5
Set No : 0 947447 08 3

VOLUME IV

Instruments, Techniques and Studies

Table of Contents

1.0 INTRODUCTION

This final volume of the Final Report on the PAWS research to determine the feasibility of rain enhancement is the book in which we set down in considerable detail all of the techniques and tools developed and the studies carried out in arriving at our assessment. It is the underpinning of all that has been described in the preceeding volumes. Not every reader of Volumes I to III will need everything which can be found in Volume IV, but each reader will need something of it.

This volume is as complete as possible. Some of the items included are in a preliminary state only and are actively being pursued at the time of writing. They are included here in order to show the ground we are attempting to cover, and as a solicitation for suggestions.

2.0 THE PAWS AIRCRAFT SYSTEM (Mather)

2.1 Introduction

A major portion of the research effort over the past 4 years has been expended collecting, storing and analysing cloud microphysical measurements. The vast majority of these measurements have been made using the PAWS Learjet 24, one of the best equipped high performance cloud physics aircraft in the world. This section of Vol. IV describes some of the performance characteristics of the aircraft that are relevant to its cloud physics measurement role, and lists the sensors that are installed on the aircraft. Finally, some of the more important computations that are used in processing the data are described.

2.2 Learjet 24

The PAWS Learjet 24, serial number 103, is one of the earlier series with the short fuselage and wide oval windows. A Howard-Raisbeck Mark II system was installed on this Lear, which reduces take-off and landing speeds by around 17 knots. Some of the pertinent characteristics of the aircraft are listed in Table 2.1. Average climb time from sea level to 30 000 feet (300mb) is 12 minutes. On-station mission time is in excess of 2 hours. Dash speed is 305 knots indicated or 0.82 Mach.

The data acquisition system (DAS) which processes the sensor data before being recorded on magnetic tape is the standard Particle Measurement Systems (PMS) DAS-20-32 which handles the output from two standard PMS laser probes as well as the analogue outputs from the sensors. An on-board computer, interfaced between the DAS and the tape recorder provides almost real-time displays of cloud physics and environmental parameters to two CRTI s; one for the pilots, the other for the mission controller. This enables changes to be made to mission profiles based upon the conditions encountered.

A complete list of the instruments and PMS probes installed on the Learjet is given in Table 2.2.

2.3 Special instrumentation

a. Decelerator.

A decelerator modelled after Hobbs et al.,(1973), (decelerator 2) is installed under the fuselage under the passenger entrance door. This device is used for collecting ice crystals on pre-cooled oil coated slides. Free stream air velocities are reduced to about 30 m/sec. Crystals captured on the slides are stored in cold silicone brake fluid and later photographed in a specially modified freezer. Excellent photographs of columns and plates were acquired on passes through glaciated Cape winter storm clouds.

Table 2.1 : The PAWS Learjet 24 : ZS-LTK

ENGINES		T/O DISTANCE (ft)	
Model	CJ610-4	S/L-ISA	
Thrust	2850 lbs each	Max T/O Wt	3200
ENVIRONMENTAL		LANDING DIST. (ft)	
Press differential	8.77 psi	S/L-ISA	
7000 ft cabin at 41000 ft		Max. Landing Wt.	2600
AIRSPEED		RATE OF CLIMB	
V_{MO}	305 knots	S/L greater than 6000 ft per min	
		S/L to 30 000 ft in 12 mins	
M_{MO}	0.82	LOAD FACTORS	
		Flaps up	+ 4.4 to -1.76 g
V_{MC}	82 knots	Max. Altitude	41 000 ft
		Max. T/O Wt	13 000 lbs
Stall at MLW	89 knots	Max. Landing Wt	11 800 lbs
Approach speed (MLW)	115 knots	Fuel capacity	5 590 lbs
		Empty wt. with equipment installed	7 561 lbs

Table 2.2 Instruments Installed on Learjet 24:ZS-LTK

Parameter Measured	Instrument Type	Manufacturer and Model Number	Range	Time Constant	Accuracy
Temperature	Platinum Resistence	Rosemount 510 BH Amplifier, Probe Model 102	± 50°C	3 sec	± 0.50°C
Dewpoint	Peltier cooled mirror	EG&G Model 137C3, Probe Model 137-S10	± 50°C	3°C/sec	± 0.5°C > 0°C
					± 1.0°C < 0°C
Altitude	Total Pressure	Rosemount 830 BA	0-15 psi	0.025 sec	0.25%
Airspeed	Differential Pressure	Rosemount 831 BA	0-15 psi	0.025 sec	0.25%
Vertical Acceleration	Linear Accelerometer	Systron-Donner 4310A-3-B	± 3 g	0.01 sec	0.01 g
Pitch Rate	Rate Gyro	Northrop GR-G5A-1.0L	± 20°/sec	0.1 sec	0.01 deg/sec
Angle of Attack	Linear Pot	Lear P/N 819802-2	± 20 deg	0.1 sec	0.1 deg
Liquid Water	Hot Wire	P M S CSIRO KLWC-100	± 0-5 gm/m³	1 sec	

Probes Installed on Learjet ZS-LTK

	FSSP	OAP-2D-C
Size Range (Dia)	0.5-45 microns	.035 - 1.12 mm
Resolution (Dia)	0.05-3 microns	0.035 mm
Sample Volume per 100 m of flight	22.9 cm³	6.8 litres

b. Aircraft radar.

A problem with the airborne laser probes is the relatively small volumes that are sampled in a single cloud penetration. A method has been developed to use the on-board aircraft weather radar to increase the cloud volume sampled.

Prior to cloud penetrations, the aircraft X-band radar is locked into a forward facing position by a switch on the instrumentation control console. A radar range gate 1800 m ahead of the aircraft is sampled 10 to 11 times each tenth of a second, then averaged. Since the aircraft radar beam width is 8.0 degrees, each 0.1 sec reflectivity value represents a sample over a volume of about 2×10^7 m^3 of cloud. The radar can be thought of as sampling a cylinder of cloud 250 metres in diameter. In a cloud 4 km in diameter, this would amount to more than 0.1 km^3 of cloud air. Over the same distance, the 2D-C samples a volume of just 0.27 m^3.

c. New methods of measuring in-cloud total and condensed water contents

Using the Learjet engine compressors as giant evaporators, two new methods of measuring total and condensed in-cloud water contents are being developed. Measurements are made in air tapped off the eighth stage of the Learjet axial compressors. Since the air temperature at this point in the engine is around 200°C, all cloud condensate will be evaporated. The two approaches are as follows:

(i) Engine-Theta technique

This approach is essentially calorimetric, in that the cooling of the compressed air due to the evaporation of the cloud condensate is calculated.

(ii) Evaporating technique

Here, the dewpoint of the air tapped off the eighth stage compressors is measured using a fast response Lyman-alpha humidiometer. By measuring the air temperature and pressure inside the Lyman-alpha measurement cell, the total water mixing ratio can be computed. Since water vapour mixing ratios outside the cloud are sampled in the clear air before and after the cloud penetration, cloud condensed mixing ratios can easily be calculated from the in-cloud and clear air differences.

Both of these concepts are examined in detail in Section 9.1 of this volume.

d. Video camera

A video camera has been installed in the Learjet. This camera, which is fixed to the co-pilot's glare shield facing forward, provides a visual record of all seeded and sampled cloud turrets. Cloud top heights can be computed from these records. Perhaps as important, the tapes can serve as a valuable aid in recalling the details of missions after some months have lapsed.

e. King liquid water meter

The CSIRO-King liquid water content probe, manufactured by PMS, has been installed on the Learjet. This instrument has been designed to measure up to 5 gm/m^3 of cloud liquid water. The short, unsheathed sensors have been used with considerable success and are sufficiently robust to stand up to millimetre size graupel. The only problem encountered with the King sensor to date is that at Learjet penetration speeds, the instrument reaches saturation between 4 and 5 gm/m^3 of cloud liquid water.

Comparisons made between the Lyman-alpha, FSSP and Johnson-Williams (JW) hot wire measurements of cloud liquid water content clearly showed that the JW measurements were unreliable. This sensor has since been removed from the Learjet.

2.4 Derived variables

The methods used to compute some of the derived variables are briefly reviewed in this section.

a. True airspeed (TAS)

$$TAS = 44.83\ (T_T)^{0.5}\ \frac{\left(P_T/P_S^{2/7} - 1\right)^{0.5}}{\left(P_T/P_S\right)^{1/7}} \qquad (1)$$

where:

T_T = total temperature

P_T = total pressure

P_S = static pressure

Recovery factor of the Rosemount probe is assumed to be 1.0. The total pressure is obtained from a differential airspeed sensor which measures $P_T - P_S$.

b. Static temperature

$$T_S = \frac{T_T}{\left(P_T/P_S\right)^{2/7}} \qquad (2)$$

c. Vertical gust velocities

$$W_g = U\alpha - \int_0^{\tau}(A_z + Uq)\,dt + lq \qquad (3)$$

where:

W_g = vertical gust velocity

U = T A S

α = angle of attack

A_z = vertical acceleration fluctuations from level flight (positive for aircraft downwards)

q = pitch rate

l = distance between angle of attack measurement and accelerometer

t = time

This expression assumes level flight conditions. In practice, if roll angles are confined to less than 10 degrees, satisfactory measurements of vertical gusts are obtained.

This system is tested by perturbing the aircraft vertically with wings level in still air (so called "roller coasters"). The resultant gust velocities are then calculated. Problems with calibrations or computations are quickly revealed by this method. Accuracies of this measurement by the Learjet are around plus or minus 1 m/sec.

2.5 Laser probes - sampling calculations

a. Forward-scattering spectrometer probe (FSSP)

It is essential to know the beam geometry of this probe. Careful measurements of beam diameter and electronic depth-of-field should be checked each time a laser tube is replaced. The beam is circular and particles that transect the edge of the beam are rejected by a velocity averaging circuit. This results in a decrease in "effective" beam width. The velocity acceptance ratio (VAR) is obtained by dividing the particles accepted by the velocity acceptance circuit (gated strobes) by all the particles that pass within the depth of field (total strobes).

The concentrations must also be corrected for "dead" time, i.e. the time during which the probe is busy processing data and not able to accept new strobes. This is done on the Lear probe by keeping track of the times between the end of the particle transit gate pulse and the reset pulse.

Corrected concentrations per unit time are computed from:

$$\text{Conc} = \frac{P_1}{\text{TAS} * A * (1-\text{ACT})}$$

where:

P_1 = particles accepted by the velocity acceptance circuit

TAS = true air speed

A = sample area

ACT = fraction of the time that the probe is inactive (dead time).

b. 2D-C image processing

One of the problems encountered with the 2D probes is the number of "artifacts" or false images that are recorded along with the valid images of drops, ice crystals and graupel. These can be largely eliminated using software techniques.

(i) Streakers (water that is shed by the upstream edge of the probe across the sampling aperture) are rejected if they are six times as long as they are wide.

(ii) Zero images are cases in which the probe circuitry is triggered but no elements are shadowed. These often correspond to small objects that are near the minimum size detectable by the probe. These are counted and used, since extremely high (greater than 1000 per litre) zero image counts are a characteristic of a recently seeded cloud.

(iii) Images with horizontal or vertical gaps are rejected as splashes.

(iv) Particles with invalid time words are also rejected.

A statistical method is used to adjust the sample area of the 2D-C imaging probe on the Learjet, as follows:

$$\text{Weighted particle count} = \frac{32.0}{(32.0 + \text{IX})}$$

where :

IX = longtitudinal length of image

All particles with X dimensions greater than 30 are truncated to 30 microns

i.e. If IX is greater than 30

IX = 30 microns

This has the effect of increasing the effective probe sample area as particle sizes increase.

3.0 THE PAWS RADAR/COMPUTER SYSTEM (Dixon)

The radar system performs the following functions:

* detection of the initiation of storm development
* collection of volume-scan digital data during storm activity
* real-time display of current storm activity, upon which the decision to launch the aircraft is based
* provision of guidance and navigational information to the aircraft
* collection of digital data on aircraft position.

The MV 4000 computer system is then used for:

* storm identification and the computation of storm properties
* storm tracking
* computation and storage of aircraft tracks
* identification of case tracks (i.e. tracks on which a seed/no-seed decision was made).

The seeding signature is identified by:

* computing track properties
* re-randomizing on the seed/no-seed split
* computing p % likeliness statistics for changes in each of the track properties
* plotting histograms of the p % statistics.

3.1 Operation

The radar system is set in operation as soon as there is a likelihood of storm activity. This usually occurs between 9 and 10 a.m. on a "Go" day. Data are collected from the start of operations, but the data tape is recycled every 30 minutes or so if no significant activity has occurred up to that time.

The real-time PPI display is then monitored for 'launch criteria'. If these criteria are met the aircraft are launched. The aircraft transponders allow the operator to locate the

aircraft, direct it to areas of interest, and then assist with navigation and storm avoidance.

During the mission the operator remains in contact with the aircraft, providing information on storm activity from a radar viewpoint. He also:

* opens, when requested, the envelope which gives the seed/no-seed decision

* informs the aircrew if they appear to be moving away from the chosen target

* decides whether a new target is a valid candidate for seeding based upon its separation from previous cases.

The radar is generally operated until about 19:00, or until activity ceases, whichever occurs first. If the aircraft lands close to 19:00 the radar watch is extended to ensure valid track data on any selected storms.

Figures 3.0 and 3.1 show examples of typical radar plots.

3.2 Progress

The following summarises development of the various components of the radar hardware/software system:

1982/83
* volume scan collection
* storm identification, 12 storm properties
* storm tracking, 8 track properties
* analysis of 82/83 data
* preparation of maps showing storm activity and storm generation
* regressions between track properties.

1983/84
* storm identification, 24 storm properties
* storm tracking, 8 track properties
* analysis of 83/84 data on NOVA 4
* installation of MV4000 computer system.

1984/85
* transfer of software to MV4000
* storm identification, 63 track properties
* digital aircraft tracking for case identification

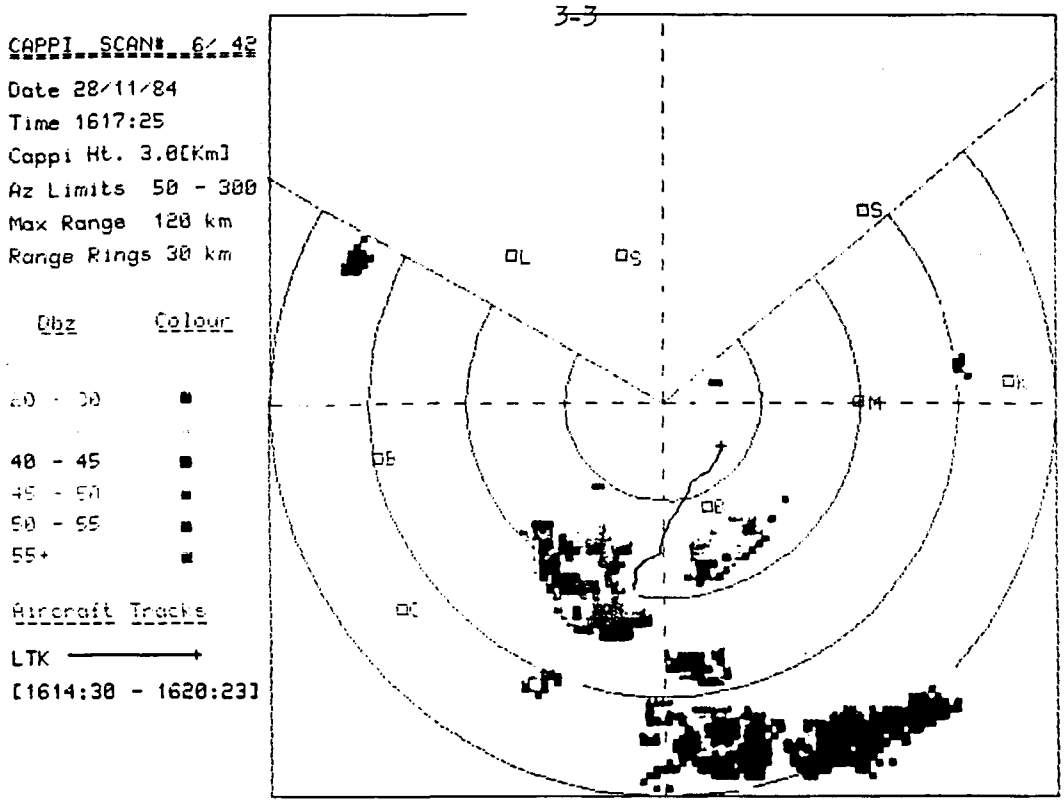

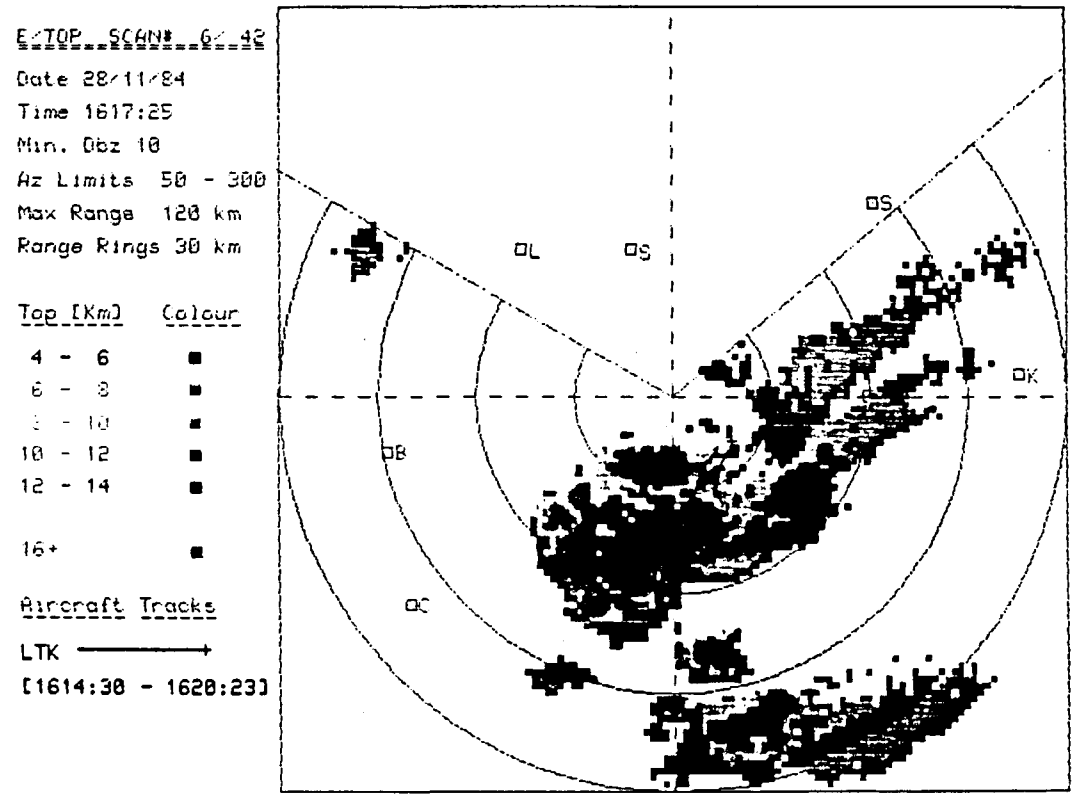

Fig. 3.0. Constant altitude map (CAPPI) and cloud echo top map.

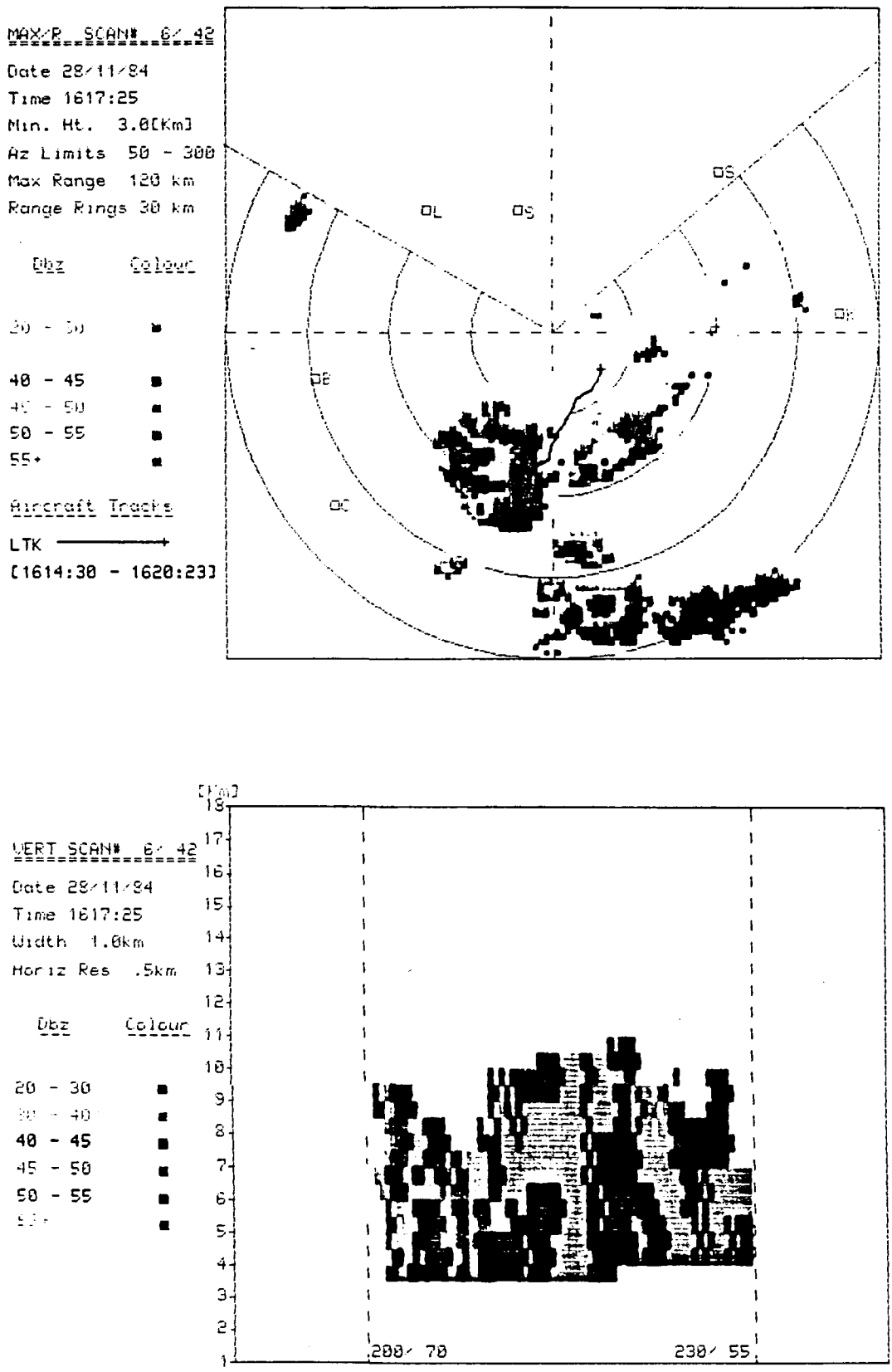

Fig. 3.1. Maximum reflectivity map and vertical section (RHI).

* storm tracking, 73 track properties

* analysis of 84/85 data

* archiving system with blue-sky suppression

* archiving of 84/85 data

* randomization scheme for seeding effect evaluation

* initial indications of radar seeding signature using re-randomization scheme

1985/86 * real-time computer-generated low-level scan display

* archiving of 82/83 and 83/84 data

* storm tracking, 244 track properties

* upgrading of re-randomization scheme to give time-dependent analysis

* analysis of 85/86 data

* confirmation of radar seeding signature using re-randomization scheme

* archiving of 85/86 data

3.3 Launch criteria and subsequent case criteria

The aircraft were launched based on the following criteria:

Cloud base aircraft - at least one storm exceeding 40 dBz within 100 km of the radar, not including storms within 10 km of the radar or over Swaziland or Mocambique.

Seeding aircraft - at least two closed 30 dBz contours containing 40 dBz or more, the location requirement being the same as for the cloud-base aircraft.

Any subsequent cases could only be chosen if the radar operator confirmed that they were at least 20 n.m. edge-to-edge from previous cases on the same flight.

3.4 The radar-computer system and its characteristics

The radar has a wavelength of 5 cm with an 8 ft parabolic antenna. Co-located with this antenna is an IFF antenna for aircraft position data acquisition. The radar characteristics are listed in Table 3.0. Figures 3.2 to 3.3 detail the beam pattern and calibration. Figure 3.4 shows the terrain angles as seen from the radar.

Table 3.0 Pacer III Radar Characteristics

	Nominal Value	Measured Value
Frequency	5.6 GHz	5.610 GHz
Average transmitted power	100W	78W
Peak transmitted power	250W	170W
Pulse duration	2 us	2.3 us
Pulse repitation frequency	200 s^{-1}	197.5 s^{-1}
Beamwidth: Azimuth	1.6 ^{o}	1.85^{o}
Elevation	1.6 ^{o}	1.5 ^{o}
Gain	40dB	38.4dB
First sidelobe level	-24dB	-25dB
Other Characteristics		
Magnetron type	7156	
Receiver	logarithmic	
Antenna type	horn fed parabola	
diameter	8 ft	
polarisation	horizontal	
feed	J-feed, tapered horn	
Average scan rate	3 rpm	

The radar processor is a Data General Nova 4 system (16-bit, 256 Kbyte RAM, 25 Mbyte Winchester, 1 floppy disk, 2 1600 bpi tape drives). The operating system is RDOS, which allows foreground/background programming.

The antenna may be driven under software control, and generally this mode of operation is used. A Tektronix 4107 graphics terminal provides a digital display of the low-level scan, while the radar VDU shows an analogue display at the current elevation.

The system calibration was checked in January 1984 by Dr. Paul Smith of the South Dakota School of Mines (Memorandum to WRC, 14 May 1984). The calibration is checked once per day during the season. However, since the radar has much solid-state circuitry, and the test equipment has not, it appears that the calibration will only indicate gross trouble, and is in fact more a test of the test equipment than the radar. New test equipment has been ordered.

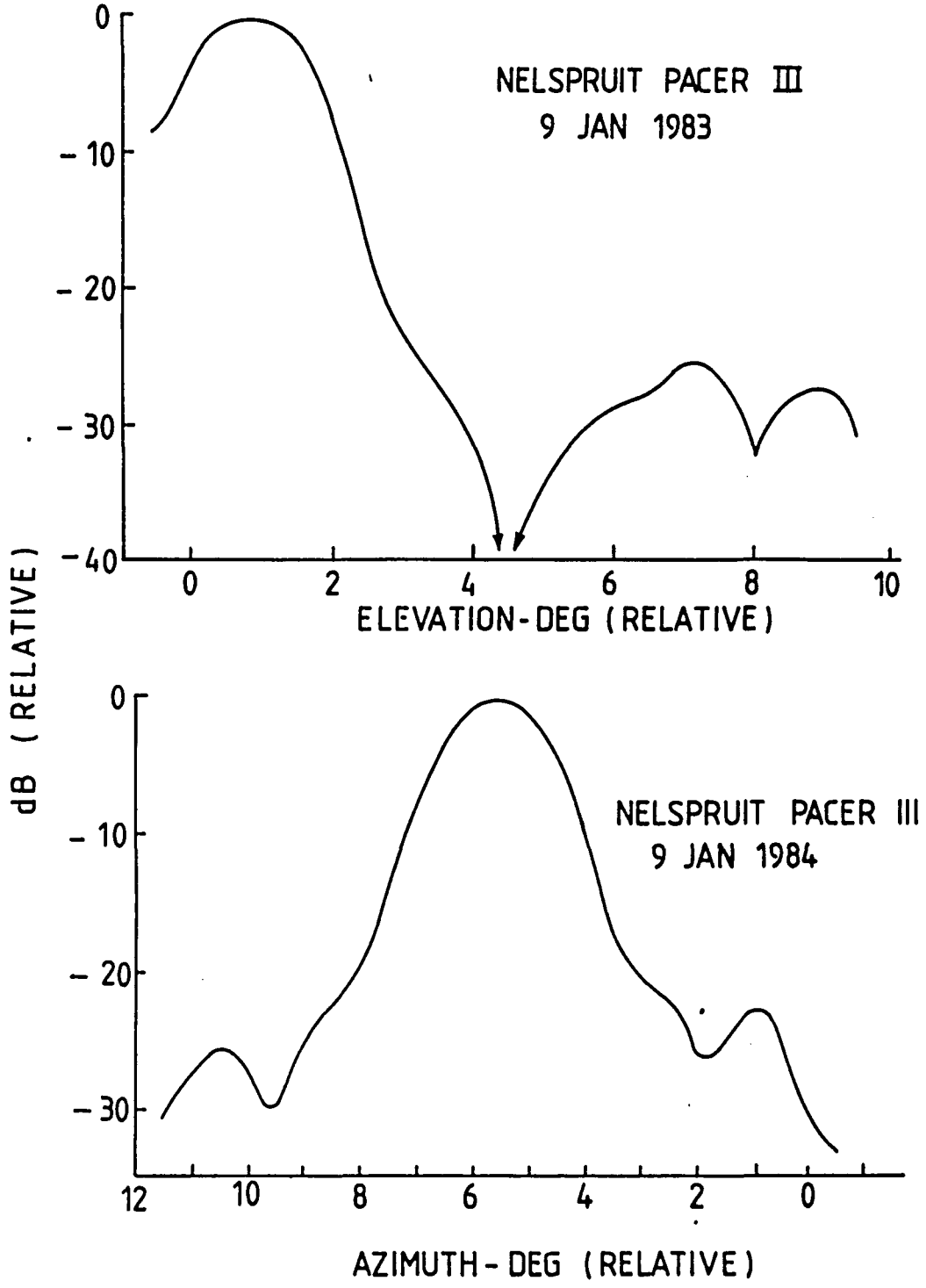

Fig. 3.2 Radar beam pattern

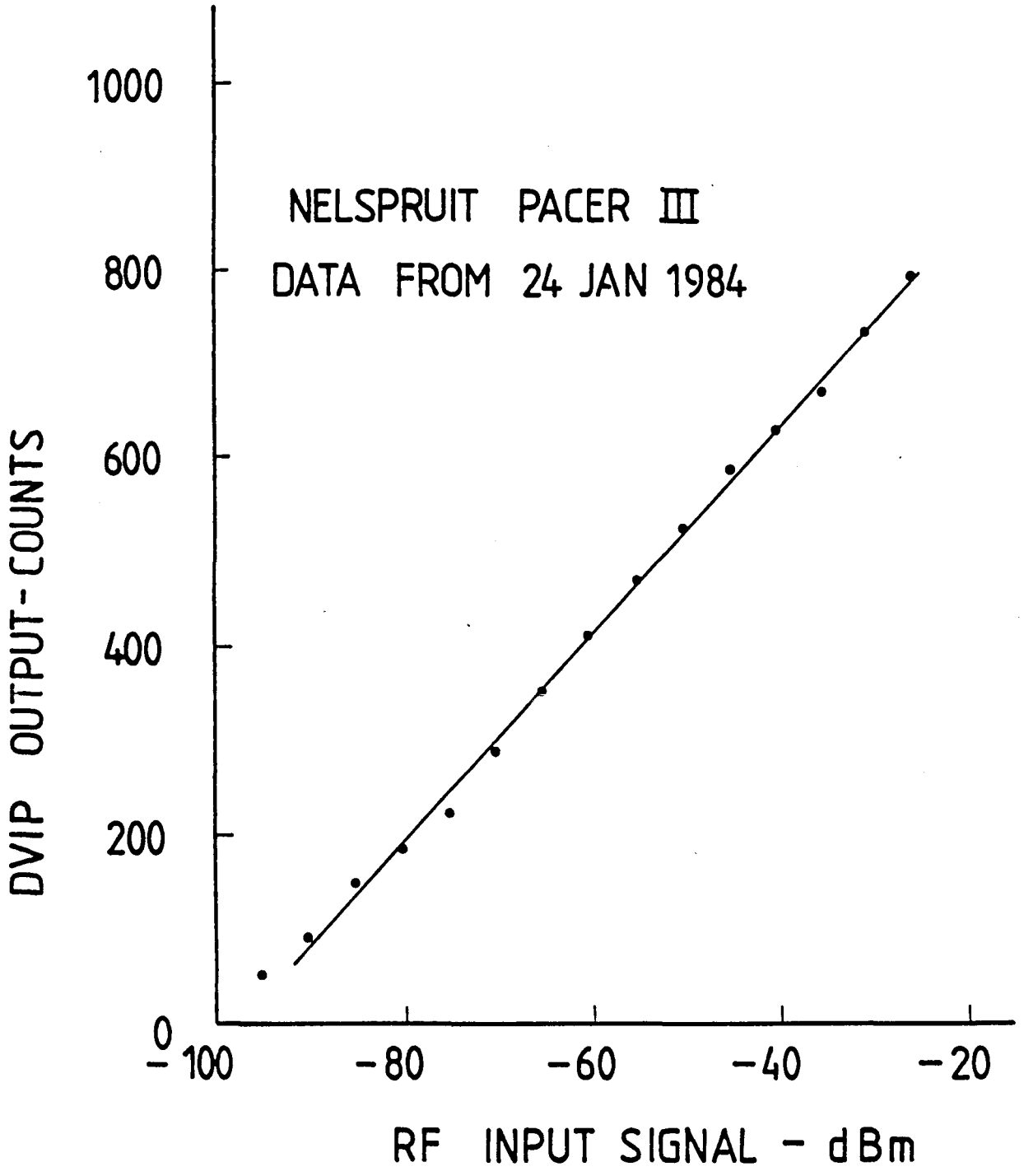

Fig. 3.3 Radar calibration

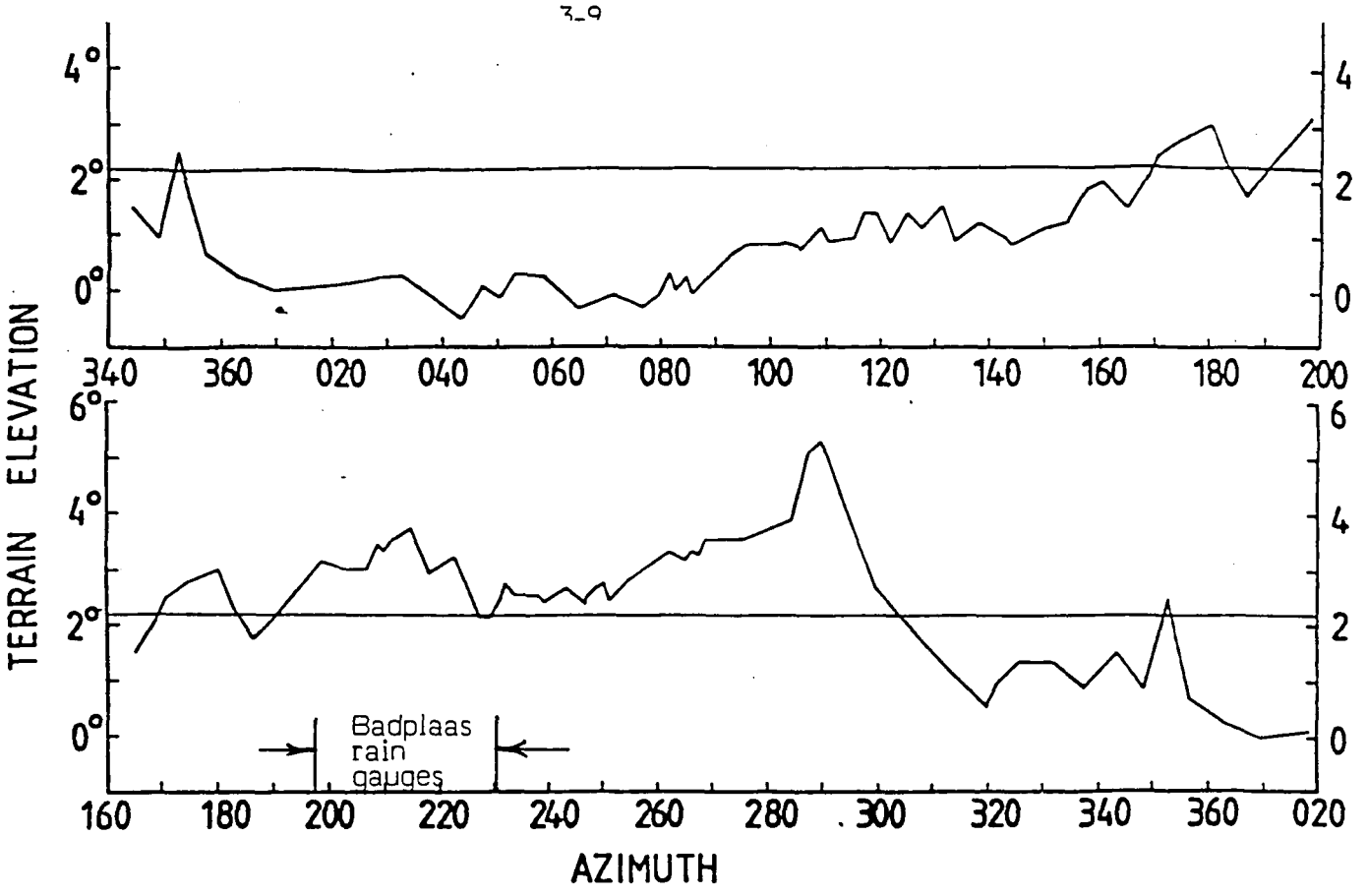

Fig. 3.4. Terrain angles as seen from the radar antenna.

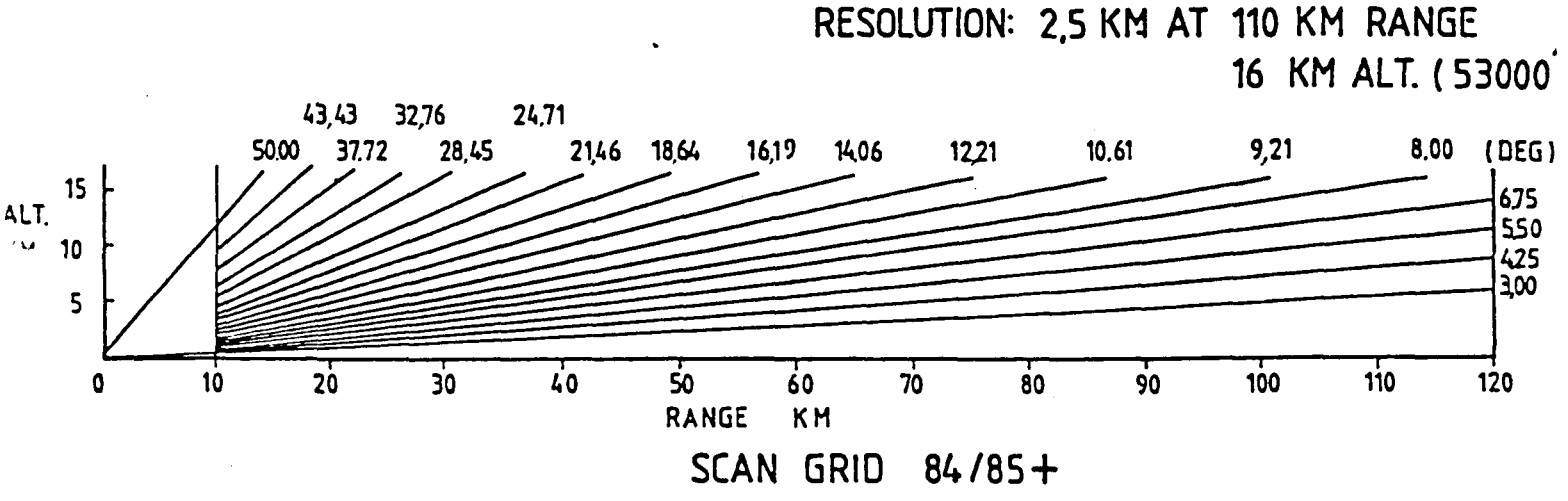

Fig. 3.5 Elevation sequence

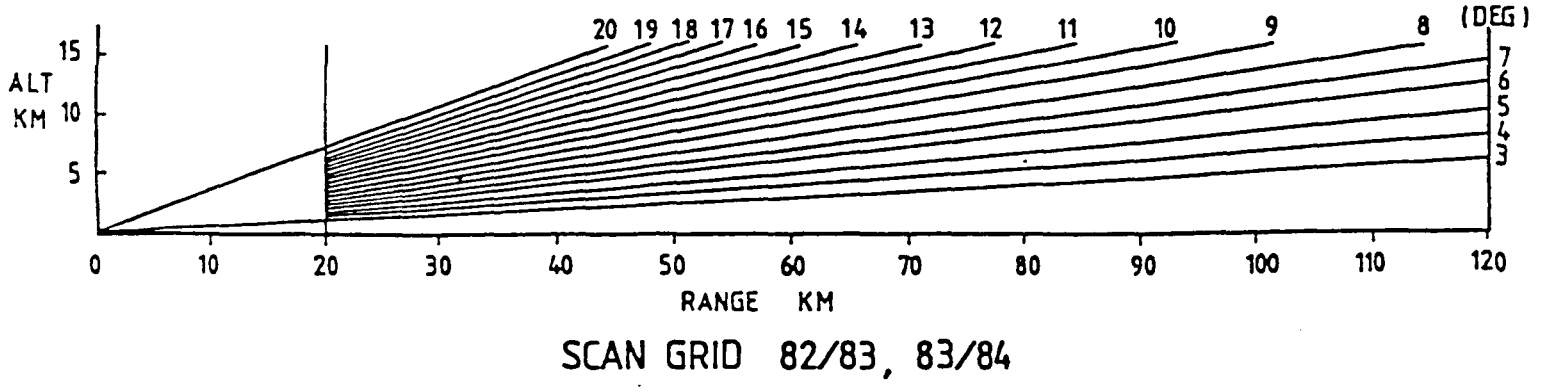

The main analysis computer is a Data General MV4000 system (32-bit, 4 Mbyte RAM, 354 Mbyte Winchester, 1 floppy disk, 1 1600 bpi tape drive, 8 terminals, Tektronix 4107 graphics, Versatec output). At present data is transferred to this system from the NOVA 4 using magnetic tapes. However, a data channel has been installed between the two systems, the intention being to transfer data to the MV4000 in real time.

3.5 The volume-scan data

The radar is operated in volume-scan mode, scanning successive PPI's at incremented elevation angles. The elevation sequence is shown in Figure 3.5.

If the storm activity is confined to some fraction of the 360 degrees scan the 'sector scan' mode is employed in which the antenna reverses direction each time it increases in elevation, and scanning is confined to a sector chosen by the operator. The full 360 degrees is scanned at the lowest elevation angle to provide a record of the activity in the sector not included in the scan. The average scan frequency is one scan in six minutes, the exact frequency depending upon the size of the sector scanned. If the entire 360 degrees is scanned, frequency is about one scan per 8.5 minutes.

In azimuth, data are stored every degree. The stored dvip level is a summation of 8 returns during the traverse of that degree, so the computed reflectivity is a mean value from eight returns approximately 0.125 degrees apart.

In range, data are stored from 10 to 130 km at 0.6 km intervals.

3.6 Aircraft Tracking

The IFF (Identification Friend or Foe) system has its own transmitter and antenna system. The antenna is mounted above the parabolic dish, and the transmitter is triggered by the main radar transmitter.

The IFF pulses trigger transponder units in the aircraft, which respond by transmitting a selected code. For each degree of rotation a maximum of eight possible returns are stored, four from each aircraft. These data are stored at the end of the data block containing the reflectivity information.

When the data are transferred from tape to the MV4000 system, the programme accesses the IFF data and decides which are valid returns and which are spurious. The valid aircraft positions are stored both on disk and in the header blocks of the archived data.

3.7 MV4000 radar software

The following Fortran 77 routines were implemented for handling and analysing the radar data:

TAPE OPERATIONS

TAPEDUMP	- loads from NOVA into MV4000
PACK-TO-TAPE	- loads repacked data to tape for archiving
TAPELIST	- produces list of files on repacked tape
REDUMP	- loads archived data back to disk for analysis
TAPECOPY	- loads archived data back to disk for copying
DISKCOPY	- makes tape copy from disk files (see TAPECOPY)
STORMS-TO-TAPE	- loads processed storms files to tape in ASCII format
AC-POSN-TO-TAPE	- loads aircraft position data to tape in ASCII format
TAPE-TO-STORMS	- reloads ASCII storm data to disk files for transfer to other systems

DATA PRESENTATION - GRAPHICS

RPLOTS - produces the following radar plot presentations

PPI - 18 elevations

CAPPI - 14 altitudes

ECHO TOPS

MAXIMUM REFLECTIVITY

HEIGHT OF MAXIMUM REFLECTIVITY

VERTICAL SECTION - any orientation

TEST PATTERN - produces a test pattern in radar data format

PPI-ZOOM - a close look at radar data in the vicinity of the aircraft at a given time

STORM ANALYSIS

STORMS	- identifies storms in each scan, and computes 63 properties for each storm
TRACK	- tracks the storms in time
STORMPRINT	- prints out storm properties
STORMPLOT	- produces x-y and time history plots of storm tracks

TRACK ANALYSIS

TRACKPROPS	- computes 244 properties for each storm track
TRACKPRINT	- prints out track properties
TRACKSTATS	- prints out statistics on the properties of a chosen group of tracks
RANDOM-STATS	- uses a re-randomization scheme to determine the significance of differences between track statistics of two track groups (e.g. seed and no-seed groups)
TRGPLOT	- produces x-y plots of track statistics
TRACK-PC	- determines the ranking of the properties of chosen tracks relative to the rest of the tracks on that day - the resulting data may then be dealt with using TRACKPRINT, TRACKSTATS and RANDOM-STATS.

3.8 Storm properties

For the purpose of the radar study, a 'storm' is defined as: 'any contiguous volume all of which exhibits reflectivity in excess of a threshold value'.

For the work done to date, the reflectivity threshold was set at 30 dBz. Experience has shown that, at this threshold, the tracking programme performs best. It also is a logical choice, since rainfall rates at reflectivities below this level are negligible (from the standpoint of this work).

In addition, a minimum volume limit of 3 cubic kilometres was set. This helped to reject isolated echo points from the data set.

For each storm at each scan time, 63 properties are computed (the 64th being the track number). These properties are listed in Table 3.1.

1 - CENTROID X
2 - CENTROID Y
3 - CENTROID Z
4 - REFLECTIVITY WEIGHTED CENTROID Z
5 - TOP
6 - BASE
7 - VOLUME TOTAL
8 - VOLUME <20 DBZ
9 - VOLUME 20-25 DBZ
10- VOLUME 25-30 DBZ
11- VOLUME 30-35 DBZ
12- VOLUME 35-40 DBZ
13- VOLUME 40-45 DBZ
14- VOLUME 45-50 DBZ
15- VOLUME 50-55 DBZ
16- VOLUME 55-60 DBZ
17- VOLUME 60-65 DBZ
18- VOLUME 65+ DBZ
19- AREA AT 3 DEG
20- MEAN REFL. AT 3 DEG
21- RAIN FLUX AT 3 DEG
22- AREA AT CUTOFF ALTITUDE
23- MEAN REFL AT CUTOFF ALTITUDE
24- RAIN FLUX AT CUTOFF ALTITUDE
25- AREA AT 3 DEG < 20 DBZ
26- AREA AT 3 DEG 20-25 DBZ
27- AREA AT 3 DEG 25-30 DBZ
28- AREA AT 3 DEG 30-35 DBZ
29- AREA AT 3 DEG 35-40 DBZ
30- AREA AT 3 DEG 40-45 DBZ
31- AREA AT 3 DEG 45-50 DBZ
32- AREA AT 3 DEG 50-55 DBZ
33- AREA AT 3 DEG 55-60 DBZ
34- AREA AT 3 DEG 60-65 DBZ
35- AREA AT 3 DEG 65+ DBZ
36- MASS G.L - 2500 METRES
37- MASS 2500 - 4000 METRES
38- MASS 4000 - 5500 METRES
39- MASS 5500 - 7000 METRES
40- MASS 7000 - 8500 METRES
41- MASS 8500 -10000 METRES
42- MASS 10000 -11500 METRES
43- MASS 11500 -13000 METRES
44- MASS 13000 -14500 METRES
45- MASS 14500 -16000 METRES
46- MASS 16000 -17500 METRES
47- MASS 17500 + METRES
48- PEAK REFL G.L - 2500 METRES
49- PEAK REFL 2500 - 4000 METRES
50- PEAK REFL 4000 - 5500 METRES
51- PEAK REFL 5500 - 7000 METRES
52- PEAK REFL 7000 - 8500 METRES
53- PEAK REFL 8500 -10000 METRES
54- PEAK REFL 10000 -11500 METRES
55- PEAK REFL 11500 -13000 METRES
56- PEAK REFL 13000 -14500 METRES
57- PEAK REFL 14500 -16000 METRES
58- PEAK REFL 16000 -17500 METRES
59- PEAK REFL 17500 + METRES
60- MEAN REFLECTIVITY
61- PEAK REFLECTIVITY
62- HEIGHT OF PEAK REFLECTIVITY
63- MAX HEIGHT OF 45 DBZ ECHO
64- TRACK NUMBER

Table 3.1 Storm properties

The following notes may help in understanding some of the properties:

Reflectivity - weighted centroid Z - this is the vertical centre of gravity weighted with respect to reflectivity, whereas property 3 is a purely geometric property. If property 4 is lower than property 3, the storm is bottom-heavy with respect to reflectivity.

Cut off altitude - this is set at 6 km, and some properties refer to this altitude, or to the region above it. The 6 km value was chosen because radar data at or above 6 km is reasonably uniform with respect to range, whereas 3 degree properties are range-dependent. Also, seeding operations occur at approximately this level.

Rain flux - computed using the Marshall-Palmer relationship:

$$Z = 200\ R^{1.6}$$

Mass - computed using the relationship (Morgan and Mueller, 1972):

$$Z = 20300\ M^{1.67}$$

Maximum height of 45 dBz echo - this property is regarded as a hail indicator. The presence of hail is considered likely if it exceeds 7.5 km.

3.9 Storm tracking

The tracking algorithm used is based on a paper by Gordon Mader (1979) of the CSIR. The description below is taken from his paper:

"Consider two consecutive scans at time t_1 and t_2.

a. Construct all possible segments of track from t_1 to t_2. To keep the number sensibly small, a constraint may be applied to their lengths - each may not be longer than 10 km or the average radius of the storm represented by the segment, whichever is the greater. This criterion allows large storms some extra space for propagation.

b. Consider any one of the aforementioned segments. Construct a set consisting of all possible segments which either have the same starting point or the same ending point.

c. Add to this set all possible segments which both start and end on points within the set, apart from those already found.

d. A branch may be defined as any point which starts or terminates more than one segment. Find the longest segment which has branches at both ends, if any such segments exist, and delete them.

e. Repeat step (d) until there are no segments with branches at both ends.

f. Commence at step (b) again and continue until no more sets are found in which there are segments with branches at both ends.

g. If several of the remaining segments end on the same branch point, delete all but the shortest segment. In effect, this separates any two tracks which merge, terminating one and allowing the other to continue.

h. The tracking process corresponding to the first scan is now complete. Repeat it, using the second scan as a starting time, then join all the segments which have a common point".

The basic algorithm was modified by replacing the distance moved with a statistic which incorporates both the distance moved and the relative change of volume of the storm from one scan time to the next. This refinement improves accuracy by inhibiting tracks between storms close to one another but of very different size. The number of possible tracks was restricted by imposing an upper limit to the speed of movement, which for the analyses to date has been set at 80 km/hr.

It is important to recognize that the algorithm tracks the storm centroid. Therefore the maximum speed refers to 'real' translation speed and 'apparent' translations as a result of shifts in the centroid position (storm splits and merges).

The nature of the algorithm is such that if a real merger occurs, the 'most likely' track is continued after the merger while the 'least likely' track is terminated. Likewise if a real split occurs a new track is commenced, this new track being the one which has the worst match with the track prior to the split.

On the whole the tracking algorithm works well. In squall-line situations it does become confused, and may produce physically unlikely tracks.

Its main feature is that it produces objective tracking under all circumstances - errors made in seed cases are just as likely to be made in no-seed cases.

Figures 3.6 and 3.7 show examples of storm track plots and time histories. The tracks are depicted as circles with joined tangents. These circles have the same area as the storm at the height of the low level scan, and are centred on the storm volume centroid.

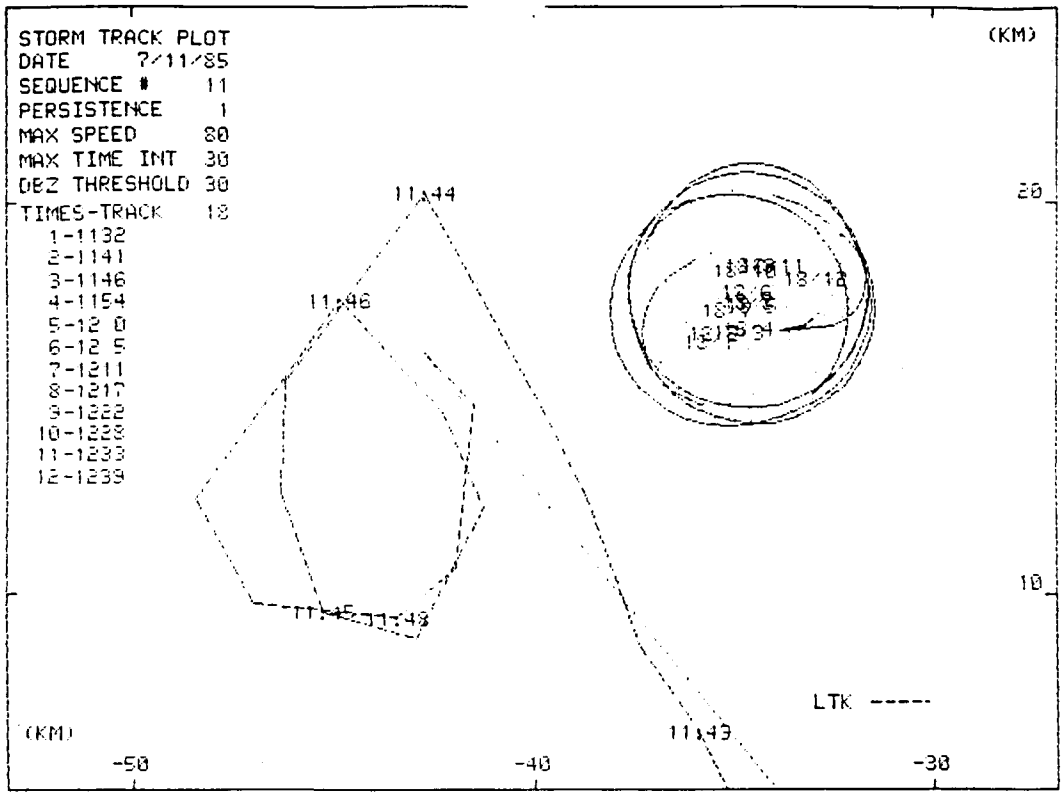

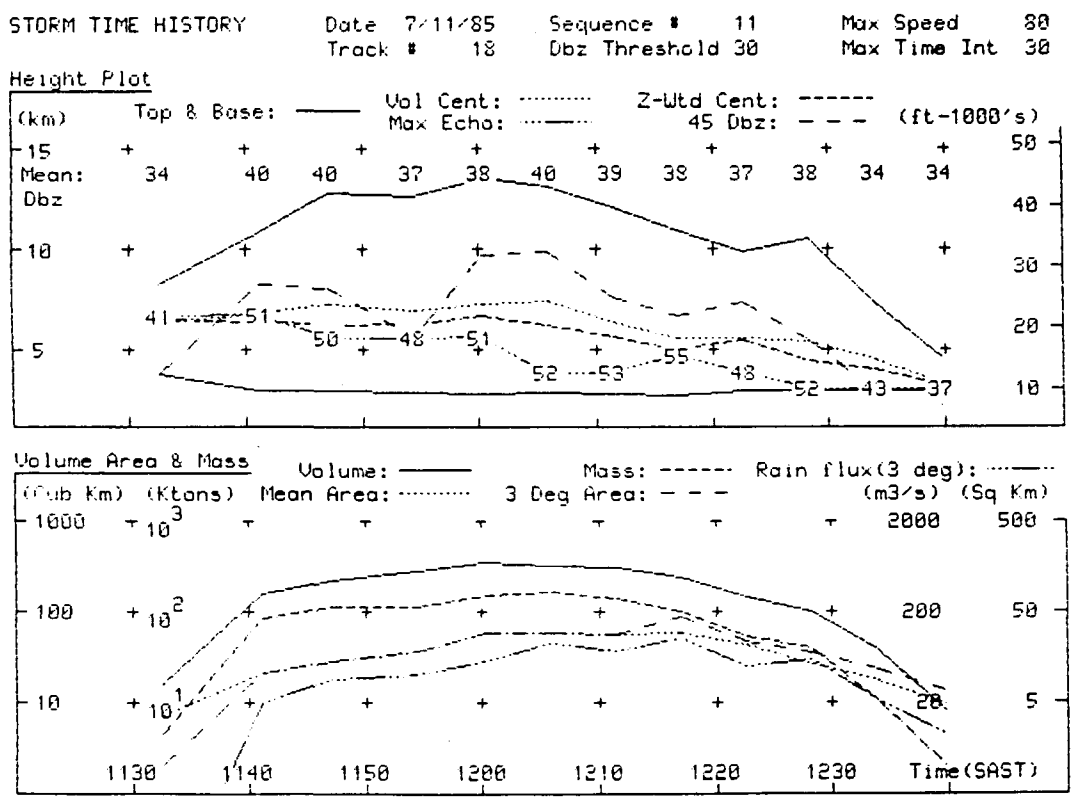

Table 3.6 A slow moving storm

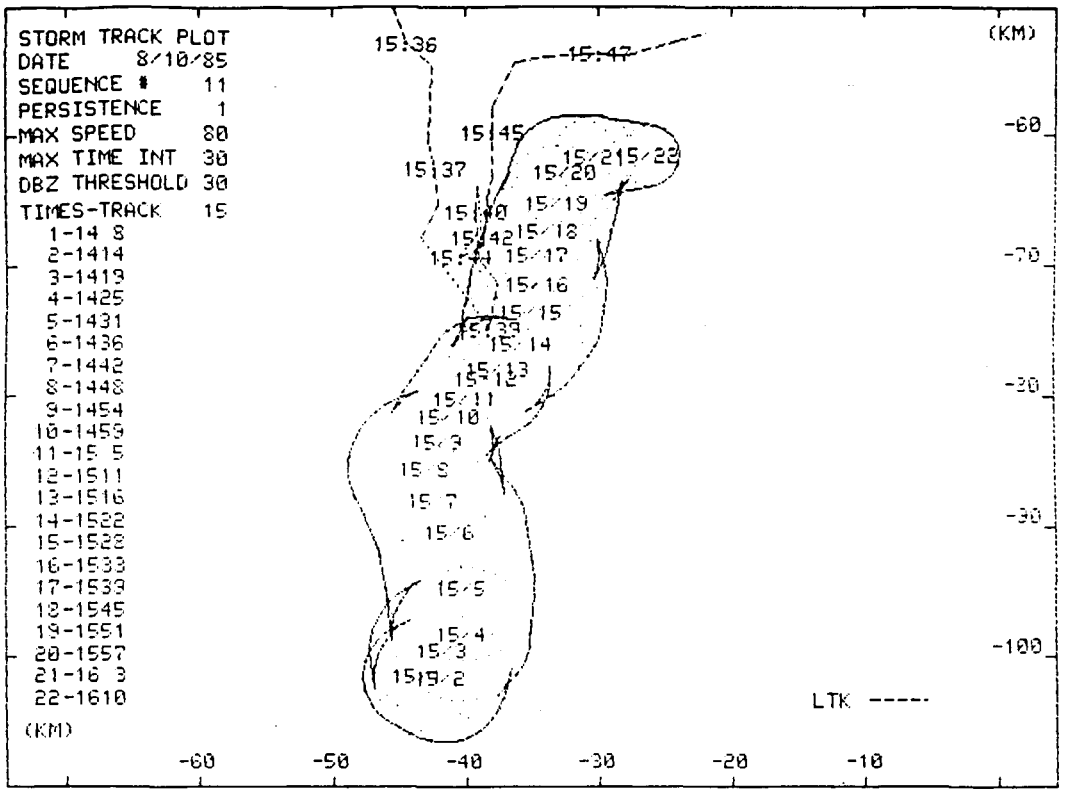

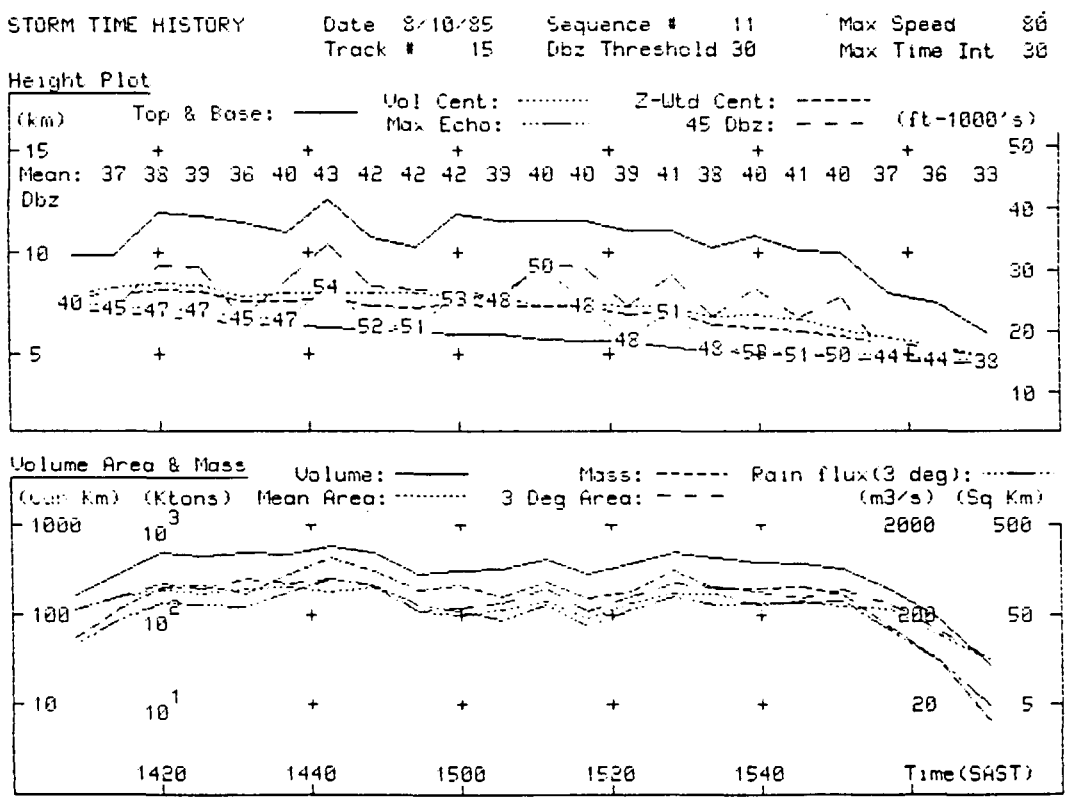

Fig. 3.7 A fast moving storm (LTK is the Lear Seeding Aircraft)

3.10 Case identification

It is necessary to identify those radar storm tracks which were selected as candidates for the seeding experiment. Figures 3.6 and 3.7 show examples of the aircraft tracks alongside or over the storm tracks. Case identification is merely a matter of determining which storm track coincides with the aircraft track in both space and time at the time the seeding/sampling was carried out.

If a seed or no-seed/sample decision is drawn, the aircraft tends to follow a 'race-track' pattern for the duration of the seeding or sampling. In these cases identification is simple.

If a no-seed/no-sample decision is drawn, the pilot is required to make at least one pattern to the side of the storm, and if possible to fly over the active zone and 'mark' the storm position by informing the radar when he is over it.

In many of the cases the aircraft appears to orbit to the side of the storm track. This occurs for the following reasons:

- for much of the time the aircraft is clear of the storm, i.e. between seeding or sampling runs;

- seeding or sampling takes place in growing turrets, which frequently are not yet visible to the radar. The storm track is plotted as circles centred on the storm 'centroid' which may be well removed from the position of the new development.

3.11 Track properties

For each track a total of 244 properties are computed. These are listed in Table 3.2. (There are 6 spare slots in the 250). These properties may be computed for the entire lifetime of the storm, or for some portion of that lifetime relative to the time of the seed/no-seed decision. For example, the properties may be computed for the period from decision time to 20 minutes later. Certain of the properties (for example, 'persistence' and 'max ratio') are not relevant if overall lifetime properties are computed.

There are a number of properties which are considered 'control properties' which will not change due to seeding. These are 9, 10 and 241-250.

The following notes provide some detail on those properties which do not have self-explanatory names:

Decision time - the time at which the seed/no-seed decision is taken.

GROUP 1 - GEOMETRY,TIME

1 DURATION
2 TIME OF ORIGIN
3 SPEED OF MOVEMENT
4 DIRECTION OF MOVEMENT
5 MEAN X CO-ORD
6 MEAN Y CO-ORD
7 MEAN RANGE
8 ENVELOPE DECISION TIME
9 VOLUME AT DECISION TIME
10 PEAK DBZ AT DECISION TIME

GROUP 2 - TOP,DEPTH,VOLUME,MASS

11 ECHO TOP - MAX
12 ECHO TOP - MAX RATE OF INCREASE
13 ECHO TOP - MEAN
14 ECHO TOP - TIME TO MAX
15 ECHO TOP - TIME TO MAX ROI
16 ECHO TOP - PERSISTENCE
17 ECHO TOP - MAX RATIO
18 DEPTH - MAX
19 DEPTH - MAX RATE OF INCREASE
20 DEPTH - MEAN
21 DEPTH - TIME TO MAX
22 DEPTH - TIME TO MAX ROI
23 DEPTH - PERSISTENCE
24 DEPTH - MAX RATIO
25 VOLUME - MAX
26 VOLUME - MAX RATE OF INCREASE
27 VOLUME - TIME INTEGRAL
28 VOLUME - MEAN
29 VOLUME - TIME TO MAX
30 VOLUME - TIME TO MAX ROI
31 VOLUME - PERSISTENCE
32 VOLUME - MAX RATIO
33 MASS TOT - MAX
34 MASS TOT - MAX RATE OF INCREASE
35 MASS TOT - TIME INTEGRAL
36 MASS TOT - MEAN
37 MASS TOT - TIME TO MAX
38 MASS TOT - TIME TO MAX ROI
39 MASS TOT - PERSISTENCE
40 MASS TOT - MAX RATIO
41 MASS A.C.- MAX
42 MASS A.C.- MAX RATE OF INCREASE
43 MASS A.C.- TIME INTEGRAL
44 MASS A.C.- MEAN
45 MASS A.C.- TIME TO MAX
46 MASS A.C.- TIME TO MAX ROI
47 MASS A.C.- PERSISTENCE
48 MASS A.C.- MAX RATIO

GROUP 3 - AREA,RAIN,PRECIP,RATIOS

49 AREA 3 DEG - MAX
50 AREA 3 DEG - MAX RATE OF INCREASE
51 AREA 3 DEG - TIME INTEGRAL
52 AREA 3 DEG - MEAN
53 AREA 3 DEG - TIME TO MAX
54 AREA 3 DEG - TIME TO MAX ROI
55 AREA 3 DEG - PERSISTENCE
56 AREA 3 DEG - MAX RATIO
57 AREA CUTOFF - MAX
58 AREA CUTOFF - MAX RATE OF INCREASE
59 AREA CUTOFF - TIME INTEGRAL
60 AREA CUTOFF - MEAN
61 AREA CUTOFF - TIME TO MAX
62 AREA CUTOFF - TIME TO MAX ROI
63 AREA CUTOFF - PERSISTENCE
64 AREA CUTOFF - MAX RATIO
65 RFLUX 3 DEG - MAX
66 RFLUX 3 DEG - MAX RATE OF INCREASE
67 RFLUX 3 DEG - MASS
68 RFLUX 3 DEG - MEAN
69 RFLUX 3 DEG - TIME TO MAX
70 RFLUX 3 DEG - TIME TO MAX ROI
71 RFLUX 3 DEG - PERSISTENCE
72 RFLUX 3 DEG - MAX RATIO
73 RFLUX CUTOFF - MAX
74 RFLUX CUTOFF - MAX RATE OF INCREASE
75 RFLUX CUTOFF - MASS
76 RFLUX CUTOFF - MEAN
77 RFLUX CUTOFF - TIME TO MAX
78 RFLUX CUTOFF - TIME TO MAX ROI
79 RFLUX CUTOFF - PERSISTENCE
80 RFLUX CUTOFF - MAX RATIO
81 PRECIP WATER - MAX
82 PRECIP WATER - MAX RATE OF INCREASE
83 PRECIP WATER - TIME INTEGRAL
84 PRECIP WATER - MEAN
85 PRECIP WATER - TIME TO MAX
86 PRECIP WATER - TIME TO MAX ROI
87 PRECIP WATER - PERSISTENCE
88 PRECIP WATER - MAX RATIO
89 MTI/RAIN MASS - 3 DEG
90 MTI/RAIN MASS - CUTOFF
91 MEAN MASS/RAIN MASS - 3 DEG
92 MEAN MASS/RAIN MASS - CUTOFF

GROUP 4 - VERTICAL CENTROIDS

93 VERT CENTROID - MAX
94 VERT CENTROID - MAX ROI
95 VERT CENTROID - MEAN
96 VERT CENTROID - TIME TO MAX
97 VERT CENTROID - TIME TO MAX ROI
98 VERT CENTROID - PERSISTENCE
99 VERT CENTROID - MAX RATIO
100 Z WT VERT CENT - MAX
101 Z WT VERT CENT - MAX ROI
102 Z WT VERT CENT - MEAN
103 Z WT VERT CENT - TIME TO MAX
104 Z WT VERT CENT - TIME TO MAX ROI
105 Z WT VERT CENT - PERSISTENCE
106 Z-WT VERT CENT - MAX RATIO
107 DELT VERT CENT - MAX
108 DELT VERT CENT - MAX ROI
109 DELT VERT CENT - MEAN
110 DELT VERT CENT - TIME TO MAX
111 DELT VERT CENT - TIME TO MAX ROI
112 DELT VERT CENT - PERSISTENCE
113 DELT VERT CENT - MAX RATIO

GROUP 5 - SPARE

114 SPARE
115 SPARE
116 SPARE
117 SPARE
118 SPARE

GROUP 6 - REFLECTIVITY

119 PEAK DBZ TOT - MAX
120 PEAK DBZ TOT - MAX ROI
121 PEAK DBZ TOT - MEAN
122 PEAK DBZ TOT - TIME TO MAX
123 PEAK DBZ TOT - TIME TO MAX ROI
124 PEAK DBZ TOT - PERSISTENCE
125 PEAK DBZ TOT - MAX RATIO
126 MEAN DBZ TOT - MAX
127 MEAN DBZ TOT - MAX ROI
128 MEAN DBZ TOT - MEAN
129 MEAN DBZ TOT - TIME TO MAX
130 MEAN DBZ TOT - TIME TO MAX ROI
131 MEAN DBZ TOT - PERSISTENCE
132 MEAN DBZ TOT - MAX RATIO
133 MEAN DBZ 3 DEG - MAX
134 MEAN DBZ 3 DEG - MAX ROI
135 MEAN DBZ 3 DEG - MEAN
136 MEAN DBZ 3 DEG - TIME TO MAX
137 MEAN DBZ 3 DEG - TIME TO MAX ROI
138 MEAN DBZ 3 DEG - PERSISTENCE
139 MEAN DBZ 3 DEG - MAX RATIO
140 MEAN DBZ CUTOFF - MAX
141 MEAN DBZ CUTOFF - MAX ROI
142 MEAN DBZ CUTOFF - MEAN
143 MEAN DBZ CUTOFF - TIME TO MAX
144 MEAN DBZ CUTOFF - TIME TO MAX ROI
145 MEAN DBZ CUTOFF - PERSISTENCE
146 MEAN DBZ CUTOFF - MAX RATIO
147 MAX HT 45'S - MAX
148 MAX HT 45'S - MAX ROI
149 MAX HT 45'S - MEAN
150 MAX HT 45'S - TIME TO MAX
151 MAX HT 45'S - TIME TO MAX ROI
152 MAX HT 45'S - PERSISTENCE
153 MAX HT 45'S - MAX RATIO
154 HT PEAK DBZ - MAX
155 HT PEAK DBZ - MAX ROI
156 HT PEAK DBZ - MEAN
157 HT PEAK DBZ - TIME TO MAX
158 HT PEAK DBZ - TIME TO MAX ROI
159 HT PEAK DBZ - PERSISTENCE
160 HT PEAK DBZ - MAX RATIO

GROUP 7 - MASS=f(HT)

161 MASS=f(HT) ; MEAN - MEAN
162 MASS=f(HT) ; MEAN - MAX
163 MASS=f(HT) ; MEAN - MIN
164 MASS=f(HT) ; MEAN - MAX ROI
165 MASS=f(HT) ; MEAN - MAX ROD
166 MASS=f(HT) ; S.D. - MEAN
167 MASS=f(HT) ; S.D. - MAX
168 MASS=f(HT) ; S.D. - MIN
169 MASS=f(HT) ; S.D. - MAX ROI
170 MASS=f(HT) ; S.D. - MAX ROD
171 MASS=f(HT) ;-SKEW - MEAN
172 MASS=f(HT) ;-SKEW - MAX
173 MASS=f(HT) ;-SKEW - MIN
174 MASS=f(HT) ;-SKEW - MAX ROI
175 MASS=f(HT) ;-SKEW - MAX ROD
176 MASS=f(HT) ; MODE - MEAN
177 MASS=f(HT) ; MODE - MAX
178 MASS=f(HT) ; MODE - MIN
179 MASS=f(HT) ; MODE - MAX ROI
180 MASS=f(HT) ; MODE - MAX ROD

GROUP 8 - PEAK DBZ=f(HT)

181 DBZ=f(HT) ; MEAN - MEAN
182 DBZ=f(HT) ; MEAN - MAX
183 DBZ=f(HT) ; MEAN - MIN
184 DBZ=f(HT) ; MEAN - MAX ROI
185 DBZ=f(HT) ; MEAN - MAX ROD
186 DBZ=f(HT) ; S.D. - MEAN
187 DBZ=f(HT) ; S.D. - MAX
188 DBZ=f(HT) ; S.D. - MIN
189 DBZ=f(HT) ; S.D. - MAX ROI
190 DBZ=f(HT) ; S.D. - MAX ROD
191 DBZ=f(HT) ;-SKEW - MEAN
192 DBZ=f(HT) ;-SKEW - MAX
193 DBZ=f(HT) ;-SKEW - MIN
194 DBZ=f(HT) ;-SKEW - MAX ROI
195 DBZ=f(HT) ;-SKEW - MAX ROD
196 DBZ=f(HT) ; MODE - MEAN
197 DBZ=f(HT) ; MODE - MAX
198 DBZ=f(HT) ; MODE - MIN
199 DBZ=f(HT) ; MODE - MAX ROI
200 DBZ=f(HT) ; MODE - MAX ROD

GROUP 9 - %VOLUME=f(DBZ)

201 %VOL=f(DBZ) ; MEAN - MEAN
202 %VOL=f(DBZ) ; MEAN - MAX
203 %VOL=f(DBZ) ; MEAN - MIN
204 %VOL=f(DBZ) ; MEAN - MAX ROI
205 %VOL=f(DBZ) ; MEAN - MAX ROD
206 %VOL=f(DBZ) ; S.D. - MEAN
207 %VOL=f(DBZ) ; S.D. - MAX
208 %VOL=f(DBZ) ; S.D. - MIN
209 %VOL=f(DBZ) ; S.D. - MAX ROI
210 %VOL=f(DBZ) ; S.D. - MAX ROD
211 %VOL=f(DBZ) ;-SKEW - MEAN
212 %VOL=f(DBZ) ;-SKEW - MAX
213 %VOL=f(DBZ) ;-SKEW - MIN
214 %VOL=f(DBZ) ;-SKEW - MAX ROI
215 %VOL=f(DBZ) ;-SKEW - MAX ROD
216 %VOL=f(DBZ) ; MODE - MEAN
217 %VOL=f(DBZ) ; MODE - MAX
218 %VOL=f(DBZ) ; MODE - MIN
219 %VOL=f(DBZ) ; MODE - MAX ROI
220 %VOL=f(DBZ) ; MODE - MAX ROD

GROUP 10 - % 3 DEG AREA=f(DBZ)

221 %AREA=f(DBZ); MEAN - MEAN
222 %AREA=f(DBZ); MEAN - MAX
223 %AREA=f(DBZ); MEAN - MIN
224 %AREA=f(DBZ); MEAN - MAX ROI
225 %AREA=f(DBZ); MEAN - MAX ROD
226 %AREA=f(DBZ); S.D. - MEAN
227 %AREA=f(DBZ); S.D. - MAX
228 %AREA=f(DBZ); S.D. - MIN
229 %AREA=f(DBZ); S.D. - MAX ROI
230 %AREA=f(DBZ); S.D. - MAX ROD
231 %AREA=f(DBZ);-SKEW - MEAN
232 %AREA=f(DBZ);-SKEW - MAX
233 %AREA=f(DBZ);-SKEW - MIN
234 %AREA=f(DBZ);-SKEW - MAX ROI
235 %AREA=f(DBZ);-SKEW - MAX ROD
236 %AREA=f(DBZ); MODE - MEAN
237 %AREA=f(DBZ); MODE - MAX
238 %AREA=f(DBZ); MODE - MIN
239 %AREA=f(DBZ); MODE - MAX ROI
240 %AREA=f(DBZ); MODE - MAX ROD

GROUP 11 - CONTROL

241 AV MIXING RATIO FOR LOWEST 50 MB
242 CCL TEMP
243 BUOYANCY AT 500 MB
244 TCCL/DT500
245 # OF TRACKS FOR THE DAY
246 CUMULATIVE 3 DEG A.T.I. FOR THE DAY
247 MAX VOLUME OF ANY STORM FOR THE DAY
248 MAX RATE OF INCR OF VOLUME OF ANY STORM
249 MAX TOPS OF ANY STORM FOR THE DAY
250 MAX DBZ OF ANY STORM FOR THE DAY

NOTES

ROI is max rate of increase
ROD is max rate of decrease
TOT means for whole storm
A.C. means above cutoff altitude
CUTOFF means at cutoff altitude
RFLUX is rain flux
MTI is mass time integral
TCCL is temp at the CCL
DT500 is buoyancy at 500 mb

Table 3.2. Track properties.

t_1, t_2 - the start and end times for time-dependent properties (e.g. for properties from decision time to 20 minutes later, t_1 = 0 and t_2 = 20)

Pt_1, Pt_2 - value of a storm propety (e.g. volume) at times t_1 and t_2 respectively

Pm - maximum value of storm property between times t_1 and t_2 inclusive.

Persistence - $(Pt_2-Pt_1)/Max(Pt_1,Pt_2)$, range -1 to +1 (Tsonis 1983)

Max ratio - $(Pm-Pt_1)/Pm$, range 0 to +1 (Dixon and Mather, 1986)

Note: persistence and max ratio were introduced because they are bounded variables and therefore do not introduce the statistical problems common to long-tailed distributions.

Depth 18 - 24 - (top minus base), which tends to be somewhat range dependent, since base is generally measured by the low-level scan.

Time to Max - the time to the maximum value of the storm property from (a) the start of the storm for overall properties or (b) time t_1 for time-dependent properties.

Time to Max ROI - the time to the maximum rate of increase of the storm property, calculated from the times given in 'time to max'.

Precipitable mass (81-88) - this is an estimate of the amount of precipitable water in the storm at any time. It is computed by adding the mass to the (rain flux) x (scan time interval). Changes in precipitable water should give an indication of the rate of precipitation generation.

Z-wt Vert Cent (100-106) - vertical storm centroid weighted with respect to reflectivity (as opposed to properties 93-99 which are computed geometrically, with respect to volume).

Delt Vert Cent (107-113) - delta vertical centroid - calculated as (volumetric vertical centroid) - (reflectivity-weighted vertical centroid). A negative value indicates that the storm is bottom heavy with respect to reflectivity.

Peak dBz tot and Mean dBz tot (119-132) - refers to reflectivities in the entire storm volume.

Mean dBz 3 dgs and Mean dBz cut off (133-146) - refers to reflectivities at 3 degrees and at the cut off altitude respectively.

Mean = f(HT) (161-180) - the distribution of mass with height. This is not a statistical distribution but statistical computations are used to give an indication of the shape of this distribution. Therefore, mean, standard deviation, the negative of the skewness and mode are computed (in units of height). These properties apply to the storm at any one time. From these basic properties the mean, maximum, minimum, maximum rate of increase and maximum rate of decrease are computed for the track during the time period of interest (or for the entire track).

dBz = f(HT) (181-200) - the distribution of maximum reflectivity with height (see Mass = f(HT) above)

%Vol = f(dBz) (201-220) - this is an authentic density function for the distribution of reflectivity within the storm volume. The mean, standard deviation, negative skewness and mode are computed at each scan time, these being basic storm properties. From these the mean, maximum, minimum, maximum rate of increase and maximum rate of decrease are computed for the time period of interest.

%Area = f(dBz) (221-240) - the distribution of dBz in the 3 degree storm area (see %VOL = f(dBz) above)

TCCL/DT500 - 'temperature ratio' = temperature at CCL/buoyancy at 500 mb. This is used as a measure of the likelihood of coalescence, since the higher the ratio the longer the time taken for air to travel from the CCL to the -10°C level.

3.12 Track property statistics

Provision has been made for obtaining statistics for any or all of the track properties, and for many partitions of the data.

For any chosen group of tracks the following may be computed for each property:

- minimum
- maximum
- arithmetic mean
- geometric mean
- standard deviation
- skewness

In addition the cross-correlation matrix for selected (or all) properties may be obtained.

Inspection of the property histograms has led to the classification of the properties into two groups, 'LOG' for those which resemble a log-normal distribution with high positive skewness, and 'LINEAR' for those which do not.

The statistics may be obtained for many partitions of the data. Examples are :

- all tracks
- all case tracks
- seed tracks only
- no-seed/no sample tracks only
  etc

In addition the partition may be generated by setting limits for any of the track properties. For example, it may be specified that only tracks with a duration exceeding 30 minutes and with a mean volume between 200 and 400 cubic kilometres, be considered for the analysis.

3.13 Testing for seeding effects - the re-randomization scheme

The seed/no-seed decisions were drawn from a list of pre-prepared random decisions, which results in a split of the tracks into seed and no-seed pools (the same applies to the sub-partition of the no-seed pool into sample and no-sample sub-pools).

Therefore it is logical to use a re-randomization technique to test for significant differences between the pools.

Let us suppose we are testing for a difference between the mean values of some track property, for example rain mass. Then the test statistic would be :

(mean rain mass seed)-(mean rain mass no-seed)

(Similarly one can test for changes in minima, maxima, geometric mean, standard deviation, skewness or cross-correlation coefficient).

We then generate a large number (say 500 or 1000) of 'dummy' random lists, using the same technique as that which produced the 'real' list. For each of these 'dummy' lists a 'dummy' test statistic is computed. The 'real' test statistic is then ranked relative to the 'dummy' list, and the resulting rank, called 'p' is expressed as a percent.

The 'p' value is then a measure of the likelihood that there is a significant difference between the seed and no-seed values of the chosen statistic. A value close to 100 indicates a significant increase, while a value close to 0 indicates a significant decrease.

When this technique is applied, a printout is obtained which lists the 'p' values of the chosen statistics, as well as the % difference between the seed and no-seed value of the statistics. In addition, histograms of the 'p' values are printed out. These

have proved to be extremely useful in detecting trends in the p values, even when the individual p results look inconclusive and confusing.

The splits which may be tested using this technique are:

seed	vs	no-seed
no-seed/sample	vs	no-seed/no-sample
seed	vs	no-seed/sample
seed	vs	no-seed/no-sample
sample (incl seed)	vs	no-seed/no-sample

The data may also be partitioned by imposing limits on the track properties, for example minimum duration, or maximum volume at decision time. Any one or a combination of the track properties may be used to create a partition.

The control properties provide an essential check on the split between the various data partitions. Biases in the control properties indicate that the partition should be modified to remove the bias. A time prior to decision (say from -10 minutes to 0) or very soon after decision (say from 0 to 5 minutes) also produces properties which can be considered as controls.

3.14 Ranking the cases relative to other tracks on the day.

It was considered desirable to investigate how the storms selected as seeding candidates compare to the other storms which occur on the same day.

The TRACK-PC programme does just this. It ranks the various track properties for the case track relative to the properties of all the other storms on that day. It produces data which are analogous to the track property data, with the track property value replaced by the rank of that property relative to the other storms.

Statistics on these ranks may be produced using the same programme which computes property statistics, and the data may be subjected to re-randomization as well.

3.15 Range effects on radar echoes (Mather)

The so-called pencil beam of the Nelspruit radar is in the form of a narrow cone. For this reason its resolution in volume, in height and in horizontal distance normal to the beam are functions of range. This causes distortions of certain echo properties. Unfortunately, the distortion is a function not only of the beam angles but also of the distribution in space of the reflective properties of the echo itself (beam filling; gradients). This makes it impossible to correct for the distortion in, for example, the echo top height. Under the assumption that the true characteristics of large numbers of

storms should not be dependent on range from the radar, it is possible to use actual storm observations to evaluate the importance of such distortions, as a function of range.

The 1985/86 volume scan radar data were examined for range effects and effects of the 3 degree scan limitation on the storm track statistics. This was done by stratifying the average storm tracks into 20 km annuli, as shown in Table 3.3.

Table 3.3 Number of storm tracks in each analysed annulus

RANGE	0	10	20	30	40	50	60	70	80	90	100
ANNULUS	20	30	40	50	60	70	80	90	100	110	120
MEAN RANGE	10	20	30	40	50	60	70	80	90	100	110
NO OF STORM TRACKS	155	359	578	868	1058	1087	1002	801	578	427	307
NORM AREA	1	2	3	4	5	6	7	8	9	10	11
NORM TRACKS	1	2.3	3.7	5.6	6.8	7.0	6.5	5.2	3.7	2.8	2.0

↑——————VALID RANGE——————↑

Mean storm track properties such as radar echo heights, areas, volumes, rain fluxes and reflectivity factors were computed and are plotted in Fig. 3.8. Both arithmetic and geometric means are considered. These analyses show that:

- the validity of the radar data degrades rapidly at ranges greater than about 80 km

- arithmetic means in some cases (mean 3^{o} areas, rain fluxes) appear more stable than their geometric counterparts.

- the attenuation problem at radar wavelengths of 5 cm in large convective storms is demonstrated in the analysis of maximum reflectivity factors

- mean reflectivity factors at 3 degrees (lowest scan) are remarkably constant with range (+-0.5 dBz).

On the basis of the above results, the statistical analyses in Vol. III, Section 3 were restricted to those storm tracks contained in an annulus beginning at 10 and ending at 80 km radius from the radar.

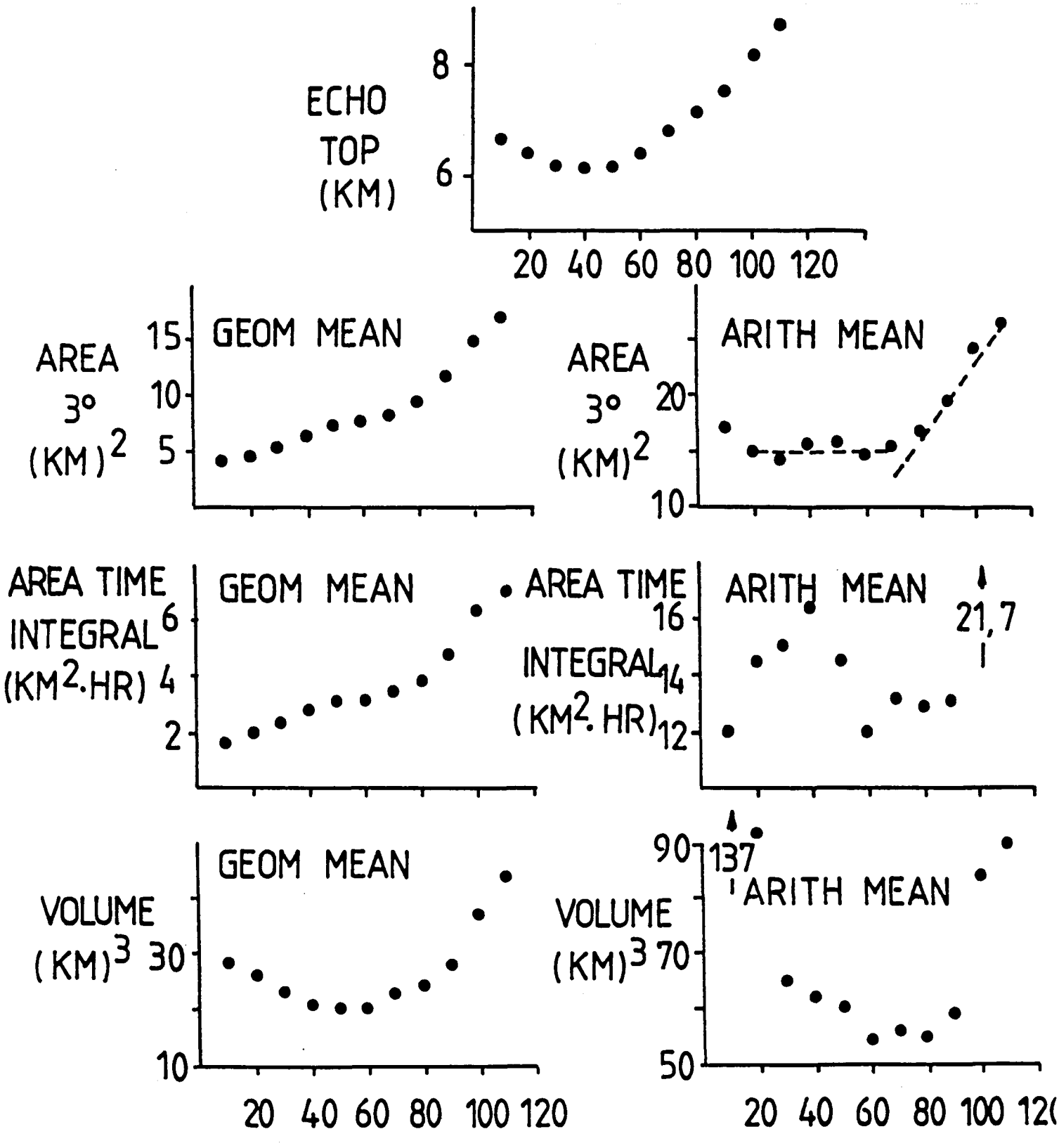

Fig. 3.8. Average track properties versus range (in km) from radar.

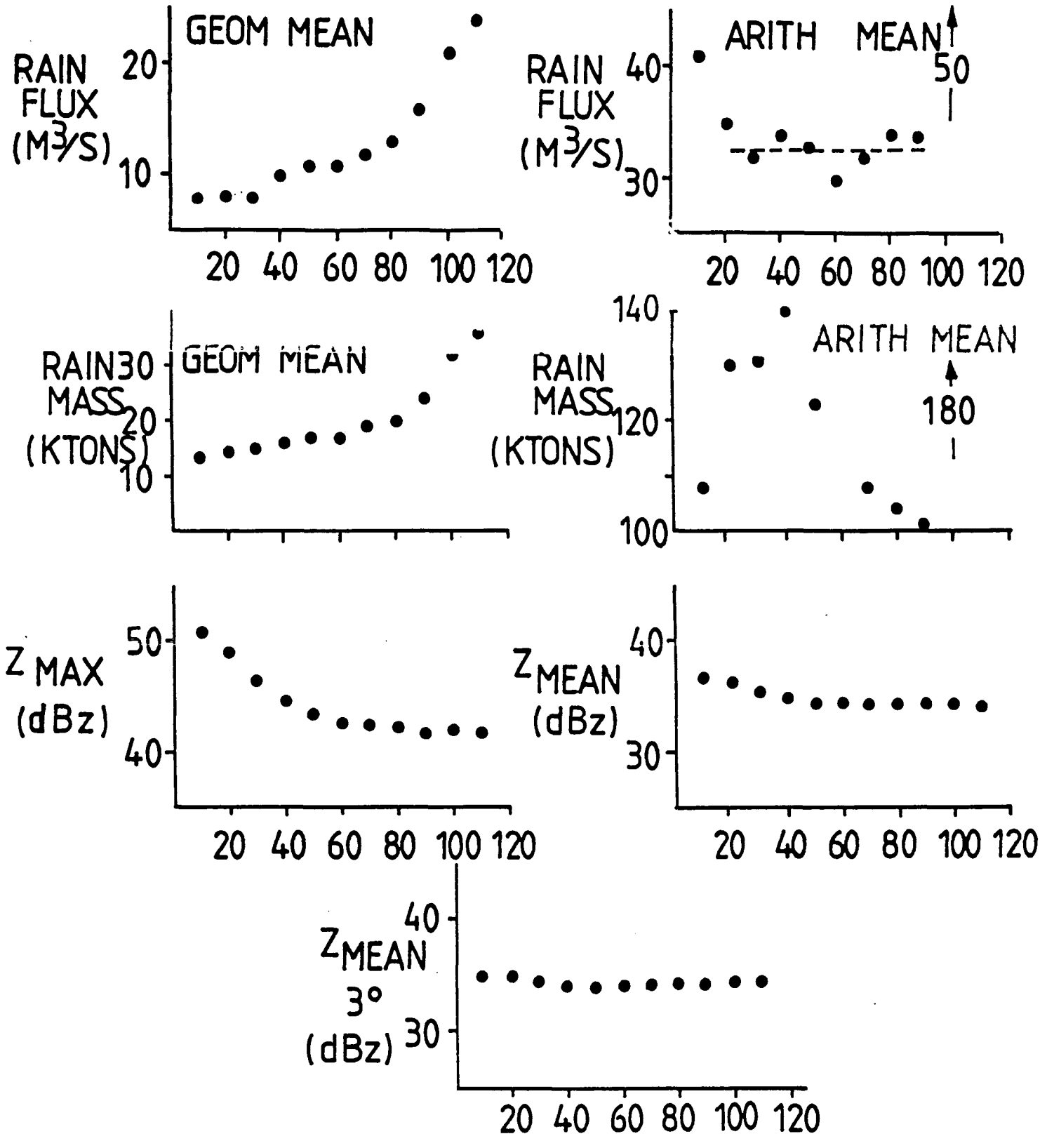

Fig. 3.8 (Cont). Average track properties versus range (in km) from radar.

4.0 THE PAWS MESOSCALE NETWORK

4.1 MEASUREMENTS

4.1.1 Introduction

A network of automated weather stations collected data in the Nelspruit area during the 1984-85 and 1985-86 operational seasons. In general there were 8 or 9 stations operating, evenly distributed from the highveld, across the escarpment and into the lowveld (Fig. 4.1). These stations archived the measurements, and the data was collected twice monthly during site visits. The data was transferred to the mainframe computer at CIC in Nelspruit for subsequent data processing and analysis. All manipulation of the information collected by the stations was performed by computer and required little human intervention to maintain the large data base as it was acquired.

4.1.2 Site Locations

Pertinent information on each instrumented site is given in Table 4.1. A brief description of each site is given here, with some factors to consider when interpreting the data.

Lower Sabie: This is the most easterly of the sites, located in Kruger National Park, and was originally placed to provide a measurement that would be influenced only by lowveld effects. Its location greatly extended the time required for site servicing, and so the site was discontinued after one month of operation. The site was several hundred meters from the Sabie River, in low bush, with good exposure from all directions.

Numbi Gate: This tower is located inside Kruger National Park, on a slightly elevated site. There are some trees in the area higher than the anemometers, although none were closer than about 100 meters. The general terrain is flat. Exposure is in general good in all directions.

Kaapmuiden: This site is located in the Boulders area, on a ridge to the south of and above the Crocodile gorge. The instruments are slightly shielded from the north east by a ridge. The site however is well exposed in all other directions. The local terrain is comprised of rolling hills.

Nelspruit: This site is located at the Nelspruit Municipal Airport, approximately 50 meters west of the runway. There is some shielding of the instruments from the south and southwest, due to a copse of wood and airport hangers within about 100 meters. Exposure is good in all other directions. The rain gauge for this site is separated from the tower by several hundred meters, being located near the CIC offices. The general terrain is characterized by rolling hills.

Barberton: This site is located on Lone Tree Hill, at the northern edge of the Barberton Mountains. This site experiences the most pronounced local effects, since some terrain in this area is quite rugged. To the north lays the Barberton valley, and 1 km to the south are the Barberton Mountains. Certain wind directions may have had large topographic influences at this site.

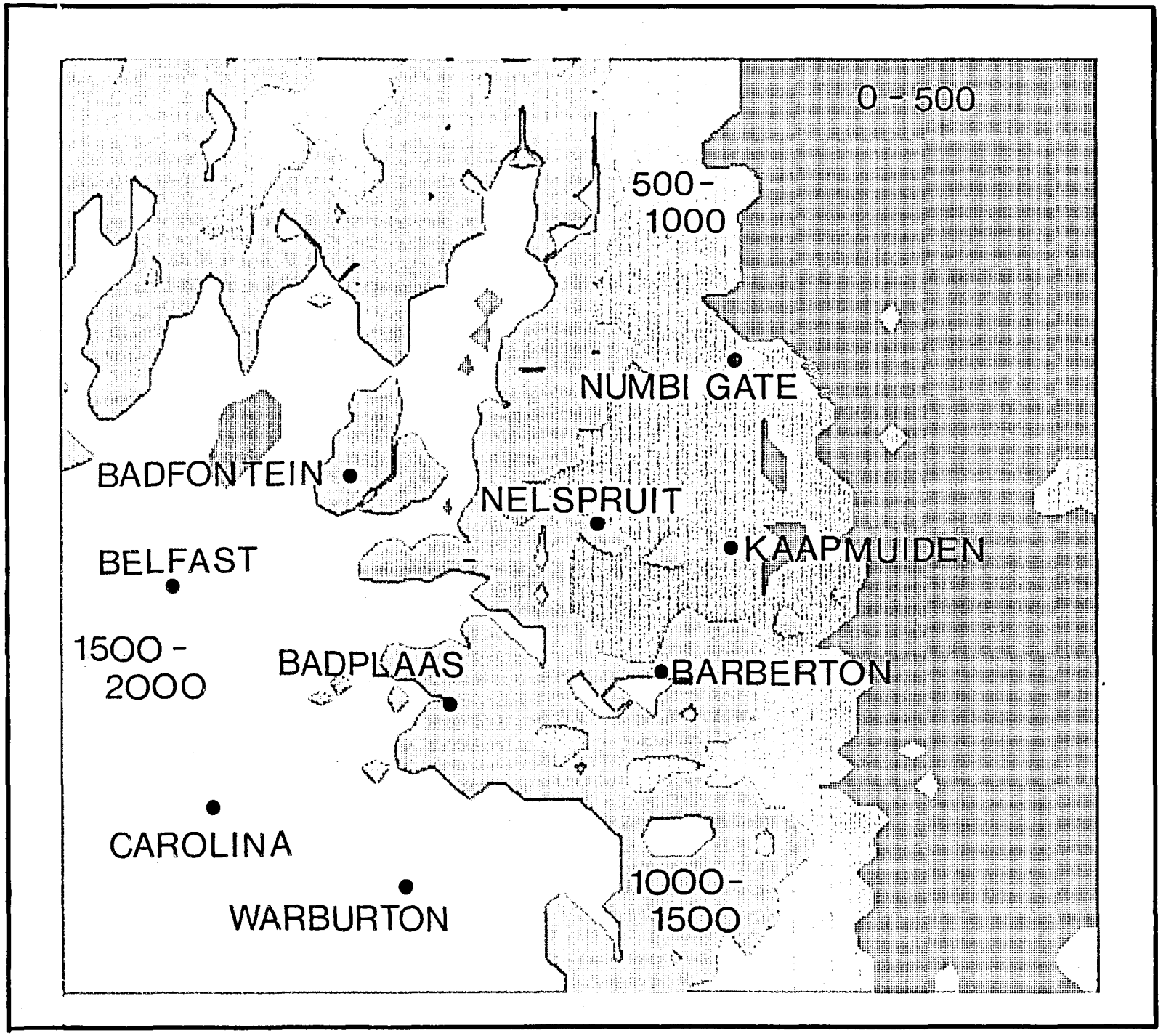

Figure 4.1. Mesoscale network site locations. Elevations of the contoured regions are given in meters above mean sea level.

Table 4.1. Site information.

	Lat.	Lon.	Elevation (m)
Badfontein	25° 24' 13'' S	30° 22' 56'' E	1326
Badplaas	25° 52' 10'' S	30° 36' 9'' E	1119
Barberton	25° 48' 06'' S	31° 03' 22'' E	1289
Belfast	25° 37' 00'' S	30° 00' 28'' E	1865
Carolina	26° 05' 00'' S	30° 05' 00'' E	1683
Kaapmuiden	25° 32' 36'' S	31° 11' 31'' E	1012
Nelspruit	25° 30' 00'' S	30° 55' 00'' E	884
Lower Sabie	25° 07' 21'' S	31° 55' 17'' E	168
Numbi Gate	25° 09' 48'' S	31° 12' 48'' E	640
Warburton	26° 15' 07'' S	30° 30' 06'' E	1762

Badplaas: The tower is located on a treeless peninsula that forms part of the western boundary of the Vygeboom Dam. The exposure is generally good with water within several 100 meters on three sides and flat terrain to the west.

Badfontein: This site is located in the eastern part of the Elands River valley, near the Braam Rabenheimer Dam. The terrain is quite flat in this area, although the escarpment rises sharply, approximately 5 km to the west. The instrument exposure is good in all directions at this site.

Belfast: This site is located several kilometers north of Belfast, on a slight rise of land. The general terrain is slightly rolling. Instrument exposure is good in all directions.

Carolina: This site is located at the Carolina Municipal Airport, 100 meters east of the airstrip. The surrounding terrain is flat, and the instruments have good exposure from all directions.

Warburton: This site is located about 10 km east of Lothair. The local terrain is rolling, and the instruments have good exposure from all directions.

4.1.3 Equipment

A diagram of the instrumentation at each site is shown in Fig. 4.2. The basic components are the power supply system, tower, sensors and data loggers. The rain gauge was not connected to the main system, but rather had its own battery and data logger.

The parameters measured by each station included the two wind components U and V, dry bulb temperature, wet bulb temperature and rainfall (Table 4.2). The data is recorded once every five minutes, and during the site visit is transferred to a portable microcomputer. The microcomputer then transfers the data to the mainframe when back in Nelspruit. It should be noted that the temperature and wind speed measurements are true 5 minute averages, rather than instantaneous samples taken at 5 minute intervals. This is because these sensors produce a frequency train proportional to the measurand, and this train is counted over the total measurement period. A scaled value of the pulse count is saved as the data value.

The rain gauge and its data recorder are the same as is used in the Badplaas rainguage network. This data recorder is based on a semiconductor random access memory which stores the time, date and quantity of tips observed during a five minute interval. It only records information when tips have occurred, and has a capacity to observe approximately 44 hours of rainfall.

Two R. M. Young-Gill propeller anemometers are used to sense wind speed and direction. They are mounted in an orthogonal configuration, and each one produces an output square wave whose frequency is proportional to wind speed. A separate output indicates the direction of rotation.

The psychrometer uses two linear thermistor networks to sense dry and wet bulb temperatures. These are mounted in a housing which provides shielding from solar radiation, and also provides airflow over the sensors. The wet bulb thermistor is kept moist with a reservoir and wick arrangement. An interface converts the thermistor readings to a square wave signal whose effective frequency is proportional to temperature.

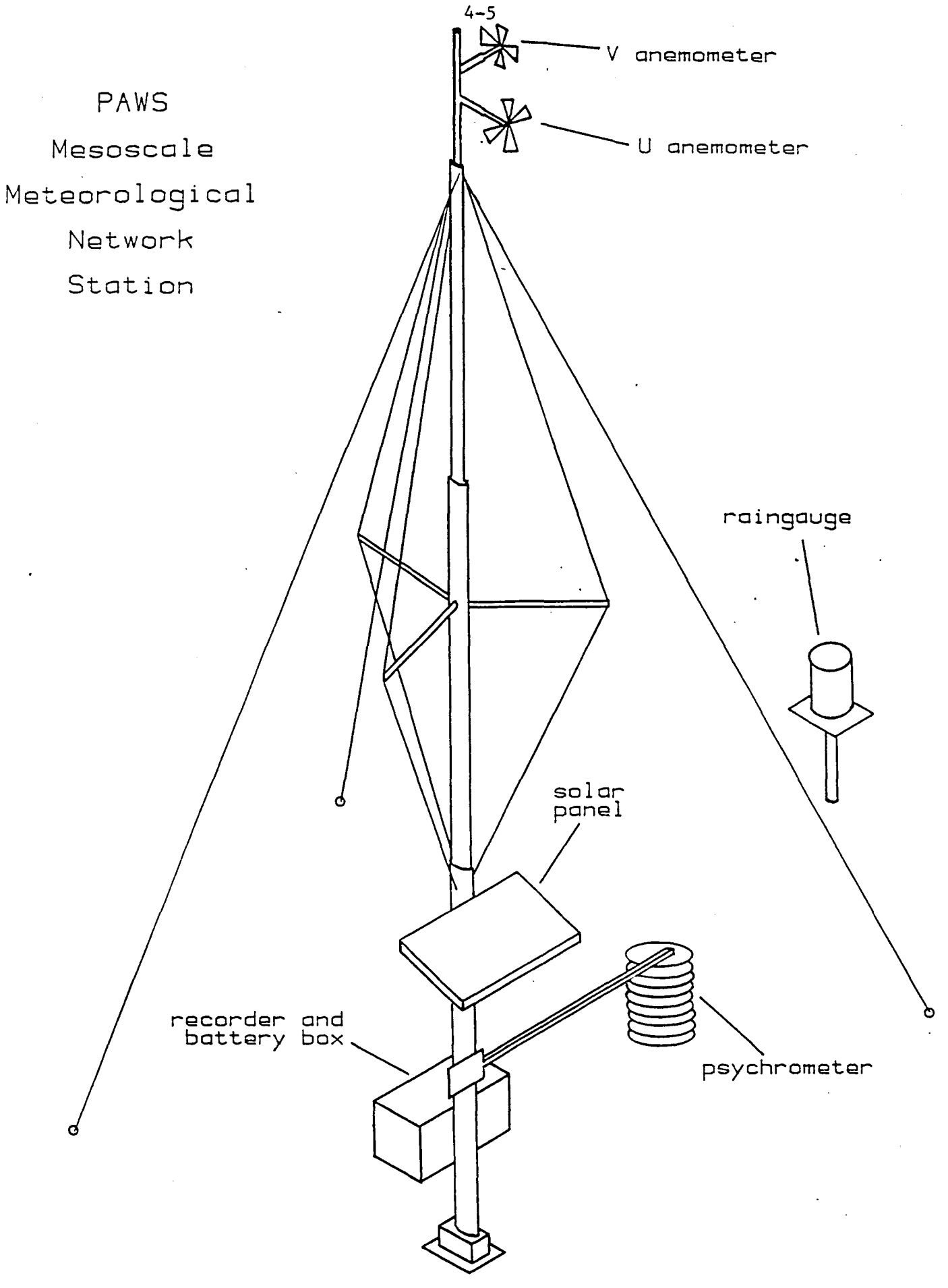

Figure 4.2. Tower and instrumentation.

Table 4.2. Sensor characteristics

Sensor	Transducer	Technique	resolution	accuracy
anemometers	R.M. Young - Gill propeller anemometer	light chopper	0.2 m/s	0.2 m/s
dry and wet bulb thermometers	Fenwall LTN-2 linear thermistor network	R/C oscillator	0.3 deg C	0.6 deg C
raingauge	tipping bucket	counts	0.25mm	0.25mm

Two microprocessor based data loggers, referred to here as solid state recorders, average and store the signals from the anemometers and psychrometer. The software in each recorder is configured for the sensor attached to it, and averages the signal over the sampling period. These averages are stored in erasable, programmable, read only memories (EPROM's). The memories have the desirable characteristic that they will retain data even when power is removed, and can be erased by exposure to ultraviolet light. To dump data from the recorders, a circuit card containing the EPROMs is removed and attached to the portable microcomputer, which saves the data and other information on diskette. A blank EPROM card is inserted in the recorder and the instrument is restarted for a new sampling run.

4.2 DATA SET

4.2.1 Calibration and Conversion to Engineering Units

4.2.1.1 Anemometers

For this discussion it will be convenient to refer to the two anemometers as the u sensor and the v sensor. The two sensors were mounted according to the recommendations of the manufacturer, R. M. Young. They suggest that the main support be a vertical pipe with two tees in line, each one having mounting hardware for one anemometer shaft. The tees are in an orthogonal configuration, when viewed from above. From a side view the tees are separated in height by at least the diameter of one propeller. This separation is made so that the wind shadow of one propeller will not influence the other. A short section of pipe extends vertically above the upper tee at least a distance equal to one half propeller diameter. This is in order to present the upper anemometer with the same wind shadow from the vertical pipe as is seen by the lower anemometer. Thus by presenting the same wind shading effects to both anemometers, a single angle of attack correction can be applied to either sensor. R. M. Young then provides a calibration curve (Fig. 4.3) which was determined for a single anemometer mounted on a shaft which extends vertically above and below the sensor. This curve gives the response of the anemometer in this configuration as a function of the wind direction.

The measurement recorded by the data logger was a count in the range -127 to + 128. This is converted to a nominal wind speed as:

speed (m/s) = 0.2 * counts

To convert the measurements taken by the anemometer into wind speed and direction, the following technique was developed. As stated above, in the given mounting configuration both sensors of the orthogonal pair will have the same response, except that the incident wind angle will be 90 degrees greater for the v sensor than the u sensor. However, since measured values U_N and V_N are uncorrected values, the true wind angle can not be found by taking the arc tangent of the nominal values. Instead the following approach is used to recover the true wind angle from U_N and V_N.

We define the true wind angle as ϕ, and the true wind components as U and V. A calibration curve $C(\phi)$ (Fig. 4.3) as a function of wind direction

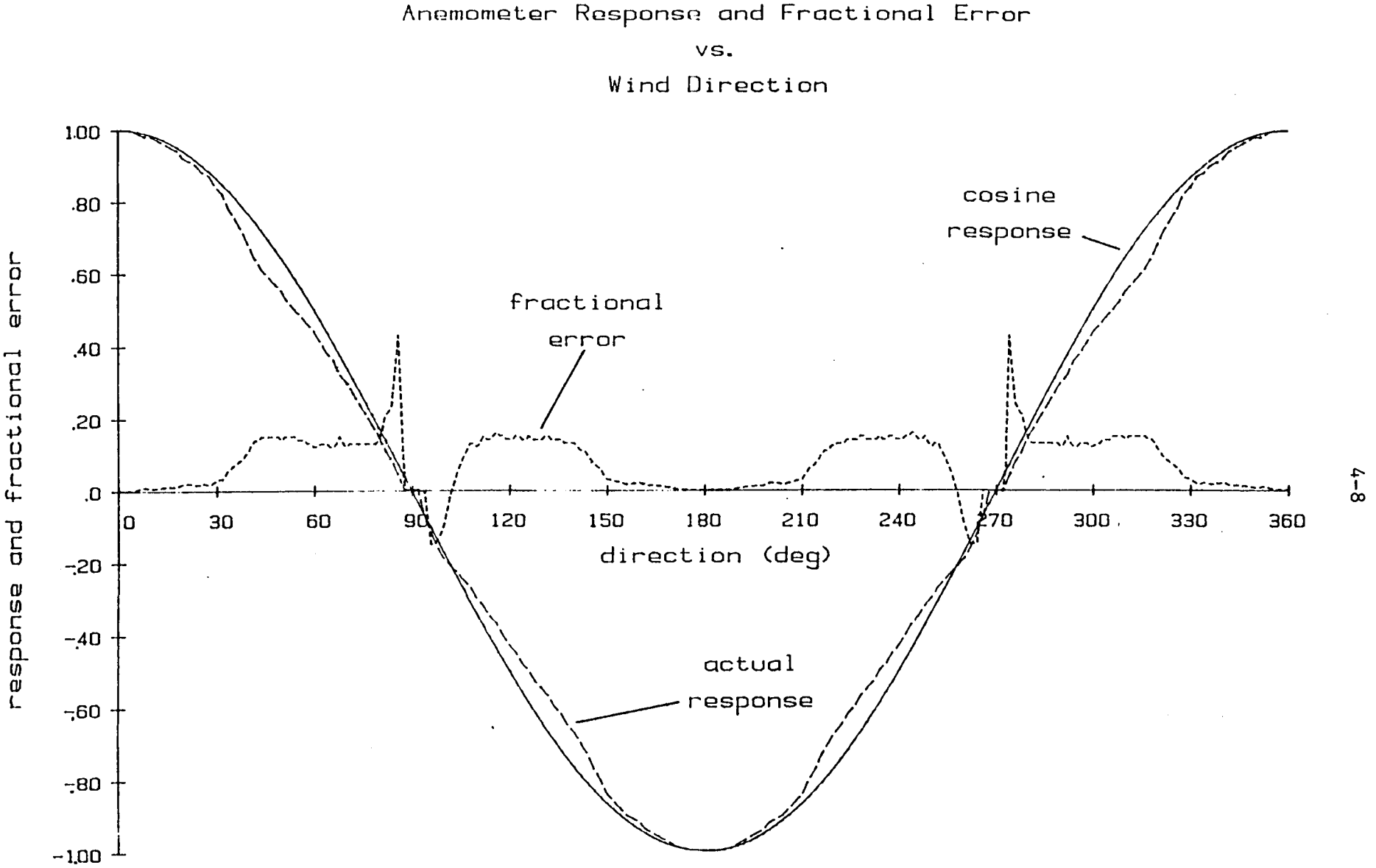

Figure 4.3. R.M. Young anemometer calibration.

is constructed from the R. M. Young calibration, where $C(\phi)$ is the fractional difference between a cosine response and the measurement at a given wind direction. U and V are then related to U_N and V_N as:

$$U = U_N/(1 - C(\phi))$$
$$V = V_N/(1 - C(90 - \phi))$$

Then the true wind angle is given by:

$$\tan(\phi) = V/U = \frac{V_N\,(1 - C(90 - \phi))}{U_N\,(1 - C(\phi))}$$

and

$$\tan(\phi)\,\frac{1 - C(\phi)}{1 - C(90 - \phi)} = \frac{V_N}{U_N}$$

A table (Fig. 4.4) of the right hand side of the above relation as a function of ϕ was computed. Thus, by knowing the ratio of the measured values V_N and U_N, the true wind angle ϕ is obtained from a table look-up.

The true wind components are easily computed from the earlier relations between U, V and U_N, V_N, and ϕ. The wind magnitude is $(U^2 + V^2)^{1/2}$.

4.2.1.2 Psychrometer

The linear thermistor networks are produced with a documented linearity, so that calibration consisted mainly of setting the gains and offsets of the thermistor interfaces for dry and wet sensors. The initial accuracy after calibration was to within .3 deg C over the span 0 to 40 deg C. A post measurement recalibration was not performed, but periodic checks during the experiment suggested that most instruments stayed within an accuracy of about 0.6 deg C.

The calibration of the thermistors simply involved cycling the sensors between cold and hot water baths and adjusting the gain and offset to provide a predefined response. The dry and wet thermistors for a given psychrometer were calibrated together, so that they would track together. The calibration was set so that the data count recorded for the sampling interval could be converted to temperature as:

$$T \text{ (deg C)} = 0.3 * \text{count}$$

$$T_w \text{ (deg C)} = 0.3 * \text{count}$$

4.2.1.3 Raingauge

The digital raingauge counted tips of the tipping bucket. Each raingauge was calibrated to give 0.25 mm of rain per tip.

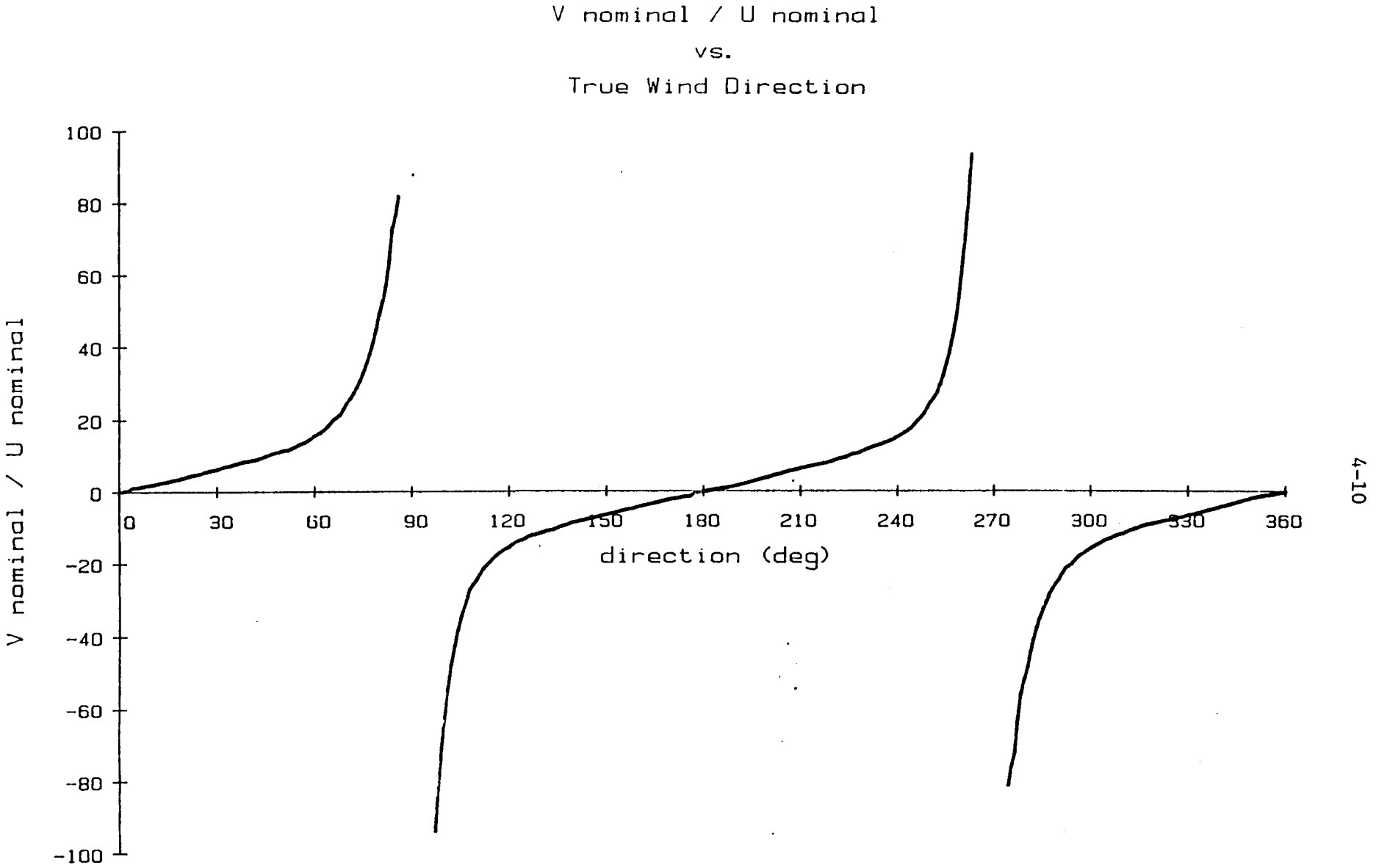

Figure 4.4. Nominal V_N/U_N versus true wind direction.

4.2.2 Coverage

The primary data set obtained from the network consists of the basic measurements made at each site: u and v components of wind velocity, dry and wet bulb temperatures, and rainfall. Figures 4.5 and 4.6 show example plots for one day of data. This type of plot was used to make quality checks of the data. Other meteorological parameters are calculated from quantities in the primary data set when needed for a particular analysis.

Data was collected during the 1984-1985 and 1985-1986 operational seasons. During the 1984-1985 season, problems developed with the psychrometers' thermistor potting method so that temperature data after November of that season are not reliable. Table 4.3 details the extent of the data set coverage.

4.3 ANALYSES

4.3.1 Calculation of meteorological parameters

Certain parameters were often used in the analysis of the mesoscale network data. These variables and the methods used for calculating them are given here.

4.3.1.1 Station pressure

Station pressure in all calculations was taken as a constant for each station, determined from the U. S. standard atmosphere according to the station elevation. It was assumed that the horizontal pressure gradient across the network would be small, and thus departures from the standard atmosphere would produce a small network-wide bias in the calculated thermodynamic values.

4.3.1.2 Dew point temperature

The dew point temperature (T_{dp} deg C) was calculated from the dry bulb temperature (T_d deg C), wet bulb temperature (T_w- deg C) and station pressure (P mb) using the following empirical procedure:

$$e0 = 6.11 * 10^{(7.5T_d/237.3 + T_d)}$$

$$e1 = 6.11 * 10^{(7.5T_w/237.3 + T_w)}$$

$$e2 = .00066 * (1 + .00115T_w) * P * (T_d - T_w)$$

$$e = e1 - e2$$

$$g = (\log^{-1}(e) - \log^{-1}(6.11)) / 7.5$$

$$T_{dp} = 237.3 * g / (1 - g)$$

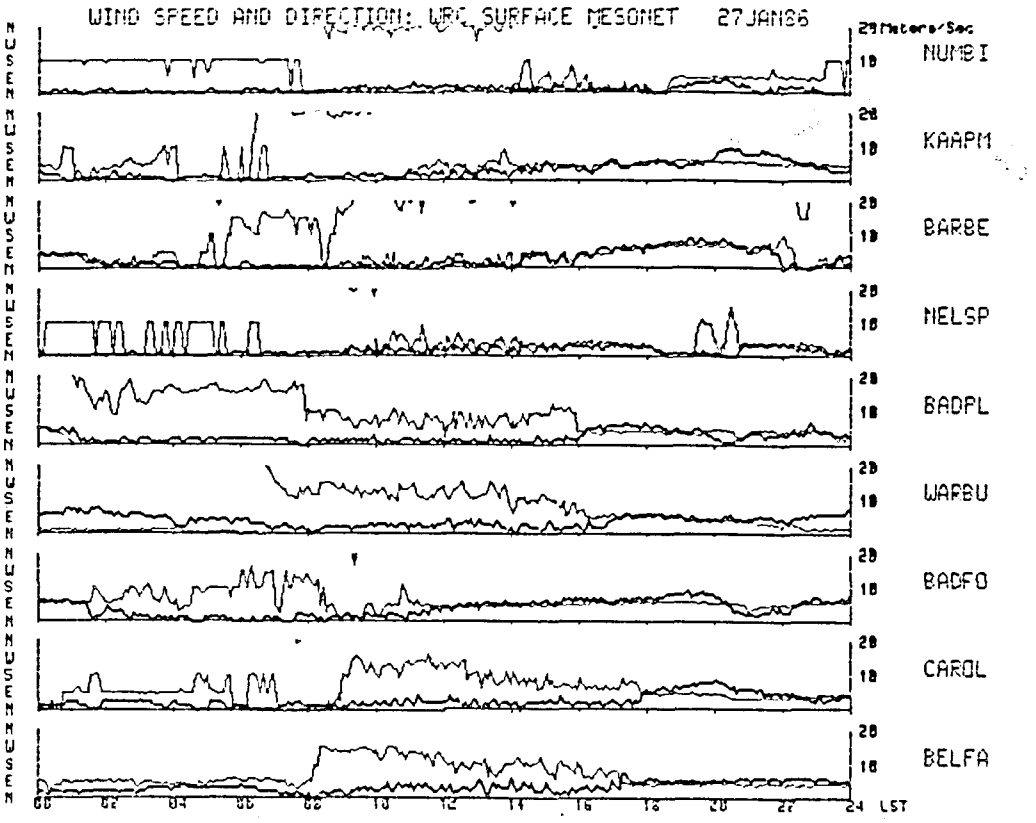

Figure 4.5. Sample anemometer data.

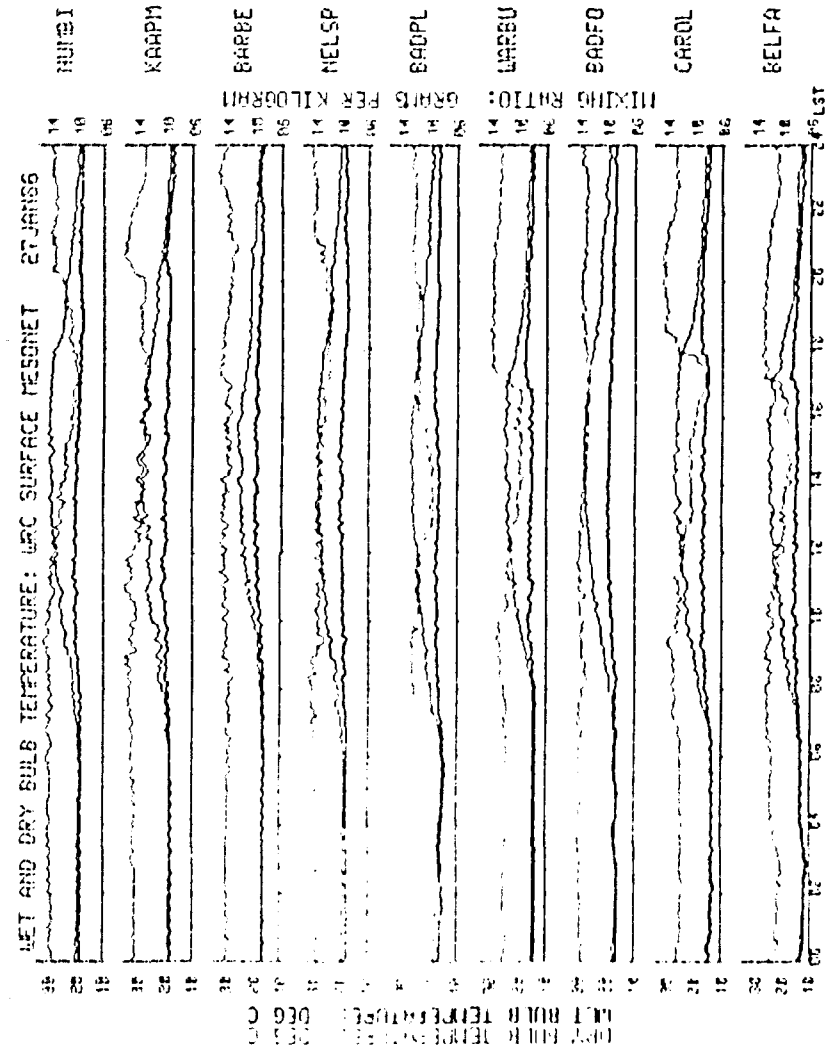

Figure 4.6. Sample of psychrometer data.

Table 4.3. Data set coverage

Season	Sites	Comments
1984-1985, September-March	Lower Sabie, Kaapmuiden, Numbi Gate, Barberton, Nelspruit, Badfontein, Badplaas, Belfast, Warburton	Lower Sabie operated only during November. Numbi Gate wind speeds unreliable after November.
1985-1986, October-March	Kaapmuiden, Numbi Gate, Barberton, Nelspruit, Badfontein, Badplaas, Belfast, Warburton, Carolina	Psychrometer data begins 13 November. Carolina data begins 5 December.

4.3.1.3 Potential temperature

The standard formula for calulating potential temperature (θ deg K) from T_d and P is used:

$$\theta = (T_d+273.15)*(1000/P)^{0.286}$$

4.3.1.4 Mixing ratio and equivalent potential temperature

The mixing ratio (r g/kg) and equivalent potential temperature (θ_e deg K) were calculated using the empirical methods described in Bolton, 1980.

4.3.2 Objective Analysis

In a number of the calculations involving network data it was necessary to interpolate data values between the station locations. The objective analysis method described by Cressman (1959) and modified by Barnes (1973) was utilized to estimate to a regularly spaced grid from the irregularly located stations. Several features of the scheme are particulary useful:

- The area containing interpolated grid points can be defined with an irregular boundary, and thus the area of interest was defined to have a boundary approximately 30 km outside of the outermost stations. Therefore estimates were made only for points which fell between two stations or within 30 km of at least one station.

- A "radius of influence" is a parameter in the scheme. This should relate to the station spacing and in our case was set to 50 km.

- The scheme is iterative in nature, and part of the procedure is to make estimates coincident with the station locations. The estimates at a station location will be based mainly on the data from that location, but will be influenced by errors from the weightings applied to the other stations within the network. When these errors become small enough (ie. the estimate at the station comes close to the observed value) the iteration is terminated. The convergence criteria is appropriately chosen to be the instrument resolution of the given parameter being estimated.

- Stations which do not have data at that particular time are easily removed from the objective analysis.

4.3.3 Mass Divergence and Integrated Mass Transports

Throughout these analyses an attempt has been made to use the mesoscale network as a single integrated sensor with which to characterize network scale processes. With only 9 stations it is impossible to resolve fine details within the network. However, based on our experience wth much denser networks in Florida and Illinois (Ulanski and Garstang, 1978, Cooper et al., 1982), surprisingly realistic patterns do appear in fields created by the objective analysis. It helps to justify these calculations in the sense

that we do not see the objective analysis producing short wavelength signals (noise) which would be simply artifacts of the procedure.

Using objectively analyzed fields of the u and v components of velocity, calculations of some surface mass quantities were performed. These were done for each 5 minute measurement interval so as to provide a time series on the day being analyzed. The grid points for which u and v were calculated are shown in Figure 4.7. All of these calculations depend upon the determination of the divergence at each grid point:

$$\text{div } (1/\text{sec}) = du/dx + du/dy$$

A cubic spline (Ahlberg and Walsh, 1967, Reinsch, 1967) was used to calculate the partial derivatives at each grid point, since a "by product" of the spline calculation is the derivative at the data points. The advantage of the spline is that it attempts to produce "smooth" fits to the data, and the derivatives are defined at the actual grid points. A simple finite difference would produce derivatives between the grid points, and a centered finite difference would smooth over three data points. In addition, a controlled amount of smoothing can be specified for the spline, and once again it was specified to be related to the resolution of the instrument.

The procedure was a simple one of fitting the cubic spline first to all of the x transects of u in the interpolated grid, and saving the derivatives for each grid point. Next the same is done for y transects of v, and finally the du/dx and dv/dy terms summed to give the divergence at each grid point. Using these values, the following time series were produced:

- The area averaged divergence computed from the total of the divergence over all grid points divided by the number of grid points.

- Total upward mass transport within the network was also obtained. This calculation is the sum of mass transports at grid points showing negative divergence. Assuming a linear wind profile with 0 at the surface to the value measured at the anemometer height, the average divergence within this layer is half the amount calculated at height. The upward mass transport is thus determined from:

$$\text{transport (cubic meters/ sec)} = (\text{divergence}/2) * \text{deltax} * \text{deltay} * h$$

  where:

  h - anemometer height
  deltax - grid box x dimension
  deltay - grid box y dimension

- Total downward mass transport within the network is calculated in the same manner as the upward mass transport, but using only grid points showing positive divergence.

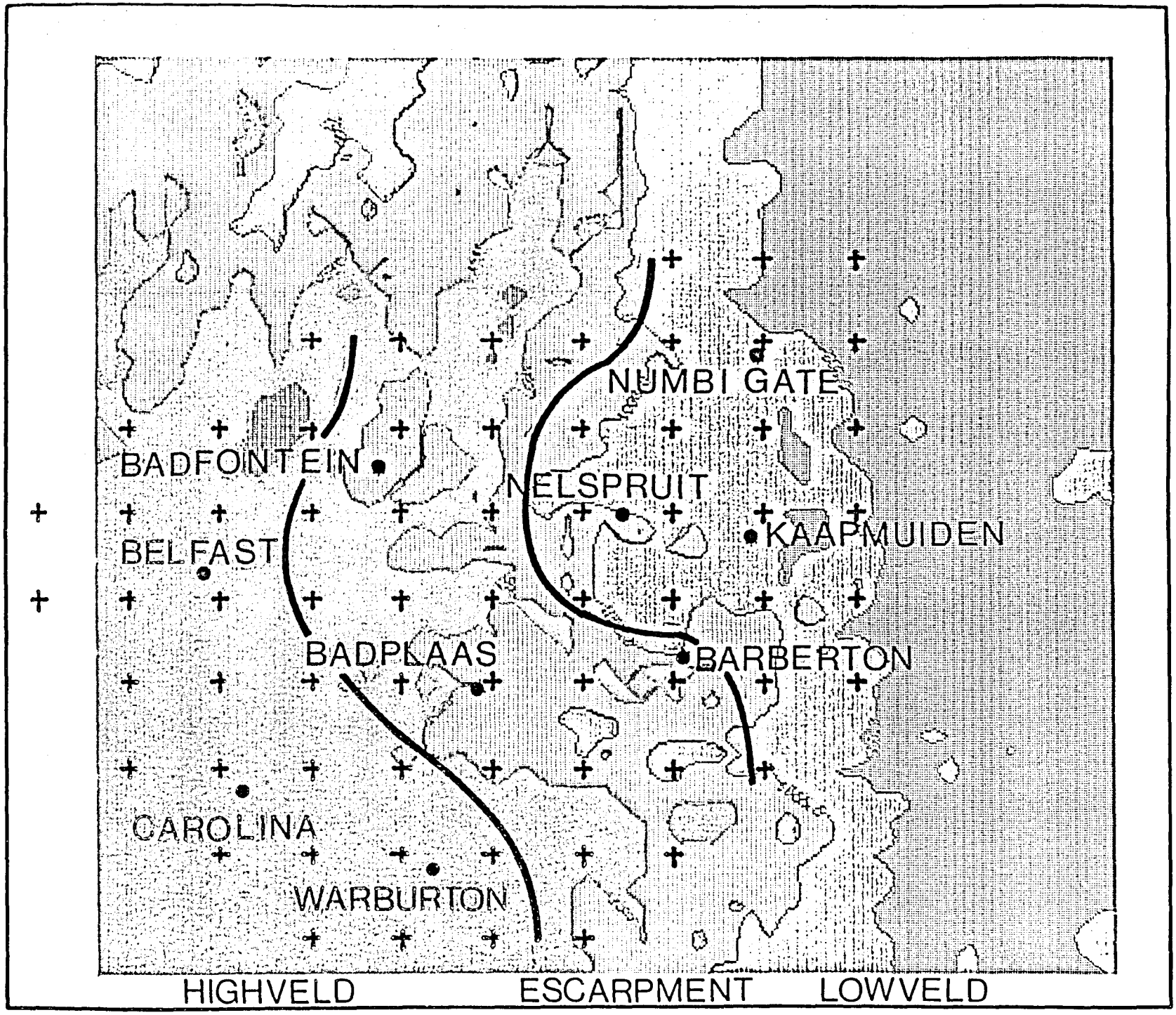

Figure 4.7. Grid used for divergence, mass transport and moisture flux convergence calculations. The three regions used in the moisture flux convergence analysis are delineated. Elevation contour indices are the same as in Fig. 4.1.

- Integrated mass transport is the net mass transport (sum of the upward and downward components) within the network. This is determined for each 5 minute interval, and integrated throughout the day, choosing 0600 LST as an arbitrary starting point.

4.3.4 Moisture Flux Convergence

The moisture flux is the product of the wind vector and mixing ratio. This quantity was calculated for each of the stations, and then interpolated to the grid using the objective analysis. The divergence of the moisture flux was then calculated in order to examine the inflow or outflow of moisture within the network. In addition, the grid was subdivided into three regions, based upon elevation and location, characterized as highveld, escarpment and lowveld areas (Figure 4.7). Time series of the moisture flux convergence for each area were produced to investigate correlations between the moisture regimes in each area and convective activity within the network.

4.3.5 Continuing Efforts

A sample of objectively analyzed wind and θ_e fields is shown in Fig. 4.8. In this case a finer grid has been utilized than is used in the calculations described earlier. The objectively obtained wind field is depicted by the wind vectors at each grid point. The objectively obtained θ_e field is shown by dashed contours, and the calculated divergence field is indicated by solid contours.

Several additional calculations are being explored or considred at present. These include examination of relationships between surface data and upper air measurements, such as determination of the LCL from the network data and its behavior across the network, relationships between thermodynamic quantities at the surface and those measured by the aircraft, and statistical analysis of surface data (means, variances, max's and min's) when stratified by various parameters, such as 800 mb flow, etc.

Preliminary work has been done using least square fits of a surface to the network data to characterize the network scale responses. This has a computational advantage over the objective analysis, being several orders of magnitude more efficient. A simple plane fit will provide a magnitude and direction of the maximum gradient across the network, and thus provide good indicators of network wide forcings (or responses). Preliminary plane fits to the u and v fields and calculation of the network wide divergence from the resulting gradients shows almost exact agreement with the results from the objective analysis. Plane fits to the θ_e and mixing ratio fields show interesting behavior as well. The fitting of higher order surfaces, such as a sphere, may also have interesting implications.

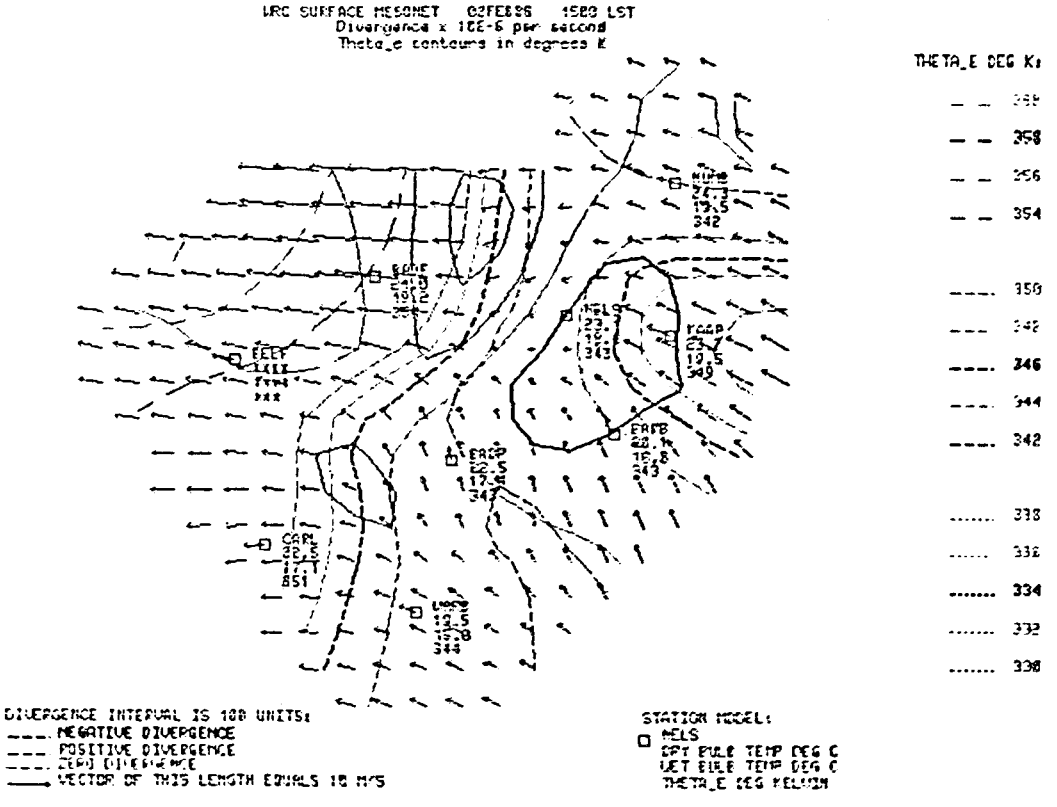

Figure 4.8. Typical objective analysis of surface wind and θ_e fields, and divergence calculations.

5.0 THUNDERSTORM OUTFLOW AND INTERACTION ALGORITHM

5.1 INTRODUCTION

The algorithm is a parameterization of some of the dynamic processes which drive larger storms and deals with the mature and decaying stages of the parent storm's lifecycle and the potential development of new convection. Complex storm systems are simulated by constructing the entire storm system from a number of "differential" cylinders one kilometer in radius. Basic potential flow theory is applied to each cylinder with base at the ground and top at a level where the vertical speed is taken to be zero. A downdraft is initiated within the cylinder at some height H, above the ground level. The effects of the imposition of the downdraft on the infinite fluid surrounding the cylinder conforms to flows that have been observed around precipitating systems.

Although there is no thermodynamical treatment in the simulation scheme, the imposition of the downdraft is in essence a parameterization of the microphysical and dynamical forces which produce local downdrafts, and the imposition of the lid at the top of a given cylinder parameterizes the upper level stability and the dynamic controls which operate on the whole system on larger scales. The combination of the two yields flow patterns similar to those which have been observed at all levels.

Recent years have seen increasing recognition within the scientific community of the importance of larger than storm scale motions and fluxes of moisture on the development of convective complexes and their production of rainfall.

A study of convective rainfall in Florida by Cooper et al. (1982) yielded two basic results:

1. Under conditions of almost constant lapse rate of temperature, there was found a good relationship between the flux of mass into the surface layers, and the amount of rainfall associated with that flux (see Figs. 5.1 and 5.2).

2. The development of convective complexes (which produce the most rainfall) appeared to depend upon the interactions between thunderstorm outflows and the larger scale convergence, which organized mesoscale areas of flux convergence within which convective scale interactions took place (Fig. 5.3).

The first result allows an association to be made between low-level radar estimations of rainfall, and the probable position and intensity of downdrafts can be broadly estimated from radar. In the Florida study, it was also noted that the near surface divergence (approximately 10.0 m height) when measured on a spatial scale of about 5 kilometers was consistently on the order of 10^{-3} sec^{-1}. Application of the algorithm can then be used to simulate the wind patterns which result when any number of storms are present over the area of interest, and allows us to display the general spatial distribution of small scale upward and downward motions.

A diagnostic use of the potential flow algorithm provides an objective method of evaluating low level ($\sim$ 1000 m) flow field in regions of convective activity and the nature of the storm/storm interaction.

Figure 5.1. The average vertical mass transports downward through 4 meters height estimated from observations of near surface divergence beneath precipitating summertime convection in south Florida.

The near-surface vertical velocities were observed using a high resolution ($\sim$ 5 x 5 km) surface wind-set array. More than 100 storms were observed. Knowledge of the surface rainfall from radar will allow estimates of downdraft intensity and location.

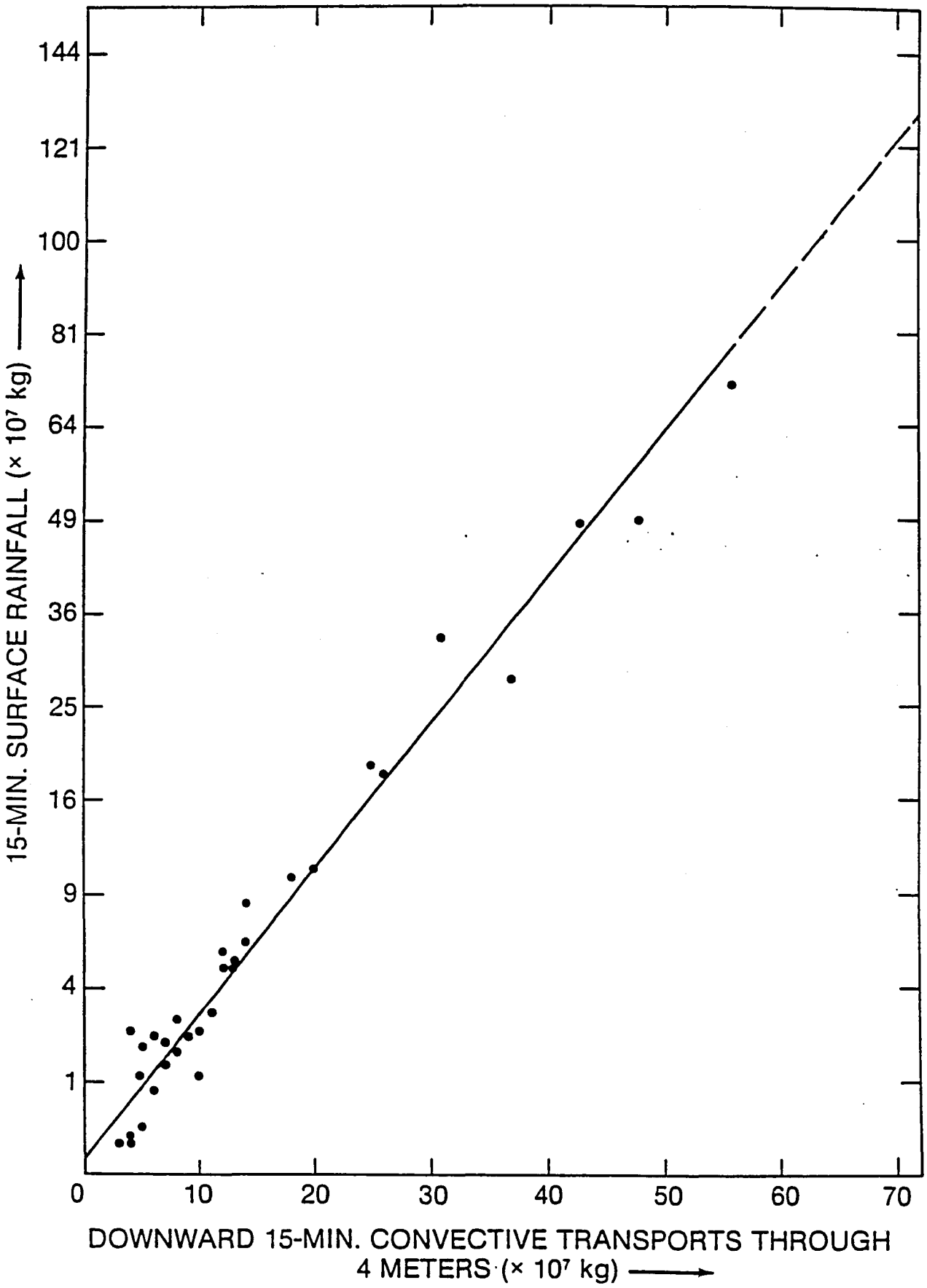
144
121
100
81
64
49
36
25
16
9
4
1
0
10
20
30
40
50
60
70
15-MIN. SURFACE RAINFALL (× 10⁷ kg) ⟶
DOWNWARD 15-MIN. CONVECTIVE TRANSPORTS THROUGH
4 METERS (× 10⁷ kg) ⟶

Figure 5.1.

Figure 5.2. (a) An example of spatial relationship between surface rainfall and vertical transports through the surface layer. These observations were made in Florida during FACE (Florida Area Cumulus Experiment) 1975. The network scale surface convergence is shown by the solid line. The upward (dashed-dot) and downward (dashed) "convective scale" transports are due only to grid scale divergence $\geq |\pm 4 \times 10^{-4}| s^{-1}$.

(b) The shaded areas are regions of divergence with isolines of divergence in units of 10^{-4} sec^{-1}. Rainfall is shown as closed circles for heavy rain ($\geq$ 1.5 cm in 5 min) and open circles for light rain (< 1.5 cm in 15 min). Radar echo return intensities from the Miami WSR-57 radar are shown by solid lines.

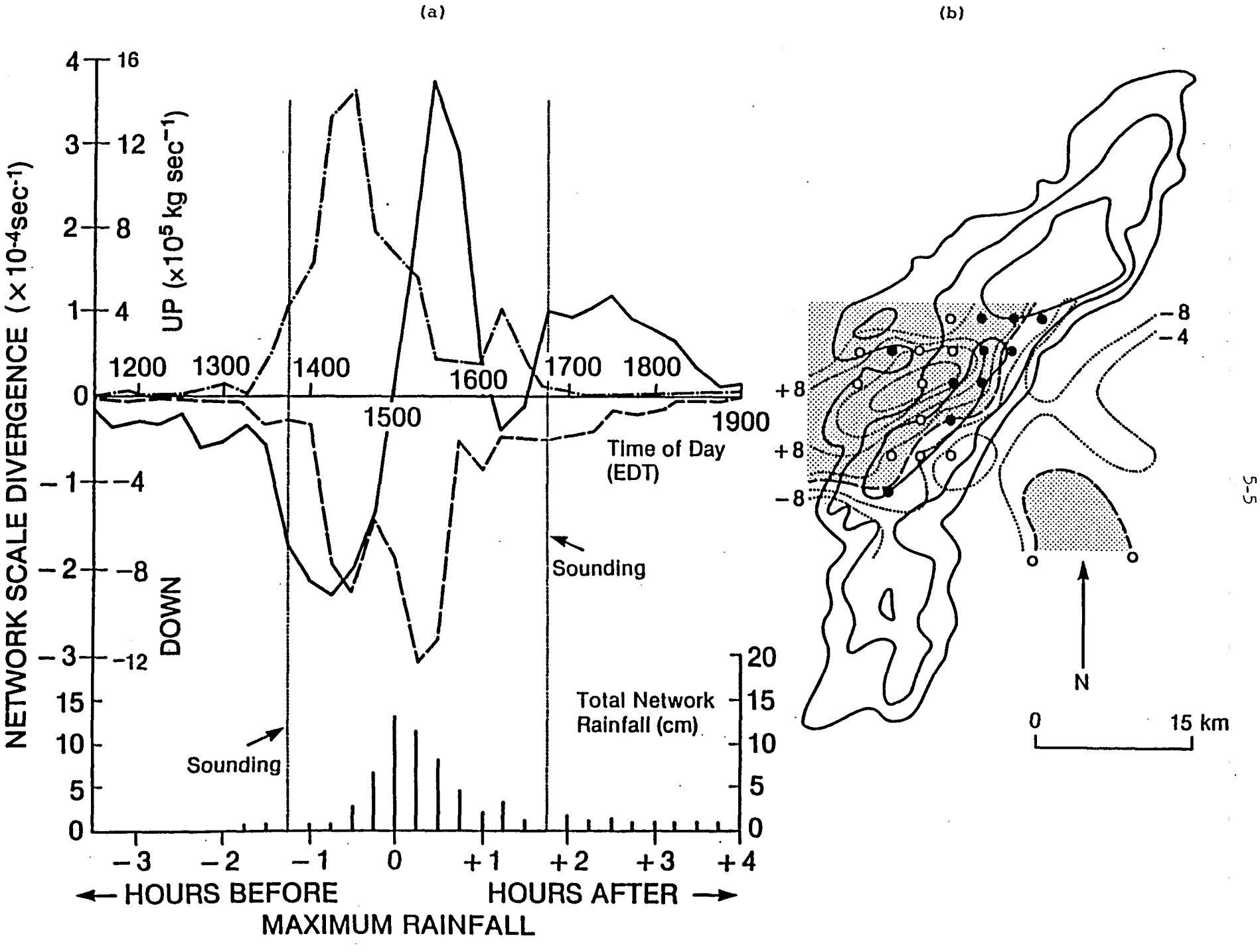
(a)
(b)
NETWORK SCALE DIVERGENCE (×10⁻⁴sec⁻¹)
UP (×10⁵ kg sec⁻¹)
DOWN
4
3
2
1
0
−1
−2
−3
16
12
8
4
−4
−8
−12
1200
1300
1400
1500
1600
1700
1800
1900
Time of Day (EDT)
Sounding
Sounding
Total Network Rainfall (cm)
20
15
10
5
0
−3
−2
−1
0
+1
+2
+3
+4
← HOURS BEFORE
HOURS AFTER →
MAXIMUM RAINFALL
+8
+8
−8
−8
−4
N
0
15 km

Figure 5.3. The relationships found in Florida between larger scale convergence and convective scale mass transports through the surface layer. The solid line is the rate of change of the peninsular scale convergence estimated by Frank (1967). The dashed line is the upward convective scale transports measured through 5 m, and the dash-dot line is the downward convective scale transports. The dotted line is the ratio of the upward transports to downward convective scale transports.

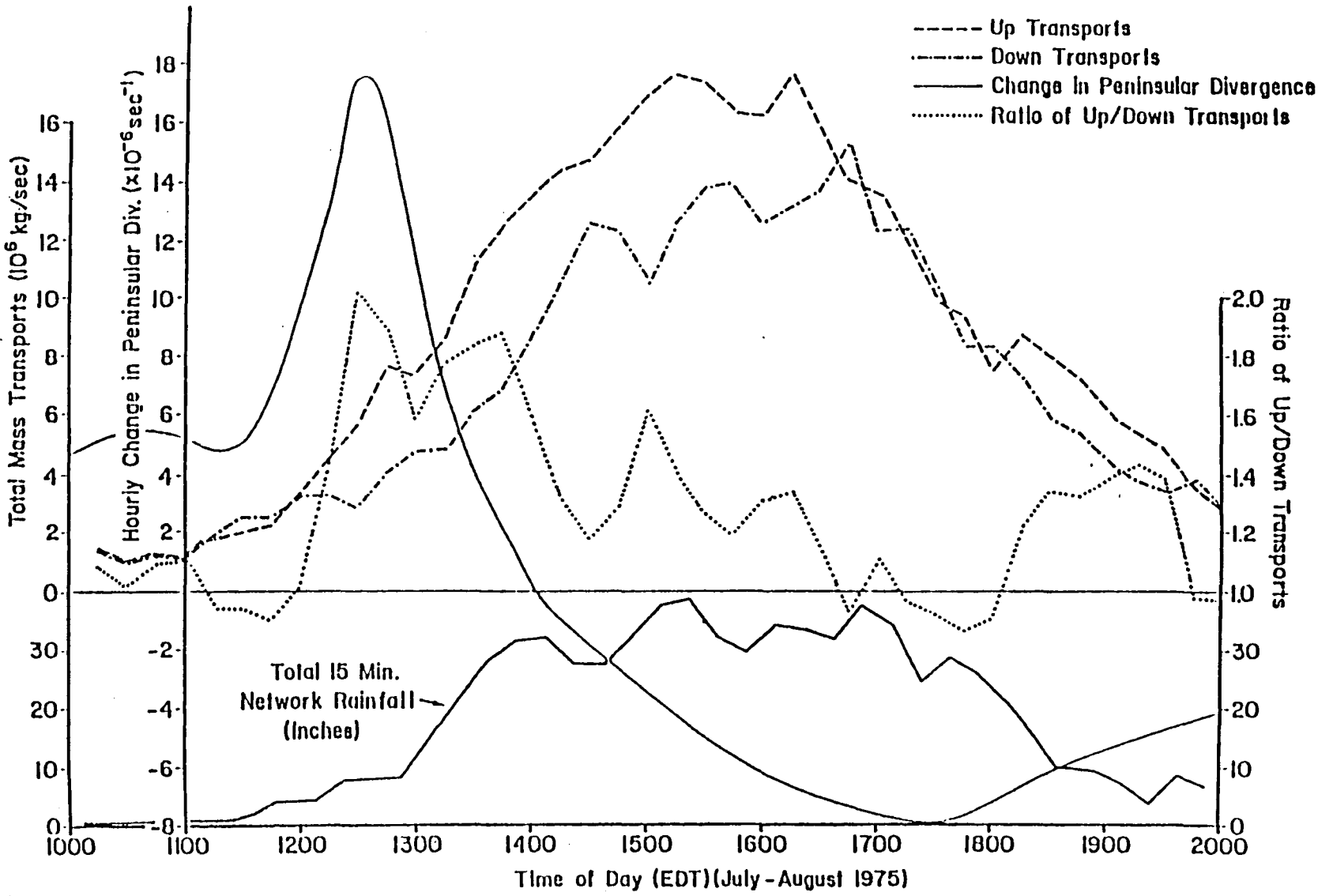
Up Transports
Down Transports
Change in Peninsular Divergence
Ratio of Up/Down Transports
Total Mass Transports (10^6 kg/sec)
Hourly Change in Peninsular Div. ($\times 10^{-6}$ sec^{-1})
Ratio of Up/Down Transports
Total 15 Min. Network Rainfall (Inches)
Time of Day (EDT) (July - August 1975)
1000
1100
1200
1300
1400
1500
1600
1700
1800
1900
2000

5.2 THEORY

There have been many attempts to completely model the evolution of a convective storm from basic equations (e.g., Schlesinger, 1975). Due to the nature of the problem, any three-dimensional convective cloud model which is capable of simulating the growth and decay of a convective storm is inevitably very complex, expensive and time-consuming. In addition, few can also simulate storm to storm interactions. These elaborate models also require access to large, fast computing machines.

The basic equations for such a model take the form (from Lilly, 1979):

(1) $\frac{d\vec{V}}{dt} = -\vec{\nabla} p/\rho - g\hat{k}$ Equation of motion

(2) $\frac{d\rho}{dt} = -\rho \vec{\nabla} \cdot \vec{V}$ Equation of mass continuity

(3) $\frac{d\theta_e}{dt} = 0$ Equation of thermodynamic energy

(4) $\frac{d}{dt}(q_v + q_e + q_i) = 0$ Equation of water substance conservation

If density is assumed constant following a parcel, and the density is approximately 1.0 kg m^{-3}, then equation (2) becomes

$$\vec{\nabla} \cdot \vec{V} = 0 \tag{5}$$

That is, this equation constrains solutions included in Eqns. (1), (3), and (4), subject to the appropriate boundary and initial conditions. Under these conditions, eq. (2) is the simplest of all of the above equations to deal with, and may be thought of as providing the background framework (in the necessary compliance with continuity) within which the other equations must operate.

Since any vector field $\vec{V}$ can be written as the sum of irrotational and non-divergent parts, we may write

$$\vec{V} = \vec{V}_r + \vec{V}_d$$

where $\vec{V}_r$ is a non-divergent vector field and $\vec{V}_d$ is an irrotational vector field. Then from eq. (5)

$$\vec{\nabla} \cdot \vec{V} = \vec{\nabla} \cdot (\vec{V}_r + \vec{V}_d) = 0$$

$$= \vec{\nabla} \cdot \vec{V}_r + \vec{\nabla} \cdot \vec{V}_d \cdot$$

Since $\vec{V}_r$ is non-divergent,

$$\vec{\nabla} \cdot \vec{V} = \vec{\nabla} \cdot \vec{V}_d = 0 \tag{6}$$

in this case. Since $\vec{V}_d$ is an irrotational field (6) may be written in terms of a velocity potential as

$$\vec{\nabla}^2 \phi = 0 \tag{6a}$$

where $\vec{\nabla}\phi$ represents the irrotational part of the velocity field and $\vec{\nabla}\phi = \vec{V}_d$.

The flow in intense thunderstorm downdrafts is, of course, highly rotational, but, if we consider the rotation during the mature stage of the storm to be confined mostly to the high shear zones at the surface and along the edges of the downdraft/updraft region, it is profitable to consider the irrotational part of the flow field and compare solutions of (6a) to observed wind fields around raining convection, in the hope that the broad nature and sense of the flow can be obtained easily and simply via an application of potential flow theory.

It may be mentioned at this point that the variation in density across lines of equal potential, which must be expected in real thunderstorm outflows does not invalidate the application of potential flow theory, but it must be assumed that mixing does not occur. We consider only the downdraft branches of the storm circulation assuming, for the time being, that the location and strength of the downdrafts can be estimated in the lower levels by surface instrumentation or radar observations.

The general approach is to break the downdraft region down into small ($\simeq$ 1 km radius) cylinders, each with its base at the surface and its top at some level T, and then to solve (6a) for each cylinder together with appropriate boundary conditions, taking into account a measured vertical speed in each small cylinder of WM m s^{-1} at z = M.

For a given cylinder, in cylindrical co-ordinates:

(7) $\vec{\nabla}^2\phi = 0$

(8) $w(r,z) = \frac{\partial\phi}{\partial z}$, $u_r(r,z) = \frac{\partial\phi}{\partial r}$, (u_r is the radial velocity in the horizontal, w is the vertical velocity)

(9) $w(r,0) = 0$

(10) $w(r,M) = WM$ which is measured at z = M

(11) $w(r,H') = 0$ for some H' such that $0 < M < H' \leq T$

(12) $w(r,T) = 0$.

It is also required that ϕ remain finite within the small cylinder of radius R. Axial symmetry for each small cylinder is also assumed. The assumption of axial symmetry for each small cylinder does <u>not</u> mean that assymetric flows cannot be represented, since the overall flow in the downdraft region is taken to be the accumulated effect (in the sense of Gauss' theorem) of many small "differential" cylinders similar to the one now under consideration.

The solution to (7), (9), (10) and (12) above is well known. It is:

$$\chi(r,z) = A \cos(az)\, I_o(ar) \qquad (13)$$

where $0 \leq z \leq T$; $0 \leq r \leq R$, and $I_o(ar)$ is a zero-order modified Bessel function. However, (13) cannot simultaneously satisfy (7), (8), (9), (10), (12)

and also (11).

The conditions in (11) reflect the requirement that the downdraft must originate ($w(H') = 0$) at some level in the troposphere. To satisfy (11), use is made of the well-known solution for potential flow near a stagnation point (see Batchelor, 1970), which is

$$\psi(r,z) = k(z^2 - \frac{r^2}{2}) \quad .$$

This potential is chosen in keeping with the general philosophy of providing the simplest overall solution. Then

$$\phi(r,z) = \chi(r,z) + \psi(r,z) \tag{14}$$

or

$$\phi(r,z) = A \cos(az)\ I_o(ar) + k(z^2 - \frac{r^2}{2}) \quad . \tag{15}$$

Then the vertical speed is given by

$$\frac{\partial \phi}{\partial z} = -a\ A \sin(az)\ I_o(ar) + 2\ kz = w(r,z) \tag{16}$$

and the radial velocity is given by

$$\frac{\partial \phi}{\partial r} = a\ A \cos(az)\ I_1(ar) - kr = u_r(r,z) \tag{17}$$

An average vertical velocity, $\bar{w}$, is defined for each differential cylinder as follows

$$\bar{w}(z) = \frac{1}{A} \int_A w(r,z)dA \tag{18}$$

where A is the horizontal area of the differential cylinder. Then

$$\bar{w}(z) = \frac{1}{\pi R^2} \int_o^{2\pi} \int_o^R w(r,z)rdrd\theta \quad . \tag{19}$$

Since

$$w(r,z) - -a\ A \sin(az)\ I_o(ar) + 2\ kz \tag{20}$$

$$\bar{w}(z) = \left[\frac{-a\ A \sin(az)}{\pi R^2} \int_o^{2\pi} \int_o^R I_o(ar)rdrd\theta\right] + \int_o^{2\pi} \int_o^R \frac{2kz}{\pi R2}\ rdrd\theta, \tag{21}$$

so that

$$\bar{w}(z) = -\frac{2}{R} A \sin(az)\ I_1(aR) + 2kz \tag{22}$$

(12) is satisfied if

$$\bar{w}(T) = -\frac{2A}{R} \sin(aT)\ I_1(aR) + 2kT = 0 \tag{23}$$

therefore,

$$A = \left[\frac{kTR}{\sin(aT)\ I_1(aR)}\right] \tag{24}$$

(10) is satisfied if $\bar{w}(M) = -\frac{2}{R} A \sin(aM)\ I_1(aR) + 2kM$ (25)

therefore

$$k = \frac{\bar{w}(M)}{2}\left[\frac{\sin(aT)}{M \sin(aT) - T \sin(aM)}\right] \tag{26}$$

Setting

$$F = M \sin(aT) - T \sin(aM) \quad (T \neq M,\ M <) \tag{27}$$

and substituting for k and A in (20) yields

$$\bar{w}(z) = \frac{\bar{w}(M)}{F}\left[z \sin(aT) - T \sin(az)\right] \tag{28}$$

for the vertical speed, and

$$u_r(R,z) = \frac{\bar{w}(M)}{2F}\left[RTa \cos(az) - R \sin(aT)\right] \tag{29}$$

for the horizontal radial speed. All of the conditions in (7)-(12) are satisfied by (28) and (29) with the exception of (11).

In eq. (14), the total potential is broken down into two independent potentials $\chi(r,z)$ and $\psi(r,z)$. $\chi(r,z)$ may be thought of as the convective potential, i.e., representing the potential field generated by microphysical processes and cloud scale dynamics. $\psi(r,z)$ may be thought of as a restraining potential which operates over the entire troposphere and which reacts to and constrains the convective potential, imposing the required conditions on the larger tropospheric scale. The convective potential is, therefore, chosen such that the vertical speeds generated by it go to zero at z = H. That is,

$$a = \frac{\pi}{H} \qquad \text{(where H is not always the same as H')} \tag{30}$$

Then

$$\bar{w}(z) = \frac{\bar{w}(M)}{F}\left[z \sin(\frac{\pi T}{H}) - T \sin(\frac{\pi z}{H})\right] \tag{31}$$

and

$$u_r(R,z) = \frac{\bar{w}(M)}{2F}\left[\frac{RT\pi}{H}\cos(\frac{\pi z}{H}) - R \sin(\frac{\pi T}{H})\right] \tag{32}$$

Since we must require the flow to be irrotational, there is a full slip condition at z = 0.

Equations (14) through (32) deal with the flow inside and at the boundaries of a differential cylinder of radius R.

Immediately outside the cylinder, the vertical speed is assumed to be zero. We require that the first derivative of the radial speed be continuous at r = R. This gives

$$u(r,z) = (C + 2)\, u(R,z)\, \frac{R^c}{r^c} - (C + 1)\, u(R,z)\, \frac{R^{C+1}}{r^{C+1}} \quad ,$$

for r > R, and C is a constant,

and the vertical speeds at each location outside the cylinder are estimated by vertical integration of the convergence in the horizontal winds.

Since there is, at present, no frictional or turbulent dissipation in the algorithm, for the sake of simplicity, the winds are calculated at the estimated boundary layer height, and a power profile is applied to reduce the wind speeds to observed magnitudes in the near surface levels.

In the real-data comparison in Figs. 5.4(a) and 5.4(b) a roughness of 4.0 cm yields a boundary layer $\sim$ 300 m thick and a coefficient (n) of 6.0 (Plate, 1971). The power profile used in this case is therefore:

$$u(z) = u(h)\, \frac{z}{h}^{\frac{1}{n}}$$

$$u(z) = u(300)\, \frac{z}{300}^{\frac{1}{6}} \qquad z \leq 300 \text{ m}$$

where 300 m is the top of the boundary layer.

The wind fields inside the cylinder can be adjusted by the user so as to fit the estimated stage (mature, decaying), and cell top height of the cells being observed by the radar. The best estimate of cell top height may be taken from the dBz - top height relationship found by Gagin and Lopez (1985) (see also Adler and Mack (1984)). An estimate is then made of the speed of translation of the storm, either from current radar observations or the current sounding. The cylinder is then translated at this speed and the advective effects of the translation into the observed low level flow produce convergence in the low level wind fields on the appropriate flank of the cylinder.

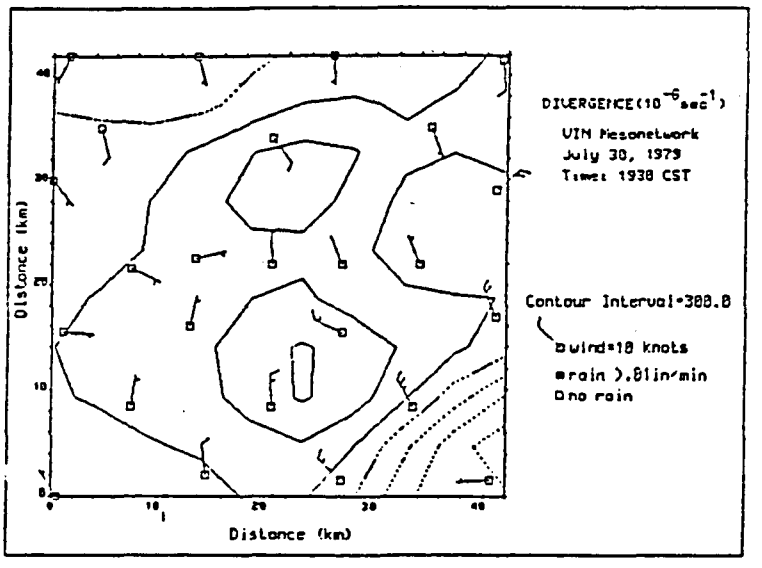

Figure 5.4(a). The observed winds beneath the 30 July 79 VIN storm.

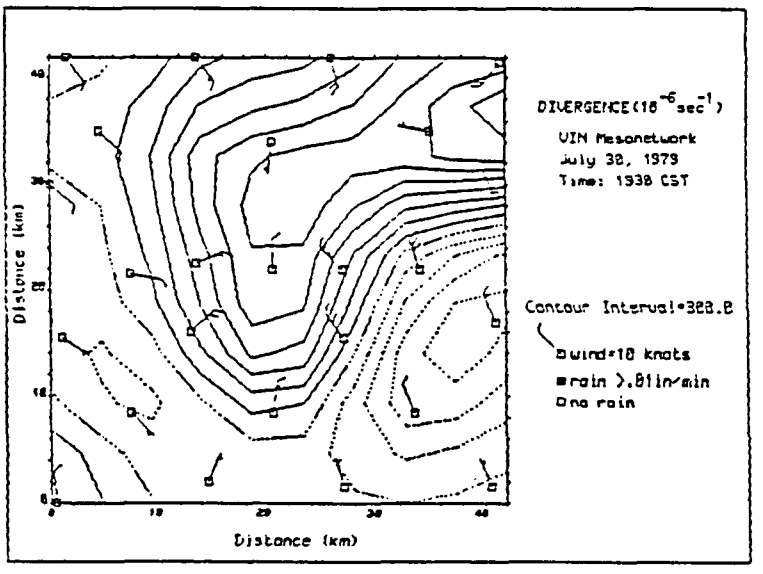

Figure 5.4(b). The winds produced by the algorithm for the 30 July 79 VIN storm.

Using the basic building block described above, we can assemble them to simulate any storm complex observed by a conventional radar. An attempt to do this has been made using conventional PPI observations taken by the CHILL radar during the Virginia/Illinois/NOAA experiment in 1979. Figure 5.4(a) shows the wind fields observed by the PAM network at 1930 LST, and Fig. 5.4(b) shows the estimated wind fields calculated for the same time using the algorithm, the radar and the local conventional sounding.

In summary:

1) The conventional radar PPI is used to identify areas where rainfall generated convective scale downdrafts are likely to be occurring (currently defined as anywhere dBz $\geq$ 35.0).

2) The conventional sounding is used to determine the wind shear in the environment surrounding the storm complex.

3) The algorithm then associates a cylindrical outflow pattern at 10 meters height with each selected radar pixel.

4) The vertical and horizontal flow are calculated inside and outside each cylinder.

5) The cylindrical flows are put together and advected in the direction of the shear vector to give estimates of the winds over the entire domain of the storm complex.

In order to preserve short computation time ($\leq$ 1 minute) for a large field, care has been taken to preserve the simplicity of the scheme whenever possible and to maintain the independence of each solution. The downdraft profile, heights of origin of downdrafts, function profiles, can all be improved. But even with these crude representations, the general sense and intensity of the low level wind fields can be simulated.

5.3 DISCUSSION

5.3.1 Inside the Cylinder

Figures 5.5(a) through 5.5(f) show the results of running the simulation for R (the radius of the downdraft region) of 2.5 km, for a 'measured' downward speed of 10 m/sec at 2000 m and for tropopause heights of 10, 13 and 15 km. In each of the figures, the parameter H was assigned values of 4000 m, 6000 m, 8000 m and 10,000 m.

As H increases toward the height of the tropopause, the nature of the flow in the cylinder changes from a flow suggestive of growing/mature storms (upward and downward speeds present) to a flow suggestive of a dissipating/mature storm (downward speeds throughout the troposphere). There is radial outflow in the low levels, inflow in the mid levels and outflow aloft in the mature growing stage. Examination of the many subjective storm flow patterns based upon observations (Fig. 5.6) reveals that the schematic flows presented in Fig. 5.6 can be represented in terms of the circulations represented in Figs. 5.5(a) through 5.5(f) (Newton, 1963; Browning and Ludlam, 1962; Moncrieff and Miller, 1976).

From these figures it can be seen that there appears to be a 'phase shift' in the nature of the simulated flow as the level of initiation of the downdraft

Figures 5.5(a), (b) and (c). The magnitude of the radial velocity, u(R,z), as a function of height for 4 values of H. H is the level at which the downdraft originates. The values are for a cylinder 2.5 km radius, with "measured" vertical speed of -10 m s^{-1} at 2.0 km height (AGL). T is set as indicated. The solid lines are flows for H = 4000 m, the two-dashed lines are for H = 6000 m, the single-dashed lines are for H = 8000 m and the dash-dot lines are for H = 1000 m.

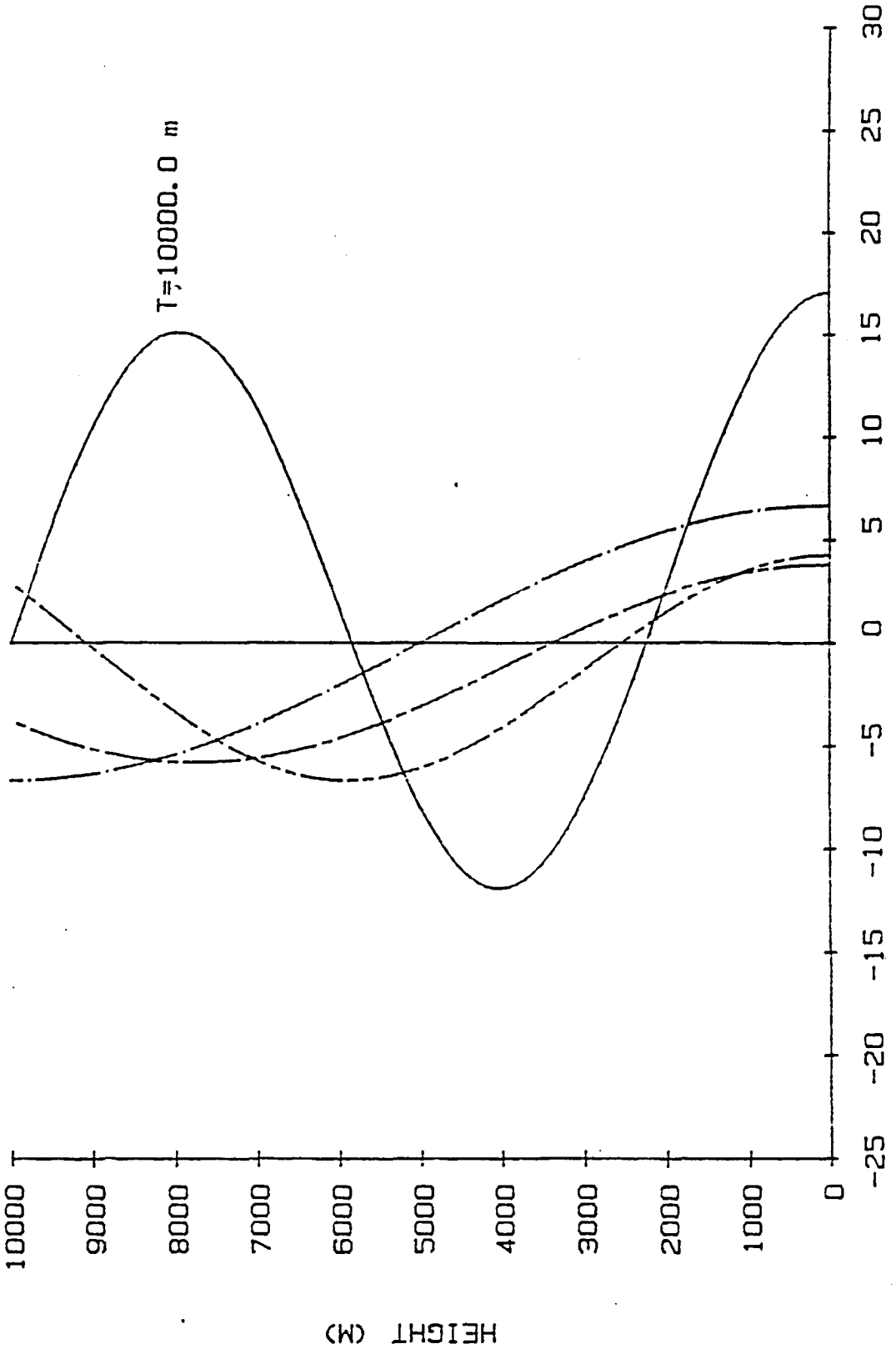
T=10000.0 m
HEIGHT (M)
10000
9000
8000
7000
6000
5000
4000
3000
2000
1000
0
-25
-20
-15
-10
-5
0
5
10
15
20
25
30
U COMPONENT (M/SEC)

Figure 5.5(a).

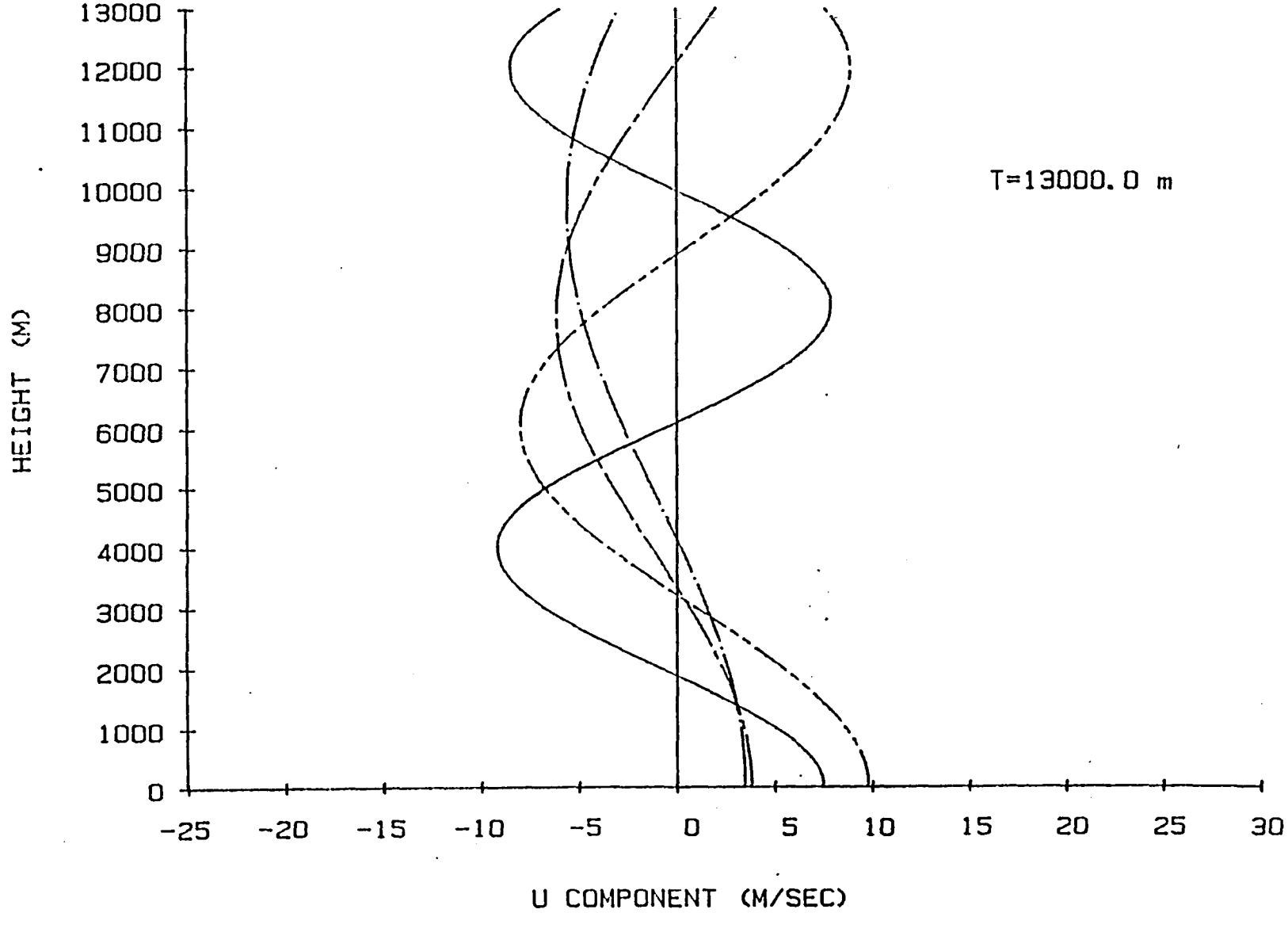
13000
12000
11000
10000
9000
8000
7000
6000
5000
4000
3000
2000
1000
0
HEIGHT (M)
T=13000.0 m
-25
-20
-15
-10
-5
0
5
10
15
20
25
30
U COMPONENT (M/SEC)

Figure 5.5(b).

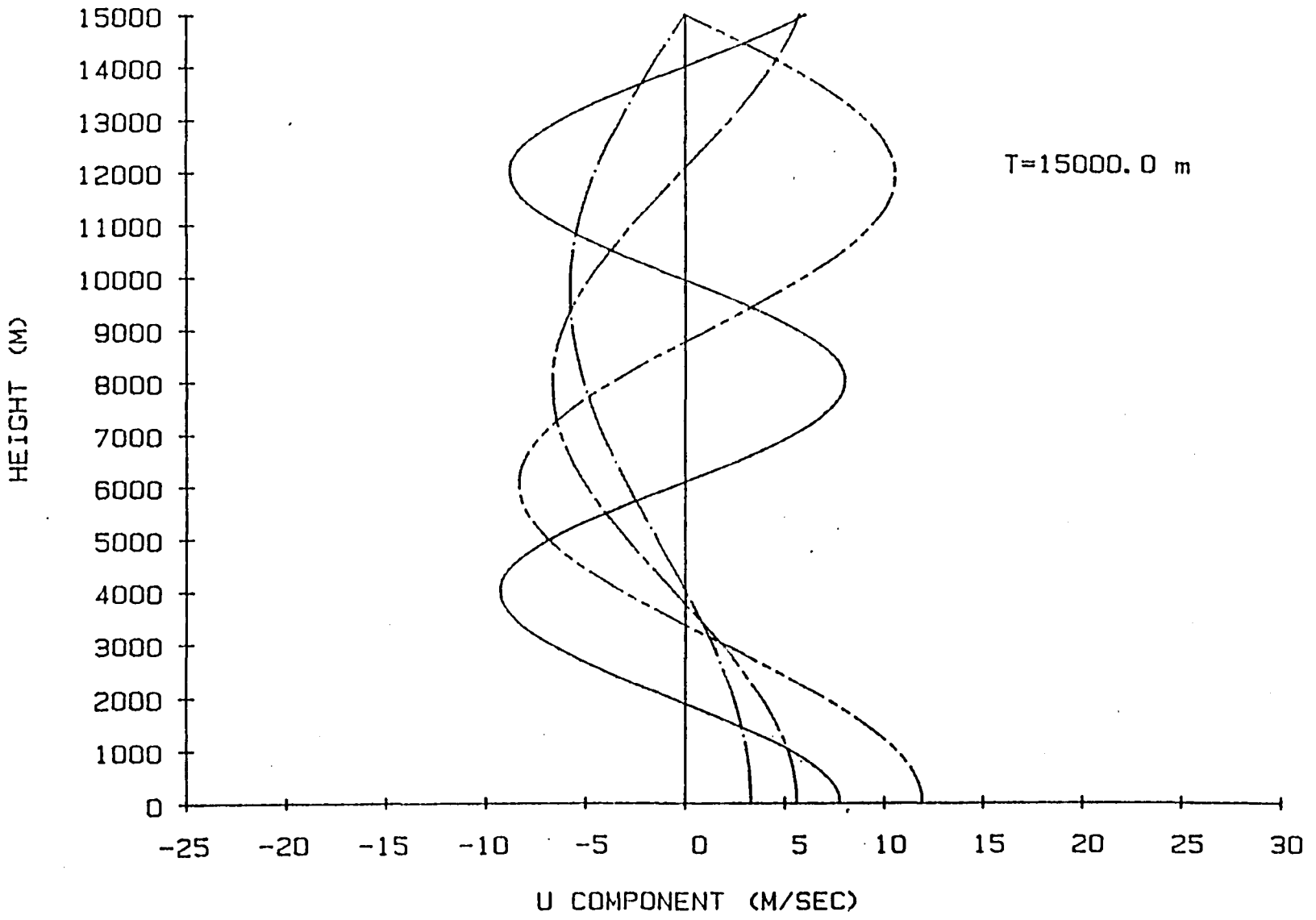
15000
14000
13000
12000
11000
10000
9000
8000
7000
6000
5000
4000
3000
2000
1000
0
HEIGHT (M)
-25
-20
-15
-10
-5
0
5
10
15
20
25
30
U COMPONENT (M/SEC)
T=15000.0 m

Figure 5.5(c).

Figure 5.5(d), (e) and (f). Same as Figures 5.5(a), (b) and (c) except for the vertical speed, $\bar{w}(z)$. The strong vertical speeds in the upper middle troposphere are often observed by Doppler radars.

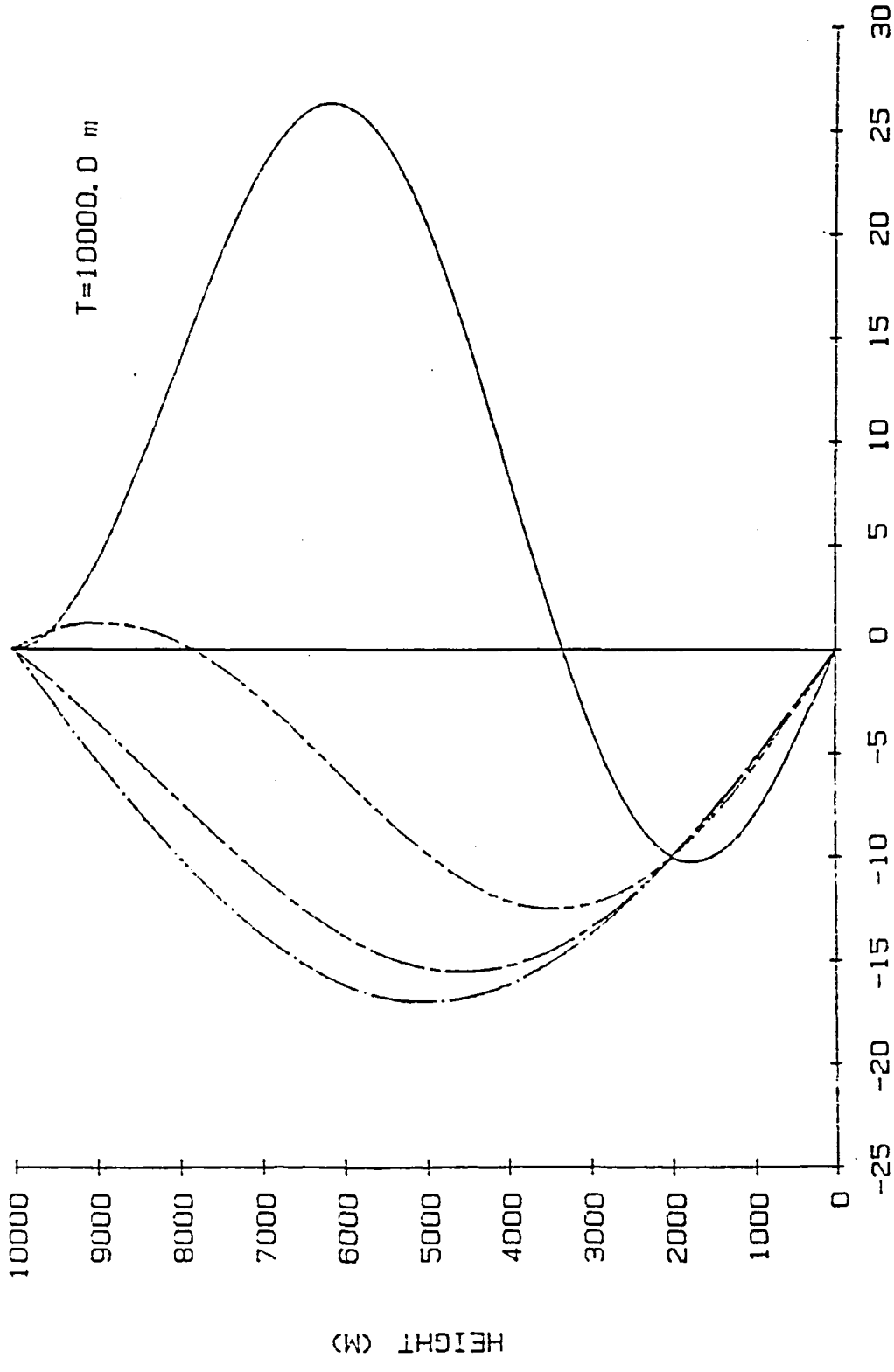
T=10000.0 m
HEIGHT (M)
10000
9000
8000
7000
6000
5000
4000
3000
2000
1000
0
-25
-20
-15
-10
-5
0
5
10
15
20
25
30
W COMPONENT (M/SEC)

Figure 5.5(d).

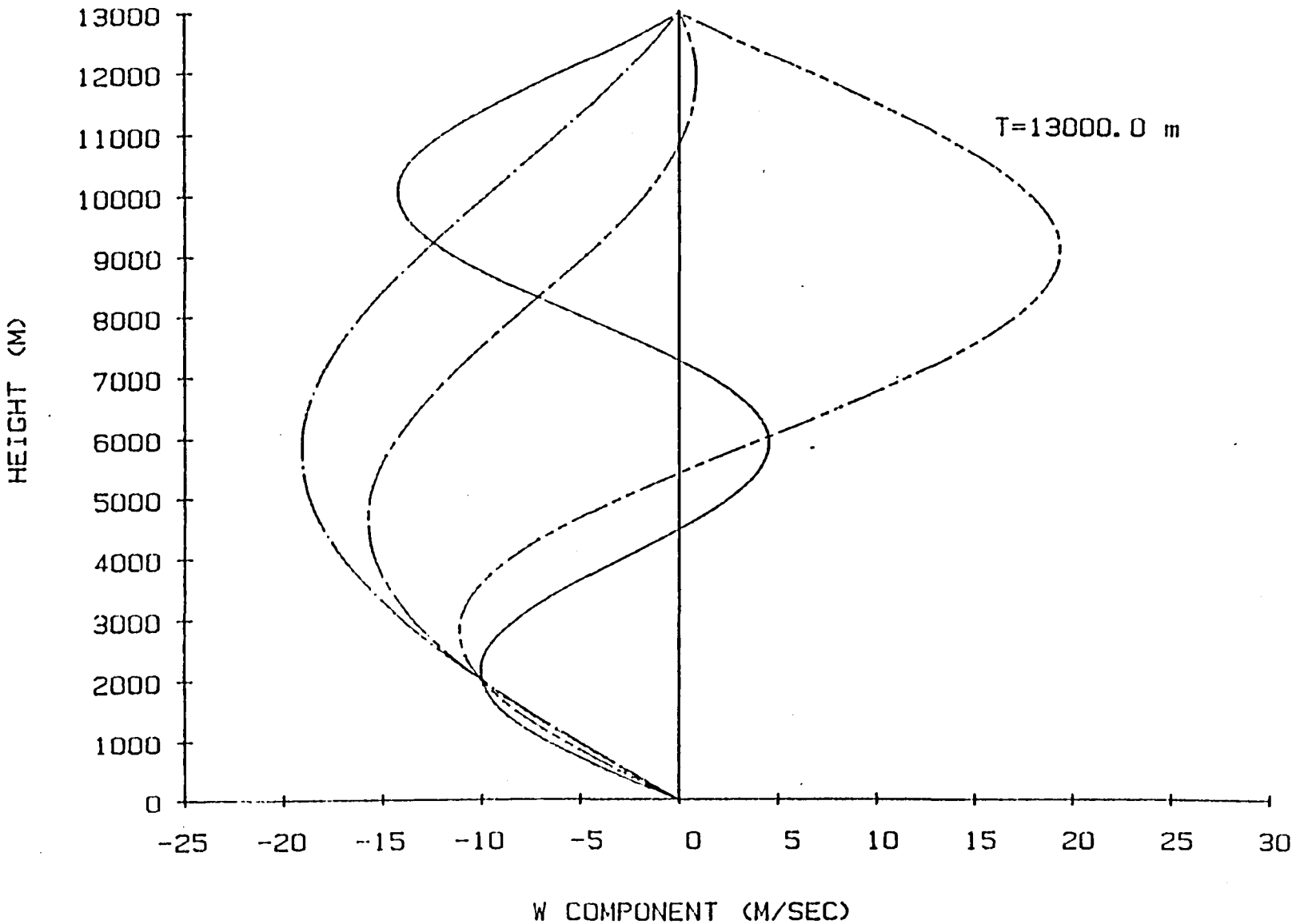
T=13000.0 m
HEIGHT (M)
13000
12000
11000
10000
9000
8000
7000
6000
5000
4000
3000
2000
1000
0
-25
-20
-15
-10
-5
0
5
10
15
20
25
30
W COMPONENT (M/SEC)

Figure 5.5(e).

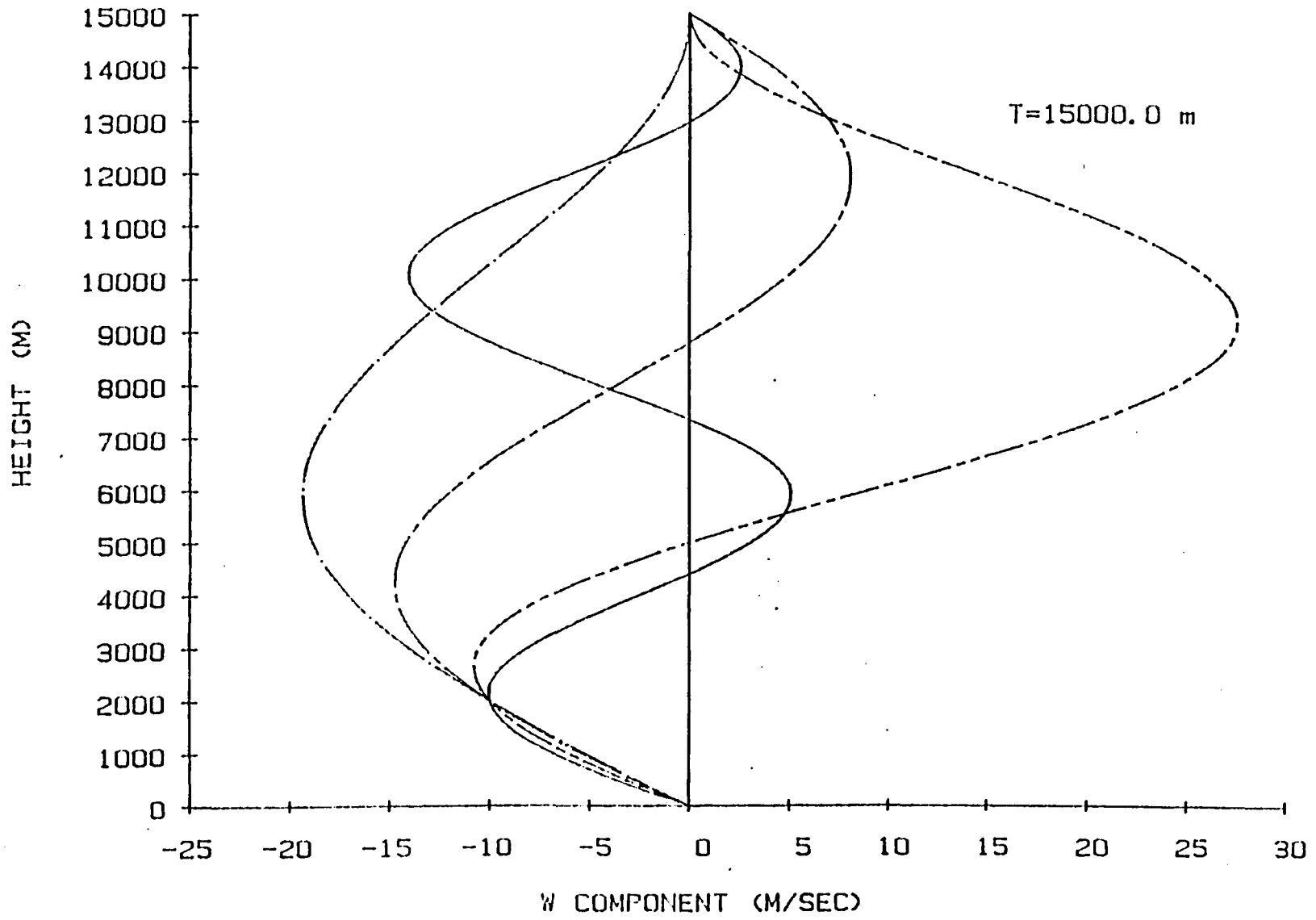
T=15000.0 m
HEIGHT (M)
15000
14000
13000
12000
11000
10000
9000
8000
7000
6000
5000
4000
3000
2000
1000
0
-25
-20
-15
-10
-5
0
5
10
15
20
25
30
W COMPONENT (M/SEC)

Figure 5.5(f).

Figure 5.6. A comparison of the flow within a mature storm as suggested by simple potential flow theory and other schematic flows suggested by observations. The four dashed solenoids represent the potential flow suggested by $\phi(r,z) = \chi(r,z) + \psi(r,z)$ in eq. (14).

The dotted streamlines are those suggested by Browning and Ludlam (1962) for the Wokingham storm. The solid streamlines represent the flow suggested by observations in Newton (1963). Moncrieff and Miller (1976) drew the flow in squall lines following a pattern similar to the dashed streamlines. The three observational schematic flows are consistent with the flow suggested by elementary potential flow.

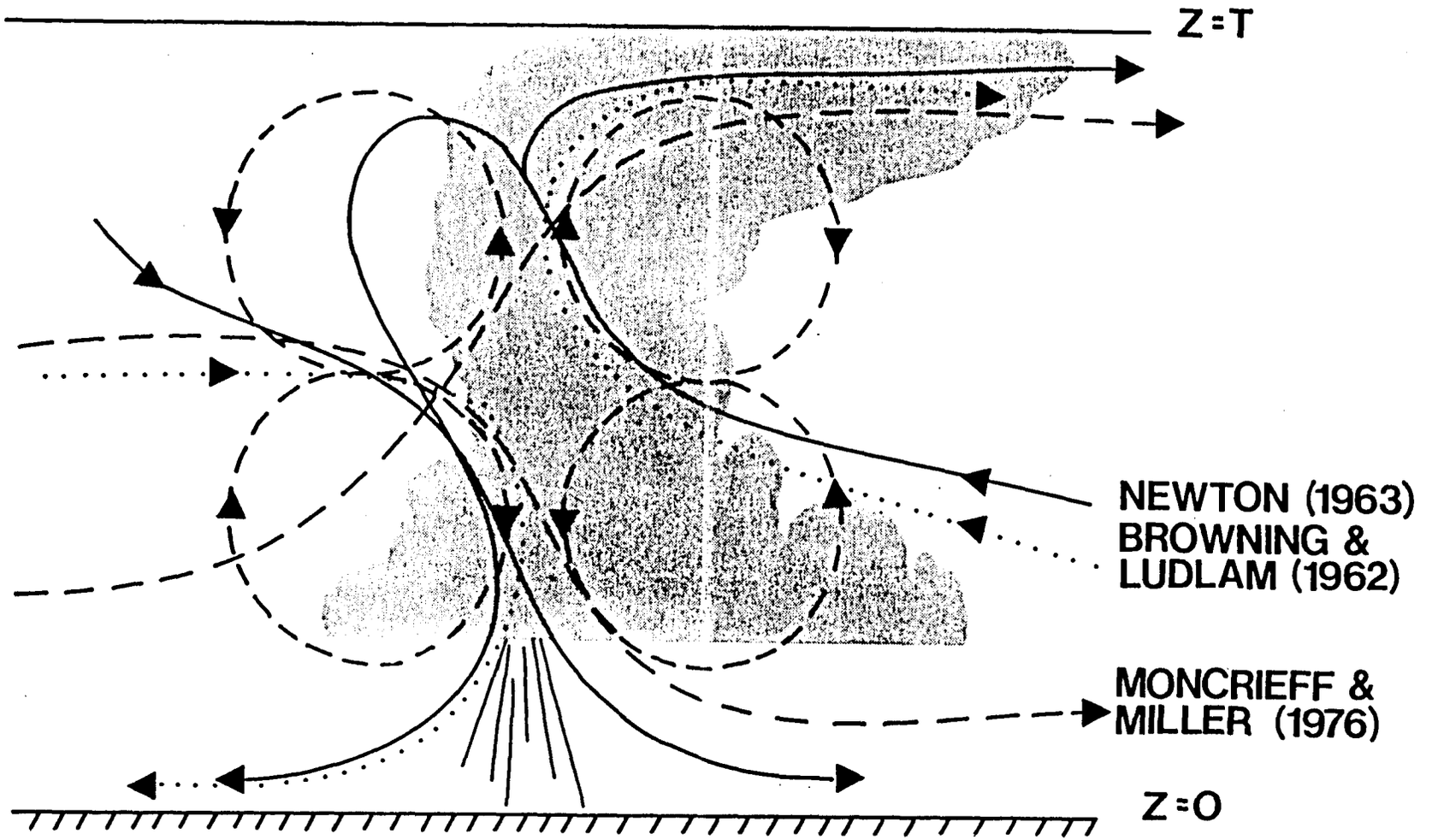
Z=T
NEWTON (1963)
BROWNING &
LUDLAM (1962)
MONCRIEFF &
MILLER (1976)
Z=O

Figure 5.6.

varies. Byers and Braham's (1949) description of the life cycle of thunderstorms, which is still accepted today, has 3 stages. They noted that in the earlier stages of a storm's lifetime the volume of the storm consisted of updrafts. Later in the cycle the lower part of the storm was occupied by downdrafts, while the upper parts were occupied by updrafts more powerful than the downdrafts beneath them. In the final stages, downdrafts occupied the entire storm volume.

These stages are reflected in the simulation. As the level of origin of the downdraft increases, the model storm goes through the mature and dissipating phases described by Byers and Braham.

If the downdraft originates too low in the troposphere, the nature of the flow is best described as a series of toroidal rolls, and in a sense, is disorganized. For example, the solid line plots in Figs. 5.5(c)-5.5(f). In Figs. 5.5(c,d) H was set at 4000 m, and T at 13 km. The resulting flow pattern is not similar to that of a mature storm. The level of H for which the flow becomes organized depends upon the depth of the troposphere. A similar, disorganized pattern results in Figs. 5.5(e) and 5.5(f), for T = 15,000.0, and H set at 4000 m. However, when the height of the tropopause is lowered to 10,000 m, the result of initiating a downdraft with H = 4000 m is an organized flow (Figs. 5.5(a,b), solid line).

In Figs. 5.5(a-f) the strength of the surface layer outflow is also seen to vary as the height of the top of the cylinder changes. Since the strength of the low level outflows from storms is important in the initiation of new, flanking convection, and in the convective scale feedback processes described in an earlier section of this report, it is instructive to investigate the change in strength of low level outflows with a variation in the levels of T and H.

In Fig. 5.7, the solid line is associated with a top height of 10 km, the dashed line with T = 13 km and the dash-dot line with T = 15 km. H (representative of the level of origin of the downdraft), is then allowed to vary from 3000 m to the top of the cylinder.

The plots show a series of maxima and minima in the resulting surface outflow speeds, which differ for each value of T, in the levels at which they occur and in their strength. Thus for a 'measured' downdraft speed of -10.0 m/sec at 2000 m, a cylinder radius of 2.5 km, and a given height for the level of origin of the downdraft and top, the strength of the outflows in the lower levels varies dramatically from minima of around 5 m/sec, to a maximum of greater than 20 m/sec.

In order to investigate further the effects of the relative variation of H and T, three top heights were selected. The three levels of T selected were 11.5 km (a typical summer high latitude height), 15.0 km (a height typical in the summertime for 30 degrees latitude) and 17.0 km (a typical tropical tropopause height).

The tropopause heights were then normalized to 1.0, and H was allowed to vary as before from the proportional level of 3000 m to the top of the troposphere where H = 1.0. The values for R and the downdraft speed at 3000 m (-10.0 m/sec) remained the same (Fig. 5.8).

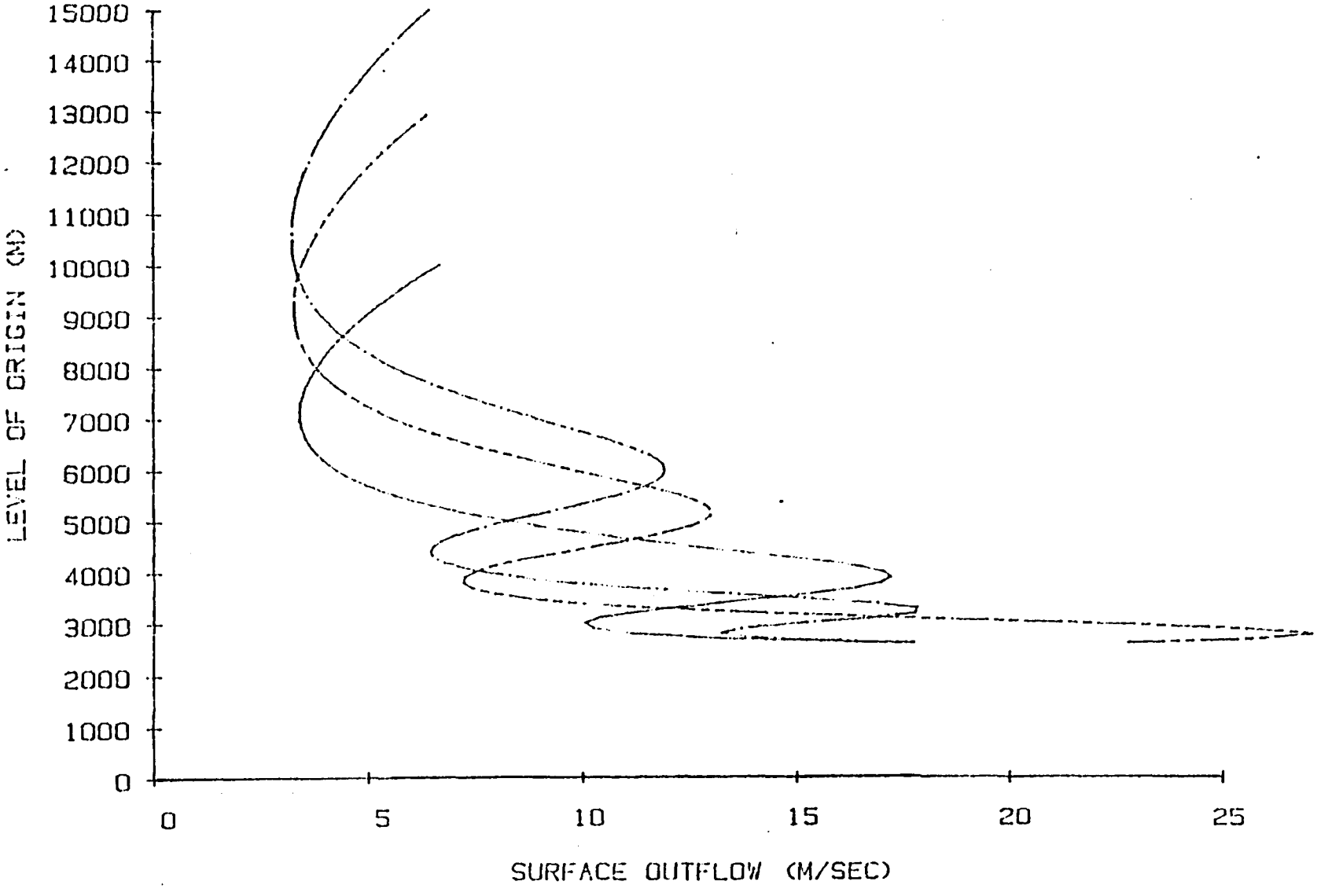

Figure 5.7. Changes in the strength of the surface outflows as the level of origin of the downdraft, H varies from 3000 m to T, for T = 10 km (solid line), T = 13 km (dashed line) and T = 15 km (dash-dot line).

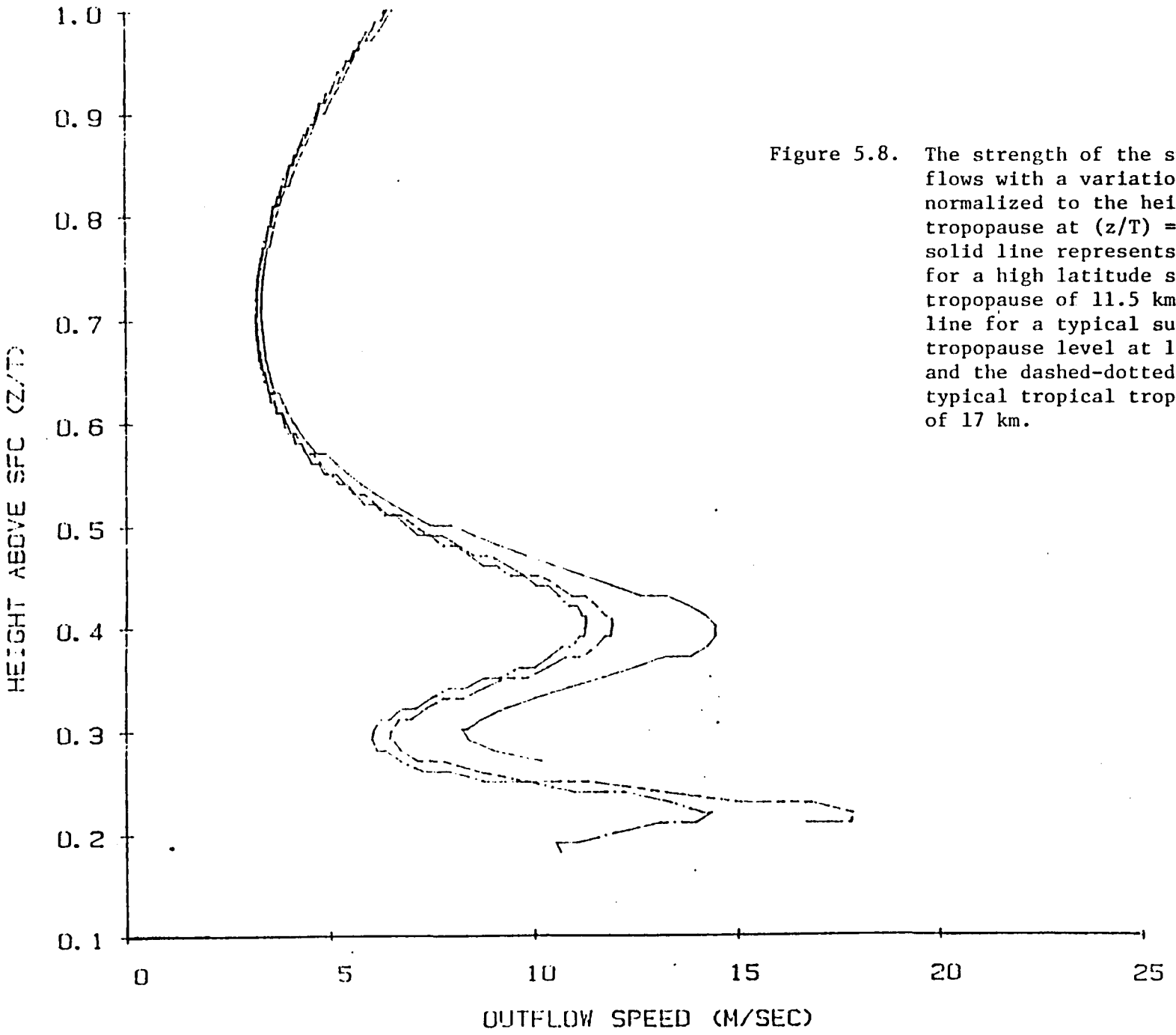

Figure 5.8. The strength of the surface outflows with a variation in H, normalized to the height of the tropopause at (z/T) = 1.0. The solid line represents the results for a high latitude summer tropopause of 11.5 km, the dashed line for a typical summertime tropopause level at 15 km at 30°N, and the dashed-dotted line is for typical tropical tropopause height of 17 km.

In Fig. 5.8 the solid line is the result of setting T = 11.5 km, the dashed line represents a T of 15.0 km (for 30°N), and the dashed-dot line is the tropical height of 17 km.

The graphs show two levels of origin which produce maximum outflows in the lower latitudes, and one level of maximum for the high latitude tropopause level. The two lower levels of maximum outflow available in the lower latitudes result in the type of 'disorganized' flow illustrated by the solid line in Figs. 5.5(c-f). The other, higher maximum at H = 0.40 x T, is available in all latitudes. The minima at H = 0.30 x T and around 0.70 x T are also present for all latitudes. The strength of the outflows produced by downdrafts originating at H = 0.40 x T is greater for the high latitude storms than for the lower latitude ones. Furthermore, this level of optimum production of outflows coincides with the level of minimum equivalent potential temperature in higher latitudes, where thermodynamically, the downdrafts produced would be most intense. The level of the trade wind inversion in the tropics, which is the level of minimum equivalent potential temperature there, is much lower, and the optimum level for downdraft production in Fig. 5.8 does not coincide.

Figures 5.9(a) and (b) show the horizontal and vertical speeds for the optimum levels of H for the three tropopause heights. Since the strongest outflows appear in the lower levels with the strongest upward and outward flows in the upper levels, a possible signal that the outflows in the low levels are at a maximum would be the initial appearance of cirroform anvils in the upper layers of the atmosphere.

This may be useful in selecting suitable candidate cells for analysis.

From this analysis, it would be expected that higher latitude storms are more likely to 'resonate' on the scale of the tropopause height, and so violent, long lived, and propagating convective storms would be more frequent in the higher latitudes than in the tropics.

5.3.2 Outside the Cylinder

The requirement that the space derivative of the radial speed at the edge of each cylinder be continuous leads to a radial speed of

$$u(r,z) = (c + 2)\, u(R,z)\, \frac{R^c}{r^c} - (c + 1)\, u(R,z)\, \frac{R^{c+1}}{r^{c+1}}$$

outside of each cylinder.

The constant c is determined from observations. During the FACE experiment, observations of surface wind fields from a 6.4 x 6.4 km station grid confirmed the findings of the Thunderstorm report that the divergence on the surface beneath moderate rainshafts was on the order of 10^{-3} sec^{-1}.

Figure 5.10 shows the frequency distribution of convergence of various magnitudes associated with maximum daily rainfall as recorded by 66 recording raingages in the FACE array during the summer of 1975. Figure 5.10 shows that > 90% of the time, during the maximum rainfall rate (i.e., when the storm was directly over the raingages and wind stations) convergence $\geq 10^{-3}$ sec^{-1} was generated in the wind station grid.

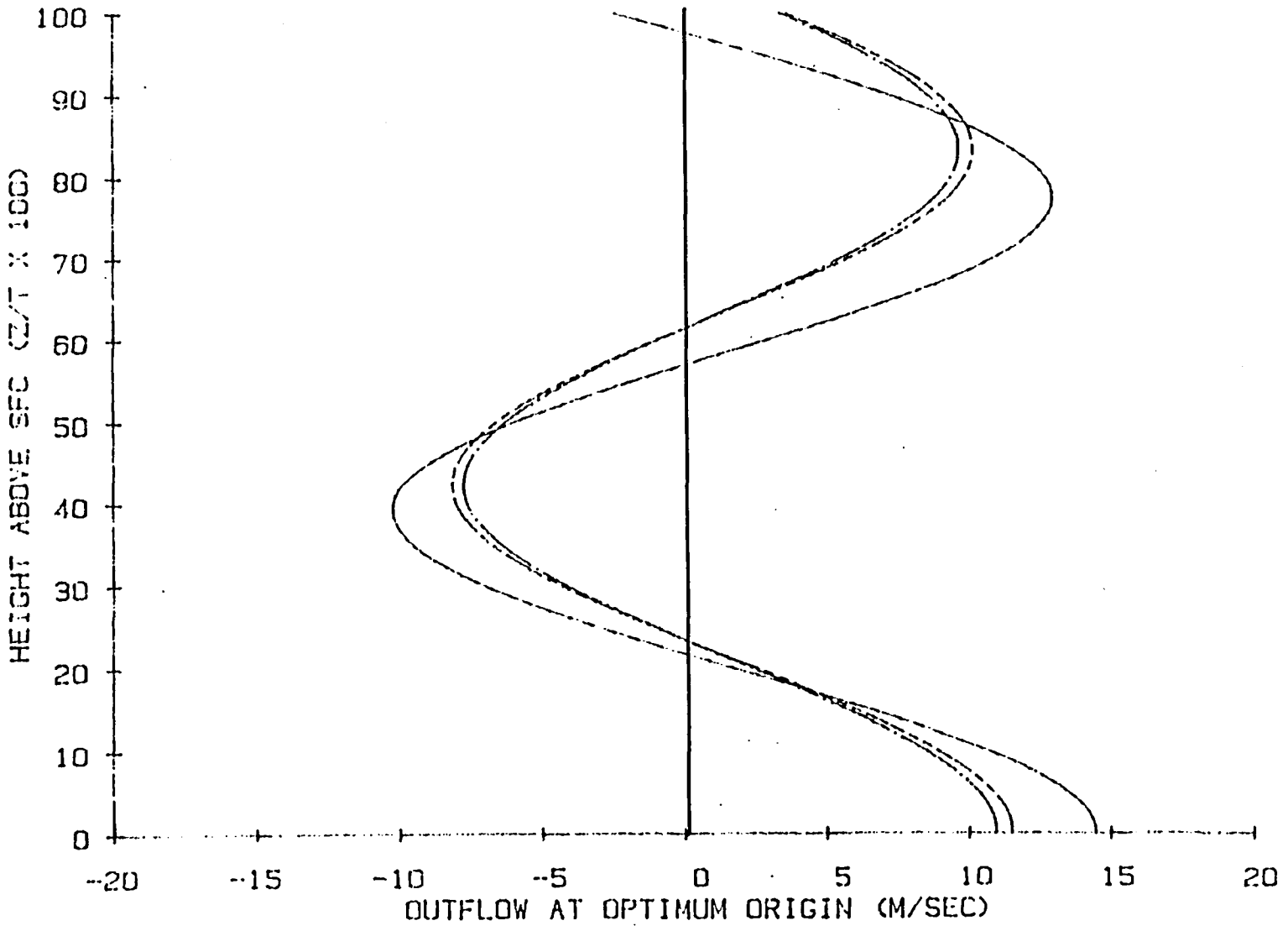

Figure 5.9(a). The horizontal component of wind as a function of height for the three tropopause heights of Fig. 5.8, but with H set at the optimum level to produce the strongest outflows in the lower layers. The height above ground is expressed as a percentage of the height of the tropopause.

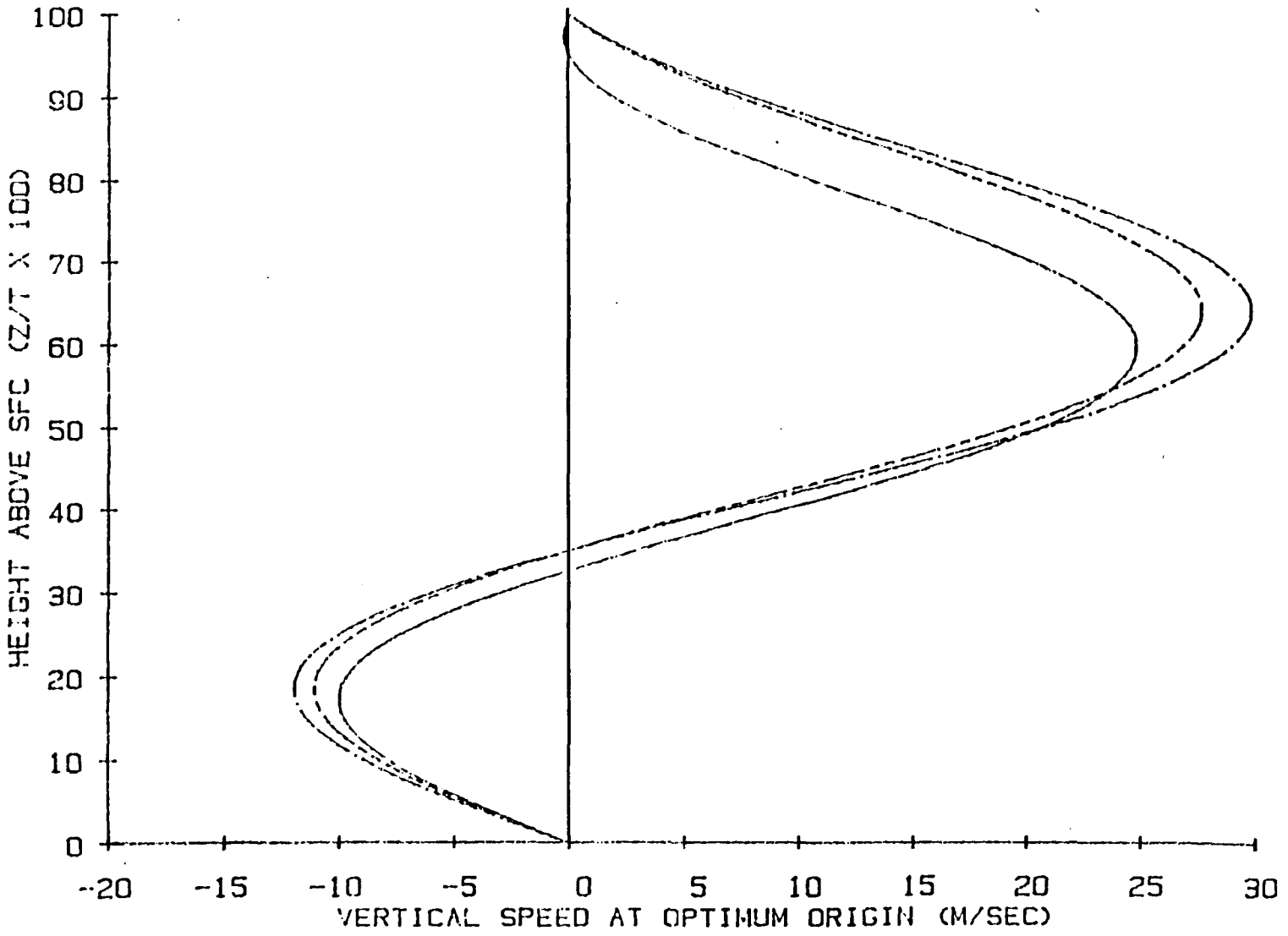

Figure 5.9(b). The same as Fig. 5.9(a) except for the vertical speed.

Figure 5.10. The frequencies of times of onset, before the time of maximum network rainfall, of continuous rainfall greater than 2.5 mm in 15 min at at least one station (thick solid line), and of continuous convergences within the network $\leq -4 \times 10^{-4}$ sec^{-1} (thin solid line), $\leq -6 \times 10^{-4}$ sec^{-1} (dashed) and $\leq -10^{-3}$ sec^{-1} (dash-dot). The rainfall and convergences are continuous within the network from the time of onset to the time of maximum network rainfall rate.

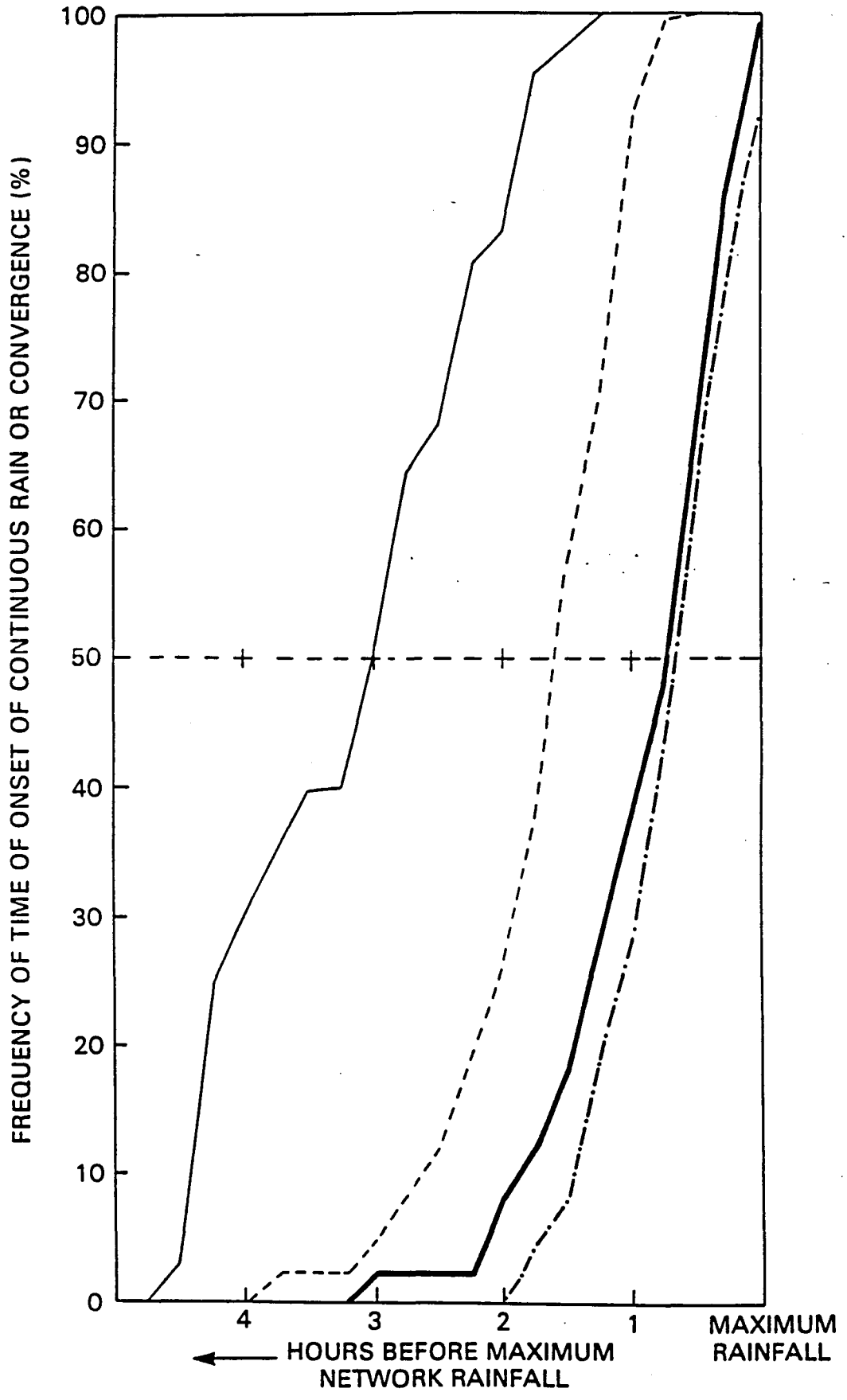
FREQUENCY OF TIME OF ONSET OF CONTINUOUS RAIN OR CONVERGENCE (%)
100
90
80
70
60
50
40
30
20
10
0
4
3
2
1
MAXIMUM RAINFALL
HOURS BEFORE MAXIMUM NETWORK RAINFALL

Figure 5.10.

The typical area of radar returns of 35 dBz in Florida was found by Gagin and Lopez (1985) to be about 30 km^2. This translates into a circular area of radius 3.09 km. To find the value of c, nine 2 x 2 km pixels with 35 dBz were placed at the center of a 6.4 x 6.4 km grid. The algorithm was set up with a vertical speed value at the top of the Florida boundary layer ($\sim$ 300 m) appropriate to divergence of 10^{-3} sec^{-1} at 4 meter height, which was the height of the anemometers during FACE.

The algorithm was then run with an all-top height of 6.8 km AGL (from Gagin and Lopez (1985)) in a zero-shear environment. The constant c was then numerically adjusted so that divergence of 10^{-3} sec^{-1} was generated in the 6.4 x 6.4 km square beneath the echo. The value of c was found to be 1.9165.

Values of dBz were divided into six categories as in the Table 5.1 below, and the divergence associated with each category of dBz weighted relative to 35 dBz and 10^{-3} sec^{-1}.

$$\text{i.e.,} \quad DIV(L) = 10^{-3}\left[\frac{DBZ(L)}{35}\right]^{1/1.5}$$

where the exponent 1/1.5 is taken from the Marshall-Palmer Z-R relationship.

Table 5.1.

DBZ(L)	L	DIV(L) * 10^{-3} sec^{-1}
37.5	1	1.047
42.5	2	1.138
47.5	3	1.226
52.5	4	1.311
57.5	5	1.393
$\geq$ 62.5	6	1.472

5.3.3 The Inclusion of Shear

Shear is included in two ways, first by assuming that the air being emitted through the sides of each cylinder carries with it the momentum of the middle layer air (this effect is assumed to decay radially at the same rate as does the radial component of the cylindrical flow), and second, by the advection of these effects in the direction of the appropriate shear vector for a period of five minutes (the approximate time between radar scans).

Relative to the moving cylinder, the horizontal velocity field of the environment is

$$\vec{V} = -\left[(ULO - ULZ)\hat{i} + (VLO - VLZ)\hat{j}\right]$$

where $\vec{V}_o = ULO\hat{i} + VLO\hat{j}$

is the motion vector of the cylinder, and

$$\vec{V}_L = ULZ\hat{i} + VLZ\hat{j}$$

is the motion vector of the larger-scale environmental flow at any level. We set UM = $\vec{V} \cdot i$ and VM = $\vec{V} \cdot j$.

Then the advection terms can be written as

$$u \frac{\partial u}{\partial x} = (u_x - um) \left[\frac{\partial u_x}{\partial x} - \frac{\partial um}{\partial x}\right]$$

where u_x is the component of the radial speed in the $\hat{i}$ direction. We will have similar terms in the j-direction.

We take the acceleration over a period of time Δt to be approximately

$$\Delta u = - \left[u \frac{\partial u}{\partial x} + v \frac{\partial u}{\partial y}\right] \frac{\Delta t}{2} \qquad (1)$$

Here we divide by 2 to get an "average" 5-minute wind speed.

In the advection terms,

$$\frac{\partial ux}{\partial x} = \frac{\partial}{\partial x} \left[u(r,z) \cos\theta\right]$$

$$= \frac{\partial}{\partial x} \left[u_o f(r) \frac{x}{r}\right] \quad ,$$

where $f(r) = (c + 2) \frac{R^c}{r^c} - (c + 1) \frac{R^{c+1}}{r^{c+1}}$

Here $u_o = u(R,z)$, and θ is the angle $\vec{r}$ makes with the $\hat{i}$-direction.

Then

$$\frac{\partial ux}{\partial x} = u_o \left[\frac{f(r)}{r} + \cos^2\theta \left(\frac{\partial f}{\partial r} - \frac{f(r)}{r}\right)\right] .$$

Assuming the same radial decay rate for the momentum carried with the radial outflow

$$\frac{\partial um}{\partial x} = um \cos\theta \frac{\partial f}{\partial r}$$

also $$\frac{\partial ux}{\partial y} = u_o \left[\cos\theta \sin\theta \left(\frac{\partial f}{\partial r} - \frac{f(r)}{r}\right)\right]$$

and $$\frac{\partial um}{\partial y} = um \sin\theta \frac{\partial f}{\partial r} \quad .$$

Similar calculations can be made for

$$\frac{\partial v_y}{\partial x}, \quad \frac{\partial v_y}{\partial y}, \quad \frac{\partial v_m}{\partial x} \quad \text{and} \quad \frac{\partial v_m}{\partial y},$$

and the accelerations at a point due to advection can be estimated by assuming the conditions to be steady over the period of one radar scan.

Table 5.2 below is a list of a series of tests using the average Florida 35 dBz cell mentioned above with varying advection times and varying shears and grid sizes.

Table 5.2.

Figure	GRID SIZE (km)	ULZ ($m\ s^{-1}$)	VLZ ($m\ s^{-1}$)	ULO ($m\ s^{-1}$)	VLO ($m\ s^{-1}$)	Δt (sec)
A.1	2x2	-5.0	0	10.0	0	300
A.2	5x5	-5.0	0	10.0	0	300
A.3	10x10	-5.0	0	10.0	0	300
A.4	2x2	-5.0	0	10.0	0	150
A.5	2x2	-5.0	0	10.0	0	60
B.1	2x2	-5.0	0	0	0	300
B.2	2x2	0	0	10.0	0	300
B.3	2x2	5.0	0	-10.0	0	300
B.4	2x2	3.53	3.53	-7.07	-7.07	300
B.5	2x2	-3.53	-3.53	7.07	7.07	300
B.6	10x10	0	0	10.0	0	300

In looking at Figures 5.A.1 through 5.B.6 one should be aware of the grid sizes. Figures A.1 and A.2 show that a 5x5 grid spacing retains the form of the low-level convergence fields generated by the algorithm. Even at 10x10 km resolution (Fig. 5.A.3) the general sense of the fields is retained, but at this resolution, we are likely to lose some of the important regions of convergence due to an unhappy relative positioning of radar pixels on grid points. The radar pixels are of course totally independent of the grid point spacing. Figures A.5, A.4 and A.1 show the effects of increasing the advection time from 1 min to 5 min. Air is 'piled up' on the downshear side of the cylinder as time progresses.

Figure 5.B.1 shows a stationary storm embedded in an easterly low-level flow of 5 m s^{-1}, with the weaker convergence on the eastern flank of the cylinder than in Fig. A.1. Figure 5.B.2 represents the dispersion of momentum from aloft by a storm moving to the east at 10 m s^{-1} through low-level air that is perfectly still. The distribution of westerly momentum from aloft around the storm that is shown is a result of the assumption

that this momentum is carried with the radial flow, and decays in intensity with distance at the same rate that the radial outflow speeds decay. Figure 5.B.6 shows that the amount of momentum re-distributed in this way dwindles rapidly to zero about 10 km from the center of the "storm".

Figures 5.B.3, B.4, and B.5 show how the strong convergence zones rotate around the flanks of the "storm" with varying middle-level and low-level flow.

Wind Field for 32/13/96 @ 2501 LST
Center: 0 0 km from radar

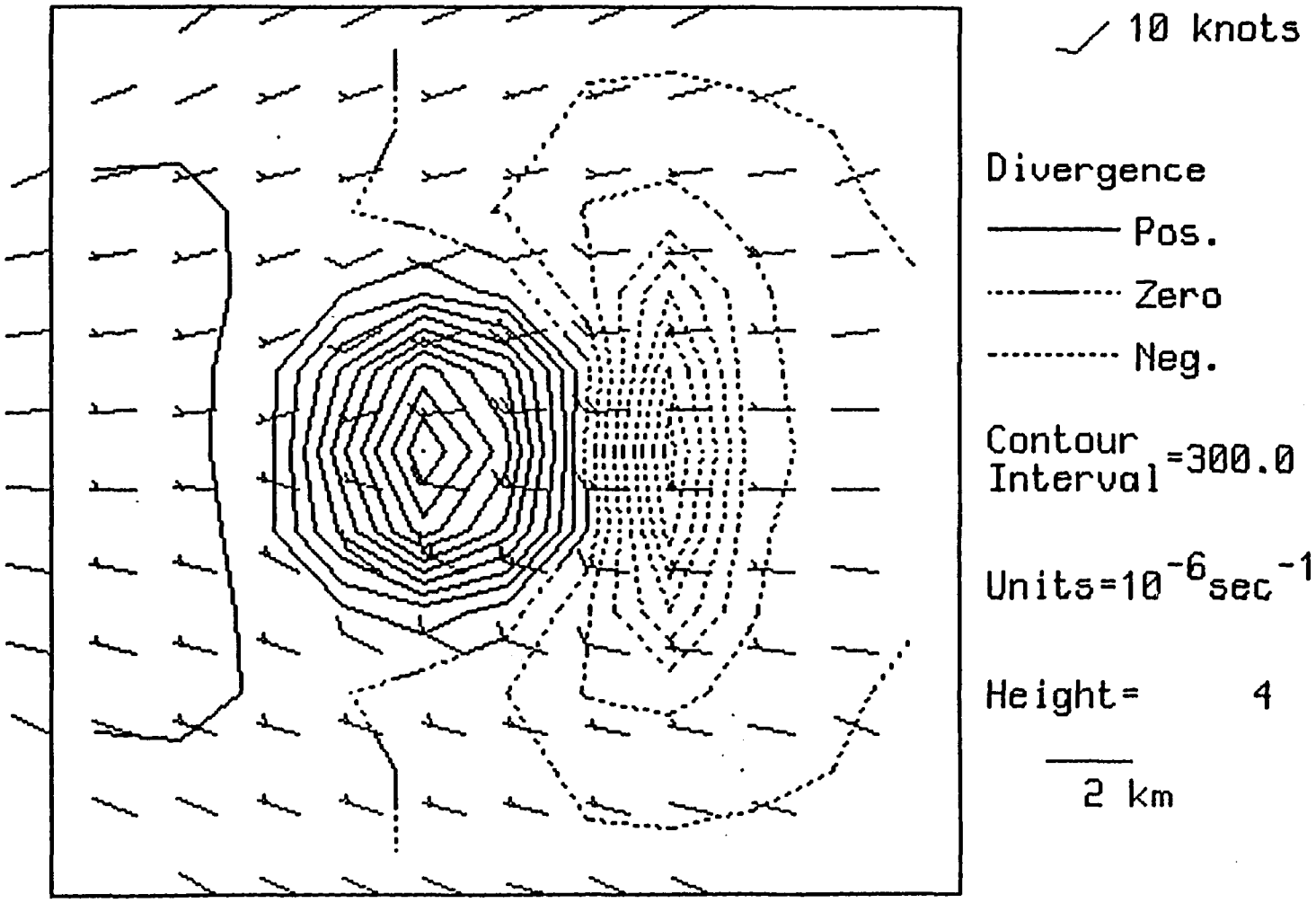

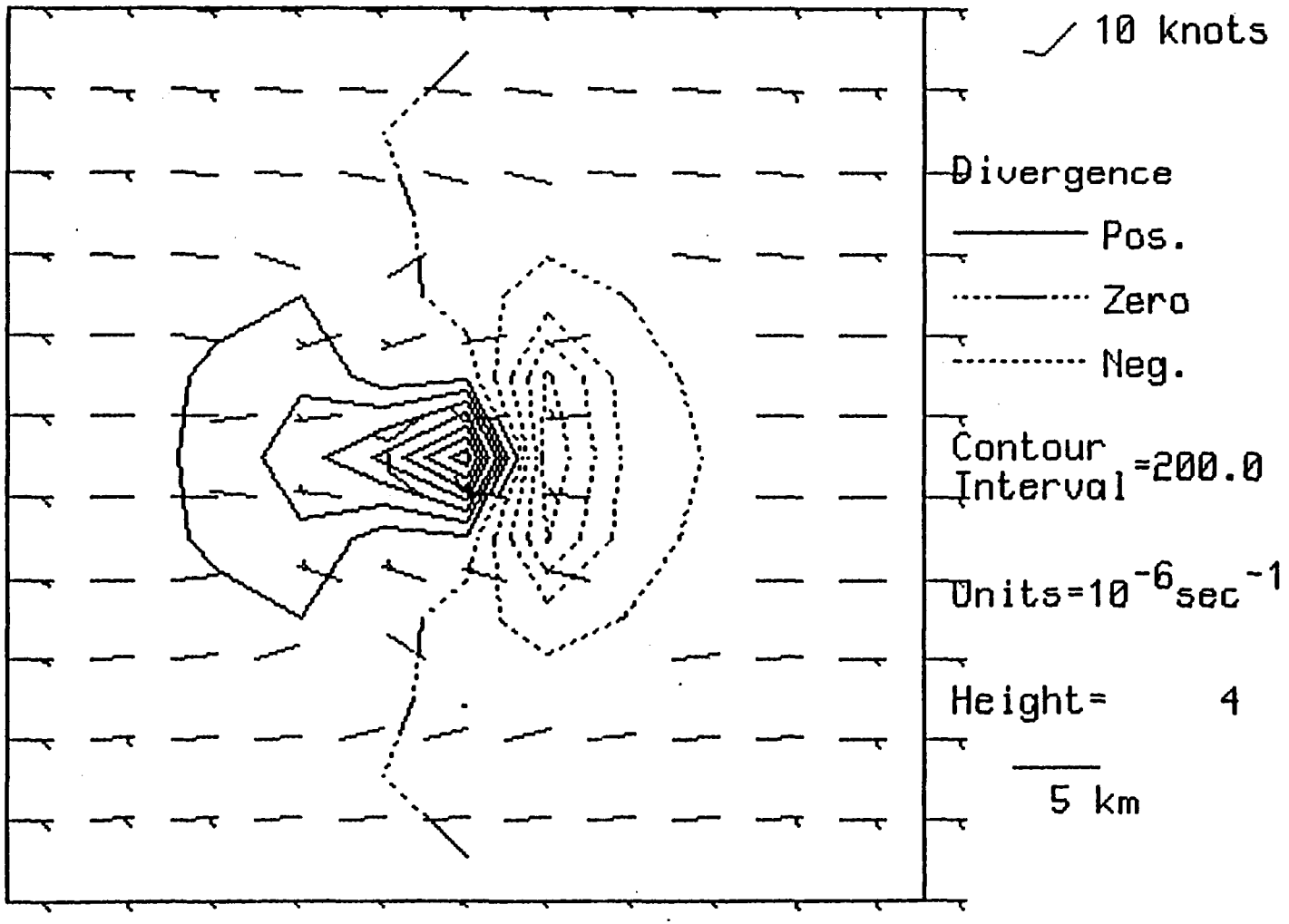
Wind Field for 32/13/96 @ 2501 LST
Center: 0 0 km from radar
10 knots
Divergence
Pos.
Zero
Neg.
Contour Interval =200.0
Units=10^-6 sec^-1
Height= 4
5 km

A.2

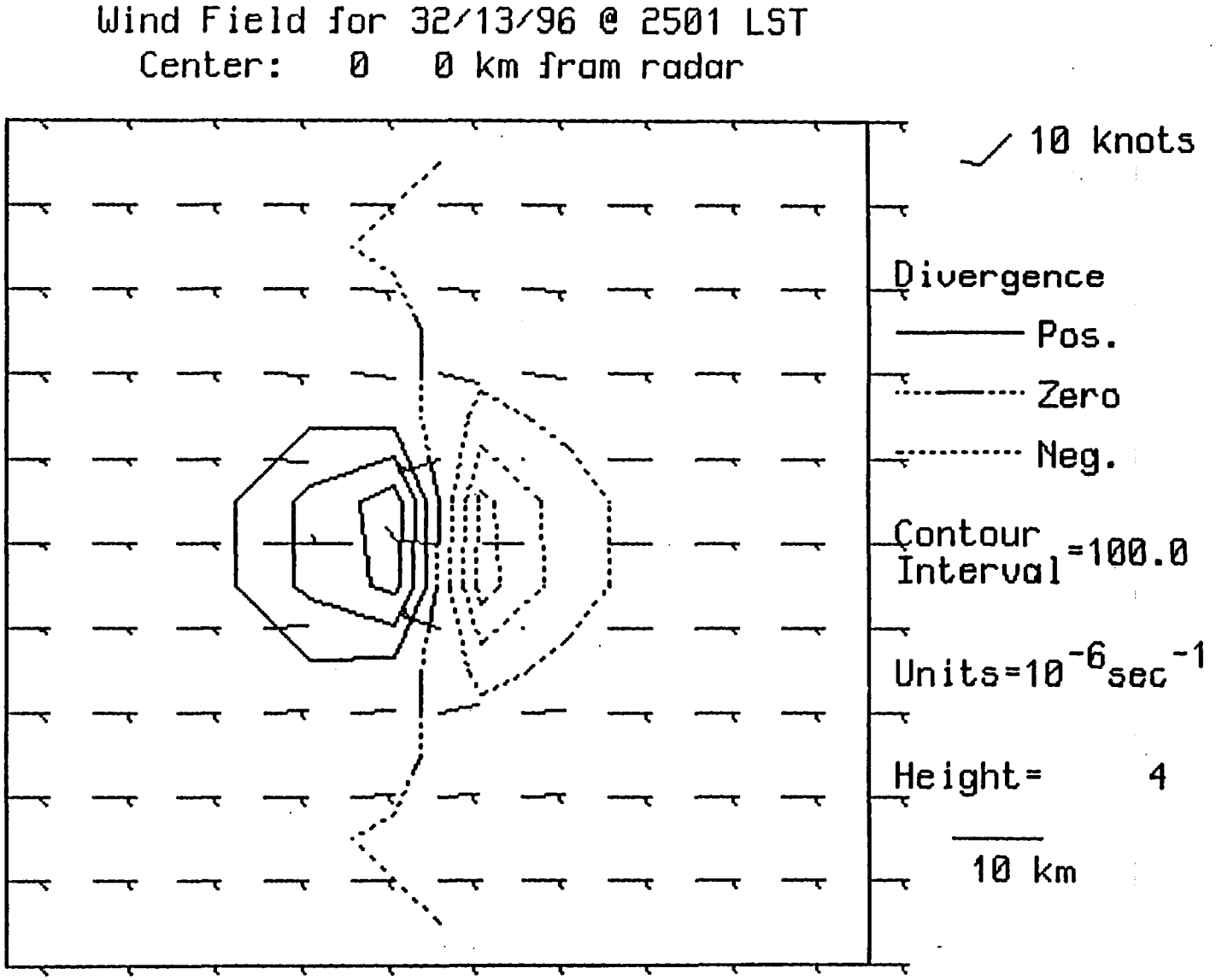
Wind Field for 32/13/96 @ 2501 LST
Center: 0 0 km from radar
10 knots
Divergence
Pos.
Zero
Neg.
Contour Interval=100.0
Units=10^-6 sec^-1
Height= 4
10 km

Wind Field for 32/13/96 @ 2501 LST
Center: 0 0 km from radar

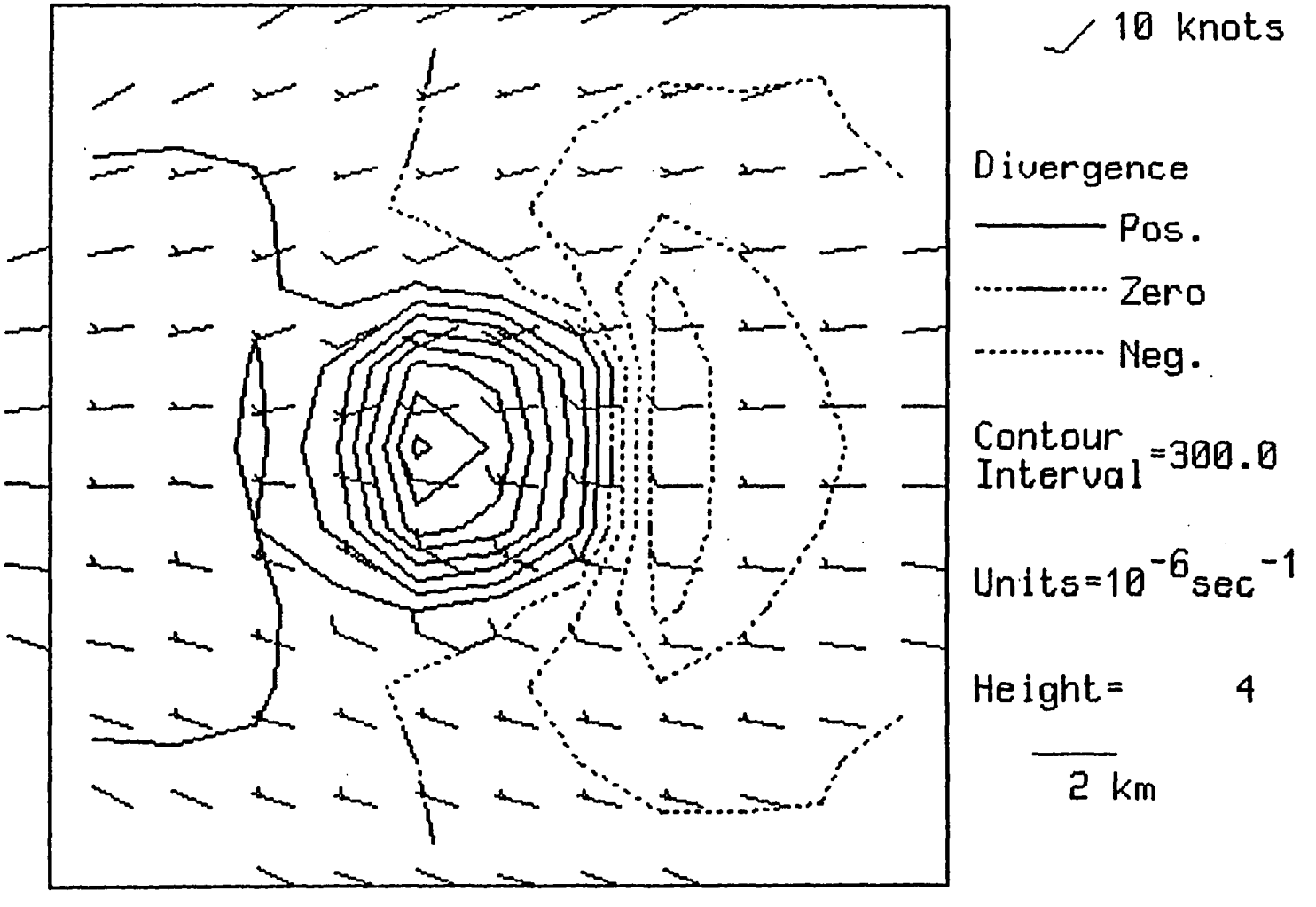

A.4

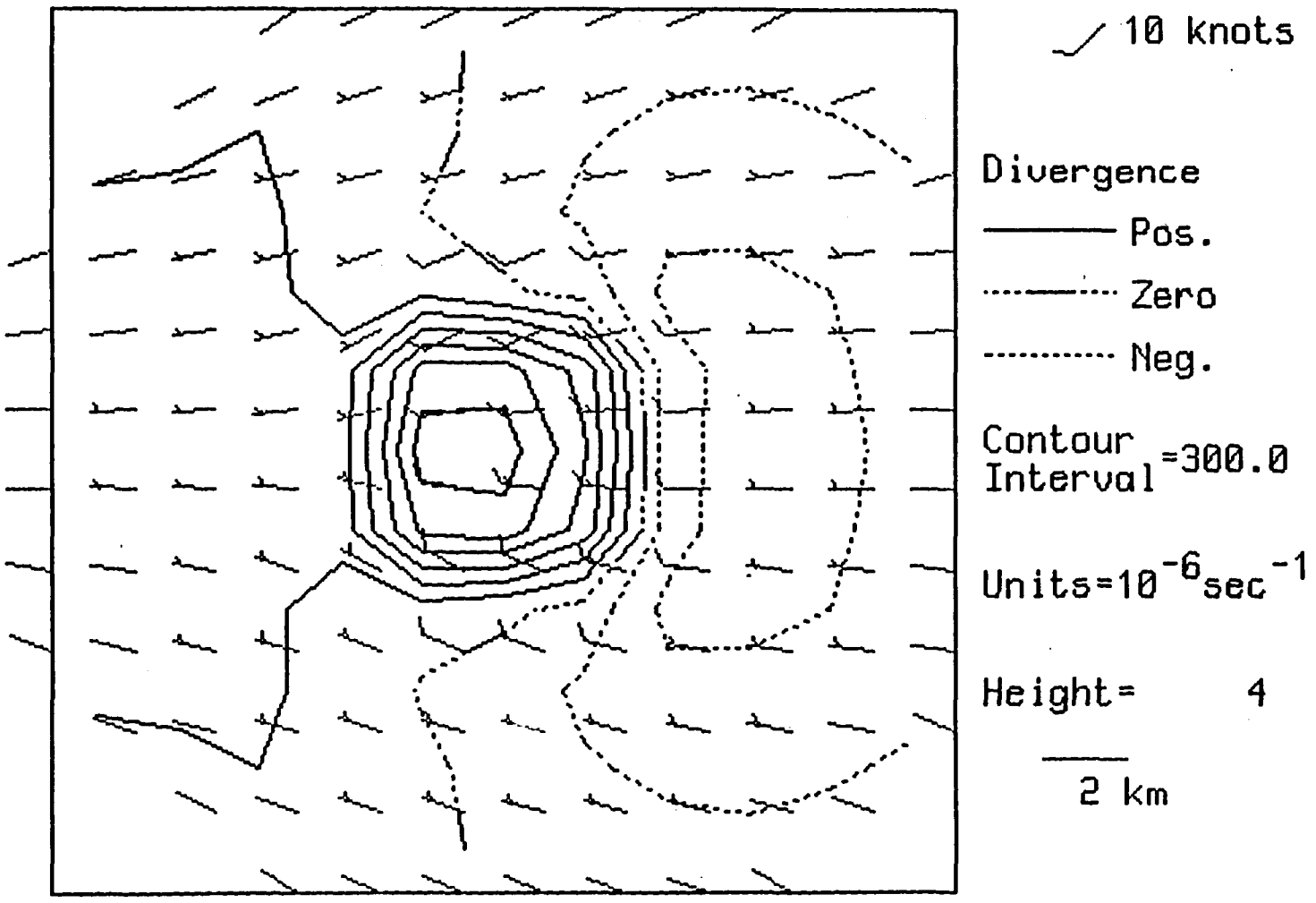
Wind Field for 32/13/96 @ 2501 LST
Center: 0 0 km from radar
10 knots
Divergence
Pos.
Zero
Neg.
Contour Interval=300.0
Units=10^-6 sec^-1
Height= 4
2 km

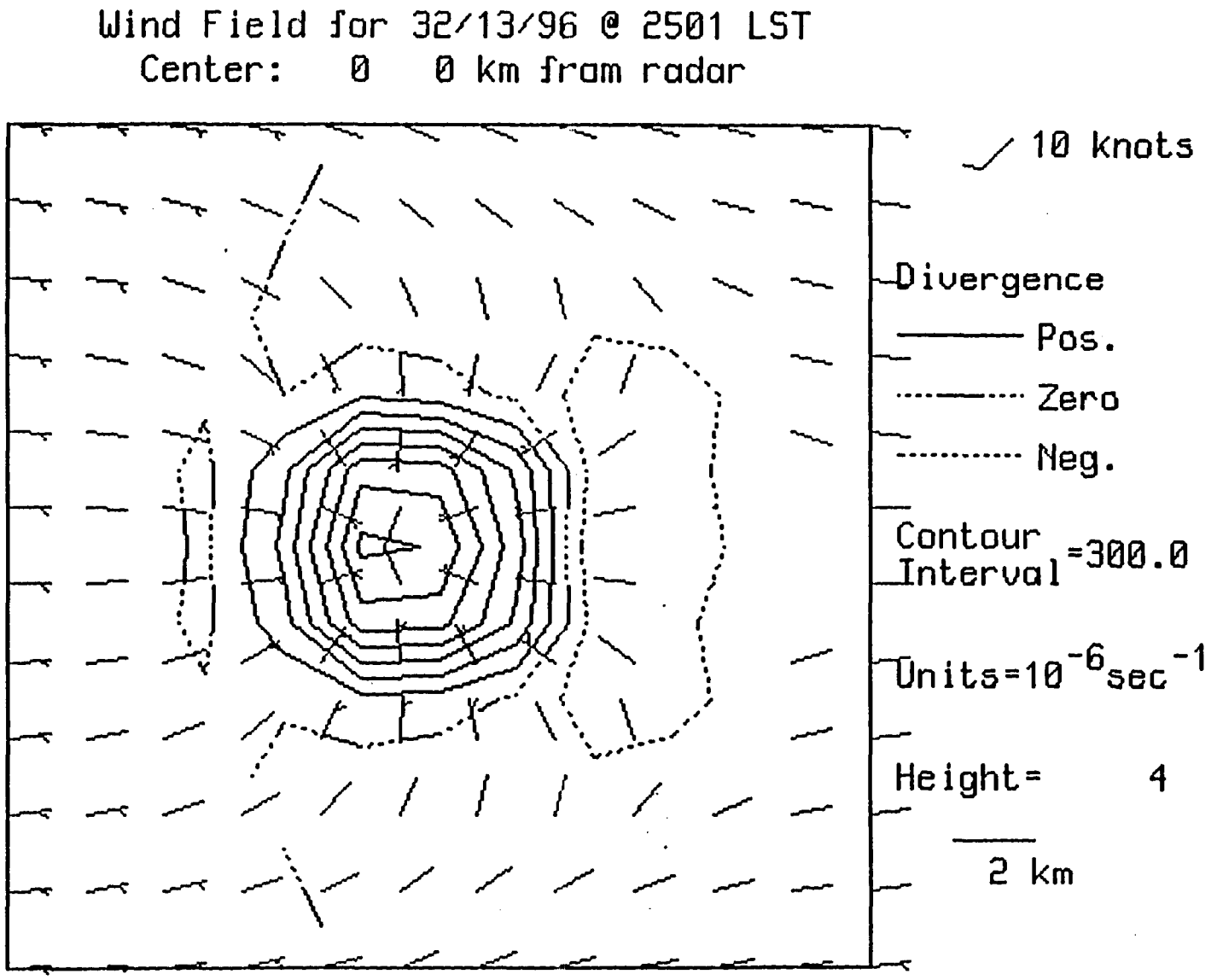
Wind Field for 32/13/96 @ 2501 LST
Center: 0 0 km from radar
10 knots
Divergence
Pos.
Zero
Neg.
Contour Interval =300.0
Units=10^-6 sec^-1
Height= 4
2 km

B.1

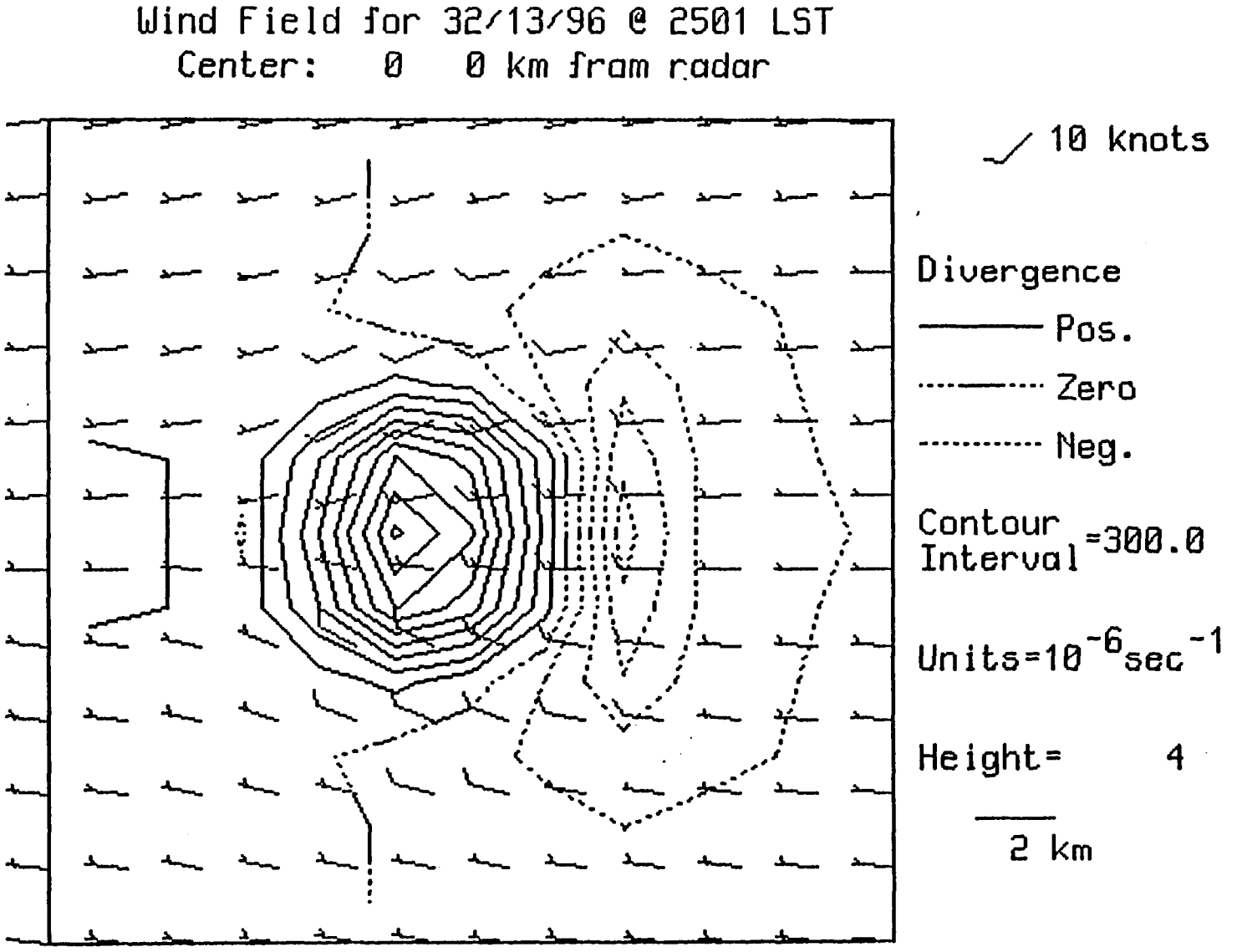
Wind Field for 32/13/96 @ 2501 LST
Center: 0 0 km from radar
10 knots
Divergence
Pos.
Zero
Neg.
Contour Interval =300.0
Units=10^-6 sec^-1
Height= 4
2 km

B.2

Wind Field for 32/13/96 @ 2501 LST
Center: 0 0 km from radar

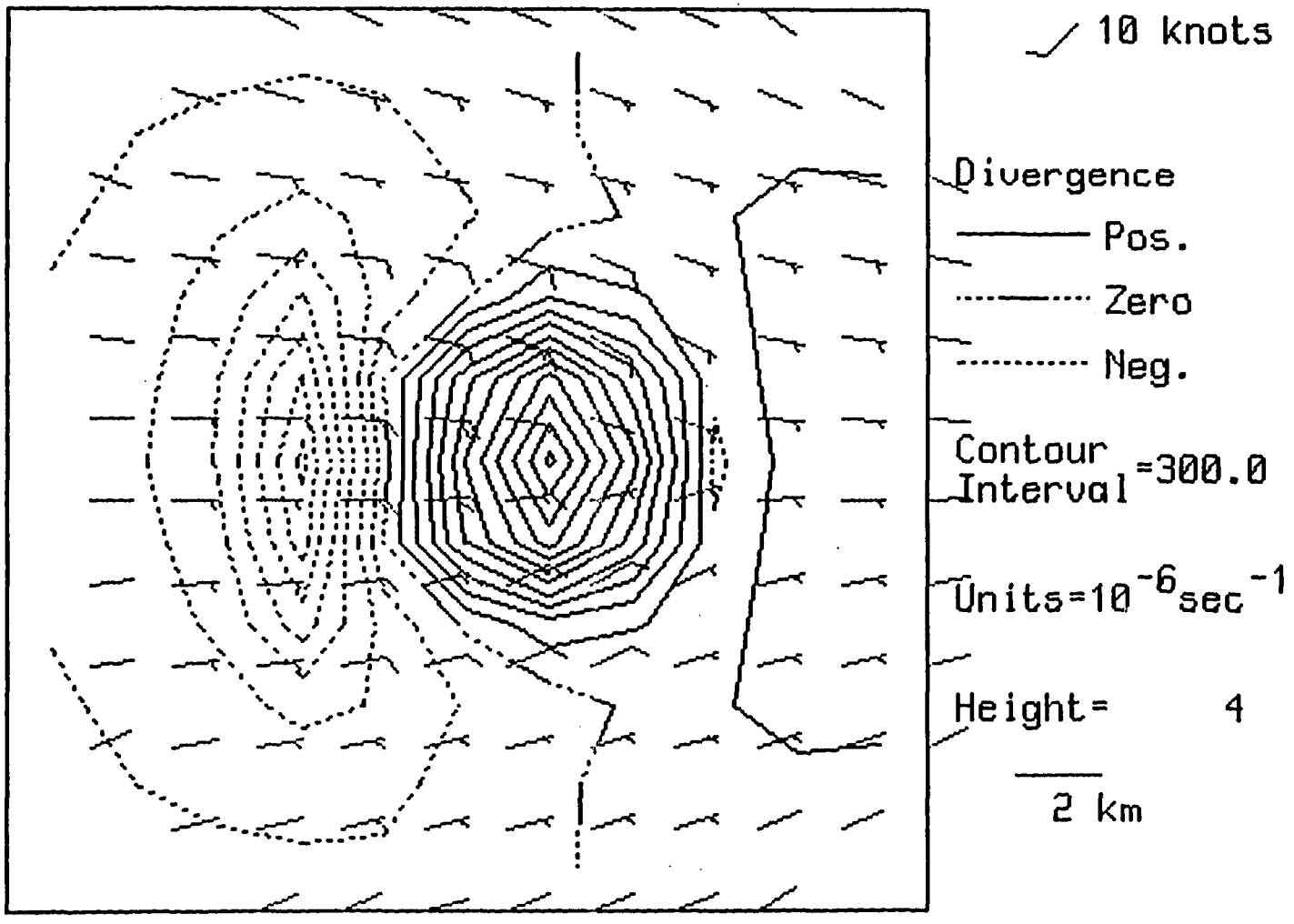

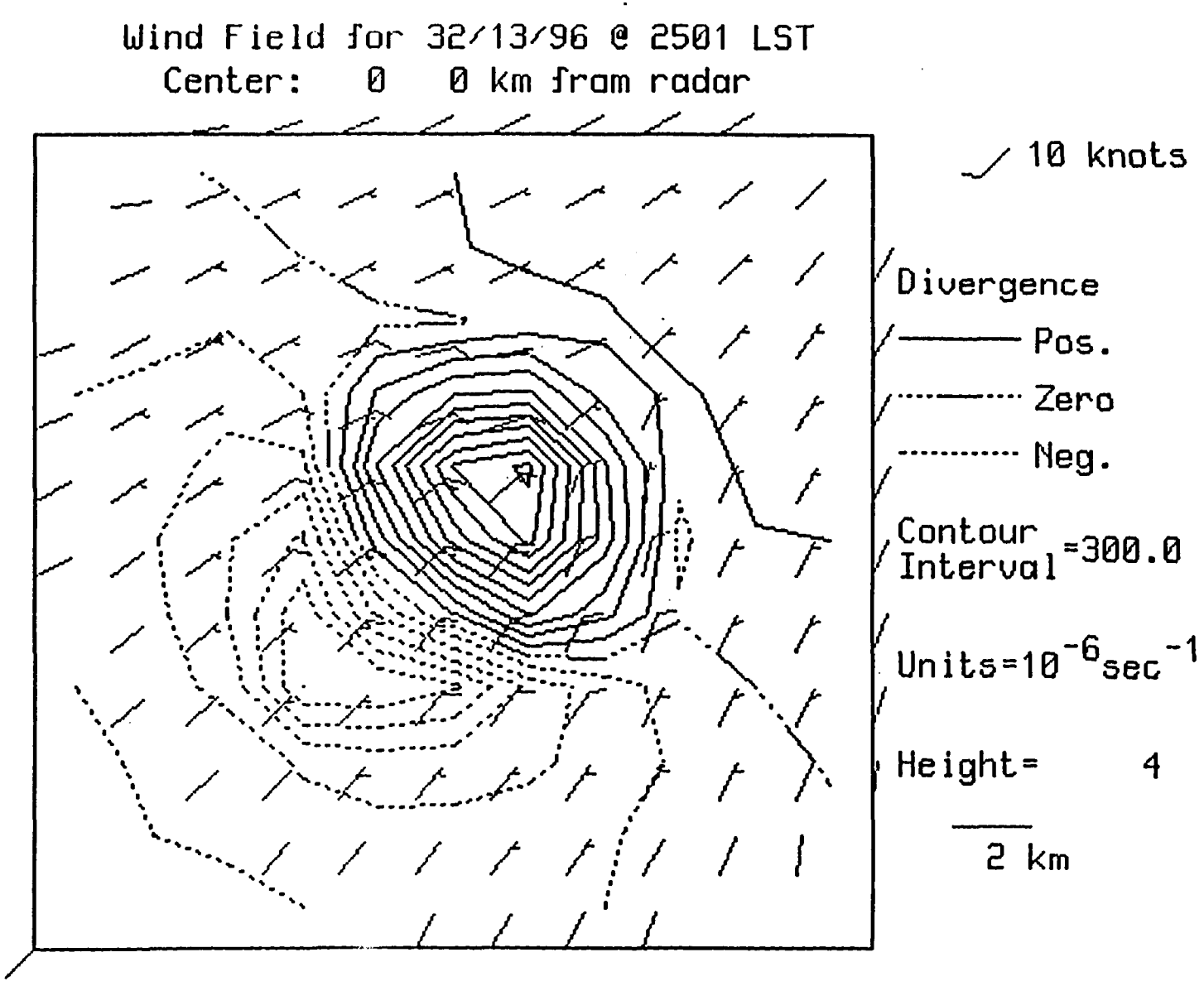
Wind Field for 32/13/96 @ 2501 LST
Center: 0 0 km from radar
10 knots
Divergence
Pos.
Zero
Neg.
Contour Interval=300.0
Units=10^-6 sec^-1
Height= 4
2 km

B.4

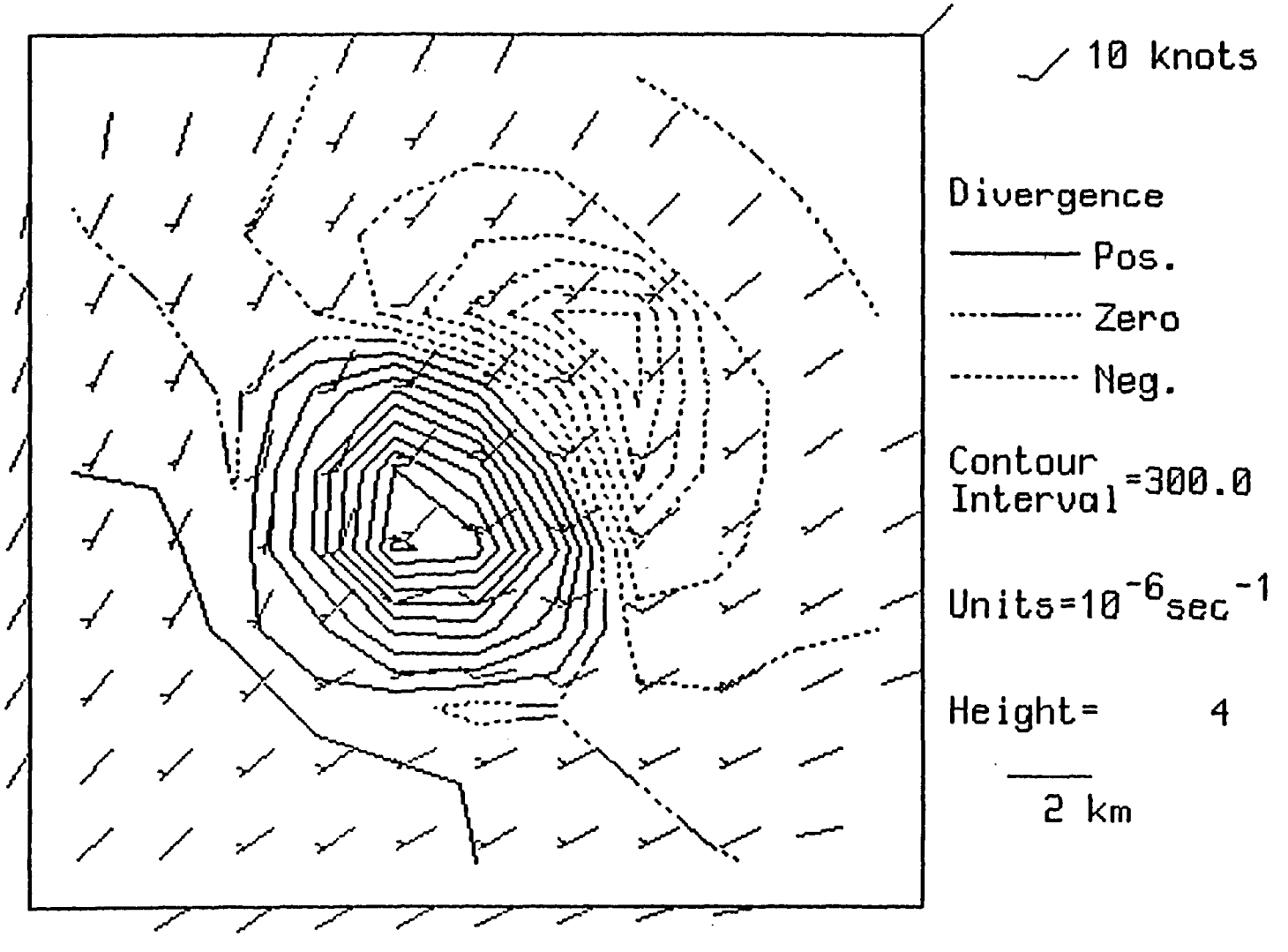
Wind Field for 32/13/96 @ 2501 LST
Center: 0 0 km from radar
10 knots
Divergence
Pos.
Zero
Neg.
Contour Interval =300.0
Units=10^-6 sec^-1
Height= 4
2 km

B.5

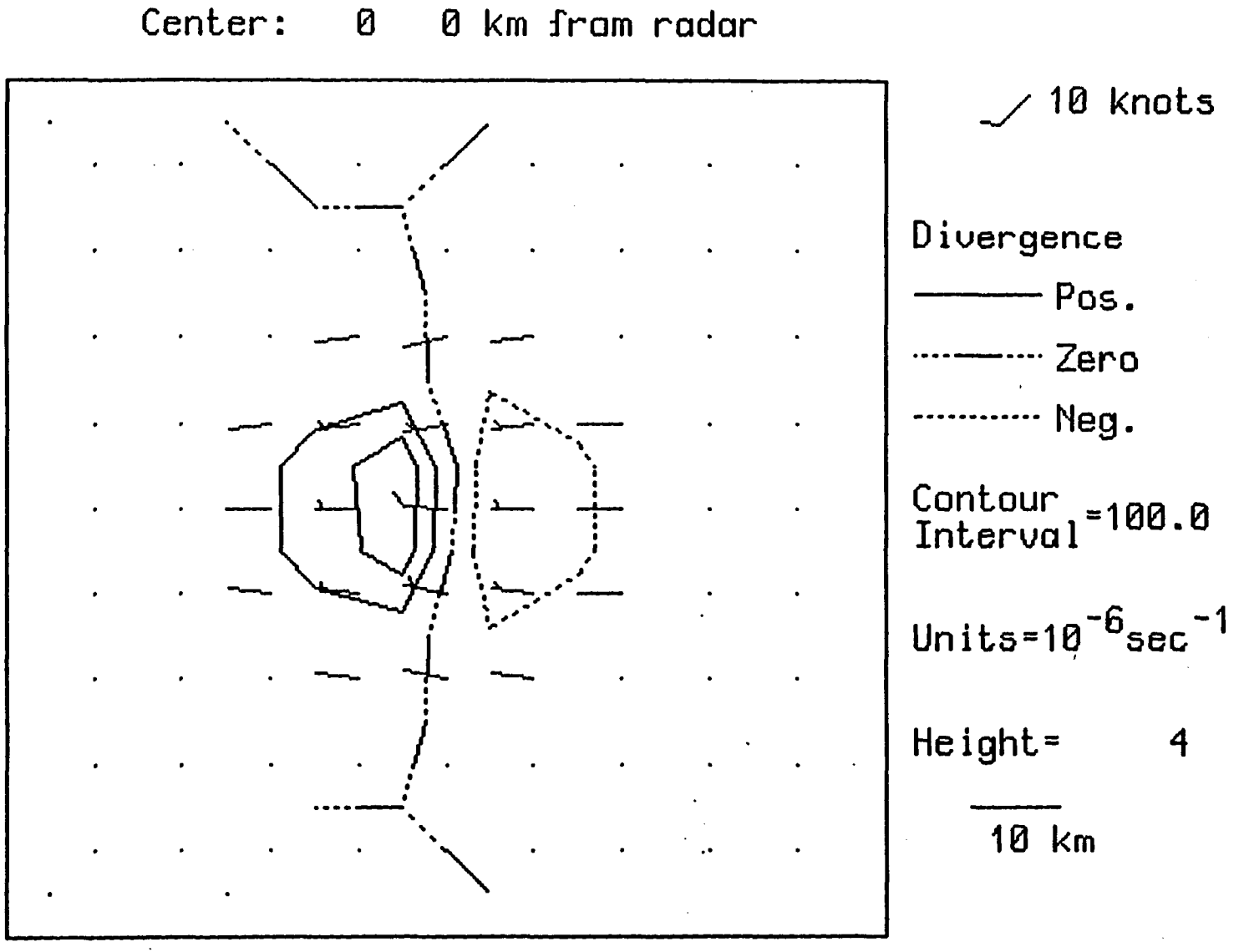
Center: 0 0 km from radar
10 knots
Divergence
Pos.
Zero
Neg.
Contour Interval =100.0
Units=10^-6 sec^-1
Height= 4
10 km

5.4 APPLICATIONS OF THE THUNDERSTORM OUTFLOW AND INTERACTION ALGORITHM USING PAWS DATA

5.4.A NOWCASTING

At present, there is no satisfactory way to observe the details of the kinematic fields within and around convection and convective complexes in the PAWS area. There is no other way to estimate the fine structure (say 5x5 km scale) of the vertical motions around storms except by inference from the conventional radar data which currently is used during operations.

The outflow algorithm outlined in this section has been specifically developed with this problem in mind. The algorithm puts together the radar echo return distribution, the observed vertical shear in the horizontal large scale winds and the conventional wisdom about how low level outflows from storms are likely to interact with one another. It is flexible enough to allow a local forecaster to introduce his/her knowledge of local conditions.

The simplest form of the algorithm has been run on the Nelspruit radar record for twenty days. The twenty days were selected for the variety of the conditions they represent and serve as case studies in the use of the algorithm. They comprise a total of about a thousand five-minute radar records. Six of the twenty days were selected at random for complete analysis.

5.4.1 Observations and Simulations

The rough terrain around Nelspruit was initially cause for concern, and undoubtedly affects the near surface flows from the storms. However, if we insist on using the algorithm in a diagnostic and relative sense, then it will be seen from what follows that useful information can be extracted from the radar record by its application.

First, we examine how the algorithm behaves over flat terrain. During 1979, 27 PAM (Portable Automated Mesonetwork) meteorological stations were deployed in Illinois for use during the VIN (Virginia/Illinois/NOAA) experiment. On 30 July of that year a large, well organized system passed over the network. Figure 5.11(a) shows the area-averaged divergence observed by the PAM system compared to the area-averaged divergence estimated by using the outflow algorithm. Two differences are evident:

1) The algorithm over estimates the area-averaged divergence (positive divergence) and under estimates the area-averaged convergence (negative divergence).

2) The signal produced by the algorithm is out of phase (precedes) with the signal observed.

The first difference in Fig. 5.11(a) can be explained by noting that the algorithm deals only with the convective scale response to the local convective scale rainfall-driven downdrafts, and is totally unaware of any other sources of motion. A reasonable large scale convergence of 10^{-4} s^{-1}

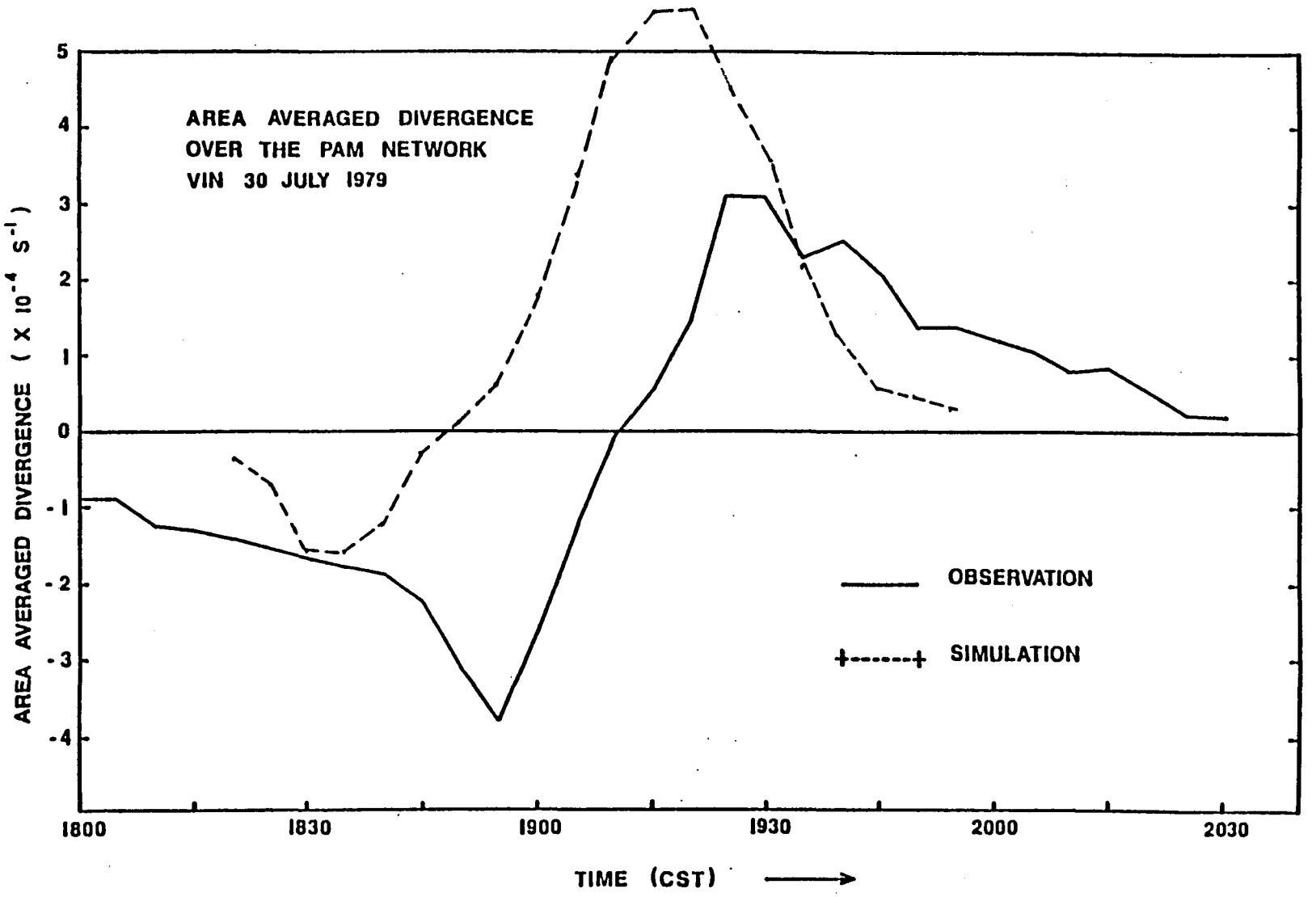
AREA AVERAGED DIVERGENCE
OVER THE PAM NETWORK
VIN 30 JULY 1979
AREA AVERAGED DIVERGENCE (X 10⁻⁴ S⁻¹)
5
4
3
2
1
0
-1
-2
-3
-4
1800
1830
1900
1930
2000
2030
TIME (CST)
OBSERVATION
SIMULATION

Figure 5.11(a).

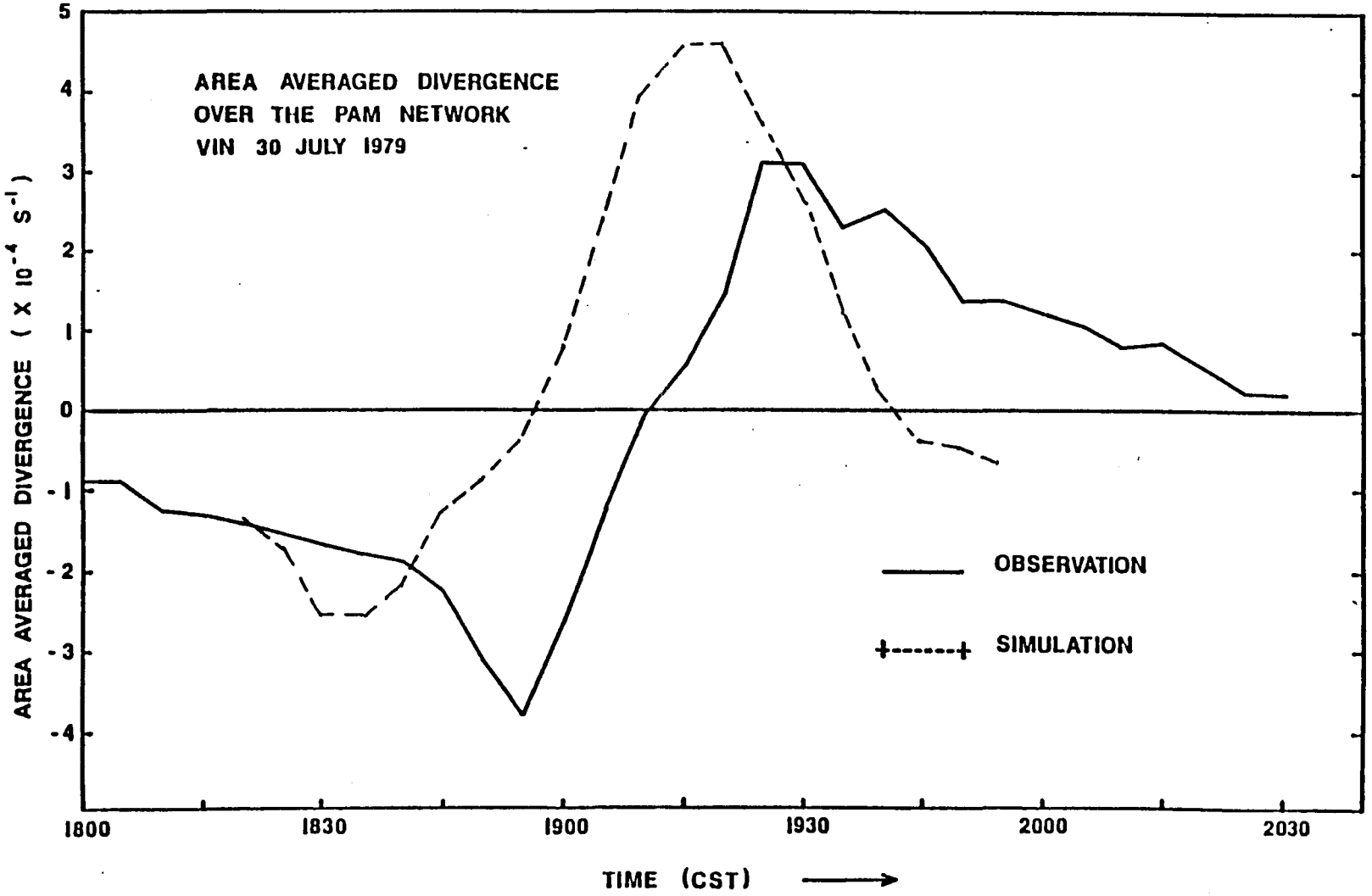
AREA AVERAGED DIVERGENCE
OVER THE PAM NETWORK
VIN 30 JULY 1979
AREA AVERAGED DIVERGENCE (X 10⁻⁴ S⁻¹)
5
4
3
2
1
0
-1
-2
-3
-4
1800
1830
1900
1930
2000
2030
TIME (CST)
OBSERVATION
SIMULATION

Figure 5.11(b).

added to the algorithm area-averaged divergence results in Fig. 5.11(b). Therefore, most of the differences in magnitude between the observed and simulated peaks in area-averaged divergence can be explained by introducing a reasonable background 'larger scale' convergence within which real systems are indeed observed to form.

If, in addition to the larger scale convergence, we assume that there will be a time lag of $\sim$ 10-15 min between the time that the rainfall was observed aloft by radar and the time that it produces outflow as it hits the ground, the phase differences between the observations and simulation disappear. A rain drop fall speed of 5 m s^{-1} from 4.5 km gives a time lag of 15 min. The result of these two adjustments is shown in Fig. 5.11(c). A comparison between the observed surface winds and simulated surface winds for this storm can be found in Figs. 5.4(a) and 5.4(b) in this volume.

The algorithm reproduces the main features (area-averaged convergence, approximate locations of regions of low level convergence and divergence) of the low level kinematic fields. In viewing the results of the calculations, we must bear in mind the phase adjustments and the fact that the algorithm will tend to over estimate divergence and under estimate convergence. We can assume that, given the correct inputs (which include timely upper-air observations), the algorithm will provide a good estimate of the larger scale convectively induced divergence and the general locations of regions of where we would expect to observe maxima and minima in local divergence induced by the interaction of cell outflows. At present, the configuration of the algorithm restricts these applications to the lower levels ($\leq$ 1000 m).

For the VIN case depicted in Fig. 5.11(a)-(c), the network consisted of 27 stations spaced approximately 10 km apart covering an area 50x50 km in length and breadth. The WRC surface wind network deployed around Nelspruit is a much coarser one and is in very rough, mountainous terrain. There were only 9 stations spaced 50 km apart, covering an area with a length scale of about 150 km. We cannot, therefore, expect the values of area-averaged network divergence estimated by the algorithm over this network to be as close to observed values as those obtained for the PAM network. Nevertheless, the algorithm was run for five days when the radar record was long enough to merit a comparison between the estimated divergence and the observed divergence. Figures 5.12(a)-(e) show the results. Again, if we adjust the "background" divergence level on each day, and allow for a 15 min time lag, the agreement is remarkably good. Figures 5.12(a)-(e) are unadjusted. On 7 DEC 85, 7 FEB 86 and 11 FEB 86, the time series in the area-averaged divergence over this coarse and mountainous network area is represented well by the algorithm, suggesting that on these days changes in the area-averaged divergence over the entire network could be attributed mostly to local convection acting within a background of escarpment-scale convergence.

On 3 JAN 86 and 12 FEB 86, the general agreement is not so good after the passage of the main storm system. On 3 JAN 86, both the observed and simulated area-averaged divergence become increasingly divergent until the storm passage, at which point the simulated area-averaged divergence becomes more convergent as the actual observations show a tendency towards greater divergence. Similarly, on 12 FEB 86 later in the day, the observations show an increase in network divergence while the

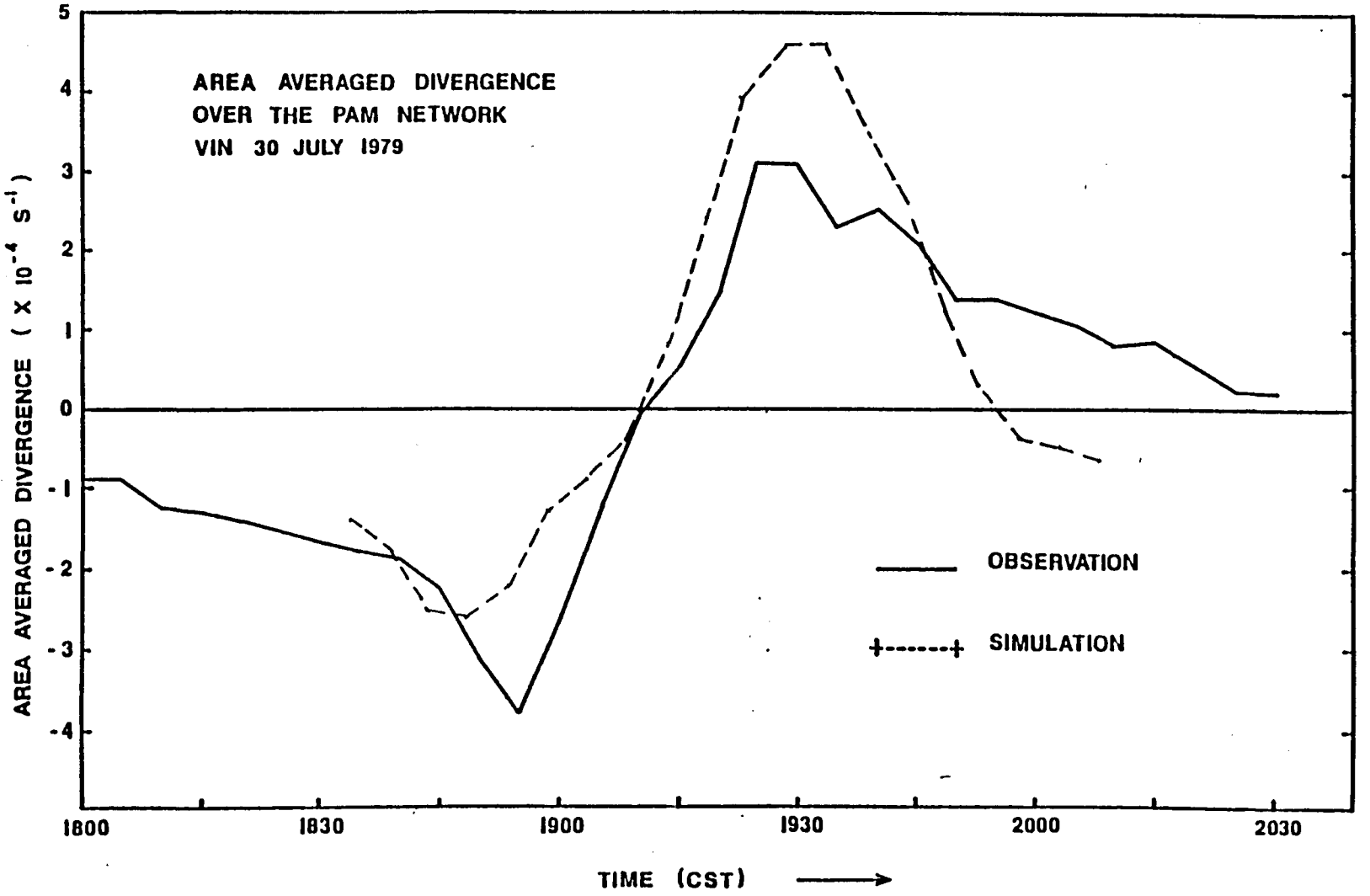
AREA AVERAGED DIVERGENCE
OVER THE PAM NETWORK
VIN 30 JULY 1979
AREA AVERAGED DIVERGENCE (X 10⁻⁴ S⁻¹)
5
4
3
2
1
0
-1
-2
-3
-4
1800
1830
1900
1930
2000
2030
TIME (CST)
OBSERVATION
SIMULATION

Figure 5.11(c).

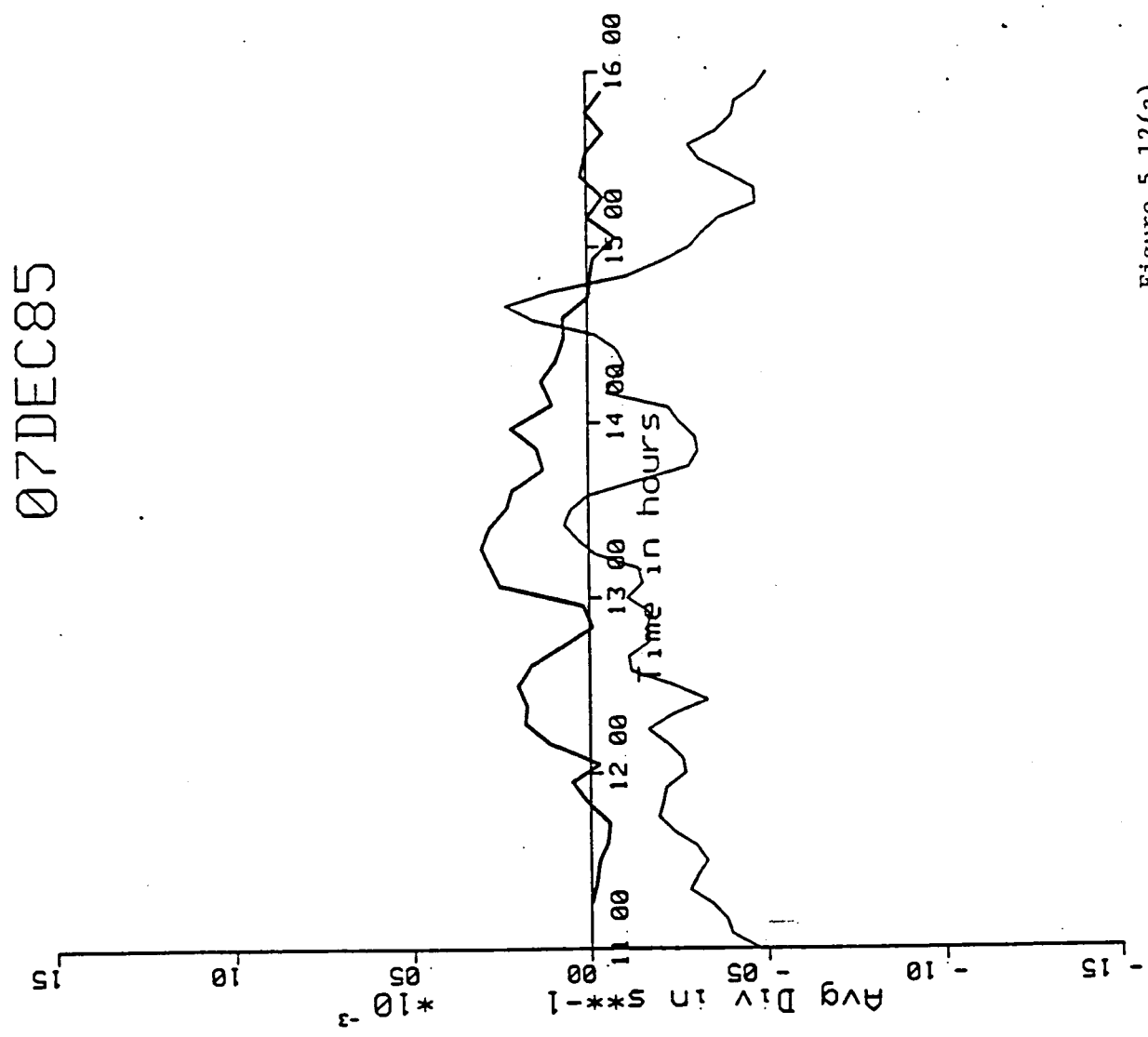
07DEC85
Avg Div in s**-1
*10 -3
-15
-10
-05
00
05
10
15
11 00
12 00
13 00
14 00
15 00
16 00
Time in hours

Figure 5.12(a).

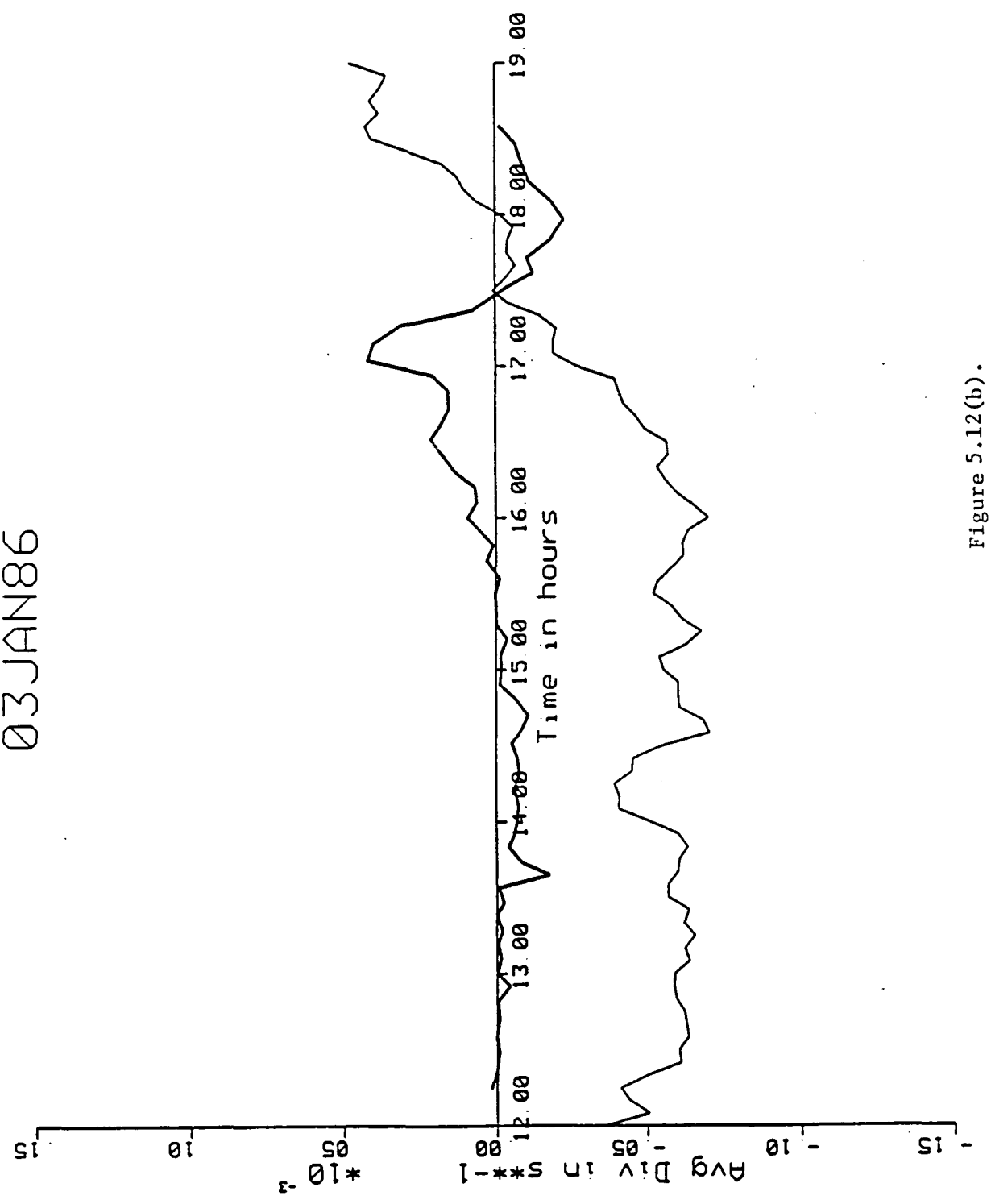
03JAN86
Avg Div in s**-1
*10 -3
-15
-10
-05
00
05
10
15
12.00
13.00
14.00
15.00
16.00
17.00
18.00
19.00
Time in hours

Figure 5.12(b).

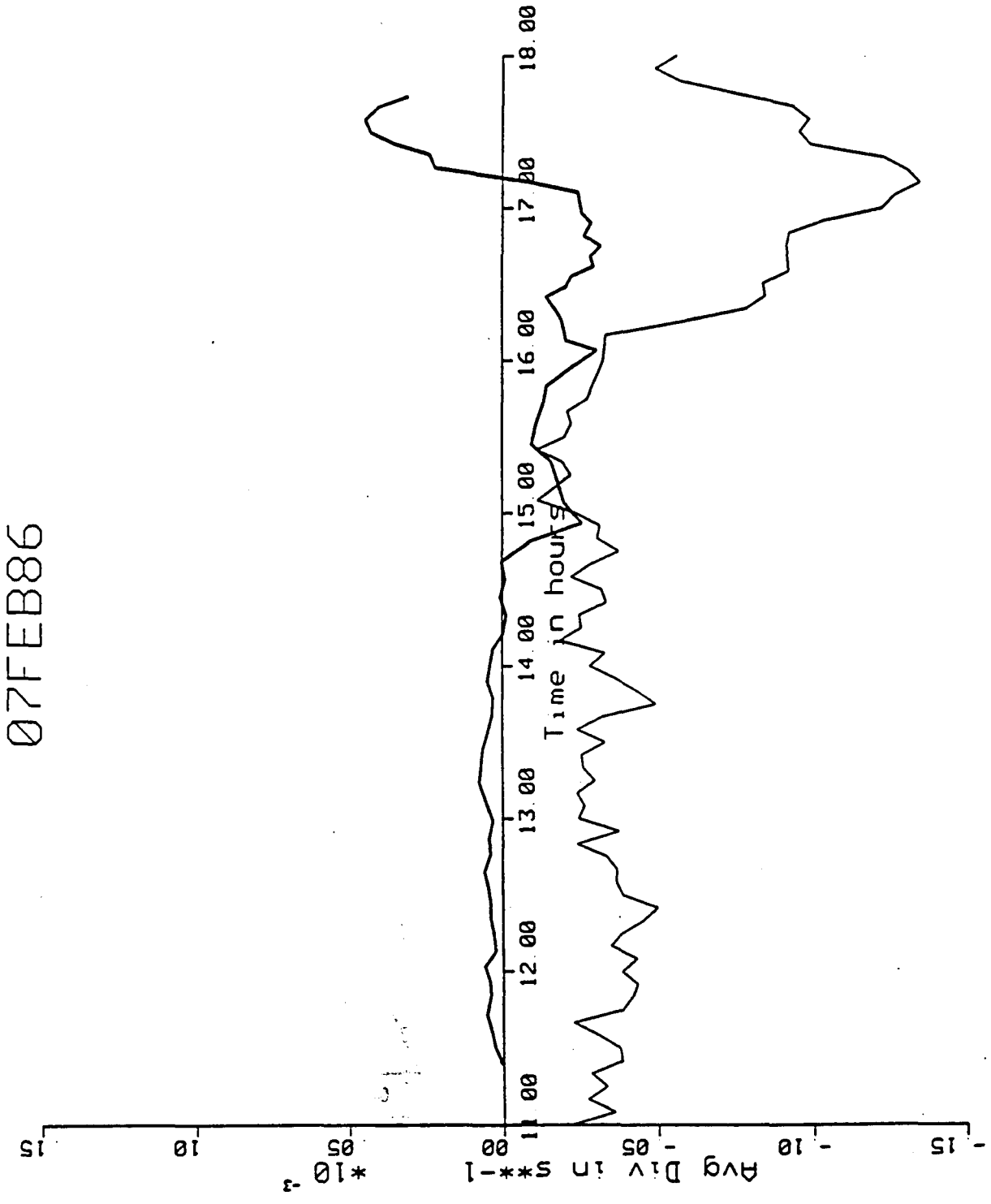
07FEB86
Avg Div in s**-1
*10 -3
-15
-10
-05
00
05
10
15
11.00
12.00
13.00
14.00
15.00
16.00
17.00
18.00
Time in hours

Figure 5.12(c).

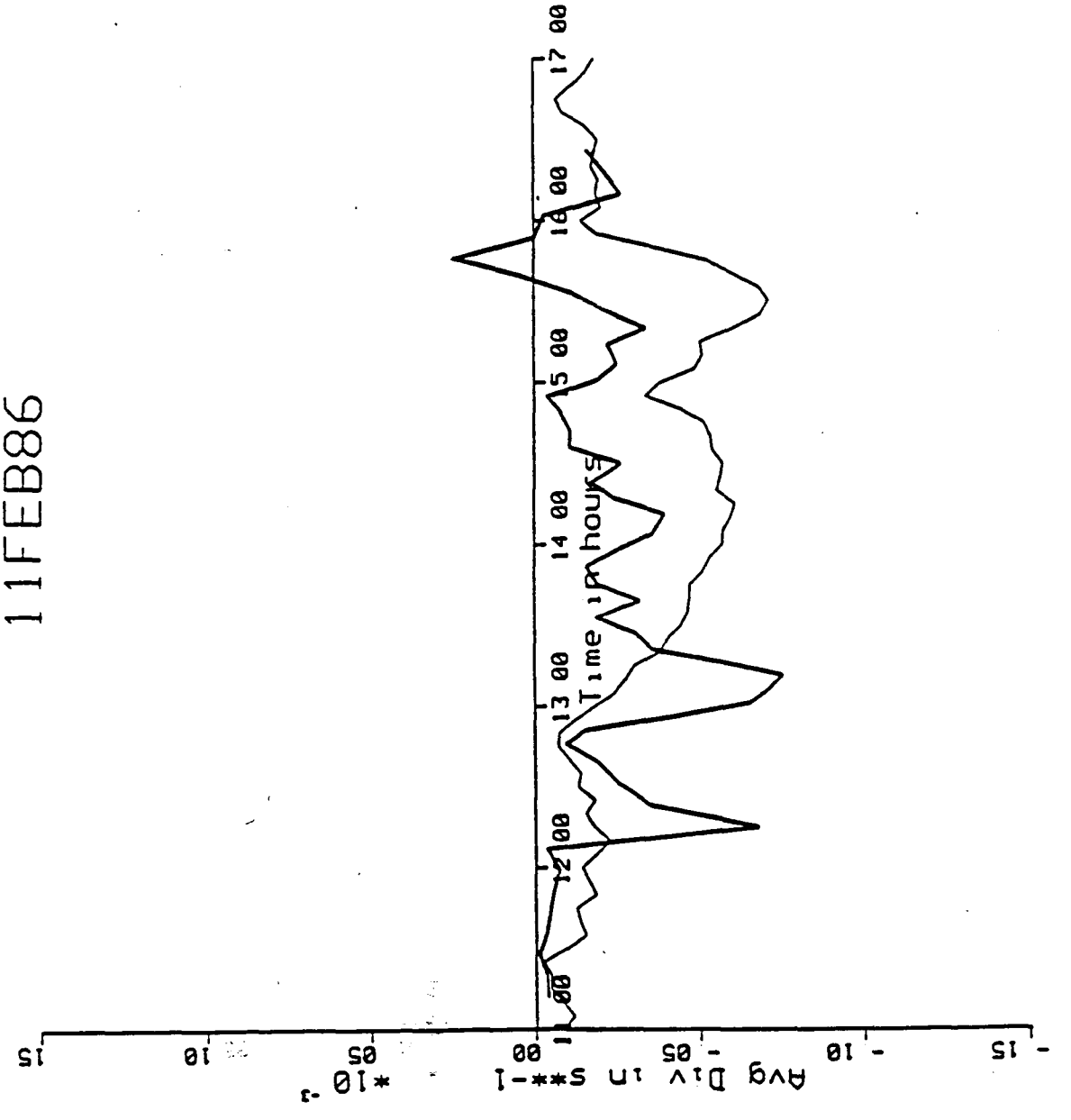
11FEB86
Avg Div in s**-1
*10 -3
15
10
05
00
- 05
- 10
- 15
Time in hours
11 00
12 00
13 00
14 00
15 00
16 00
17 00

Figure 5.12(d).

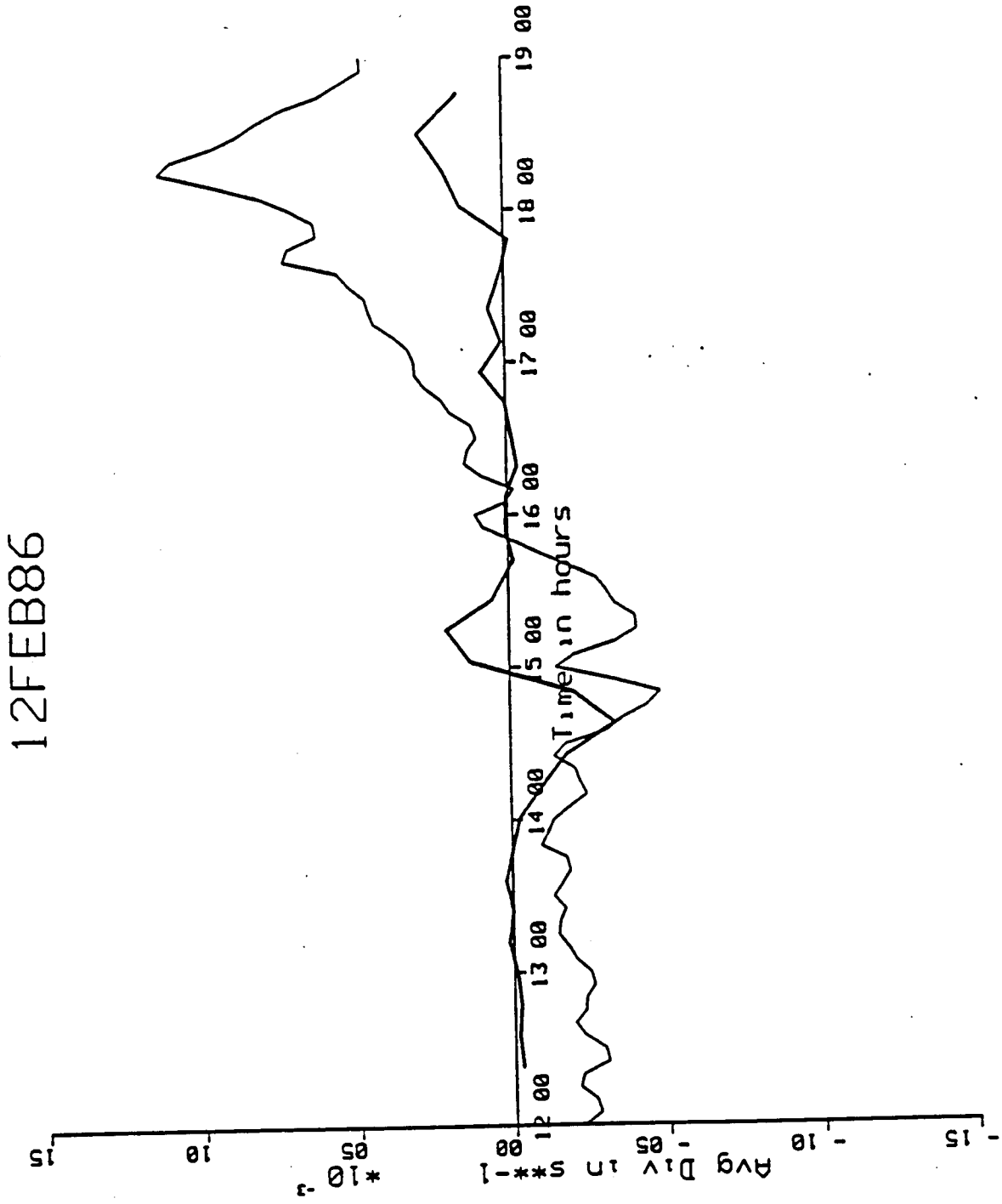
12FEB86
Avg Div in s**-1
*10 -3
15
10
05
00
- 05
- 10
- 15
12 00
13 00
14 00
15 00
16 00
17 00
18 00
19 00
Time in hours

Figure 5.12(e).

simulation shows much less divergence. These periods of strong divergence in the network cannot be explained by the algorithm but it may be said that they are probably not due to the action of convective scale downdrafts.

5.4.2 Case Studies

Seven case studies were chosen at random from the 20 days under study to be presented here. They provide examples of the use of the algorithm as a diagnostic tool and as a short-term forecasting aid. The calculations can be performed rapidly enough to be displayed in real time, ideally overlayed on the radar screen. They hold out the possibility of contributing to the selection and classification of seeding targets.

The algorithm was run for each five minute radar record during which the cloud physics aircraft (the Lear) was in the air. A 5x5 km grid was then set up with the mean position of the aircraft for that radar record located at the center. Then the estimated winds for a 50x50 km area around the aircraft were calculated at each of the 121 grid points. Thus, a 50x50 km box with 5x5 km spacing followed the aircraft around.

Each figure which follows shows:

a) The radar echo return at the time indicated, with dBz between 35 and 40 represented as blue, dBz between 40 and 45 as yellow, between 45 and 50 dBz as red, 50-55 as green and above 55 dBz as purple.

b) The solid light green line is the line of zero divergence, the dashed green lines are lines of convergence (negative divergence) drawn every $2.0 * 10^{-4}$ s^{-1}. Positive divergence is not plotted.

c) The solid blue contours are the outlines of the 35 dBz radar return approximately 20 min later than the color-contoured return. The actual time is indicated.

d) The 30 km range rings from the Nelspruit radar are plotted to give a sense of position relative to Nelspruit.

e) The transponder track of the Lear jet is plotted as a red line joining red squares.

All runs were for 1000 m AGL, and all winds are storm-relative. The position of the center of the box relative to the Nelspruit radar is noted at the top of each frame.

The 'rear' of the storm is taken to be the divergent side, while the convergent side is referred to as the 'front' of the storm, regardless of absolute orientation.

5.4.2.1 Case 1: 27 NOV 84

The morning sounding shows strong westerly/southwesterly flow in the middle and upper layers and light northeasterlies below 5000 ft. The radar area increases from about 20 km^2 around 1245 LST to a peak of 170 km^2 around 1420, then declines to 27 km^2 by 1601. Figure 5.13 shows the estimated fields around the aircraft at 1235 LST. If there are no aircraft tracks plotted, then the aircraft was not in the air at the time.

The radar before 1235 LST showed little or no activity although the aircraft appeared to have spotted a suitable cell which has not yet reached 35 dBz in intensity. By 1235 LST a cell appears with echo greater than 35 dBz, and the algorithm puts in a downdraft at that location, integrates the shear from the sounding, and produces the convergence fields of Fig. 5.13.

The aircraft track during the 1235 LST radar scan arcs around the western edge of the storm, starting on the left flank, flying around the rear left flank towards the center, and then over the main convergence zone at the front. The new development occurred within the area outlined over the convergence zone in Fig. 5.13. All of the new development in the 30 min after 1235 LST occurs within that area.

This represents a case of isolated cells with little or no outflow interaction.

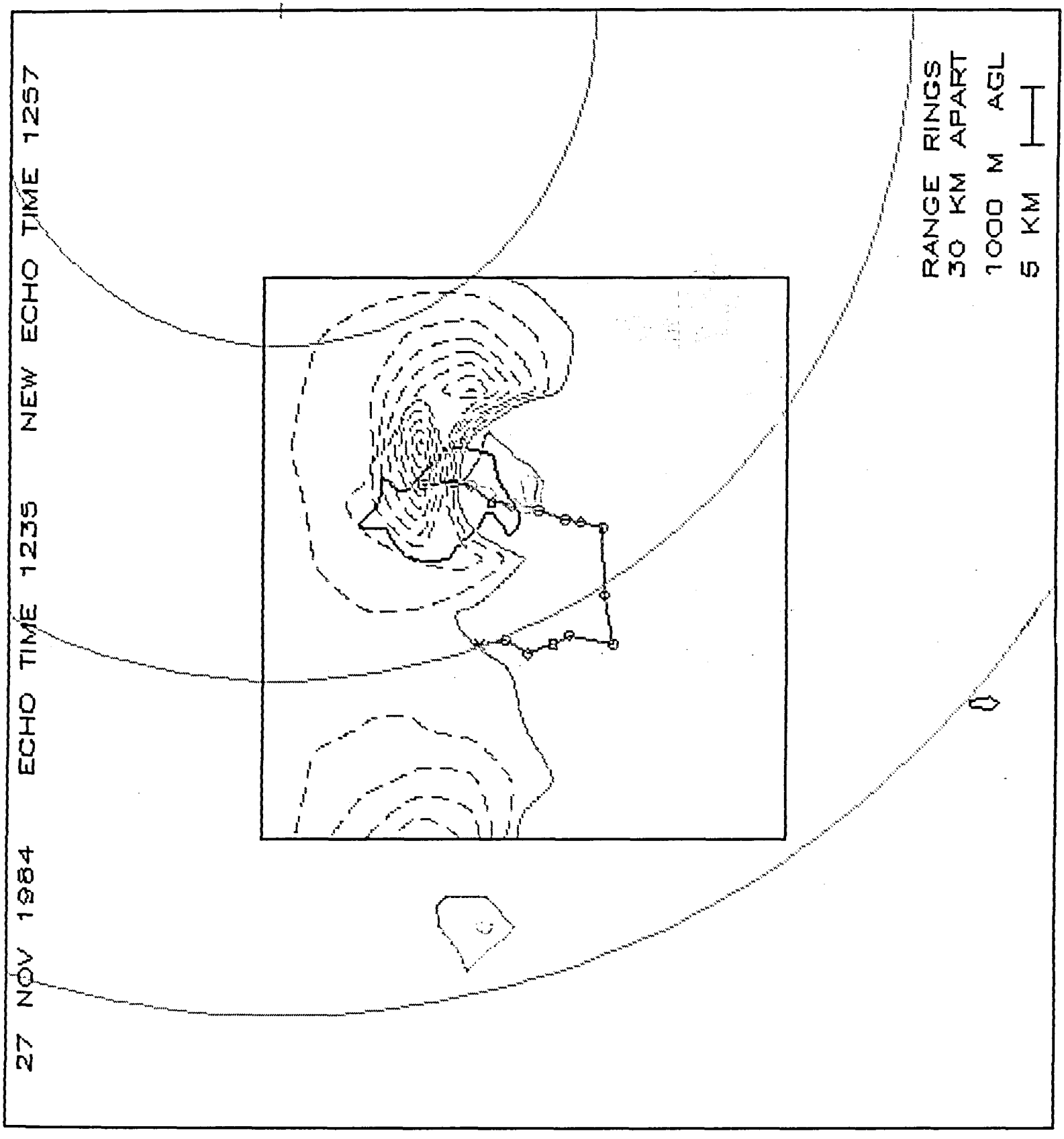
27 NOV 1984 ECHO TIME 1235 NEW ECHO TIME 1257
RANGE RINGS
30 KM APART
1000 M AGL
5 KM

Figure 5.13

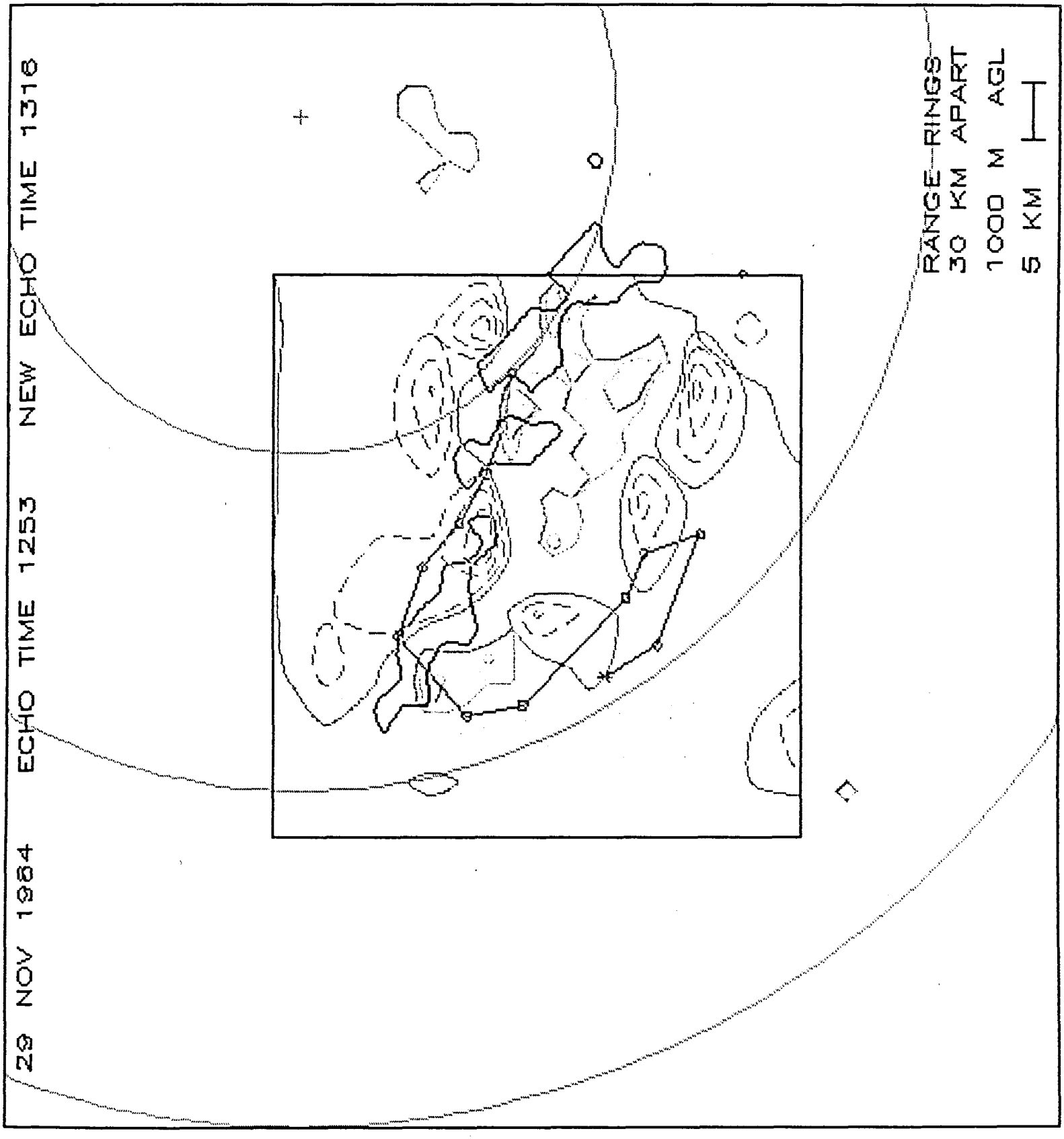
29 NOV 1984 ECHO TIME 1253 NEW ECHO TIME 1318
RANGE RINGS
30 KM APART
1000 M AGL
5 KM

Figure 5.14(a)

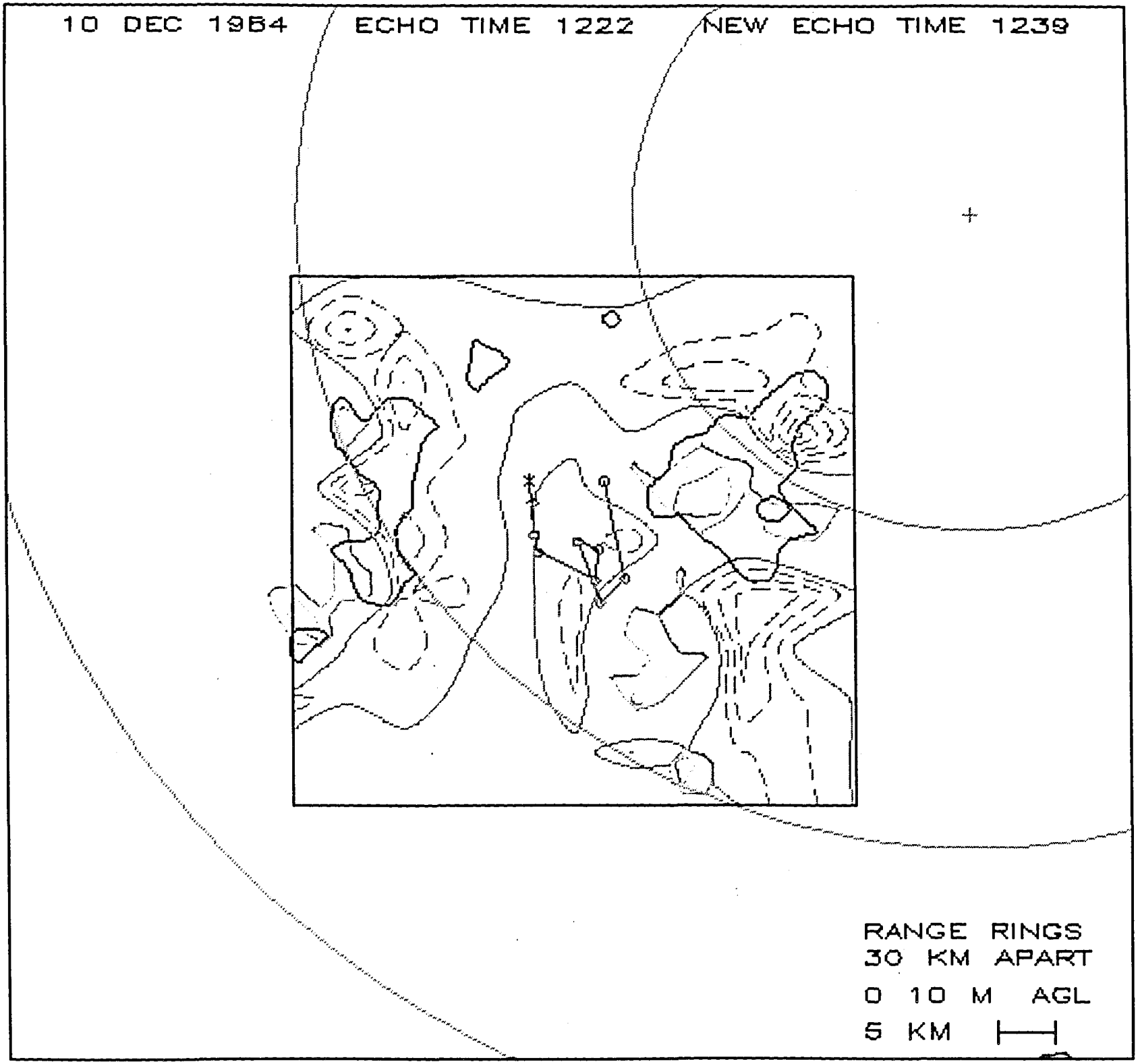
10 DEC 1984 ECHO TIME 1222 NEW ECHO TIME 1239
RANGE RINGS
30 KM APART
0 10 M AGL
5 KM

Figure 5.15(a)

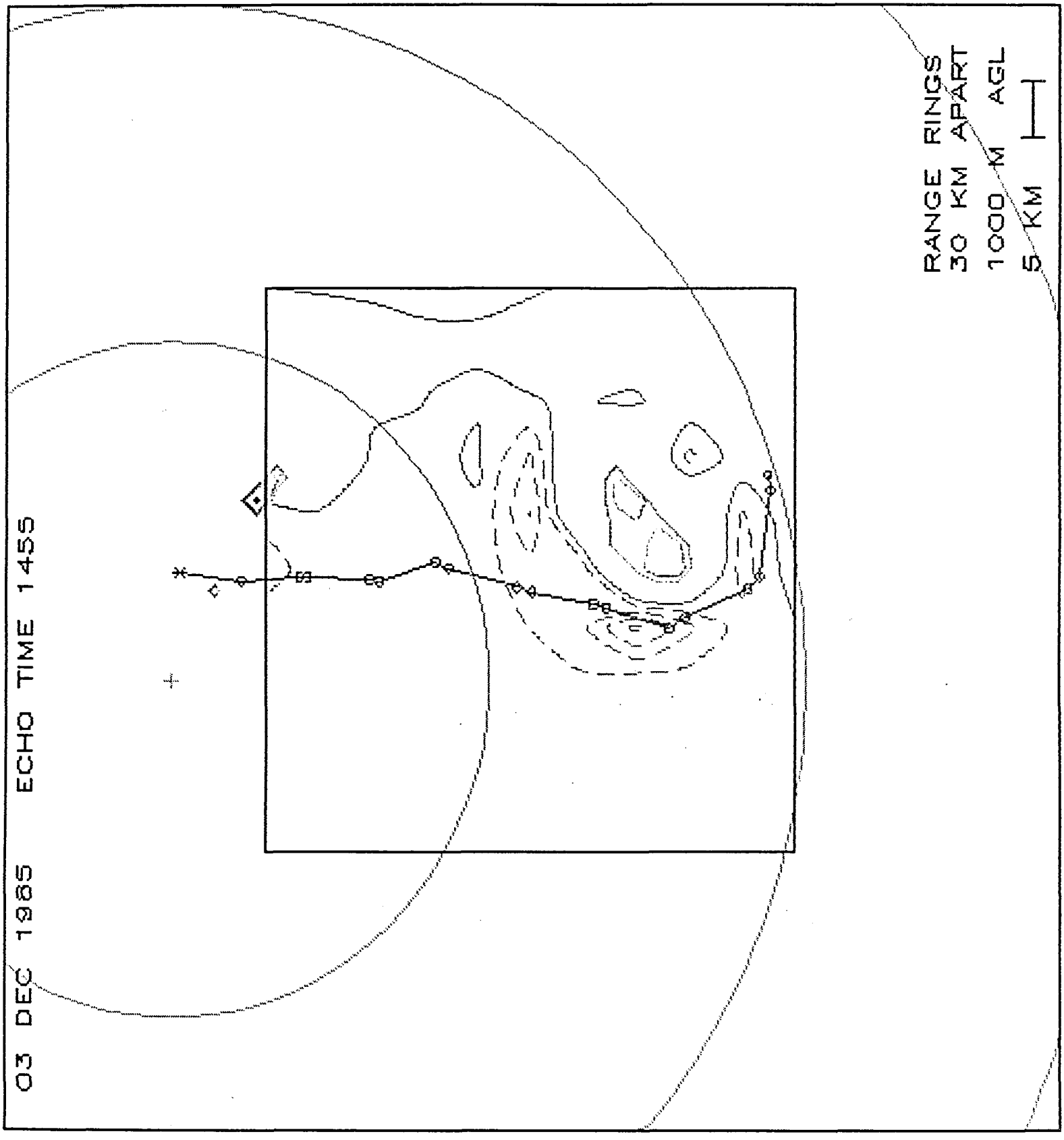
RANGE RINGS
30 KM APART
1000 M AGL
5 KM
03 DEC 1985 ECHO TIME 1455

Figure 5.16(a)

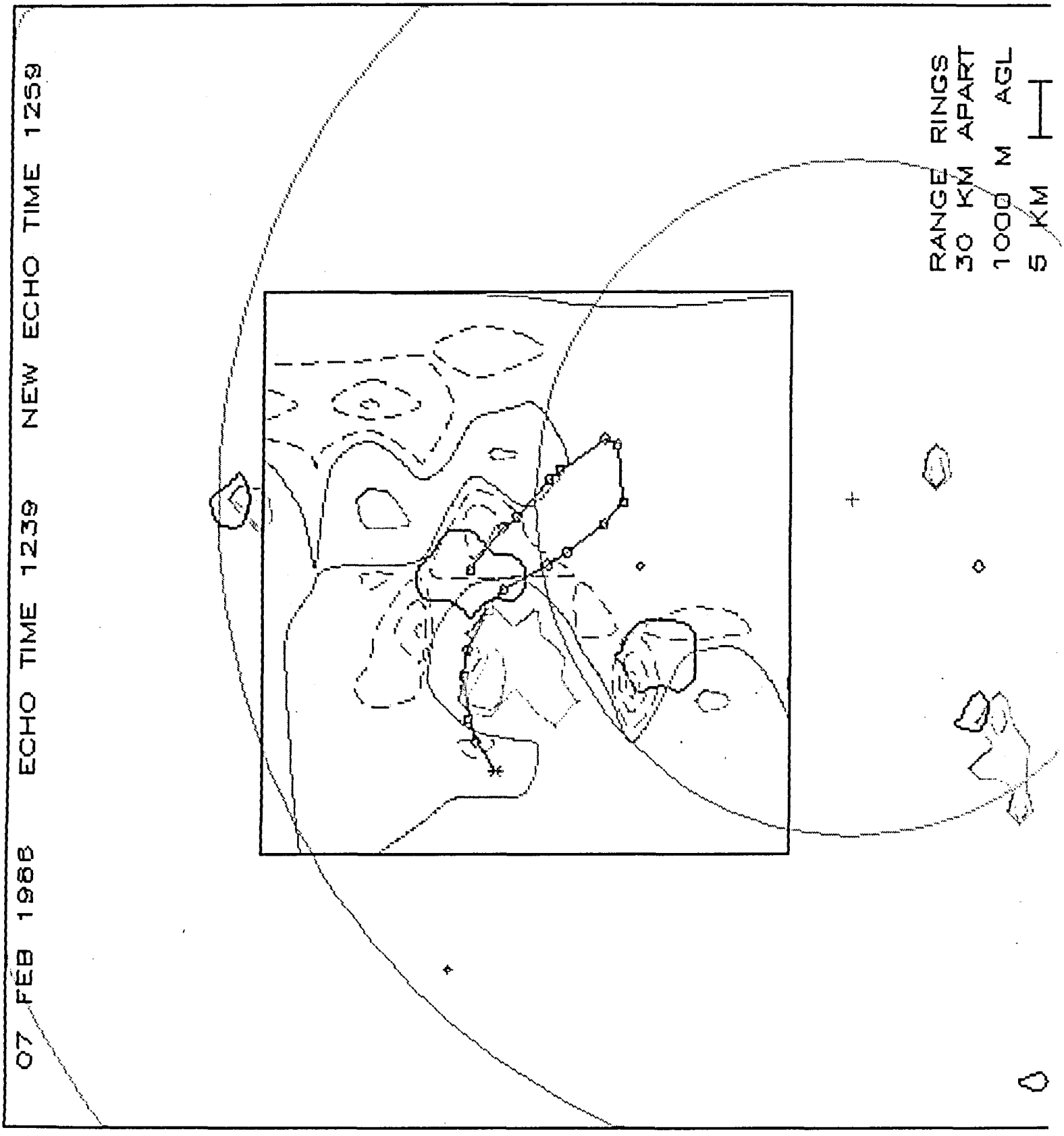
07 FEB 1988 ECHO TIME 1239 NEW ECHO TIME 1259
RANGE RINGS
30 KM APART
1000 M AGL
5 KM

Figure 5.17(a)

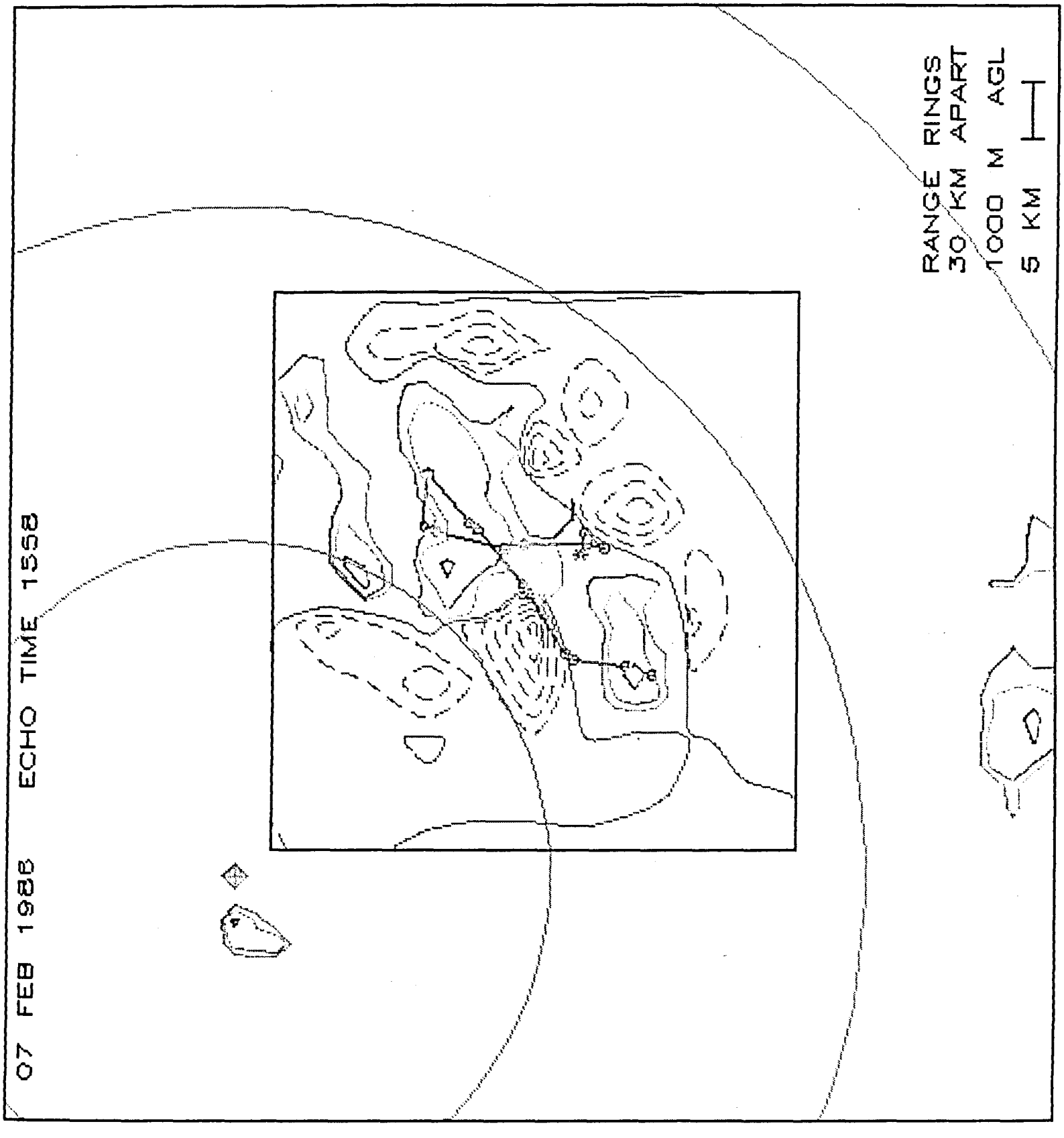
07 FEB 1988 ECHO TIME 1558
RANGE RINGS
30 KM APART
1000 M AGL
5 KM

Figure 5.18(a)

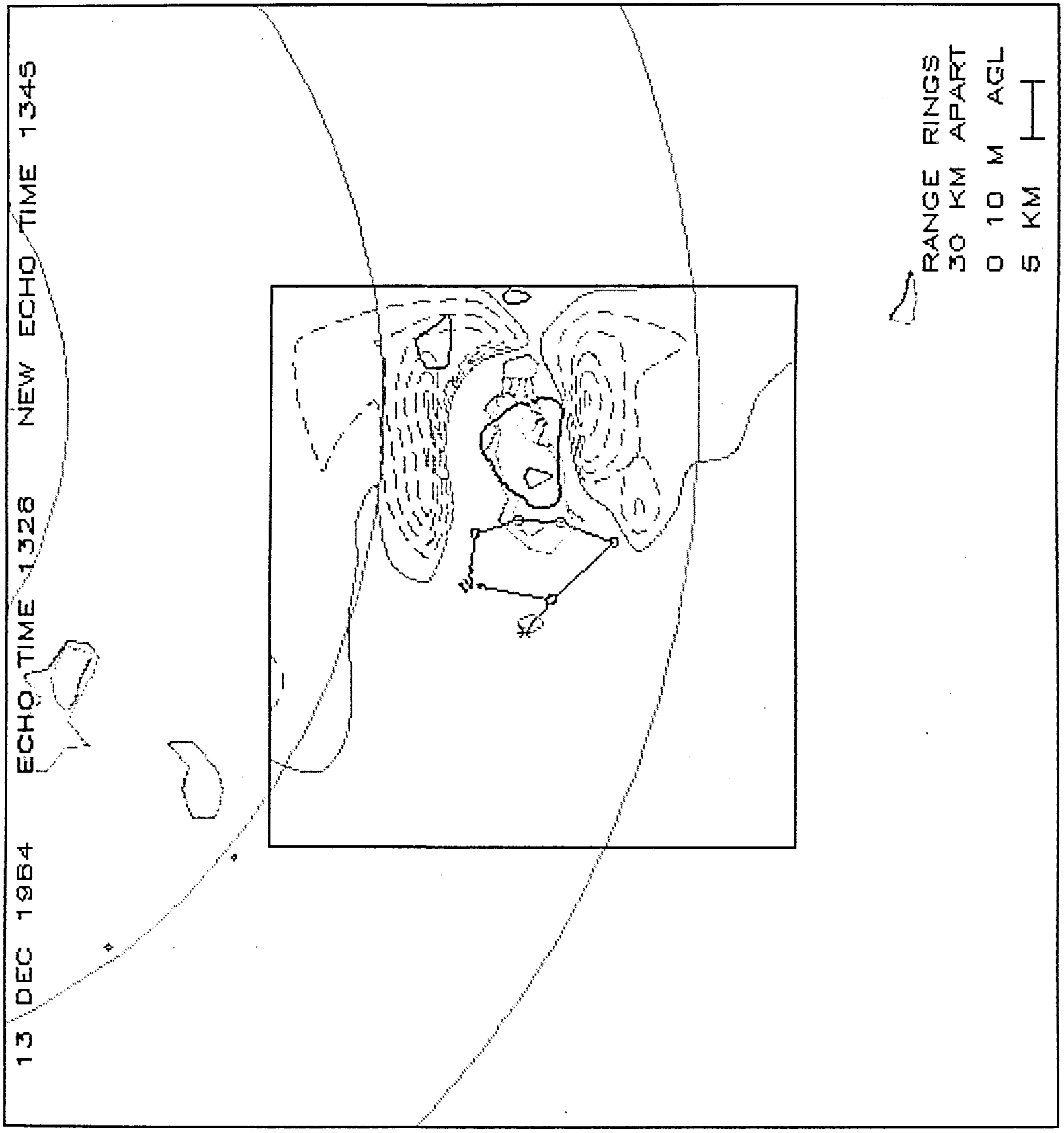
13 DEC 1964 ECHO TIME 1328 NEW ECHO TIME 1345
RANGE RINGS
30 KM APART
0 10 M AGL
5 KM

Figure 5.19(a)

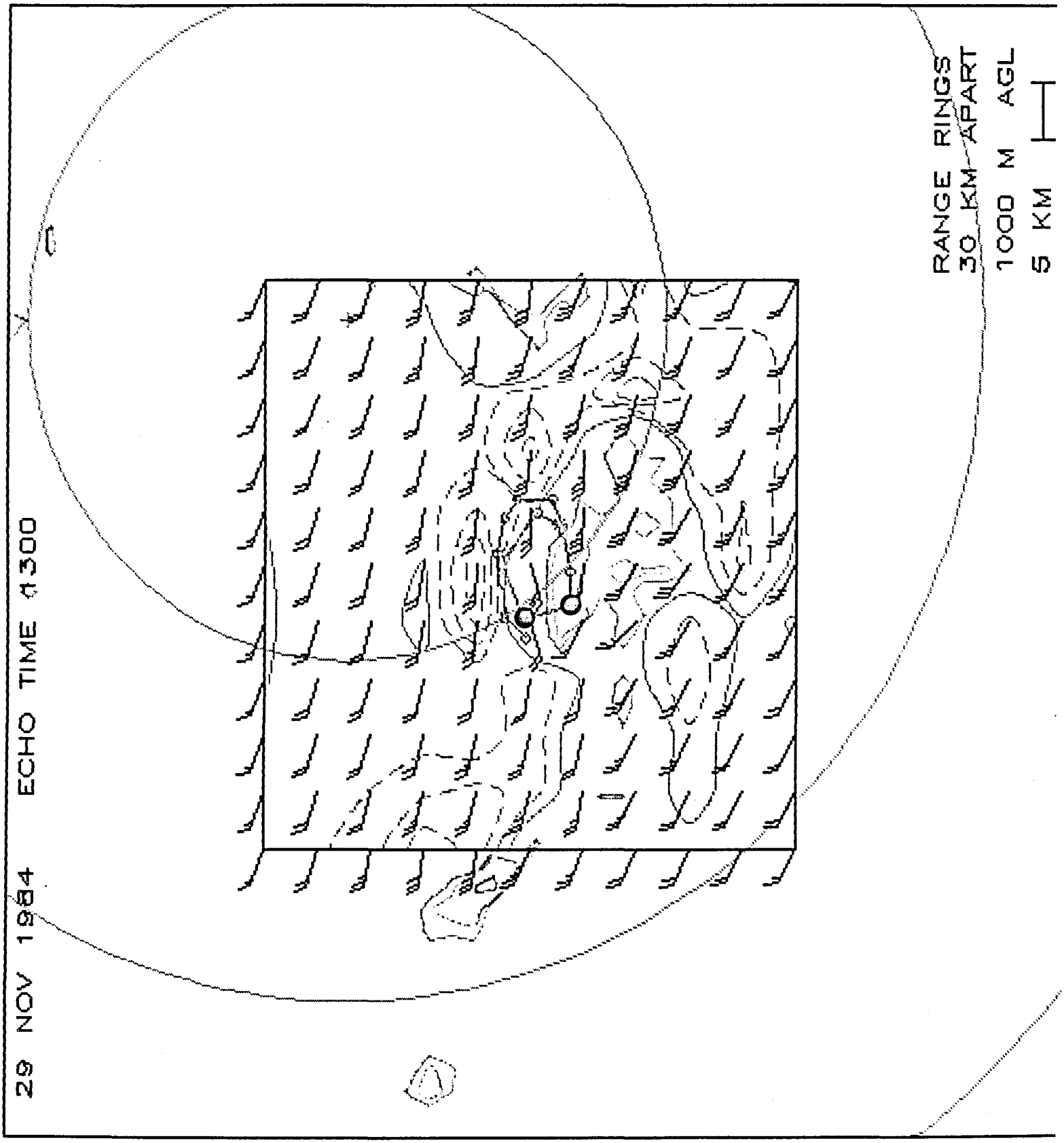
29 NOV 1984 ECHO TIME 1300
RANGE RINGS
30 KM APART
1000 M AGL
5 KM

Figure 5.21(a)

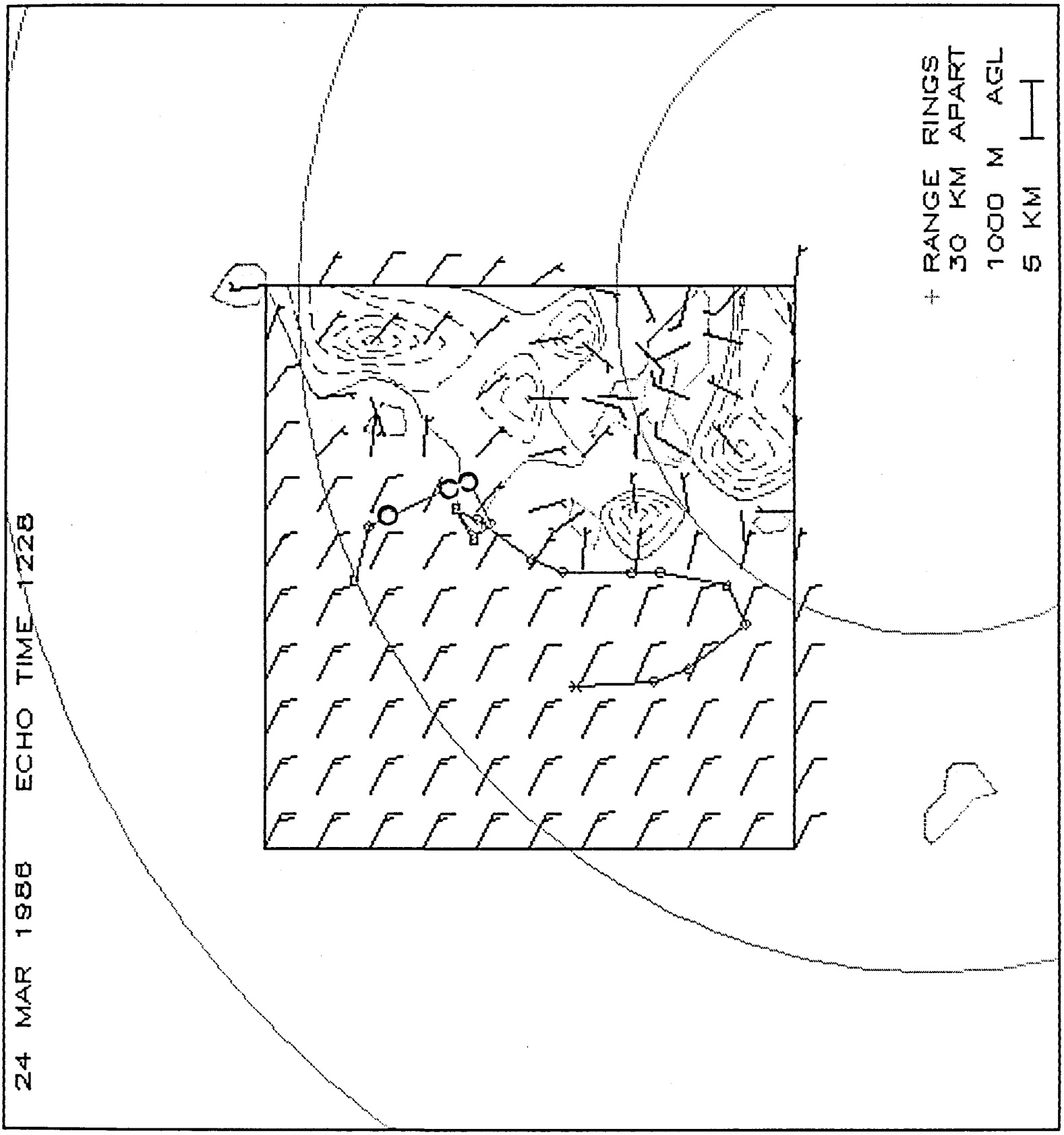
24 MAR 1988 ECHO TIME 1228
+ RANGE RINGS
30 KM APART
1000 M AGL
5 KM

Figure 5.21(d)

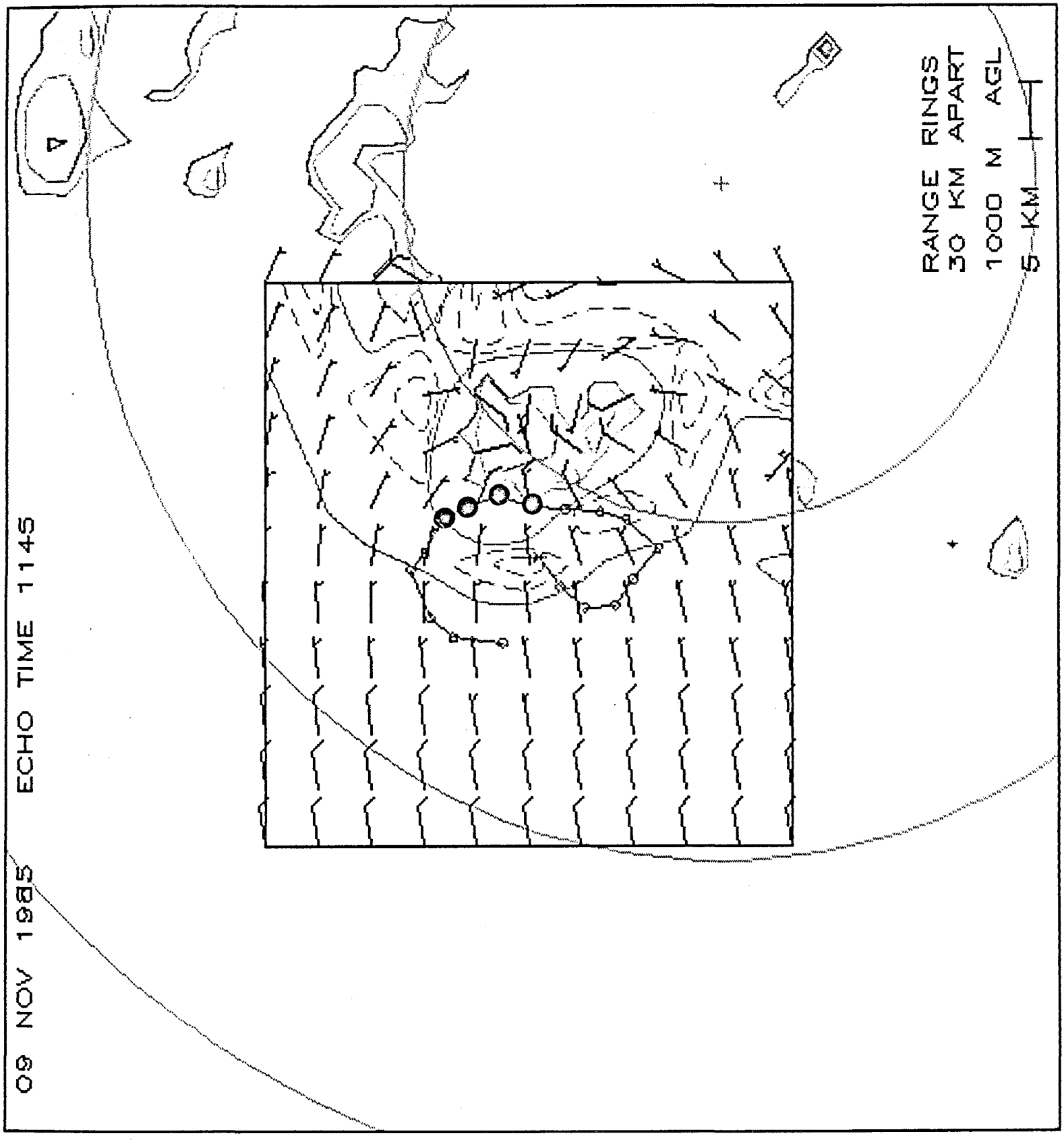
09 NOV 1985 ECHO TIME 1145
RANGE RINGS
30 KM APART
1000 M AGL
5 KM

Figure 5.21(g)

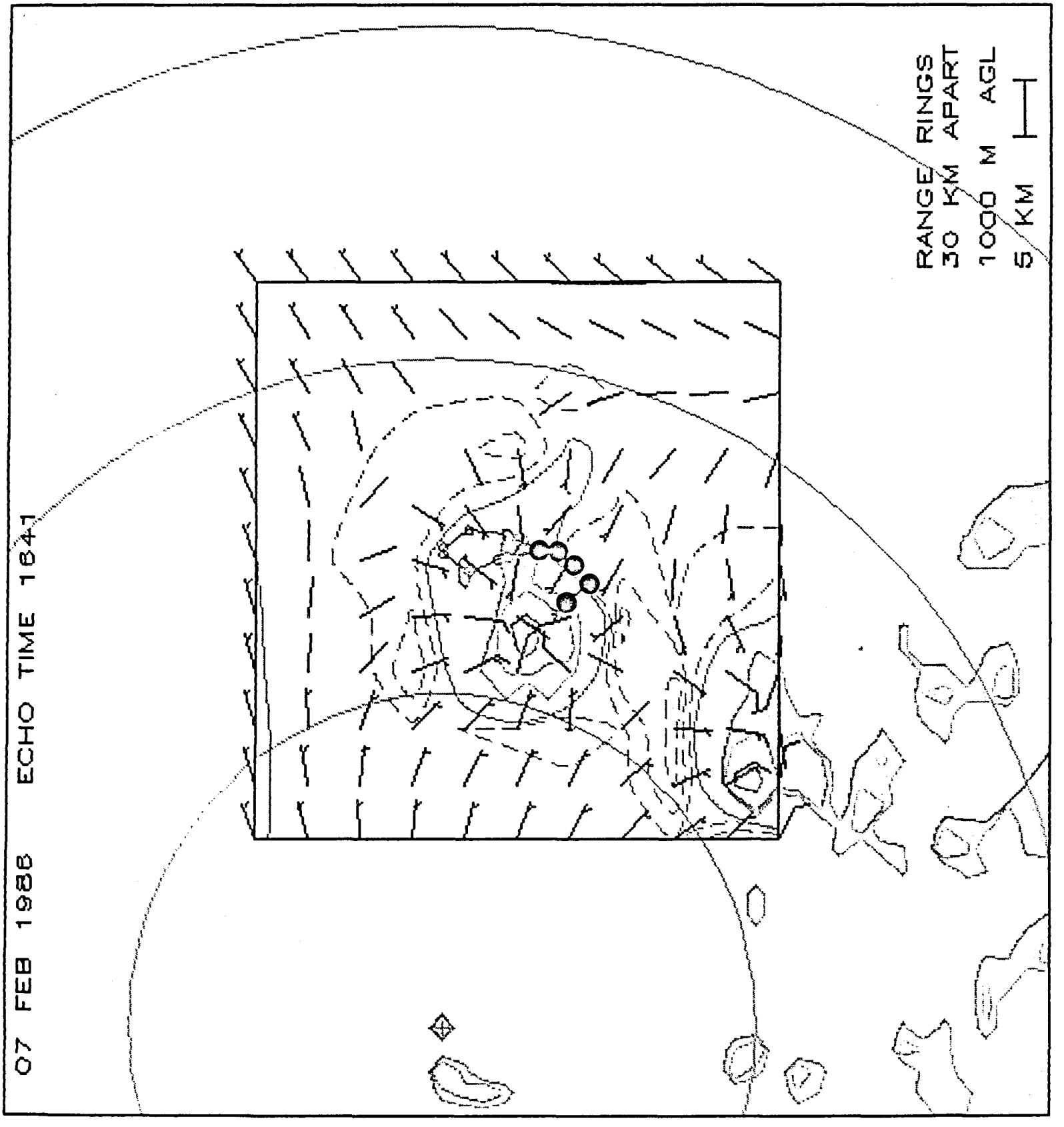
RANGE RINGS
30 KM APART
1000 M AGL
5 KM
07 FEB 1988 ECHO TIME 1841

Figure 5.21(J)

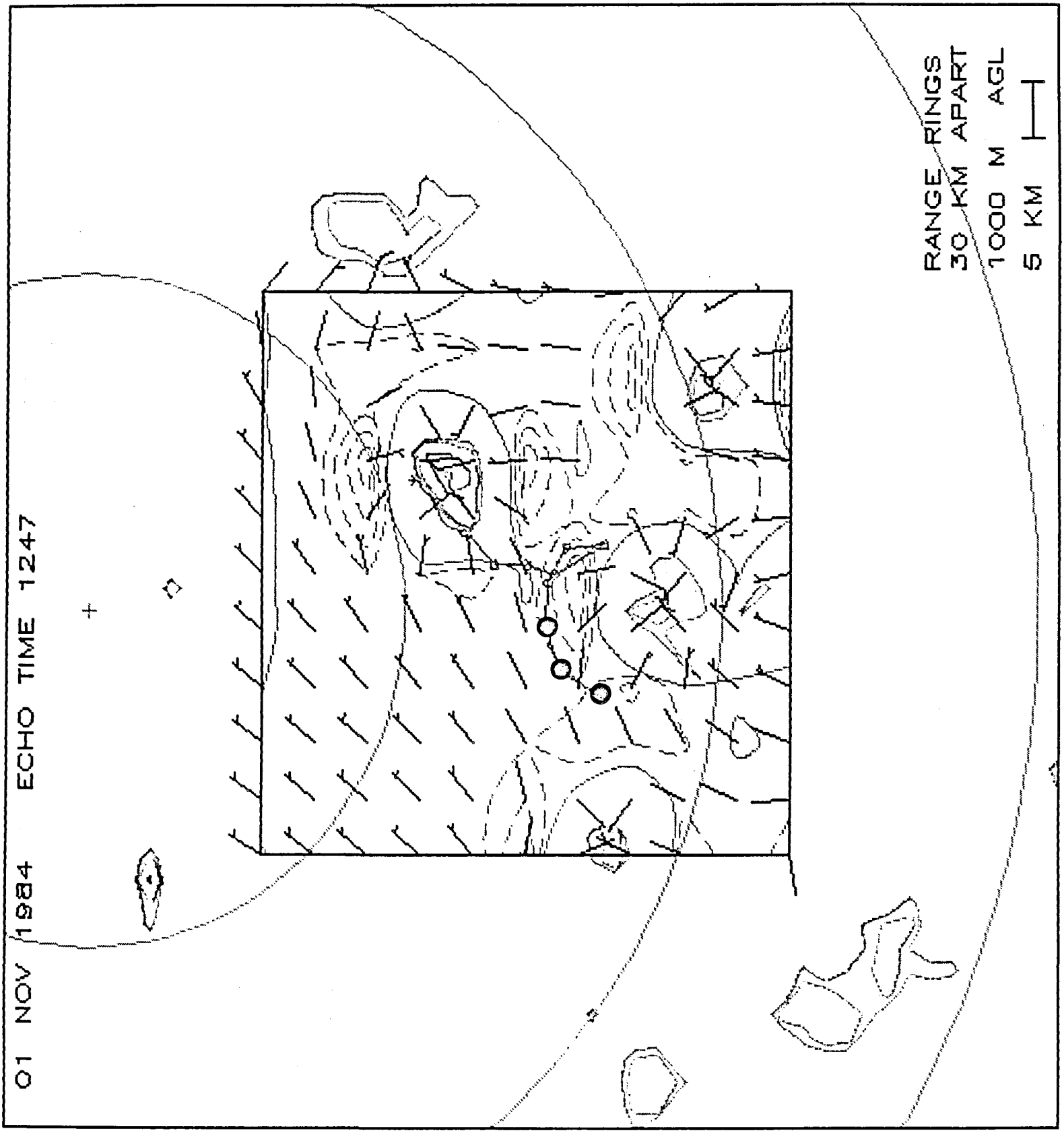
01 NOV 1984 ECHO TIME 1247
RANGE RINGS
30 KM APART
1000 M AGL
5 KM

Figure 5.21(m)

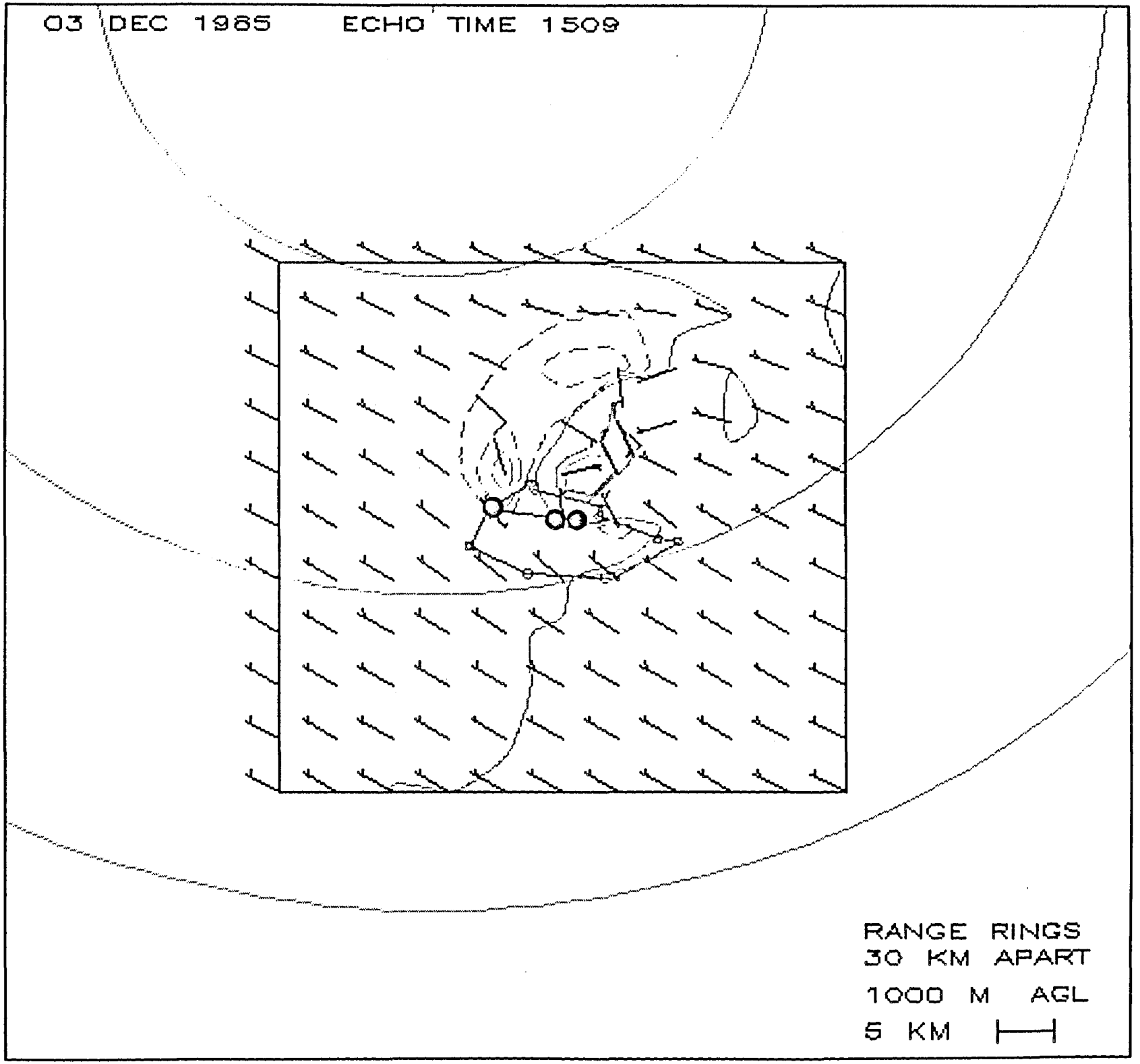
03 DEC 1985 ECHO TIME 1509
RANGE RINGS
30 KM APART
1000 M AGL
5 KM

Figure 5.21(q)

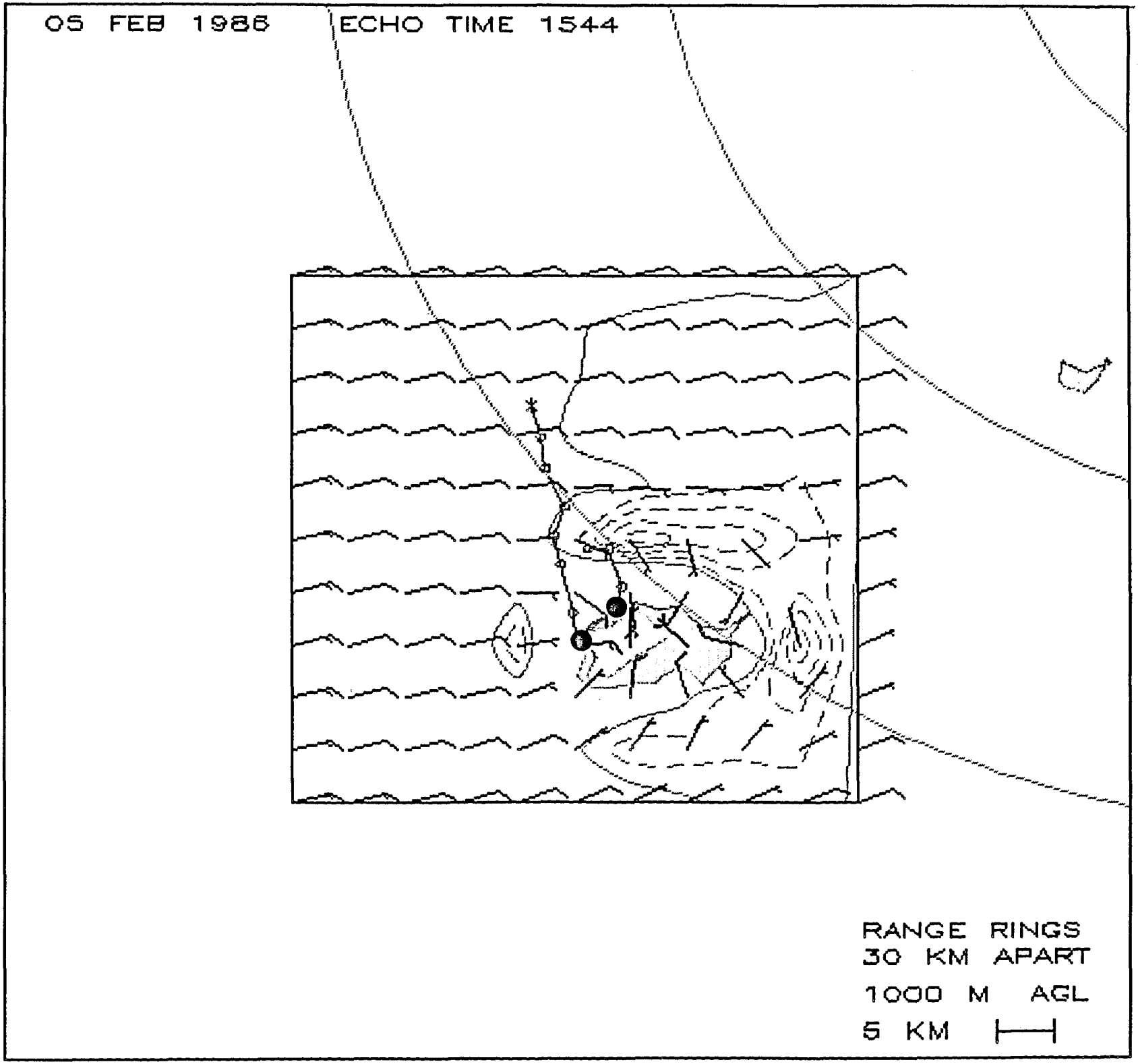
05 FEB 1986
ECHO TIME 1544
RANGE RINGS
30 KM APART
1000 M AGL
5 KM

Figure 5.21(v)

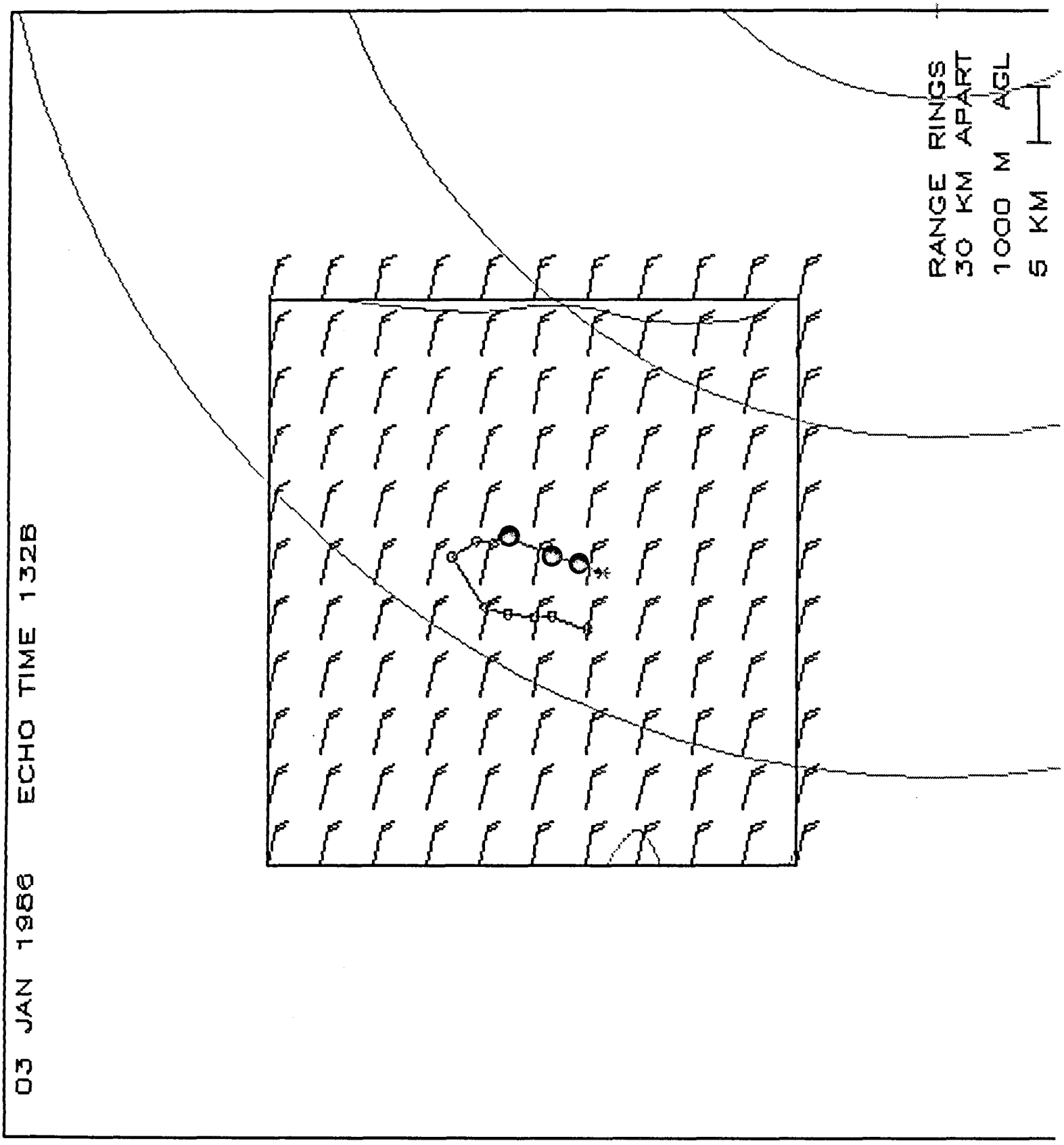

Figure 5.21(bb)

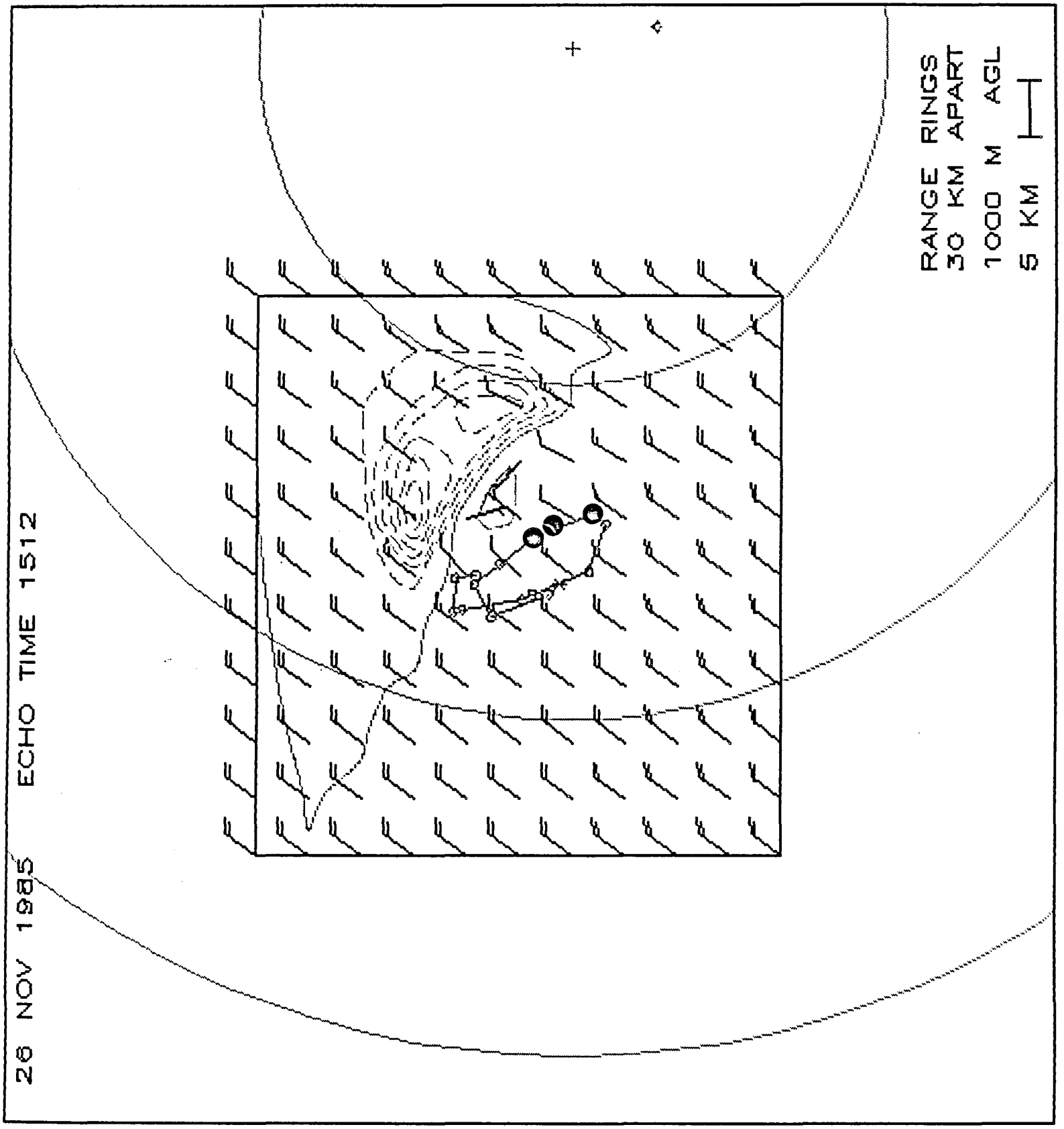

Figure 5.21(gg)

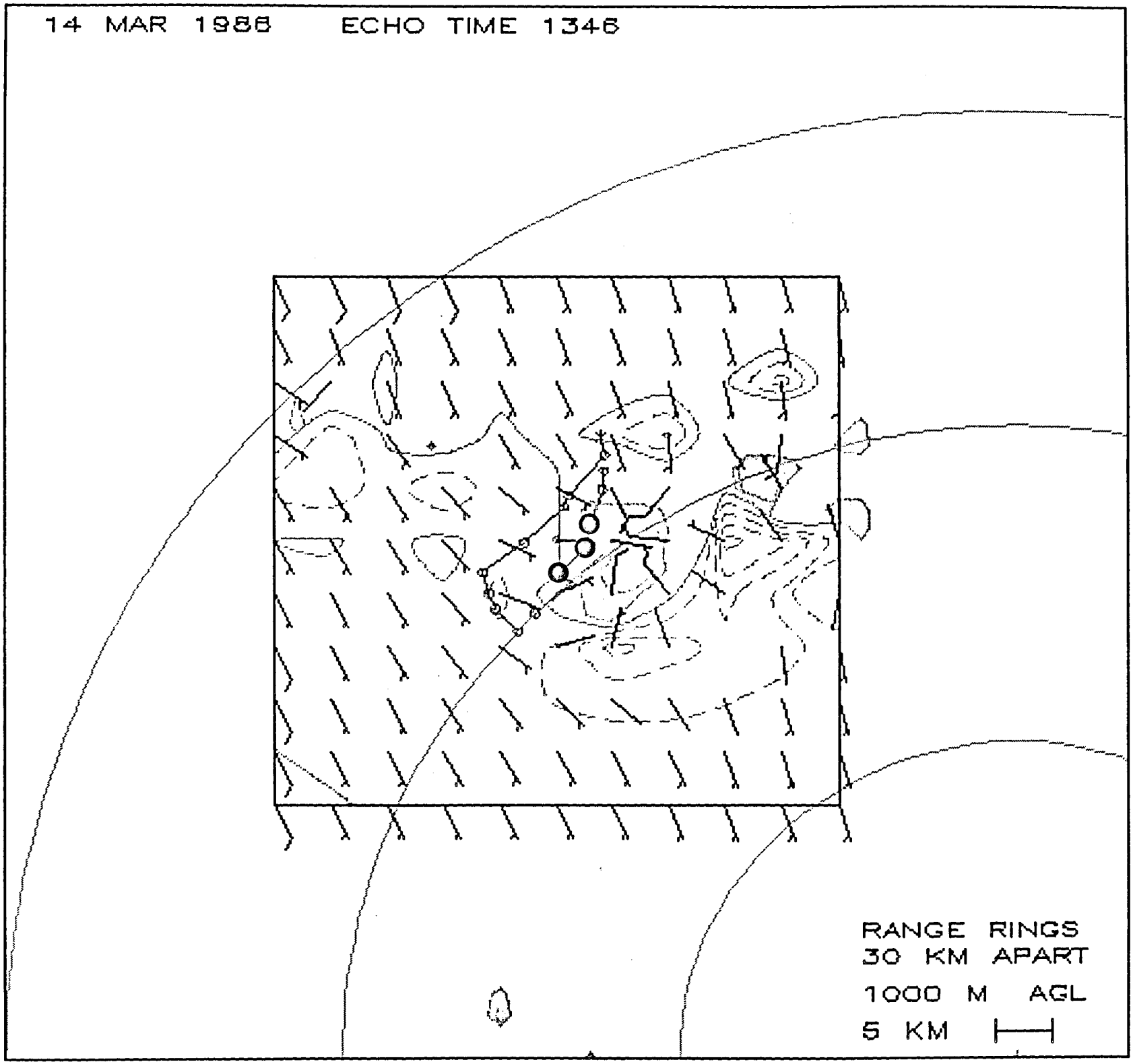

Figure 5.21(11)

6.5 The PAWS sounding database (Morrison and Morgan)

6.5.1 Introduction

The CIC-PAWS Sounding Database was generated at CIC in Nelspruit to provide rapid and simple access to processed aircraft and rawinsonde sounding data taken at Nelspruit. As many meaningful sounding parameters as possible have been computed in the database to eliminate the need for any intermediate processing of data between the database and statistical/graphical analysis programmes. The database was structured in a record-oriented ASCII format in order to take advantage of the SORT/MERGE utility available on the CIC MV4000 which permits high-speed, unlimited stratifications of disk files. Quality control has been very strict in assembling the database; any soundings with bad or questionable data have been excluded.

6.5.2. Physical structure of the database

As of 22 July 1986 the database is just over 1.25 MB in size. It consists of 921 records (715 Nelspruit rawinsonde, 176 Learjet, and 29 Aero-Commander soundings; and 1 terminator record) each of which is 1400 bytes long. The data begin with the 1982/83 summer season and currently run through the end of the 1985/86 season.

6.5.3. Logical structure of the database

Each record has a 200A7 FORTRAN format. The terminator record at the end of the database consists of all 9's. The contents of each data word is detailed in file ":UDD BRIAN:SOUNDING DB: SOUNDING DB PARAMS". The general categories of parameters in each record are listed below:

* identification parameters (date, time, ID code, etc)
* surface data parameters
* sounding vertical limits
* wind parameters (valid for rawinsonde soundings only)
* standard level temperature and mixing ratio data
* classical stability indices (K-index, etc)
* average boundary layer theta-e and mixing ratios
* cloud base and related parameters (e.g. LFC computed from cloud base, delta-T at 500 mb assuming moist adiabatic ascent from cloud base, etc)
* CCL and related parameters
* dry-bulb and wet-bulb freezing level parameters
* parcel ascent times from cloud base or CCL to $-10^{o}C$
* experimental stability-related parameters (Theta-e max, etc)
* database management parameters
* spare (blank) words for future database expansion.

The file SOUNDING DB PARAMS mentioned above also contains the necessary information for decoding each data word, as well as the physical location of each data word and flag for including individual data words in statistical and graphical summaries.

6.5.4. Decoding database records

The data words in each record are either ASCII character strings, integer or real numbers encoded into an A7 word. Decoding is done according to the conversion equation assigned for each data word, described at the end of file SOUNDING DB PARAMS. The suggested sequence for decoding numerical data words is as follows: The subroutine READ SOUNDING DB PARAMS reads the file SOUNDING DB PARAMS, loads the parameter description and unites strings into string arrays, then loads the conversion equations and factors into integer arrays. These arrays are stored in COMMON blocks. Once this is done the subroutine CODE SOUND PARAMS can be called to decode any numerical parameter. Bad, missing or inapplicable data are represented by either a blank (" ") or flagged ("-999999") string prior to parameter decoding or by a value of -99 or -99.9 after decoding.

Only 2 of the data words in each record are non-numerical parameters. Parameter number 5 ("Sounding ID") identifies the sounding as from the Nelspruit rawinsonde ("Nst RAW"), CIC Learjet 24 ZS-LTK ("Lear 24"), or CIC Aero-Commander ZS-IZN ("Aer-Com"). All the rawinsonde soundings were taken at CIC, and all of the aircraft soundings were taken during ascent from or descent back into the Nelspruit airfield. Parameter number 6 ("Aircraft Mission") serves as a flag to identify operational days: "No Ops" for days on which no research aircraft missions were flown, "ERSE" for days on which the Exploratory Randomized Seeding Experiment was conducted, and "CldPhys" for all other days on which cloud physics research missions were flown.

6.5.5. Description of individual parameters

Most of the parameters are self-explanatory and will not be discussed here. Readers are referred to the subroutine SOUND DBASE COMPS for details on how most of the parameters were computed. Specific parameters requiring elaboration are briefly described below:

* params 24 to 27: Sounding top descriptors. Learjet upsoundings out of the Nelspruit airfield generally terminate at about 300 mb, although they may terminate as low as 350 mb. To permit computation of an equilibrium level from these soundings, the Nelspruit 06Z morning sounding data above the termination level is appended to the Lear soundings. If this has been done the minimum sounding pressure will be that of the morning rawinsonde sounding. Learjet downsoundings and Aero-Commander soundings are not modified in any way.

* Params 40 to 43: Low-level jet descriptors. We define the low level jet as the wind speed maximum 5 km AMSL.

* Params 45, 46, 48, 49: Wind shear vectors. These are the vectors constructed by the vectorial addition of the wind vectors for the specified levels.

* Params 69 to 72: Average boundary layer theta-e and mixing ratio. These quantities are averaged over either the lowest 60 mb or the lowest 100 mb for the given sounding.

* Params 73 to 92: Cloud base related parameters. We define cloud base as the point where the average theta-e and mixing ratio over the lowest 60 mb intersect. No LFC is computed if there is no conditionally unstable layer above the cloud base. No equilibrium level is computed if there is no LFC or if the sounding does not extend at least up to the top of the conditionally unstable layer. The adiabatic updraft for a parcel ascending from cloud base to the -10°C level is not computed if the parcel is not positively buoyant by the time it reaches the -10°C level. The delta-T's at 700, 500 and 300 mb are all computed assuming moist adiabatic ascent of a parcel from cloud base.

* Params 95 to 110: CCL related parameters. The CCL is found by following the temperature sounding downwards until the saturation mixing ratio intersects the average mixing ratio over the lowest 60 mb. Except for the absence of a separate LFC, all the computations in the paragraph above also apply here.

* Params 125 to 148: Experimental stability related parameters. Theta-e_{max} and Theta-es_{max} are found between the surface and 700 mb. Theta-e and theta-es_{min} are found above the theta-es_{max} level.

* Params 149 to 156: Special freezing level parameters. These parameters are computed at the intersection of the 0 degree isotherm and the specified line of constant theta-e.

6.5.6. Errors found in the database

One inconsistency has been found in the database. The CCL mixing ratio should be the mixing ratio of a parcel at the CCL which is equal to the average mixing ratio over the lowest 60 mb. Instead, the CCL mixing ratio computed in the database is computed from the CCL pressure and corresponding environmental dewpoint. The CCL mixing ratio should then be taken to be the same as that given in parameter 71 ("Avg Mix Ratio - 60 mb").

6.5.7. Support software

The Sounding Database software package contains four main programmes:

* GENERATE SOUND DBASE: This programme creates new database records. It reads in the raw data from rawinsonde or aircraft sounding disk files and computes all the derived parameters for

inclusion in the database. The SORT/MERGE utility is automatically run after each execution of this programme to merge new records into the proper database sequence.

* SOUND DBASE REPORTS: This programme prints out the contents of any selected database record.

* SOUND DBASE STATS: This programme computes simple statistics for each flagged numerical database parameter. It will also print out distributions of flagged parameters in histogram format. The SORT/MERGE utility is run prior to execution of this programme to select out the data desired for the statistical analysis.

* SOUND DBASE PLOT: In its current version, this programme does an X-Y plot on the Tektronix 4107 graphics terminal of any selected Nelspruit morning sounding parameter versus any selected Learjet upsounding parameter for the same days. Optional linear and polynomial regressions can be run and plotted for the given data. Once again, the SORT/MERGE utility can be run prior to programme execution to select the desired data.

* DATABASE XY PLOT: This programme plots any two parameters in the SAME database records against each other in an X-Y plot. The SORT/MERGE utility can be run prior to programme execution to extract the desired data. This programme is also shared with the Cloud Sample Database software (i.e. it works for BOTH databases).

6.6. Meteorological analyses related to thunderstorm forecasting at Nelspruit (Morgan and Morrison)

The radiosonde data collected over four seasons (82/83, 83/84, 84/85, 85/86) have been organized in a database format. With this fund of meteorological information we can begin to develop techniques for forecasting the stratification and stability of the atmosphere and the probable cloud type and characteristics.

What follows here is mainly intended to display the normal ranges of important parameters, their variations from month to month and over the four years (1982-1986). These are mere beginnings in the exploitation of the sounding data.

6.6.1. The mean trend of instability

Fig. 6.6.1(a) gives for the individual seasons, the monthly means of the low level maximum in Theta-e, Theta-e averaged over the lowest 60 mb (Theta-e 60) and the mid-level minimum of Theta-es. Also shown are monthly means of the difference Theta-e max minus Theta-es$_{min}$. The difference Theta-e$_{max}$ minus Theta-es$_{min}$ is an index of the mid-afternoon instability, as described in Section 6.3 of this Volume. The individual seasons exhibit variations, but a general behaviour is clear. The low level Theta-e max increases rapidly during the first months of the season, while the mid-level Theta-es increases more slowly. This

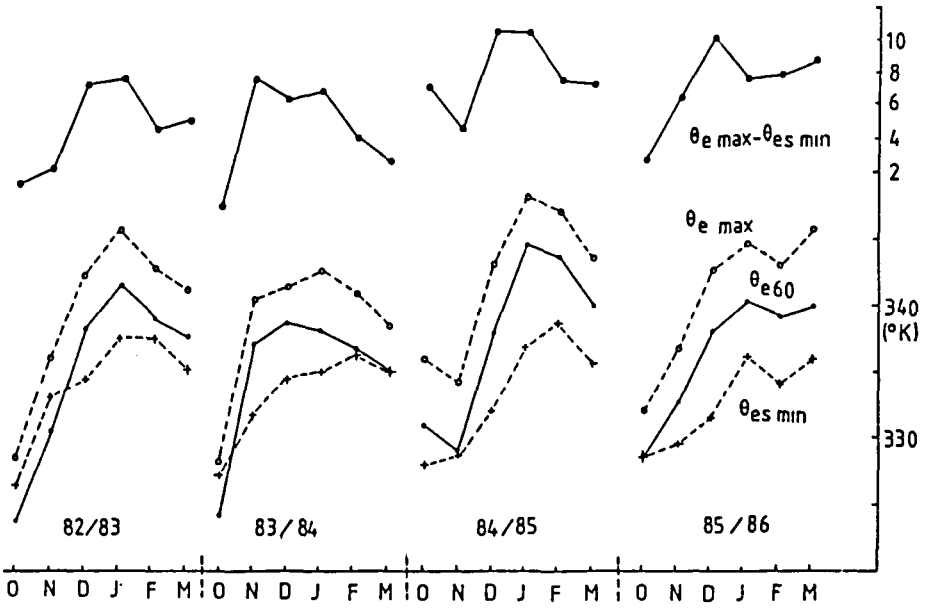

Fig. 6.6.1 (a). Seasonal monthly means of:
- Theta-e max minus Theta-e min
- low level Theta-e max
- Theta-e averaged over lowest 60 mb
- mid-level Theta-es min

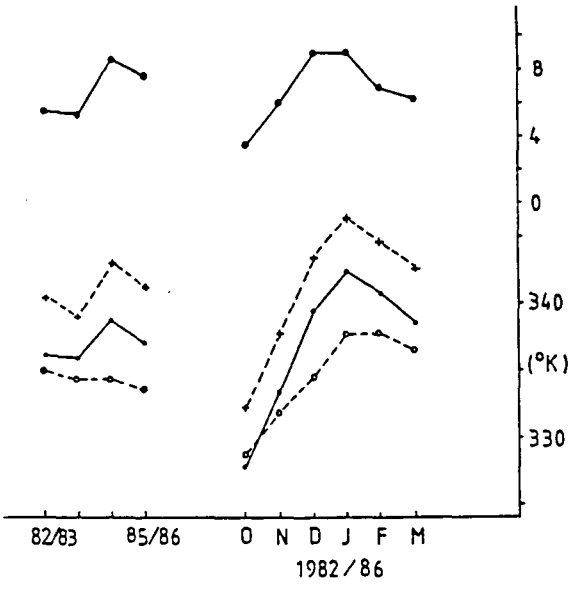

Fig. 6.6.1 (b) Four years means of the monthly means plotted in Fig. 6.6.1 (a).

is reasonable as the heating is applied to the atmosphere from the surface, and is diffused upward through mixing (turbulence and convective clouds). The result is an increase of the instability, seen as an increasing difference between the two quantities. The mean development of instability shown here is similar to that shown, for example, in northern Italy (Morgan 1973). The overall four year means of the monthly means are shown in Fig 6.6.1 (b). The means for the months, combining all four seasons, show steady warming near the ground and aloft through January, a strong reversal at the ground after that, and a lag in the reversal in the mid troposphere.

The instability peaks in December and January. The mean curve of instability does not correspond quite with our understanding of the month-to-month variations in storm activity. An examination of the standard deviations of instability and its components (Fig. 6.6.1 (c)) helps to explain why. The standard deviation can be taken as a measure of "storminess". This shows high values in November, a peak month of storm activity, and in March, offsetting the decreasing instability in that month.

Note the curves of the annual means (Fig. 6.6.1 (b)) which show a measurable cooling of the middle troposphere and a warming of the lowest layers, resulting in an average increase of instabilty over the four year period. This may be a sign of emergence from a dry period.

6.6.2. Wind speeds

Another environmental factor, to be combined with instability in seeking an explanation for the seasonal march of instability, is the strength of wind flow over the area. This is an index of cyclonic activity and mean proximity to the polar front. Figs. 6.6.2 and 6.6.3 show the mean wind speeds at 850, 700 and 500 mb for each month, by seasons and combined (82-86) and the seasonal (Oct-Mar) means for four years. The pattern which shows up in the four-year monthly means is quite strong and visible in each of the component years. November has the highest winds in the middle troposphere in each year, and November has been our peak month for storm activity.

The great instability of December-January is offset by weaker winds, while February, our second most stormy month, shows a secondary peak in 700 mb wind speed. October, the month of greatest instability, is nevertheless a month of high wind speeds and can be fairly stormy.

6.6.3. Depth of convection

Figure 6.6.4 shows some altitudes (in km amsl) of significant parameters on the sounding for the four seasons combined, month-by-month. The bottom curve is the mean altitude of the minimum of Theta-e, the hypothesized level of downdraft origin. It rises through the first half of the season and then levels off at around 4000m. The total variation is from just over

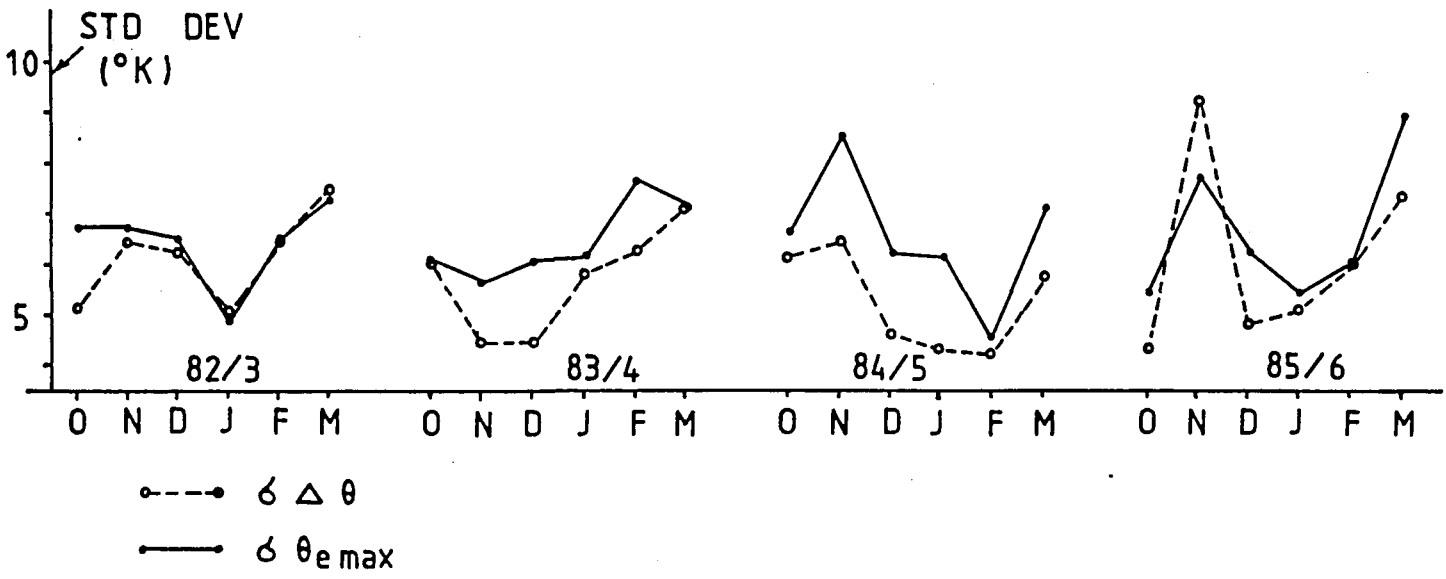

Fig. 6.6.1 (c). Standard deviations of Theta-e max and Theta-e max minus Theta-es min

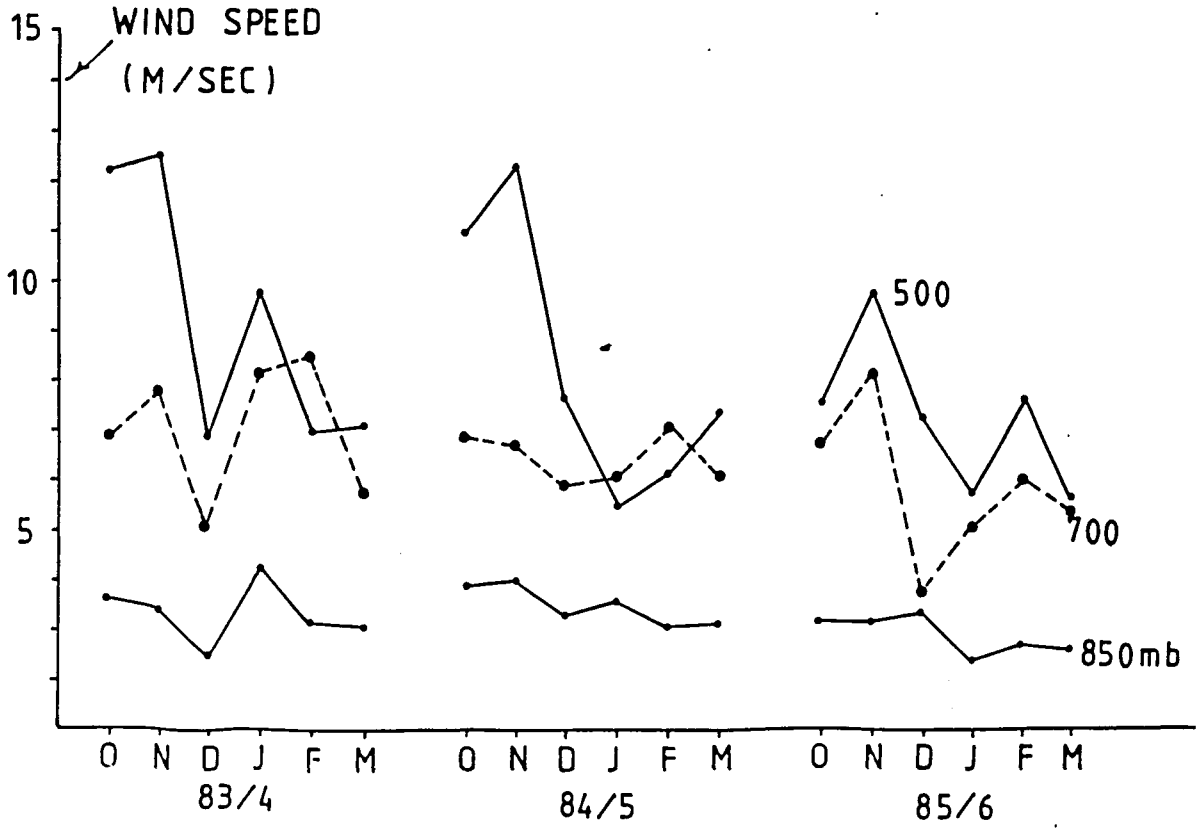

Fig. 6.6.2. Mean seasonal wind speeds: 500, 700 and 850 mb.

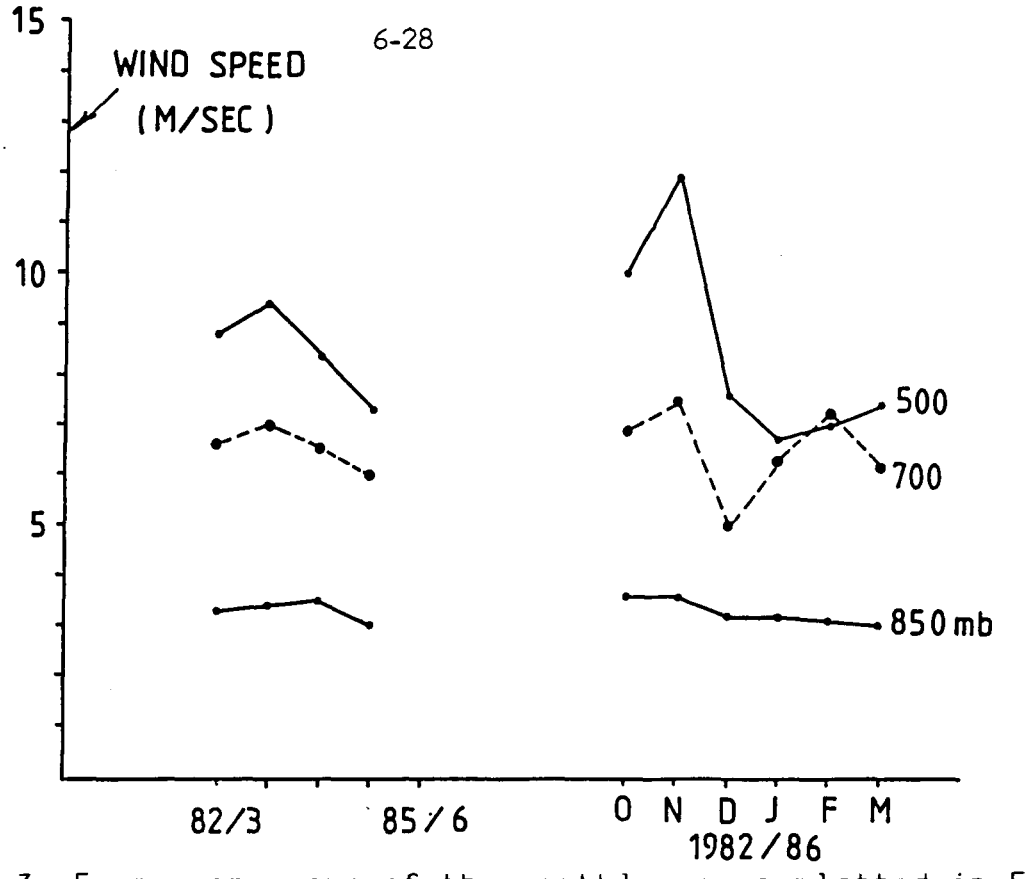

Fig. 6.6.3. Four year means of the monthly means plotted in Fig. 6.6.2.

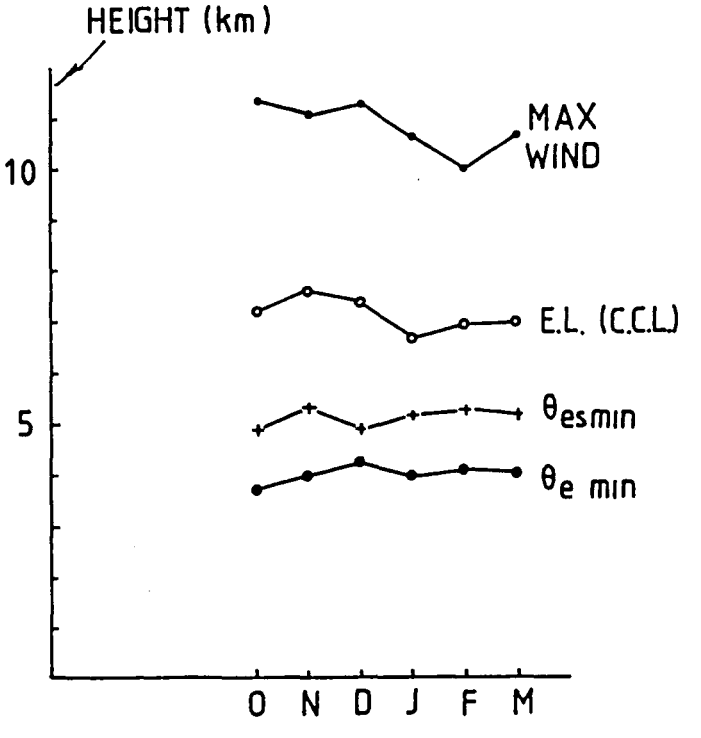

Fig. 6.6.4. Heights of seasonal means of:
- maximum wind
- convective equilibrium
- Theta-es min
- Theta-e min

3600 to just over 4200 m.

The next curve is the mean altitude of Theta-es minimum, the top of the conditionally unstable layer and the base of the layers of absolute stability. Here again, not a large variation, but November stands out, compared to its neighbour months.

The curve labelled E.L. (CCL) is the mean altitude of the equilibrium level (sometimes referred to as the "top of the positive area") for parcels rising from the CCL. This is the altitude where Theta-es of the environment equals Theta-es at the CCL. This shows a tendency for deeper convection in the early months of the season, again underlining the fact that, in the four year sample, November has been the most active month overall.

The top curve is the mean altitude of the maximum wind on the sounding. This has been shown here because the Nelspruit sounding seldom reaches the tropopause. The maximum wind is usually below the tropopause and follows it in its height variations. The tropopause is often a natural lid on convective storms, even when they are overshooting their equilibrium. Here, again, there is evidence for deeper convective storms in the early part of the season.

6.6.4. Freezing levels

The levels in the sounding at which certain temperatures equal $0^{o}C$ are important to the character and strength of convective storms, and their means are another useful way of displaying the character of a month or season.

Fig. 6.6.5 shows the behaviour of the mean heights of three types of freezing levels. The lowest curves are the wet-bulb-freezing-level or wet-bulb-zero (WBZ). This is the level at which the environmental wet-bulb temperature is $0^{o}C$. This is the lowest level to which hail or graupel can fall in the environment, without beginning to melt. It is an important hail forecasting parameter according to the USAF Severe Weather Warning Center (Miller, 1967). This has been questioned by Morgan (1970), based on observed correlations between WBZ and mean (over a layer) low level mixing ratio. This will be dealt with further on.

The middle (solid) curves are the environmental freezing level or freezing level, where the environmental temperature is $0^{o}C$.

The upper (dashed) curve is an estimate of the freezing level in the updraft. The updraft temperature profile is based on the constant Theta-e process (moist adiabatic) through Theta-e max.

There are other freezing levels in the sounding database, but they will not be dealt with here.

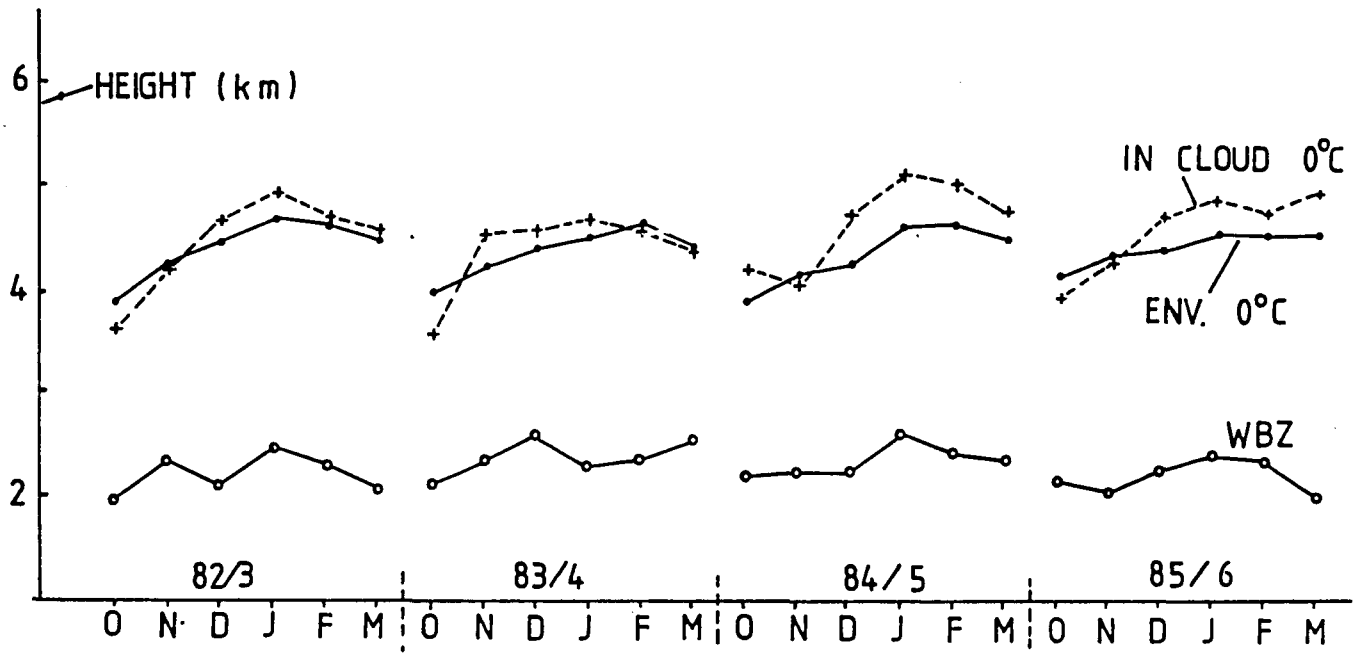

Fig. 6.6.5. Seasonal changes in mean heights of in-cloud, environmental and wet-bulb freezing levels.

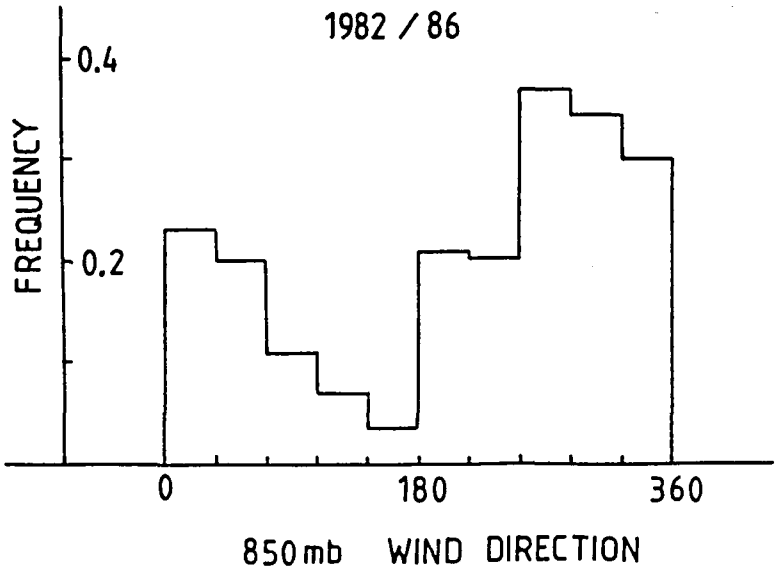

Fig. 6.6.6. Probability of operations versus morning (Nelspruit sounding) 850 mb wind direction.

850 mb Wind Direction (degrees)

ops Season	0	0-36	36-72	72-108	108-144	144-180	180-216	216-252	252-288	288-324	324-360	Total
all 82/83	11	18	16	11	21	15	13	13	24	15	18	175
all 83/84	11	19	9	13	32	27	11	12	9	20	18	181
all 84/85	5	16	10	12	20	25	8	14	15	22	23	170
all 85/86	9	17	10	17	27	20	15	5	13	15	21	169
all seasons	36	70	45	54	100	87	47	44	61	72	80	695
ops only	9	15	9	6	7	3	10	9	23	25	24	140
ratio	.25	.21	.2	.11	.07	.03	.21	.20	.37	.347	.30	.2

Table 6.6.1 Distribution of 850 mb wind direction - Nelspruit morning sounding.

Theta-es min

Season	321	321 323.5	323.5 326	326 328.5	328.5 331	331 333.5	333.5 336	336 338.5	338.5 341	341 343.5	343.5 346	346	Total
82/83	5	3	1	8	19	25	32	40	27	12	2	1	175
83/84	4	4	5	13	21	25	31	39	29	9	1	0	181
84/85	1	5	8	14	25	24	26	23	23	16	3	2	170
85/86	4	2	11	8	18	31	40	33	14	7	1	0	169
all seasons	14	14	25	43	83	105	129	135	93	44	7	3	695
ops days	0	0	3	7	18	24	25	32	20	7	2	2	140
ratio	0	0	.12	.163	.216	.23	.19	.24	.21	.16	.28	.67	.20

Instability

Theta-e max - Theta-es min

	-15	-15 -11	-11 -7	-7 -3	-3 +1	1 5	5 9	9 13	13 17	17 21	21 25	Total
all seasons	2	5	13	31	78	146	169	139	79	28	5	695
ops days	0	0	0	1	4	15	35	31	37	15	2	140
ratio	0	0	0	.032	.051	.103	.206	.223	.468	.535	.40	.20

Table 6.6.2 Distribution of equivalent potential temperatures - Nelspruit morning sounding (see text for details).

Theta-e min (°K)

Season	≤ 310	310 - 312.5	312.5 - 315	315 - 317.5	317.5 - 320	320 - 322.5	322.5 - 325	325- 327.5	327.5- 330	330- 332.5	332.5- 335	> 335	Total
82/83	8	7	8	8	23	21	31	20	27	13	7	2	175
83/84	3	7	3	20	30	32	37	18	10	7	10	4	181
84/85	4	2	14	22	29	29	28	14	10	10	1	7	170
85/86	5	7	12	30	30	26	16	17	13	11	2	0	169
all seasons	20	23	37	80	112	108	112	69	60	41	20	13	695
ops days only	0	1	2	7	12	21	33	18	25	15	3	3	140
ratios	0	.04	.054	.087	.107	.185	.294	.246	.416	.366	.15	.23	.20

Theta-e max (°K)

Seasons	≤ 325	325- 329	329 - 333	333 - 337	337 - 341	341 - 345	345 - 349	349 - 353	353 - 357	357 - 361	361- 365	> 365	Total
82/83	7	13	17	20	33	29	31	19	4	2	0	0	175
83/84	10	10	23	24	35	34	27	12	4	1	0	1	181
84/85	5	7	17	10	23	33	30	32	6	5	2	0	170
85/86	6	10	17	16	28	31	34	20	4	3	0	0	169
all seasons	28	40	74	70	119	127	122	83	18	11	2	1	695
ops days	0	1	3	12	16	29	31	29	10	8	0	1	140
ratio	0	.025	.040	.171	.134	.23	.262	.35	.55	.72	0	1.00	.20

Table 6.6.2 Cont/.

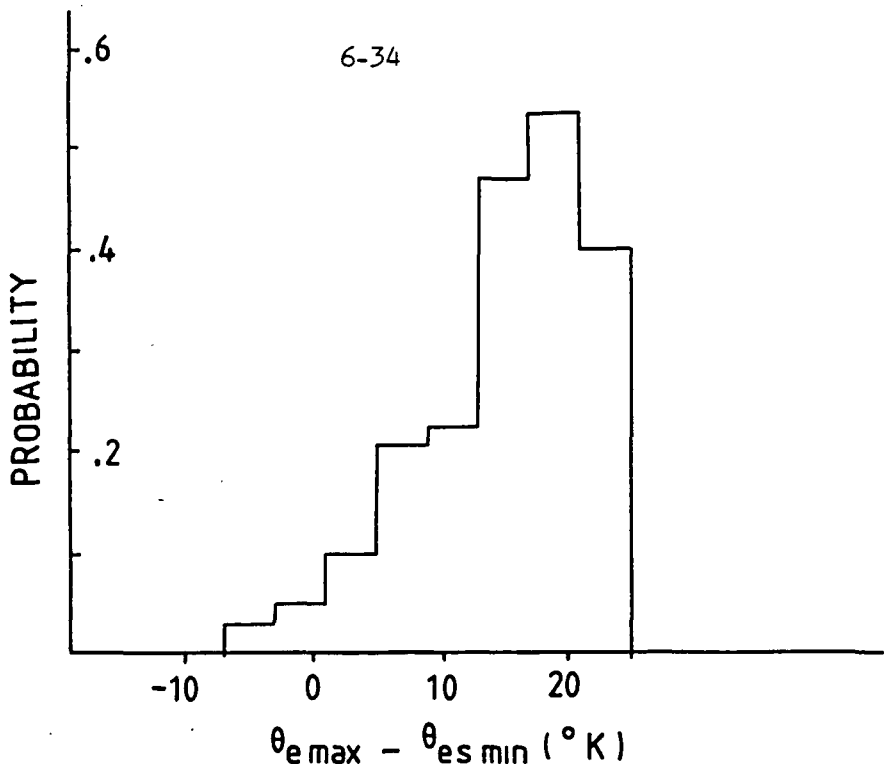

Fig. 6.6.7. Probability of operations versus Theta-e max minus Theta-es min from morning radiosonde.

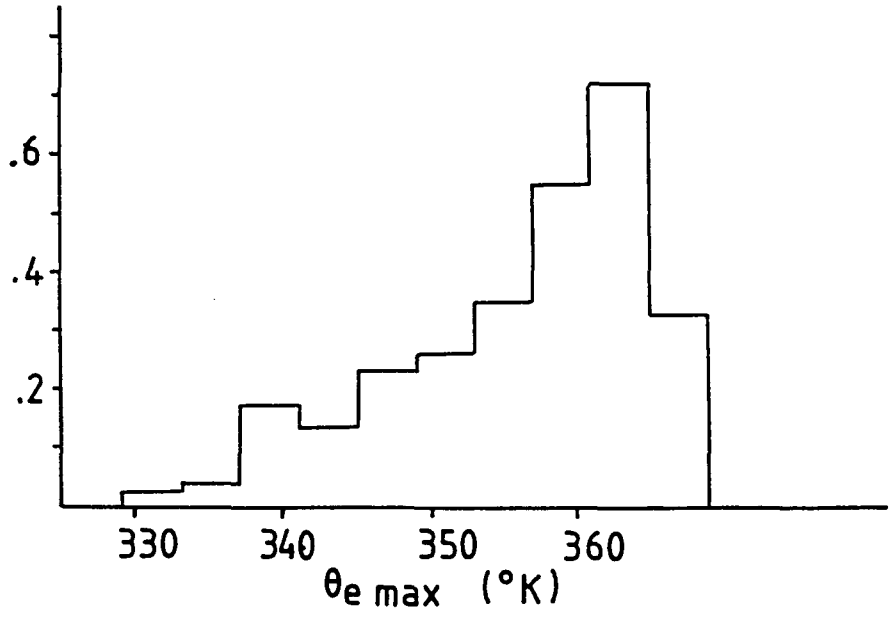

Fig. 6.6.8 (a). Same as Fig. 6.6.7 for Theta-e max.

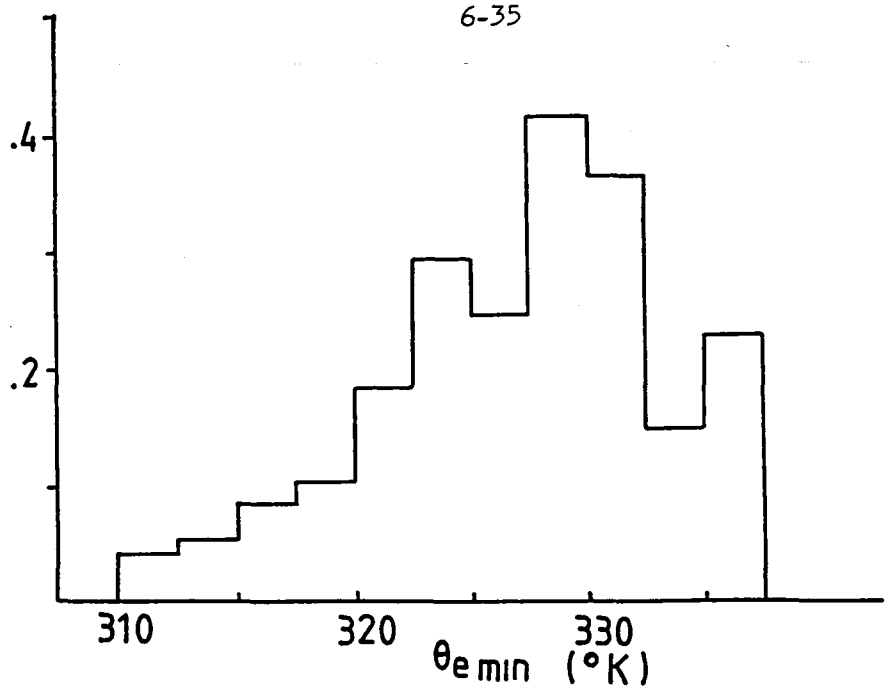

Fig. 6.6.8 (b). Same as Fig. 6.6.7 for Theta-e min.

6.6.5. Low-level wind direction

The winds in the lowest levels are an importnt element in any convective storm forecast scheme. Winds at and near the surface respond in characteristic ways to the approach and passage of synoptic systems and also are then highly correlated with the character of the advection of heat and moisture.

The importance of low level winds in favouring storms in Nelspruit is readily shown based on the wind direction at 850 mb, as measured by the morning sounding. Table 6.6.1 gives the distributions by 850 mb wind directions of all the morning soundings for each of four seasons and for all four combined. The last line gives the 850 mb morning winds for all operational days during the four seasons.

The following graph (Fig. 6.6.6) shows the ratio of operational days to all days for each 850 mb wind interval, and hence the probability of operations given only the morning 850 mb wind direction. The northwesterly wind direction preference is quite strong, a third of days being operational when the wind lies between 250 and 360 degrees. Even stronger is the probability minimum associated with southeastern wind direction.

The underlying cause for this is quite well known, the southeasterly winds being generally post-frontal (cool and moist). Though northwest winds (often pre-frontal) blow downslope, our experience with the metmaps (Section 6.4) has shown that such winds often bring higher mixing ratios into the area (and higher Theta-e, as well).

6.6.6. Equivalent potential temperatures and related measures.

The equivalent potential temperatures have been treated in the same manner as the 850 mb wind directions and the results are displayed in Tables 6.6.2 (a and b) and the graphs of Figs. 6.6.7 and 6.6.8. The probabilities of operations exceed 50 percent for certain classes of some of these variables. It should be noted that the overall probability of an ops day (number of ops days divided by total numbers of days) is 0.2 (20 percent) and so values above and below that show some effect of the variables. It should also be kept in mind that some of these variables are correlated with each other.

The uninteresting behavior of Theta-es min is somewhat surprising. Its combination with Theta-e max to form the difference (a stability index) however, seems a strong variable. The high probability in the last category of Theta-es min probably is the result of a few days with very tropical showers (low tops - strong coalescence).

6.6.7. Relationship between morning sounding parameters and Lear soundings later in the day

The parameters calculated from the morning sounding are really predictions of conditions during the afternoon, based on certain simplified assumptions about mixing of the lower layers. We can investigate the accuracy of these predictions by comparing them to values observed on soundings carried our later in the day. The largest number of such soundings are those made by the Learjet. This sample is, of course, biased by the fact that the Lear is launched only when storms of sufficient intensity break out. We have a very limited set of unbiased later soundings, from the Intensive Study Period of November 1984. Fig. 6.6.16 shows a sample regression plot based on these.

The regressions shown here have been determined using the Lear up-soundings only. It was felt that the down-soundings were too often contaminated by cloud and to use them would require too much screening effort.

The following plots (Fig. 6.6.9 to 6.6.16) show the scatter of the data, and regression equations relating the early to the later data. In many cases a curvilinear regression is also shown. The plots are presented, for the moment, without detailed comment. A few general comments follow:

1. The morning calculation of CCL tends to overestimate the variability of quantities later measured. For example, low morning CCL heights (high pressure) almost always are followed by higher cloud-bases.

2. Buoyancy (Delta-T 500) is generally overestimated by CCL.

3. Max Theta-e seems a better predictor of subsequent mean Theta-e than the early value of mean Theta-e. This seems quite natural given the heating that takes place.

These curves or linear regressions can be introduced into the morning sounding analysis package to give improved predictions of the afternoon cloud properties.

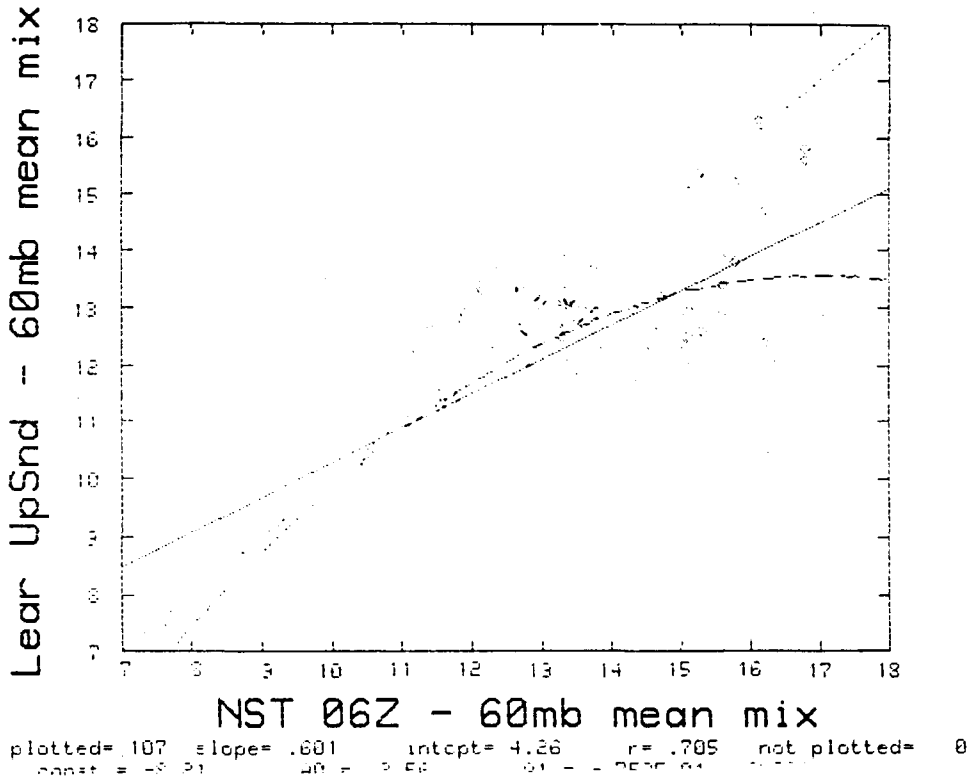

Fig. 6.6.9. Average mixing ratio in lowest 60 mb layer of the morning (0600Z) Nelspruit sounding versus the same mean mixing ratio for the subsequent Learjet climb out sounding.

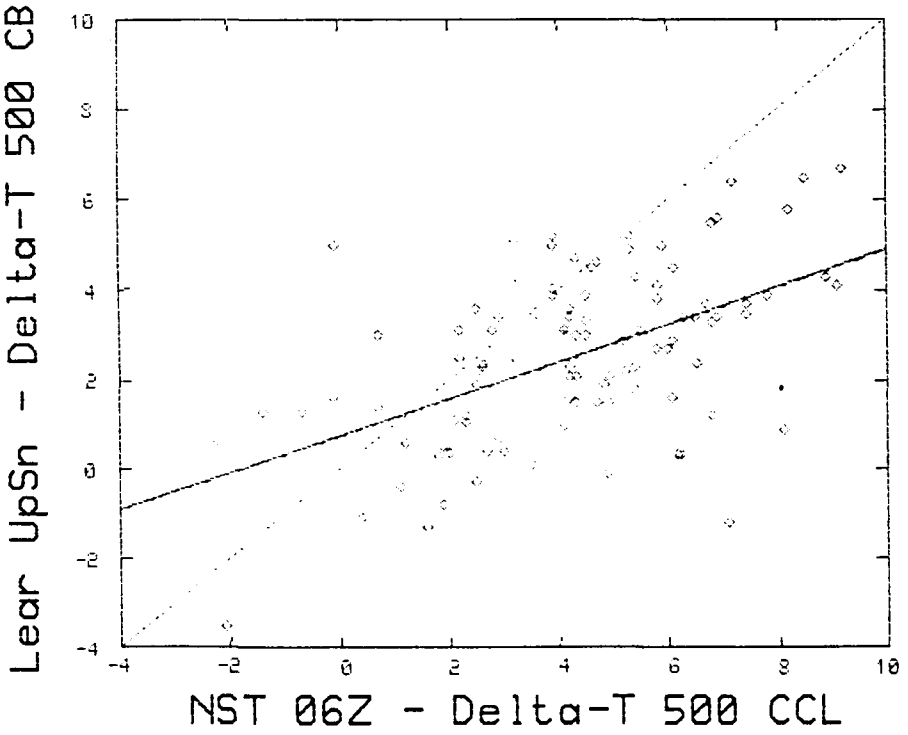

Fig. 6.6.10. As in 6.6.9, but for the 500 mb buoyancy estimated from the paired soundings.

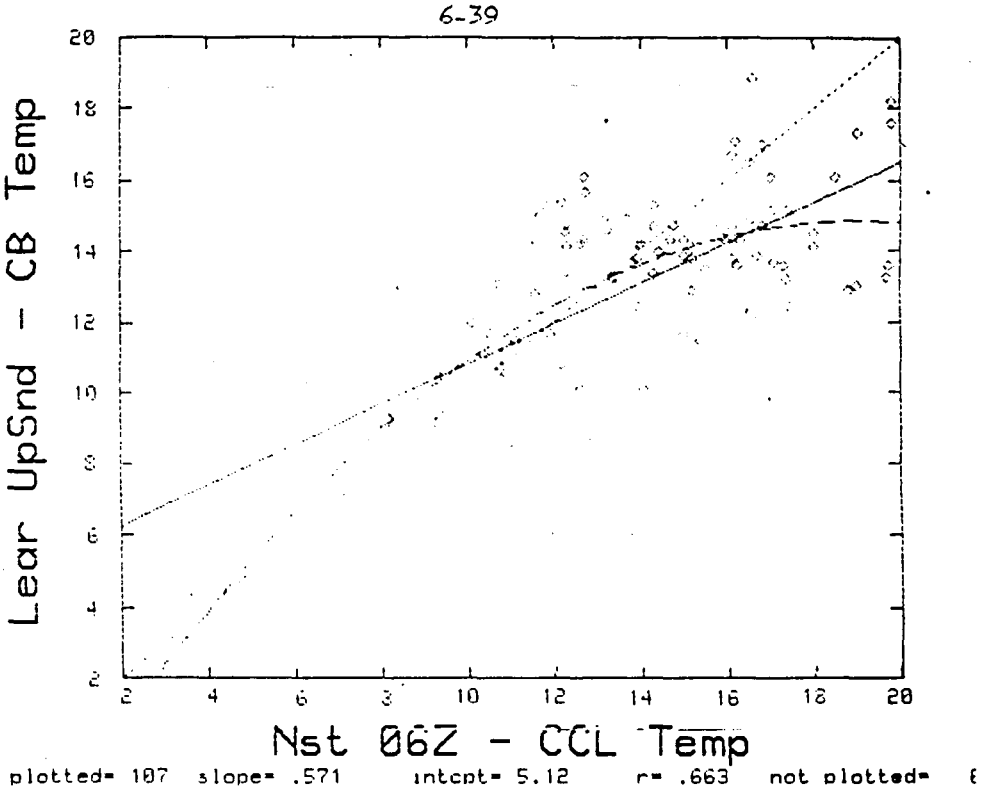

Fig. 6.6.11. As in 6.6.9, but showing the afternoon cloud base temperature against the morning CCL temperature.

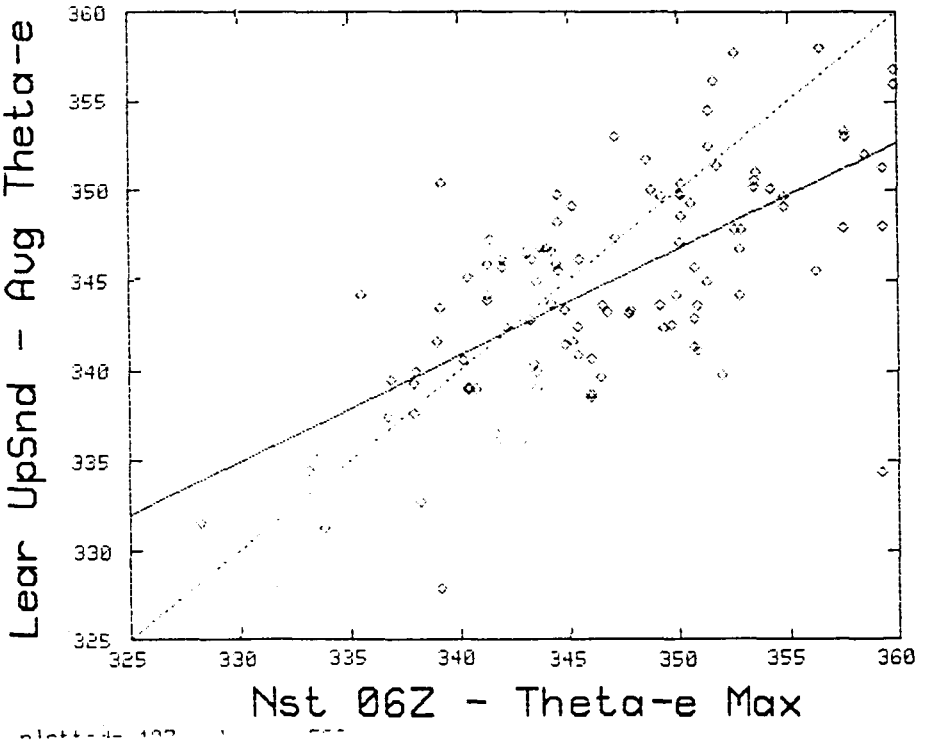

Fig. 6.6.12. As in 6.6.9, but showing the 60 mb average Theta-e in the afternoon versus the maximum Theta-e near the ground on the morning.

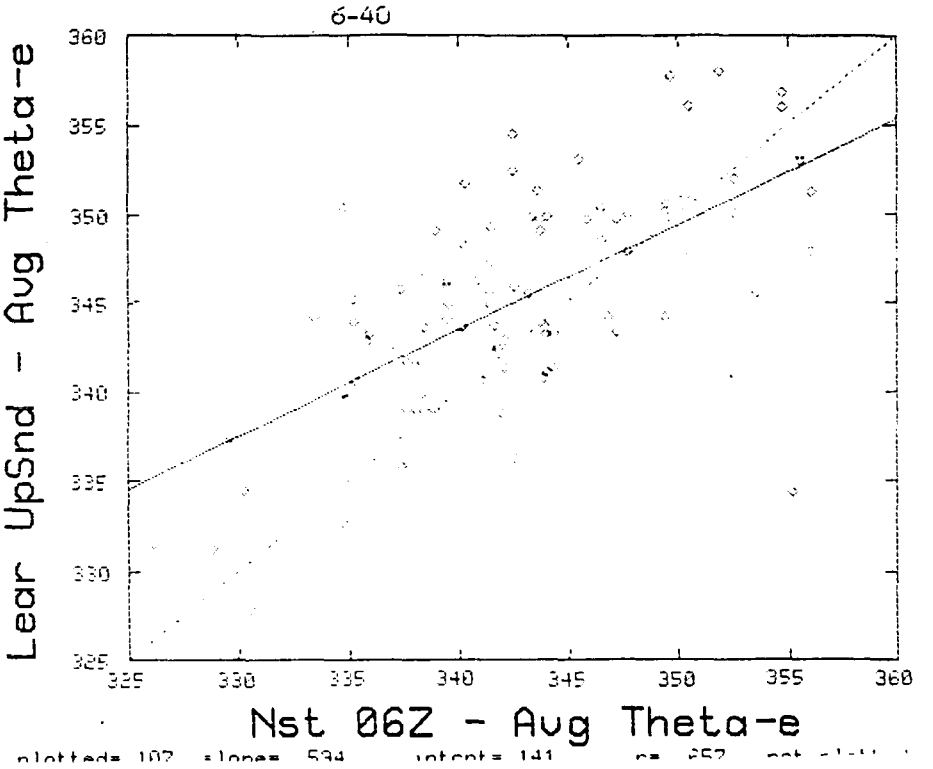

Fig. 6.6.13. As in 6.6.9, but showing the afternoon average 60 mb Theta-e versus the same quantity estimated from the morning sounding.

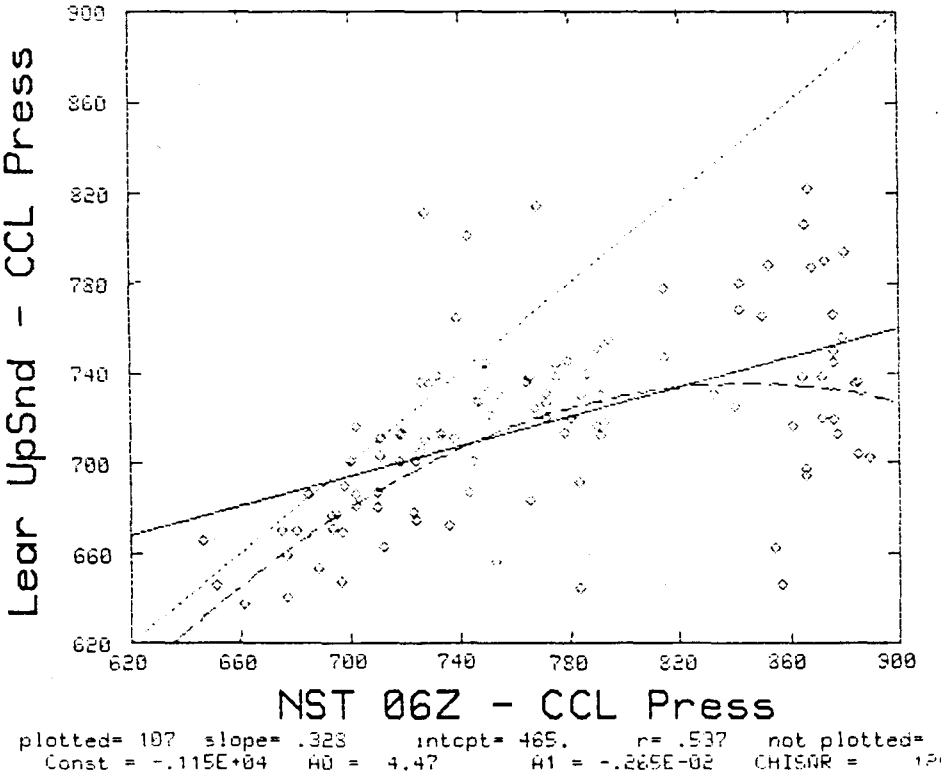

Fig. 6.6.14. As in 6.6.9, but comparing the CCL pressure estimated from the paired soundings.

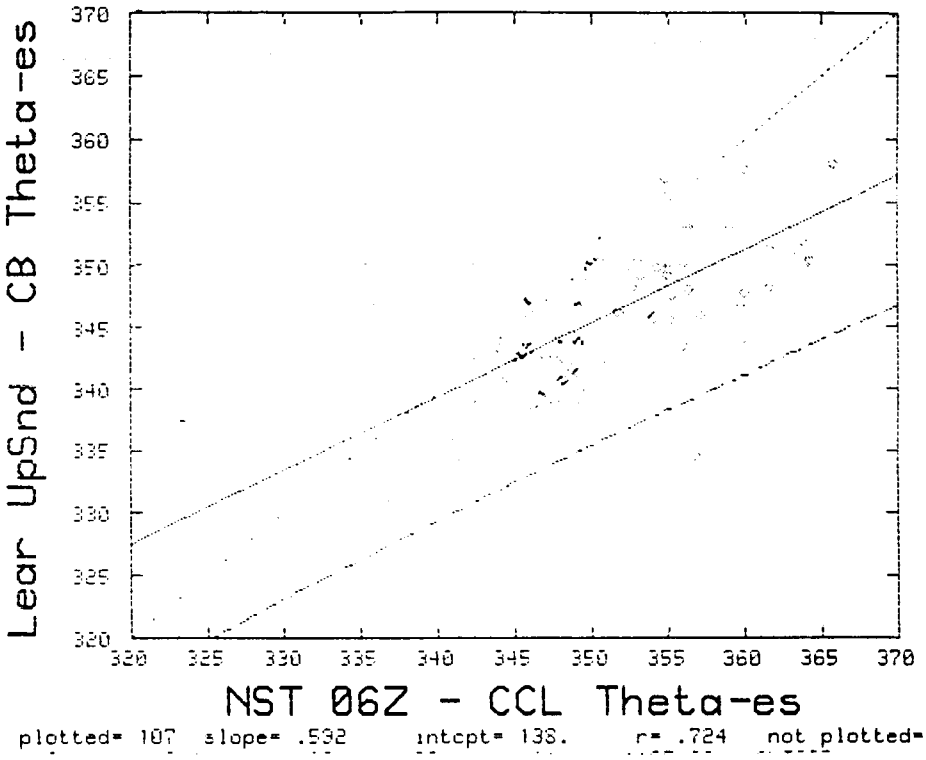

ig. 6.6.15. As in 6.6.9, but comparing the Theta-es at cloud base estimated from the afternoon (Learjet) sounding to the Theta-es at the CCL on the morning sounding.

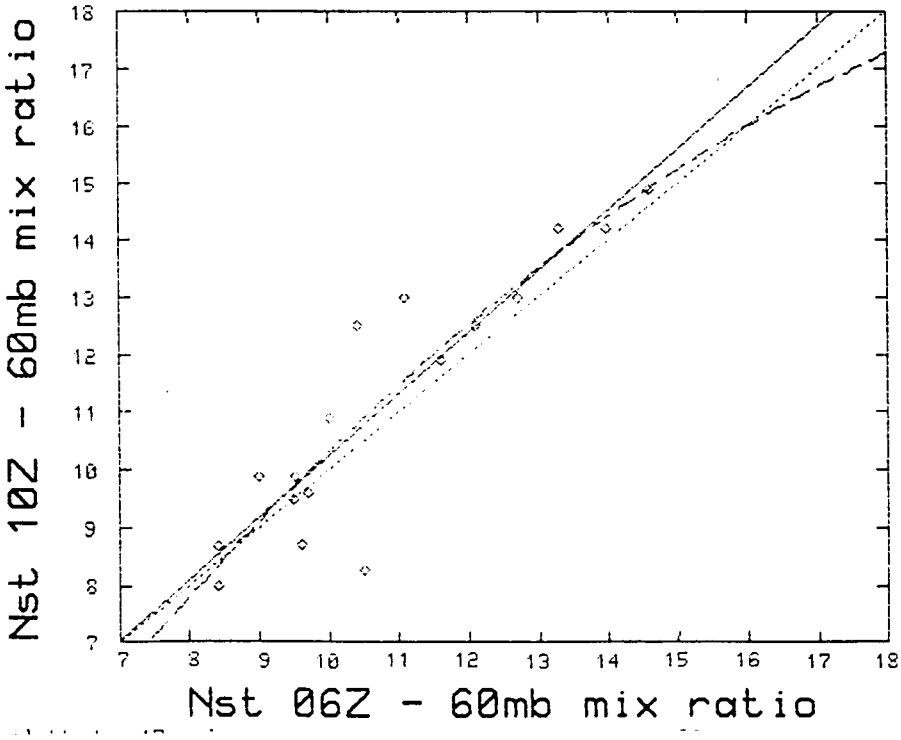

Fig. 6.6.16. A regression example from the small set of morning (0600Z) and local noon (1000Z) soundings performed during the Intensive Study Period of November 1984.

7.0 PROPERTIES OF DRY ICE AS A GLACIOGENIC SEEDING AGENT

For nearly forty years dry ice has been one of the most often used materials for glaciogenic seeding. The effectiveness of dry ice, i.e. how many detectable ice particles are generated per gram of dry ice sublimed, has been the focus of several field and laboratory experiments (Eadie and Mee, 1963; Fukuta, et al., 1971; Allee, et al., 1972; Holroyd, et al., 1978; Lozowski and Kochtubajda, 1980). More recent work by Morrison, et al. (1984), in the Colorado State University simulation laboratory has added evidence of not only a higher effectiveness than previously reported but also a temperature dependence for the ice production.

The laboratory work at CSU was a continuation of a series of experiments begun during the RAIN (Rain Augmentation in Nelspruit) project to examine, in detail, various aspects of dry ice pellet behavior in supercooled clouds. Some questions addressed during RAIN involved the size distribution of the pellets actually being delivered to the cloud, pellet lifetimes, variation of pellet fall velocities as pellet shape and size change, sublimation rates as a function of cloud liquid water content (LWC), and the significance of the ice "whiskers" that are shed from the falling pellets. A complete report of those experiments is contained in Emmitt, Roos and Morrison (1984).

7.1 LABORATORY ESTIMATES OF DRY ICE EFFECTIVENESS[1]

Despite the fact that dry ice has been widely utilized as a cloud seeding agent for several decades, there are misconceptions and deficiencies in the knowledge about dry ice nucleation that limit the scientific basis for its use. Laboratory experiments conducted at the Colorado State University (CSU) Cloud Simulation and Aerosol Laboratory used the 960 liter isothermal cloud chamber to address this problem. As part of the research an accurate effectiveness spectrum was established, rates of ice crystal production determined, and nucleation mechanism investigated. The laboratory effectiveness spectrum was also compared to values derived from a simple numerical model which estimates dry ice effectiveness using cloud physics data from aircraft observaations of dry ice seeding signatures.

7.1.1 Dry Ice Effectiveness

An electro-mechanical precision catapult apparatus was used to launch small spherical dry ice pellets vertically into the CSU cloud chamber at speeds up to 82% of terminal velocity. The pellets were exposed to the cloud over a 10.2 cm path length and then caught behind a motor-driven shutter in a trapping tube. A small fan was simultaneously operated for 4 seconds to minimize aggregation of ice embryos in the pellet plume and to mix them uniformly throughout the chamber. Ice crystal yields were measured by

---

[1]Material in this section (7.1) based solely upon conference paper by Morrison, Finnegan, Horn, and Grant. However, the research was funded by SWA and the Water Research Commission.

counting ice crystals under a microscope and the rates of ice crystal production were measured using a capillary type acoustic sensor system. The supercooled cloud was continuously replenished and monitored during the experiment.

The effectiveness spectrum for 5 mm diameter spherical pellets at a cloud liquid water content of 1.5 g m^{-3} is shown in Fig. 7.1. This result is substantially different from that of Fukuta et al. (1971) which shows no temperature dependence. Their effectiveness spectrum after correction for a computational error pointed out by Horn et al. (1982) is plotted as a dashed line in Fig. 7.1. The flat spectrum may be an artifact due to overseeding with subsequent sublimation loss of many ice embryos (Horn et al., 1982).

Model effectiveness values derived from RAIN field data are plotted in Fig. 7.1 as the circled numbers (Volume III, Section 2.0). They are generally within an order of magnitude of the laboratory-derived effectiveness spectrum and also imply a temperature dependence. This relative agreement is encouraging considering the simplicity of the model and the numerous assumptions involved.

7.1.2 Rates of Ice Crystal Production

Figure 7.2 illustrates the rates of ice crystal production in the form of kinetic plot. In this plot the total number of ice crystals counted by the acoustic sensor is taken to be the total number of viable ice embryos present after pellet transit at time t = 0. Then the depletion of these embryos with time as they grow to ice crystals and fall out is plotted from 100% on a natural log scale. For example, 90% of the ice crystals at $-2^{o}C$ are produced in 2.4 minutes and at $-15^{o}C$ in 1.3 minutes. The rate of ice crystal production is proportional to the slope of the resulting curve. These rates are generally faster than those observed for most aerosol type nucleants under the same conditions.

7.1.3 Nucleation Mechanism

A frequently held misconception is that dry ice functions primarily by the freezing of cloud droplets (Vonnegut, 1981). Our data confirms the preliminary experimental work by Horn et al. (1982) that this is not the case. If we assume a 100% droplet freezing efficiency at up to 4 times the pellet diameter from the axis of the path traversed by the 5 mm pellets, the number of cloud droplets that could be frozen amounts to only 2.5% of our total ice crystal yield at $-5^{o}C$ and 0.8% at $-15^{o}C$. In natural clouds, these percentages would be even less. Therefore, the predominant nucleation mechanism must be vapor dependent. This implies that the ice crystal yields in any cloud at a given temperature under the same seeding conditions should be similar regardless of droplet concentration and size distribution as long as the vapor supply is sufficient.

From these analyses we draw the following conclusions:

1) Dry ice effectiveness is temperature dependent and varies from 2.2×10^{11} ice crystal g^{-1} dry ice sublimed at $-2^{o}C$ to 8.9×10^{12} at $-20^{o}C$.

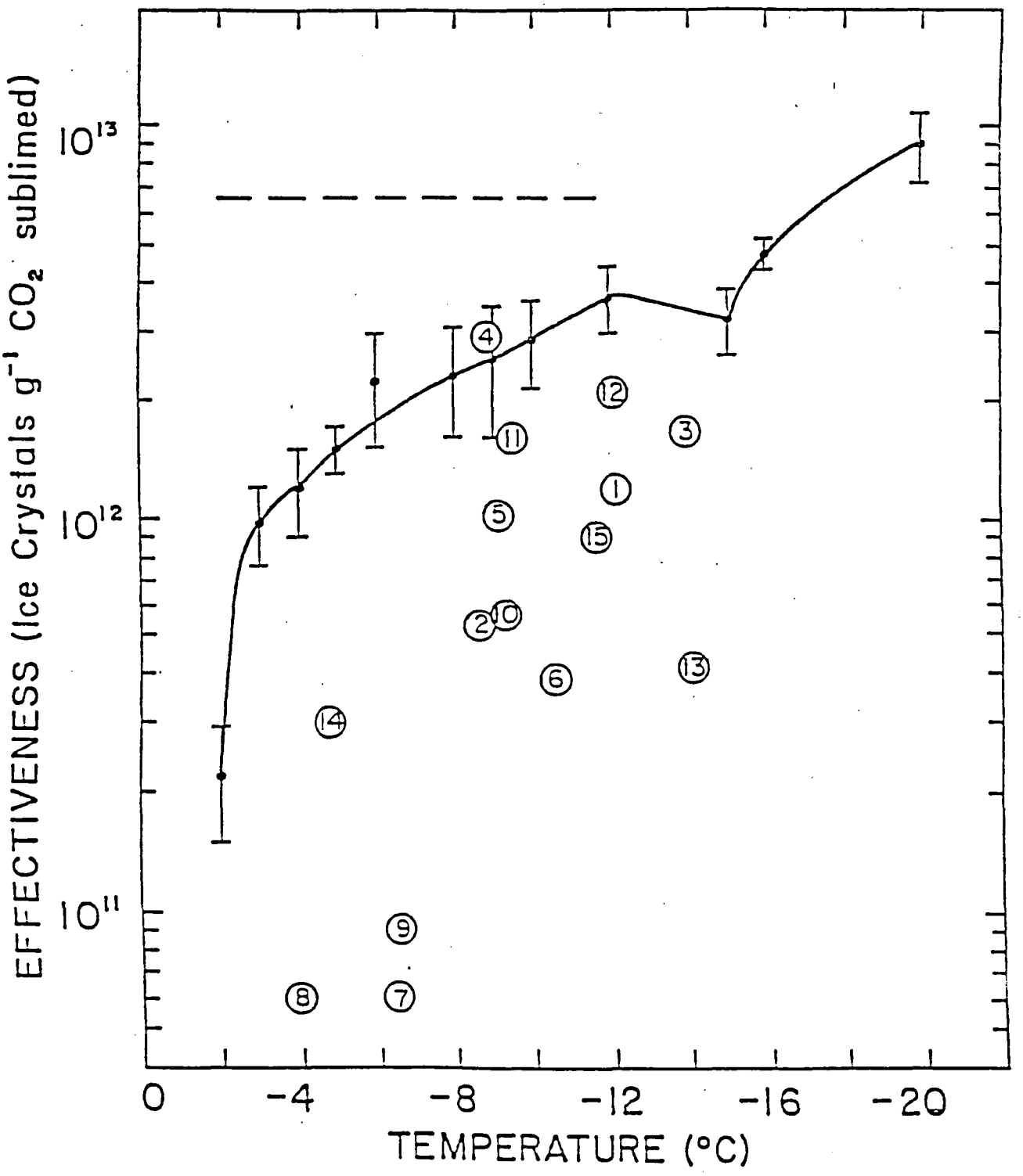

Figure 7.1. Laboratory derived effectiveness spectrum for 5 mm diameter dry ice pellets at 12.3 m s^{-1} and at a cloud liquid water content of 1.5 g m^{-3} (solid line). Simulation effectiveness values from field data of 15 clouds are plotted as the circled numbers. The Fukuta et al. (1971) spectrum after correction for a computational error (Horn et al., 1982) is shown as the dashed line.

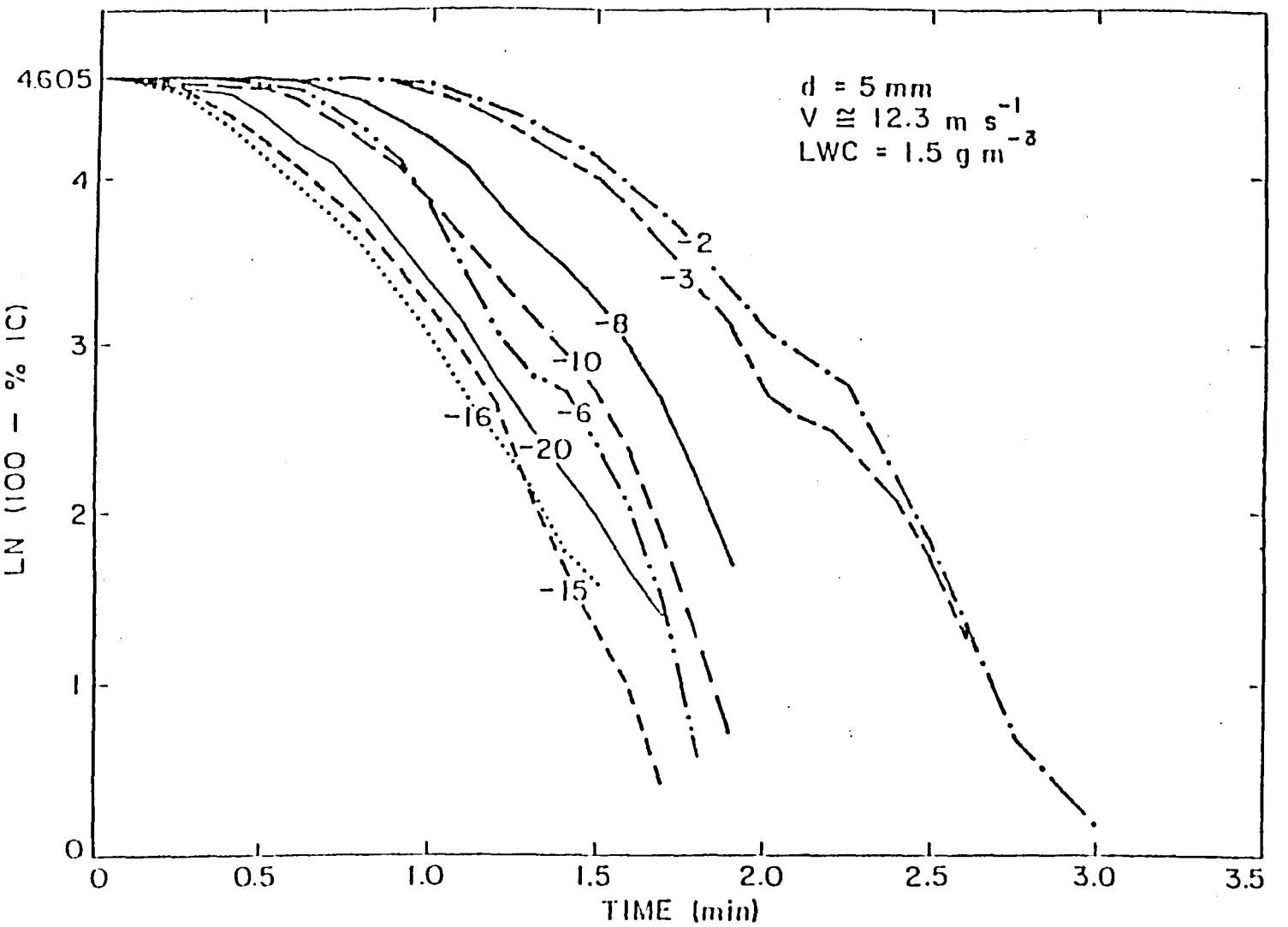

Figure 7.2. Composite kinetics plots for 15 mm dry ice pellets over a range of temperatures. The plots for -5, -9, and -12°C have not been included in order to reduce confusion in the figure.

2) Model derived effectiveness values using field data are generally within an order of magnitude of the laboratory values and also imply temperature dependence.

3) Rates of ice crystal production are much faster than most aerosol nucleants.

4) The predominant nucleation mechanism is vapor dependent.

7.2 FIELD EXPERIMENTS TO CHARACTERIZE PELLET BEHAVIOR

There were two phases of experimentation to empirically determine the terminal fall velocity and sublimation rate of the cylindrical dry ice pellets being used in the South African project. The first phase included dropping pellets from a slow (-80 kts) flying aircraft at heights ranging from 150 to 2100 meters above ground level (AGL). The second phase was carried out in the South African Council for Scientific and Industrial Research's (CSIR) cold room.

The pellets used in the field and laboratory were cylindrical in form with length to diameter ratios of - 1.0. These pellets are dispensed from the seeding aircraft at a controlled rate expressed in terms of kg/sec (.2 kg/sec for current equipment). To effectively describe the seeding treatment several key characteristics of the pellets were determined and are summarized in Table 7.1.

Table 7.1. Summary of dry ice pellet characteristics after dispensing through aircraft delivery system

	Small
Average pellet diameter (cm)	.89 (.02)*
Average pellet length (cm)	.87 (.62)
Average pellet density (g cm^{-3})	1.52 (.06)
Number density of pellets (#/kg)	-1300

*(Standard Deviations are Noted in ( ).)

The primary reasons for performing some of the field experiments in cloud free air were: 1) targeting the collection area with an aircraft would be nearly impossible from within clouds, and 2) the droplet free environment tests would provide baseline information for the laboratory experiments on

sublimation rates, terminal velocities and pellet survivability. The aircraft tests were the closest that we could get to examining the dynamical behavior of tumbling cylindrical dry ice pellets. The data thus obtained would then serve to assess our ability in the laboratory to simulate the evolution of the pellets in cloud free air. Once certain of the laboratory similarity in dry conditions, the effects of cloud droplets could then be examined.

The aircraft drops were conducted over a 150,000 m^2 sporting complex. The 3 to 5 cm high grass provided a cushion for the pellets (radius = .42 cm) and resulted in very little breakage upon impact. The fall time for the first pellet observed to contact the ground was recorded and used to compute terminal speeds. Pellet diameters and lengths were then measured within 2 minutes after the pellets reached the ground. The loss of mass during those two minutes was measured and found to be insignificant ($<5.0 \times 10^{-4}$ gm s^{-1}).

The 22 drops were carried out over a period of 4 days and repeated drops from reference heights showed little day-to-day variations. A complete discussion of these field tests is given in Emmitt, et al. (1984). However, as background for the laboratory tests, a summary of some of the field results is presented in Table 7.2.

Table 7.2. Summary of clear air dry ice pellet field experiments.

Summary of Clear Air Dry Ice Pellet Field Experiments

z (km)	°K	P (mb)	r (cm)	dm/m	$\bar{V}$ (m s^{-1})	dm/dz (gm cm^{-1})
2.0	284	720	.15	.87	12.6	3.6×10^{-6}
1.5	287	770	.23	.70	15.3	3.9×10^{-6}
1.0	290	820	.30	.49	17.2	4.1×10^{-6}
.5	293	870	.36	.26	17.8	4.4×10^{-6}
0	298	920	.42	-	-	-

z = drop height AGL; T_a = air temperature at drop height; P = pressure at drop height; r = radius of pellet after falling distance z; dm/m = fraction of mass loss over distance z; $\bar{V}$ = average fall speed over distance z; dm/dz = average mass sublimed per cm fall distance (per unit pellet length)

In general, the following two conclusions were drawn after completing the pellet experiments in cloud free air and developing models to determine pellet performance at seeding altitudes:

1) The cylindrical pellets fall at terminal velocities described in Fig. 7.3.

2) The average lifetime of pellets will be ~ 3-5 minutes depending upon the strength of the updrafts. Laboratory experiments show that the lifetime is also effected by the presence of supercooled water.

7.3 LABORATORY EXPERIMENTS TO DETERMINE EFFECTS OF SUPERCOOLED WATER

Study of the effects of supercooled water droplets on the sublimation rate of dry ice pellets and the production of ice "whiskers" necessitated the use of the sub-zero temperature vertical wind tunnel facility at CSIR in Pretoria. The wind tunnel was located in a 23 m^3 cold room with a -20°C capability. The spray nozzle, producing a controllable spectrum of supercooled droplets, was positioned on the tunnel axis, 1.2 m below the exit. The LWC of the induced cloud was determined from the measured air and water flow rates. For some of the experiments an additional LWC measurement was obtained with a Forward Scattering Spectrometer Probe (FSSP) positioned at the tunnel exit. A typical droplet size-distribution as measured by the FSSP at an airspeed of 15 m s^{-1} is shown in Figure 7.4. Comparison with spectra derived from gelatine coated slides shows a reasonable agreement except for the high counts in the smallest size bin.

The pellets used in the cold room experiments had radii of .55 cm and lengths ranging from 2-3 cm. Since we were looking for a % change in sublimation rates due to supercooled water droplets, the tunnel speed (15 m s^{-1}) and pellet exposure (rotation speed) were held constant throughout the experiments.

A complete set of runs was made at the three temperatures -5°C, -11°C and -16°C. More than 50 pellets were used to obtain sublimation values for LWC's of 0.0, 1.5, and 4.5 gm m^{-3}. The pellets were placed in the exit of the tunnel for 1 minute periods after which they were weighed to within $\pm$0.03 gm and then reexposed for additional one minute intervals until they could no longer survive for measurement. The results of these tests are summarized in Table 7.3. Figure 7.5 illustrates the pellet sublimation for T_{air} ~ -5°C. Since these experiments were made at a constant speed (15 m s^{-1}), only during the first minute or so should a comparison of the laboratory sublimation rates be made with values determined in the field (previous work by Emmitt et al., 1984).

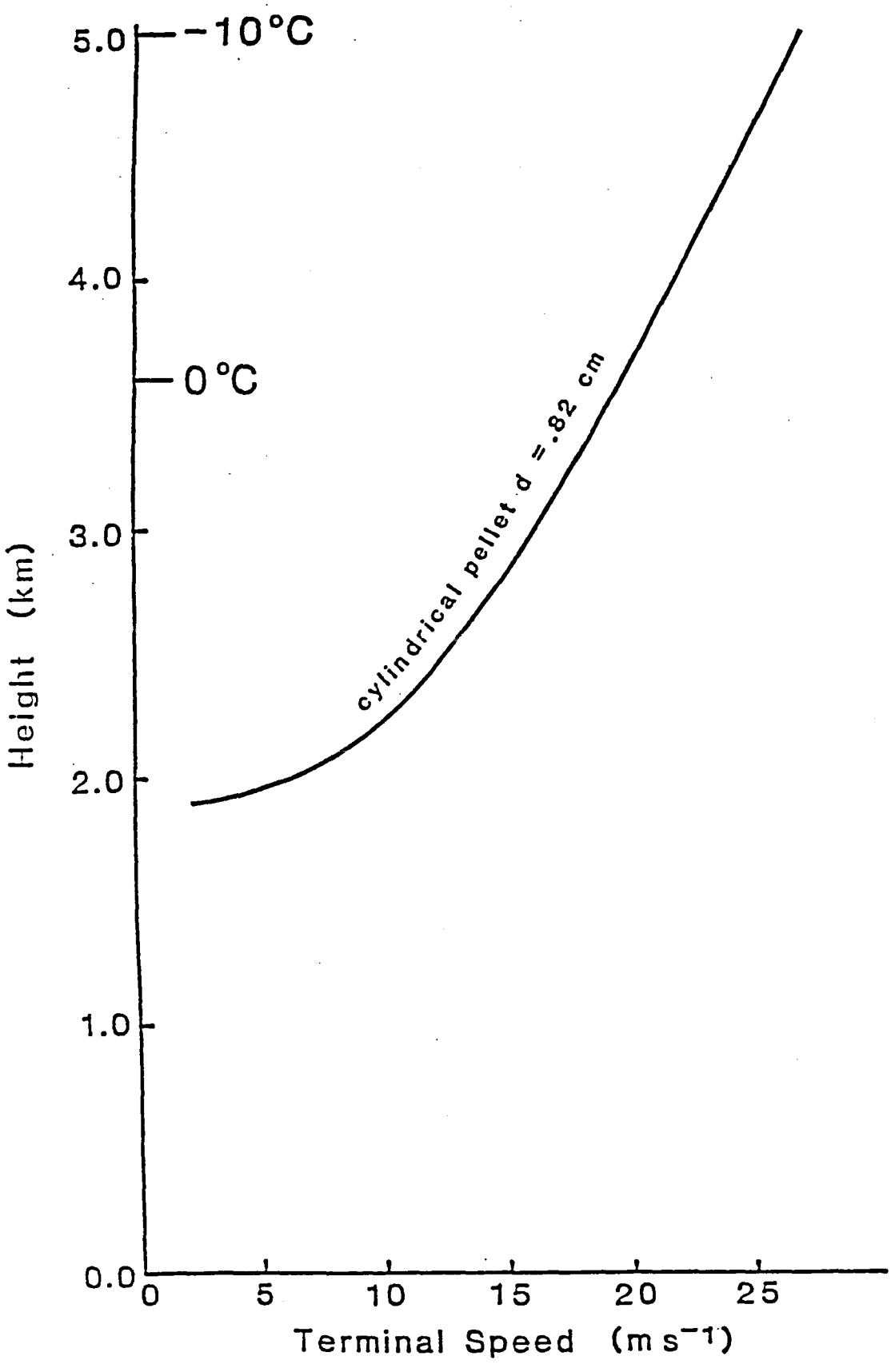

Figure 7.3. Model simulation of pellet speed as a function of height for a release at -10°C in cloud-free air.

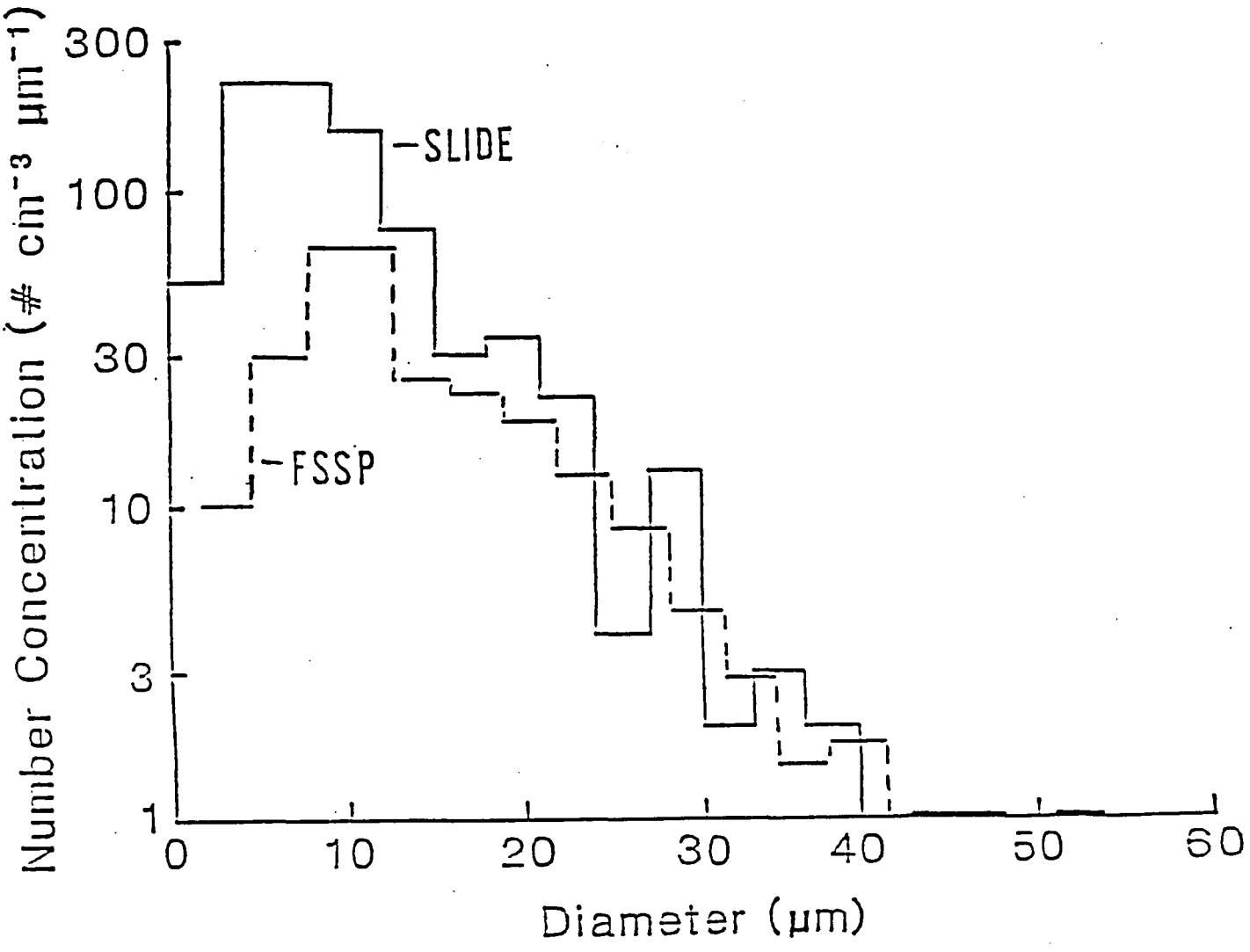

Figure 7.4. A supercooled water droplet spectra used in CSIR vertical wind tunnel. Solid line was obtained with FSSP; dashed line spectra was obtained with gelatine coated slides.

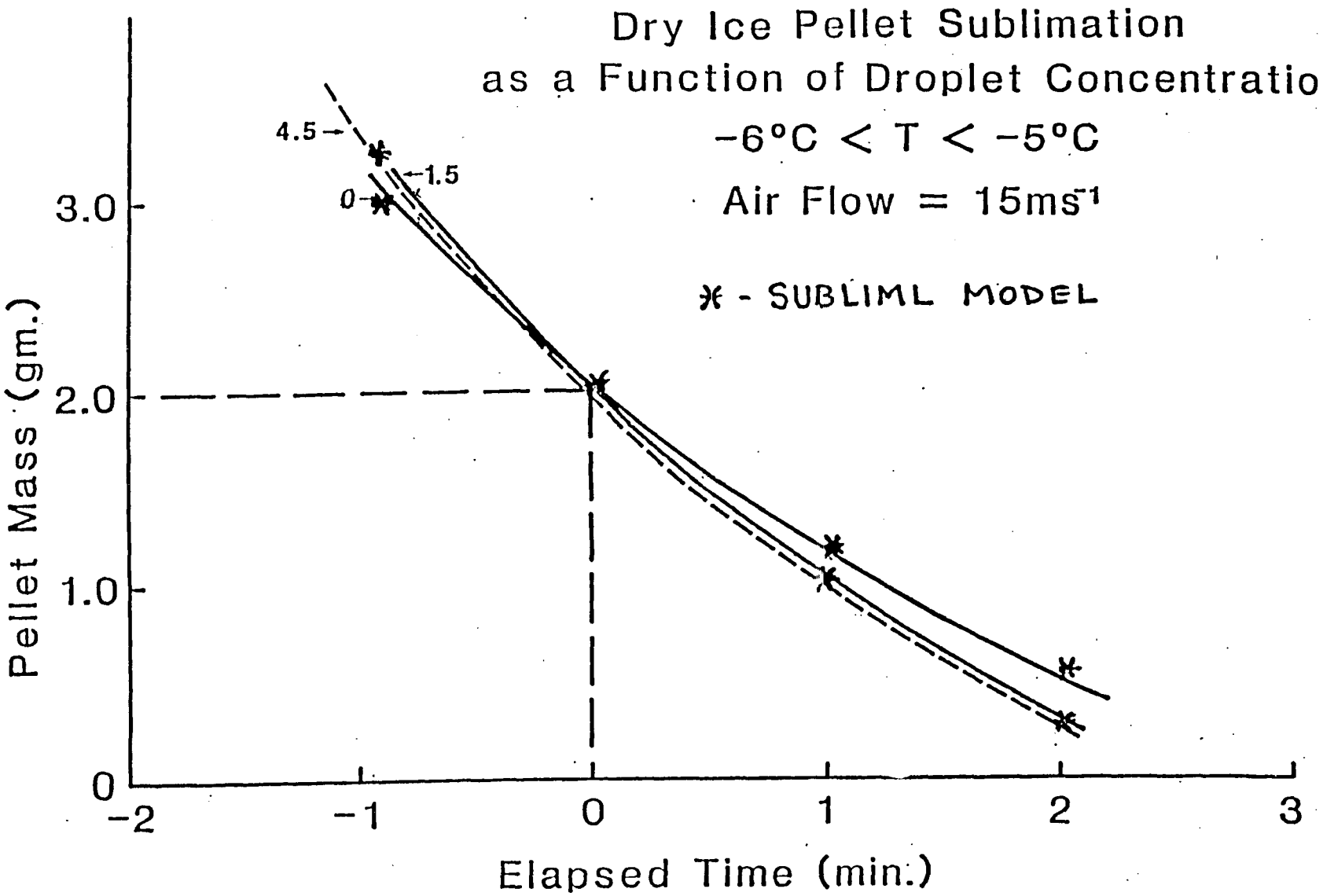

Figure 7.5. Laboratory measured and model predicted pellet sublimation at -5°C, airflow of 15 m s^{-1} and three liquid water contents (0, 1.5 and 4.5 gm m^{-1}).

Table 7.3. Pellet mass loss (%) after 1 minute time intervals.

Temp (°C)	LWC (gm m^{-3})	1 min	2 min	3 min
-5	0	37	66	90
	1.5	46	81	98
	4.5	44	76	97
-11	0	34	62	80
	1.5	40	69	92
	4.0	42	74	96
-16	0	38	67	85
	1.5	39	70	91
	4.5	41	76	96

An examination of Table 7.3 shows that the largest (24% increase) percentage change in rate of sublimation during the first minute occurred at -5°C and for 1.5 gm m^{-3} LWC; the smallest (3% increase) first minute change occurred at -16°C and 1.5 gm m^{-3}. This decrease in supercooled water effect with a decrease in temperature is consistent with the observation of a buildup of an ice layer on the pellet and its subsequent shedding. Riming was also noted by Lozowski and Kochtubajda (1980) and more recently Lozowski (personal communication) reported detecting a decrease in the effect of supercooled water with decreasing temperature. Although no attempt has been made to theoretically estimate the effect that riming may have on the sublimation rate, it is conceivable that the reduced heat conduction through the ice coating could actually reduce the cloudy air sublimation rate below the clear air rate, depending upon how often the ice was shed.

Although keeping the tunnel speed and pellet exposure constant gave us better control in the experiment, it did not allow for the tumbling action of the pellet which may affect the amount and pattern of riming which, in turn, could affect the aerodynamics of the pellet and therefore its tumbling behavior. However, in the judgement of the experimenters, the shedding of the ice coating seemed to be random and not particularly in phase with the pellet rotation. Whether the pellet was tumbling or not, the tendency to rime would be greater at the colder temperatures and thus the decreasing effect of the supercooled water on the dry ice sublimation rates would be in the same sense as was found in the laboratory.

In summary, these laboratory experiments have shown that:

1) in the presence of supercooled water droplets there is an increase in the sublimation rates of cylindrical dry ice pellets (range 3% - 25%),

2) the sublimation rate increase is largest at warm temperatures and while the pellets are large, and

3) in the seeding temperature range (-5°C to -15°C), the lifetimes of the pellets are reduced by 10-15%.

7.4 LABORATORY EVALUATION OF DRY ICE PELLET "WHISKERS"

Besides the riming of the dry ice pellets, there was visible evidence of frost particles being blown or knocked from the pellets' surface. A considerable effort went into examining the physical characteristics and quantifying number concentrations of these ice "whiskers" shed by the subliming dry ice pellets, both with and without supercooled water droplets.

The ability of dry ice to produce large and unnatural concentrations of ice particles in clouds has been demonstrated in laboratory and field experiments (Emmitt, 1984, Fukuta, et al., 1971), although the exact magnitude of the effectiveness (# ice particles/gm dry ice) may still be debated (Morrison, et al., 1984). It is generally accepted that the primary means of ice production by dry ice is homogeneous nucleation due to the low temperature ($-79^{o}C$) of solid CO_2. Ice particles thus produced grow by vapor deposition for several minutes until they are large enough to grow by the accelerated process of riming. Contact freezing is considered a secondary process.

PAWS laboratory experiments have provided evidence of a way in which dry ice may produce instantly large ice particles of riming size. Because of their filament appearance under a microscope these particles are referred to as "whiskers."

7.4.1 Nature of Dry Ice Pellet "Whiskers"

Shortly after being made, a dry ice pellet exposed to the air will form a jacket of frost. Left undisturbed, the frost layer grows until an equilibrium between frost production and ice sublimation is achieved (Lozowski and Kochtubajda, 1980). When the pellet is subjected to an airflow of a few meters per second, a plume of frost "whiskers" can be seen being stripped off the pellet. Questions arise regarding the crystalline structure, maximum size (at terminal fall velocity of the pellet in clear and cloudy conditions) and the number concentrations of these particles. A primary question is, do the ice "whiskers" shed from a tumbling dry ice pellet provide a significant number of instantly large riming centers?

By re-orienting the CSIR wind tunnel into a horizontal position, the whisker plumes of dry ice pellets held at the tunnel outlet were sampled utilizing a PMS OAP-2D probe and formvar replicating slides. Typically, the 2-D probe was located at about 10 cm from the pellet and simultaneous formvar samples were taken just downstream of the 2D probe.

Whiskers in the plumes of dry ice pellets in dry airflows were clearly observed in the 2-D images (Figure 7.6). Concentrations of whiskers longer than 100 m derived from both formvar examination and computer processing of the 2-D images are in good agreement -- on the order of 40 to 50 per liter. Concentrations computed for these laboratory experiments should not be confused with concentrations that would be sensed with an aircraft two to three minutes after a seeding run. Further discussion of concentrations is presented in Section 7.4.2.

When small pieces of dry ice were observed under the laboratory microscope under a normal room environment with little air motion, dendrite or

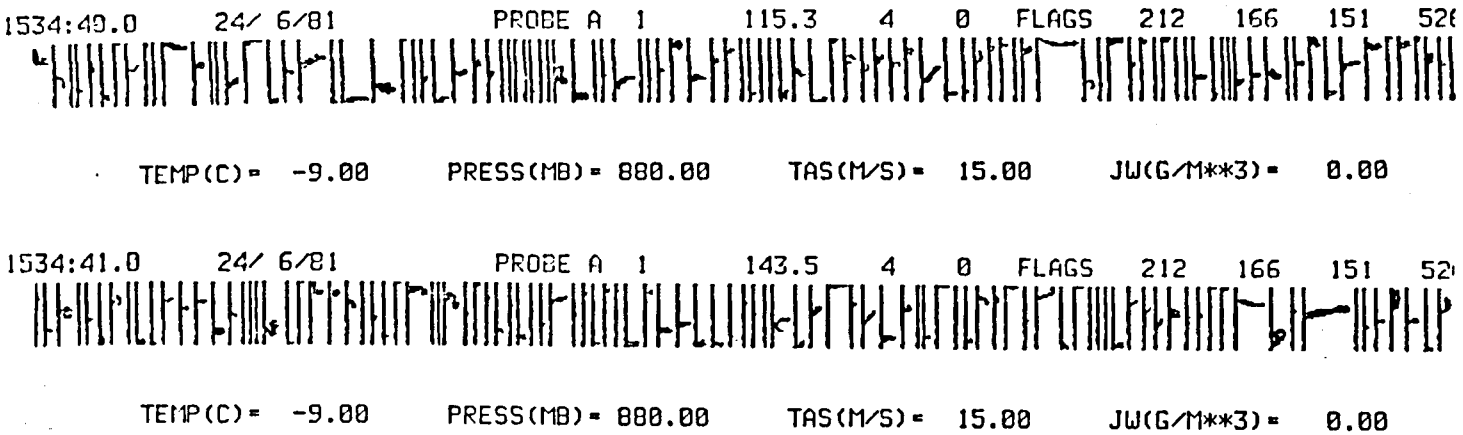

Figure 7.6. PMS-OAP-2D-C images of particles shed by dry ice pellet without any supercooled water droplets present.

fern-like structures Fig. 7.7 were readily seen growing as appendages outward from the frost jacket enveloping the sublimating dry ice pellet. These structures grow to tens of microns in length, sometimes becoming intertwined with neighboring structures and then breaking off from the jacket of frost due to turbulence caused by the strong temperature gradient near the dry ice surface.

In the cold room experiments with an airflow present these "whiskers" lost their crystalline appearance (Fig. 7.8) apparently due to mechanical stresses on the surface of the pellet. More recent experiments by SWA in Charlottesville have produced videos of "whisker" growth and shedding using a special mini-wind tunnel and a large laboratory microscope. Review of that video shows clearly why the "whiskers" lose their dendritic structure. The "whiskers" are actually an agglomeration of very small ice crystals that agglomerate by rolling along the surface of the pellet until enough ice is collected to be entrained into the strong airflow a few 10's of microns above the pellet surface. An attempt to estimate whisker number concentrations leads to numbers an order of magnitude larger than those obtained with the 2-D probe but showed similar sizes and shapes.

7.4.2 The Interaction of Whiskers with Supercooled Water Droplets

Formvar samples collected downwind of a pellet in cloudy air using the wind tunnel in the cold room showed large numbers of droplets in clusters, but no direct evidence of whiskers or fragments of whiskers. SEM examination of collected pellet products plus droplets revealed tiny objects, roughly rectangular in shape, on some of the drops.

Inspection of the FSSP droplet spectrum prior to the introduction of a dry ice pellet showed it agreed reasonably well with gelatine-derived spectra except for the very high counts in the first bin (see Figure 7.4). The mean total concentration of particles was 871 cm^{-3}, and mean particle diameter 10.6 microns with a dispersion of 0.64. When a dry ice pellet was added to the cloudy air of the wind tunnel, there was a slight increase of the FSSP particle count in the higher bins. The mean total concentration of particles in this case was 917 cm^{-3}; the mean particle diameter, 11.8 microns; and the dispersion, 0.66.

A typical 2-D spectrum of the supercooled droplets alone is shown in Fig. 7.9. The mean concentration of particles less than 105 microns was 400 per liter while the concentration of particles greater than 105 microns was 24 per liter. The addition of a dry ice pellet to the supercooled droplet environment caused an increase in the number of large particles imaged by the 2-D. Although the 2-D images still showed large numbers of zero images with a few large water droplets, some whiskers were also observed (2-D spectra in Fig. 7.10. The mean concentration of particles less than 105 microns decreased to 172 per liter, while those greater than 105 microns increased to 36 per liter.

The 2-D probe shows the apparent survival of a significant number of whiskers in the presence of supercooled water droplets. It is unclear as to why no evidence of whiskers was seen in formvar samples under the same conditions, unless their evidence was destroyed by the clustering of the droplets

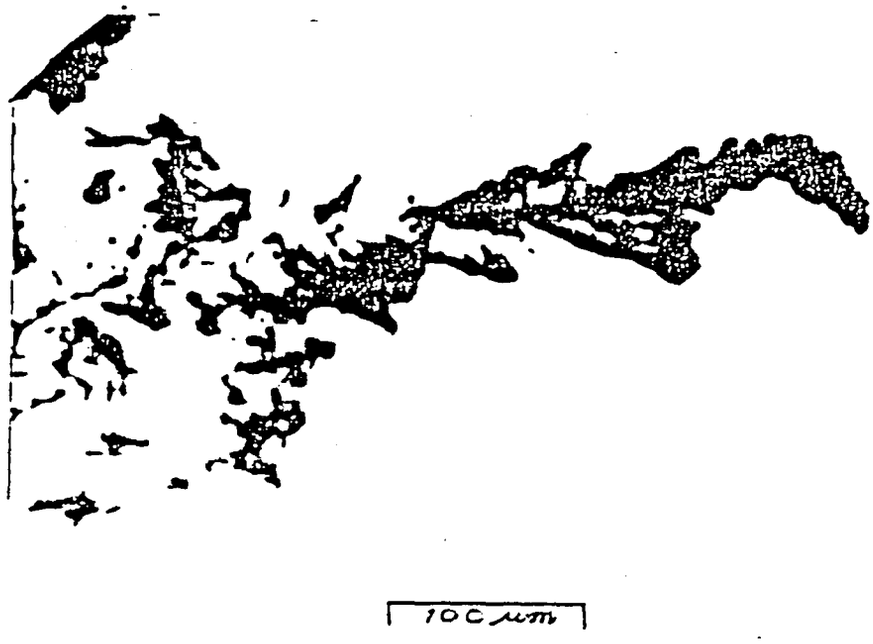

Figure 7.7. Replica of a whisker brushed off the dry ice showing a dendritic structure.

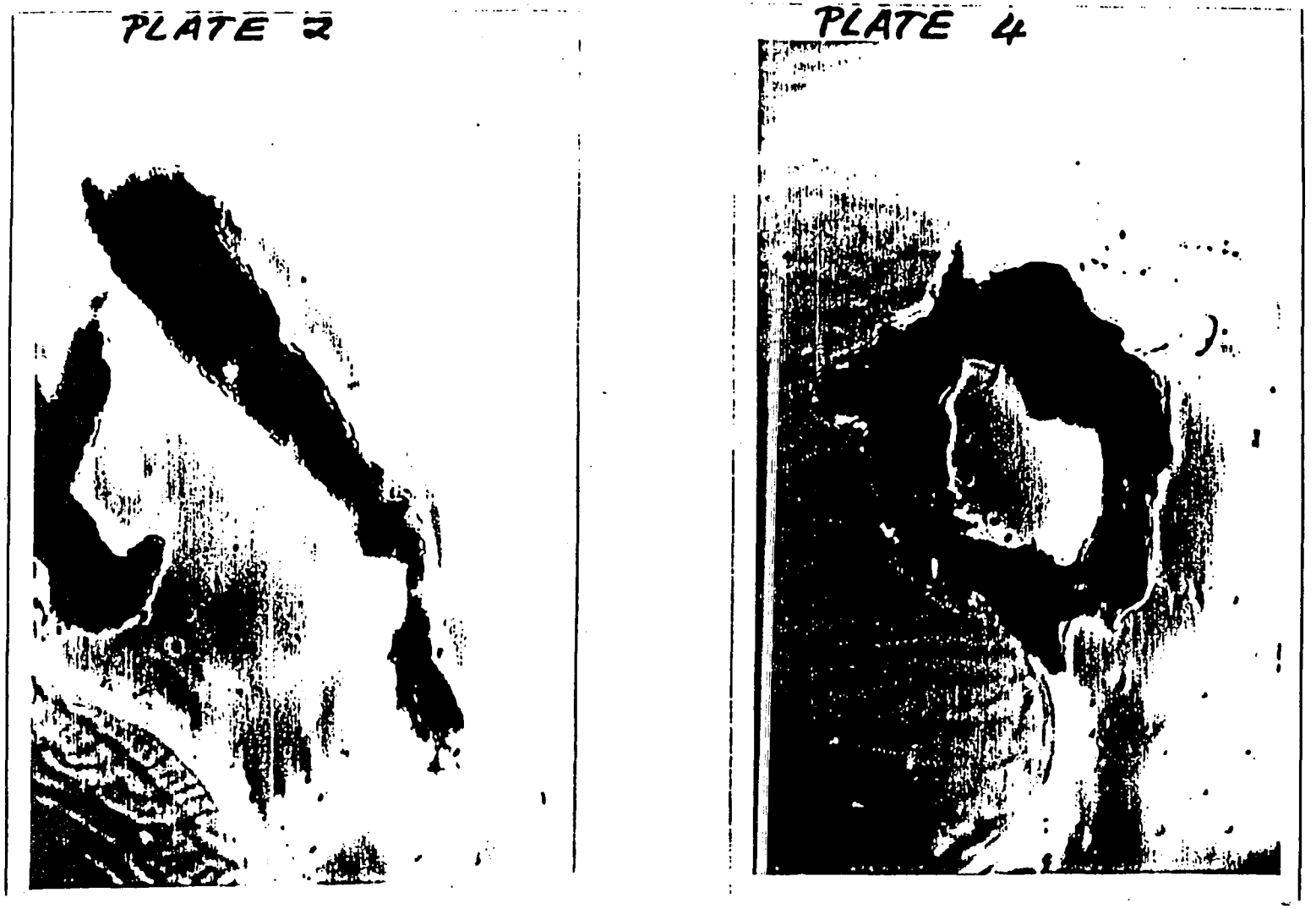

Figure 7.8. Formvar "whisker" replications as seen under a standard laboratory microscope.

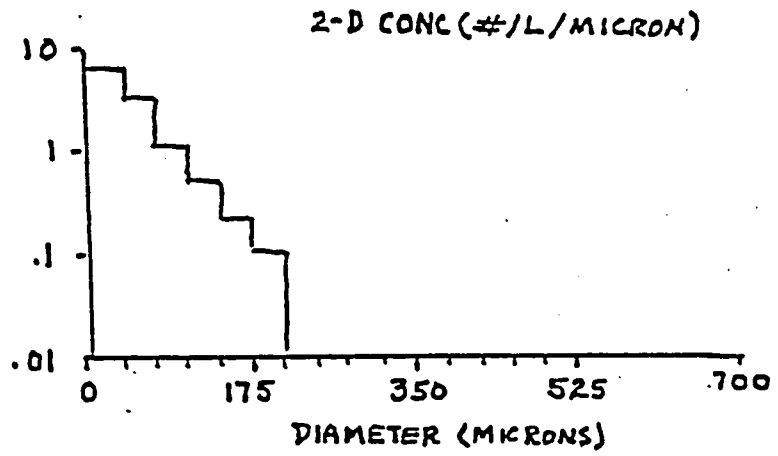

Figure 7.9. 2-D supercooled droplet only spectra.

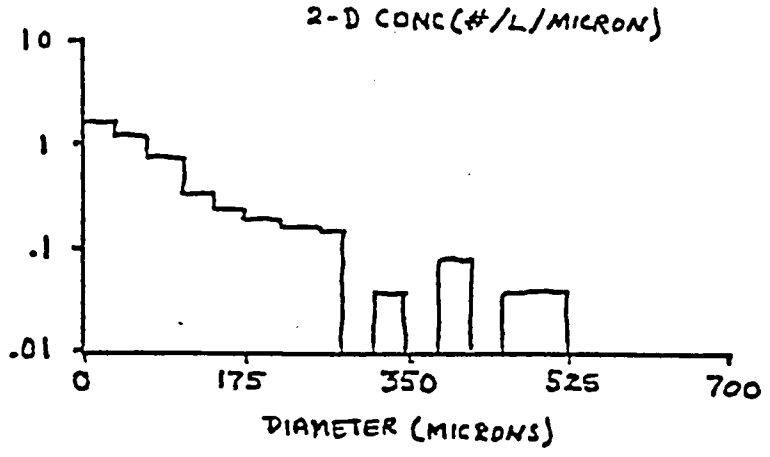

Figure 7.10. 2-D supercooled droplet with dry ice pellet spectra.

in the formvar film subsequent to sampling. As an alternative to formvar sampling, petri dishes filled with liquid hexane were subsequently used.

In one experiment, a dry ice pellet was held at the mouth of the tunnel and a dish of liquid hexane was quickly moved through the airflow at about 30 cm downstream. Large numbers of droplets, but only a few whiskers, were collected. Most of the droplets were still liquid when they entered the hexane. However, a few frozen droplets were observed. Nearly all the whiskers had frozen droplets attached to them; one such example is shown in Figure 7.11 where dendritic crystalline features can actually be seen inside the frozen drop, diverging from the point on the surface where the whisker had nucleated the supercooled bulk.

7.4.3 Significance of Whisker Products

The particle concentrations measured in the wind tunnel are not the same as those that would be measured by an aircraft flying through a dry ice seeding plume. To estimate the scale factor between the tunnel and aircraft measurements, the following arguments are made:

1. during seeding the pellets have a line density of -1 m^{-1} along the aircraft track;

2. an average pellet sublimes at a rate of approximately .010 g s^{-1}, falls initially at -25 ms^{-1} and thus sublimes -4.0 x 10^{-4} gm/m;

3. the lateral turbulent diffusion spreads the ice pellet products out to a distance of .5 km on either side of the seeding track in 3 minutes after seeding.

After three minutes the particles generated in the first meter of pellet fall will be dispersed into nearly 10^3 m^3. With a fall speed of 25 m s^{-1} we need to divide any laboratory production rate (s^{-1}) by 2.5 x 10^4 m^3 s^{-1} to get a reasonable estimate of the particle concentration to be realized in a real seeding situation.

Next, the sampling efficiency of the formvar replicator and the 2D probe are estimated. The formvar slides have sample areas of .6 cm^2 while the 2D probe has a sample area of .7 cm^2. The area of the total ice plume of the pellets was visually estimated to be 10 cm^2 at the sampling distance of 10 cm. Therefore both the formvar slides and the 2D probe are intercepting -6-7% of the ice products. Converting the formvar and 2D laboratory large (>100 m) particle concentrations of $\doteq 10^{-1}$ to number of particles per second of flow we get -100 particles/second. Converting this number to its equivalent field concentration we get 4.0 x 10^{-3} m^3. Based upon the more recent visual counts using the micro-wind tunnel, a field concentration for the >100 μm whiskers may be $\doteq$ .1 m^{-3}. By comparison the generally accepted activity rate for dry ice (10^{12}/gm) yields 4.0 x 10^5 m^{-3} of the < 100 μm particles.

Review of initial cloud penetrations with an instrumented aircraft reveals frequent occasions when there is little ($<<10^3$ m^{-3}) or no 2-DP probe activity. The laboratory studies suggest that dry ice may deliver to these clouds the first large (>100 μm) ice particles at concentrations of 10^{-1} to 10^{-3} m^{-3}. In terms of growth by riming these particles have a several minute

Figure 7.11. Example of a supercooled droplet (diameter = 250 m) that had been nucleated by a "whisker" in mid-air. Dendritic arms, showing up at a result of air bubble contrasts in the ice, are seen diverging from the point of nucleation.

lead on the smaller dry ice produced particles which must first grow by vapor deposition. How important these particles are to the evolution of the cloud precipitation production process remains a question to be addressed by cloud models that can handle the broad range of number concentrations represented by these results.

8.0 RADAR ECHO CLIMATOLOGY STUDIES (Morgan, Parsons and Wightman)

8.1 The geographical patterns of radar echo frequency

The terrain over the area of coverage by the PAWS radar is such that one expects and observes a nonuniform geographical distribution of echo activity. The role of even small terrain features in triggering convective storms has been noted since the earliest days of radar meteorology and even before.

The geographical dependence of echo occurrence in the PAWS experimental area is readily shown utilizing the radar analysis software package developed by Dixon and described in Section 2.0 of this volume.

The radar coverage area (120 km radius from Nelspruit) has been divided into 10 km blocks and echo events occurring in those blocks are summed. The events are based on the entities which are tracked by the cell tracking software. The unit is the three-dimensional cell and an event consists of the presence of the centre of a cell in a block.

A simplified version of the terrain over the same area is shown in Fig. 8.1.1 based on a digitized terrain file provided to the Project by Prof. R E Schulze of the University of Natal. The height value in each block (the same blocks as used for the radar echo frequency patterns) is the average terrain elevation in each block.

The following geographical frequency distributions have been determined:

a. First Detection Distribution (FDD)

The First Detection Distribution is the frequency of occurrence of the beginnings of storm tracks. Each track appears only once on this frequency map, at its point of origin, thus the total of all the individual block frequencies is the total number of cells tracked by the software.

b. Limited Storm Frequency Distribution (LSFD)

This is the geographical distribution of the frequency of occurrence of storms over each block. A given storm (cell) can enter a given block total only once. So, if a storm passed over three blocks, spending three radar scan periods (about 7 min each) in each of them, it would enter each of the three block totals with a count of one.

c. Storm Frequency Distribution (SFD)

In this distribution a given storm contributes to the count in a given block a number equal to the number of scans on which it was centred somewhere over the block. The frequencies appearing in the blocks are thus a measure of the amount of time

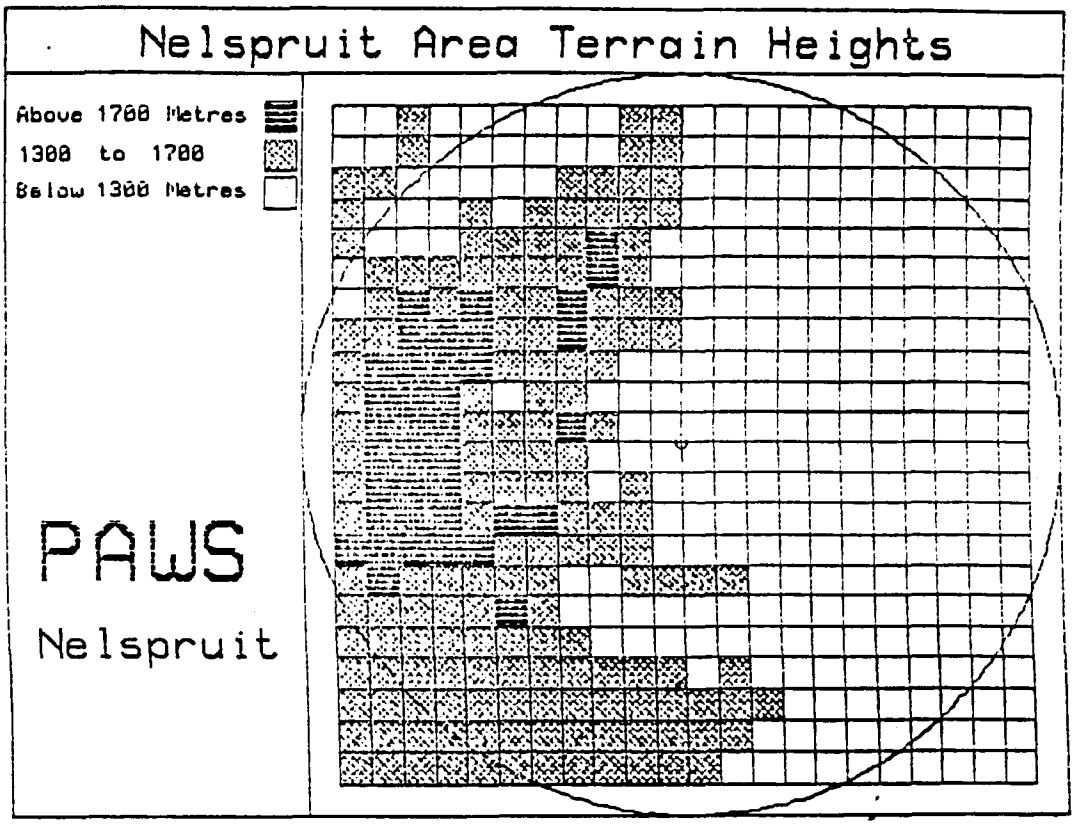

Fig. 8.1.1. Schematic relief map of terrain surrounding Nelspruit.

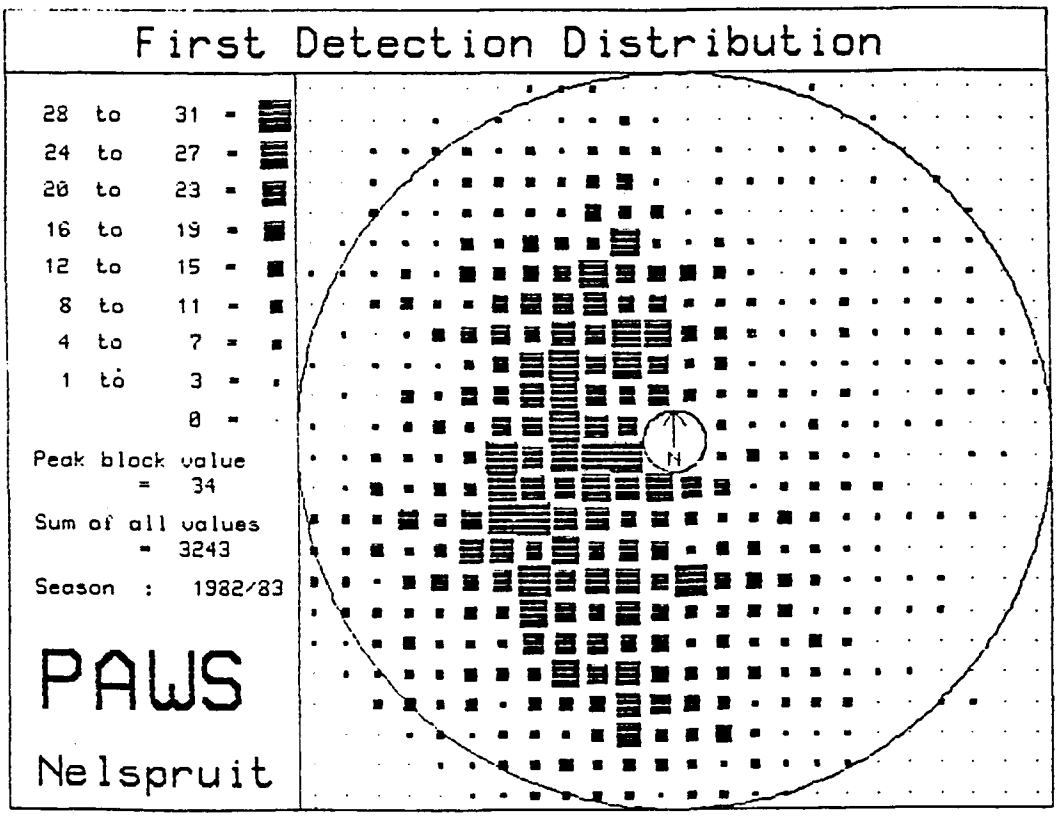

Fig. 8.1.2. Geographical distribution of first storm echo detection - 1982/83 season.

storms (centres) existed in the blocks.

d. Last Detection Distribution (LDD)

This is completely analogous to the First Detection Distribution except that each storm track enters the distribution only once, at the point of its demise.

8.1.1 Seasonal distributions

The most interesting seasonal maps, and the easiest to interpret, are the First Detection Distributions. Fig. 8.1.2 to 8.1.5 show the seasonal FDD's for 1982/83, 83/84, 84/85 and 85/86. There are differences between these, but they certainly have some common features. The most striking differences concern the varying relative strength of the activity to the southwest of the radar. It is quite pronounced in the 1982/83 sample, nearly absent in 1983/84, pronounced again in 1984/85, and very much attenuated in 1985/86. The high first detection frequencies to the northwest do not exhibit these dramatic variations. The differences that appear among these seasonal distributions are interesting and we shall seek explanation of them.

8.1.2 Combined distributions for the 1982 - 86 period

It is desirable to combine the four years to yield an "average" pattern. This has been done by dividing each seasonal field by the total number of storm initiations, then averaging. This produces an average pattern shape rather than a pattern of average frequencies, and accounts for the different modes of operation and incidental breaks in the data which affect the sample size. The 1982/83 season, for example, was not fully operational; software and operational volume scan procedures were being developed. This resulted in a low total number of storms being tracked, but the observations are well distributed through the season and can be considered an unbiased selection. In 1984/85, operations were carried out as needed, seven days per week, whereas during most of the rest of the time, Sundays were always considered non-operational. In 1983/84, most of the month of January was non-operational due to the loss of an engine on the Lear.

The average normalized pattern of First Detections for the 1982 - 1986 period is shown in Fig. 8.1.6 and confirms what had been learned over many years (since 1972) of radar operations in Nelspruit. The pattern of storm generation is closely tied to the major terrain features of the escarpment.

The Storm Frequency Distribution for the 1982 - 86 period is shown in Fig. 8.1.7.

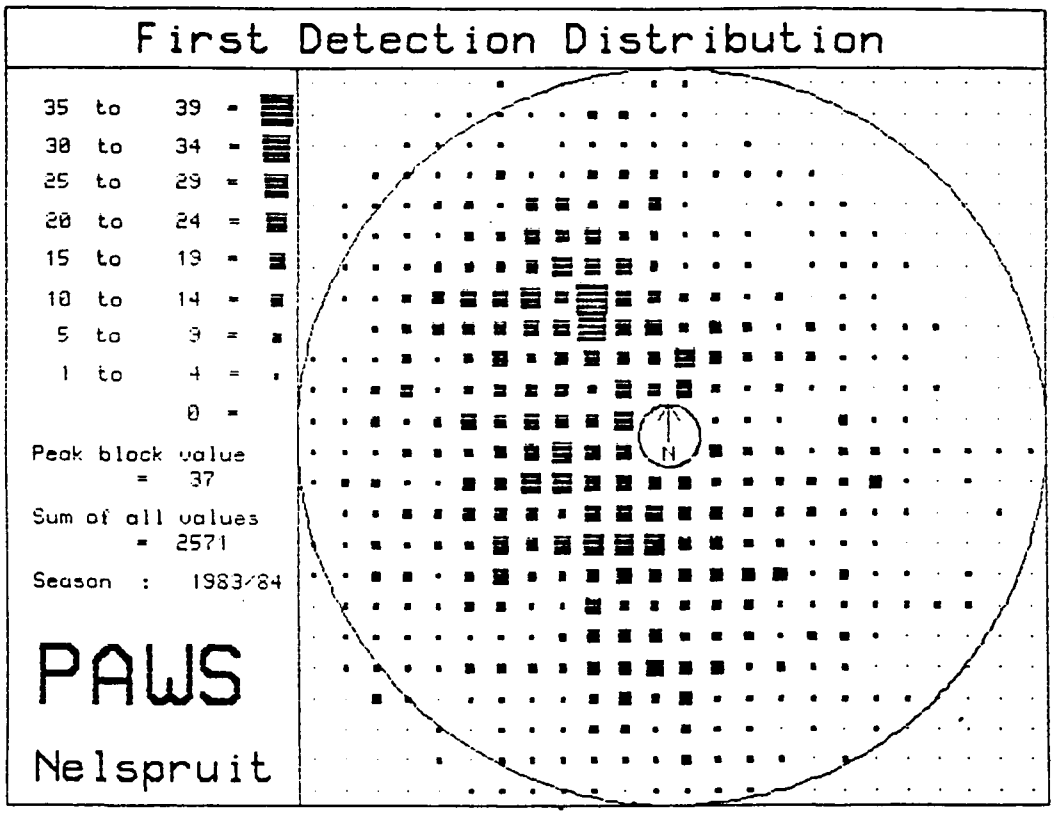

Fig. 8.1.3. As in Fig. 8.1.2 - 1983/84.

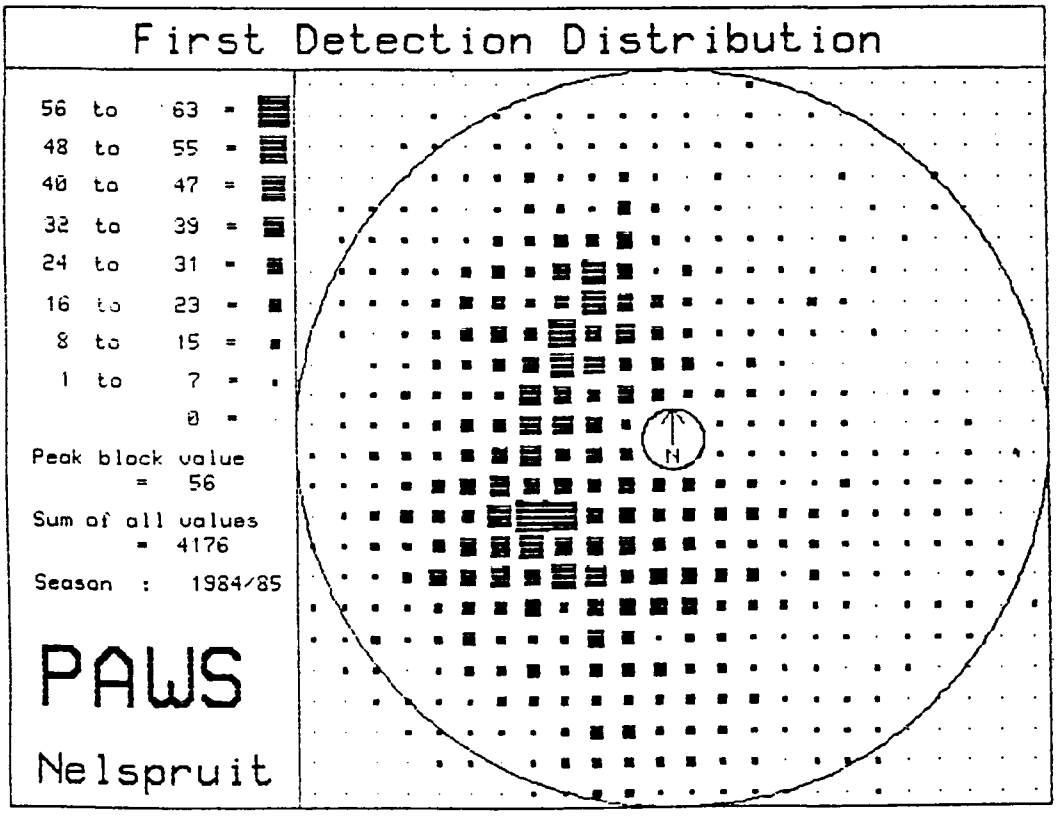

Fig. 8.1.4. As above - 1984/85.

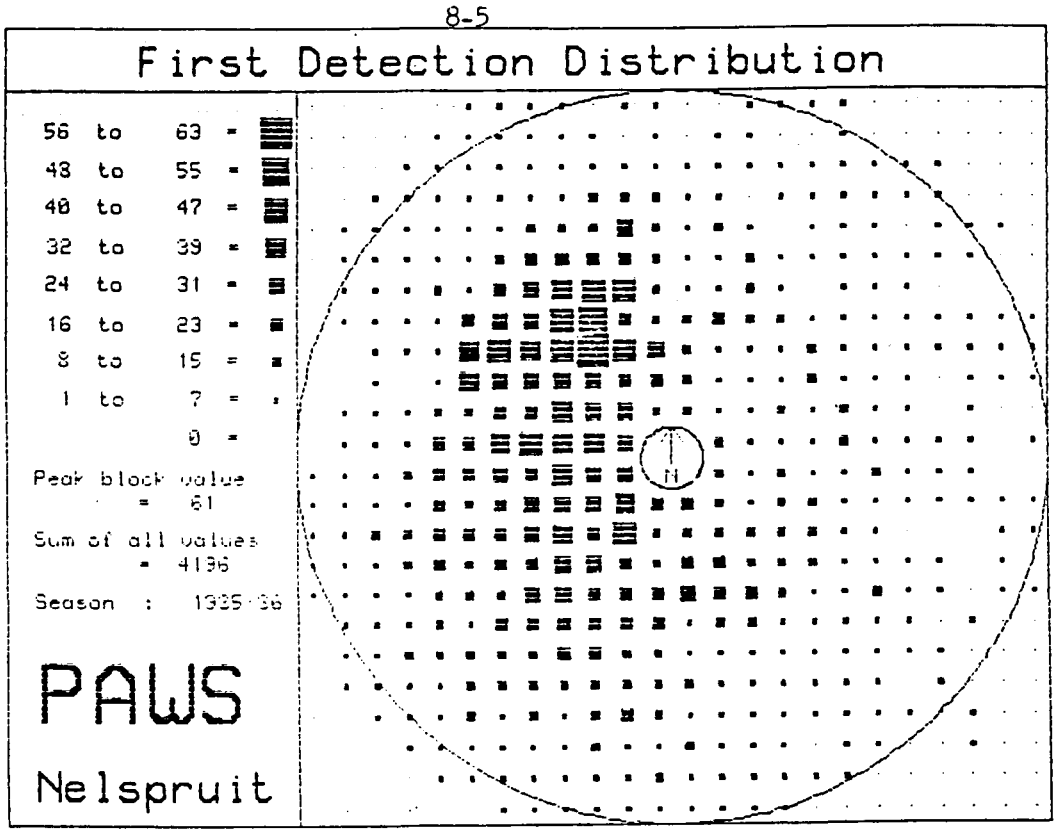

Fig. 8.1.5. As in Fig. 8.1.2 - 1985/86.

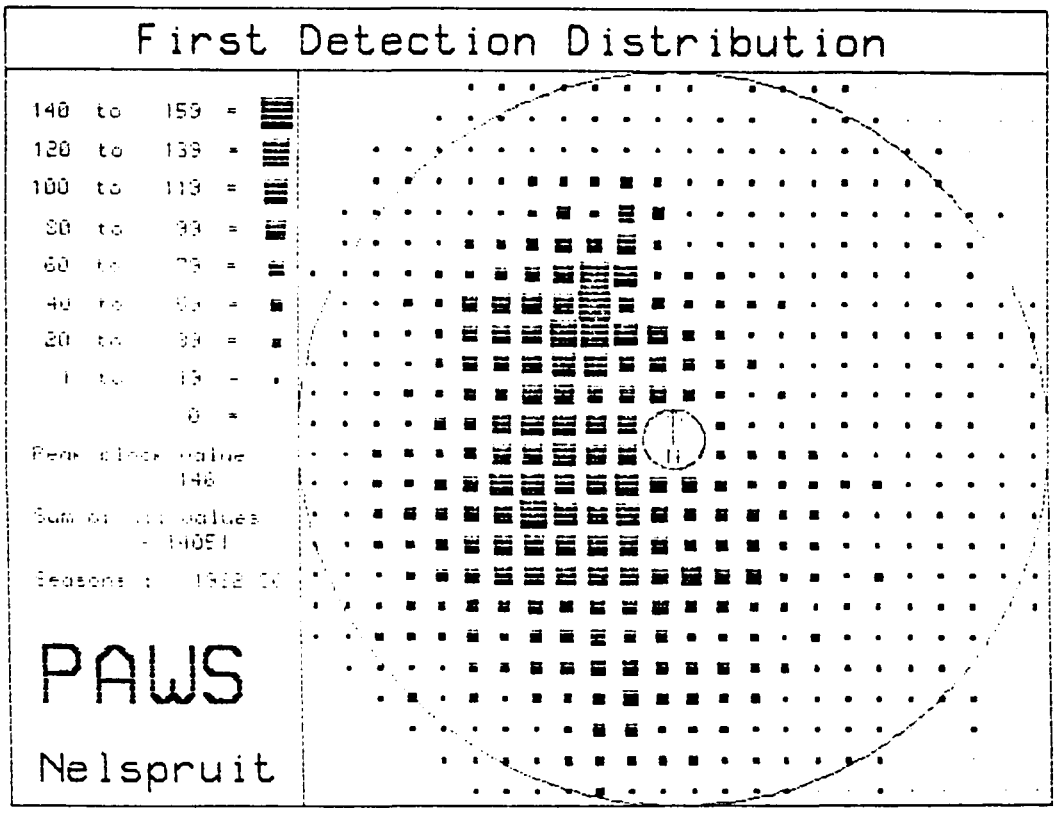

Fig. 8.1.6. Four season average of first storm echo detection.

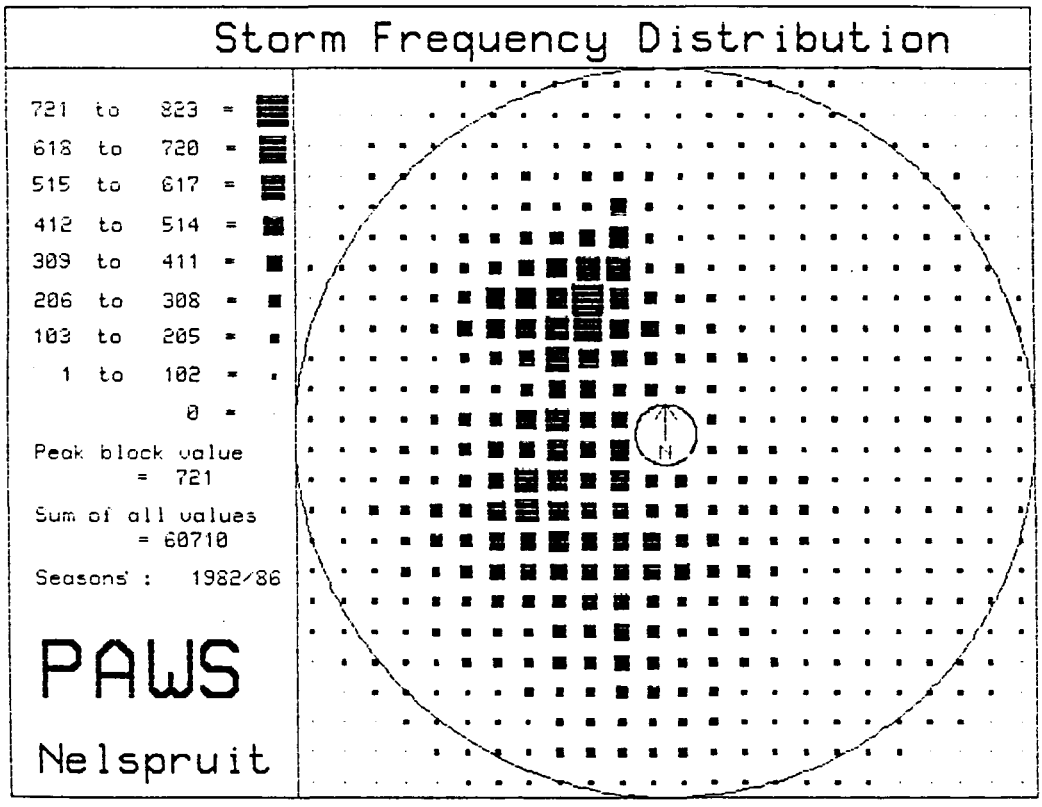

Fig. 8.1.7. Four season average of geographical distribution of storm frequency.

8.1.3 Storm speeds and lifetimes

We have four fields for each season. First Detection Distribution (FDD), Storm Frequency Distribution (SFD), Limited Storm Frequency Distribution (LSFD) and Last Detection Distribution (LDD). From these we may derive a few more fields.

The LSFD and SFD are related in such a way that if we divide, block-by-block, the SFD by the LSFD, the result is the field of average number of scans per storm per block. High values of this will indicate a tendency for storms to linger in the block, low values a tendency toward short lifetimes or rapid motion through the box.

The distributions resulting from the estimates of the ratios of SFD to LSFD are very ragged in the single seasons. When the four seasons were added together, the geographical distribution was of such astonishing uniformity, at a value of 2 scans per block per storm, that there is no point in presenting it graphically. This result is important and permits us to state that there is no localization of the combined effects of storm speed and lifetimes to be detected anywhere in the radar observational area.

8.1.4 Storm sources and sinks

The LSFD is interesting. It can be decomposed into distinct components which can be given letter names.

LSFD = A+B+C+D where
- A = number of storms which start and die within the block
- B = number of storms which start in the block and then leave the block
- C = number of storms which enter the box and then leave it
- D = number of storms which enter the block and die there

Using these behaviours, which are exclusive we see that

FDD = A + B, and
LDD = A + B

Further,

LSFD - FDD = C + D, the total number of storms which enter the block

LSFD - LDD = B + C, the total number of storms which leave the block and so on. Taking the difference between these yields the "divergence" of storms and this, since the storms which pass

right through the block (c) do not contribute, is just

(SFD-LDD)-(SFD-FDD) = FDD-LDD = B - D

Positive values of this mean that more storms leave the block than enter it, negative values mean that more storms enter and die in the block than start out there and leave it.

The terrain has been averaged in columns and rows in the same way as the various storm properties, to emphasize the relationship between the terrain and the storm behaviour.

The FDD - LDD distributions for single years are noisy. So, they are summed for all the four seasons (not shown). In this distribution, which we call the Storm Source-Sink Distribution (SSSD), a general area of predominant storm production is easily discernible to the West of Nelspruit, and a more distributed sink area can also be seen. To show this more dramatically, the columns and rows can be summed to give the E-W and N-S profiles of storm 'divergence'. The columns and row averages are calculated taking into account the length of the chord of the radar circle at each averaging position. The actual procedure consisted in applying fractional weights to the 10 x 10 km boxes on the border of the 120 km radius limit of radar observation. This results in the graphs of Figs. 8.1.8 and 8.1.9 The N-S profile (Fig. 8.1.8) has a noisy characteristic, no clear pattern. There is a tendency for more production of storms to the south, and more storm disappearance to the north. The E-W profile, however, shows a very strong and easily interpreted pattern. The peak to the W of Nelspruit is the storm generating effect of the escarpment. The deep trough immediately west of the Nelspruit axis is the effect of storms dying as they are moved off the higher ground by the prevailing westerlies. This supports the view that most storms in this area are generated and supported by the thermally direct circulation which develops over the higher ground. Storms do not often show rapid movement, but tend to drift away from their source area with the upper winds. They tend to die when they lose the support of the terrain and there may be a storm suppression mechanism (subsidence) east of the escarpment. This is, of course, not true for all storms; certainly not for the night-time storms which were not routinely recorded by our radar. The negative peak between 70 and 120 km is doubtless due to the faster moving storms. To some extent the character of the column averaged SSSD is a product of the shape of the FDD column averages and a tendency for storms to move from the west. If every storm just moved into the next box, a similar SSSD would result. The LDD, column averaged, would be just the FDD displaced one box to the right, and the SSSD would be determined mainly by the slope of the FDD. Storms, however, move a spectrum of distances and directions between birth and death, producing a more complex result.

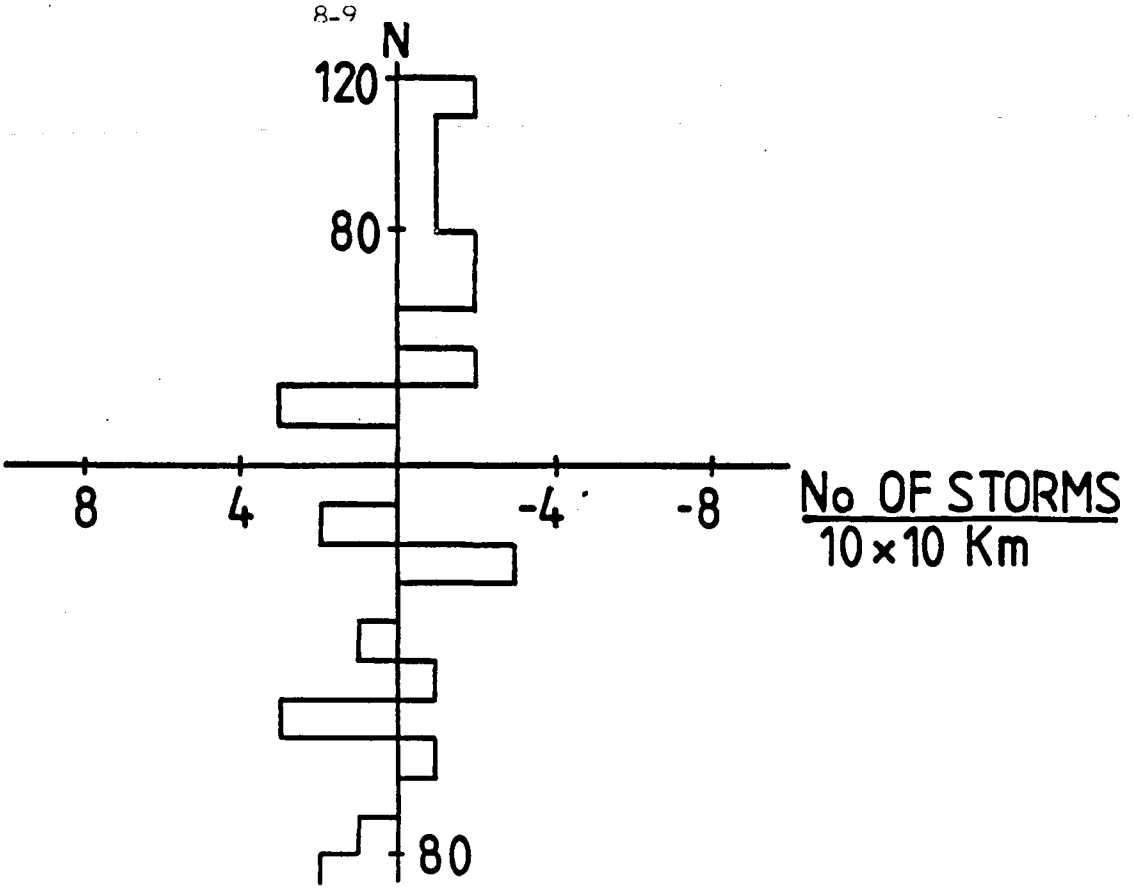

Fig. 8.1.8. North/south pattern of storm sources and sinks.

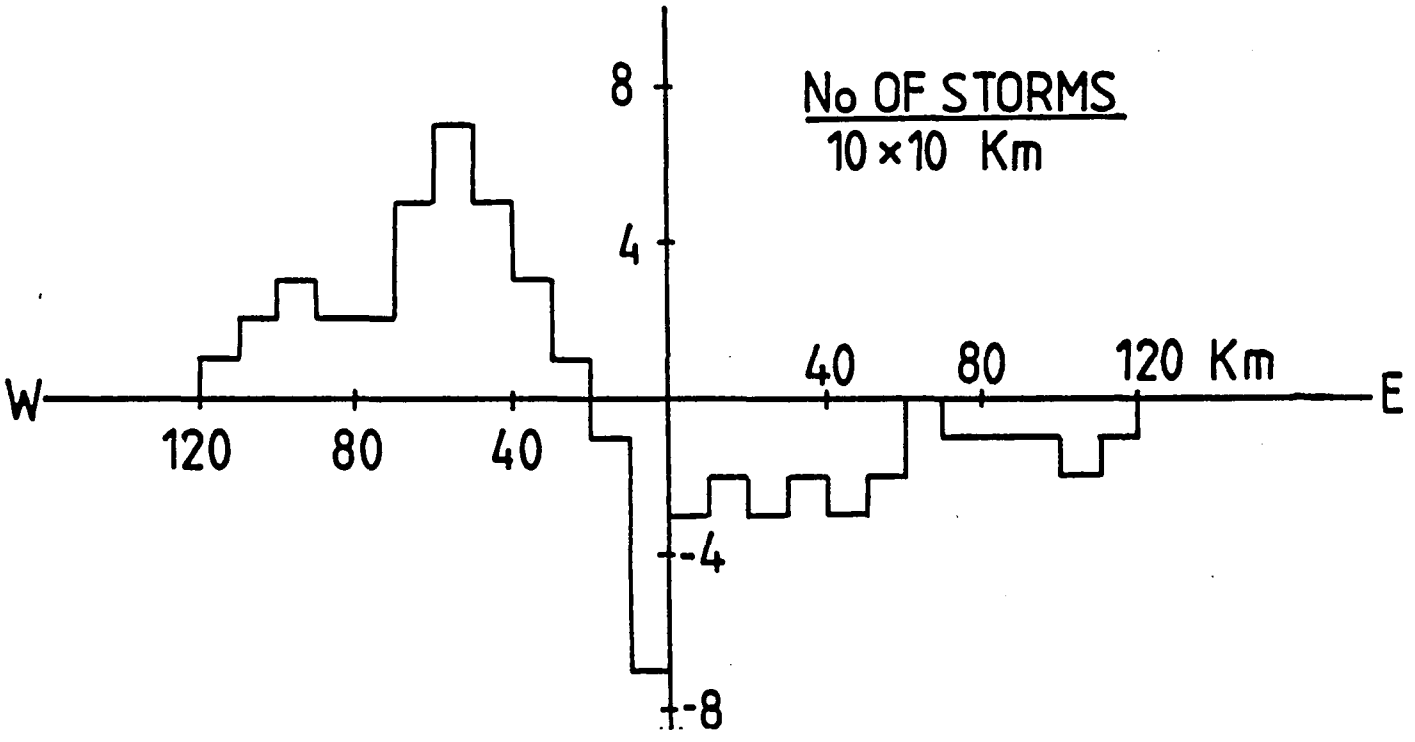

Fig. 8.1.9. West/east pattern of storm sources and sinks.

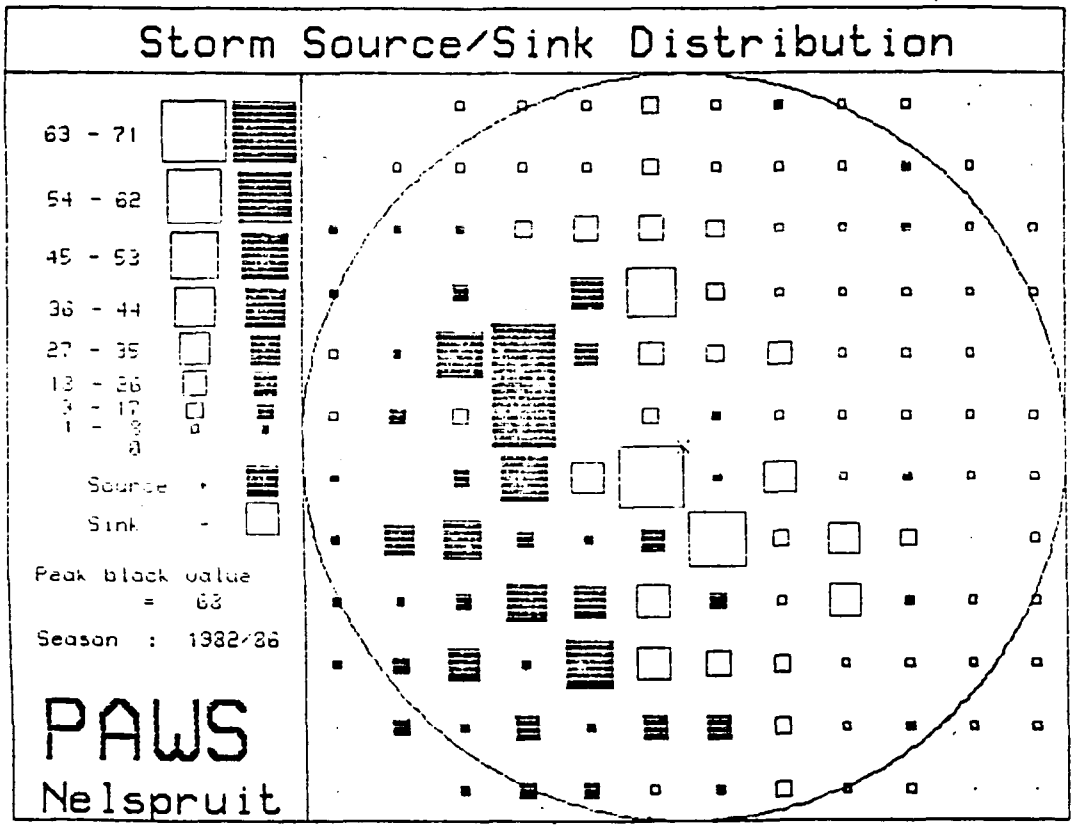

Fig. 8.1.10. Geographical distribution of storm sources and sinks - four season average.

The clarification resulting from summing the data in rows and columns suggests that some smoothing in the two-dimensional SSSD might be profitable. Fig. 8.1.10 results from changing the 10 x 10 km box size to 20 x 20 km (by summing four adjacent boxes). Here the pattern has been greatly clarified and seems highly significant.

The 20 x 20 km boxes adjacent to Nelspruit have had their values altered to account for the effect of the 10 km ring within which no radar data is analysed. Because of this ring, the 10 x 10 km boxes closest to Nelspruit do not contain valid data. The 20 x 20 boxes closest to the radar thus are composed of only three 10x10 km boxes each, and the numbers in them have been multiplied by 4/3.

8.1.5 Geographical effects on the direction of storm movement

It has been shown above that there are no significant variations in storm speed which are dependent on position. It remains to be shown whether there are or are not any significant connections between geographical position and preferred directions of storm movement. A straightforward computer analysis of the storm track data shows that in this case there are strong geographical effects.

In each 10 x 10 km block, as in previous analyses, as many estimates as possible of storm direction (vector) were made. These were assigned as frequencies to 30 degree sectors and these divided by the total number of estimates of direction in each block. This produces a relative frequency distribution, by 30 degree direction sectors, for each block. Maps were plotted of relative frequency for each 30^{o} sector and then adjacent sectors were combined in various ways to produce further maps. The accompanying two plots give a strong demonstration of directional preference in different areas. Values are plotted here, only for blocks in which the total number of direction estimates exceeded 100. The first (Fig. 8.1.11) shows the relative frequencies for the sector 330^{o} - 060^{o}, and one sees that in the northern portions of the area, and in a few other spots, over 40 percent of radar storms move with directions in that sector.

The second (Fig. 8.1.12) is an analogous plot for the sector 060 - 150^{o}. Here the pattern has virtually reversed itself, and in large areas of the southern part of the map, it is seen that over 50 percent of storms move with directions in the sector 060^{o} - 150^{o}.

These large shifts in direction are due to a combination of terrain and meteorology (winds). We shall attempt to separate the two effects as the research proceeds. The principal terrain effect on direction would appear to be the fact that the valleys to the north tend to run northeast-southwest, while those to the south are east-west. Storms tend to propogate along the terrain contours.

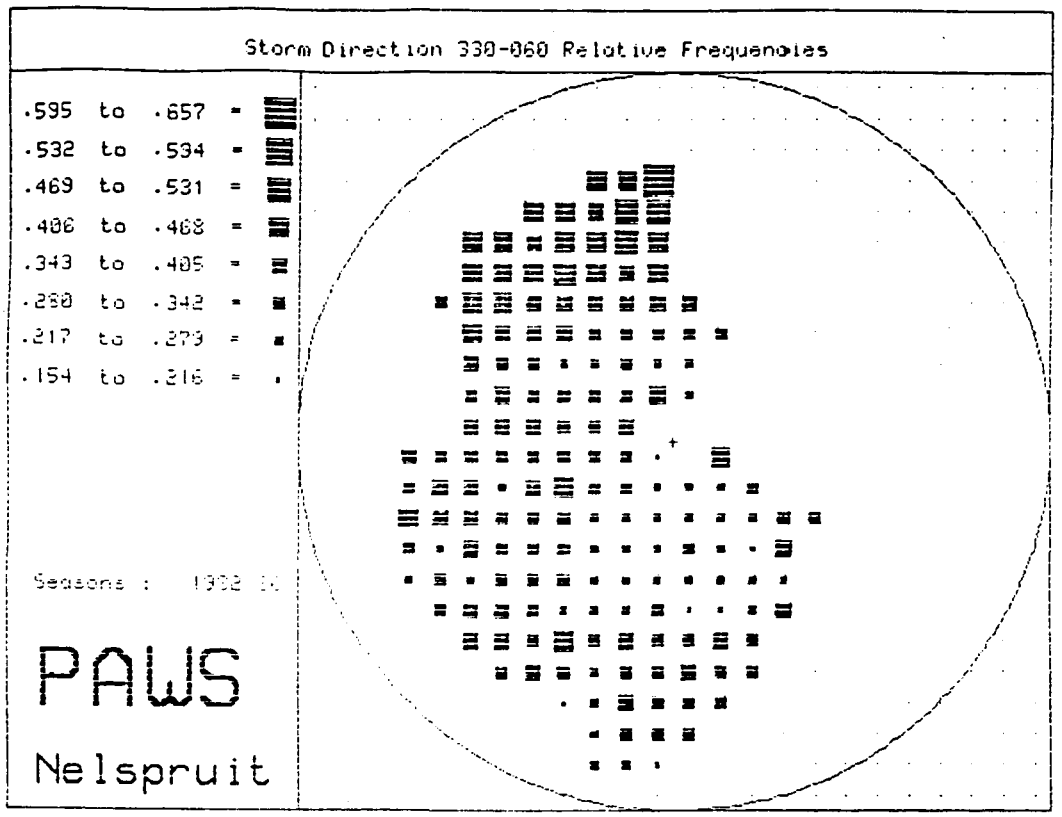

Fig. 8.1.11. Relative frequency of storm directions - northwest quadrant.

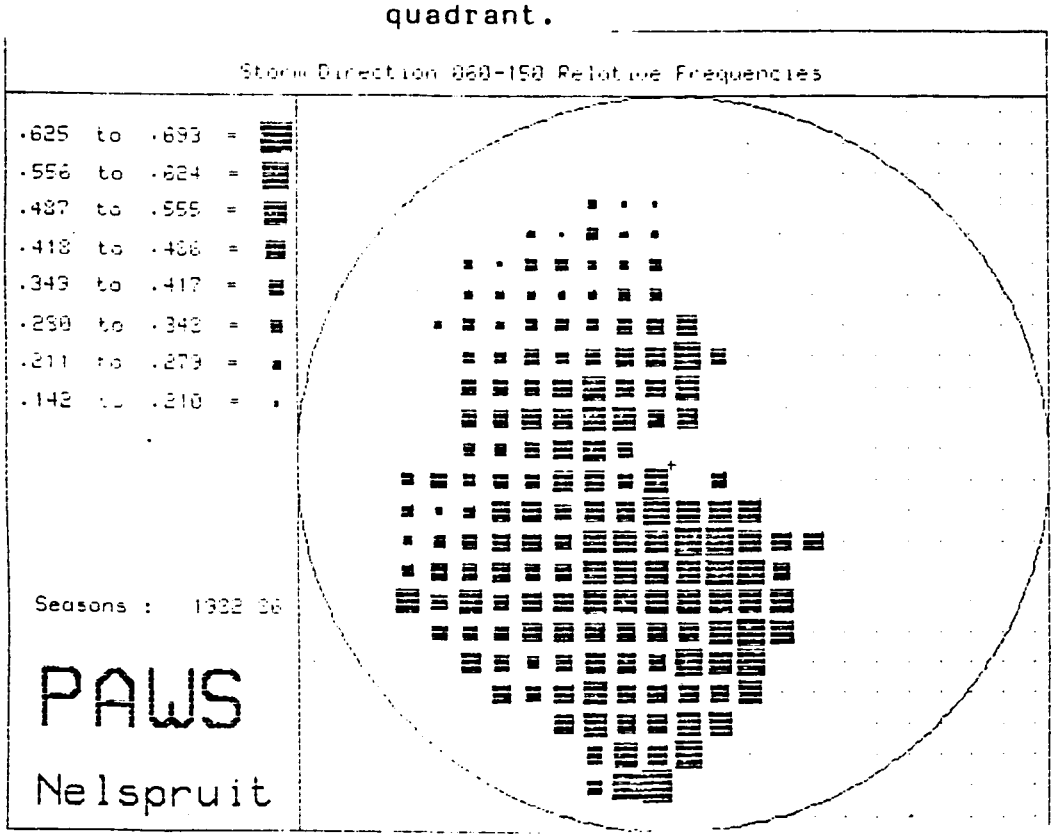

Fig. 8.1.12. As above - southwest quadrant.

8.2 A climatological Z-R relationship for the Nelspruit area (Mather and Parsons)

The rainfall analysis in this report uses the Marshall-Palmer relationship between radar reflectivity and rainfall:

$$Z = 200\ R^{1.6} \qquad (1)$$

where

Z = reflectivity in mm^6/m^3
R = rainfall rate in mm/hr

Efforts to develop a Z-R relationship for Nelspruit using individual rain gauge versus radar range bin comparisons have not been successful. This result echoes the efforts of many other studies of this sort.

A more promising approach, outlined in Smith et al. (1985), is to use non-simultaneous radar and rain gauge data to arrive at a "climatological" Z-R relationship for an area.

The 5 minute rain rates in excess of 15 mm per hour from the 16 automatic rain gauge network in the Badplaas valley are summed for the 1984/85 and 85/86 seasons. A threshold level of 15 mm per hour was used to eliminate most of the non-convective rainfall from the sample, resulting in a total of 3634 rainfall rate measurements. These data were used to construct the cumulative frequency distribution shown in Fig. 8.2.0.

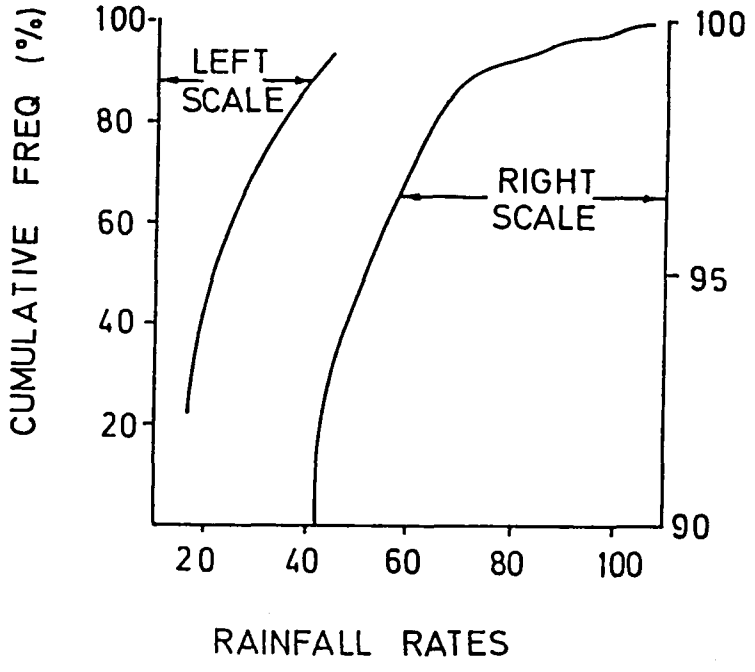

Fig. 8.2.0. Cumulative frequency distribution of rainfall rates from automatic rain gauge network - Badplaas valley.

Next, radar reflectivities in 2072 range bins (an area of 1098 km^2) over the gauge network for the same two seasons were summed and plotted as cumulative frequencies in Fig. 8.2.1. The curve in Fig. 8.2.2 was generated by pairs of Z and R values from Figs 8.2.0 and 8.2.1 chosen at corresponding cumulative frequency values resulting in a climatological Z-R relationship for the Nelspruit area of:

$$Z = 126\ R^{1.7} \qquad (2)$$

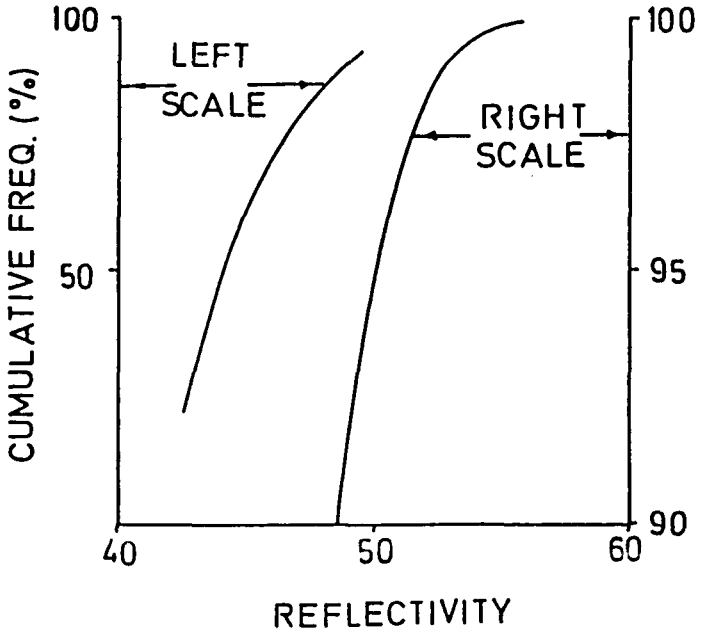

Fig. 8.2.1. Cumulative frequency distribution of reflectivities greater than 42 dBz from radar range bins over Badplaas valley.

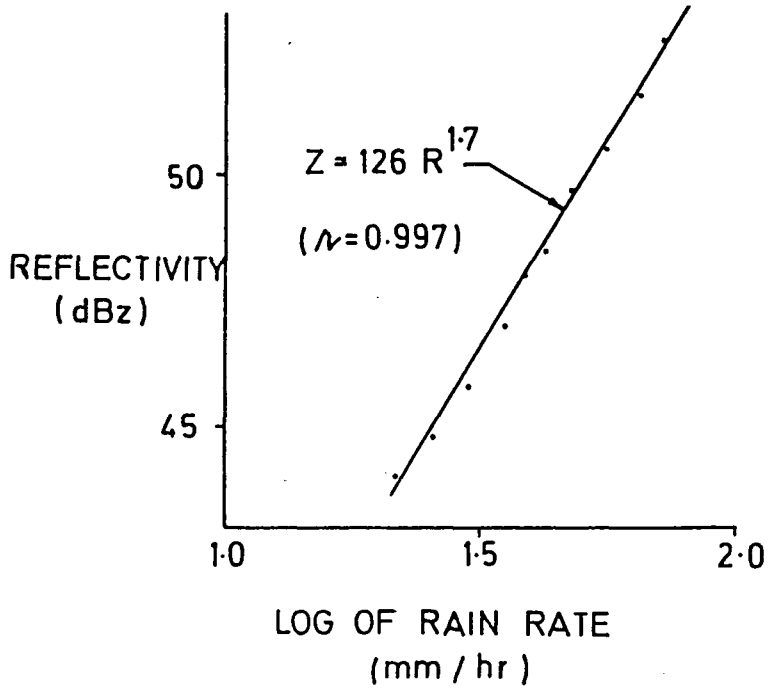

Fig. 8.2.2. Pairs of Z and R values from Figures 8.2.0 and 8.2.1.

The two Z-R relationships are compared in Fig. 8.2.3. This study indicates that the Marshall-Palmer Z-R relationship is entirely suitable for use in the current experiment.

In Section 5.0, Vol. III, the use of this Z-R relationship underestimates the actual rainfall as recorded by the recording rain gauge network in the Badplaas valley by about 70 percent (see Table 5.2, Vol. III). We believe that this is almost entirely explained by the poor siting of the radar at the Nelspruit airport.

a. The terrain rises to over 3^{o} in the sector where the radar is scanning over the rain gauge network (see Fig. 3.4, Section 3.4, this Volume), thus blocking the radar view in this direction.

b. The 3^{o} low level scan angle means that the radar is looking at about the 4 km level in clouds over the rain gauge network. This is more than 1 km above the usual cloud bases in the area.

Further meaningful comparisons of radar/rain gauge measurements of rainfall will have to await the re-siting of the rain gauge network and/or the radar.

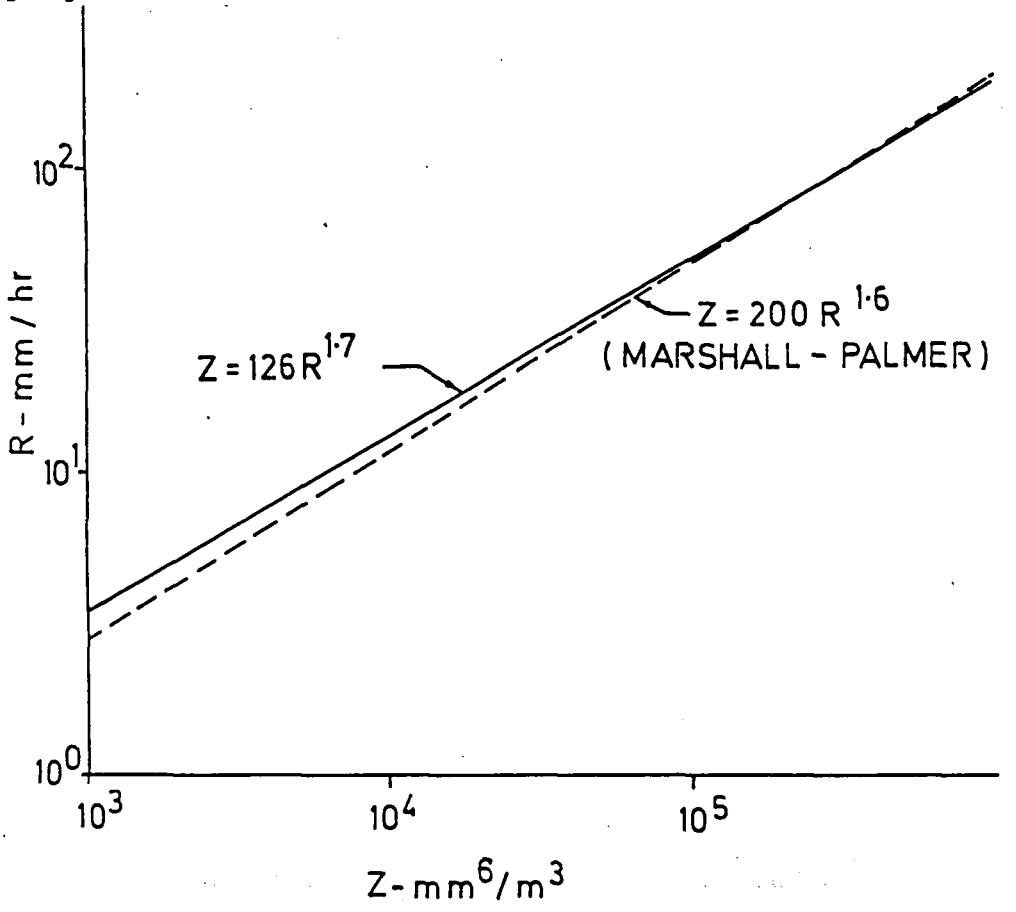

Fig. 8.2.3. Comparison of Nelspruit climatological and Marshall - Palmer Z-R relationships.

9.0 STUDIES AND DEVELOPMENTS IN CLOUD PHYSICS

9.1 Measurement of total and condensed water mixing ratios in warm based cumulus clouds (Morgan, Morrison and Mather)

One of the principal areas of the PAWS research concerns the description of natural precipitation processes and related environmental and cloud characteristics. Perhaps the most important specialized area of this has been the measurement and description of liquid water content.

Cloud exploration is carried out with a Learjet 24 aircraft equipped with a sophisticated instrumentation system. From the beginning of the research programme the aircraft carried the state-of-the-art equipment for measuring liquid water quantities:

a. Johnson-Williams hot wire (JW)

b. Particle Measurement Systems (PMS) Forward Scattering Spectrometer Probe (FSSP)

c. PMS 2D-C cloud particle image detector.

The JW is intended to measure the liquid water content contained in cloud droplets smaller than about 30 microns in diameter. The FSSP estimates the size-spectrum of cloud particles at diameters less than 47 microns and, by integration of their masses, the liquid water content contained in that range. The 2D-C, using a diode-shadowing principle, records the shadow images of particles out to diameters of 1.2 mm (and beyond). If shape and density are known one can determine water content from those images.

It became apparent early in the programme that this instrument set was not capable of describing the clouds we were interested in. The main problem seemed to be that the spectrum of particles in Transvaal clouds was one not dealt with in other cloud research projects. Transvaal clouds often develop precipitation through coalescence and contain large supercooled water drops (Mather et al., 1986). The three instruments listed above will not account for all the liquid water in such clouds for the following reasons:

a. When large (greater than 50 microns) drops are present in high concentrations the JW responds partially to them, giving uninterpretable readings (Morgan and Mather, 1984)

b. The 2D-C does not consistently detect liquid water particles smaller than some unknown size, which we suspect to lie in the 100-150 micron region, though it does detect ice particles below that size (Morgan and Mather, 1984)

c. When large rain drops are present their concentrations are poorly estimated by the 2D-C due to its small sample volume.

Thus, during important stages of the coalescence and rain development processes, liquid water is present which is either poorly sensed or totally invisible to the above instruments.

To fill this gap in our measurement capabilities, several developments were undertaken, two of which have succeeded in a very satisfactory manner. These have been reported in a series of papers (Morgan, Morrison and Mather, 1986 a; 1986 b; 1986 c).

9.1.1. The Engine-Vapour technique

9.1.1.1. Principles

The total water mixing ratio of a unit mass of cloud air is the sum of its vapour, its liquid (cloud and rain), and its ice contents. There are well known ways for estimating certain fractions of the above components of the total water mixing ratio, each with its problems and limitations. The small diameter (less than 30 microns) fraction of the liquid water content (LWC) is commonly sensed with the Johnson-Williams (J-W) hot wire sensor. The CSIRO-King hot wire sensor is used to sense LWC to somewhat larger sizes (about 100 microns). The Particle Measuring Systems (PMS) Forward Scattering Spectrometer Probe (FSSP) can estimate the size spectrum of cloud droplets up to 47 microns in diameter and this can be integrated to produce an estimate of the LWC in those sizes. The PMS 2D-C optical array probe images larger cloud particles and the spectrum of these can be integrated to yield an ice or water content if the proper assumptions are made concerning shape and density of the particle. Vapour content can be estimated in clear air with a dew point sensor and in clouds by measuring the air temperature and pressure and assuming saturation.

Early experience in using the J-W hot wire probe in the warm-based, wet cumulus congestus clouds of the Nelspruit area led to serious doubts about our ability to describe their character and evolution (Morgan and Mather, 1984). This was only natural since the J-W responds primarily to the LWC in the condensation peak below a diameter of about 30 microns and we strongly suspected the presence of much larger cloud droplets. For this reason the more promising King hot wire device was added to the aircraft in 1985; first a shielded version, which was later replaced by the unshielded probe.

It was hoped that the King device measures the liquid water up to diameters of 100 microns, although there is no information in the literature concerning the response of the instrument to drops around that size. Wind tunnel calibrations have not been performed with particles of that size and, in fact, such tests would be very difficult to perform. In a recent publication on

wind tunnel calibrations of the King instrument, King et al., (1985) stated "quantitative studies to examine the probe response to higher LWC (e.g. 4 - 5 g m^{-3}) at typical aircraft speeds and to drizzle and precipitation size drops are needed". Our experience in the field is that the King instrument shows a saturation effect at about 4.0 g m^{-3} for the unshielded sensor. We have concluded that, at least at the airspeeds at which the Learjet penetrates clouds (around 150 m s^{-1}), existing hot-wire devices are not capable of measuring liquid water contents in excess of that value.

An entirely different principle can be exploited which largely solves the liquid water measurement problem. This is the evaporation technique.

A turbojet engine has three main sections: a compressor at the front, a combustion section and, at the back, a turbine section. Air entering the inlet of the engine is compressed and heated in the compressor section, converting any water or ice in the air to vapour. The water vapour mixing ratio in the compressed air is then equal to the total water mixing ratio in the environmental air. Independent knowledge of the vapour mixing ratio of the outside (cloud) air permits the condensed water mixing ratio, w_c, to be calculated as a difference.

Evaporators have been applied in cloud investigations several times (Kyle, 1975; Gayet et al., 1977; Coulman and Parker, 1982; Ruskin and Scott, 1974). The instruments have all been limited by small inlet diameters and low volume flow rates. The inlets of the Learjet engines are large (0.1 m^2) and the air volume flow through the two engines on the aircraft is on the order of 30 m^3 s^{-1}. This huge sample volume assures that even the largest precipitation particles in the cloud are adequately sampled.

During the development of the system to be described here, the authors were apprised of an early, similar approach to total water content measurement (Roys, 1963; Roys and Kessler, 1966). An infrared sensor was used to measure water vapour from the 4th stage compressor bleed-air of the J-57 engine in an F100F aircraft. There were drawbacks to the infrared sensing equipment, such as very slow time response, and perhaps other problems, so that the investigation was never reported in the open literature. The approach, nevertheless, was essentially the same as taken here.

Engine compressor bleed-air is sampled from the line which feeds hot air to the external windscreen defoggers. This air sample flows through the measurement cell of a Lyman-alpha UV absorption humidiometer (Buck, 1976). Absorption at the Lyman-alpha line wavelength of 121.56 nm is proportional to the densities of water vapour and molecular oxygen. The molecular oxygen contribution is small and can be easily estimated. Given the water vapour density in the Lyman-alpha cell, the total and condensed water mixing ratios of outside cloud air can be

computed as follows.

The total water mixing ratio of the outside air, w_{ta}, is

$$w_{ta} = w_{va} + w_{la} + w_{ia} = w_{va} + w_{ca} \quad (1)$$

where the liquid and ice mixing ratios, w_{la} and w_{ia}, are combined into the condensed water mixing ratio, w_{ca}.

In the Lyman-alpha measurement cell, vapour density, ρ_{vc}, is the observed quantity. The dry air density in the cell, ρ_{ac}, may be computed from the ideal gas law. The pressure and temperature in the cell are measured by a pressure transducer and thermocouple, respectively.

The total water content mixing ratio for the outside air can then be computed as

$$w_{ta} = \frac{\rho_{vc}}{\rho_{ac}} \quad (2)$$

If the vapour content of the air is known, the condensed water mixing ratio can be directly calculated from equation (1) as

$$w_{ca} = w_{ta} - w_{va} \quad (3)$$

In cloud we assume that the water vapour mixing ratio, w_{va}, is equal to the saturation mixing ratio of the cloud air, $w_s(T_a,P_a)$, so that we can re-write equation 3 as

$$w_{ca} = w_{ta} - w_s\,(T_a,P_a) \quad (4)$$

The air temperature is measured by a Rosemount temperature probe.

The gap between UV source and detector in the Lyman-alpha test cell is a critical parameter which must be precisely known. It can be varied over a wide range, but we have not yet considered optimizing it for our particular types of measurements. It does offer a degree of freedom to the user and could be increased to give excellent resolution in clouds such as Great Plains cumulus clouds where condensed water contents are not expected to exceed 1 or 2 g m^{-3}. In our studies, the gap is set at between 4.0 - 4.5 mm.

9.1.1.2. Testing

Problems have been encountered and, we believe, solved during the testing of the Lyman-alpha humidiometer for the measurement of the bleed air vapour content. These derived mainly from our unique measurement environment. The instrument was not designed to operate over the wide range of pressures and temperatures encountered in jet engine bleed air lines.

Time was lost in the development of the instrument due to the presence of what appeared to be a slowly varying bias in the measurement. This appeared most clearly as a high value of the mixing ratio in the clear air; where the value would be expected to lie in the vicinity of 0.1 to 1.0 g kg^{-1} at -10°C the values fell repeatedly in the neighborhood of 3.0 g kg^{-1}. Suspicion first fell on the estimates of air density, based on the measurements of pressure and temperature in the Lyman-alpha measurement cell. However, after many checks it became clear that the bias could only be due to a contaminant in the bleed air sample. The contaminant is probably a hydrocarbon such as engine oil. This could enter the system via an oil seal at the front of the compressor or from the walls of the tubing of the bleed air system.

The bias due to the contaminant varies with parameters which determine the flow through the bleed air tubing. Most important of these are the engine power setting and outside air pressure (altitude). The sense of the variation is such that the higher the bleed air flow, the lower the bias. This is consistent with a fairly steady production of the contaminant by the tubing walls.

The Lyman-alpha system must therefore be baselined during a mission not only to determine the zero water vapour output (system gain) of the humidiometer, but also to calculate the bias added by the contaminant. In order to explicitly establish the system gain the instrumental setup includes a bottle of high purity nitrogen and appropriate plumbing to allow flushing of the Lyman-alpha measurement cell with the inert nitrogen. The contaminant term is found by baselining the system against the aircraft Cambridge EG&G dewpoint hygrometer. A drawback with this method is that, although the dewpoint hygrometer has good accuracy, its time response at relatively cold temperatures is poor. As a consequence, baselining in clear air at penetration altitudes is generally done before and after "working" a storm (after the dewpointer has stabilized) to provide good baselines for comparison against those values obtained in the unsaturated air prior to each individual cloud penetration. Any erroneous baseline values prior to cloud penetration can then be corrected.

Although not ideal, the above calibration technique has proved satisfactory. Any error introduced in the baselining operation with the dewpoint hygrometer, due to incorrect recovery from a previous cloud pass, would reduce the computed value of total water mixing ratio. The contaminant problem can probably be eliminated by installing dedicated, cleanable airlines to bring

the compressor air directly to the Lyman-alpha measurement cell.

9.1.1.3 Demonstration of Measurements

There are no standards of comparison for testing measurements of any internal cloud properties. We proceed here by inference, first by showing examples that illustrate the full spectrum of results obtained with this system over five months of routine operation and second, by showing that the cloud total water mixing ratios are bounded by the values to be expected for unmixed adiabatic ascents through the cores of clouds. We note here that a completely different method for measurement of cloud condensed water mixing ratio using one of the Lear turbojet engines has been developed and preliminary results support the validity of the engine vapour technique (Morgan et al. 1986(a)).

The examples that follow consist of four panels of strip chart plots of Learjet penetrations at the -10°C level through cumulus congestus turrets growing on the flanks of multicellular thunderstorms. The bottom panel shows the total water mixing ratio measured by the engine vapour system as a function of distance run (integration of aircraft true air speed). Also plotted in the bottom panel are the saturation mixing ratio (computed from the aircraft temperature and pressure sensors) and the cloud base mixing ratio computed from the routine Lear sounding during climb out from the Nelspruit airfield. For unmixed adiabatic ascent from cloud base in the absence of any significant accretional particle growth processes, the total water mixing ratios of the cloud air should equal the cloud base mixing ratio. The second panel is a plot of condensed water mixing ratio from the engine vapour system compared to the liquid water mixing ratio measured by the CSIRO-King hot wire. The third panel shows the cloud particle concentrations obtained from a PMS 2D-C optical array probe (35 micron resolution) using the particle weighting computational technique after standard artifact rejection. Finally, the top panel is a plot of reflectivity from the aircraft X-band radar. This measurement is obtained from a single range gate set approximately 1.5 km ahead of the aircraft. The signal is lagged in the plots to adjust for its displacement relative to the aircraft. Some of the plots appear incomplete because the recording was started when the range gate was already well inside the cloud.

The first example (Fig. 9.1) is from a cloud with relatively low liquid water content and almost no particles detectable by the 2D-C. The agreement between the engine vapour measurement and that of the King hot wire is excellent, except for a small tract at around 2.8 km where the mixing ratio exceeded 5 g kg^{-1}, the level at which we experienced saturation of the King instrument at this altitude. (The saturation of the King at this low value, equivalent to 3 g m^{-3}, was found later to be due to electronic saturation. This has been corrected, and for all flights subsequent to 15 December 1986 the saturation value occurs at about 4.0 g m^{-3}, or 6.0 g kg^{-1}). This cloud was sub-adiabatic throughout, as indicated by the total water mixing ratio being

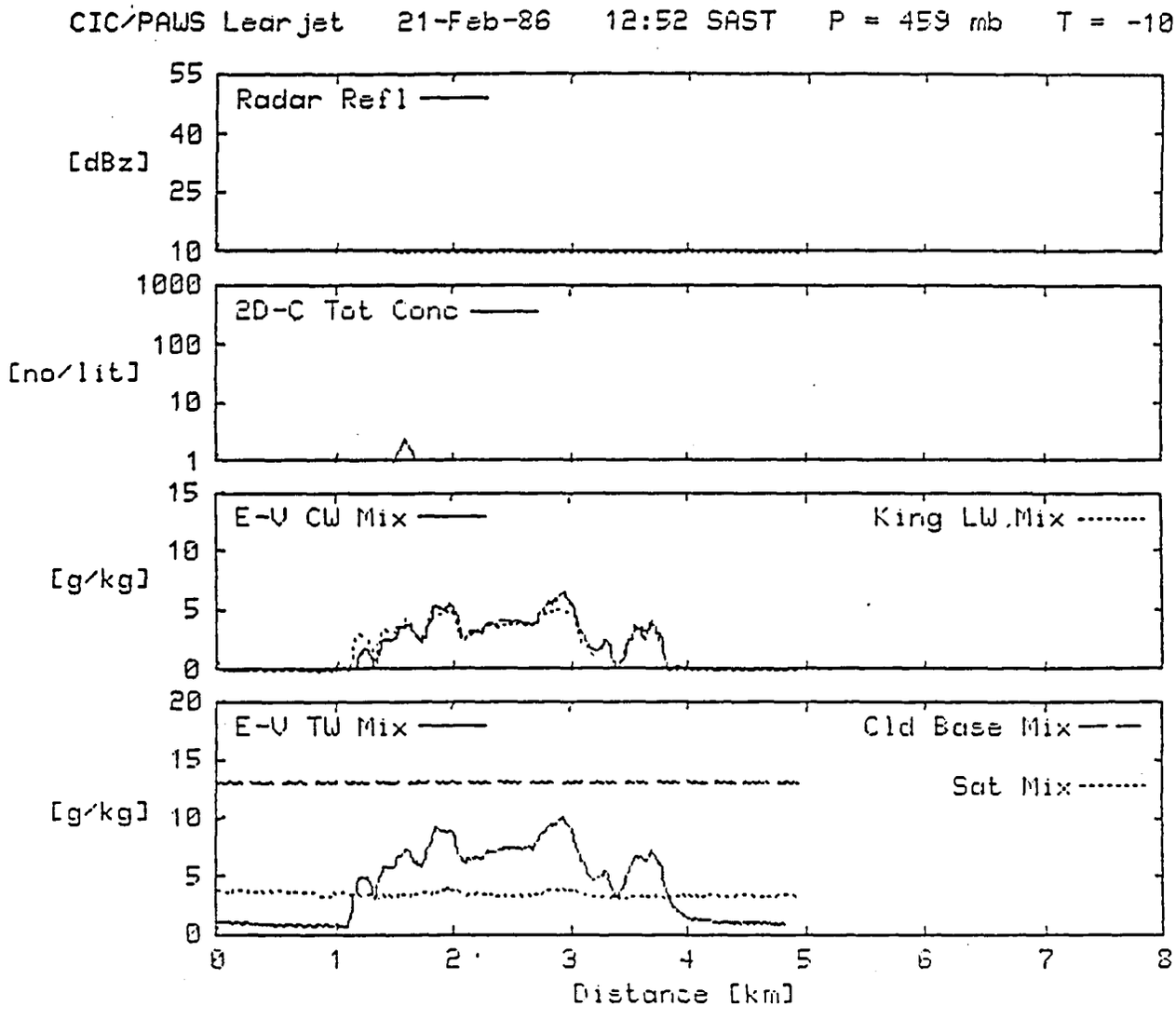

Figure 9.1. An example of agreement between the engine-vapor method and the CSIRO-King hot-wire probe, in a cloud with no large (liquid or ice) precipitation particles.

everywhere less than the cloud base mixing ratio.

Taken on the same mission the second example (Fig. 9.2) is from a well-iced cloud in which the 2D-C probe detected high concentrations of small, irregular particles showing only a weak proved satisfactory. Any error introduced in the baselining operation with the dewpoint hygrometer, due to incorrect recovery from a previous cloud pass, would reduce the computed value of total water mixing ratio. The contaminant problem can probably be eliminated by installing dedicated, cleanable airlines to bring the compressor air directly to the Lyman-alpha measurement cell.

The third example (Fig. 9.3) is taken from a cloud with a well developed graupel population. The King appears not to saturate here, probably because the graupel is consuming the cloud. A more substantial radar signal is evident for this penetration.

A fourth example (Fig. 9.4) shows a cloud with almost no 2D-C activity in which the King hot wire is saturated almost throughout. The lack of any significant radar return also implies an absence of cloud particles with large radar cross-sections. The liquid water mixing ratio exceeds the King saturation value by perhaps 50% almost everywhere. The total water mixing ratio hovers near the cloud base mixing ratio over much of the pass, implying a moist adiabatic unmixed cloud core.

The last example (Fig. 9.5) is a cloud in which liquid water accumulation appears is taking place (big drop zone). Between about 1.5 and 3.4 km the 2D-C images show predominantly large clearly defined liquid water drops. The response from the aircraft radar and examination of the videotape record of the cloud penetration also demonstrate the liquid phase of these large particles. These observations are not unusual in the turrets that occur in the experimental region (Mather et al., 1986). The King remains unsaturated throughout most of the record because the large drops are consuming the cloud water. It saturates in a small region near 3.5 km where the 2D-C concentration falls off. The total water mixing ratio indicates strongly super-adiabatic values where the 2D-C concentration is high, but is nearly moist adiabatic where the King reaches saturation and the cloud particle habit changes to mostly low concentrations of graupel. The aircraft data collected over the 1985/86 summer season contain even more spectacular examples of accumulation of supercooled water (Morgan et al. 1986(b)).

A check for internal consistency of data in this example is worthwhile. A cloud water budget is calculated in Table 9.1. If we subtract the King liquid water content from the E-V cloud water content, the remaining liquid water should be contained in the drops. This water content, calculated from the 2D-C images is 7.0 g/kg leaving just 0.7 g/kg unaccounted for. With such large drops present, the 2D-C has known sampling problems. A second budget calculations is carried out using measured radar reflectivity and the relationship (Brown and Braham, 1969),

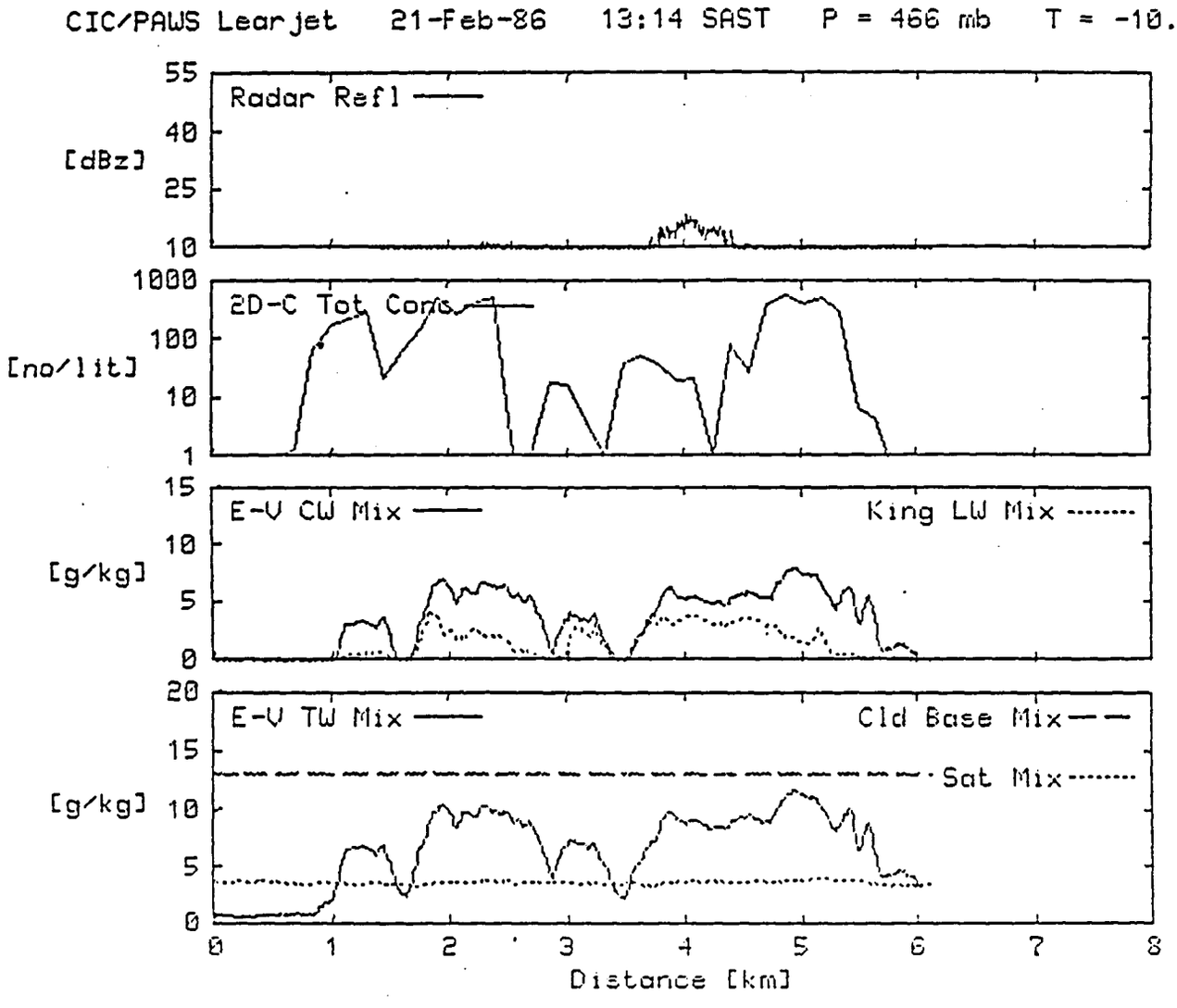

Figure 9.2. An example of the relative readings of the engine-vapor instrument and the CSIRO-King hot-wire probe in a glaciating cloud.

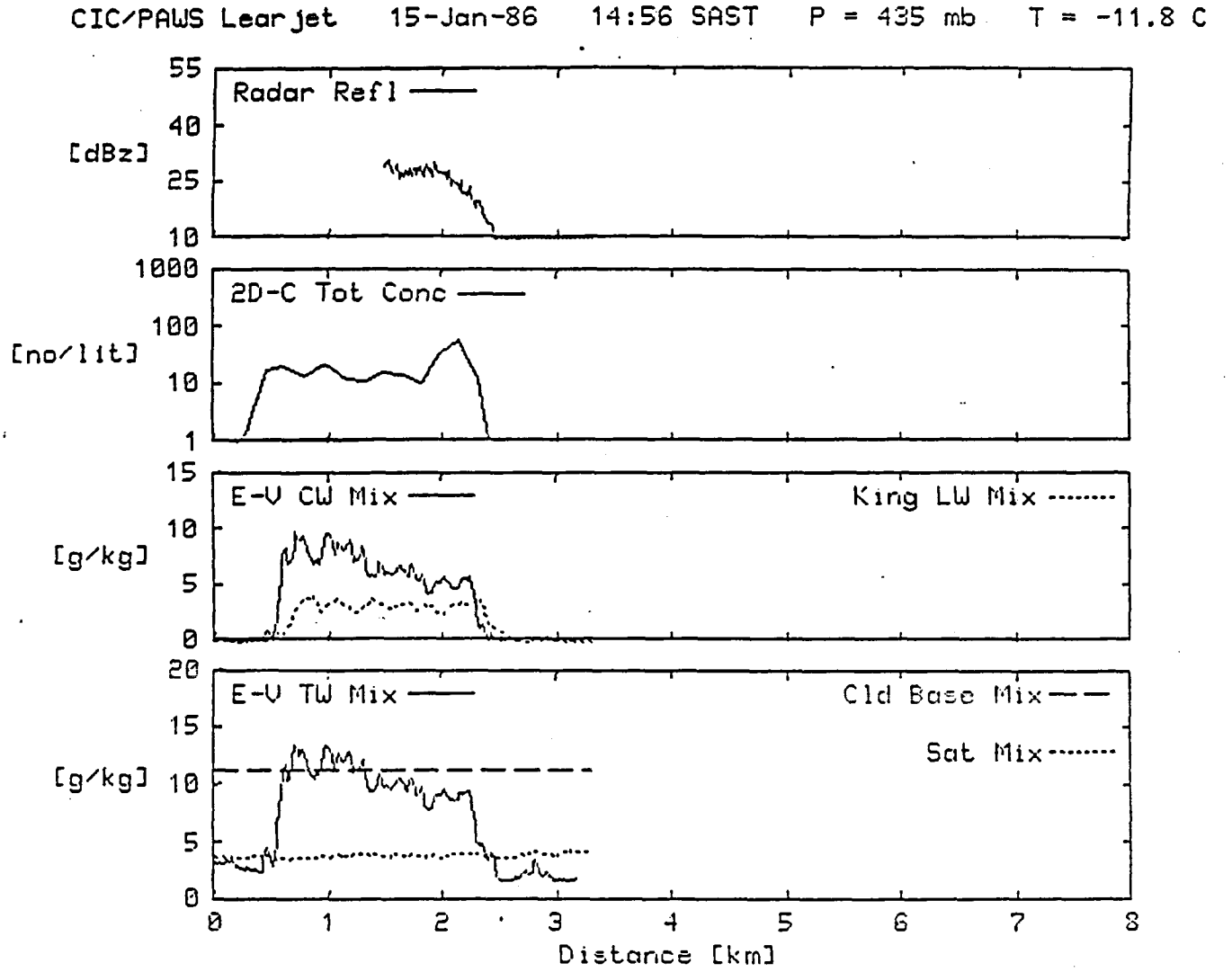

Figure 9.3. An example of engine-vapor and CSIRO-King hot-wire probe performance in a cloud with well-developed graupel.

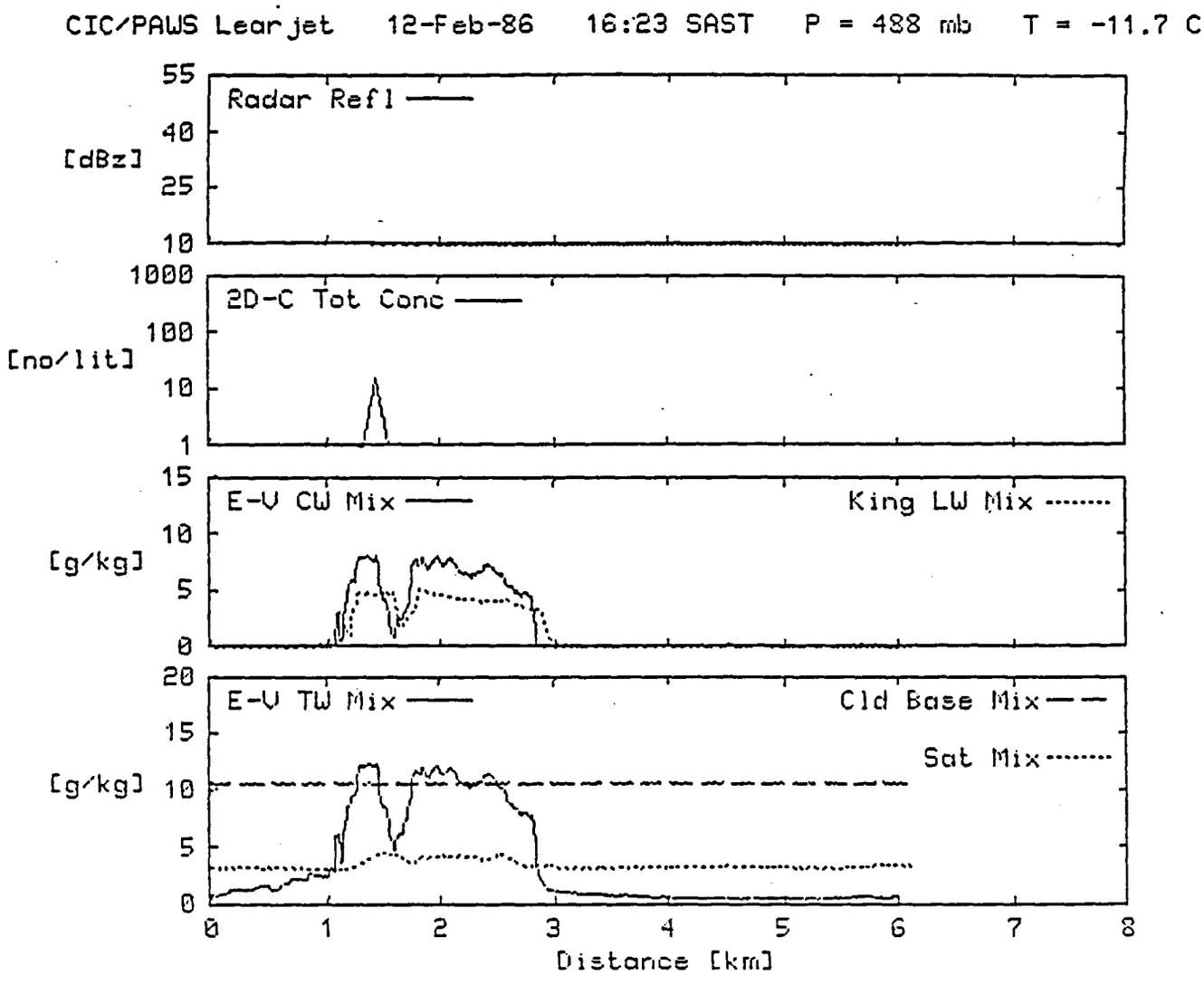

Figure 9.4. An example of a cloud with almost no significant 2D-C activity that exhibits saturation of the CSIRO-King hot-wire.

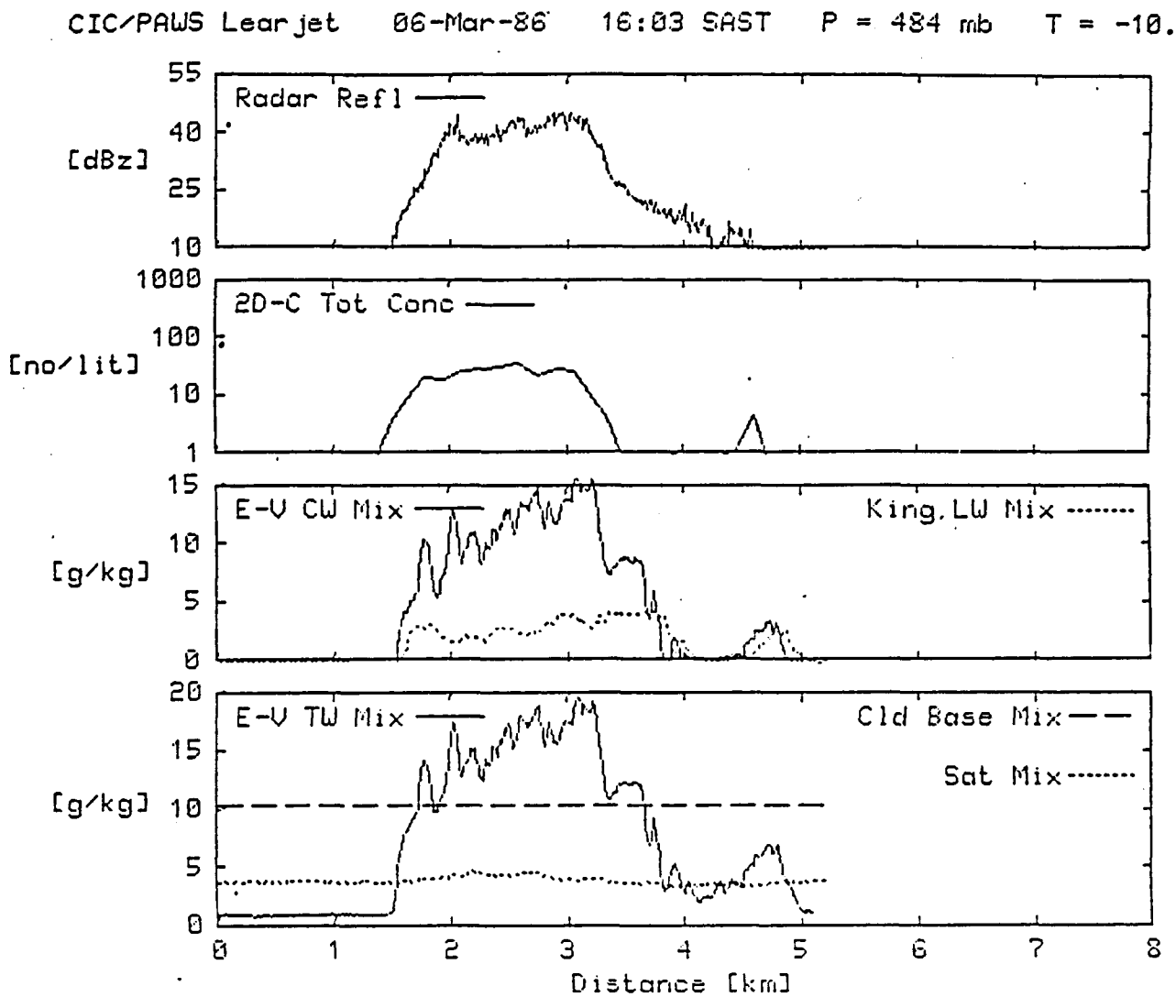

Figure 9.5. An example of engine-vapor and CSIRO-King hot-wire performance in a cloud with moderate accumulation of liquid water.

$$Z = 380\ M^{1.46}$$

where Z is the equivalent radar reflectivity factor (mm^6/m^3) and M is the liquid water content (g/m^3). Here, the budget using the radar estimate of liquid water to calculate the cloud water content and the E-V estimate are within 0.3 g/kg. Such internal consistency generates confidence in these measurements, measurements that have, in the past, been intractable. Both estimates confirm super-adiabatic values of total cloud water content in this example.

Table 9.1 Check on internal consistency of data (see Fig. 9.5). These results are averages over the event, defined as that period during which the 2D-C mean diameters exceed 100 microns (see Fig. 9.6).

E-V - cloud water content	10.54	g/kg
King-liquid water content	2.82	
	7.72	
2D-C water content	7.00	
	0.72	g/kg
RADAR: 36.1 dBz = 4074 Z; M = 5.08 g/m^3 = 8.05 g/kg		
RADAR - water content	8.05	
King	2.82	
	10.87	
E-V - cloud water content	10.54	
	0.33	

It is also instructive to briefly examine a larger ensemble of data from the 1985/86 season. Table 9.2 shows the ratio between peak measured total water mixing ratio and cloud base mixing ratio for 21 cloud penetrations during which the 2D-C probe was not triggered (zero concentration). Only one case showed a total water mixing ratio greater than 1.05 times the calculated cloud base value. Also shown in Table 9.2 is the same ratio for 61 cloud passes with low (less than 10 $litre^{-1}$) 2D-C total particle concentrations and for 41 cases with high (greater than 10 $litre^{-1}$) concentrations. As the 2D-C concentrations increase the distribution changes from one skewed toward sub-adiabatic values to one skewed toward super-adiabatic values. Taken together, the three distributions in Table 9.2, particularly the first, argue that the engine vapour system

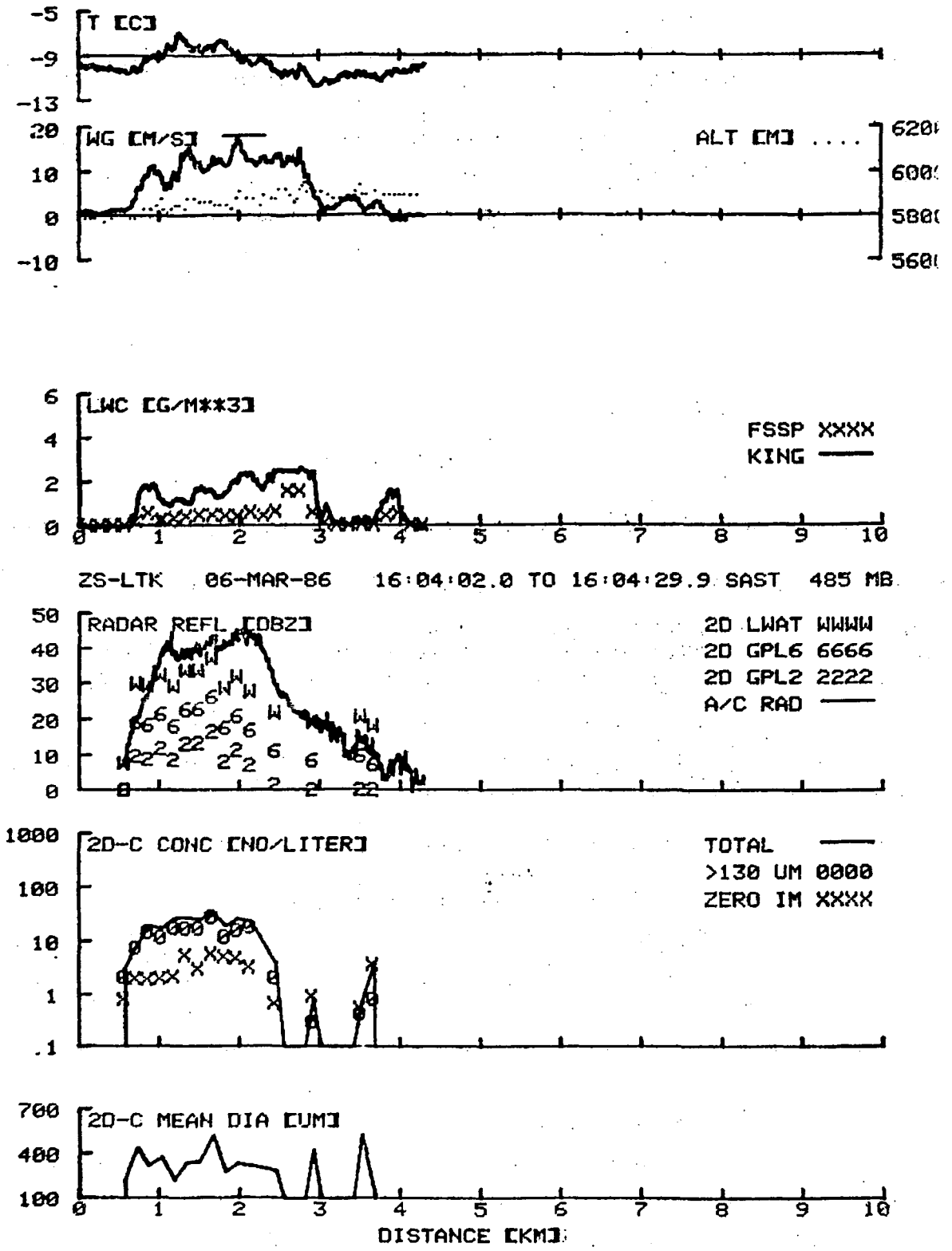

Fig. 9.6. Time histories of some of the measurements used in the cloud water budget in Table 9.1.

Max. Total Water Mixing Ratio/Cloud Base Mixing Ratio

2D-C Conc. (ℓ^{-1})	.3 to .45	.45 to .60	.60 to .75	.75 to .90	.90 to 1.05	1.05 to 1.20	1.20 to 1.35	1.35 to 1.50	1.50 to	N	Avg	σ
0	-	1	2	4	13	1	-	-	-	21	.88	.14
< 10	1	4	3	15	30	5	2	1	-	61	0.9	.18
> 10	-	1	1	4	8	16	5	2	4	41	1.13	.23

TABLE 9.2 : Peak Total Water mixing ratios, from engine-vapor instrument, divided by cloud base mixing ratio.

performs well and yields reasonable values of total water. Additionally, and these will be critically dealt with in a later paper, they suggest that Nelspruit cloud turrets have adiabatic cores, little affected by mixing and that as precipitation particles begin to develop in these clouds there is on some occasions a transient accumulation phenomenon.

Table 9.3 presents a comparison of simultaneous peak liquid water estimates from four different instruments available on the Learjet: the engine vapour system, CSIRO-King hot wire, Johnson-Williams (J-W) hot wire, and integration of the FSSP cloud droplet spectra from 2 to 47 microns. The data shown are for penetrations through 20 turrets between -9.5 and -14.0°C where the average total 2D-C particle concentrations are less than 10 litre^{-1} (no significant ice or large liquid water particles present). The engine vapour system shows an average peak liquid water content of 4.0 g m^{-3}.

9.1.1.4. Discussion

The jet engine vapour measurement of cloud total water mixing ratio is relatively inexpensive and easy to accomplish. The time response is excellent and its high volume sampling rate ensures adequate sampling of the entire spectrum of hydrometeors present in the air. No other system presently available is capable of measuring total and condensed water contents in the warm based wet eastern Transvaal clouds.

The Lyman-alpha humidiometer has proved to be a robust instrument, well adapted to routine day to day use. The system is considered fully operational and is being employed in a study of the feasibility of cloud seeding enhancement of rainfall from convective clouds in the eastern Transvaal. The measurements with the bleed air system have allowed us to demonstrate the existence of liquid water contents beyond the reach of other state-of-the-art instrumentation.

The rapid development of graupel particles following dry ice seeding of eastern Transvaal clouds has been often noted in past years. This rapid graupel growth can now be understood in terms of the results of the engine vapour measurements. The large particles, often water drops, once frozen, can grow rapidly in the high liquid water contents we now know to exist in the Nelspruit clouds.

The ability to apply the engine vapour technique for measurement of water quantities is further justification for the employment of high performance jet aircraft for research in cumulus clouds. The airborne instrumentation system described here is capable of assessing the liquid water in warm based cumulus congestus. The use of hot wire liquid water meters in clouds outside of semi-arid regions is likely to produce misleading assessments of their liquid water contents.

TABLE 9.3

A) LIQUID WATER CONTENT [g m^{-3}]

	0-1	1-2	2-3	3-4	4-5	5-6	6-7	Avg	σ
Engine-vapor system	0	1	4	2	11	1	1	4.02	1.10
CSIRO-King hot-wire	0	4	14	2	0	0	0	2.47	0.46
J-W hot-wire	1	13	6	0	0	0	0	1.71	0.42
FSSP	0	14	6	0	0	0	0	1.91	0.44

B) LIQUID WATER MIXING RATIO [g kg^{-1}]

	0-1	1-2	2-3	3-4	4-5	5-6	6-7	7-8	8-9	9-10	Avg	σ
Engine-vapor system	0	0	1	3	1	1	5	6	1	2	6.48	1.86
CSIRO-King hot-wire	0	1	1	6	12	0	0	0	0	0	3.96	0.80
J-W hot wire	0	3	8	9	0	0	0	0	0	0	2.75	0.70
FSSP	0	1	11	6	2	0	0	0	0	0	3.06	0.69

9.1.2 The Engine Theta technique

9.1.2.1 Principles

A completely different physical principle may be employed to measure the condensed water mixing ratio alone, again using the engine compressor. This new approach is calorimetric in character, making use of the cooling of the compressed air due to evaporation of the cloud condensate. Test trials have been carried out using this technique in parallel with the engine vapour method, and it is now possible to demonstrate the soundness of the principle. Since employment of the technique by others will require adaptation to the particular engines involved, it is considered useful to report on the technique at this stage of development.

Dry air entering the engine compressor at outside pressure P_a and temperature T_a (hence potential temperature Theta-a) undergoes compression and heating. The heating is mostly adiabatic but also in part due to frictional work as the air is driven through the eight stages of the compressor. The air that is bled out of the compressor expands to some intermediate pressure in the utility lines of the aircraft. At a suitable point in the engine bleed-air line the potential temperature in the measurement cell, should be

$$\theta_c = \theta_a + \Delta\theta_f \qquad (1)$$

where $\Delta\theta_f$ is the increase in θ_c due to the frictional heating. $\Delta\theta_f$ is a function of engine performance and the air viscosity. It can be evaluated by flying at different altitudes and power settings.

In fact, during research flights it can be evaluated at the beginning of each run, after the aircraft has been stabilized for cloud penetration. In cloud air, there will be an additional change in θ_c due to the evaporation of the condensate, $\Delta\theta_{cond}$, such that

$$\theta_c = \theta_a + \Delta\theta_f - \Delta\theta_{cond} \qquad (2)$$

can be specified as a function of the mixing ratios of ice and liquid water in the air. We compute this term as follows:

An amount dw_l of liquid water is evaporated into a kilogram of air at temperature T. This results in a temperature change

$$dT = \frac{L_e(T)\ dw_l}{c_p} \tag{3}$$

and, consequently, a potential temperature change

$$d\theta = \left(\frac{1000}{P}\right)^{\gamma} dt = \left(\frac{1000}{\bar{P}}\right)^{\gamma} \frac{L_e(T)\ dw_l}{c_p} \tag{4}$$

where $\gamma = 0.286$, P is pressure, $L_e(T)$ is the latent heat of evaporation of water, and c_p is the specific heat of dry air at constant pressure.

Similar equations hold for the sublimation of ice, with the latent heat of sublimation, $L_s(T)$, and the ice mixing ratio, w_i, taking the place of the latent heat of evaporation and the liquid water mixing ratio. For a mixture of liquid and ice the net change in will be

$$d\theta = \left(\frac{1000}{P}\right)^{\gamma} \frac{L_e(T)\ dw_l + L_s(T)\ dw_i}{c_p} \tag{5}$$

Since,

$$L_s(T) = L_e(T) + L_f \tag{6}$$

then we can rewrite equation 5 as

$$d\theta = \left(\frac{1000}{P}\right)^{\gamma} \frac{L_e(T)\ (dw_l + dw_i) + L_f\ dw_i}{c_p} \qquad (7)$$

The condensed water mixing ratio, w_c, is the sum of the liquid and ice water mixing ratios and therefore

$$d\theta = \left(\frac{1000}{P}\right)^{\gamma} \frac{L_e(T)\ dw_c + L_f\ dw_i}{c_p} \qquad (8)$$

A difficulty arises due to the temperature dependence of L_e. This can be taken care of empirically by flying in all-water clouds and determining an effective value of L_e or, equivalently, an effective evaporation temperature. Substituting equation 8 into equation 2 we get

$$\theta_c = \theta_a + \Delta\theta_f - \left(\frac{1000}{P}\right)^{\gamma} \frac{L_e(T)\ w_c}{c_p} - \left(\frac{1000}{P}\right)^{\gamma} \frac{L_f\ w_i}{c_p} \qquad (9)$$

The condensed water mixing ratio can be independently determined using the engine vapour technique. Then, knowing all the terms in equation 9 but the last, we can solve for the ice water mixing ratio as

$$w_i = \frac{c_p}{L_f} \left(\frac{P}{1000}\right)^{\gamma} \left[\theta_a + \theta_c + \Delta\theta_f - \left(\frac{1000}{P}\right)^{\gamma} \frac{L_e(T)\ w_c}{c_p}\right] \qquad (10)$$

The temperature change due to the presence of ice is not large, about $0.33^{\circ}C\ g^{-1}\ kg^{-1}$. Ability to make estimates of w_i will depend on the stability of the engine behaviour.

At this stage of development of the engine theta technique we set aside the refinement of distinguishing between ice and liquid, and show only the ability to make reasonable estimates of total condensed water content. For this we can use equation 9 solved for the condensed water mixing ratio, neglecting the ice

water term. The latent heat of evaporation will be fixed at its $0^{o}C$ value of 2.500×10^{6} J kg^{-1} as a first approximation.

Sensors of pressure and temperature have been mounted directly on the port engine of the Learjet and their signals recorded. The pressure and temperature sensors employed in these trials were chosen primarily on the basis of ready availability at limited cost and they are not optimum. They are nevertheless adequate for demonstrating the feasibility of the engine theta technique.

Measurements were made in the tops of growing cloud turrets on the flanks of multi-cellular thunderstorms in the vicinity of the $-10^{o}C$ level (near 6.0 km ASL altitude).

9.1.2.2 Results

Fig. 9.6 shows the result of a cloud penetration at 1155 SAST on 10 March 1986, at 468 mb and $-11.2^{o}C$. The drop in temperature due to the evaporation of condensate is clear in the records of both engine temperature and engine potential temperature. Note that just prior to cloud entry the potential temperature in the engine (right scale) is approximately 30 ^{o}K higher than that of the environment (left scale). That is typical of the frictional heating which occurs in the compressor (the compressor consists of eight stages rotating at 12000-15000 rpm). Pressure in the engine is about 2.6 atmospheres and the temperature in the neighbourhood of $190^{o}C$. The condensed water mixing ratio, derived from application of equation 9 (neglecting the ice water term) shows excellent similarity to that derived from the engine-vapour system. The general shape of the two curves and the overall values are in quite good agreement, but the engine theta measurements obviously respond sluggishly. This is due to the engine temperature measurement, which is the most important element of the technique. This should be solved by a combination of a higher response sensor and perhaps more careful placement of the sensor in the engine bleed air outlet.

9.1.2.3 Summary

The principle of measuring changes of potential temperature in jet engine compressor bleed air as an estimate of condensed water mixing ratio in clouds has been tested and shown to be quite sound. Problems remain to be solved in order to realize the full potential and accuracy of the technique. The reasonable agreement shown to occur between the engine theta measurements and the engine vapour technique indicates that the condensed water estimates from the engine vapour method are indeed due to water evaporated in the engine compressor and not some quirk of the Lyman-alpha device and its associated electronics and plumbing.

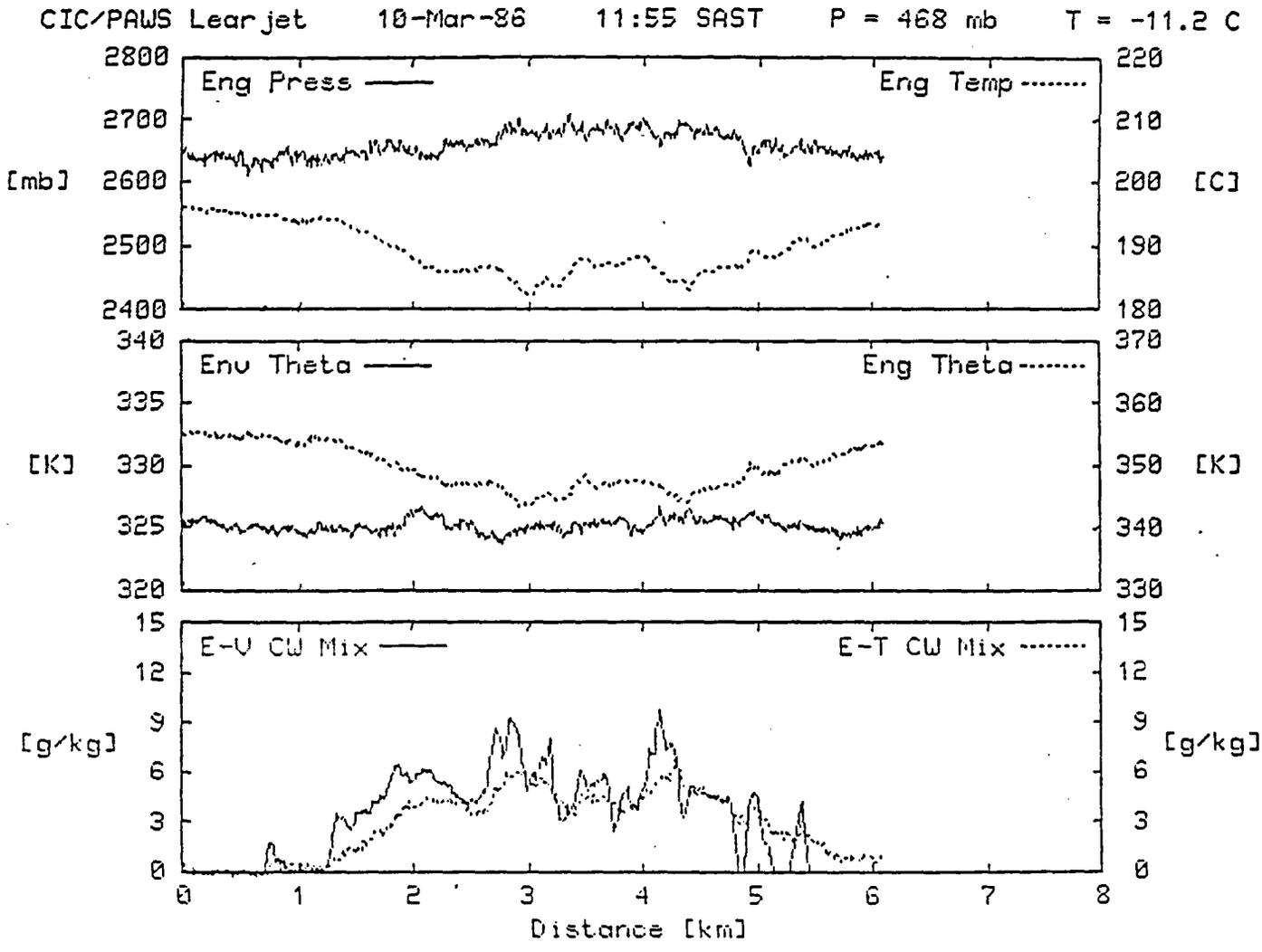

Figure 9.6. Engine-theta and engine-vapor measurements from the cloud pass at 1155 SAST, 10 March 1986. Three panels are shown displaying analog traces as a function of distance run (integration of aircraft true air speed and time). The top panel shows the pressure (solid line; left scale) and temperature (dotted line; right scale) in the port Learjet engine through the run. The middle panel displays the potential temperature computed for the ambient environment (solid line; left scale) and in the engine (dotted line; right scale). The condensed water mixing ratios using the engine-vapor technique (solid line) and the engine-theta technique (dotted line) are given in the bottom panel.

The time response of the thermocouple mounted in the engine is undesireably slow. This may be due not only to the thermocouple itself but also to its positioning in the engine bleed air outlet. Much also remains to be done in precisely determining the frictional heating by the compressor as a function of engine power setting and environmental parameters, and in specifying the effective evaporation temperature of the water.

Given the successful resolution of these engineering problems, the engine theta technique combined with the engine vapour method will provide a unique system for obtaining accurate water content measurements in convective clouds, a goal currently beyond the capabilities of standard airborne cloud physics measurement systems.

9.2 Evidence for the accummulation of very high concentrations of supercooled water in thunderstorms

9.2.1 Background

During the 1960's western scientists became aware of claims by Soviet researchers of great success in reducing hail damage to crops through ice phase cloud seeding. The Soviet method of hail prevention was based on a largely conceptual model of natural hail formation and growth, at whose core lay the concept of an "accumulation zone" (sometimes called the "Big Drop Zone" or BDZ). The accumulation zone (AZ) occurred above the updraft speed maximum where the vertical air velocity was in the range of the fall speeds of the smallest and largest rain drops. In such a region the numbers of drops and the liquid water content increase rapidly (a more complete explanation of this phenomenon is given in Morgan, 1972) and, according to the Soviets, could reach values in excess of 40 $g\,m^{-3}$. The accumulation zone was small, of the order of a few km^3, and was identified with a rapidly developing elevated peak in the radar reflectivity profile. In the AZ, it was claimed, hail could grow very rapidly, and its prevention could be affected by shooting a nucleant into the AZ with a rocket. Haman (1967) and later Morgan (1972), pointed out problems with this concept and attempted to show alternative ways in which the accumulation could be brought about.

The Soviet claims to great success in hail suppression led to American interest in hail suppression and eventually to the undertaking known as the National Hail Research Experiment (NHRE) in northeast Colorado. The history of NHRE is recounted by Morgan and Squires (1982) and by Morgan and Crow (1982). The NHRE, established in a semi-arid region, failed to produce evidence for the AZ.

An announcement by Kyle and Sands (1973) of having measured very high (40 g m^{-3}) liquid water contents in a Colorado storm was later criticized by Smith (1976) and the observation shown to be due to the low volume sampling rate of Kyle's evaporator.

Attempts were made during Grossversuch IV, the three nation hail suppression experiment in Switzerland, to detect evidence for the accumulation zone phenomenon (Musil et. al. 1984; Musil and Smith, 1985) using the T-28 armoured aircraft. After 14 cloud penetrations on three hailstorms it was reported that no evidence even for the presence of large water drops was found.

In the eastern Transvaal, the average cloud base temperature is 14°C (Mather et al., 1986) and at times values as high as 20°C are observed. By comparison, NHRE was carried out in a region where average cloud base temperature was 4.4 °C (Faukhauser and Wade, 1982) with maximum values of less than 12 °C. Ackerman et al., 1979 , using a Ruskin evaporator in clouds with average base temperatures of 19.5°C (range 15.3 to 21.8°C), found the total water content to exceed the adiabatic value on two thirds of cloud passes near the 0°C level. On several occasions the total water reached 20 g m^{-3}. They concluded that accumulation was occurring.

On two occasions the new instruments described here have detected condensed water contents in warm based Transvaal clouds which suggest the existence of accumulation zones.

9.2.2 The observations

March 12, 1986 was one of the first operational days on which both engine vapour and engine theta instruments were on board the aircraft. During a cloud penetration at -10°C at 1537 SAST, the engine vapour method produced a peak estimate of condensed (liquid and ice phase) water mixing ratio of 39.6 g kg^{-1} (23.7 g m^{-3}) as shown in the third panel of figure 9.7. This was a mixture of large raindrops and round graupel. There had been a previous occurrence of very high water content, as will be shown below, which had been set aside for study because of the suspicion that something had malfunctioned in the Lyman-alpha humidiometer. In the present case, however, we were able to analyze the engine-theta records, resulting in the dotted curve in the bottom panel of Fig. 9.8. The pressure, temperature and theta curves of Fig. 9.8 should be compared to similar curves shown in section 9.3 above, to fully appreciate how extraordinary this case was.

The pilots and observer on the flight described the experience as similar to driving through a downpour; the high water content was very apparent to all three. A video tape record furnished dramatic documentation of enormous water drops striking and streaming across the copilot's windscreen. An additional data record from the Learjet lends further support to the measurement. Radar Z_e values, shifted by 1.5 km to correspond, point for point, with the rest of the data set, are shown in the

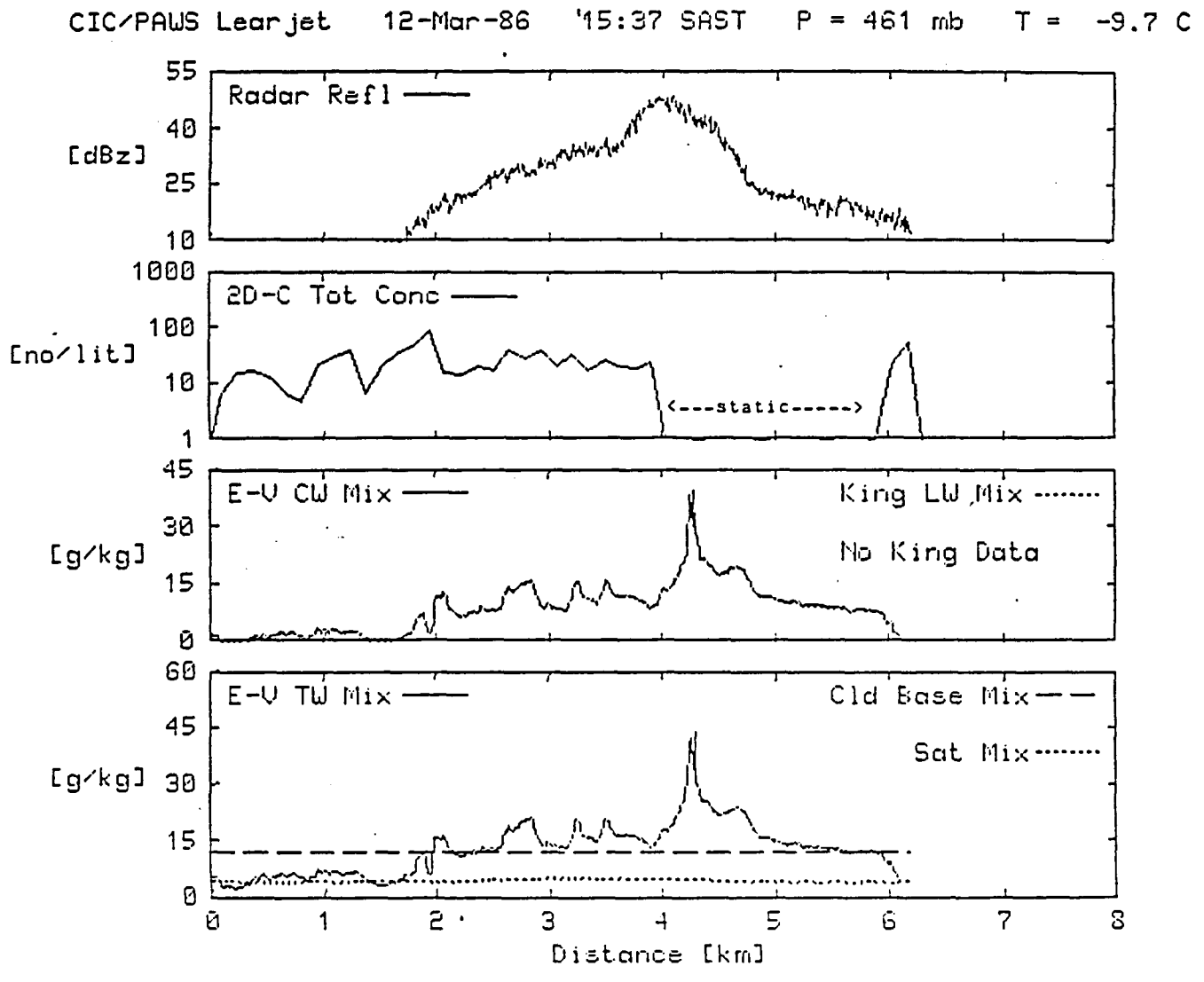

Figure 9.7. The 12 March 1986 accumulation zone observations. Analog traces are shown as a function of distance run. The bottom panel shows the total water mixing ratio by the engine-vapor system (solid line), saturation mixing ratio (dotted line) and cloud base mixing ratio (dashed line). The second panel displays the engine-vapor system condensed water mixing ratio (solid line) and King liquid water mixing ratio (dotted line if data is present). 2D-C probe total particle concentration is shown in the third panel and aircraft 3 cm radar reflectivity (adjusted for horizontal displacement ahead of the aircraft) is shown in the top panel.

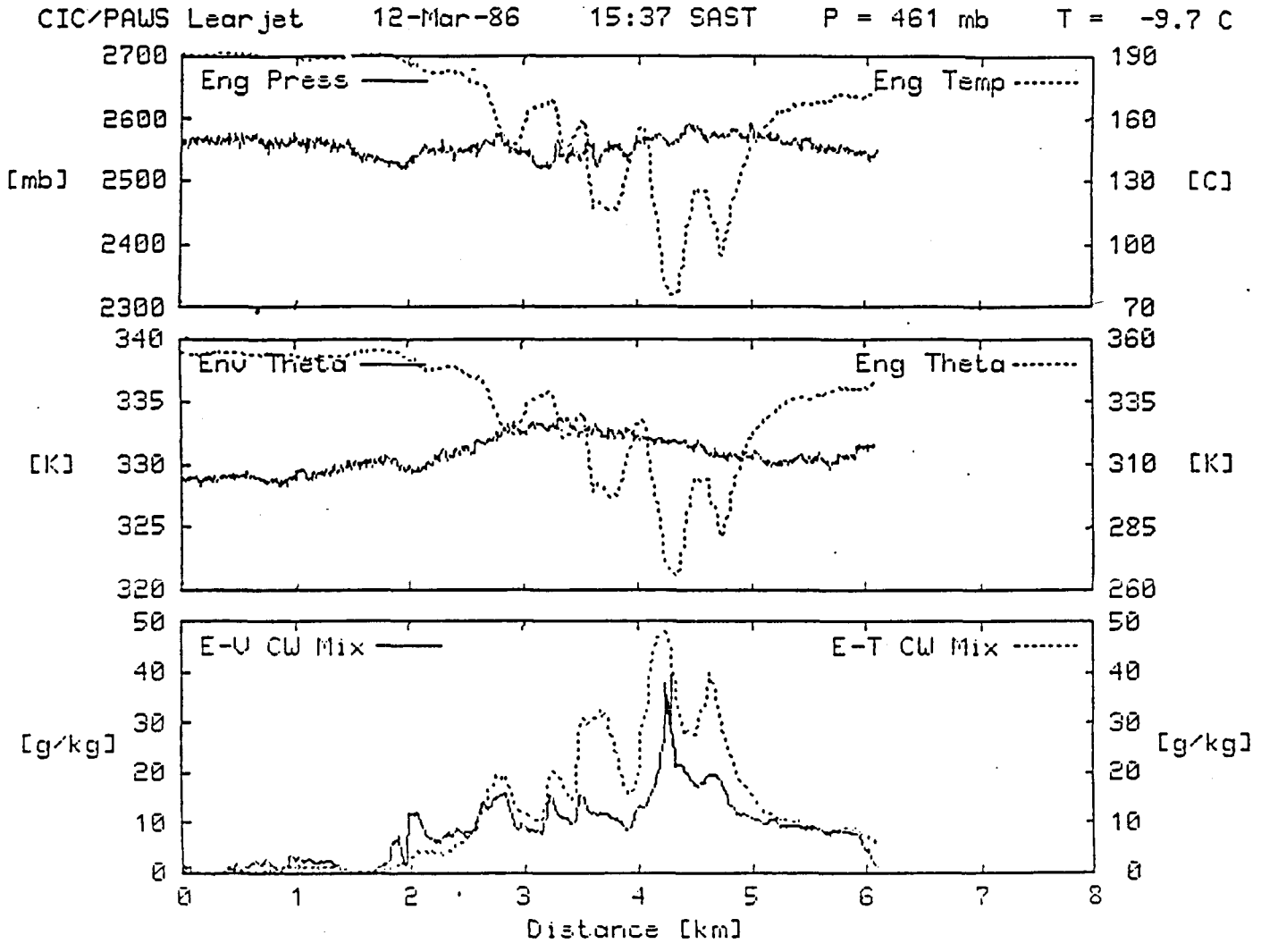

Figure 9.8. A comparison of the condensed water mixing ratio computed using the engine-vapor method for the 12 March 1986 observation is shown in the bottom panel as the solid line, and using the engine-theta technique as the dotted line. The other two panels show data relevant to the engine-theta technique: potential temperature for the environment (solid line) and computed in the engine (dotted line) are shown in the second panel; and the pressure (solid line) and temperature (dotted line) in the engine are displayed in the top panel.

top panel of Fig. 9.7. The radar indicates a much broader feature than is apparent in the condensed water profile. This is due to the resolution of the radar; the half pulse length is about 350 m. Had the radar been able to measure at the same scale as the engine instruments, a much higher value of Z_e would clearly have resulted. A peak reflectivity of 48.8 dBz coincides well in position with the peak in water content. The updraft speed was close to 9.10 m s^{-1} in the vicinity of the high Z_e and high water contents. Such a value would be consistent with accumulation of millimetre sized drops.

Recorded volume scan data from the project's ground based C-band radar showed reflectivities up to 47 dBz along the aircraft's flight track on this penetration. The adjacent parent storm contained a peak reflectivity of 56 dBz.

Since the above case apparently ruled out instrument malfunction as an explanation for the exceptionally high condensed water measurements, an earlier and even more spectacular flight was re-examined. Fig. 9.9 shows the observations from a cloud penetration made at -10°C at 1504 SAST on 15 January 1986. This cloud, too, consisted of large drops, and graupel. The engine theta instruments were not installed at that time.

The peak engine vapour condensed water mixing ratio recorded on this pass was 80 g kg^{-1}, corresponding to 46 g m^{-3}. The crew's sensations of driving through a rainstorm on this pass were similar to those on the penetration just described above. Unfortunately, the video recorder ran out of tape just prior to this run. However, there was a video recording which fully justified a report of very heavy rain at around -10°C on a previous run, where no cloud physical data were recorded. On leaving this cloud the Lear was forced to pass through a neighbouring tower in which it encountered hail causing minor damage to the airframe and exposed instruments.

The full value of 80 g kg^{-1} shown is not a real measure of the cloud content. What had happened in this case is that condensation had taken place in the measurement cell. The pressure and temperature in the cell were 750 mb and 35°C. The corresponding saturation mixing ratio is 50.5 g kg^{-1}. When the mixing ratio rose to that value, condensation must have occurred in the cell and the narrow copper pipe leading to it. The apparent mixing ratio remained at about 80 g kg^{-1} for a long period as the condensate re-evaporated. So, what we do know is that for an indeterminate period the total water mixing ratio exceeded 50.5 g kg^{-1} (29 g m^{-3}) by an indeterminate amount. Once the mixing ratio exceeded that amount, the instrument saturated. It is very likely that something similar to this occurred to produce the exceptional value of 44 g m^{-3} reported by Roys (1963).

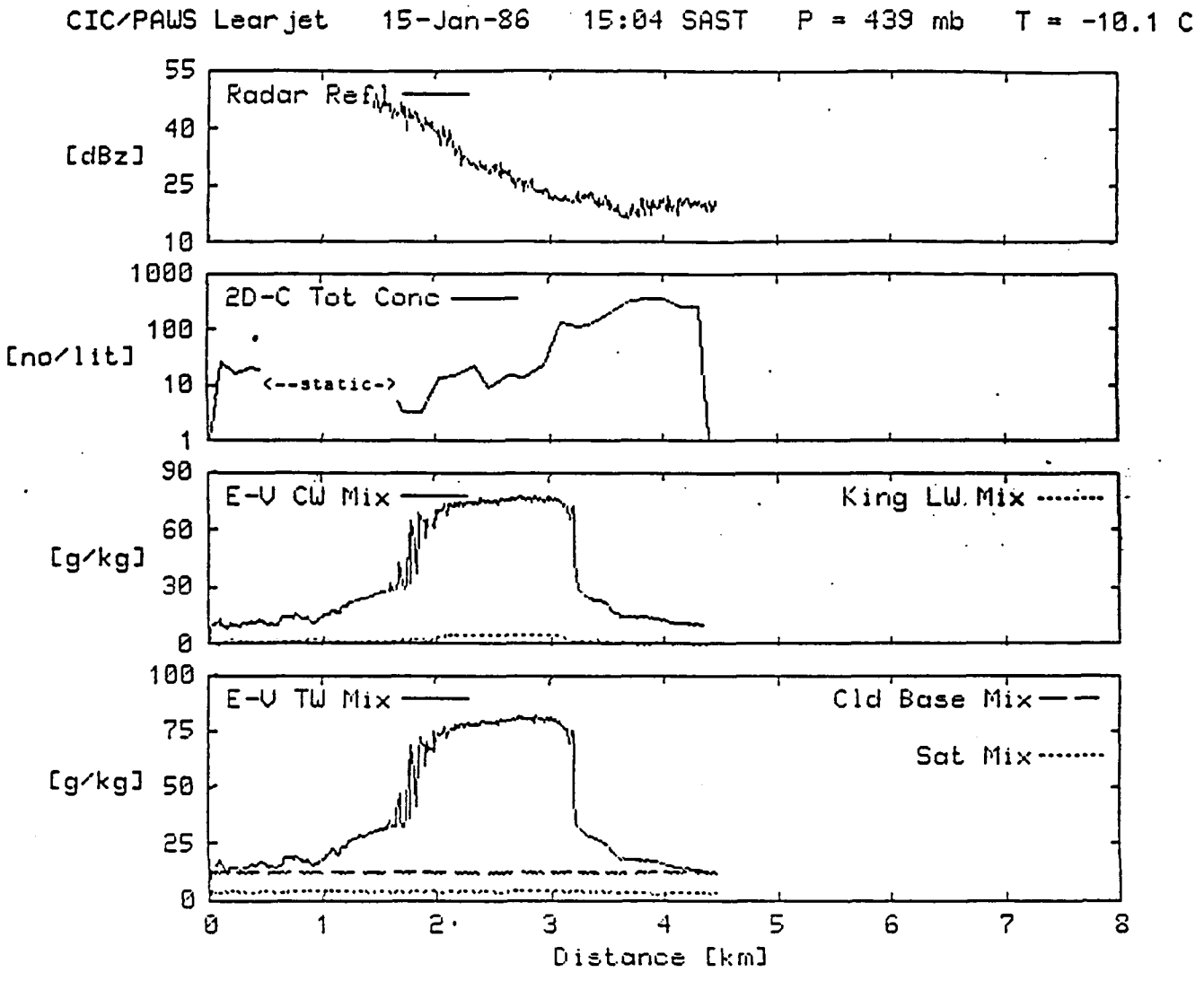

Figure 9.9. The 15 January 1986 accumulation zone observations. Figure shown is the same format as Fig. 8.9 except that the scales in the bottom two panels have been expanded.

In the absence of the engine theta measurement, the main support for the reality of the exceptional water content value must come from the on board radar recording. Unfortunately, on this pass, the tape recorder was turned on late, at the time when the flying range gate was just passing the region of high water content. Nevertheless, as the radar recording was begun the Z_e value was around 50 dBz.

The ground based radar at Nelspruit recorded radar reflectivities as high as 49 dBz along the aircraft's track on this cloud penetration and the adjacent parent storm contained reflectivities as high as 54 dBz.

9.2.3 Comments

How often does this accumulation phenomenon occur? That would be a difficult question to answer at this point, but the following observations are relevant.

A total of 30 flight days have occurred on which the engine vapour instrument was operational on the aircraft; the phenomenon has been observed on two of them. The flight programme is not designed to look for the AZ. Flights are performed so as to sample, and, when dictated by a randomization procedure, to seed clouds at about the -10°C level. Only a fraction of the cloud turrets which occur are sampled. In fact, one possible outcome of the randomization procedure dictates that the turrets on a selected storm be neither seeded nor sampled.

In the years from 1973 to 1981, the Learjet was employed in an operational hail suppression project (without its present sophisticated instrument complement) penetrating cloud turrets over a wide range of temperatures. During those years the experience of "driving through a downpour" while flying at sub-zero temperatures, was not uncommon. Heavy clear icing on unheated surfaces was common in clouds at -20°C and -25°C.

The observations reported here which could not have been made with conventional instrumentation are interpreted as indicating that the accumulation phenomenon exists. Its significance in the clouds in question is unknown; there are no reliable records of hail occurrence or non-occurrence in the region of study.

Though it is suggested above that accumulation occurs only in clouds with high cloud base temperatures, that is not a proven fact since adequate measurements in Colorado and Switzerland have not been made. Certainly, if the AZ phenomenon exists, as these observations suggest, any attempt to numerically model thunderstorms must deal with that fact. Model results should display the AZ phenomenon at times. A major factor in the occurrence or absence of the liquid water AZ must be the ice nucleation behaviour of the cloud. Underlying the AZ phenomenon is a major mechanism for precipitation development, coalescence. Mather et al. (1986), have shown the importance of coalescence

in Transvaal clouds and determined the conditions under which it clearly predominates. They also pointed out that ice nucleation can interfere with that process, producing a graupel population at the sampling level (-10°C) rather than drops.

The AZ of Sulakvelidze et al. (1967), which has been so poorly esteemed in Western scientific circles must be seriously reconsidered. So, too, must be the report by Roys (1963) of a liquid water content of 44 g m^{-3} in an Oklahoma thunderstorm. At the same time, the conceptual model of hail formation and hail suppression advanced by Sulakvelidze must be re-examined.

9.3 Studies on the state of mixing in Nelspruit clouds (Morgan and Morrison)

Cumulus clouds are the visible elements of a very complex spectrum of mixing processes in the atmosphere. The spectrum of mixing processes is a continuous one with much interaction and movement of energy through the spectrum. The rising masses of warm air which make up the cumulus clouds are not like corks, bobbing to the surface of a pail of water, but are constantly mingling with their surroundings, taking in environmental air and shedding some of their mass into the environment. This has a profound effect on the lifetimes of clouds and on their internal precipitation forming processes.

Theory concerning mixing is a very complex problem and not at a satisfactory stage of development. It would be completely beyond the scope and means of the PAWS project to attempt theoretical studies or the development of models to deal with this important problem which most certainly has impact on the weather modification problem. It is also not likely that significant theoretical advancement for our purposes is forthcoming from any quarter. We can, however, attempt to describe the impact of the mixing in an empirical way and present an overall view of the clouds, seen as being composed of zones of varying degrees of mixing.

In Section 9.1 it was shown, using measurements of total water mixing ratio, that clouds in which no precipitation has formed at about the -10°C level have adiabatic cores. We can now take this small sample of such clouds and examine the question of the importance of these cores.

The approach is based on fluxes. The calculations of the fluxes are discussed in Section 10. We pose the question, what portion of the upward flux of air in the cloud is adiabatic or nearly adiabatic? It is important to discuss this in terms of flux because there is a correlation between the upward air velocities and the total water content, the quasi-adiabatic regions tending to be in the faster moving interior of the cloud.

We can form, for each traverse the relative frequency and cumulative frequency distributions of upward flux (percent of total) versus total water mixing ratio expressed as a fraction of the adiabatic value (we actually assume that the peak value in the cloud is the adiabatic value, small departures from adiabatic being due to local values of low level mixing ratios being slightly different from those estimated on the aircraft sounding at Nelspruit). An example of this is the pass made at 1348 SAST on 29 October 1985, shown in Fig. 9.3.1. Examination of this plot shows that in this cloud, at the penetration level, 50 percent of the upward flux of air contained total water mixing ratios within 10 percent of the adiabatic value.

Fig. 9.3.2 is a combined result for 14 cloud passes in which there were no 2D-C images and the total water mixing ratio was greater than 0.9 times the adiabatic value. This shows that for this ensemble, over thirty percent of the upward flux was within 10 percent of adiabatic and 60 percent of the upward flux was within 20 percent of adiabatic. These were clouds averaging 2.0 km in diameter and almost 4.0 km^2 in cross-sectional area. The mean flux of air was 14.65 Kton sec^{-1}. Separating the up and down portions of the vertical speed record resulted in an average up flux of air of 16.37 Kton sec^{-1} and an average down flux of 1.72 Kton sec^{-1}. At least one of the clouds contained no downdraft and in one the updraft occupied only about 8 percent of the traverse; the average of the set of clouds was 70 percent updraft and 30 percent downdraft.

We next enlarge our sample by including cases in which there was a very small amount of precipitation in the cloud (2D-C average concentration less than 10 l^{-1}). Here we look at cases with a peak total water mixing ratio from 0.9 to 1.05 times the adiabatic value. The result is Fig. 9.3.3 for 25 cases, and is almost identical to the previous figure.

The percent of each traverse which is updraft is an interesting parameter which is related to mixing and is recorded in the cloud sample database. It varies from zero to 100 percent. In an attempt to determine relations between this and other cloud parameters, a number of scatter plots similar to Fig. 9.3.4 have been examined. Here, the percent of each traverse which is updraft is plotted against the maximum vertical velocity measured on the traverse, for traverses performed between -5 and -10°C. There is a very clear tendency for clouds with weak updrafts to contain large percentages of downdraft, and for clouds with strong updrafts to contain large amounts of updraft. Similar plots for other temperature intervals look the same. One conclusion from this is that the mixing and development of downdrafts in the cloud cause it to arrive at the penetration level with a weak updraft.

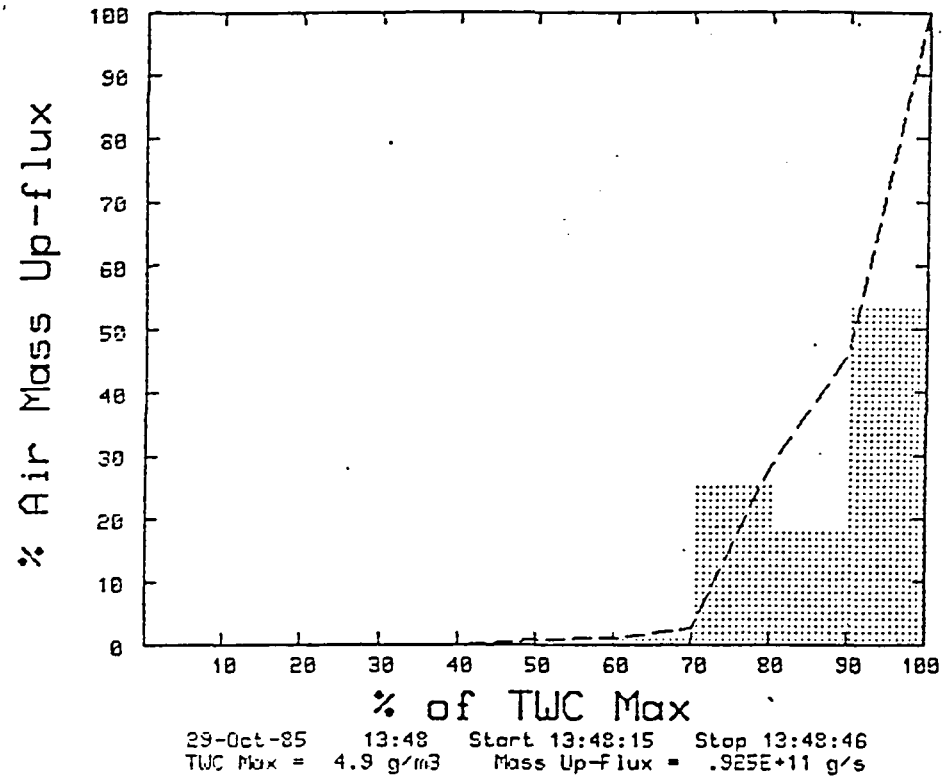

Fig. 9.3.1. Cumulative frequency distribution of upward air flux versus the total water mixing ratio expressed as a percent of the adiabatic value.

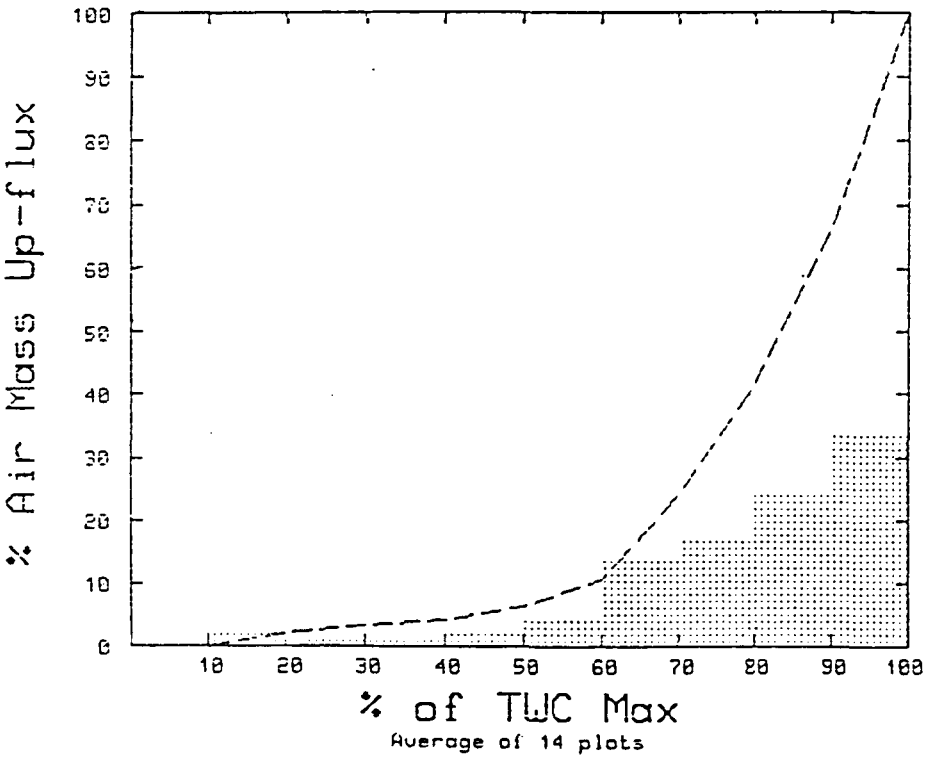

Fig. 9.3.2. As above, for 14 passes containing no 2D-C images and total water mixing ratios greater than 90 percent of the adiabatic value.

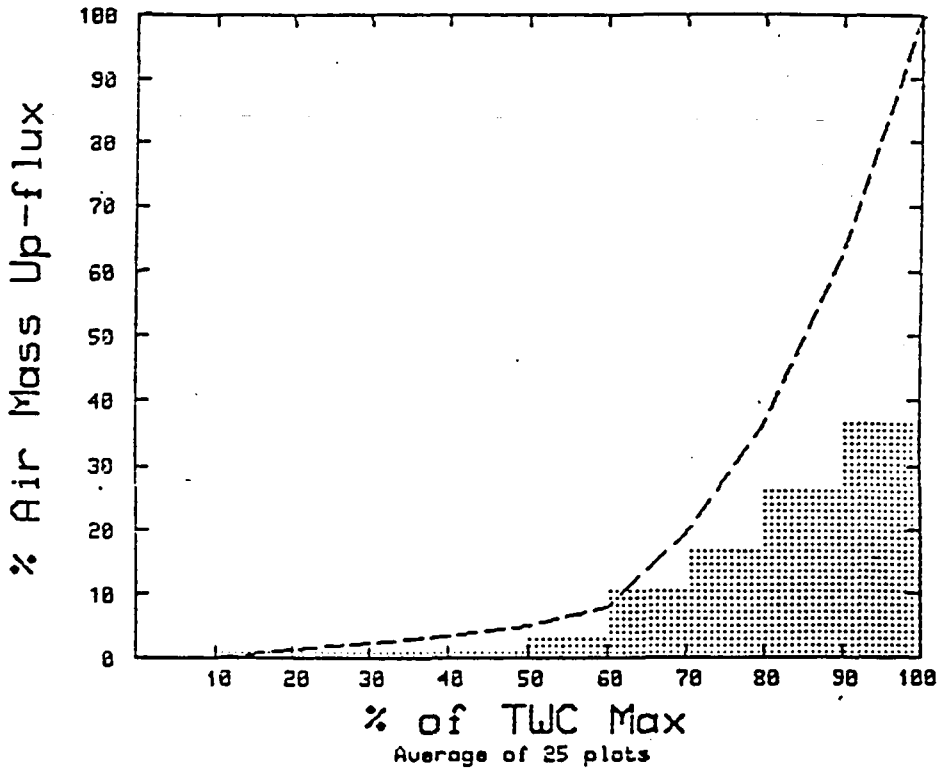

Fig. 9.3.3. As in Fig. 9.3.1, with average 2D-C concentrations less than 10 l^{-1} and total water mixing ratios 90 to 105 percent of the adiabatic value.

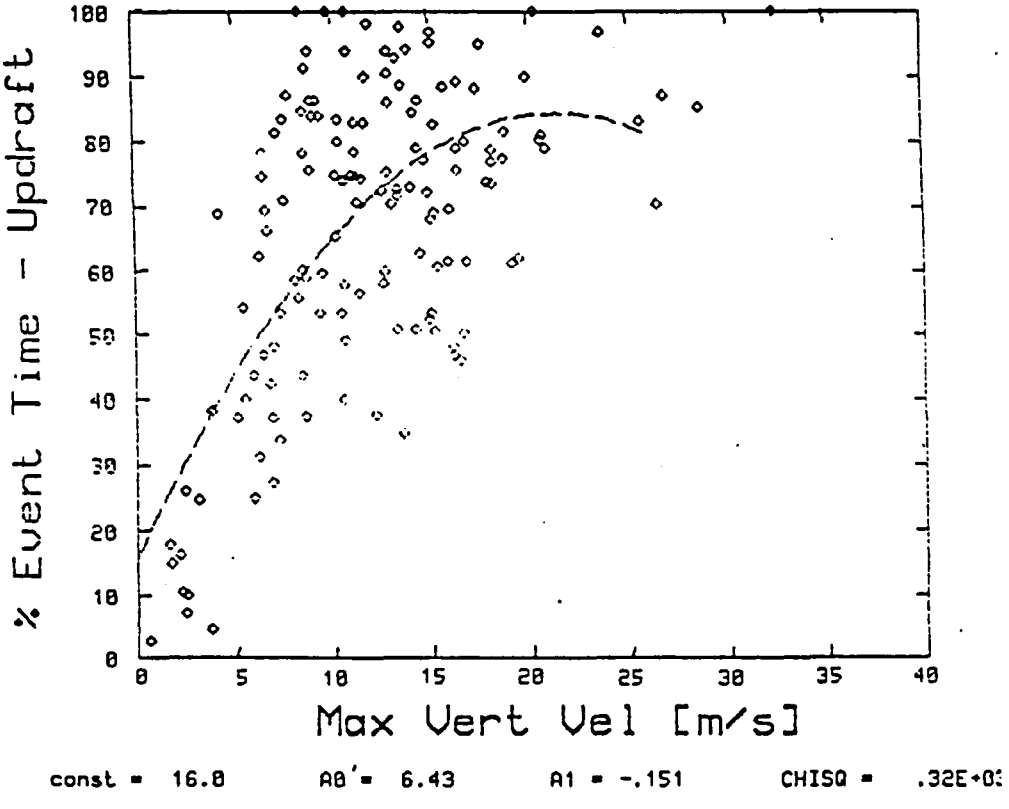

Fig. 9.3.4. The percent of a cloud traverse that is updraft versus maximum vertical velocity.

9.4 The dependence of the frequency of occurrence of certain cloud properties in the -15 to -5°C layer, on terrain height (Morgan and Morrison)

The terrain over the experimental area varies from near 200 m asl in the East to around 2200 m to the northwest of Nelspruit. This should have influences on the internal properties of clouds as they are viewed in a fixed altitude or temperature interval. Two main effects expected to play a role in determining cloud characteristics are:

a. The higher the terrain, the shallower the moist layer, hence the higher and cooler the bases of the clouds

b. The lower the terrain the greater the distance between the surface and any fixed altitude or temperature level, and, following a), the greater the distance from cloud base to that level. The importance of this to the development of precipitation through coalescence is documented in Section 5.2 of Vol. III and in Mather et al., (1986).

A very simple test of the existence of these influences has been performed using the cloud sample database. All data from Learjet missions between October 1982 and April 1986 have been sorted to select first passes occurring between - 15 and -5°C (environmental temperature) with valid 2D-C data, then sorted into sets according to the terrain elevation below each sampled cloud.

The terrain intervals in Tables 9.4.1 and 9.4.2 are unequal and chosen for convenience, with due respect for sample sizes. The lowest interval includes all terrain lying below the base of the Nelspruit sounding. Clouds over that region have beneath them a layer of moisture which is not sensed by our soundings and which can extend as much as 700 m below it. The other intervals were set by examining the overall histogram of underlying terrain heights and attempting to split the sample up meaningfully. Table 9.4.1 shows the probability (percent) of encountering large liquid drops in clouds for four categories of terrain height. This probability goes from 11 percent over the highest terrain to 67 percent over the lowest terrain east of Nelspruit.

The average peak radar reflectivity factor for clouds in the same terrain height intervals (Table 9.4.2) also varies in a way which is consistent with the above. The general decrease of Z with height can be expected, due to a greater percentage of clouds with large particles over the lower ground, and a greater role being played by coalescence generated large drops there.

No other cloud parameters in the database showed consistent or marked tendencies under this stratification.

Table 9.4.1 The dependence of the relative frequency of occurrence (percent of 1st cloud passes) of drops in the 2D-C images on terrain height. Data from 1982 to 1986, first passes only in the environmetal temperature range -15 to -5°C.

Terrain ht interval (m)	Number of clouds	Number with drops	Percent with drops	Number with no 2D	Percent with no 2D
900	37	24	65	2	5
900-1500	89	27	30	19	21
1500-1700	128	30	23	24	19
1700	46	5	11	9	20

Table 9.4.2 The Mean peak radar reflectivity factor Z (dBz), in turret clouds sampled over four categories of terrain height.

Terrain height interval (m)	Max radar reflectivities (dBz)	No of cases
900	23.7	24
900 - 1500	18.1	67
1500 - 1700	16.3	109
1700	13.3	41

9.5 The efficiency of precipitation formation (Morgan and Morrison)

Precipitation efficiency is a term often discussed in the weather modification context. It is often used in a loose way or without clear reference to its definition. Perhaps the most common definition is that the precipitation efficiency is the total amount of precipitation falling to the ground during the life of a cloud divided by the total amount of water vapour which enters the base of the cloud during its life. Difficulties with this are obvious. It is extremely difficult to monitor either the

rainfall or the inflow. Nevertheless, such concepts allow one to discuss the major limits to precipitation efficiency, even if it cannot be practically measured. Efficiency is limited by factors such as mixing and by evaporation below cloud base, and by exhaustion of water through anvils, to name a few.

Efficiency as defined above is an important concept to PAWS, but we will try and approach it from a point of view most suited to the types of data we have. We will attempt to discuss efficiency from a "local" point of view, as we can estimate it from data collected in clouds.

This will be done by estimating the sizes of terms in a simple precipitation formation equation and pointing out their relative values. By taking this local point of view we do not want to imply that it presents the whole picture. Local conditions may be completely offset by conditions at other places or times.

9.5.1 Analysis of first passes

Precipitation growth rate is computed for each 2D-C data record assuming precipitation particle densities of 0.2, 0.4, 0.6, 0.8, or 1.0 g cm^{-3}. For use in the calculations described below, a bulk particle density was assumed for each cloud penetration according to the 2D-C image classification parameter stored in the Cloud Sample Database using the following scheme: Penetrations consisting predominantly of water drops were given a bulk density of 1.0. Runs that were predominantly graupel were assigned a density of 0.6. All-ice runs were assigned a density of 0.2. Mixtures of graupel and drops were assumed to have a density of 0.8. Images that were too small to discriminate phase (ice versus small water drops) were assigned a value of 0.8. Zero images were assumed to be ice and were given a density of 0.2.

Three terms described above have been computed across the updraft of turrets penetrated by the Learjet and are combined into two parameters which were stored in the Cloud Sample Database. These parameters are the "conversion efficiency", CE, and the "reservoir effect", RE, and are defined as follows.

The conversion efficiency is defined as :

$$CE = \frac{AC + PGR}{CR}$$

where AC = autoconversion rate [g m^{-3} s^{-1}]
PGR = precipitation growth rate [g m^{-3} s^{-1}]
CR = condensation rate [g m^{-3} s^{-1}]

This dimensionless parameter is the ratio of the rate of precipitation production (AC + PGR) to the rate of cloud water production (CR). Small values (less than 1.0) imply that little of the cloud liquid water being produced is being converted to precipitation suggesting a locally inefficient precipitation mechanism. A value of 1.0 implies that precipitation is being produced at the same rate as that of cloud liquid water. If we assumed a steady state supply of cloud liquid water and precipitation embryos (which is not realistic for convective clouds), this would be optimal. However, this does not take into account the substantial reservoir of supercooled liquid water, frequently in excess of 3 g m^{-3}, which already exists when precipitation production begins. Values of the conversion efficiency somewhat greater than 1.0 would therefore be more ideal. Excessively high values much greater than 1.0 could exhaust both the production of liquid water and the existing supply resulting in a decline in efficiency.

The reservoir effect parameter, RE, directly addresses the question of the exhaustion of the supply of liquid water. It is defined as :

$$RE = \frac{AC + PGR}{LWC}$$

where LWC = cloud liquid water content from J-W or FSSP [g m^{-3}]

It has units of s^{-1}. The cloud liquid water content is taken from the J-W hot wire data or, if the J-W data is missing or bad, from the integrated FSSP liquid water spectrum. This parameter is inversely proportional to the rate at which precipitation scavenges the cloud liquid water. Very small values imply a slow rate of cloud water uptake and, therefore, inefficient utilization of cloud water. Very large rates, however, could lead to depletion of the local liquid water supply required for continued precipitation development and growth.

Recognizing the assumptions and limitations inherent in these parameters, and emphasizing that they address only LOCAL precipitation efficiency and not that of the overall cloud or cloud system, we can make some general statements concerning the natural clouds in the study area.

Figure 9.5.1 shows the cumulative curves for the updraft conversion efficiency over four temperature ranges in untreated (first pass) turrets. In the -4 to -8°C range precipitation efficiency is the lowest. Only 10% of the penetrations show precipitation developing at a rate equal to or faster than the condensation rate. This figure increases to 38% in the -8 to -12°C range, then decreases slightly to 28% in the -12 to -16°C range, then increases to about 42% in the -16 to -20°C range. This implies that there is a significant population of inefficient and therefore potentially seedable turrets.

Cumulative curves for the reservoir effect in natural turrets over the same temperature ranges are shown in Fig. 9.5.2. We can assume that the time to deplete the cloud liquid water supply is about 1.0/RE. Therefore, at the 50th percentile this time would be 1515 seconds in the -4 to -8°C temperature range, 625 seconds in the -8 to -12°C range, and 588 seconds in both the -12 to -16°C and -16 to -20°C ranges. Even at the colder temperatures, this time scale of about 10 minutes (588 secs) implies locally inefficient utilization of the available cloud liquid water supply.

9.5.2 Analysis of seeding effects

Given that there is opportunity for static mode glaciogenic seeding to enhance precipitation efficiency, how does seeding with dry ice pellets affect natural efficiency? To answer this question we must examine changes in the efficiency parameters defined above in unseeded and seeded turrets.

Figures 9.5.3 and 9.5.4 show the cumulative frequencies of CE and RE, respectively, for all first Learjet passes (natural cloud state), and subsequent repenetrations into seeded and unseeded turrets in the temperature range -10 to -20°C. The data on repenetrations was insufficient to allow examination of narrower temperature ranges. In both the seeded and unseeded turrets there is a positive shift towards higher values of CE and RE from first passes to repenetrations. The shift is greater in the seeded cases.

These results must be interpreted with caution because of the limited sample size. The values of CE and RE from the first passes on the seeded and unseeded turrets are plotted against all first passes available in the data set in the temperature range from -10 to -20°C in Figures 9.5.5 and 9.5.6. These figures show that, while the turrets selected for the unseeded cases are reasonably representative of the entire population of natural turrets (especially in the CE parameter), the turrets in the seeded cases show initially higher values of CE and RE than are found in the natural population. Definitive statements about the effects of dry ice seeding, as revealed by this analysis, will have to await the acquisition of further measurements from seeded turrets.

9.6 The dependence of cloud droplet concentration on precipitation development (Morgan and Morrison)

As a parcel of air rises through the cloud base, a cloud forms in it. This cloud is composed of droplets with diameters less than 30 - 35 microns. The FSSP mounted on the port tip-tank of the Lear is capable of counting and sizing the droplets in this size range.

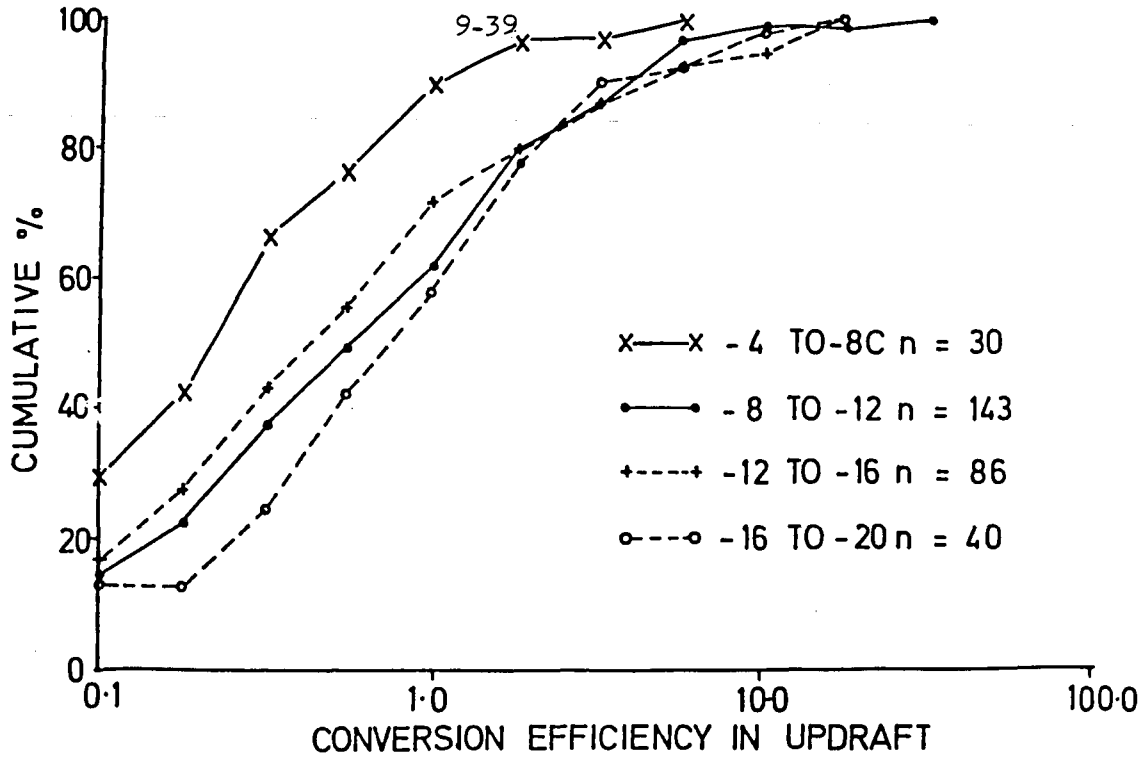

Fig. 9.5.1. Updraft conversion efficiency (CE) over 4 temperature ranges in untreated clouds.

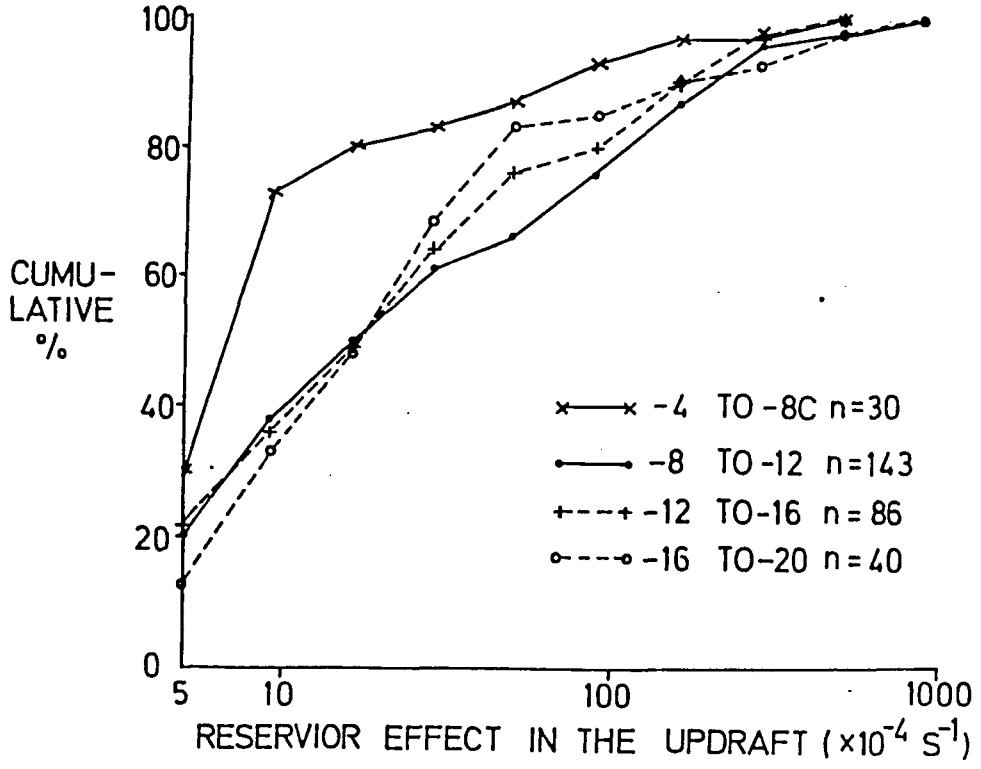

Fig. 9.5.2. Reservoir effect (RE) for above samples.

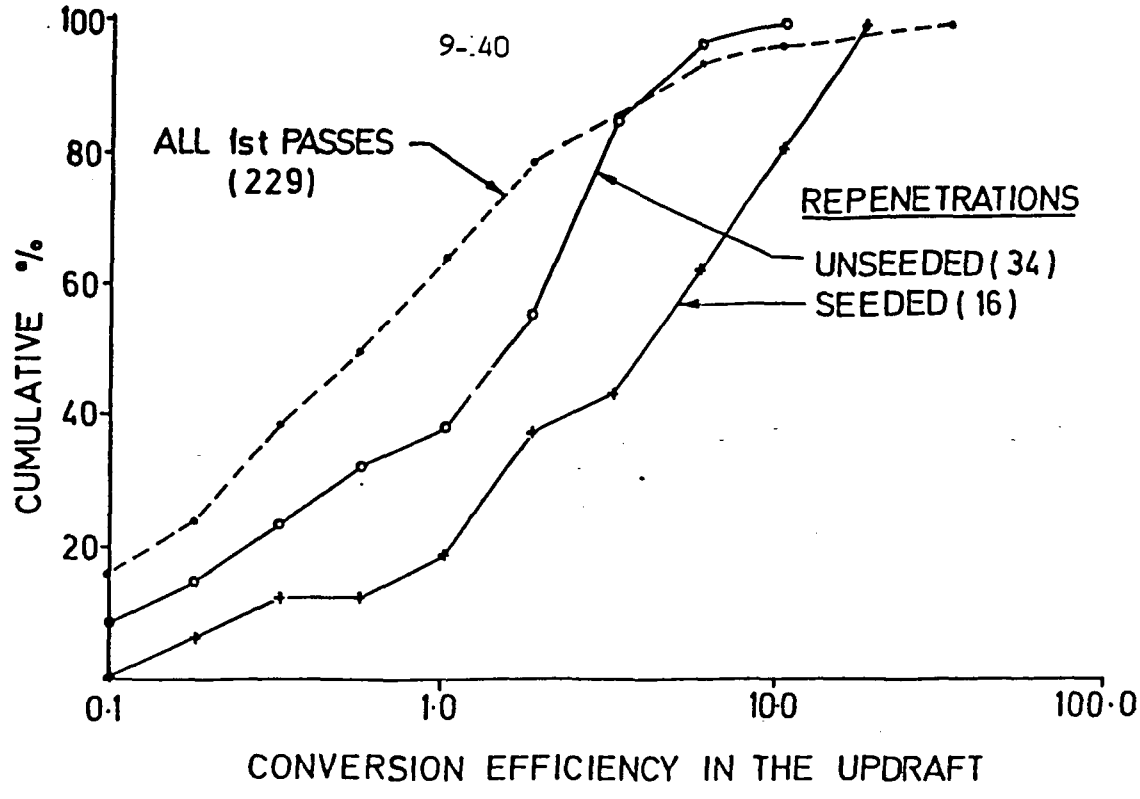

Fig. 9.5.3. CE for all first passes and subsequent repenetrations between -10 and -20°C.

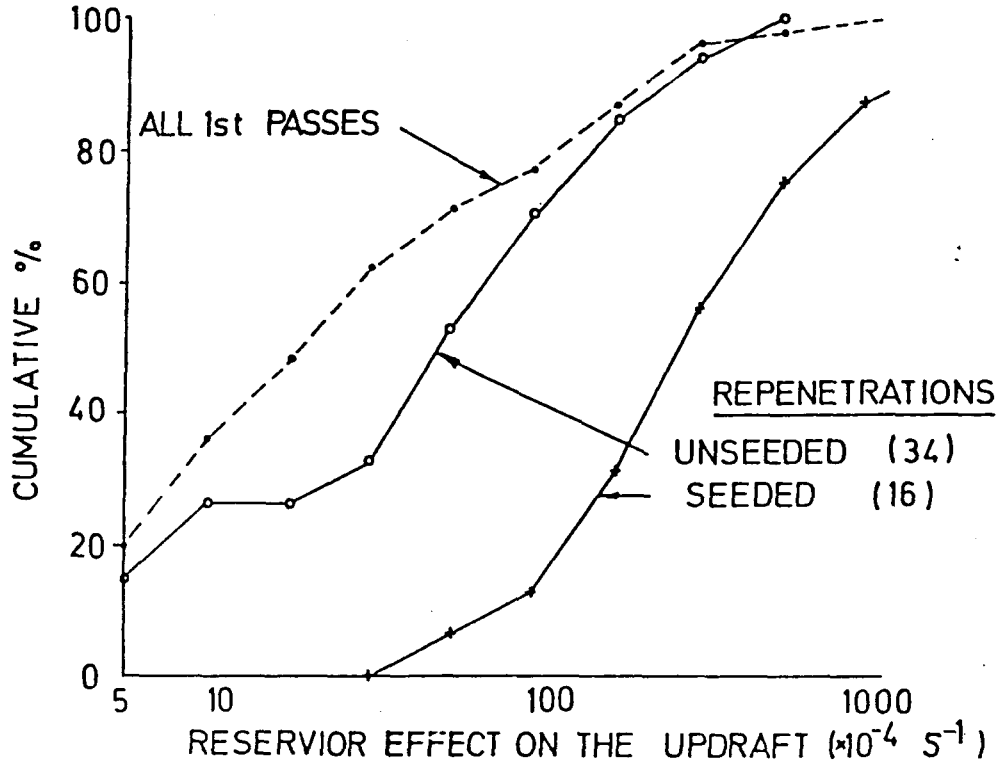

Fig. 9.5.4. RE for above samples.

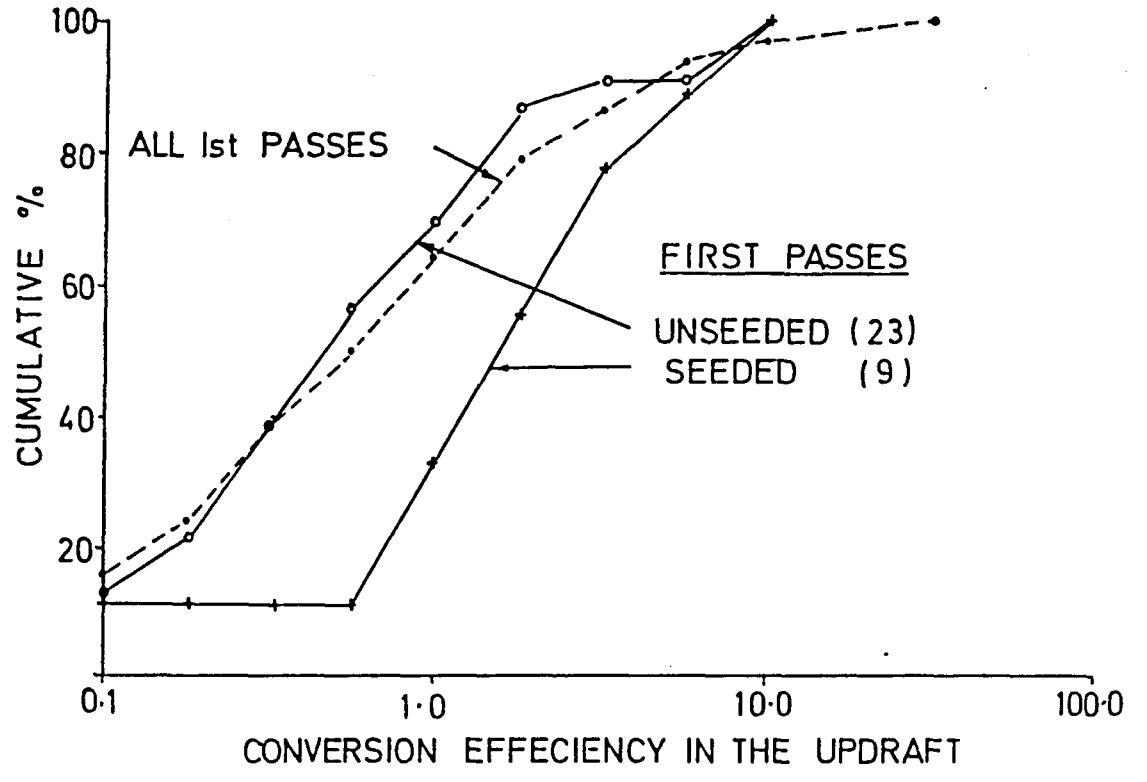

Fig. 9.5.5. CE for first passes through seeded and unseeded clouds.

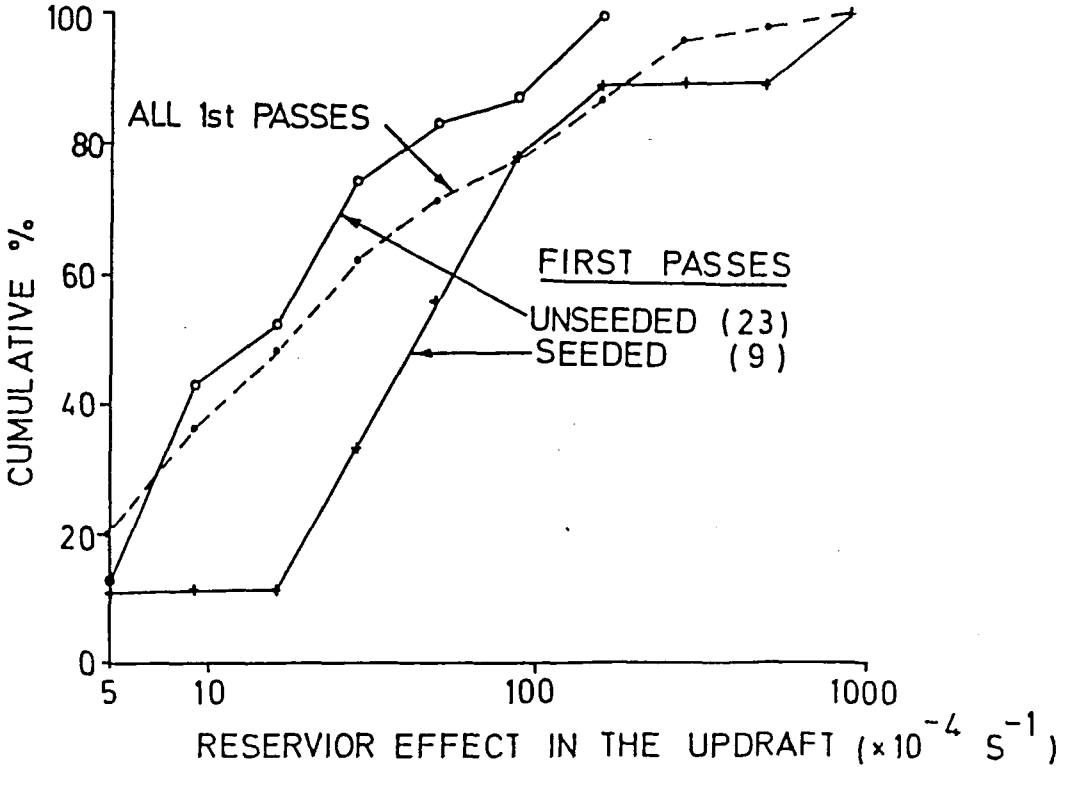

Fig. 9.5.6. RE for above samples.

With further rise in the atmosphere, more and more water condenses onto these particles, the mass of the cloud water increases, and , if sufficient time elapses, coalescence will begin to take place. When sufficient coalescence has taken place, droplets will have been formed which are too large to appear in the 0 - 47 micron window of the FSSP. At this point, the early stages of coalescence precipitation formation, the development of the cloud and precipitation are governed by: a. the condensation rate since virtually all of the water condensed out can be considered as going to increase the volume of cloud water, because the total surface area of the cloud drops is orders of magnitude greater than that of the larger coalescence products; b. the rate at which new coalescence products are being created, and c. the rate at which the coalescence products are sweeping out the cloud water.

We deal in a separate section with the relative values of the terms of the precipitation equation just described.

Here, we describe a simple attempt at detecting an effect which should exist as a consequence of the above interacting and competing phenomena. Detecting the effect would provide evidence that we do indeed know the important factors of the problem and that our measurements are of sufficient quality to promise fruitful investigations in this problem area.

During the early stage of precipitation development, water flows from the vapour to the cloud and then to the nascent precipitation. The cloud water content at any time may be increasing or decreasing, depending on the condensation rate and the amount of precipitation present. However, the number of cloud droplets (given no resupply of droplets) must be decreasing steadily.

To show this effect, we look for an inverse relationship between the condensed water content, estimated with the Engine Vapour (E-V) instrumentation described in Section 9 of this volume, and the FSSP concentration. To assure that we restrict ourselves to the earliest stages of precipitation formation we consider only cloud passes on which the average 2D-C total concentration was less than 10 l^{-1}, and we consider only cloud passes occurring between -8 and -12^{o}C.

The result is displayed in Fig. 9.6.1. The negative relationship is clear, apart from two wild points, and in spite of day to day variability.

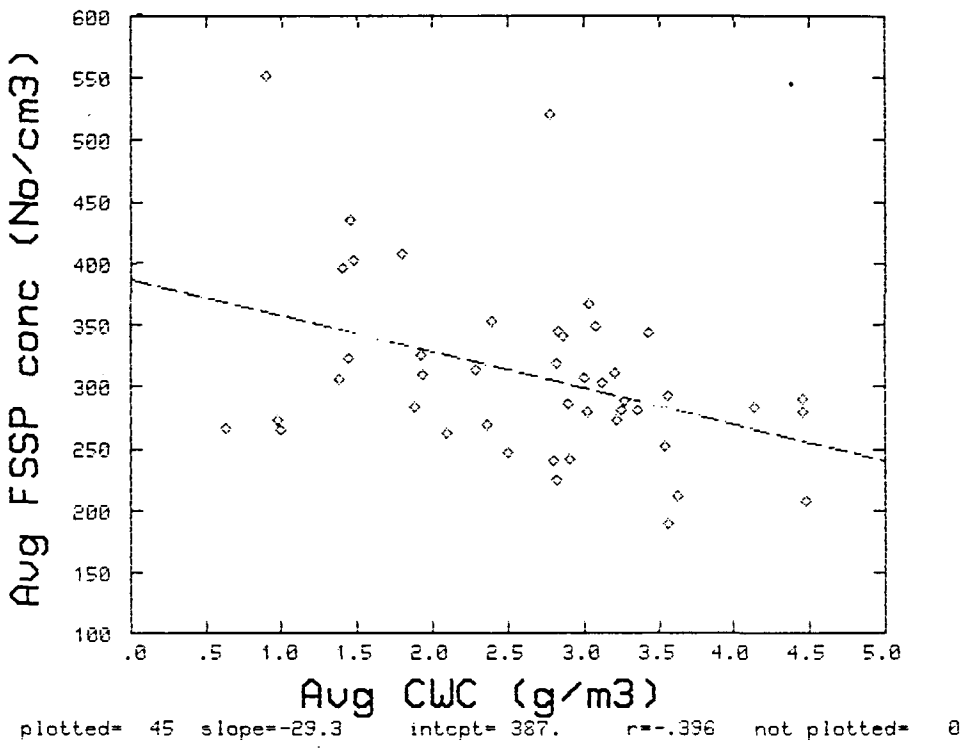

Fig. 9.6.1. The dependence of FSSP cloud particle concentrations on the condensed water content in clouds with little or no precipitation. Temperature range -8 to -12°C.

9.7 The variation of in-cloud equivalent potential temperature with time and location (Morgan and Morrison)

The temperature (or equivalent potential temperature) in the storm is one of the elements which we attempt to forecast in arriving at our various estimates of stability or cloud updraft strength. The measurements of quantities such as in-cloud Theta-es, and updraft speeds by the instrumented Learjet are our most direct physical measure of the strengths of convection, at least during its early (cloud turret) stages. These same measures also constitute the most direct means of detecting small scale (cloud scale) terrain influences on convection.

An intensive search for terrain effects on clouds has been carried out using the cloud sample database and the digitized terrain file. Theta-es measured during cloud penetrations has been plotted against terrain height; Theta-es has been normalized by subtracting out Theta-e_{max} from the morning sounding; daily and mission averages have been subtracted. None of these manipulations has led to the detection of any coherent effect of terrain heights on cloud properties . This is true for in-cloud Theta-es, updraft speeds, water quantities of various kinds and FSSP and 2D concentrations. The only terrain height effect which has been seen is the large drop frequency effect described in Section 9.4 above.

In pursuing this attempt to see a terrain effect, a concerted effort was made to detect a consistent time effect on Theta-es in cloud. This appears to be weakly present, but so immersed in noise that it is not worth presenting.

This finding is preliminary, and further attempts will be made in future to discover meaningful influences of terrain height and configuration on cloud properties.

9.8 Variability of ice concentration in Nelspruit clouds (Morgan and Morrison)

The ice content of Nelspruit cumulus turrets is quite variable. This bears importantly on the question of seedability of these clouds and so it is important to display the variations that are observed.

Four temperature intervals, centred on -5, -10, -15 and -20°C, were selected and the Cloud Sample Database was searched for clouds (first passes only) with average vertical velocities greater than 2.5 m sec^{-1} (to ensure they are growing turrets). This produced a sample of 201 cloud passes.

Setting aside ambiguous cases, the remaining cases can be classed as containing ice or no ice, drops or no drops, ice only or drops only. Table 9.8.1 summarizes the results. One sees that some water drops are found even at -20°C, and that ice is found even at -5°C.

The cloud passes which contained only images which were unmistakably ice (image classes: large graupel, small graupel, ice) were then re-analysed to display the concentrations and variabilities. An examination of the data showed that the sample size was inadequate at -5°C (1 case) and at -20°C (5 cases) and that there was no strong trend with height (for example, the average total 2D concentration at -10° C was 20.5 l^{-1}, and at -15°C, 25.5.) so the results for the -8 to -17°C layer were combined in Table 9.8.2.

Table 9.8.1 The occurrence of 2D-C image categories as a function of temperature for growing cloud turrets (average vertical velocity 2.5 m sec^{-1}) sampled from 1981 to 1986. Total number of cloud penetrations, 201. Figures in () are percent

Degrees C	-3 to -7	-8 to -12	-13to -17	-18 to -22
no 2D-C images	3	27	10	1
graupel or ice	0	28	15	5
mixed ice and water	2	45	14	4
water drops	5	17	1	0
unclassified, zero images, streakers)	1	16	5	2
TOTAL	11	133	45	12
containing ice	2 (20)	73 (62)	29 (72)	9 (90)
containing no ice	8 (80)	44 (38)	11 (28)	1 (10)
TOTAL	10	117	40	10
containing drops	7 (70)	62 (52)	15 (37)	4 (40)
containing no drops	3 (30)	55 (48)	25 (63)	6 (60)
TOTAL	10	117	40	10
% no precipitation	(30)	(23)	(25)	(10)
% ice only	(0)	(24)	(37)	(50)
% water only	(50)	(15)	(2.5)	(0)

Table 9.8.2 The variability of ice concentration in clouds with average updraft speeds 2.5 m sec^{-1}, with 2D-C image classifications graupel and ice

	avg	max	std.dev	N
Average over cloud	20.3	137.1	29.3	52
Maximum over cloud	78.4	684.5	140.9	52
Average 0 images	6.1	50.3	10.8	52
Maximum 0 images	21.7	196.7	38.3	52
Average < 128 microns	10.4	79.0	17.2	52
Maximum < 128 microns	41.3	438.6	80.2	52
Average > 128 microns	10.5	61.7	12.9	52
Maximum > 128 microns	44.2	455.0	79.8	52
Average > 1067 microns	0.2	1.1	0.3	38
Maximum > 1067 microns	1.8	16.9	3.6	38

9.9 Empirical estimation of coalescence rate (Morgan and Morrison)

Coalescence is an important part of the precipitation formation process in all rain producing clouds in Nelspruit, and the dominant one in a large percentage of them. In Vol.II Section 5.6, and in Mather et al., (1986) it has been shown that the probability of encountering larger drops in cumulus turrets at the -10°C level can be predicted by a parameter based on the time of rise of a cloud parcel from cloud base to that level.

Here we wish to explore the possibility of expressing the degree of development of coalescence in a more quantitative way.

The detailed physics of coalescence is a complex one, and in fact the theoretical field cannot be considered settled. A good introduction to its state is given in an important study by Leighton and Rogers (1974).

We will examine the possibility of employing a very simple bulk parameterization of the coalescence process and of determining the coefficients of the parameterization empirically, using observations of cloud water content, updraft speed, and condensed water content (CWC).

9.9.1 A simple parameterization

The observations on which this study are based are those cloud passes in the neighbourhood of $-10^{o}C$ in which there were few or no 2D-C images and the total water content indicated moist adiabatic ascent from cloud base.

The parameterization we will test is based on a simple equation for the rate of change of cloud liquid water content, m, under the competing influences of condensation and coalescence. Coalescence is described in terms of two effects:

1. Cloud coalescence, described in the manner of Kessler (1969)

$$\left(\frac{dm}{dt}\right)_{cloud} = 0 \quad \text{for } m \leq 1.0 \text{ gm m}^{-3} \qquad (1)$$

$$= B(m - 1.0) \quad \text{for } m > 1.0 \text{ gm m}^{-3}$$

and

2. An interaction between the cloud (droplets less than 35 microns diameter) and the nascent precipitation (the coalescence products).

$$\left(\frac{dm}{dt}\right)_{coal.} = A(cwc-m)m \qquad (2)$$

The rate of change is

$$\frac{dm}{dt} = \text{cond.} - A(cwc-m)m - B(m - 1.0) \qquad (3)$$

where cond. is the condensation rate (Section 10.3). The problem now is the estimation of the constants

$A(g^{-1}\ kg\ sec^{-1})$ and $B\ (sec^{-1})$

This can be integrated over time, from cloud base to penetration level (subscript p denotes penetration level, b is base level)

$$m_p = \int_{t_b}^{t_p} \text{cond. } dt - A \int_{t_b}^{t_p} (cwc - m)m\ dt - B \int_{t_b}^{t_p} (m - 1.0)\, dt \qquad (4)$$

$$w_1 = w_s(T_1) \approx \varepsilon \frac{e_s(T_1)}{P} \tag{1}$$

The one gram of water is frozen, releasing 79.7 calories of heat, resulting in a new temperature, T_2, given by

$$T_2 = T_1 + \frac{79.7}{C_p d} = T_1 + 0.33°C \tag{2}$$

C_p is the specific heat of air at constant pressure

This first step temperature rise is not a function of P and T.

The parcel at this stage has a temperature T_2 and a mixing ratio $w_s(T_1)$. It now undergoes a wet bulb process (see Rogers, 1979) which cools it to T_3 and restores saturation with respect to water.

The wet bulb process is described by

$$\frac{T - T_w}{w_s(T_w) - w} = \frac{L}{C_p} \tag{3}$$

which results in a temperature change, ΔT_2, given by

$$\Delta T_2 = \frac{e_{s_o} \varepsilon L}{C_p P} \left[\exp \frac{L}{R_v} \left(\frac{1}{T_o} - \frac{1}{T_3} \right) - \exp \frac{L}{R_v} \left(\frac{1}{T_o} - \frac{1}{T_1} \right) \right] \tag{4}$$

(2)

The net change in temperature then, is

$$\Delta T = \Delta T_1 - \Delta T_2 \tag{5}$$

For an arbitrary amount, m of water frozen, this becomes

$$\Delta T(m) = 0.33\ m - (2) \tag{6}$$

This is not linear in m because of the non-linearity of the wet bulb process.

The first term integrates to the condensed water content. We change time integration to integration over height by introducing

dt = dz/W, where W is the updraft speed

$$m_p = CWC_p - A\int_{z_b}^{z_p} \frac{(cwc - m)m}{W}\, dz - B\int_{z_b}^{z_p} \frac{(m - 0.5)}{W}\, dz \qquad (5)$$

We assume a linear updraft profile, with 1.0 m sec^{-1} at the cloud base.

$$W_{(z)} = W_b + \frac{(Wp - Wb)\,(Z - Z_b)}{(Z_p - Z_b)} \qquad (6)$$

$w_b = 1.0$ m sec^{-1}

$$T_z = T_p + \int_{z_p}^{z} \frac{dT}{dz}\, dz \qquad (7)$$

Calculation of dT/dz is described in Section 10.5

$$\text{cond.} = \text{C.M.}\ (P,T)\ W(Z) \qquad (8)$$

where C.M. is the condensation multiplier described in Section 10.3.

$$P(z) = P_p + \int_{z_p}^{z} \rho g\, dz = P_p + g\int_{z_p}^{z} \frac{P(z)}{R_d T(z)}\, dz \qquad (9)$$

$$CWC(z) = \rho_a\,(w_{sb} - w_s(z))$$

$w_{sb} = (TWCMIX)_p$; TWCMIX is the Total Water Mixing Ratio at penetration level (See Section 9.1) (10)

$$w_s(z) = W_{sp} - \int_{z_p}^{z} \text{C.M.}\, dz \qquad (11)$$

$$m(z) = \int_{z_b}^{z} \text{C.M.}\, dz - A\int_{z_b}^{z} \frac{(cwc - m)m}{W}\, dz - B\int_{z_b}^{z} \frac{(m - c)}{W}\, dz \qquad (12)$$

The cloud base is where

$$W_{sp} + \int_{z_p}^{z} C.M.\ dz = TWCMIX_p \qquad (13)$$

The constants are determined by running the integrations for a matrix of values for A and B.

We have tested this approach on a set of 24 cloud passes for which the 2D-C average total concentration was less than 5.0 l^{-1}. The result, not entirely satisfying, was that, though the average error in predicting m, the cloud liquid water content, could be reduced to just over 0.6 g m^{-3}, this occurred when the coefficient of the autoconversion term was 6.5 x 10^{-3} (compared with Kessler's value of 1.0 x 10^{-3}), and the interaction term was zero.

This would mean that the (invisible) droplets in the coalescence portion of the spectrum have not grown to such sizes as to collectively capture a significant amount of the cloud water.

The results were best for clouds with TWMR less than about 12.0 g kg^{-1}, suggesting that perhaps the role of the interaction is more important in warmer clouds with more water at play, but requires a more complex form than we have given it.

We will continue to pursue this approach to the study of coalescence, as it will be important to be able to predict the coalescence development as it can be described by our measured quantities.

9.10 Aircraft observations of target turrets on multi-cellular storms showing radar response to dry ice seeding (Morrison, Mather and Morgan)

9.10.1 Introduction

Microphysical and radar studies of natural and experimentally seeded storms and an Exploratory Randomized Seeding Experiment (ERSE) began in October 1984. To date (early March, 1986) 98 convective complexes developing within 100 km of the project C-band radar near Nelspruit have been selected by the objective criteria of the ERSE randomization procedures; of these 48 have been seeded with dry ice pellets and 50 have not been seeded. Of the unseeded cases 23 have been sampled by the aircraft and 27 have not been touched.

Preliminary analyses using re-randomization techniques indicate an overall net positive radar response to seeding.

The objective of the ERSE was to generate a sample of randomly selected seeded and unseeded storms upon which to perform analyses which would lead to the definition of hypotheses and procedures for a subsequent confirmatory experiment. This exploratory study is a first attempt to compare aircraft observations of target cloud turrets on seeded storms that show an apparent positive radar seeding response to those storms that show no or negative responses.

9.10.2 General characteristics of target clouds

Newly developed cumulus congestus turrets rising vigorously through the -10°C level are targetted for seeding and/or sampling by the project Learjet aircraft. The turrets on the selected storms must show no signs of glaciation, have firm and well defined bases, and must not be excessively sheared.

Studies conducted prior to the ERSE by CIC and SWA showed that the target turrets contain large amounts of supercooled water, frequently in excess of 1.5 g m^{-3} at -10°C. The concentrations of natural ice in these turrets is relatively low with average 2D-C concentrations of particles greater than 105 microns of about 7 per litre. The predominant ice particle habit is well rimed graupel. Pristine ice crystals are rarely observed. Cloud base temperature is highly variable between about 7 to 16 °C, generally averaging around 14°C at an altitude of 2 km AMSL with an average mixing ratio of 13 g kg^{-1}. Vertical air velocities average 3.5 m s^{-1} with updraft around 12 m s^{-1}.

9.10.3 Radar response to seeding

The radar analysis technique and results are detailed in Dixon (1986). The storm track property selected for this study is a relative echo height change parameter (EHC) defined as :

$$EHC = \frac{EHEIGHT\ 1 - EHEIGHT\ 0}{MAX\ (EHEIGHT\ 0,\ EHEIGHT\ 1)}$$

where EHEIGHT 0 = Height of the 30 dBz echo at storm selection time

EHEIGHT 1 = The maximum height of the 30 dBz echo from 5 to 30 minutes after storm selection time

This is simply the difference between the maximum 30 dBz echo top height measured from 5 to 30 minutes after "decision time" and the 30 dBz echo height at decision time divided by the maximum value of the two parameters. If the echo top height does not change within the given time "window", the statistic has a value of 0, if the 30 dBz echo top height increases it is positive, if it decreases it is negative.

The distributions of EHC for 41 NO-SEED case tracks and 35 SEED (as of February 1986) case tracks is shown in Figure 9.10.1. Of the SEED cases, 79% have values greater than or equal to 0.05 compared to 41% of the NO-SEED cases. Values of 1.00 can occur if the maximum echo reflectivity did not exceed 30 dBz at decision time. Similarly, values of -1.00 can occur if the maximum echo reflectivity dropped below 30 dBz in the 5 to 30 minute window after decision time. For all valid case tracks up to 17 January 1986 the difference in EHC between the seeded and unseeded storms is significant at a p-value of 93%, the difference being tested by re-randomization.

NO-SEED cases (n=41)				SEED cases (n=35)		
60%	30	0		0	30	60%
n						n
2		**	1.00	*****		5
1		*	0.30 to 0.35			
3		***	0.25 to 0.30	.		
2		**	0.20 to 0.25	**		2
4		****	0.15 to 0.20	**********		9
5		*****	0.10 to 0.15	***		3
			0.05 to 0.10	*****		5
7		*******	0.00 to 0.05	****		4
2		**	-0.05 to 0.00	**		2
5		*****	-0.10 to -0.05	**		2
3		***	-0.15 to -0.10	**		2
3		***	-0.20 to -0.15			
1		*	-0.25 to -0.20			
1		*	-0.30 to -0.25	*		1
1		*	-0.35 to -0.30			
1		*	-1.00			

Fig. 9.10.1. Distribution of EHC for no seed and seed cases.

For the analysis presented in this paper, the EHC parameter was chosen as a means of testing for possible dynamic seeding effects. The values of EHC for all the SEED cases were ranked from highest to lowest. The five values of 1.00 were rejected leaving 30 values from 0.248 to -.285. The ranked values were divided into thirds so that the top ten cases were selected as the "best" seed cases possibly due to a dynamic seeding response and the bottom ten cases selected as the "worst" seed cases exhibiting an apparent nil or negative response. The range of EHC for the "best" cases is 0.248 to 0.150 and for the "worst" cases range from -0.285 to 0.016. The aircraft data for the "best" cases were then compared to the "worst" cases to search for any significant differences between the two data sets that might provide some support for the presence or absence of a dynamic seeding response.

9.10.4 Aircraft measurements

Summary data and derived parameters for each cloud penetration are stored in a Cloud Sample Database (Section 10.2 of this volume) on disk in the project MV4000 computer. Currently, over 170 parameters are stored in the database for each penetration. A partial list of the major categories of

parameters is shown in Table 9.10.1.

Table 9.10.1 Major Categories of Cloud Sample Database Parameters

1. Identification
2. Seed/No-seed parameters
3. Aircraft position
4. Terrain beneath a/c position
5. Cloud dimensions
6. Environmental state parameters
7. Cloud state parameters
8. Liquid water contents
9. Total and condensed water contents
10. Vertical air velocity parameters
11. Turbulence
12. FSSP particle concentrations and sizes
13. Aircraft radar parameters
14. 2D-C particle concentrations and sizes
15. Vertical fluxes of various thermodynamic and particle parameters
16. Data management parameters.

9.10.5 Data analysis

After a storm has been selected as a SEED/SAMPLE case the Learjet commences seeding runs through the growing turrets at around the $-10^{o}C$ level. Usually the aircraft simultaneously samples the cloud during these penetrations to document the untreated cloud state. The turrets are seeded only once although they may be re-penetrated by the Lear for "post-seed" samples. In the present analysis, the database parameters for the first runs on each sampled turret in the 10 "best" and 10 "worst" seed cases are compared. This amounts to 40 turrets in the "best" cases and 43 in the "worst" cases.

Some of the database parameters show no significant differences between the two data sets. These include cloud length (approx. 3 km), adiabatic water mixing ratio (approx. 12.6 g kg^{-1}), average downdraft speed (approx. 2.5 m s^{-1}), and average turbulance dissipation (approx. 830 cm^{2} s^{-3}).

A large number of parameters however, did show some important differences. A list of some of the more interesting parameters in this category is given in Table 9.10.2.

One important difference is the apparent presence of higher supercooled liquid water in the "best" cases. JW measurements of liquid water between the two data sets show little difference, but, as already pointed out, the JW probe has proved to be inadequate in the high liquid water environments encountered in these clouds. The King-CSIRO probe, however, shows a clear tendency for the "best" cases to have greater liquid water contents.

Further support for the creation of conditions conducive to higher water contents can be implied from some of the other parameters. On average, vertical air velocities in the "best" cases are lower permitting more time for particle growth. This is further borne out by the lower cloudy air buoyancy computed for the "best" cases (difference between environmental virtual temperature and cloud virtual temperature). Additionally, the average cloud saturated equivalent potential temperature is nearly 2.5 degrees higher in the "best" cases which can imply a warmer cloud base neglecting any ice formation. There is also some evidence that the "best" suffer less entrainment than the "worst" cases. The difference between the maximum cloud saturated equivalent potential temperature and cloud base equivalent potential temperature computed from the Learjet upsounding at the start of a mission is less in the "best" cases which can imply turret cores closer to adiabatic conditions.

Table 9.10.2 Selected parameters showing significant differences between the "best" and "worst" cases.

Parameter (units)	"Worst" Cases n	"Worst" Cases avg value	"Best" Cases n	"Best" Cases avg value
Avg cloud θ_{es} (K)	43	341.0	40	343.4
Max cloud θ_{es} - cloud base θ_e (K)	43	- 2.3	40	0.4
Excess Tv (C)	43	0.6	40	0.1
Max CSIRO- King LWC (g m^{-3})	20	2.14	28	2.55
Avg vertical air velocity (m s^{-1})	42	5.0	38	2.8
Max vertical air velocity (m s^{-1})	42	14.0	38	11.0
Avg FSSP particle conc (cm^{-3})	43	305	40	265
Avg. FSSP conc in 32-47μm range (cm^{-3})	43	0.929	40	1.499
Avg FSSP mass-weighted mean dia (μm)	43	21.5	40	23.1
Max aircraft radar reflectivity(dBz)	43	10.3	40	23.9
Avg 2D-C total particle conc (litre^{-1})	36	13.2	39	33.2
Max 2D-C total particle conc (litre^{-1})	36	37.2	39	131.2

Given that the liquid water content is higher in the "best" cases, how does this extra water manifest itself? We can first examine the liquid water in the small cloud droplet range as measured by the FSSP from 2 to 47 microns. The liquid water content integrated over the range of the FSSP does not show much change between data sets (averaging about 1.1 g m^{-3}) despite the fact that the average total concentration is somewhat less in the "best" cases. The increase in FSSP mass weighted mean diameter and the increase in particle concentrations at the high end of the FSSP spectrum from 32 to 47 microns (Table 9.10.2) suggests a shift in the size distribution of liquid water drops away from the small cloud droplet range.

The 2D-C array imaging probe data show a nearly three-fold increase in average total particle concentration in the "best" cases. Interestingly enough, much of this increase in concentration occurs in the lower range of the probe below particle diameters of about 130 microns. Unfortunately, for these

small sizes, it is very difficult to distinguish between graupel and water drops by visual inspection of the 2D-C images. However, clear images of some water drops greater than about 300 microns are observed in 35% of the turrets in the "best" cases compared to 15% of the turrets in the "worst" cases. It is therefore possible that some of the extra supercooled water observed in the "best" cases is in the higher end of the cloud droplet spectrum.

Further evidence arguing for the presence of liquid water in the form of large cloud droplets is seen when examining the difference in maximum aircraft radar returns for the "best" versus the "worst" cases. The maximum reflectivity observed in penetrations in the "best" cases is better than double that of the "worst" cases. The implication is that the observed higher reflectivities may be due to higher concentrations of large cloud droplets in the "best" cases.

The presence of higher concentrations of large supercooled cloud droplets in the "best" cases would be consistent with a dynamic seeding response. Lamb, Hallet and Sax (1981) have shown that maximum latent heat release available for dynamic invigoration of deep convective clouds can be crucially dependent on the presence of large supercooled water droplets.

9.10.6 Conclusions

In an exploratory investigation a radar measured storm track property which may help to identify possible dynamic seeding effects was used to group aircraft observations of cloud turrets prior to seeding into cases showing an apparent dynamic response and cases showing a nil or negative apparent response. Comparison of the two sets of aircraft observations strongly suggests that the cases with an apparent positive response had lower vertical air velocities, warmer cloud bases, and higher concentrations of supercooled liquid water possibly in the form of relatively large cloud droplets.

Further analyses will be made along these lines using other radar storm track properties and also to test the NO-SEED/SAMPLE data set as a control. The environmental characteristics on days with "good" and "bad" cases will also be examined.

9.11 Heating of cloud air by the freezing of the large diameter fraction of the condensed water content. (Morgan and Morrison).

The calculation of the maximum possible temperature increase due to the freezing of supercooled water is described in Section 10.6. The equation shown there has been used to calculate this quantity for each applicable cloud pass and the results have been entered into the cloud sample database.

We are not at present able to deal with problems related to the rate at which drops freeze, so the following estimates of temperature increase must be considered upper estimates. The calculations were done on the assumption that the water which can be most quickly frozen is the particles with diameters larger than those sensed by the FSSP or the JW. This is estimated as the difference between the CWC mixing ratio minus FSSP liquid water mixing ratio. If this difference is assumed to be all liquid then it is the amount entered into the temperature change equation. The 2D-C image classes: No data, Rain and Water Drops correspond to this case. For other classes, fractions of the difference were assumed to be freezable. For Mixed BD, 75% was frozen and for Graupel BD, 50% was frozen. Figure 9.11.0 shows the distribution of temperature changes for those passes in the 1985/86 season for which the calculations could be made. Sixty additional cloud passes gave a value of zero due to the 2D-C image class indicating graupel or mixed water and ice. We did not venture to assign a freezable fraction value to this class of image.

These estimates of temperature change are based on CWC and FSSP LWC which are averaged over each cloud pass. They nevertheless yield values which would be significant. These changes should be viewed against the background of the observed buoyancies (Vol. II, Section 5; the values of buoyancy shown are also averages over each pass) which tend to be quite low.

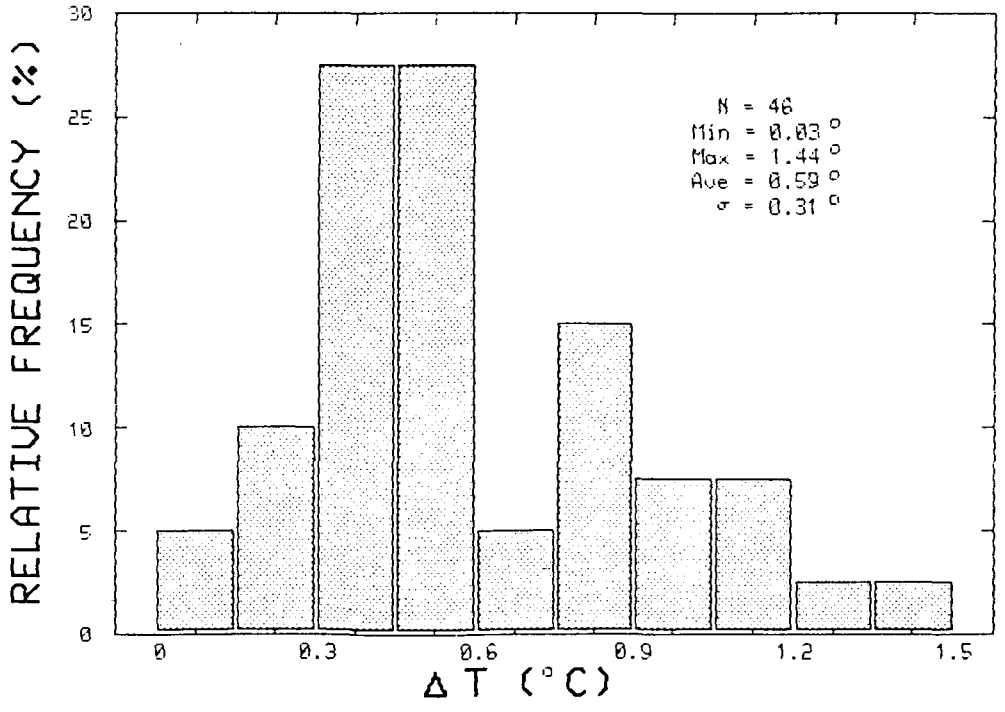

Fig. 9.11.0. Calculated temperature rise due to freezing the large diameter of the liquid water.

10.0 DETAILS OF CALCULATIONS

10.1 Calculations of the condensation rate (Morgan and Morrison)

The condensation rate (g kg^{-1} sec^{-1}) for a moist adiabatic ascent is given by

$$\frac{dm_c}{dT} = -\frac{dw_s}{dT} = -W\frac{dw_s}{dZ} \qquad (1)$$

where W is the updraft speed (m sec^{-1}) and m_c is the cloud water mixing ratio. dw/dz, which we call the condensation multiplier, can be computed assuming that for moist adiabatic ascent, the static energy per unit mass, σ is constant, and

$$\sigma = \text{const.} = CpT + LW_s + gz$$

$$d\sigma = 0 = CpdT + Ldw_s + gdz \qquad (2)$$

With the aid of the definition of W_s ($W_s = \epsilon \sigma s/p$), the hydrostatic equation and the Clausius-Clapeyron equation, this results in

$$\frac{dw_s}{\partial z} = \frac{g\epsilon}{PR_d}\,\frac{(611)\exp\left[\frac{L}{R_v}\left(\frac{1}{273}-\frac{1}{T}\right)\right]\left(CpR_vT - R_dL\right)}{\left(CpR_vT^2 - \frac{L^2\epsilon}{P}(611)\exp\left[\frac{L}{R_v}\left(\frac{1}{273}-\frac{1}{T}\right)\right]\right)} \qquad (3)$$

This is just a function of temperature and pressure. To display this, we have put isolines of the condensation multiplier on Thetaplot, in place of saturation mixing ratio lines. This appears in Fig. 10.1.1.

The condensation rate is an important quantity in the microphysics of cumulus clouds. The amount of water condensed in moist adiabatic ascent is, of course, strictly a function of vertical displacement. The rate of displacement plays an important role in precipitation development since it is proportional to the rate at which cloud water is made available for precipitation growth. The sweep up of cloud by larger particles, however, is at any instant independent of the rate of vertical displacement.

Rapid precipitation growth can lead to exhausting the cloud water if the condensation rate is not such as to replenish it at a pace as great as its depletion.

Figure 10.1.2 shows the range of values of condensation rate estimated from flight level temperature, pressure and vertical velocity over the entire 1984-85 cloud sample of the season. Values fall over a wide range, from -.022 to + .047 g kg^{-1} sec^{-1}.

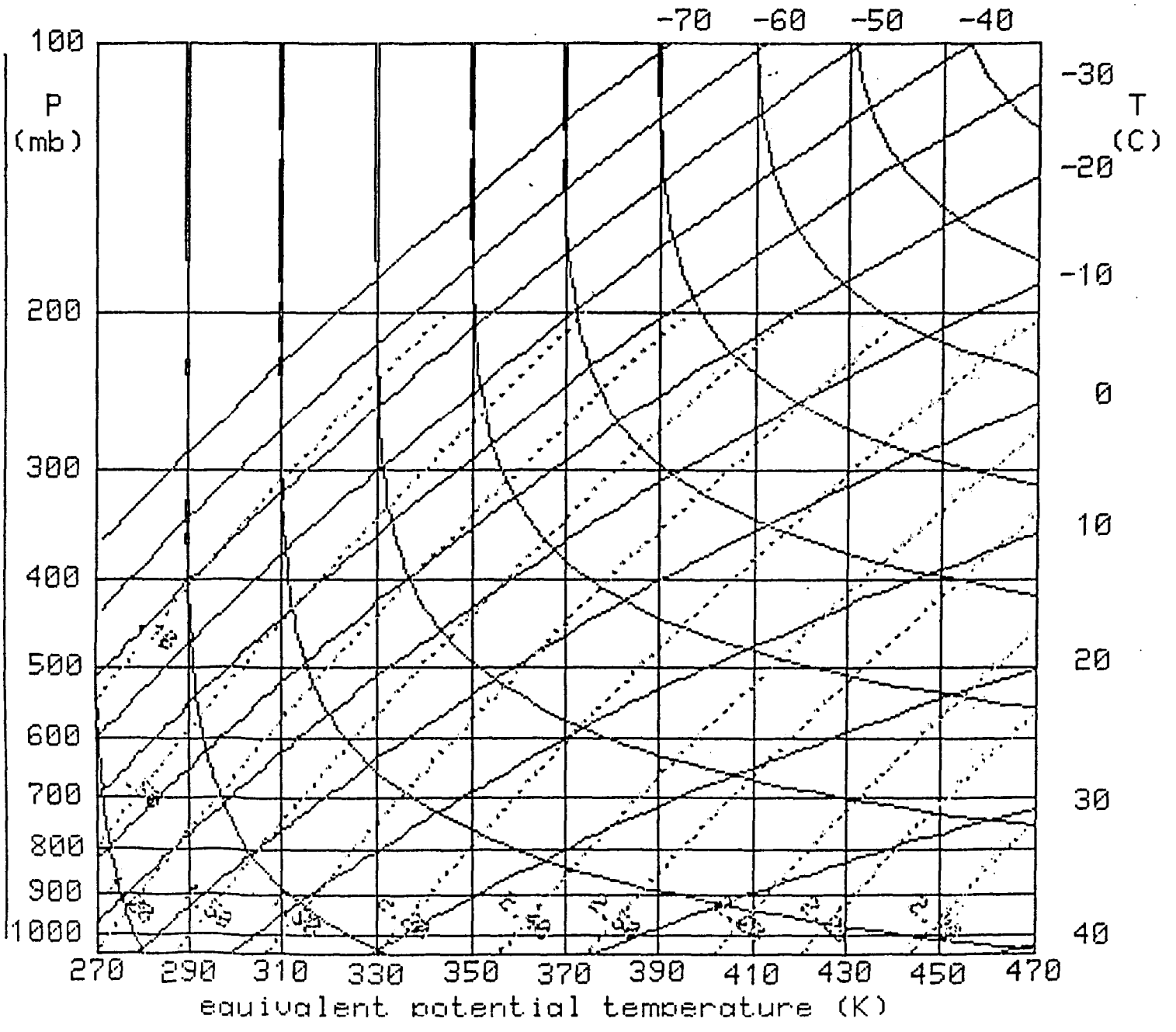

Fig. 10.1.1. The condensation multiplier plotted on Thetaplot, in place of the saturation mixing ratio. Values are multiples of 10^{-3} g kg^{-1} sec^{-1}.

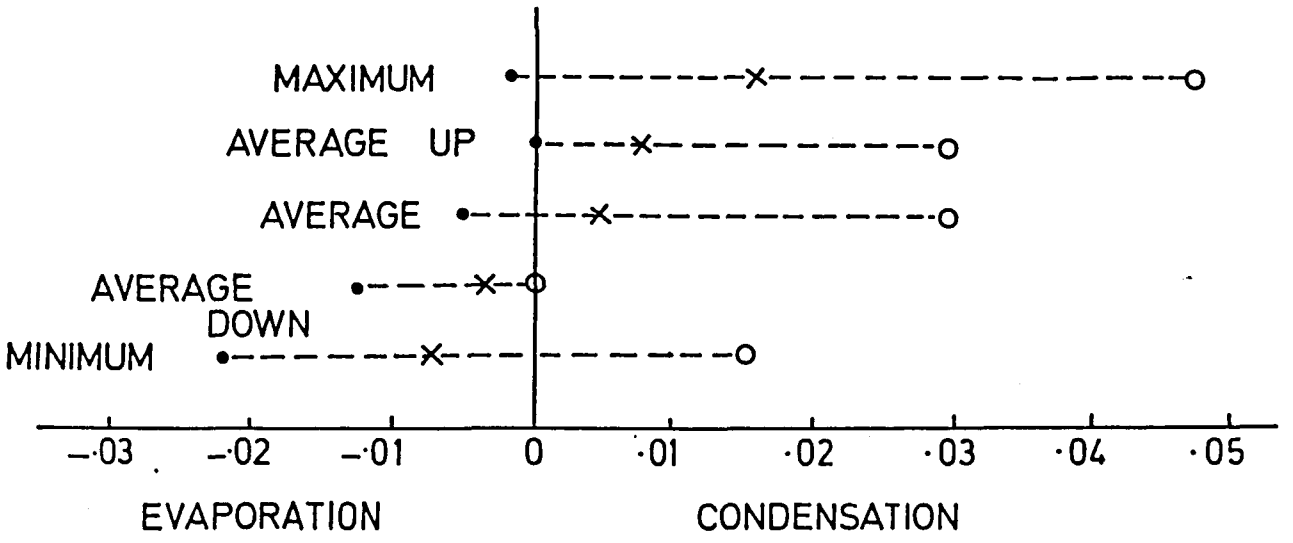

Fig. 10.1.2. Estimates of condensation rates (g kg^{-1} sec^{-1}).

On a very few passes, the average condensation rate was actually negative (evaporation).

Condensation rates in the updrafts were generally stronger than were the evaporation rates in the downdrafts, reflecting the relative strength of updraft and downdraft observed at our penetration altitudes.

10.2 Calculations of vertical fluxes (Morgan and Morrison)

Vertical fluxes of several quantities measured in cloud by the aircraft have been calculated and some of these require assumptions which cannot be rigorously defended.

Point flux values are straightforward and are all of the form:

$$F_p = P \rho_a W \qquad (1)$$

where F_p is the flux property P which can be in the form of a mixing ratio or a density.

We have also calculated total fluxes based on the assumption that the measured profiles of the vertical velocity and the property are representative random samples of a cloud which is not radially symmetric. The total flux of property P is then

$$F_p = P \rho_a W \cdot \frac{\pi}{4} D^2 \qquad (2)$$

where D is the diameter of the cloud, assumed circular. D is determined from the true air speed (TAS) and the time in cloud. Single estimates of F determined in this way can be greatly in error, but a large number of such estimates will allow us to gain a "feel" for the typical magnitude of these fluxes and their variations in the vertical.

The histograms of Fig. 10.2.1. show the distributions of the fluxes of water vapour (tons per sec) and of air (in kilotons per sec). The analysis also presents the important fractions of the various fluxes, the up flux, and the down flux.

10.3 Calculations of the variations of temperature with pressure on a moist adiabat (Morgan and Morrison)

The aircraft experiences vertical displacements as it traverses a cumulus cloud. These result in difficulties in trying to estimate the buoyancy from the temperature profile as plotted in time-history format. It is convenient, then, to correct for these height displacements and graph out a profile of the temperature which is corrected to the pressure at the beginning

tons/s		0 25 50 75 100 %			
(=	-100.00	I*	1	N	205
-100.00 to	-50.00	I*	3		
-50.00 to	.00	I*******	31	Minimum	-113.07
.00 to	50.00	I**********************	95		
50.00 to	100.00	I*********	40	Maximum	551.63
100.00 to	150.00	I***	15		
150.00 to	200.00	I*	5	Average	55.31
200.00 to	250.00	I**	7		
250.00 to	300.00	I*	2	Std Dev	86.43
300.00 to	350.00	I*	3		
350.00 to	400.00	I*	1	Skewness	2.204
)	400.00	I*	2		

170 Vapor flux

ktons/s		0 25 50 75 100 %			
(=	-30.00	I		N	205
-30.00 to	-20.00	I*	3		
-20.00 to	-10.00	I**	7	Minimum	-27.67
-10.00 to	.00	I******	27		
.00 to	10.00	I**************	76	Maximum	141.24
10.00 to	20.00	I*******	34		
20.00 to	30.00	I*******	27	Average	14.71
30.00 to	40.00	I***	13		
40.00 to	50.00	I*	2	Std Dev	23.16
50.00 to	60.00	I*	4		
60.00 to	70.00	I*	2	Skewness	2.340
)	70.00	I**	8		

191 Air mass flux

Fig. 10.2.1. Frequency distributions of the fluxes of water vapour (tons per sec) and of air (kilotons per sec).

of the traverse. For this we require the temperature as a function of pressure along any moist adiabat. This is easily derived by using the static energy as the characteristic value of the moist adiabat (see equation 2, Section 10.1). Making use of the Clausius-Clapeyron equation, the equation of state, and the hydrostatic equation:

$$\frac{\partial T}{\partial P} = \frac{1}{P}\left(\frac{LW_s + RT}{Cp + \frac{W_s L^2}{R_v T^2}}\right) \qquad (1)$$

This is used at every point of the traverse to correct the temperature to the pressure at the beginning of the record.

10.4 Aircraft sounding frost points and dew points (Morgan and Morrison)

The Cambridge dew point sensor on the Lear measures dewpoint (T_d) in the lower part of the atmosphere but measures frost point (T_f) when the dew point is below 0 degrees C.

T_f is a higher temperature than T_d and will yield for example, higher mixing ratios if it is treated as dewpoint in the sounding programme. This can be allowed for in several ways, but we have chosen to calculate T_d given T_f.

A first order correction factor for converting frost point values to dew points has been added to the aircraft sounding software.

The correction is as follows:

$$\frac{T_d}{T_f} = \frac{L_{cond}}{T_f\left(\frac{L_{cond} - L_{sub}}{273}\right) + L_{sub}} \qquad (1)$$

The correction is not exact due to our use of Clapeyron's equation and constant values of Lc and Ls. We have introduced values valid at $-10^{o}C$, taken from a standard text.

The introduction of frost points into the calculations only extends the usefulness of the Cambridge dewpointer down to about $T_d = -10^{o}C$.

10.5 Engine vapour signal processing (Morrison)

Lyman-alpha hygrometry is based upon the absorption of monochromatic radiation in the absence of scattering as described by Beer's law (Buck, 1976). This can be expressed as

$$I = I_o \exp(-k\rho x/\rho_o) \qquad (1)$$

where I = received intensity of radiation at wavelength

I_o = transmitted intensity

k = absorption coefficient of the gaseous medium at wavelength i

ρ = density of the gaseous medium

X = length of the absorbing path

ρ_o = density of the gaseous medium at standard temperature and pressure (0°C, 1013 mb)

At the Lyman-alpha line wavelength of 121.56 nm the only significant absorbing gases in the troposphere are water vapour and molecular oxygen. In the current application of sampling bleed air from the 8th compressor stage of the turbojet engines a hydrocarbon contaminant is apparently also acting as an obsorber. After replacing I and I_o by their sensed voltage equivalents, we may rewrite equation (1) as :

$$V = V_o \exp[-(k_{H_2O} \rho_{H_2O} x/\rho_{oH_2O}) - (k_{O_2} \rho_{O_2} x/\rho_{oO_2}) - (k_{cont} \rho_{cont} x/\rho_{ocont}) \qquad (2)$$

where V_o is system gain proportional to I_o, window transmission, and detector quantum efficiency, and V is the sensed voltage analogue output from the Lyman-alpha. The subscripts H_2O, O_2, and cont refer to water vapour, molecular oxygen, and bleed air contaminant, respectively. Solving (3) for water vapour density we get:

$$\rho_{H_2O} = \left[\frac{\rho_{oH_2O}}{k_{oH_2O}x}\right]_A \ln V_o - \ln V - \left(\frac{k_{O_2}\rho_{O_2}{}^x}{\rho_{oO_2}}\right)_B - \left(\frac{k_{cont}\rho_{cont}{}^x}{\rho_{ocont}}\right)_C \qquad (3)$$

The three unknowns in equation (3) (c) are system gain (term A), oxygen absorption (term B), and contaminent absorption (term C). The system gain term can easily be determined by flushing the Lyman-alpha with nitrogen so that the density of each absorbing gas is zero and $\ln V_o = \ln V$

The oxygen absorption term can be well estimated by computing the density of molecular oxygen, using the ideal gas law.

In the well mixed troposphere the partial pressure of oxygen can be taken to be the molar fraction of oxygen in air or 21% of total ambient pressure.

The contaminant absorption term, however, is an unknown which cannot currently be computed in a straightforward fashion. It appears to be a function of bleed air flow through the Lyman-alpha and the temperature in the bleed air system which are controlled by engine power setting, pressure altitude and the control settings for wing heat, nacelle heat, and air flow. Lacking explicit definition of this term, we are forced to calculate it implicitly through baselining of the Lyman-alpha against the EG & G dewpoint hygrometer. The main drawback of this method is that, although the EG & G dewpoint hygrometer has a reasonable accuracy, its time response at relatively cold temperatures is poor, particularly after large altitude changes or cloud penetrations. However, if sufficient time has passed to obtain a reliable dewpoint measurement at penetration altitude and if the aircraft is operated in cloud penetration configuration, then the contaminant term can be computed in the sub-saturated air just prior to penetration in the following manner.

The ambient air mixing ratio, is computed from pressure and dew point. Then, since the mixing ratio of water vapour in the Lyman-alpha cell is the same as that in the free air, the vapour density in the cell is given by:

$$\rho_{H_2O} = W\rho_d \qquad (4)$$

where ρ_d = density of dry air in Lyman-alpha cell

The dry air density in the Lyman-alpha cell is simply computed using the ideal gas law.

The temperature and pressure in the Lyman-alpha cell are measured using a thermocouple and pressure transducer. Then, the contaminant term can be obtained from equation 2.

The programme LYAL-BASELINE computes terms A, B, and C using the first two seconds of clear air data prior to a cloud penetration or using data from a straight and level baselining file. The system gain (term A) and the contaminant (term C) are then combined into a single offset term which can then be used in the data processing subroutine LYMAN-ALPHA in programme ULTRADAS using the formula derived from equation (3).

$$\rho_{H_2O} = \frac{\rho_{oH_2O}}{k_{oH_2O}{}^{x}} \left[\text{OFFSET} - \ln V - \left(\frac{k_{O_2} \rho_{O_2}{}^{x}}{\rho_{oO_2}} \right) \right] \qquad (5)$$

where OFFSET = term A - term C

Once the vapour density in the cell is computed the mixing ratio is calculated to give the total water content of the environmental air. The results from this approach seem satisfactory. However, it is desirable to control or quantify the bleed air contamination to eliminate the need for baselining against the EG & G dewpoint hygrometer.

10.6 Calculations of the heating of air by the freezing of supercooled water in it (Morgan)

The release of the latent heat of fusion by the freezing of supercooled water is the primary concept underlying the dynamic hypothesis for ice phase rainfall stimulation. It is well known that the temperature of water rises as it freezes due to the release of about 80 calories for each gram of water frozen.

The heating of the air by the freezing of supercooled water contained in it is slightly more complex than just the liberation of a certain amount of heat. The heat must be diffused into the air and a certain amount of water must be evaporated to restore the air to saturation.

The process can be broken down into two steps. First, the heat released by the freezing is thoroughly mixed with the air (ignoring the temperature dependence of the latent heat and the heat content of the condensed phases) producing a warmed and unsaturated air parcel. Then water is evaporated into the air to bring it to saturation, according to a wet bulb process. This results in less heating of the air than would result from the first step alone, due to the latent heat absorbed in evaporating the water. Our calculations will assume that enough cloud water remains at all times to maintain saturation with respect to water (the calculation can easily be done assuming saturation over ice).

Consider a water-saturated cloud parcel containing one kilogram of dry air, m grams of cloud water and one gram of water which is to be frozen. The initial temperature and pressure of the parcel are P and T_1. Its mixing ratio is

10.7 Calculations of cloud virtual temperature; the effect of condensed water content on density and buoyancy (Morgan)

Condensed water in cloudy air consists of particles falling at their terminal velocities. Terminal velocity is that fall speed at which the particles exert a drag on the air equal to their weight. Thus they contribute their weight to the weight of the whole and contribute to the total density of the air. We can take account of this in displaying temperature profiles in clouds by calculating a cloud virtual temperature, analogous to the way the effect of water vapour is accounted for by means of the conventional virtual temperature.

Cloud virtual temperature is defined as :

$$T_{cv} \equiv \frac{P}{R_d \rho} \qquad (1)$$

where T_{cv} = cloud virtual temperature

P = pressure

ρ = density (air plus condensate)

R_d = gas constant for dry air

using the ideal gas law and

$$T_v = T(1 + 0.61\ w) \qquad (2)$$

where

w = mixing ratio

T_v = virtual temperature

we can derive:

$$T_{cv} = T\left[\frac{1}{w_c + (1 + 0.61w)}\right] \qquad (3)$$

(w_c = cloud water mixing ratio)

10.8 Cloud measurement and tracking with the video camera aboard the Lear 24

The Lear 24 has been equipped with an experimental video camera and recorder which is being evaluated for several tasks:

1. Measurement of cloud dimensions (heights, widths, etc) and locations

2. Recording the character of objects (drops, graupel) striking the windscreen during cloud penetrations

3. Recording the character of ice build up on parts of the aircraft

4. Assembling case studies.

Perhaps the most important of these will be (1) and this section covers the overall procedures for carrying out the cloud measurements.

The following photogrammetric techniques are first approximations and are not intended to be high precision. An evaluation of the errors is under way.

The following calculations ignore the drift of the aircraft and the movements of the clouds over short time intervals. Aircraft drift and cloud movement are not wholly independent and there should be some compensation between them.

We are using these techniques to track and monitor development of entities which are characteristically 5 km in diameter and separated from each other by that distance and more, most of the time. These techniques are adequate to maintain separate and distinct records of these entities, give a reasonable record of their developments and movements, and assure that, on returning to a cloud tower a short time after first penetration, the aircraft is operating on the same tower.

10.8.1 Video equipment

The camera and recorder set up which we have mounted on the Lear has a zoom system and automatic focus feature. It also incorporates a small keyboard for titling and an elapsed time feature which gives the time from recorder turn-on in hours, minutes, seconds and tenths of seconds.

A video monitor is used for viewing the recorder tapes after flight missions. The camera is mounted close to the windscreen on the copilot's side of the aircraft, pointing forward and close to level. The recorder is mounted on the bulkhead just behind the pilot.

The DAS system records clock time and is sychronized to the radar computer clock. At take off the DAS recorder is turned on for the climb out sounding just prior to starting to roll, and the video recorder is turned on at the same instant. In this way, the elapsed time can be converted to clock time simply by adding the time of start of the sounding file on the DAS tape.

10.8.2 Measurement of height of cloud tower about to be penetrated

Fig. 10.8.1 shows the geometry of the measurement of cloud top height for this simplest case. The measurement time is chosen by the tape analyst and the times are taken from the sound channel of the video tape. A histogram of these measurements is shown in Fig. 10.8.2.

10.8.3 Measurements on clouds off the line of flight

Fig. 10.8.3 shows the geometry for making height measurements on clouds off the line of flight (and not penetrated).

10.8.4 Determination of cloud positions

The Lear is tracked by the ground radar by means of a transponder system. Position estimates are updated each time the radar beam sweeps the aircraft, and are recorded on the same tape as the radar data. With the position and heading of the aircraft known, and knowing the bearing and distance of the storm from the aircraft as described in Fig. 10.8.3, the ground position of the cloud can be determined. This is shown in Fig. 10.8.4. The heading of the aircraft is not at the moment directly recorded (this is planned) and must be read onto the video sound track by the pilot.

A computer programme has been prepared which allows entering measurements of bearing angles (vertical and horizontal), elapsed times, headings, altitudes and airspeeds into a file which then computes the various calculated aircraft heights and positions.

10.8.5 The screen overlay for measuring angles

The angle measurements necessary for the above calculations are made with the aid of a ruled transparent overlay on the TV screen. This overlay was prepared by recording a scene on the tape and measuring the bearing angles of points in the scene with a theodolite colocated with the camera. Then, with the scene on the screen the values of the angles are plotted on the screen and the grid interpolated from the plotted points. Further corrections are added by video taping a regular grid and measuring the resulting distortions on the screen during playback. It is planned to carry out the same process with the camera in place on its fixed mount in the Lear, so as to allow for correcting for all the optical and video distortions, including those introduced by the windscreen of the Lear.

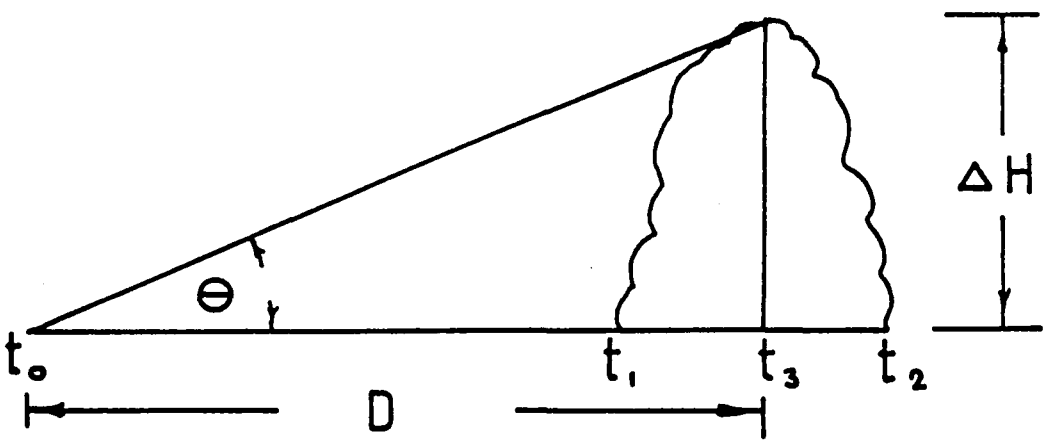

Θ = elevation angle of cloud top at t_o

t_o = time of angle measurement

t_1 = time of cloud entry

t_2 = time of cloud exit

t_3 = centre time of pass = $\frac{t_1 + t_2}{2}$

D = distance from point of angle measurement to centre of cloud
= TAS x $(t_3 - t_o)$

Δ H = height of cloud top above flight level
= D tan Θ

H = cloud top height
= ALT + Δ H

Fig. 10.8.1. Geometry of the measurement of cloud top height from the Learjet.

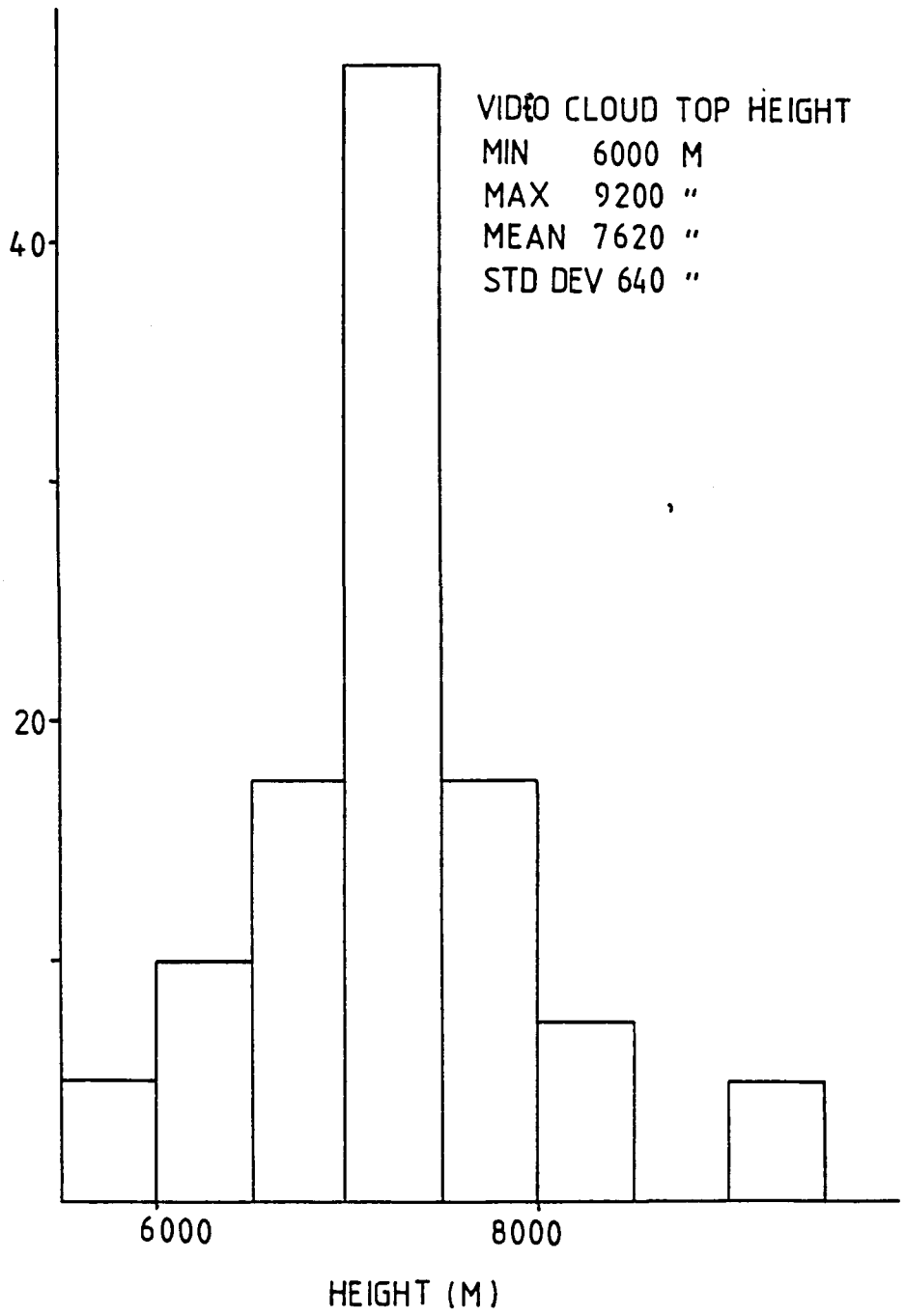

Fig. 10.8.2. A summary of measurements of cloud top heights determined from the cockpit video.

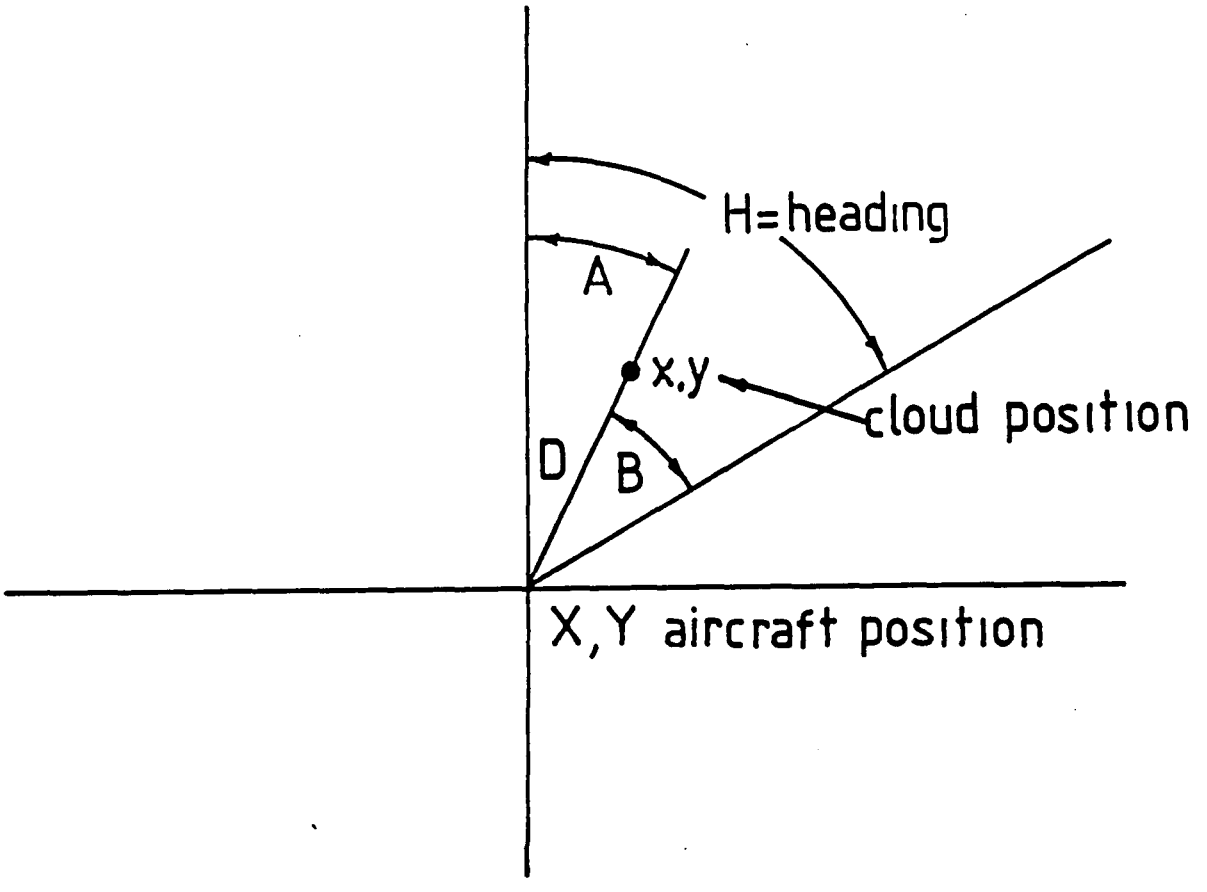

x, y	= cloud position
X,Y	= aircraft position
A	= H + B (B negative left, positive right) = true azimuth of cloud from aircraft, X,Y
x	= X + D sin A
y	= Y + D cos A
D	= distance from aircraft to cloud

Fig. 10.8.3. Geometry of making estimates of cloud top heights off the line of the aircraft flight path.

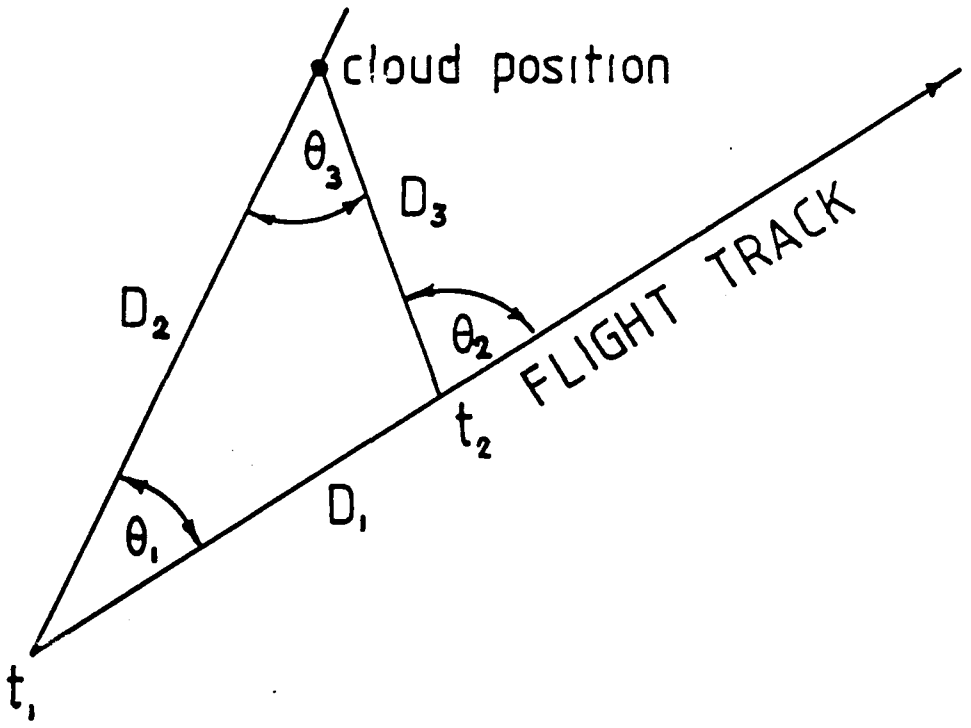

$$\frac{D_1}{\sin\Phi_3} = \frac{D_3}{\sin\Phi_1} = \frac{D_2}{\sin(\pi-\Phi_2)}$$

$$\Phi_3 = \Phi_2 - \Phi_1$$

Φ_1 = azimuth angle to cloud at t_1

Φ_2 = azimuth angle to cloud at t_2

D_1 = distance flown between measurements

= TAS x $(t_2 - t_1)$, or

$$= \int_{t_1}^{t_2} TAS\ dt$$

Fig. 10.8.4. Geometry of making estimates of the geographical (ground) position of the cloud.

In practice, the overlay is aligned as follows: the aircraft is flown level with a visible horizon and the centre line of the overlay lined up over the horizon of the resulting image. When the horizon is visible during measurements this can always be done, even if the aircraft is not perfectly level. When the horizon is not visible the aircraft must be levelled for the measurements, and the overlay lined up with the predetermined horizon.

10.9 Calculations of precipitation growth rates from 2D-C data (Morrison and Morgan)

In the initial processing of Learjet cloud penetration data using programme ULTRADAS, accretional growth rates are computed from the 2D-C imaging probe data in subroutine TWOD-CALCULATIONS according to a scheme given by Pflaum and Pruppacher (1979). In their approach they compute a collection kernel as an empirical function of particle momentum. The mass growth rate is then taken as the product of the collection kernel and the liquid water content of the air. The growth rates for valid particles are summed over each image frame and then divided by the sample volume to yield a bulk growth rate for the 2D-C image frame. Particle densities are computed as being 0.2, 0.4, 0.6, 0.8 or 1.0 g cm^{-3} resulting in five different estimates of growth rate.

In Pflaum and Pruppacher (1979), collection kernels were determined experimentally using the relation

$$K = \frac{dM/dt}{W} \qquad (1)$$

where K = collection kernel ($cm^{-3}\ s^{-1}$)
dM/dt = average particle growth rate from some initial mass to a final mass (g s^{-1})
W = average liquid water content of the air (g m^{-3})

Solving for dM/dt we get

$$dM/dt = K \times W \qquad (2)$$

Expressing the collection kernel for graupel as a function of the momentum of the individual graupel particles, the visual best-fit line to their experimental results for collection of 10 micron radius water drops is:

$$K = 10.77\ (M \times V)^{0.753} \qquad (3)$$

where M = equivalent water mass (g)
V = particle terminal velocity (cm s^{-1})

They found this scheme reasonable for graupel up to several millimetres in diameter as long as the droplets collected are small (r-collected/ r-graupel 0.1). In the special case where the collectors are large water drops rather than graupel they refer to the theoretical collection kernel by Beard and Grover (1974):

$$K = 9.13\ (M \times V)^{0.738}$$

where, once again, the water droplets that are collected are assumed to be about 10 microns in radius.

The terminal velocities for the particles in the 2D-C images are estimated in subroutines WATER-DROPLET-TERM-VELOCITY for density assumption of 1.0, and in subroutine GRAUPEL-TERMINAL-VELOCITY for density assumptions 0.2, 0.4, 0.6 and 0.8. The first subroutine computes water droplet terminal velocities over three size ranges that run from 0.5 microns in diameter to 7.0 mm as given by Beard (1976). The second subroutine estimates the terminal velocities for graupel particles for any specified density using the relationships given in Locatelli and Hobbs (1974). If the particle size is outside the range of their measurements the results are extrapolated. The terminal velocity is corrected for altitude using the method given in Pruppacher and Klett (1978).

After computation of the particle terminal velocity and its water-equivalent mass (particle volume assuming a sphere, multiplied by the assumed density) we compute the collection kernel using either equation (3) or (4) as appropriate for the density assumption. Taking the cloud liquid water content as measured from the King hot wire device (or from the J-W hot wire or FSSP if the King is not available) we then compute the mass growth rate from equation (2).

11.0 ICE NUCLEATION STUDIES (Morgan)

Elsewhere in this report (Vol. II Section 5.6, Vol. IV Section 9.9) it has been shown that the icing behavior of Nelspruit clouds is quite variable. Many clouds are ice-free at flight altitudes and others contain ice in widely varying concentrations. The degree of development of ice in clouds is important to the natural precipitation processes and to the question of seedability of the clouds. Accurate prediction of ice concentrations in clouds would be an important covariate in an evaluation of the effect of seeding clouds, and would enhance understanding of the natural rain characteristics.

The key to this problem lies in the difficult study area of ice nucleation. During the hail suppression period a few measurements of ice nuclei were made at Nelspruit (CIC 1978). These few measurements showed concentrations of the order of .04 l^{-1} (40 m^{-3}) at -18°C. The method of processing the sampling filters was one which would only detect the sorption mode of nucleation.

The collaboration of Dr Jan Rosinski of NCAR was obtained to explore the possibility that nuclei might be active by another mode, condensation-freezing. In concert with Dr. Rosinski, an exploratory programme of ice nucleus sampling was run during February and March 1986.

Air was sampled with Millipore filters. Two filters were run simultaneously and approximately 100 l of air was sampled on each filter. The dates, times and sample volumes as well as brief weather notes are given in Table 11.1.

The filters were sent to NCAR in Boulder, Colorado, for processing. Fig. 11.1 shows the ice forming nuclei (IFN) concentrations at -15°C and 2 percent supersaturation with respect to a water surface. These show variations over several orders of magnitude (from near zero to 4000 m^{-3}). Sorption IFN (zero supersaturation over water) were in very low concentration (peak, 150 m^{-3} on 12 March, otherwise well below 100 m^{-3}). Note that the concentrations show trends over consecutive days.

A paper examining these IFN concentrations and their relationship to meteorological and other conditions is in preparation.

Table 11.1 Brief weather notes - at filter times

Filter No	Date	Times (SAST)	Time Interval (min)	Volume (l)	Comments
1,2	17-2-86	1358-1413	15	105	S E flow; fine, partly cloudy day
3,4	18-2-86	1350-1409	19	147	shower in progress, light E flow
5,6	19-2-86	1443-1458	15	105	clear to scattered, fine day
7,8	20-2-86	1418-1433	15	105	clear day with isolated storms on Escarpment
9,10	21-2-86	1408-1423	15	105	gentle E wind, high moisture, storms strongly developed on escarpment
11,12	22-2-86	1488-1510	22	178	very high surface T with humidity, well developed storms on escarpment
13,14	23-2-86	1221-1238	17	119	large storms on escarpment, 29^{o} C at 1221 TW 24.5^{o} C
15,16	24-2-86	1357-1452	55		post frontal, but warm surface air, E flow
17,18	25-2-86	1411-1426	15	105	cool, post frontal, middle overcast
19,20	26-2-86	1357-1415	18	140	overcast, cool
21,22	27-2-86	1615-1630	15	105	cool, scattered clouds, light winds
23,24	28-2-86	1414-1429	15	105	almost clear, light haze, warm, wind E
25,26	01-3-86	1327-1342	15	105	warm, almost clear, no wind
27,28	02-3-86	1509-1531	22	178	warm, calm, storms on escarpment to N-W and S
29,30	03-3-86	1435-1450	15	105	scattered, very warm, few storms on escarpment

31,32	04-3-86	1350-1409	19	147	broken Cu, deep E flow, warmish
33,34	05-3-86	1410-1425	15	105	scattered and warm, still E flow
35,36	06-3-86	1439-1455	16	112	scattered, warm (front?)
37,38	07-3-86	1405-1426	21	171	scattered and quite warm, some sort of front yesterday
39,40	08-3-86	1507-1523	16	112	warm, scattered, isolated TsTms SW
41,42	09-3-86	1101-1117	16	112	warm, almost clear, storms developed later
43,44	10-3-86	1516-1531	15	105	post squall, after heavy rain, cool
45,46	11-3-86	1344-1441	57	399	1st scattered, hot, wind W. 2nd. isolated
47,48	11-3-86	1444-1459	15	105	thunderstorm S
49,50	12-3-86	1406-1426	20	154	cool here, hot on Highveld, line forming on escarpment
51,52	13-3-86	1418-1434	16	112	calm, cool to warm ($26^{o}C$) broken clouds
53,54	14-3-86	1422-1438	16	112	scattered to broken, storms all day, escarpment and Swaziland.
55,56	22-3-86	1453-1558	65	455	hot and clear

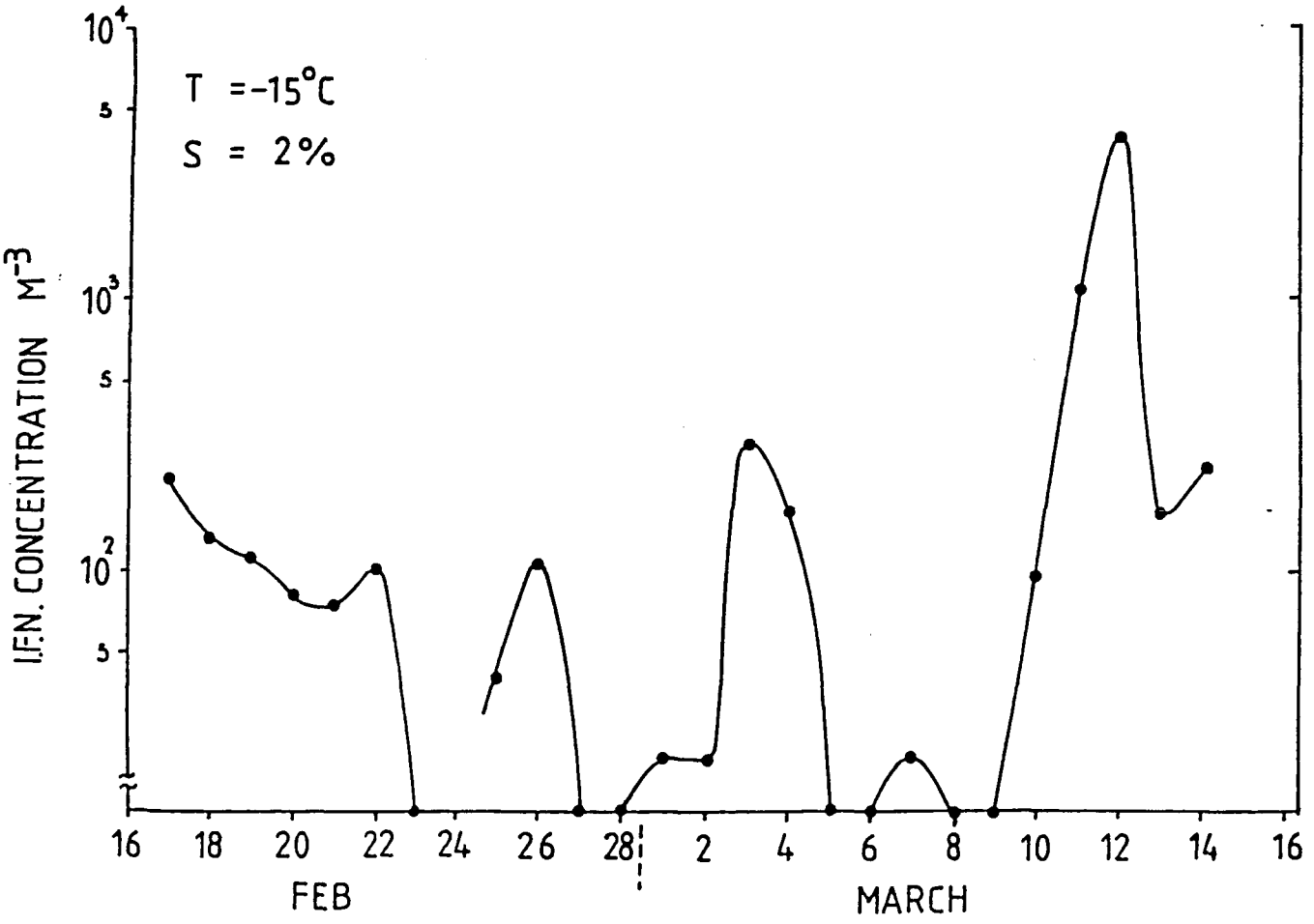

Fig. 11.1. Ice forming nulcei (IFN) concentrations at Nelspruit; February and March 1987.

12.0 PAWS DATA ARCHIVING

A data archive and software package for future data storage has been established in Nelspruit. The data base, located either on disk on the MV4000 computer or on magnetic tape at Cansas International Corporation, is copied onto magnetic tape and taken to the Subtropical Fruit and Citrus Research Institute (Nelspruit) for safe keeping. Notes and log books are also photocopied and archived. A selected portion of the data base is sent to Simpson Weather Associates in Charlottesville, Virginia, for data analyses as well as for additional storage.

This data base covers almost every aspect of the PAWS project. Table 1 shows the types of data which have been archived and the periods of record that they cover. A documentation file accompanies the magnetic tapes at the Institute. This file contains information necessary for dumping the data from tape to disk and explains what the numbers in each data set represent. In the file, each tape has an information sheet (Sample 2), a list of the files contained on the tape, a sample of the data format, and printouts of the programs used to write the data to tape or to dump it to disk.

TABLE 1

Archived Data

Data Type	Format	Period of Record
Nelspruit soundings	mag. tape	82/83, 83/84, 84/85
Rainfall network (16 stations)	mag. tape	82/83, 83/84
Rainfall network (25 stations)	mag. tape	84/85
Radar, blue sky suppressed*	mag. tape	82/83, 83/84, 84/85
WRC surface mesonetwork (9 stations - winds and temperatures)	mag. tape	84/85
Radiation	mag. tape	84/85
Aircraft	mag. tape	80/81, 81/82, 82/83, 83/84, 84/85
Radar log book	paper	82/83. 83/84, 84/85
Pilot's and observer's notes	paper	82/83, 83/84, 84/85
G. Mather's daily log book	paper	82/83, 83/84, 84/85
Principle component analysis	paper	82/83, 83/84, 84/85
Nelspruit 24-hour rainfall	paper	82/83, 83/84, 84/85
Barograph strip charts (Nelspruit)	paper	82/83, 83/84, 84/85
Hygrothermograph strip charts (Nelspruit)	paper	82/83, 83/84, 84/85

*Archiving will be completed before the start of the 85/86 season

Sample 2

SECTION : RAINFALL

TAPE NO : 2

TAPE TITLE : "Rainfall Data, 82/83, 83/84, + 84/85 Seasons"

DATE OF TAPE CREATION : 29 MAR 1985

DATA TYPE (ASCII binary, EBCDIC, etc): ASCII

TAPE DENSITY: 1600 bpi

TAPE LENGTH : 600 ft.

WHO WROTE THE DATA TO TAPE: Wendy London

NAME OF THE TAPE WRITING PROGRAM : RAINTAPE.F77

WHO WORKS WITH AND ANALYSES THIS DATA : Parsons, London, Emmitt

NUMBER OF FILES ON THE TAPE : 57

NUMBER OF BLOCKS PER FILE : Variable

NUMBER OF RECORDS PER BLOCK : 100

NUMBER OF WORDS PER BLOCK : 2000

DESCRIPTION OF THE DATA : Header record of file name such as STATION01.83, where 01 is station # and 83 is the 83/84 season, then one record per each 5 minute interval of the season that had rain. Data is: year, Julian date, time and the number of tips, where 1 tip = 0.25 mm.

OTHER COPIES OF THIS DATA ARE LOCATED AT : CIC (Nelsprint), SWA (Virginia)

IS THERE A PROGRAM TO TAKE THE DATA OFF OF THE TAPE? yes

PROGRAM NAME: RAINOFFTAPE.F77

13.0 REFERENCES

Ackerman, B., R.C. Grosh and R.Y. Sun, 1979: Assessing midwest cloud characteristics for weather modification. Final Report ENV 77-11527, National Science Foundation, Illinois Water Survey, Irbana, Illinois.

Adler, R.F., and R.A. Mack, 1984: Thunderstorm cloud height-rainfall relations for use with satellite rainfall estimation techniques. J. Climate Appl. Meteor., 23, 280-296.

Ahlberg, J.H., E.N. Nilson and J.L. Walsh, 1967: The Theory of Splines and their Applications. New York, Academic Press.

Allee, P.A., B.T. Patten and E.W. Barrett, 1972: The dynamic calibration of an airborne ice nuclei generator. J. Rech. Atmos., 6, 29-40.

Batchelor, G.K., 1970: An introduction to fluid dynamics. Cambridge University Press, 615 pp.

Barnes, Stanley L., 1973: Mesoscale objective map analysis using weighted time-series observations. NOAA Technical Memorandum, ERL NSSL 62, March 1973.

------, and S.W. Grover, 1974: Numerical collision efficiencies for small raindrops colliding with micron sized particles. J. Atmos. Sci., 31, 543-550.

Beard, K.V., 1976: Terminal velocity and shape of cloud precipitation drops aloft. J. Atmos. Sci., 33, 851-864.

Berry, F.A., and E. Bolay, 1973: Handbook of meteorology. McGraw Hill Publication.

Bolton, D. 1980: The computation of equivalent potential temperature. Mon. Wea. Rev., 108, 1046-1053.

Browning, K.A., and F.H. Ludlain, 1962: Airflow in convective storms. Quart. J. Roy. Meteor. Soc., 89, 75-84.

Buck, A., 1976: The variable-path Lyman-alpha hygrometer and its operating characteristics. Bull. Amer. Met. Soc., 57, 1113-1118.

Byers, H.R., and R.R. Braham, 1949: The thunderstorms. Wash. D.C., U.S. Govt. Printing Office.

CIC, 1978: Annual report weather modification season 1976/77. Submitted to Laeveldse Tabak Kooperasie Beperk. Cansas International Corporation.

Cooper, H., M. Garstang and J. Simpson, 1982: The diurnal interaction between convection and peninsular-scale forcing over south Florida. Mon. Wea. Rev. 110, 488-503.

Coulman, C.E., and M.A. Parker, 1982: On the calibration and performance of an instrument for measuring total water mixing ratio in cloud. J. Appl. Meteor., 21, 695-702.

Cressman, G.P., 1959: An operational objective analysis scheme. Mon. Wea. Rev., 108, 1046-1053.

Dixon, M., and G.K. Mather, 1986: Radar evaluation of a randomized rain-augmentation experiment: Some preliminary results. Tenth AMS Conf. on Planned and Inadvert. Wea. Modif., Arlington, Virginia.

Eadie, W.J., and T.R. Mee, 1963: The effect of dry ice pellet velocity on the generation of ice crystals. J. Appl. Meteor. 2, 260-265.

Emmitt, G.D., D.S. Roos and B.J. Morrison, 1984: Dry ice pellet experiments (DIPEX) - field and laboratory. Report to Water Research Commission Republic of South Africa.

Frankhauser, J.C., and C. Wade, 1982: The environment of the storms; Chapter 2 of hailstorms of the central high plains, Vol. 1, The National Hail Research Experiment. Colorado Associated University Press, Boulder, Colorado, 5-33.

Frank, N., P.L. Moore and G.E. Fisher, 1967: Summer shower distribution over the Florida peninsula as deduced from digitized radar. J. Appl. Meteor., 6, 309-316.

Fukuta, N., W.A. Schmeling and L.F. Evans, 1971: Experimental determination of ice nucleation by falling dry ice pellets. J. Appl. Meteor., 10, 1174-1179.

Gagin, A., D. Rosenfeld and R.E. Lopez, 1985: The relationship between height and precipitation characteristics of summertime convective cells in south Florida. J. Atmos. Sci., 42, 84-94.

Gayet, J.F., M. Friedlander and J.P. Pinty, 1977: Sur la mesur de la teneur en eau totale des nuages. Sci. Rep. No 22, Lab. Assoc. Meteor. Phys, Aubiere, France.

Haman, K., 1967: On the accumulation of liquid water in a buoyant jet and its relation to hail phenomena. Acta Geophys. Pol., 15, 9-27.

Hobbs, P.V., R.J. Farber and R.G. Joppa, 1973: Collection of ice particles from aircraft using decelerators. J. Appl, Meteor., 12, 522-528.

Holroyd, E.W., A.B. Super and B.A. Silverman, 1978: The practicability of dry ice for on top seeding of convective clouds. J. Appl. Meteor. 17, 49-63.

Horn, R.D., W.G. Finnegan, and P.J. DeMott, 1982: Experimental studies of nucleation by dry ice. J. Appl. Meteor., 21, 1567-1570.

Kessler, E., 1969: On the distribution and continuity of water substance in atmospheric circulations. Met. Monographs, 10, No 32, AMS. Boston.

King, W.D., J.E. Dye, J.W. Strapp, D. Baumgardner and D. Huffman, 1985: Icing wind tunnel tests on the CSIRO liquid water probe. J. Atmos. Ocean Tech., 2, 340-352.

Knight, C.A., W.A. Cooper, D.W. Breed, I.R. Paluch, P.L. Smith and G. Vali, 1982: Microphysics, Chapter 7 of hailstorms of the central high plains, Vol. 1, The National Hail Research Experiment. Knight and Squires, Eds. Colorado Associated University Press. Boulder, Colorado.

Kyle, T.G., and W.R. Sands, 1973: Water content in convective storm clouds. Science, 180, 1274-1275.

-----, 1975: The measurement of water content by an evaporator, J. Appl. Meteor., 14, 327-332.

Lamb, D., J. Hallet and R. Sax 1981: Mechanistic limitations to the release of latent heat during the natural and artificial glaciation of deep convective clouds. Quart. J.R. Met. Soc. 107, 935-954.

Leighton, H.G., and R.R. Rogers, 1974: Droplet growth by condensation and coalescence in a strong updraft. Jour. Atmos. Sci., 31, No 1, 271-279.

Lilly, D.K., 1979: The dynamical structure and evolution of thunderstorms and squall lines. Ann. Rev. Earth Planet Sci., 7, 117-161.

Locatelli, J. D., and P.V. Hobbs, 1974: Fall speeds and masses of solid precipitation particles. J. Geophys. Res., 79, 2185-2197.

Lozowski, E.P., and B. Kochtubajda, 1980: Theory and measurements of dry ice sublimation in clear air and simulated cloud. Proc. WMO Third Scientific Conf. on Weather Modification, Clermont-Ferrand, France, 409-416.

Mader, G.N., 1979: Numerical study of storms in the Transvaal. S. African Geo. J. 61, No 2.

Mandrioli, P., M.G. Negrini, G. Cesari and G. Morgan, 1983: Evidence for long range transport of biological and anthropogenic aerosol particles in the atmosphere. Grana, 23, No 1, 43-53.

Mather, G.K., B.J. Morrison and G.M. Morgan, 1986: A preliminary assessment of the importance of coalescence in convective clouds of the eastern Transvaal. Submitted to J. Clim. Appl. Meteor.

-----, 1986: The Nelspruit program - history and current status. Tenth AMS Conf. on Planned and Inadvert. Wea. Modif. Arlington, Virginia.

Miller, R.C., 1967: Semi-objective evaluation of the relative importance of parameters favouring production of severe storms. Preprints 5th Conf. Severe Local Storms, St. Louis, Amer. Meteor. Soc., 2-9.

Moncrieff, M.W., and J.J. Miller, 1976: The dynamics and simulations of tropical squall lines. Quart. J. Roy. Meteor. Soc., 102, 373-394.

Morgan, G.M., 1970: An examination of the wet-bulb zero as a hail forecasting parameter in the Po Valley, Italy. J. Appl. Meteor., 9, 537-540.

-----, and R.C. Beebe, 1971: Analysis of the time-space behaviour of the field of equivalent temperature during a severe weather situation. Preprints, 7th Conference on Severe Local Storms, A.M.S., Kansas City, Missouri, 54-59.

-----, 1972: On the growth of large hail. Mon. Wea. rev., 100, 196-205.

-----,and E.A. Mueller, 1972: The total liquid water mass of large convective storms. Preprints, 15th Radar Meteor. Conf., AMS, Boston, 4 pp.

-----, 1973: A general description of the hail problem in the Po Valley of Northern Italy. J. Appl. Meteor., 12, 338-353.

-----, and P. Squires, 1972: Introduction to Chapter 1 of hailstorms of the central high plains, Vol. 1, The National Hail Research Experiment. Colorado Associated University Press, Boulder, Colorado, 1-4.

-----, and E.L. Crow, 1982: Statistical testing of hail suppression hypothesis; Chapter 11 of hailstorms of the central high plains, Vol. 1, The National Hail Research Experiment. Colorado Associated University Press, Boulder, Colorado, 249-261.

-----, and J. Tuttle, 1982: Some experimental techniques for the study of the evolution of atmospheric thermodynamic instability. Proceedings of the Second International Conference on Hailstorms and Hail Prevention, Sofia, Bulgaria, Printing Office of the Bulgarian Hydrometeorological Service, Sofia, 192-196.

-----, and G.K. Mather, 1984: Problems in the measurement of liquid water content in Transvaal clouds. Paper presented at the Ninth Conf. on Wea. Mod., Park City, Utah, American Meteorological Society.

-----, and B.J. Morrison, 1985: Jet engine bleed air measurements of water quantities in convective clouds. Second Annual Conf., S.A. Soc. for Atmos. Sci., Pretoria.

-----, B.J. Morrison, and G.K. Mather, 1986a: Total and condensed water contents in warm based thunderstorm turrets: their estimation with a jet engine bleed air measurement technique. Submitted to J. Clim. Appl. Meteor.

-----, -----, and -----, 1986b: Sensing of cloud condensed water mixing ratio in jet engine compressor bleed air by the potential temperature method. Submitted to J. Atmos. Ocean. Tech.

-----, -----, and -----, 1986c: Evidence for the accumulation of very high concentrations of supercooled liquid water in thunderstorms. Submitted to J. Clim. Appl. Meteor.

Morrison, B.J., G.K. Mather, and G.M. Morgan, 1986: Aircraft observations of target turrets on multicellular storms showing radar response to dry ice seeding. Tenth Conf. Wea. Modif. Arlington, Virginia. American Meteorological Society.

-----, B.J., W.G. Finnegan, R.D. Horn and L.O. Grant, 1984: A laboratory characterization of dry ice as a glaciogenic seeding agent. Ninth Conference on Planned and Inadvert. Wea. Modif. 21-23 May 1984, Park City, Utah.

Musil, D.J., P.L. Smith and A. Waldvogen, 1984: Evaluation of the applicability of the accumulation zone hypothesis to Swiss hailstorms. Extended Abstracts. Ninth Conf. Wea. Mod. Park City, Utah, A.M.S. Boston, 29-30.

-----, and -----, 1985: Aircraft penetrations of Swiss hailstorms: An update. Abstracts, First European Conf. of the Wea. Mod. Assoc., Clermont-Ferrand, Toulouse, France.

Newton, C.W., 1963: Dynamics of severe convective storms. Meteorol. Monogr. 5, 33-55.

Pflaum, J.C., and H.R. Pruppacher, 1979: A wind tunnel investigation of the growth of graupel initiated from frozen drops. J. Atmos. Sci, 34, 680-689.

Plate, E.J., 1971: Aerodynamic characteristics of the atmospheric boundary layer. U.S. Dept. of Energy, Rept. prepared for the U.S. Atomic Energy Commission, 190 pp.

Pruppacher, H.R., and J.D. Klett, 1978: Microphysics of clouds and precipitation. D. Reidel, Dordrecht, Holland.

Reinsch, C.H., 1967: Smoothing by spline functions. Numerische Mathematik, 10, 177-183.

Rogers, R.R., 1979: A short course in cloud physics. 2nd Edition. Pergamon International Library, Oxford.

Roys, G.P., 1963: Airborne instrumentation system for measuring meteorological phenomena inside thunderstorms. Tech. Doc. Rept. No. ASD-TDR-63-231, Directorate of Flight Test, Aeron. Systems Div., AF Systems Command, Wright-Patterson AB, Ohio.

-----, and E. Kessler, 1966: Measurement by aircraft of condensed water in Great Plains thunderstorms. Tech. Note 49-NSSP-19. U.S. Dept. of Commerce, ESSA, Wash. D.C.

Ruskin, R.E., and W.D. Scott, 1974: Weather and climate modification. W.N. Hess, Ed., Chap. 4, Wiley.

Schlesinger, R., 1975: A three-dimensional numerical model of a violated deep convective cloud: preliminary results. J. Atmos. Sci., 32, 934-957.

Smith, P.L., Jr., 1976: Comments on the measurement of water content by an evaporator. J. Appl. Meteor., 15, 189-191.

-----, P.L., J.R. Miller, A.A. Doneand, J.H. Hursch, D.L. Pregnitz, P.E. Price, K.J. Tyler and H.D. Orville, 1985: Research to develop evaluation techniques for operational convective cloud modification projects. report SDSMT/IAS/R - 85/02, Institute of Atmospheric Sciences, South Dakota School of Mines and Technology, Rapid City S.D. 93 pp.

Sulakvelidze, G.K., N.S. Bibilashvili and V.F. Lapcheva, 1967: Formation of precipitation and modification of hail processes. Israel Program for Scientific Translations, Jerulsalem.

Tsonis, A.A., G.L. Austin and S. Lovejoy, 1984: A proposal for a new statistic and technique development for the design and evaluation of cloud seeding experiments. Atmos-Ocean 22, 67-82.

Ulanski, S.L., and M. Garstang, 1978: The role of surface divergence and vorticity in the life cycle of convective rainfall. Part 1: Observations and analysis. J. Atmos. Sci., 35, 1047-1062.

Vonnegut, B., 1981. Misconceptions about cloud seeding with dry ice. J. Wea. Modif., 13, 9-10.

GROUP 1 - GEOMETRY,TIME

1	DURATION
2	TIME OF ORIGIN
3	SPEED OF MOVEMENT
4	DIRECTION OF MOVEMENT
5	MEAN X CO-ORD
6	MEAN Y CO-ORD
7	MEAN RANGE
8	ENVELOPE DECISION TIME
9	VOLUME AT DECISION TIME
10	PEAK DBZ AT DECISION TIME

GROUP 2 - TOP,DEPTH,VOLUME,MASS

11	ECHO TOP - MAX
12	ECHO TOP - MAX RATE OF INCREASE
13	ECHO TOP - MEAN
14	ECHO TOP - TIME TO MAX
15	ECHO TOP - TIME TO MAX ROI
16	ECHO TOP - PERSISTENCE
17	ECHO TOP - MAX RATIO
18	DEPTH - MAX
19	DEPTH - MAX RATE OF INCREASE
20	DEPTH - MEAN
21	DEPTH - TIME TO MAX
22	DEPTH - TIME TO MAX ROI
23	DEPTH - PERSISTENCE
24	DEPTH - MAX RATIO
25	VOLUME - MAX
26	VOLUME - MAX RATE OF INCREASE
27	VOLUME - TIME INTEGRAL
28	VOLUME - MEAN
29	VOLUME - TIME TO MAX
30	VOLUME - TIME TO MAX ROI
31	VOLUME - PERSISTENCE
32	VOLUME - MAX RATIO
33	MASS TOT - MAX
34	MASS TOT - MAX RATE OF INCREASE
35	MASS TOT - TIME INTEGRAL
36	MASS TOT - MEAN
37	MASS TOT - TIME TO MAX
38	MASS TOT - TIME TO MAX ROI
39	MASS TOT - PERSISTENCE
40	MASS TOT - MAX RATIO
41	MASS A.C.- MAX
42	MASS A.C.- MAX RATE OF INCREASE
43	MASS A.C.- TIME INTEGRAL
44	MASS A.C.- MEAN
45	MASS A.C.- TIME TO MAX
46	MASS A.C.- TIME TO MAX ROI
47	MASS A.C.- PERSISTENCE
48	MASS A.C.- MAX RATIO

GROUP 3 - AREA,RAIN,PRECIP,RATIOS

49	AREA 3 DEG - MAX
50	AREA 3 DEG - MAX RATE OF INCREASE
51	AREA 3 DEG - TIME INTEGRAL
52	AREA 3 DEG - MEAN
53	AREA 3 DEG - TIME TO MAX
54	AREA 3 DEG - TIME TO MAX ROI
55	AREA 3 DEG - PERSISTENCE
56	AREA 3 DEG - MAX RATIO
57	AREA CUTOFF - MAX
58	AREA CUTOFF - MAX RATE OF INCREASE
59	AREA CUTOFF - TIME INTEGRAL
60	AREA CUTOFF - MEAN
61	AREA CUTOFF - TIME TO MAX
62	AREA CUTOFF - TIME TO MAX ROI
63	AREA CUTOFF - PERSISTENCE
64	AREA CUTOFF - MAX RATIO
65	RFLUX 3 DEG - MAX
66	RFLUX 3 DEG - MAX RATE OF INCREASE
67	RFLUX 3 DEG - MASS
68	RFLUX 3 DEG - MEAN
69	RFLUX 3 DEG - TIME TO MAX
70	RFLUX 3 DEG - TIME TO MAX ROI
71	RFLUX 3 DEG - PERSISTENCE
72	RFLUX 3 DEG - MAX RATIO
73	RFLUX CUTOFF - MAX
74	RFLUX CUTOFF - MAX RATE OF INCREASE
75	RFLUX CUTOFF - MASS
76	RFLUX CUTOFF - MEAN
77	RFLUX CUTOFF - TIME TO MAX
78	RFLUX CUTOFF - TIME TO MAX ROI
79	RFLUX CUTOFF - PERSISTENCE
80	RFLUX CUTOFF - MAX RATIO
81	PRECIP WATER - MAX
82	PRECIP WATER - MAX RATE OF INCREASE
83	PRECIP WATER - TIME INTEGRAL
84	PRECIP WATER - MEAN
85	PRECIP WATER - TIME TO MAX
86	PRECIP WATER - TIME TO MAX ROI
87	PRECIP WATER - PERSISTENCE
88	PRECIP WATER - MAX RATIO
89	MTI/RAIN MASS - 3 DEG
90	MTI/RAIN MASS - CUTOFF
91	MEAN MASS/RAIN MASS - 3 DEG
92	MEAN MASS/RAIN MASS - CUTOFF

GROUP 4 - VERTICAL CENTROIDS

93	VERT CENTROID - MAX
94	VERT CENTROID - MAX ROI
95	VERT CENTROID - MEAN
96	VERT CENTROID - TIME TO MAX
97	VERT CENTROID - TIME TO MAX ROI
98	VERT CENTROID - PERSISTENCE
99	VERT CENTROID - MAX RATIO
100	Z WT VERT CENT - MAX
101	Z WT VERT CENT - MAX ROI
102	Z WT VERT CENT - MEAN
103	Z WT VERT CENT - TIME TO MAX
104	Z WT VERT CENT - TIME TO MAX ROI
105	Z WT VERT CENT - PERSISTENCE
106	Z-WT VERT CENT - MAX RATIO
107	DELT VERT CENT - MAX
108	DELT VERT CENT - MAX ROI
109	DELT VERT CENT - MEAN
110	DELT VERT CENT - TIME TO MAX
111	DELT VERT CENT - TIME TO MAX ROI
112	DELT VERT CENT - PERSISTENCE
113	DELT VERT CENT - MAX RATIO

GROUP 5 - SPARE

114	SPARE
115	SPARE
116	SPARE
117	SPARE
118	SPARE

GROUP 6 - REFLECTIVITY

119	PEAK DBZ TOT - MAX
120	PEAK DBZ TOT - MAX ROI
121	PEAK DBZ TOT - MEAN
122	PEAK DBZ TOT - TIME TO MAX
123	PEAK DBZ TOT - TIME TO MAX ROI
124	PEAK DBZ TOT - PERSISTENCE
125	PEAK DBZ TOT - MAX RATIO
126	MEAN DBZ TOT - MAX
127	MEAN DBZ TOT - MAX ROI
128	MEAN DBZ TOT - MEAN
129	MEAN DBZ TOT - TIME TO MAX
130	MEAN DBZ TOT - TIME TO MAX ROI
131	MEAN DBZ TOT - PERSISTENCE
132	MEAN DBZ TOT - MAX RATIO
133	MEAN DBZ 3 DEG - MAX
134	MEAN DBZ 3 DEG - MAX ROI
135	MEAN DBZ 3 DEG - MEAN
136	MEAN DBZ 3 DEG - TIME TO MAX
137	MEAN DBZ 3 DEG - TIME TO MAX ROI
138	MEAN DBZ 3 DEG - PERSISTENCE
139	MEAN DBZ 3 DEG - MAX RATIO
140	MEAN DBZ CUTOFF - MAX
141	MEAN DBZ CUTOFF - MAX ROI
142	MEAN DBZ CUTOFF - MEAN
143	MEAN DBZ CUTOFF - TIME TO MAX
144	MEAN DBZ CUTOFF - TIME TO MAX ROI
145	MEAN DBZ CUTOFF - PERSISTENCE
146	MEAN DBZ CUTOFF - MAX RATIO
147	MAX HT 45'S - MAX
148	MAX HT 45'S - MAX ROI
149	MAX HT 45'S - MEAN
150	MAX HT 45'S - TIME TO MAX
151	MAX HT 45'S - TIME TO MAX ROI
152	MAX HT 45'S - PERSISTENCE
153	MAX HT 45'S - MAX RATIO
154	HT PEAK DBZ - MAX
155	HT PEAK DBZ - MAX ROI
156	HT PEAK DBZ - MEAN
157	HT PEAK DBZ - TIME TO MAX
158	HT PEAK DBZ - TIME TO MAX ROI
159	HT PEAK DBZ - PERSISTENCE
160	HT PEAK DBZ - MAX RATIO

GROUP 7 - MASS=f(HT)

161	MASS=f(HT) ; MEAN - MEAN
162	MASS=f(HT) ; MEAN - MAX
163	MASS=f(HT) ; MEAN - MIN
164	MASS=f(HT) ; MEAN - MAX ROI
165	MASS=f(HT) ; MEAN - MAX ROD
166	MASS=f(HT) ; S.D. - MEAN
167	MASS=f(HT) ; S.D. - MAX
168	MASS=f(HT) ; S.D. - MIN
169	MASS=f(HT) ; S.D. - MAX ROI
170	MASS=f(HT) ; S.D. - MAX ROD
171	MASS=f(HT) ;-SKEW - MEAN
172	MASS=f(HT) ;-SKEW - MAX
173	MASS=f(HT) ;-SKEW - MIN
174	MASS=f(HT) ;-SKEW - MAX ROI
175	MASS=f(HT) ;-SKEW - MAX ROD
176	MASS=f(HT) ; MODE - MEAN
177	MASS=f(HT) ; MODE - MAX
178	MASS=f(HT) ; MODE - MIN
179	MASS=f(HT) ; MODE - MAX ROI
180	MASS=f(HT) ; MODE - MAX ROD

GROUP 8 - PEAK DBZ=f(HT)

181	DBZ=f(HT) ; MEAN - MEAN
182	DBZ=f(HT) ; MEAN - MAX
183	DBZ=f(HT) ; MEAN - MIN
184	DBZ=f(HT) ; MEAN - MAX ROI
185	DBZ=f(HT) ; MEAN - MAX ROD
186	DBZ=f(HT) ; S.D. - MEAN
187	DBZ=f(HT) ; S.D. - MAX
188	DBZ=f(HT) ; S.D. - MIN
189	DBZ=f(HT) ; S.D. - MAX ROI
190	DBZ=f(HT) ; S.D. - MAX ROD
191	DBZ=f(HT) ;-SKEW - MEAN
192	DBZ=f(HT) ;-SKEW - MAX
193	DBZ=f(HT) ;-SKEW - MIN
194	DBZ=f(HT) ;-SKEW - MAX ROI
195	DBZ=f(HT) ;-SKEW - MAX ROD
196	DBZ=f(HT) ; MODE - MEAN
197	DBZ=f(HT) ; MODE - MAX
198	DBZ=f(HT) ; MODE - MIN
199	DBZ=f(HT) ; MODE - MAX ROI
200	DBZ=f(HT) ; MODE - MAX ROD

GROUP 9 - %VOLUME=f(DBZ)

201	%VOL=f(DBZ) ; MEAN - MEAN
202	%VOL=f(DBZ) ; MEAN - MAX
203	%VOL=f(DBZ) ; MEAN - MIN
204	%VOL=f(DBZ) ; MEAN - MAX ROI
205	%VOL=f(DBZ) ; MEAN - MAX ROD
206	%VOL=f(DBZ) ; S.D. - MEAN
207	%VOL=f(DBZ) ; S.D. - MAX
208	%VOL=f(DBZ) ; S.D. - MIN
209	%VOL=f(DBZ) ; S.D. - MAX ROI
210	%VOL=f(DBZ) ; S.D. - MAX ROD
211	%VOL=f(DBZ) ;-SKEW - MEAN
212	%VOL=f(DBZ) ;-SKEW - MAX
213	%VOL=f(DBZ) ;-SKEW - MIN
214	%VOL=f(DBZ) ;-SKEW - MAX ROI
215	%VOL=f(DBZ) ;-SKEW - MAX ROD
216	%VOL=f(DBZ) ; MODE - MEAN
217	%VOL=f(DBZ) ; MODE - MAX
218	%VOL=f(DBZ) ; MODE - MIN
219	%VOL=f(DBZ) ; MODE - MAX ROI
220	%VOL=f(DBZ) ; MODE - MAX ROD

GROUP 10 - % 3 DEG AREA=f(DBZ)

221	%AREA=f(DBZ); MEAN - MEAN
222	%AREA=f(DBZ); MEAN - MAX
223	%AREA=f(DBZ); MEAN - MIN
224	%AREA=f(DBZ); MEAN - MAX ROI
225	%AREA=f(DBZ); MEAN - MAX ROD
226	%AREA=f(DBZ); S.D. - MEAN
227	%AREA=f(DBZ); S.D. - MAX
228	%AREA=f(DBZ); S.D. - MIN
229	%AREA=f(DBZ); S.D. - MAX ROI
230	%AREA=f(DBZ); S.D. - MAX ROD
231	%AREA=f(DBZ);-SKEW - MEAN
232	%AREA=f(DBZ);-SKEW - MAX
233	%AREA=f(DBZ);-SKEW - MIN
234	%AREA=f(DBZ);-SKEW - MAX ROI
235	%AREA=f(DBZ);-SKEW - MAX ROD
236	%AREA=f(DBZ); MODE - MEAN
237	%AREA=f(DBZ); MODE - MAX
238	%AREA=f(DBZ); MODE - MIN
239	%AREA=f(DBZ); MODE - MAX ROI
240	%AREA=f(DBZ); MODE - MAX ROD

GROUP 11 - CONTROL

241	AV MIXING RATIO FOR LOWEST 50 MB
242	CCL TEMP
243	BUOYANCY AT 500 MB
244	TCCL/DT500
245	# OF TRACKS FOR THE DAY
246	CUMULATIVE 3 DEG A.T.I. FOR THE DAY
247	MAX VOLUME OF ANY STORM FOR THE DAY
248	MAX RATE OF INCR OF VOLUME OF ANY STORM
249	MAX TOPS OF ANY STORM FOR THE DAY
250	MAX DBZ OF ANY STORM FOR THE DAY

NOTES

ROI is max rate of increase
ROD is max rate of decrease
TOT means for whole storm
A.C. means above cutoff altitude
CUTOFF means at cutoff altitude
RFLUX is rain flux
MTI is mass time integral
TCCL is temp at the CCL
DT500 is buoyancy at 500 mb

Table 3.2. Track properties.

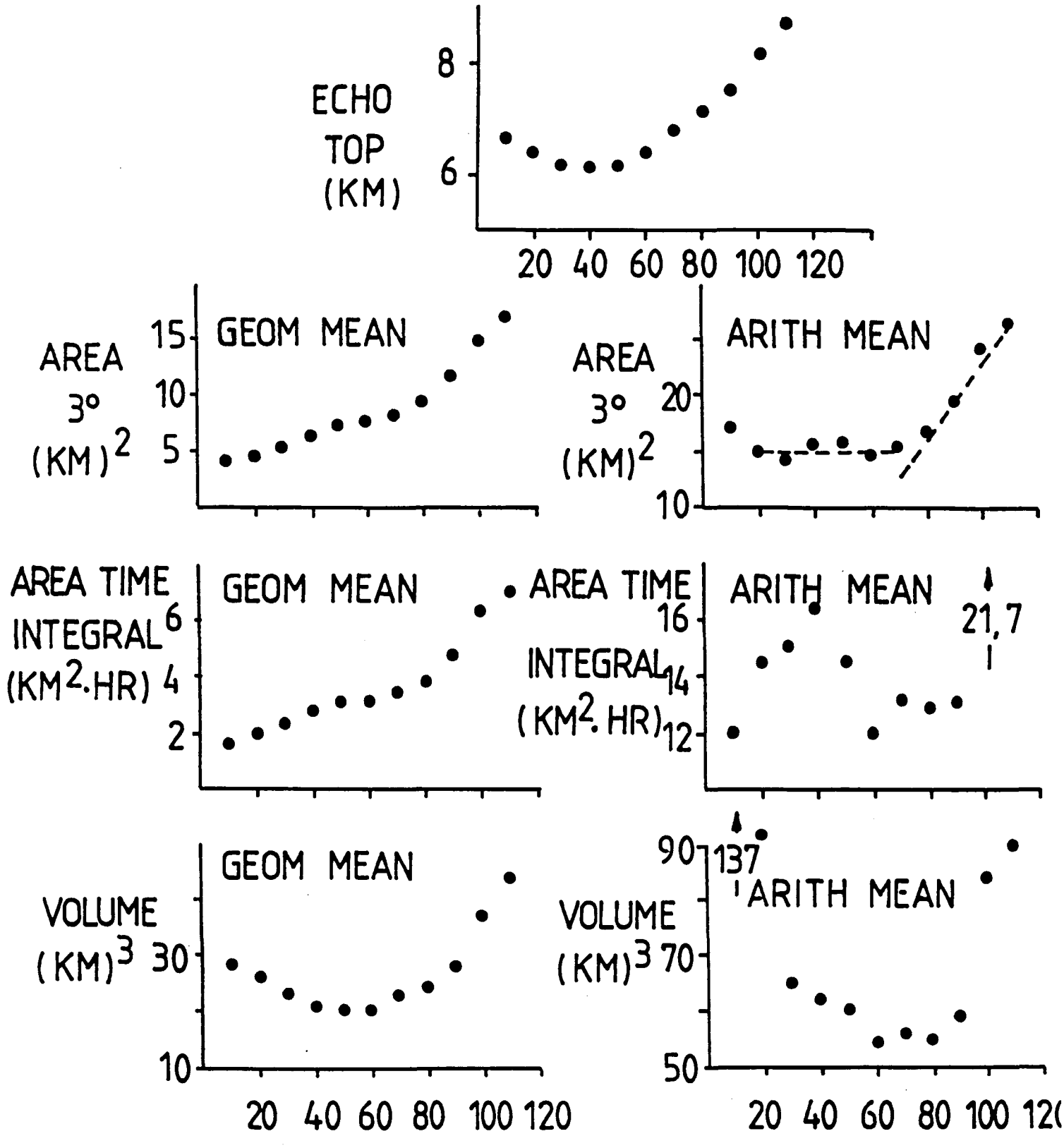

Fig. 3.8. Average track properties versus range (in km) from radar.

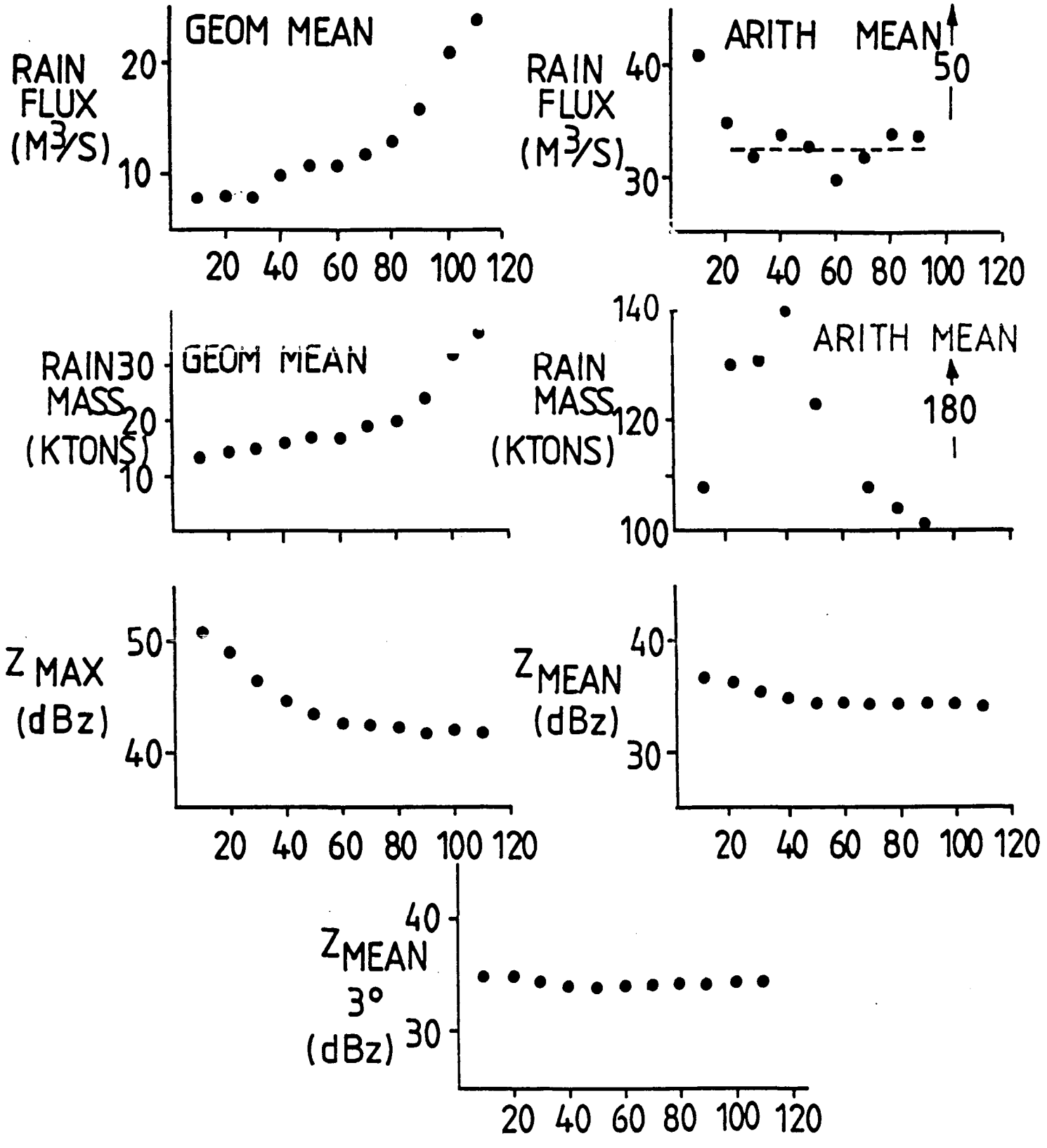

Fig. 3.8 (Cont). Average track properties versus range (in km) from radar.

4.0 THE PAWS MESOSCALE NETWORK

4.1 MEASUREMENTS

4.1.1 Introduction

A network of automated weather stations collected data in the Nelspruit area during the 1984-85 and 1985-86 operational seasons. In general there were 8 or 9 stations operating, evenly distributed from the highveld, across the escarpment and into the lowveld (Fig. 4.1). These stations archived the measurements, and the data was collected twice monthly during site visits. The data was transferred to the mainframe computer at CIC in Nelspruit for subsequent data processing and analysis. All manipulation of the information collected by the stations was performed by computer and required little human intervention to maintain the large data base as it was acquired.

4.1.2 Site Locations

Pertinent information on each instrumented site is given in Table 4.1. A brief description of each site is given here, with some factors to consider when interpreting the data.

Lower Sabie: This is the most easterly of the sites, located in Kruger National Park, and was originally placed to provide a measurement that would be influenced only by lowveld effects. Its location greatly extended the time required for site servicing, and so the site was discontinued after one month of operation. The site was several hundred meters from the Sabie River, in low bush, with good exposure from all directions.

Numbi Gate: This tower is located inside Kruger National Park, on a slightly elevated site. There are some trees in the area higher than the anemometers, although none were closer than about 100 meters. The general terrain is flat. Exposure is in general good in all directions.

Kaapmuiden: This site is located in the Boulders area, on a ridge to the south of and above the Crocodile gorge. The instruments are slightly shielded from the north east by a ridge. The site however is well exposed in all other directions. The local terrain is comprised of rolling hills.

Nelspruit: This site is located at the Nelspruit Municipal Airport, approximately 50 meters west of the runway. There is some shielding of the instruments from the south and southwest, due to a copse of wood and airport hangers within about 100 meters. Exposure is good in all other directions. The rain gauge for this site is separated from the tower by several hundred meters, being located near the CIC offices. The general terrain is characterized by rolling hills.

Barberton: This site is located on Lone Tree Hill, at the northern edge of the Barberton Mountains. This site experiences the most pronounced local effects, since some terrain in this area is quite rugged. To the north lays the Barberton valley, and 1 km to the south are the Barberton Mountains. Certain wind directions may have had large topographic influences at this site.

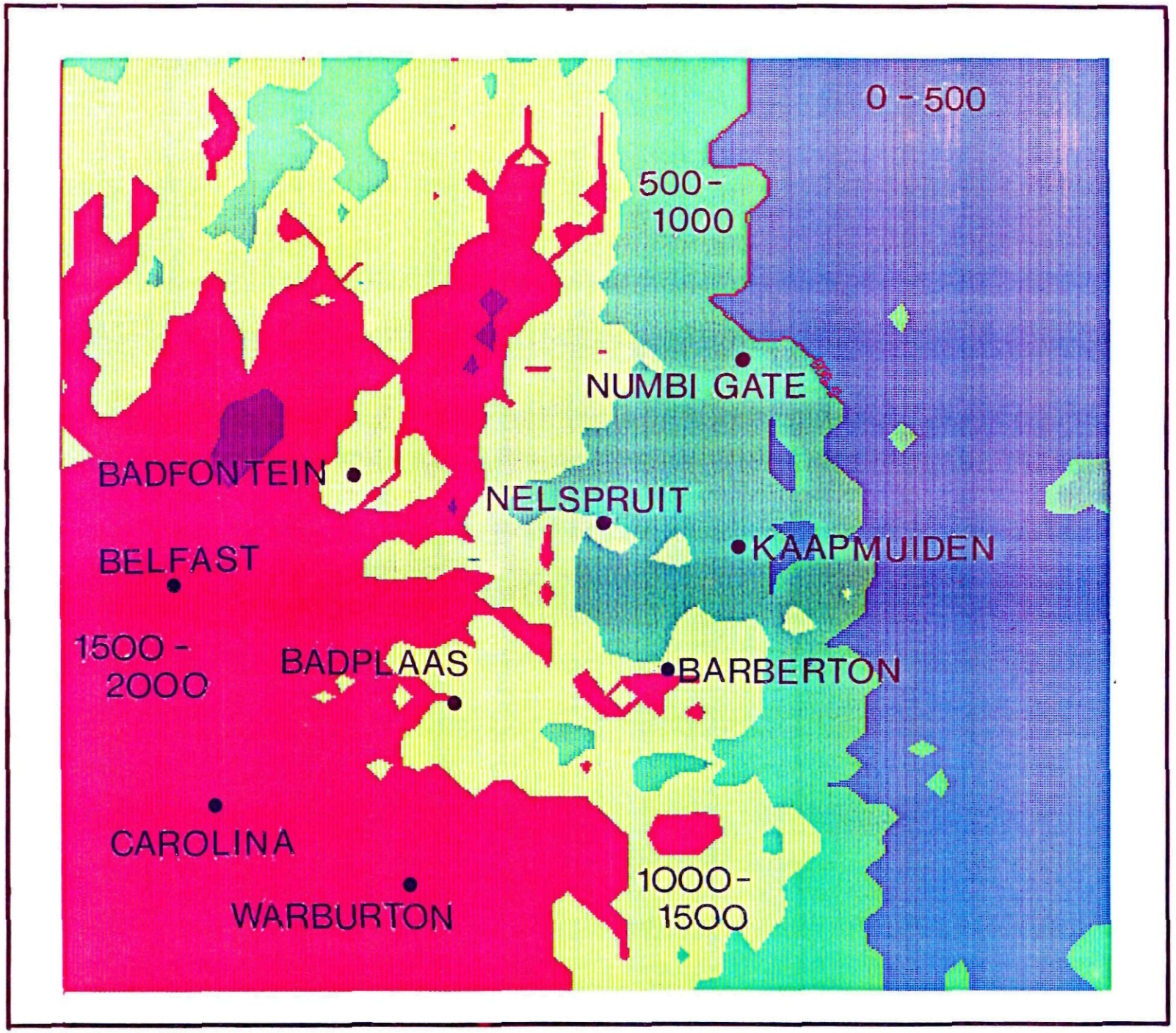

Figure 4.1. Mesoscale network site locations. Elevations of the contoured regions are given in meters above mean sea level.

Table 4.1. Site information.

	Lat.	Lon.	Elevation (m)
Badfontein	25° 24' 13'' S	30° 22' 56'' E	1326
Badplaas	25° 52' 10'' S	30° 36' 9'' E	1119
Barberton	25° 48' 06'' S	31° 03' 22'' E	1289
Belfast	25° 37' 00'' S	30° 00' 28'' E	1865
Carolina	26° 05' 00'' S	30° 05' 00'' E	1683
Kaapmuiden	25° 32' 36'' S	31° 11' 31'' E	1012
Nelspruit	25° 30' 00'' S	30° 55' 00'' E	884
Lower Sabie	25° 07' 21'' S	31° 55' 17'' E	168
Numbi Gate	25° 09' 48'' S	31° 12' 48'' E	640
Warburton	26° 15' 07'' S	30° 30' 06'' E	1762

Badplaas: The tower is located on a treeless peninsula that forms part of the western boundary of the Vygeboom Dam. The exposure is generally good with water within several 100 meters on three sides and flat terrain to the west.

Badfontein: This site is located in the eastern part of the Elands River valley, near the Braam Rabenheimer Dam. The terrain is quite flat in this area, although the escarpment rises sharply, approximately 5 km to the west. The instrument exposure is good in all directions at this site.

Belfast: This site is located several kilometers north of Belfast, on a slight rise of land. The general terrain is slightly rolling. Instrument exposure is good in all directions.

Carolina: This site is located at the Carolina Municipal Airport, 100 meters east of the airstrip. The surrounding terrain is flat, and the instruments have good exposure from all directions.

Warburton: This site is located about 10 km east of Lothair. The local terrain is rolling, and the instruments have good exposure from all directions.

4.1.3 Equipment

A diagram of the instrumentation at each site is shown in Fig. 4.2. The basic components are the power supply system, tower, sensors and data loggers. The rain gauge was not connected to the main system, but rather had its own battery and data logger.

The parameters measured by each station included the two wind components U and V, dry bulb temperature, wet bulb temperature and rainfall (Table 4.2). The data is recorded once every five minutes, and during the site visit is transferred to a portable microcomputer. The microcomputer then transfers the data to the mainframe when back in Nelspruit. It should be noted that the temperature and wind speed measurements are true 5 minute averages, rather than instantaneous samples taken at 5 minute intervals. This is because these sensors produce a frequency train proportional to the measurand, and this train is counted over the total measurement period. A scaled value of the pulse count is saved as the data value.

The rain gauge and its data recorder are the same as is used in the Badplaas rainguage network. This data recorder is based on a semiconductor random access memory which stores the time, date and quantity of tips observed during a five minute interval. It only records information when tips have occurred, and has a capacity to observe approximately 44 hours of rainfall.

Two R. M. Young-Gill propeller anemometers are used to sense wind speed and direction. They are mounted in an orthogonal configuration, and each one produces an output square wave whose frequency is proportional to wind speed. A separate output indicates the direction of rotation.

The psychrometer uses two linear thermistor networks to sense dry and wet bulb temperatures. These are mounted in a housing which provides shielding from solar radiation, and also provides airflow over the sensors. The wet bulb thermistor is kept moist with a reservoir and wick arrangement. An interface converts the thermistor readings to a square wave signal whose effective frequency is proportional to temperature.

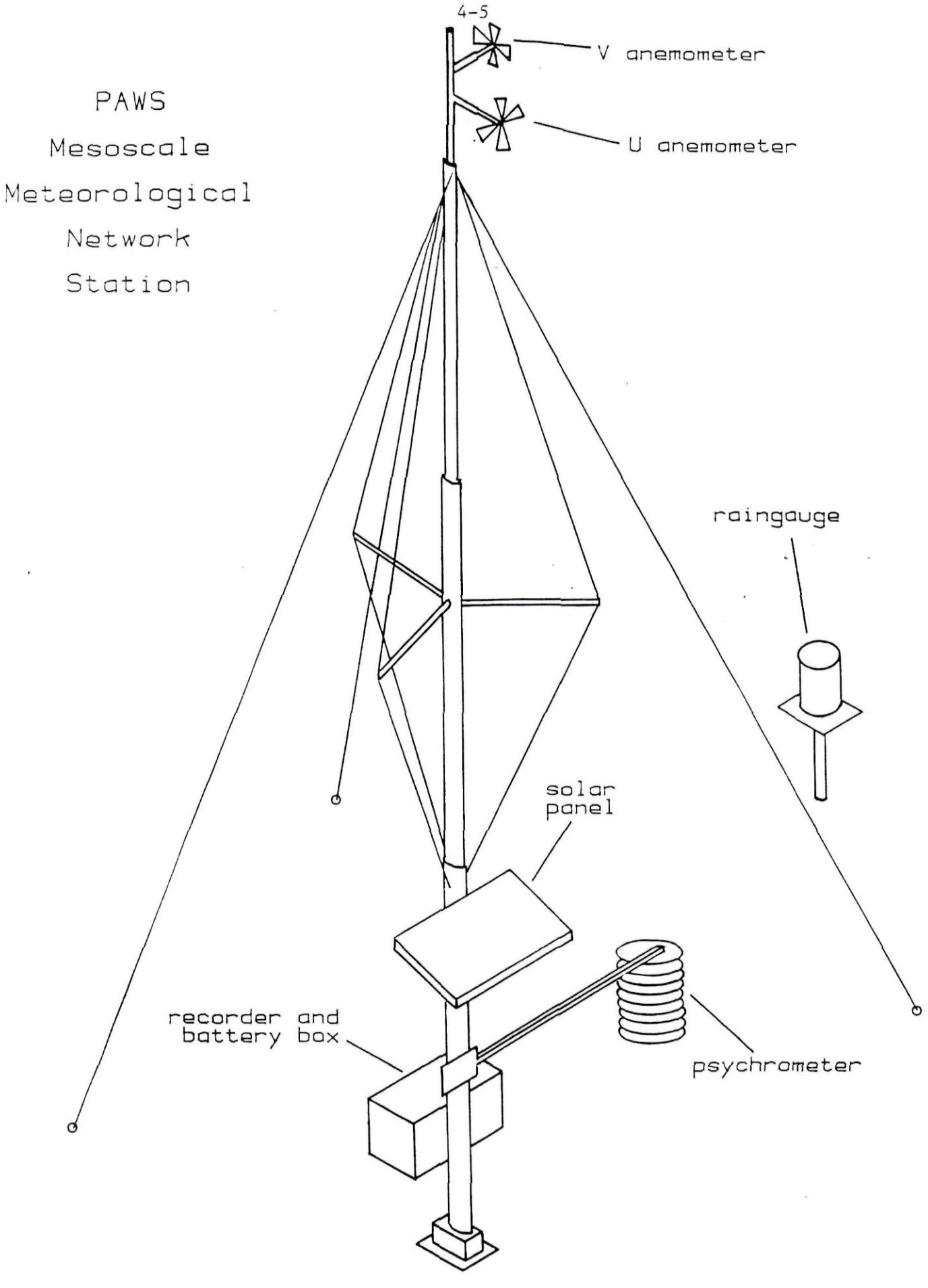

Figure 4.2. Tower and instrumentation.

Table 4.2. Sensor characteristics

Sensor	Transducer	Technique	resolution	accuracy
anemometers	R.M. Young - Gill propeller anemometer	light chopper	0.2 m/s	0.2 m/s
dry and wet bulb thermometers	Fenwall LTN-2 linear thermistor network	R/C oscillator	0.3 deg C	0.6 deg C
raingauge	tipping bucket	counts	0.25mm	0.25mm

Two microprocessor based data loggers, referred to here as solid state recorders, average and store the signals from the anemometers and psychrometer. The software in each recorder is configured for the sensor attached to it, and averages the signal over the sampling period. These averages are stored in erasable, programmable, read only memories (EPROM's). The memories have the desirable characteristic that they will retain data even when power is removed, and can be erased by exposure to ultraviolet light. To dump data from the recorders, a circuit card containing the EPROMs is removed and attached to the portable microcomputer, which saves the data and other information on diskette. A blank EPROM card is inserted in the recorder and the instrument is restarted for a new sampling run.

4.2 DATA SET

4.2.1 Calibration and Conversion to Engineering Units

4.2.1.1 Anemometers

For this discussion it will be convenient to refer to the two anemometers as the u sensor and the v sensor. The two sensors were mounted according to the recommendations of the manufacturer, R. M. Young. They suggest that the main support be a vertical pipe with two tees in line, each one having mounting hardware for one anemometer shaft. The tees are in an orthogonal configuration, when viewed from above. From a side view the tees are separated in height by at least the diameter of one propeller. This separation is made so that the wind shadow of one propeller will not influence the other. A short section of pipe extends vertically above the upper tee at least a distance equal to one half propeller diameter. This is in order to present the upper anemometer with the same wind shadow from the vertical pipe as is seen by the lower anemometer. Thus by presenting the same wind shading effects to both anemometers, a single angle of attack correction can be applied to either sensor. R. M. Young then provides a calibration curve (Fig. 4.3) which was determined for a single anemometer mounted on a shaft which extends vertically above and below the sensor. This curve gives the response of the anemometer in this configuration as a function of the wind direction.

The measurement recorded by the data logger was a count in the range -127 to + 128. This is converted to a nominal wind speed as:

$$speed\ (m/s) = 0.2 * counts$$

To convert the measurements taken by the anemometer into wind speed and direction, the following technique was developed. As stated above, in the given mounting configuration both sensors of the orthogonal pair will have the same response, except that the incident wind angle will be 90 degrees greater for the v sensor than the u sensor. However, since measured values U_N and V_N are uncorrected values, the true wind angle can not be found by taking the arc tangent of the nominal values. Instead the following approach is used to recover the true wind angle from U_N and V_N.

We define the true wind angle as ϕ, and the true wind components as U and V. A calibration curve $C(\phi)$ (Fig. 4.3) as a function of wind direction

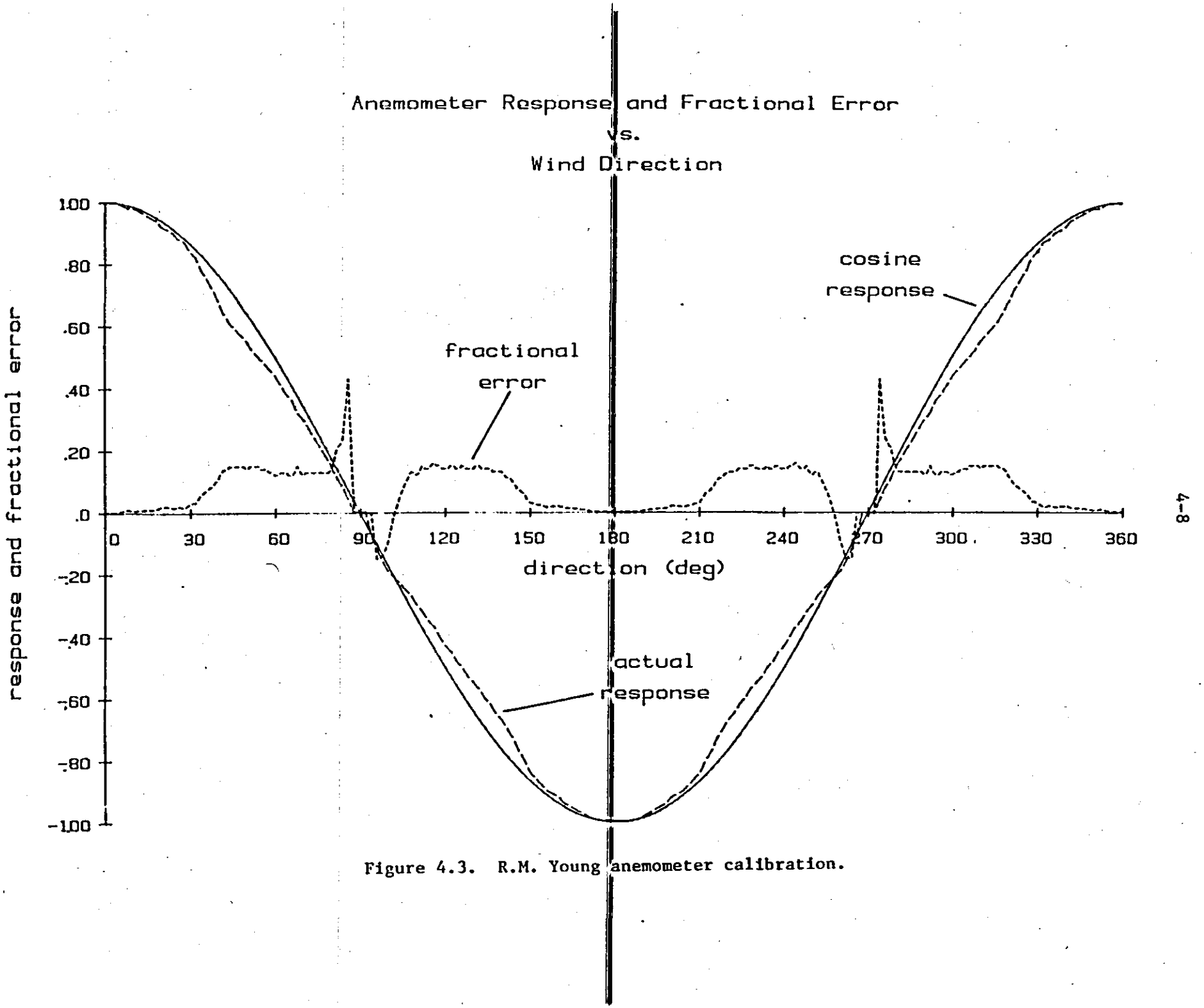

Figure 4.3. R.M. Young anemometer calibration.

is constructed from the R. M. Young calibration, where $C(\phi)$ is the fractional difference between a cosine response and the measurement at a given wind direction. U and V are then related to U_N and V_N as:

$$U = U_N/(1 - C(\phi))$$
$$V = V_N/(1 - C(90 - \phi))$$

Then the true wind angle is given by:

$$\tan(\phi) = V/U = \frac{V_N\ (1 - C(90 - \phi))}{U_N\ (1 - C(\phi))}$$

and

$$\tan(\phi)\ \frac{1 - C(\phi)}{1 - C(90 - \phi)} = \frac{V_N}{U_N}$$

A table (Fig. 4.4) of the right hand side of the above relation as a function of ϕ was computed. Thus, by knowing the ratio of the measured values V_N and U_N, the true wind angle ϕ is obtained from a table look-up.

The true wind components are easily computed from the earlier relations between U, V and U_N, V_N, and ϕ. The wind magnitude is $(U^2 + V^2)^{1/2}$.

4.2.1.2 Psychrometer

The linear thermistor networks are produced with a documented linearity, so that calibration consisted mainly of setting the gains and offsets of the thermistor interfaces for dry and wet sensors. The initial accuracy after calibration was to within .3 deg C over the span 0 to 40 deg C. A post measurement recalibration was not performed, but periodic checks during the experiment suggested that most instruments stayed within an accuracy of about 0.6 deg C.

The calibration of the thermistors simply involved cycling the sensors between cold and hot water baths and adjusting the gain and offset to provide a predefined response. The dry and wet thermistors for a given psychrometer were calibrated together, so that they would track together. The calibration was set so that the data count recorded for the sampling interval could be converted to temperature as:

$$T\ (\text{deg C}) = 0.3 * \text{count}$$

$$T_w\ (\text{deg C}) = 0.3 * \text{count}$$

4.2.1.3 Raingauge

The digital raingauge counted tips of the tipping bucket. Each raingauge was calibrated to give 0.25 mm of rain per tip.

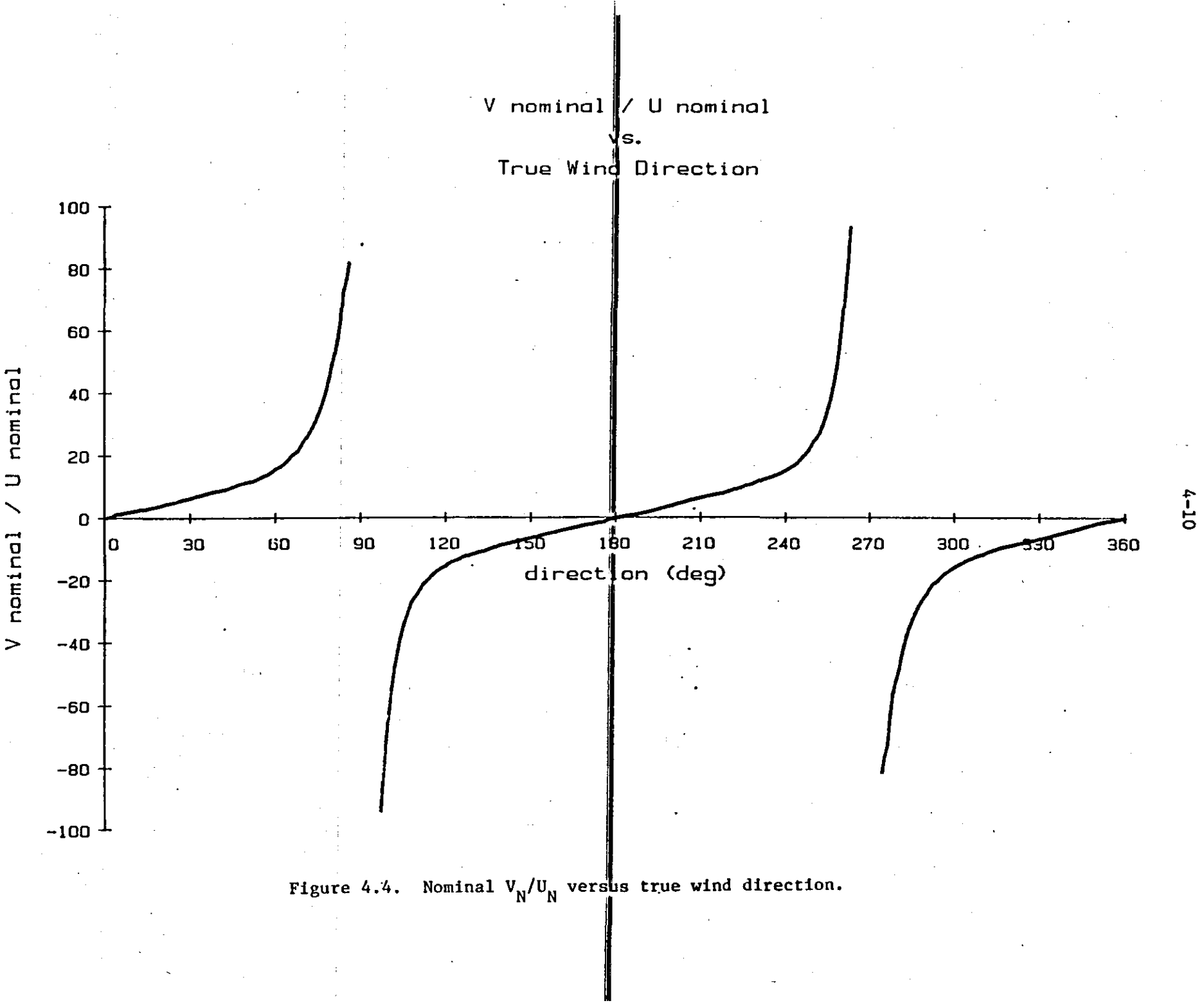

Figure 4.4. Nominal V_N/U_N versus true wind direction.

4.2.2 Coverage

The primary data set obtained from the network consists of the basic measurements made at each site: u and v components of wind velocity, dry and wet bulb temperatures, and rainfall. Figures 4.5 and 4.6 show example plots for one day of data. This type of plot was used to make quality checks of the data. Other meteorological parameters are calculated from quantities in the primary data set when needed for a particular analysis.

Data was collected during the 1984-1985 and 1985-1986 operational seasons. During the 1984-1985 season, problems developed with the psychrometers' thermistor potting method so that temperature data after November of that season are not reliable. Table 4.3 details the extent of the data set coverage.

4.3 ANALYSES

4.3.1 Calculation of meteorological parameters

Certain parameters were often used in the analysis of the mesoscale network data. These variables and the methods used for calculating them are given here.

4.3.1.1 Station pressure

Station pressure in all calculations was taken as a constant for each station, determined from the U. S. standard atmosphere according to the station elevation. It was assumed that the horizontal pressure gradient across the network would be small, and thus departures from the standard atmosphere would produce a small network-wide bias in the calculated thermodynamic values.

4.3.1.2 Dew point temperature

The dew point temperature (T_{dp} deg C) was calculated from the dry bulb temperature (T_d deg C), wet bulb temperature (T_w deg C) and station pressure (P mb) using the following empirical procedure:

$$e0 = 6.11 * 10^{(7.5T_d/237.3 + T_d)}$$

$$e1 = 6.11 * 10^{(7.5T_w/237.3 + T_w)}$$

$$e2 = .00066 * (1 + .00115T_w) * P * (T_d - T_w)$$

$$e = e1 - e2$$

$$g = (\log^{-1}(e) - \log^{-1}(6.11)) / 7.5$$

$$T_{dp} = 237.3 * g / (1 - g)$$

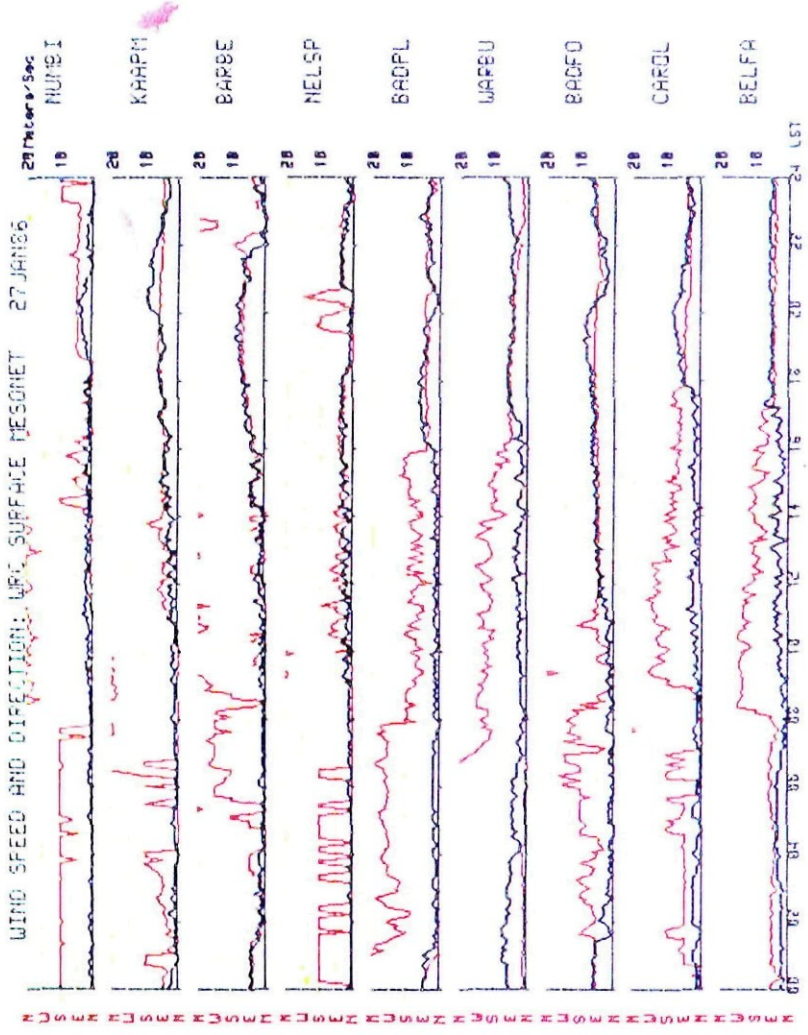

Figure 4.5. Sample anemometer data.

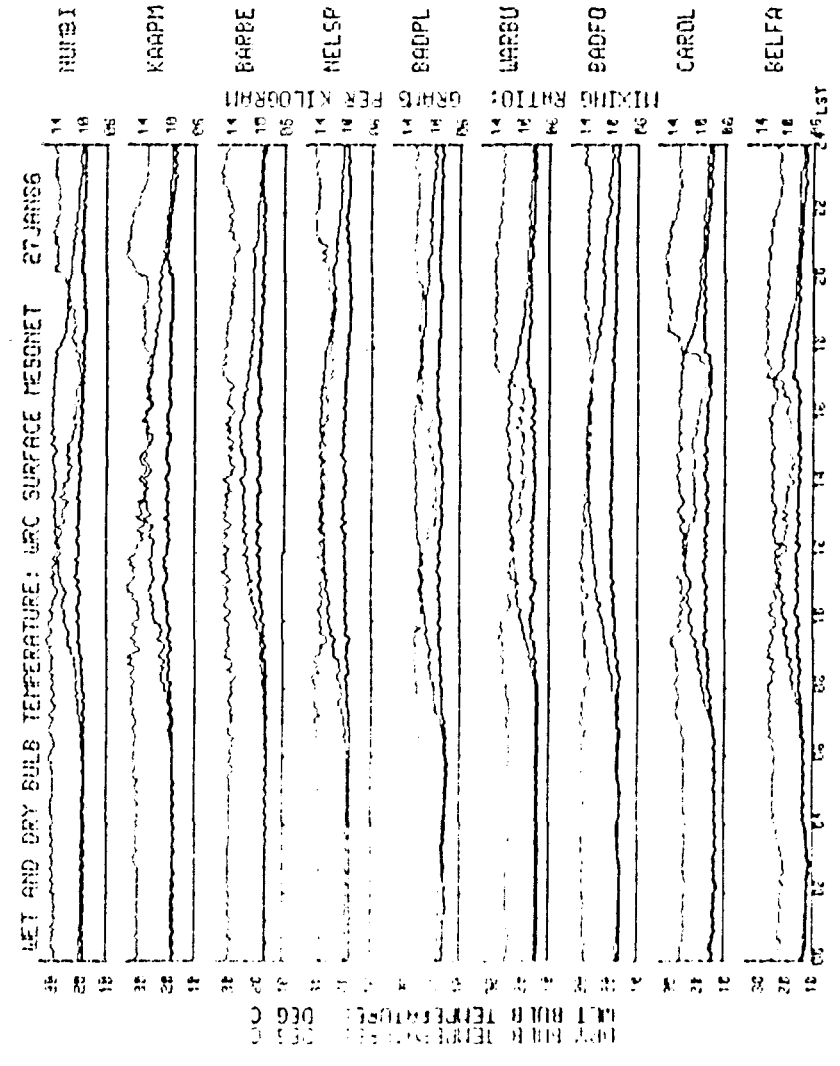

Figure 4.6. Sample of psychrometer data.

Table 4.3. Data set coverage

Season	Sites	Comments
1984-1985, September-March	Lower Sabie, Kaapmuiden, Numbi Gate, Barberton, Nelspruit, Badfontein, Badplaas, Belfast, Warburton	Lower Sabie operated only during November. Numbi Gate wind speeds unreliable after November.
1985-1986, October-March	Kaapmuiden, Numbi Gate, Barberton, Nelspruit, Badfontein, Badplaas, Belfast, Warburton, Carolina	Psychrometer data begins 13 November. Carolina data begins 5 December.

4.3.1.3 Potential temperature

The standard formula for calulating potential temperature (θ deg K) from T_d and P is used:

$$\theta = (T_d+273.15)*(1000/P)^{0.286}$$

4.3.1.4 Mixing ratio and equivalent potential temperature

The mixing ratio (r g/kg) and equivalent potential temperature (θ_e deg K) were calculated using the empirical methods described in Bolton, 1980.

4.3.2 Objective Analysis

In a number of the calculations involving network data it was necessary to interpolate data values between the station locations. The objective analysis method described by Cressman (1959) and modified by Barnes (1973) was utilized to estimate to a regularly spaced grid from the irregularly located stations. Several features of the scheme are particulary useful:

- The area containing interpolated grid points can be defined with an irregular boundary, and thus the area of interest was defined to have a boundary approximately 30 km outside of the outermost stations. Therefore estimates were made only for points which fell between two stations or within 30 km of at least one station.

- A "radius of influence" is a parameter in the scheme. This should relate to the station spacing and in our case was set to 50 km.

- The scheme is iterative in nature, and part of the procedure is to make estimates coincident with the station locations. The estimates at a station location will be based mainly on the data from that location, but will be influenced by errors from the weightings applied to the other stations within the network. When these errors become small enough (ie. the estimate at the station comes close to the observed value) the iteration is terminated. The convergence criteria is appropriately chosen to be the instrument resolution of the given parameter being estimated.

- Stations which do not have data at that particular time are easily removed from the objective analysis.

4.3.3 Mass Divergence and Integrated Mass Transports

Throughout these analyses an attempt has been made to use the mesoscale network as a single integrated sensor with which to characterize network scale processes. With only 9 stations it is impossible to resolve fine details within the network. However, based on our experience wth much denser networks in Florida and Illinois (Ulanski and Garstang, 1978, Cooper et al., 1982), surprisingly realistic patterns do appear in fields created by the objective analysis. It helps to justify these calculations in the sense

that we do not see the objective analysis producing short wavelength signals (noise) which would be simply artifacts of the procedure.

Using objectively analyzed fields of the u and v components of velocity, calculations of some surface mass quantities were performed. These were done for each 5 minute measurement interval so as to provide a time series on the day being analyzed. The grid points for which u and v were calculated are shown in Figure 4.7. All of these calculations depend upon the determination of the divergence at each grid point:

$$\text{div } (1/\text{sec}) = du/dx + du/dy$$

A cubic spline (Ahlberg and Walsh, 1967, Reinsch, 1967) was used to calculate the partial derivatives at each grid point, since a "by product" of the spline calculation is the derivative at the data points. The advantage of the spline is that it attempts to produce "smooth" fits to the data, and the derivatives are defined at the actual grid points. A simple finite difference would produce derivatives between the grid points, and a centered finite difference would smooth over three data points. In addition, a controlled amount of smoothing can be specified for the spline, and once again it was specified to be related to the resolution of the instrument.

The procedure was a simple one of fitting the cubic spline first to all of the x transects of u in the interpolated grid, and saving the derivatives for each grid point. Next the same is done for y transects of v, and finally the du/dx and dv/dy terms summed to give the divergence at each grid point. Using these values, the following time series were produced:

- The area averaged divergence computed from the total of the divergence over all grid points divided by the number of grid points.

- Total upward mass transport within the network was also obtained. This calculation is the sum of mass transports at grid points showing negative divergence. Assuming a linear wind profile with 0 at the surface to the value measured at the anemometer height, the average divergence within this layer is half the amount calculated at height. The upward mass transport is thus determined from:

$$\text{transport (cubic meters/ sec)} = (\text{divergence}/2) * \text{deltax} * \text{deltay} * h$$

  where:

  h - anemometer height
  deltax - grid box x dimension
  deltay - grid box y dimension

- Total downward mass transport within the network is calculated in the same manner as the upward mass transport, but using only grid points showing positive divergence.

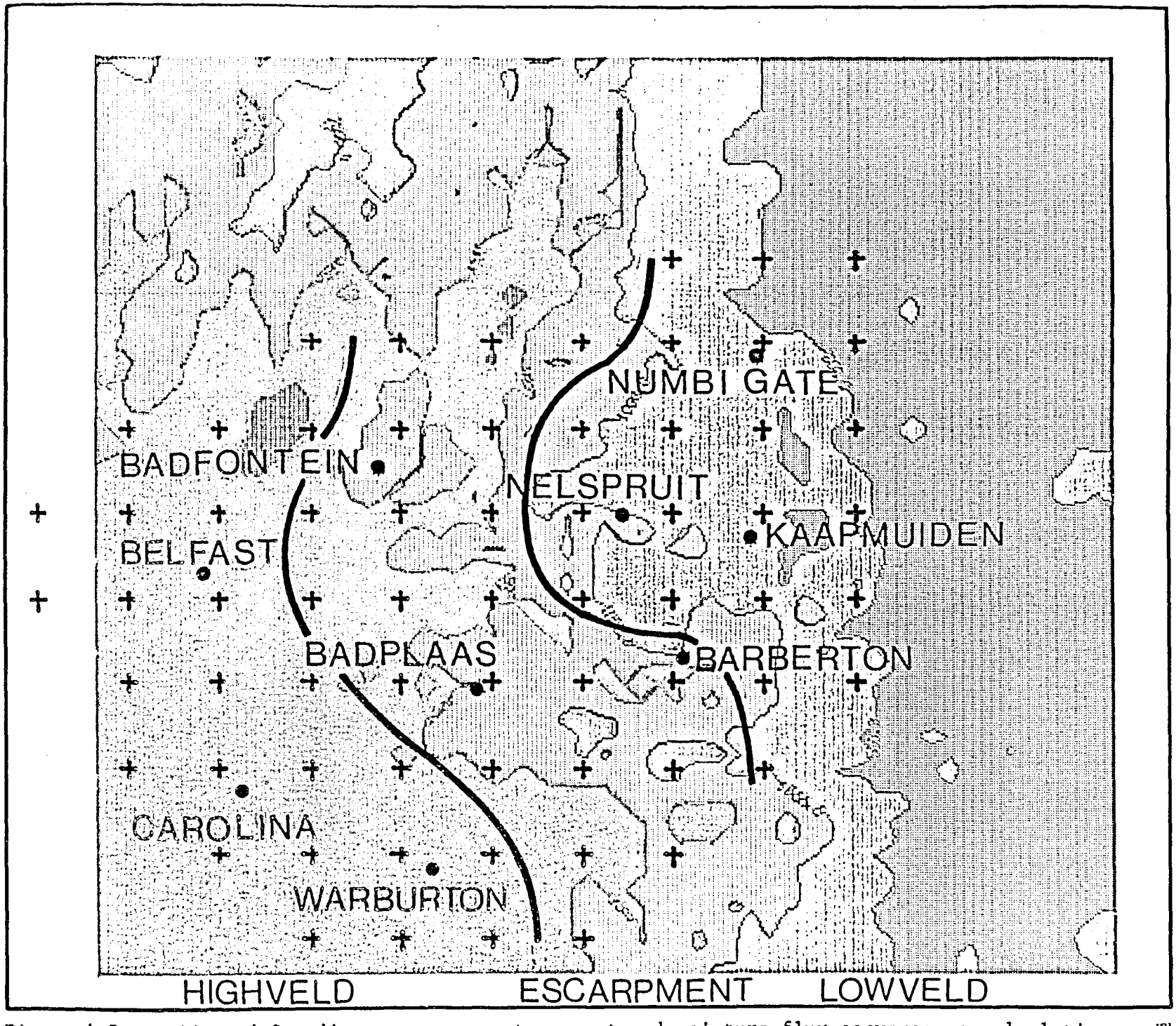

Figure 4.7. Grid used for divergence, mass transport and moisture flux convergence calculations. The three regions used in the moisture flux convergence analysis are delineated. Elevation contour indices are the same as in Fig. 4.1.

- Integrated mass transport is the net mass transport (sum of the upward and downward components) within the network. This is determined for each 5 minute interval, and integrated throughout the day, choosing 0600 LST as an arbitrary starting point.

4.3.4 Moisture Flux Convergence

The moisture flux is the product of the wind vector and mixing ratio. This quantity was calculated for each of the stations, and then interpolated to the grid using the objective analysis. The divergence of the moisture flux was then calculated in order to examine the inflow or outflow of moisture within the network. In addition, the grid was subdivided into three regions, based upon elevation and location, characterized as highveld, escarpment and lowveld areas (Figure 4.7). Time series of the moisture flux convergence for each area were produced to investigate correlations between the moisture regimes in each area and convective activity within the network.

4.3.5 Continuing Efforts

A sample of objectively analyzed wind and θ_e fields is shown in Fig. 4.8. In this case a finer grid has been utilized than is used in the calculations described earlier. The objectively obtained wind field is depicted by the wind vectors at each grid point. The objectively obtained θ_e field is shown by dashed contours, and the calculated divergence field is indicated by solid contours.

Several additional calculations are being explored or considred at present. These include examination of relationships between surface data and upper air measurements, such as determination of the LCL from the network data and its behavior across the network, relationships between thermodynamic quantities at the surface and those measured by the aircraft, and statistical analysis of surface data (means, variances, max's and min's) when stratified by various parameters, such as 800 mb flow, etc.

Preliminary work has been done using least square fits of a surface to the network data to characterize the network scale responses. This has a computational advantage over the objective analysis, being several orders of magnitude more efficient. A simple plane fit will provide a magnitude and direction of the maximum gradient across the network, and thus provide good indicators of network wide forcings (or responses). Preliminary plane fits to the u and v fields and calculation of the network wide divergence from the resulting gradients shows almost exact agreement with the results from the objective analysis. Plane fits to the θ_e and mixing ratio fields show interesting behavior as well. The fitting of higher order surfaces, such as a sphere, may also have interesting implications.

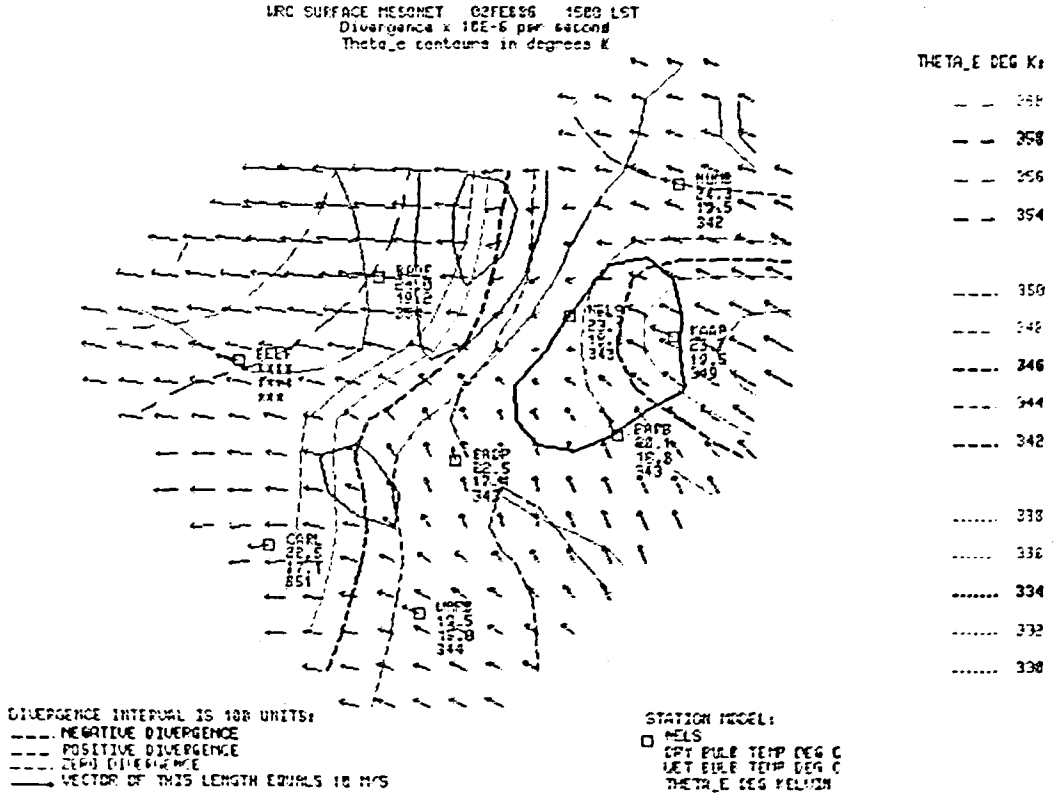

Figure 4.8. Typical objective analysis of surface wind and θ_e fields, and divergence calculations.

5.0 THUNDERSTORM OUTFLOW AND INTERACTION ALGORITHM

5.1 INTRODUCTION

The algorithm is a parameterization of some of the dynamic processes which drive larger storms and deals with the mature and decaying stages of the parent storm's lifecycle and the potential development of new convection. Complex storm systems are simulated by constructing the entire storm system from a number of "differential" cylinders one kilometer in radius. Basic potential flow theory is applied to each cylinder with base at the ground and top at a level where the vertical speed is taken to be zero. A downdraft is initiated within the cylinder at some height H, above the ground level. The effects of the imposition of the downdraft on the infinite fluid surrounding the cylinder conforms to flows that have been observed around precipitating systems.

Although there is no thermodynamical treatment in the simulation scheme, the imposition of the downdraft is in essence a parameterization of the microphysical and dynamical forces which produce local downdrafts, and the imposition of the lid at the top of a given cylinder parameterizes the upper level stability and the dynamic controls which operate on the whole system on larger scales. The combination of the two yields flow patterns similar to those which have been observed at all levels.

Recent years have seen increasing recognition within the scientific community of the importance of larger than storm scale motions and fluxes of moisture on the development of convective complexes and their production of rainfall.

A study of convective rainfall in Florida by Cooper et al. (1982) yielded two basic results:

1. Under conditions of almost constant lapse rate of temperature, there was found a good relationship between the flux of mass into the surface layers, and the amount of rainfall associated with that flux (see Figs. 5.1 and 5.2).

2. The development of convective complexes (which produce the most rainfall) appeared to depend upon the interactions between thunderstorm outflows and the larger scale convergence, which organized mesoscale areas of flux convergence within which convective scale interactions took place (Fig. 5.3).

The first result allows an association to be made between low-level radar estimations of rainfall, and the probable position and intensity of downdrafts can be broadly estimated from radar. In the Florida study, it was also noted that the near surface divergence (approximately 10.0 m height) when measured on a spatial scale of about 5 kilometers was consistently on the order of 10^{-3} sec^{-1}. Application of the algorithm can then be used to simulate the wind patterns which result when any number of storms are present over the area of interest, and allows us to display the general spatial distribution of small scale upward and downward motions.

A diagnostic use of the potential flow algorithm provides an objective method of evaluating low level ($\sim$ 1000 m) flow field in regions of convective activity and the nature of the storm/storm interaction.

Figure 5.1. The average vertical mass transports downward through 4 meters height estimated from observations of near surface divergence beneath precipitating summertime convection in south Florida.

The near-surface vertical velocities were observed using a high resolution ($\sim$ 5 x 5 km) surface wind-set array. More than 100 storms were observed. Knowledge of the surface rainfall from radar will allow estimates of downdraft intensity and location.

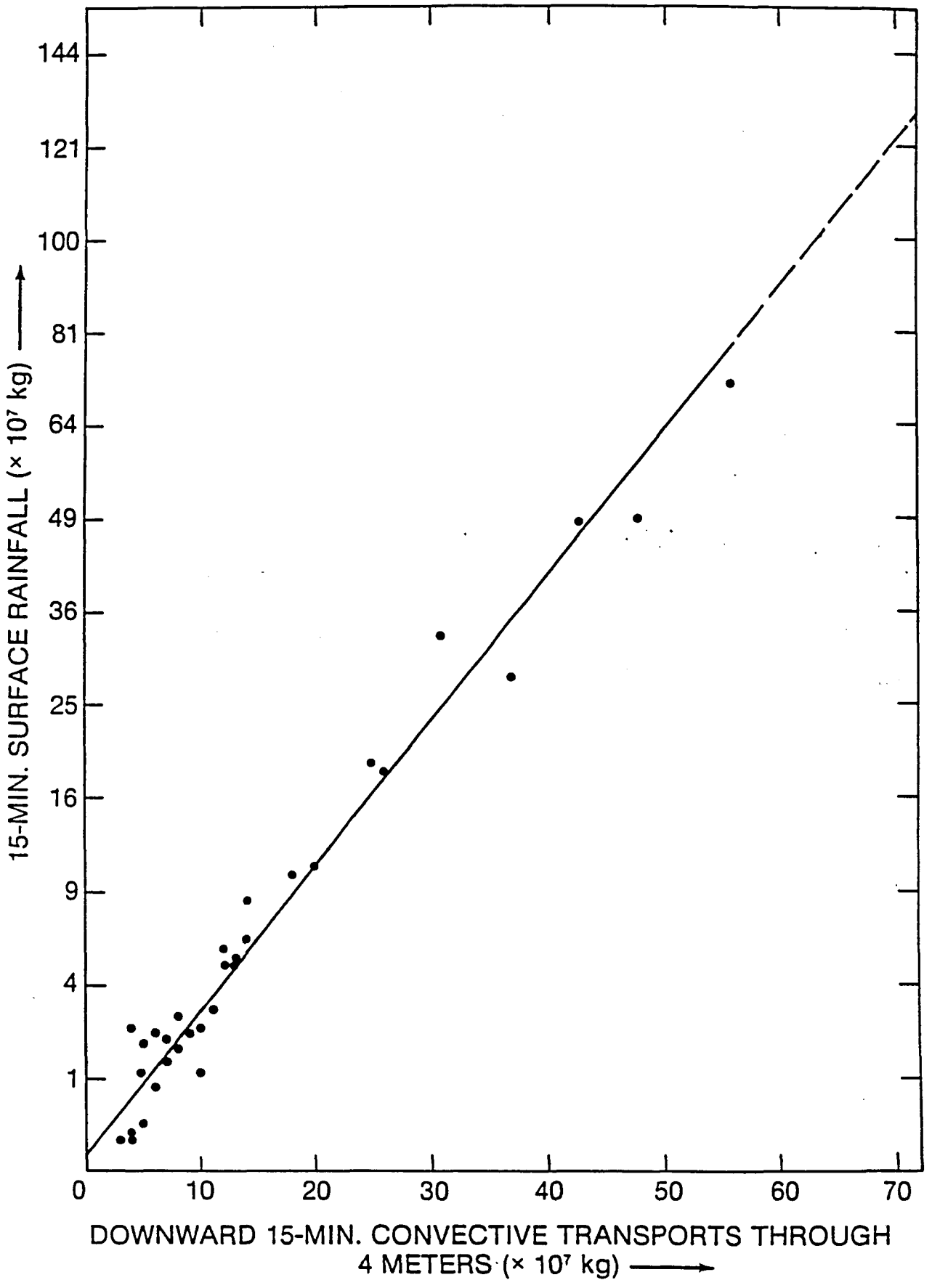
144
121
100
81
64
49
36
25
16
9
4
1
15-MIN. SURFACE RAINFALL (× 10⁷ kg)
0
10
20
30
40
50
60
70
DOWNWARD 15-MIN. CONVECTIVE TRANSPORTS THROUGH
4 METERS (× 10⁷ kg)

Figure 5.1.

Figure 5.2. (a) An example of spatial relationship between surface rainfall and vertical transports through the surface layer. These observations were made in Florida during FACE (Florida Area Cumulus Experiment) 1975. The network scale surface convergence is shown by the solid line. The upward (dashed-dot) and downward (dashed) "convective scale" transports are due only to grid scale divergence $\geq |\pm 4 \times 10^{-4}| s^{-1}$.

(b) The shaded areas are regions of divergence with isolines of divergence in units of 10^{-4} sec^{-1}. Rainfall is shown as closed circles for heavy rain ($\geq$ 1.5 cm in 5 min) and open circles for light rain (< 1.5 cm in 15 min). Radar echo return intensities from the Miami WSR-57 radar are shown by solid lines.

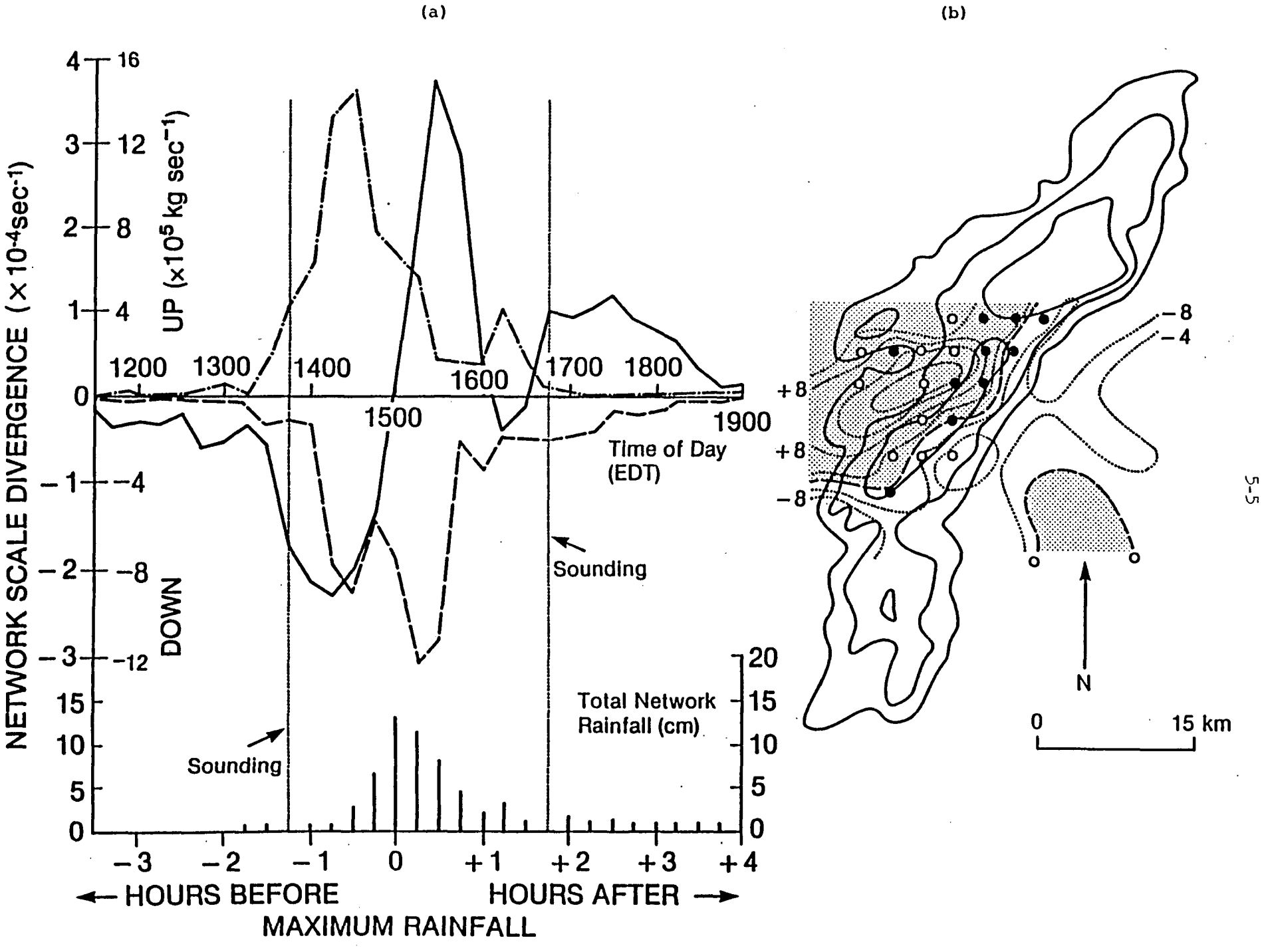
(a)
(b)
NETWORK SCALE DIVERGENCE (×10⁻⁴sec⁻¹)
UP (x10⁵ kg sec⁻¹)
DOWN
4
3
2
1
0
−1
−2
−3
16
12
8
4
−4
−8
−12
1200
1300
1400
1500
1600
1700
1800
1900
Time of Day (EDT)
Sounding
Sounding
Total Network Rainfall (cm)
20
15
10
5
0
−3
−2
−1
0
+1
+2
+3
+4
← HOURS BEFORE
HOURS AFTER →
MAXIMUM RAINFALL
+8
+8
−8
−8
−4
N
0
15 km

Figure 5.3. The relationships found in Florida between larger scale convergence and convective scale mass transports through the surface layer. The solid line is the rate of change of the peninsular scale convergence estimated by Frank (1967). The dashed line is the upward convective scale transports measured through 5 m, and the dash-dot line is the downward convective scale transports. The dotted line is the ratio of the upward transports to downward convective scale transports.

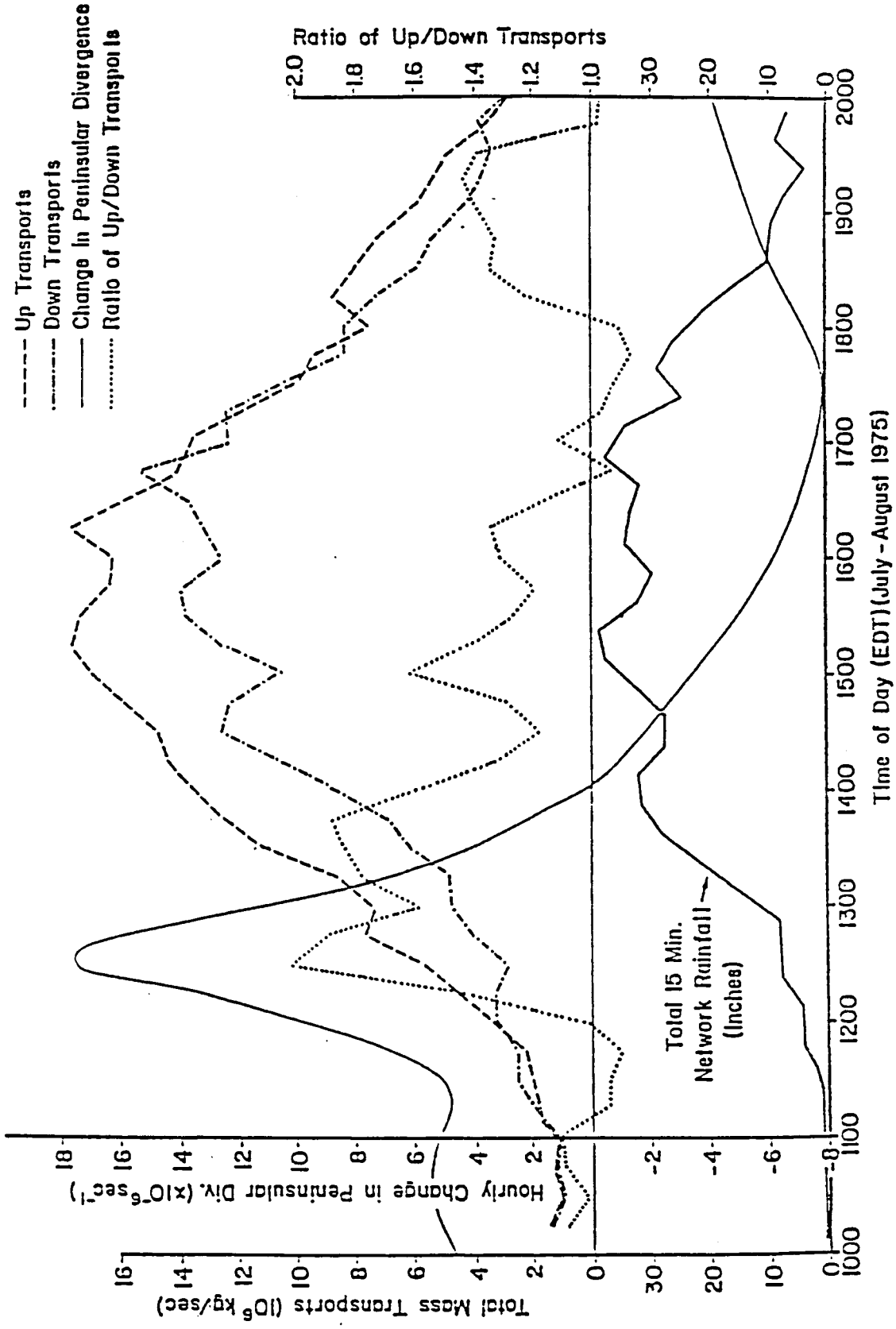
Up Transports
Down Transports
Change in Peninsular Divergence
Ratio of Up/Down Transports
Ratio of Up/Down Transports
Total Mass Transports (10^8 kg/sec)
Hourly Change in Peninsular Div. ($\times 10^{-6}$ sec^{-1})
Total 15 Min. Network Rainfall (Inches)
Time of Day (EDT) (July - August 1975)

5.2 THEORY

There have been many attempts to completely model the evolution of a convective storm from basic equations (e.g., Schlesinger, 1975). Due to the nature of the problem, any three-dimensional convective cloud model which is capable of simulating the growth and decay of a convective storm is inevitably very complex, expensive and time-consuming. In addition, few can also simulate storm to storm interactions. These elaborate models also require access to large, fast computing machines.

The basic equations for such a model take the form (from Lilly, 1979):

(1) $\frac{d\vec{V}}{dt} = -\vec{\nabla} p/\rho - g\hat{k}$ Equation of motion

(2) $\frac{d\rho}{dt} = -\rho \vec{\nabla} \cdot \vec{V}$ Equation of mass continuity

(3) $\frac{d\theta_e}{dt} = 0$ Equation of thermodynamic energy

(4) $\frac{d}{dt}(q_v + q_e + q_i) = 0$ Equation of water substance conservation

If density is assumed constant following a parcel, and the density is approximately 1.0 kg m^{-3}, then equation (2) becomes

$$\vec{\nabla} \cdot \vec{V} = 0 \tag{5}$$

That is, this equation constrains solutions included in Eqns. (1), (3), and (4), subject to the appropriate boundary and initial conditions. Under these conditions, eq. (2) is the simplest of all of the above equations to deal with, and may be thought of as providing the background framework (in the necessary compliance with continuity) within which the other equations must operate.

Since any vector field $\vec{V}$ can be written as the sum of irrotational and non-divergent parts, we may write

$$\vec{V} = \vec{V}_r + \vec{V}_d$$

where $\vec{V}_r$ is a non-divergent vector field and $\vec{V}_d$ is an irrotational vector field. Then from eq. (5)

$$\vec{\nabla} \cdot \vec{V} = \vec{\nabla} \cdot (\vec{V}_r + \vec{V}_d) = 0$$

$$= \vec{\nabla} \cdot \vec{V}_r + \vec{\nabla} \cdot \vec{V}_d \cdot$$

Since $\vec{V}_r$ is non-divergent,

$$\vec{\nabla} \cdot \vec{V} = \vec{\nabla} \cdot \vec{V}_d = 0 \tag{6}$$

in this case. Since $\vec{V}_d$ is an irrotational field (6) may be written in terms of a velocity potential as

$$\vec{\nabla}^2 \phi = 0 \tag{6a}$$

where $\vec{\nabla}\phi$ represents the irrotational part of the velocity field and $\vec{\nabla}\phi = \vec{V}_d$.

The flow in intense thunderstorm downdrafts is, of course, highly rotational, but, if we consider the rotation during the mature stage of the storm to be confined mostly to the high shear zones at the surface and along the edges of the downdraft/updraft region, it is profitable to consider the irrotational part of the flow field and compare solutions of (6a) to observed wind fields around raining convection, in the hope that the broad nature and sense of the flow can be obtained easily and simply via an application of potential flow theory.

It may be mentioned at this point that the variation in density across lines of equal potential, which must be expected in real thunderstorm outflows does not invalidate the application of potential flow theory, but it must be assumed that mixing does not occur. We consider only the downdraft branches of the storm circulation assuming, for the time being, that the location and strength of the downdrafts can be estimated in the lower levels by surface instrumentation or radar observations.

The general approach is to break the downdraft region down into small ($\simeq$ 1 km radius) cylinders, each with its base at the surface and its top at some level T, and then to solve (6a) for each cylinder together with appropriate boundary conditions, taking into account a measured vertical speed in each small cylinder of WM m s^{-1} at z = M.

For a given cylinder, in cylindrical co-ordinates:

(7) $\vec{\nabla}^2\phi = 0$

(8) $w(r,z) = \frac{\partial\phi}{\partial z}$, $u_r(r,z) = \frac{\partial\phi}{\partial r}$, (u_r is the radial velocity in the horizontal, w is the vertical velocity)

(9) $w(r,0) = 0$

(10) $w(r,M) = WM$ which is measured at z = M

(11) $w(r,H') = 0$ for some H' such that $0 < M < H' \leq T$

(12) $w(r,T) = 0$.

It is also required that ϕ remain finite within the small cylinder of radius R. Axial symmetry for each small cylinder is also assumed. The assumption of axial symmetry for each small cylinder does <u>not</u> mean that assymetric flows cannot be represented, since the overall flow in the downdraft region is taken to be the accumulated effect (in the sense of Gauss' theorem) of many small "differential" cylinders similar to the one now under consideration.

The solution to (7), (9), (10) and (12) above is well known. It is:

$$\chi(r,z) = A \cos(az)\, I_o(ar) \qquad (13)$$

where $0 \leq z \leq T$; $0 \leq r \leq R$, and $I_o(ar)$ is a zero-order modified Bessel function. However, (13) cannot simultaneously satisfy (7), (8), (9), (10), (12)

and also (11).

The conditions in (11) reflect the requirement that the downdraft must originate ($w(H') = 0$) at some level in the troposphere. To satisfy (11), use is made of the well-known solution for potential flow near a stagnation point (see Batchelor, 1970), which is

$$\psi(r,z) = k(z^2 - \frac{r^2}{2}) \quad .$$

This potential is chosen in keeping with the general philosophy of providing the simplest overall solution. Then

$$\phi(r,z) = \chi(r,z) + \psi(r,z) \tag{14}$$

or

$$\phi(r,z) = A \cos(az)\ I_o(ar) + k(z^2 - \frac{r^2}{2}) \quad . \tag{15}$$

Then the vertical speed is given by

$$\frac{\partial \phi}{\partial z} = -a\ A \sin(az)\ I_o(ar) + 2\ kz = w(r,z) \tag{16}$$

and the radial velocity is given by

$$\frac{\partial \phi}{\partial r} = a\ A \cos(az)\ I_1(ar) - kr = u_r(r,z) \tag{17}$$

An average vertical velocity, $\bar{w}$, is defined for each differential cylinder as follows

$$\bar{w}(z) = \frac{1}{A} \int_A w(r,z)dA \tag{18}$$

where A is the horizontal area of the differential cylinder. Then

$$\bar{w}(z) = \frac{1}{\pi R^2} \int_o^{2\pi} \int_o^R w(r,z)rdrd\theta \quad . \tag{19}$$

Since

$$w(r,z) - -a\ A \sin(az)\ I_o(ar) + 2\ kz \tag{20}$$

$$\bar{w}(z) = \left[\frac{-a\ A \sin(az)}{\pi R^2} \int_o^{2\pi} \int_o^R I_o(ar)rdrd\theta\right] + \int_o^{2\pi} \int_o^R \frac{2kz}{\pi R^2}\ rdrd\theta, \tag{21}$$

so that

$$\bar{w}(z) = -\frac{2}{R} A \sin(az)\ I_1(aR) + 2kz \tag{22}$$

(12) is satisfied if

$$\bar{w}(T) = -\frac{2A}{R} \sin(aT)\ I_1(aR) + 2kT = 0 \tag{23}$$

therefore,

$$A = \left[\frac{kTR}{\sin(aT)\ I_1(aR)}\right] \tag{24}$$

(10) is satisfied if $\bar{w}(M) = -\frac{2}{R} A \sin(aM)\ I_1(aR) + 2kM$ (25)

therefore

$$k = \frac{\bar{w}(M)}{2}\left[\frac{\sin(aT)}{M \sin(aT) - T \sin(aM)}\right] \tag{26}$$

Setting

$$F = M \sin(aT) - T \sin(aM) \quad (T \neq M,\ M <) \tag{27}$$

and substituting for k and A in (20) yields

$$\bar{w}(z) = \frac{\bar{w}(M)}{F}\left[z \sin(aT) - T \sin(az)\right] \tag{28}$$

for the vertical speed, and

$$u_r(R,z) = \frac{\bar{w}(M)}{2F}\left[RTa \cos(az) - R \sin(aT)\right] \tag{29}$$

for the horizontal radial speed. All of the conditions in (7)-(12) are satisfied by (28) and (29) with the exception of (11).

In eq. (14), the total potential is broken down into two independent potentials $\chi(r,z)$ and $\psi(r,z)$. $\chi(r,z)$ may be thought of as the convective potential, i.e., representing the potential field generated by microphysical processes and cloud scale dynamics. $\psi(r,z)$ may be thought of as a restraining potential which operates over the entire troposphere and which reacts to and constrains the convective potential, imposing the required conditions on the larger tropospheric scale. The convective potential is, therefore, chosen such that the vertical speeds generated by it go to zero at z = H. That is,

$$a = \frac{\pi}{H} \qquad \text{(where H is not always the same as H')} \tag{30}$$

Then

$$\bar{w}(z) = \frac{\bar{w}(M)}{F}\left[z \sin\left(\frac{\pi T}{H}\right) - T \sin\left(\frac{\pi z}{H}\right)\right] \tag{31}$$

and

$$u_r(R,z) = \frac{\bar{w}(M)}{2F}\left[\frac{RT\pi}{H}\cos\left(\frac{\pi z}{H}\right) - R \sin\left(\frac{\pi T}{H}\right)\right] \tag{32}$$

Since we must require the flow to be irrotational, there is a full slip condition at z = 0.

Equations (14) through (32) deal with the flow inside and at the boundaries of a differential cylinder of radius R.

Immediately outside the cylinder, the vertical speed is assumed to be zero. We require that the first derivative of the radial speed be continuous at r = R. This gives

$$u(r,z) = (C + 2)\, u(R,z)\, \frac{R^c}{r^c} - (C + 1)\, u(R,z)\, \frac{R^{C+1}}{r^{C+1}} \quad ,$$

for r > R, and C is a constant,

and the vertical speeds at each location outside the cylinder are estimated by vertical integration of the convergence in the horizontal winds.

Since there is, at present, no frictional or turbulent dissipation in the algorithm, for the sake of simplicity, the winds are calculated at the estimated boundary layer height, and a power profile is applied to reduce the wind speeds to observed magnitudes in the near surface levels.

In the real-data comparison in Figs. 5.4(a) and 5.4(b) a roughness of 4.0 cm yields a boundary layer $\sim$ 300 m thick and a coefficient (n) of 6.0 (Plate, 1971). The power profile used in this case is therefore:

$$u(z) = u(h)\left(\frac{z}{h}\right)^{\frac{1}{n}}$$

$$u(z) = u(300)\left(\frac{z}{300}\right)^{\frac{1}{6}} \qquad z \leq 300 \text{ m}$$

where 300 m is the top of the boundary layer.

The wind fields inside the cylinder can be adjusted by the user so as to fit the estimated stage (mature, decaying), and cell top height of the cells being observed by the radar. The best estimate of cell top height may be taken from the dBz - top height relationship found by Gagin and Lopez (1985) (see also Adler and Mack (1984)). An estimate is then made of the speed of translation of the storm, either from current radar observations or the current sounding. The cylinder is then translated at this speed and the advective effects of the translation into the observed low level flow produce convergence in the low level wind fields on the appropriate flank of the cylinder.

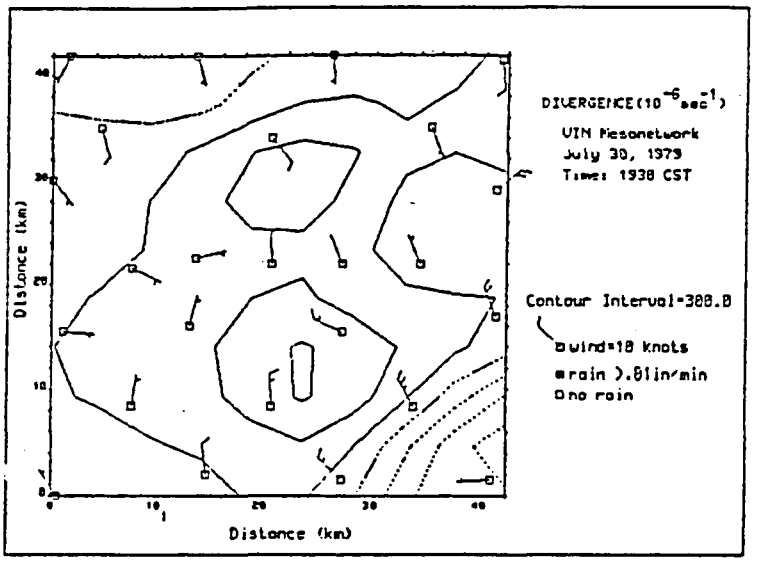

Figure 5.4(a). The observed winds beneath the 30 July 79 VIN storm.

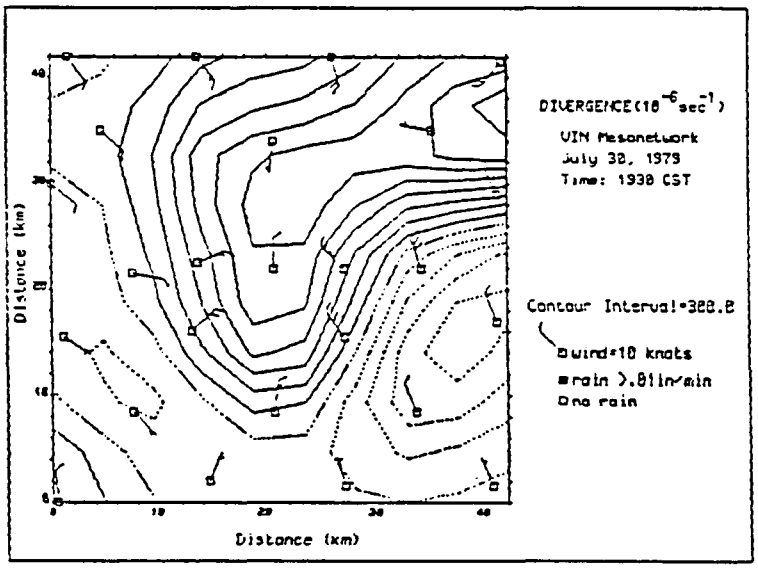

Figure 5.4(b). The winds produced by the algorithm for the 30 July 79 VIN storm.

Using the basic building block described above, we can assemble them to simulate any storm complex observed by a conventional radar. An attempt to do this has been made using conventional PPI observations taken by the CHILL radar during the Virginia/Illinois/NOAA experiment in 1979. Figure 5.4(a) shows the wind fields observed by the PAM network at 1930 LST, and Fig. 5.4(b) shows the estimated wind fields calculated for the same time using the algorithm, the radar and the local conventional sounding.

In summary:

1) The conventional radar PPI is used to identify areas where rainfall generated convective scale downdrafts are likely to be occurring (currently defined as anywhere dBz $\geq$ 35.0).

2) The conventional sounding is used to determine the wind shear in the environment surrounding the storm complex.

3) The algorithm then associates a cylindrical outflow pattern at 10 meters height with each selected radar pixel.

4) The vertical and horizontal flow are calculated inside and outside each cylinder.

5) The cylindrical flows are put together and advected in the direction of the shear vector to give estimates of the winds over the entire domain of the storm complex.

In order to preserve short computation time ($\leq$ 1 minute) for a large field, care has been taken to preserve the simplicity of the scheme whenever possible and to maintain the independence of each solution. The downdraft profile, heights of origin of downdrafts, function profiles, can all be improved. But even with these crude representations, the general sense and intensity of the low level wind fields can be simulated..

5.3 DISCUSSION

5.3.1 Inside the Cylinder

Figures 5.5(a) through 5.5(f) show the results of running the simulation for R (the radius of the downdraft region) of 2.5 km, for a 'measured' downward speed of 10 m/sec at 2000 m and for tropopause heights of 10, 13 and 15 km. In each of the figures, the parameter H was assigned values of 4000 m, 6000 m, 8000 m and 10,000 m.

As H increases toward the height of the tropopause, the nature of the flow in the cylinder changes from a flow suggestive of growing/mature storms (upward and downward speeds present) to a flow suggestive of a dissipating/mature storm (downward speeds throughout the troposphere). There is radial outflow in the low levels, inflow in the mid levels and outflow aloft in the mature growing stage. Examination of the many subjective storm flow patterns based upon observations (Fig. 5.6) reveals that the schematic flows presented in Fig. 5.6 can be represented in terms of the circulations represented in Figs. 5.5(a) through 5.5(f) (Newton, 1963; Browning and Ludlam, 1962; Moncrieff and Miller, 1976).

From these figures it can be seen that there appears to be a 'phase shift' in the nature of the simulated flow as the level of initiation of the downdraft

Figures 5.5(a), (b) and (c). The magnitude of the radial velocity, u(R,z), as a function of height for 4 values of H. H is the level at which the downdraft originates. The values are for a cylinder 2.5 km radius, with "measured" vertical speed of -10 m s^{-1} at 2.0 km height (AGL). T is set as indicated. The solid lines are flows for H = 4000 m, the two-dashed lines are for H = 6000 m, the single-dashed lines are for H = 8000 m and the dash-dot lines are for H = 1000 m.

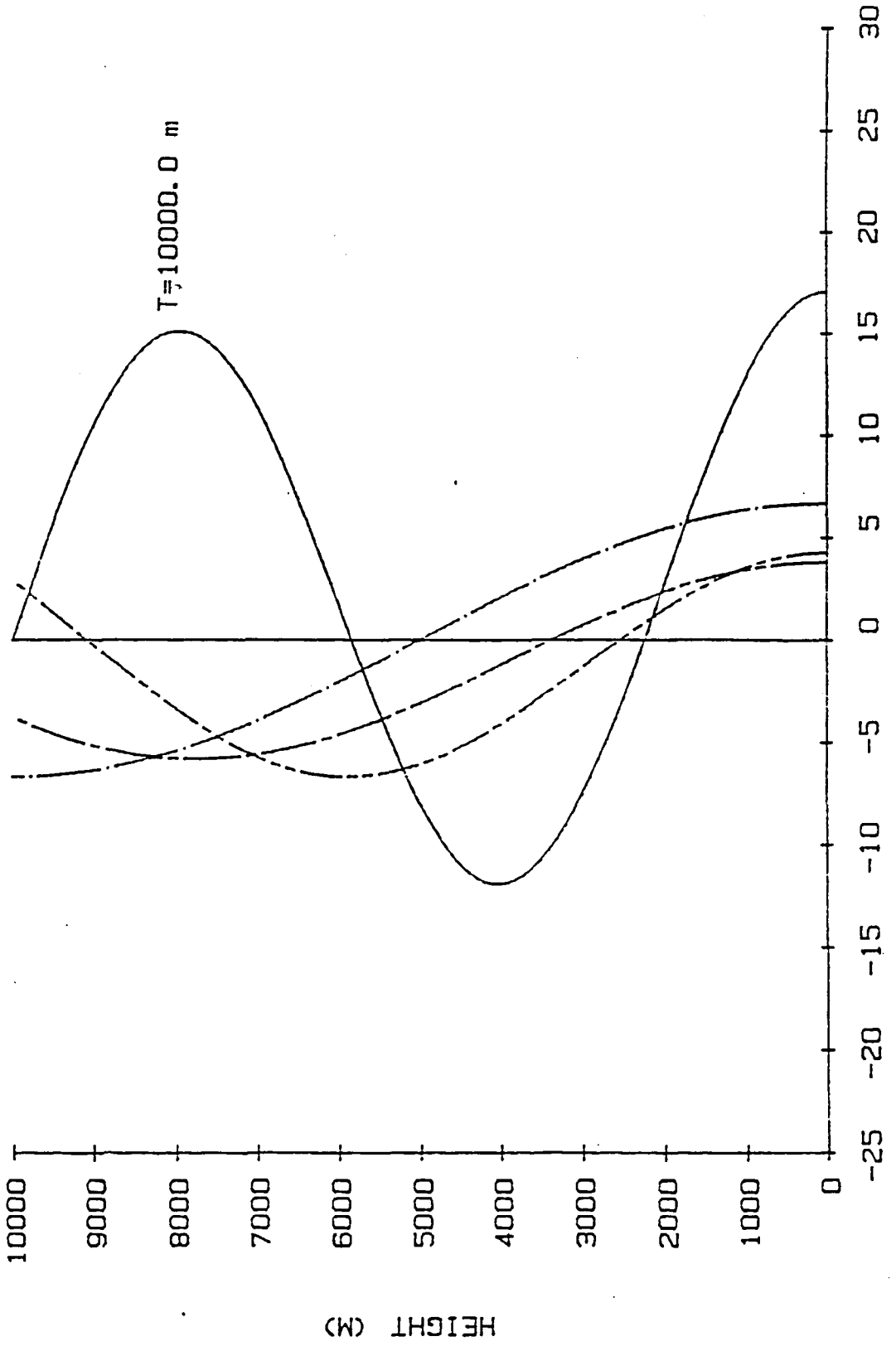
T=10000.0 m
HEIGHT (M)
10000
9000
8000
7000
6000
5000
4000
3000
2000
1000
0
-25
-20
-15
-10
-5
0
5
10
15
20
25
30
U COMPONENT (M/SEC)

Figure 5.5(a).

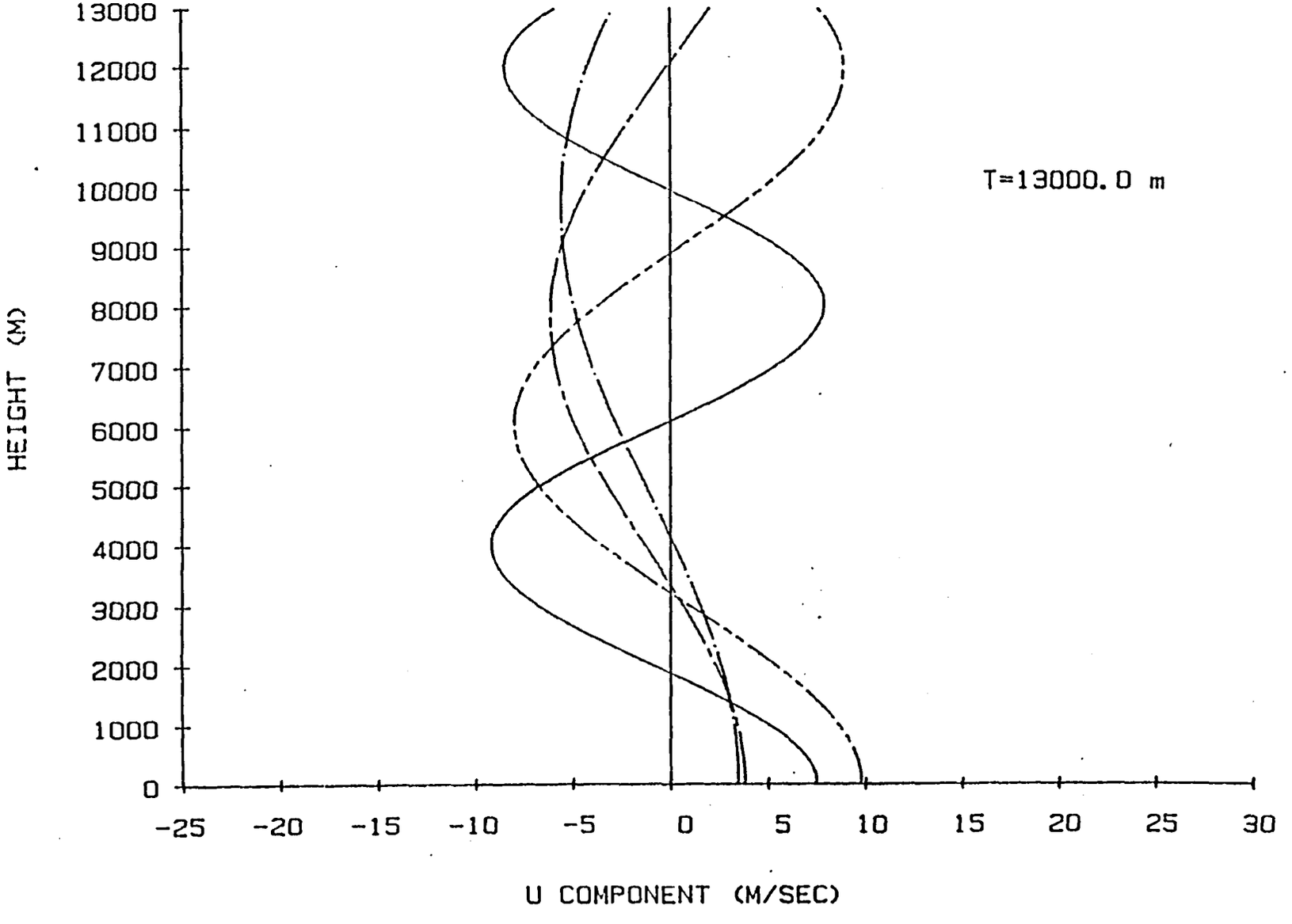
13000
12000
11000
10000
9000
8000
7000
6000
5000
4000
3000
2000
1000
0
HEIGHT (M)
T=13000.0 m
-25
-20
-15
-10
-5
0
5
10
15
20
25
30
U COMPONENT (M/SEC)

Figure 5.5(b).

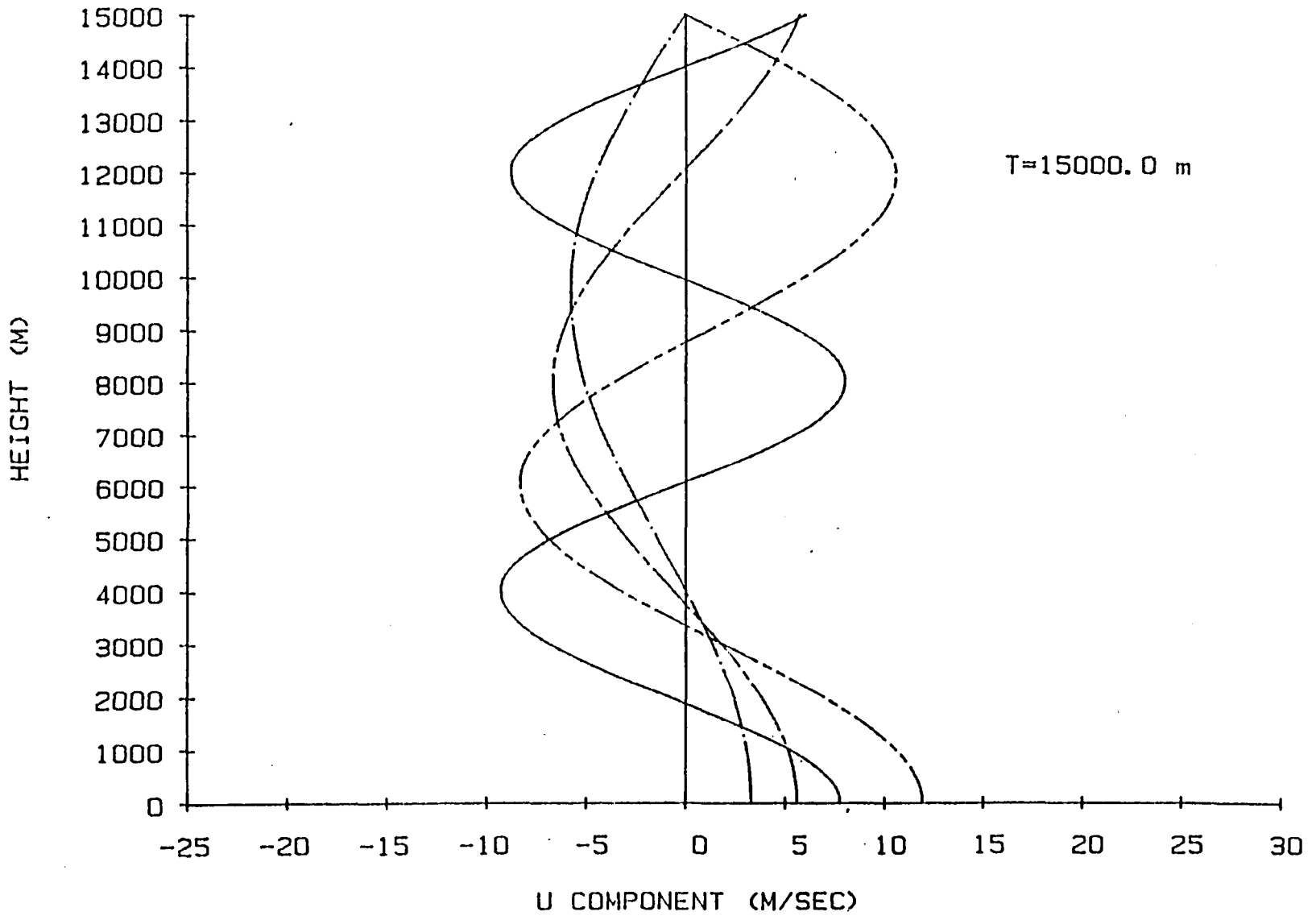
15000
14000
13000
12000
11000
10000
9000
8000
7000
6000
5000
4000
3000
2000
1000
0
HEIGHT (M)
T=15000.0 m
-25
-20
-15
-10
-5
0
5
10
15
20
25
30
U COMPONENT (M/SEC)

Figure 5.5(c).

Figure 5.5(d), (e) and (f). Same as Figures 5.5(a), (b) and (c) except for the vertical speed, $\bar{w}(z)$. The strong vertical speeds in the upper middle troposphere are often observed by Doppler radars.

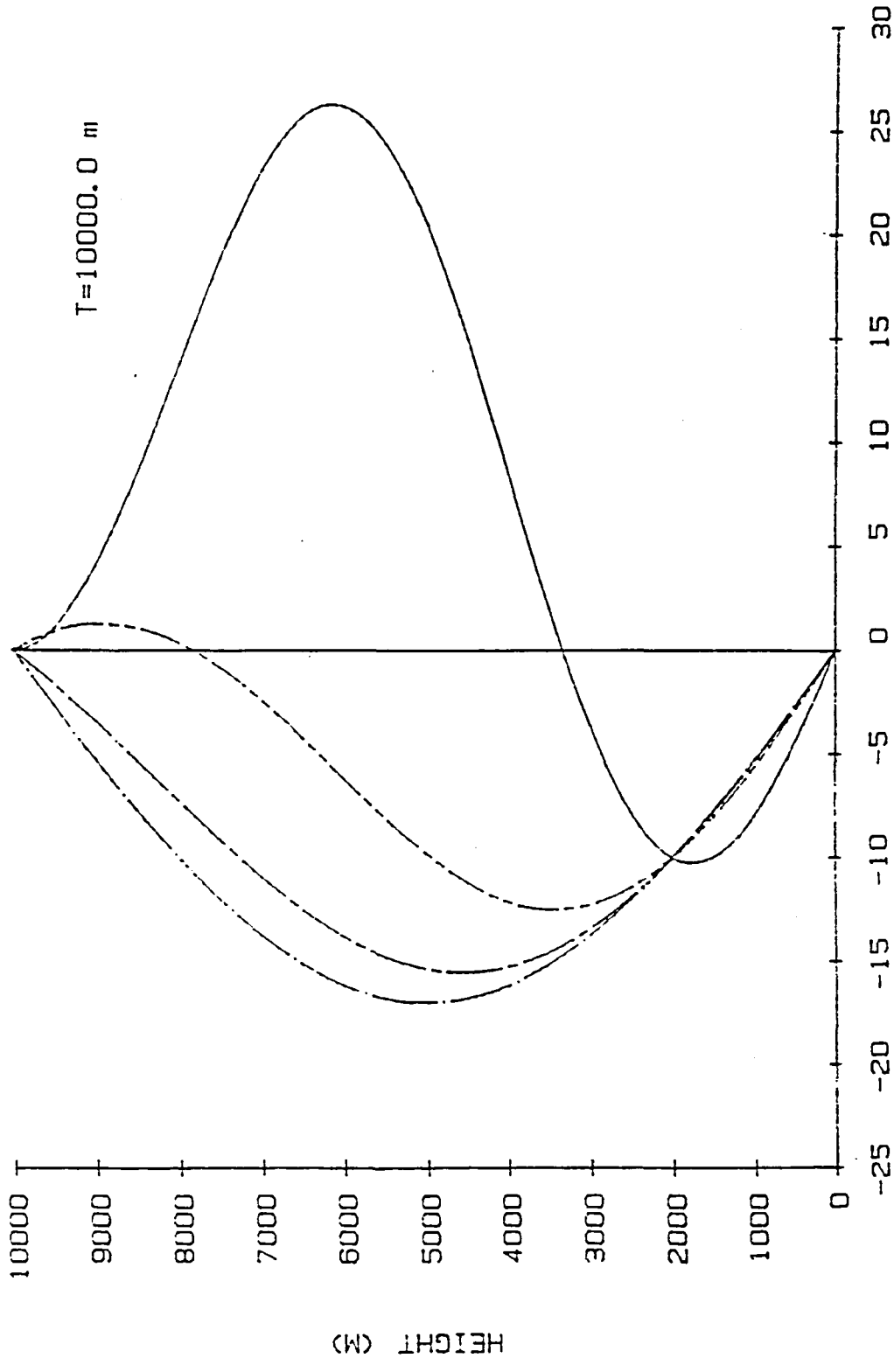
T=10000.0 m
HEIGHT (M)
10000
9000
8000
7000
6000
5000
4000
3000
2000
1000
0
-25
-20
-15
-10
-5
0
5
10
15
20
25
30
W COMPONENT (M/SEC)

Figure 5.5(d).

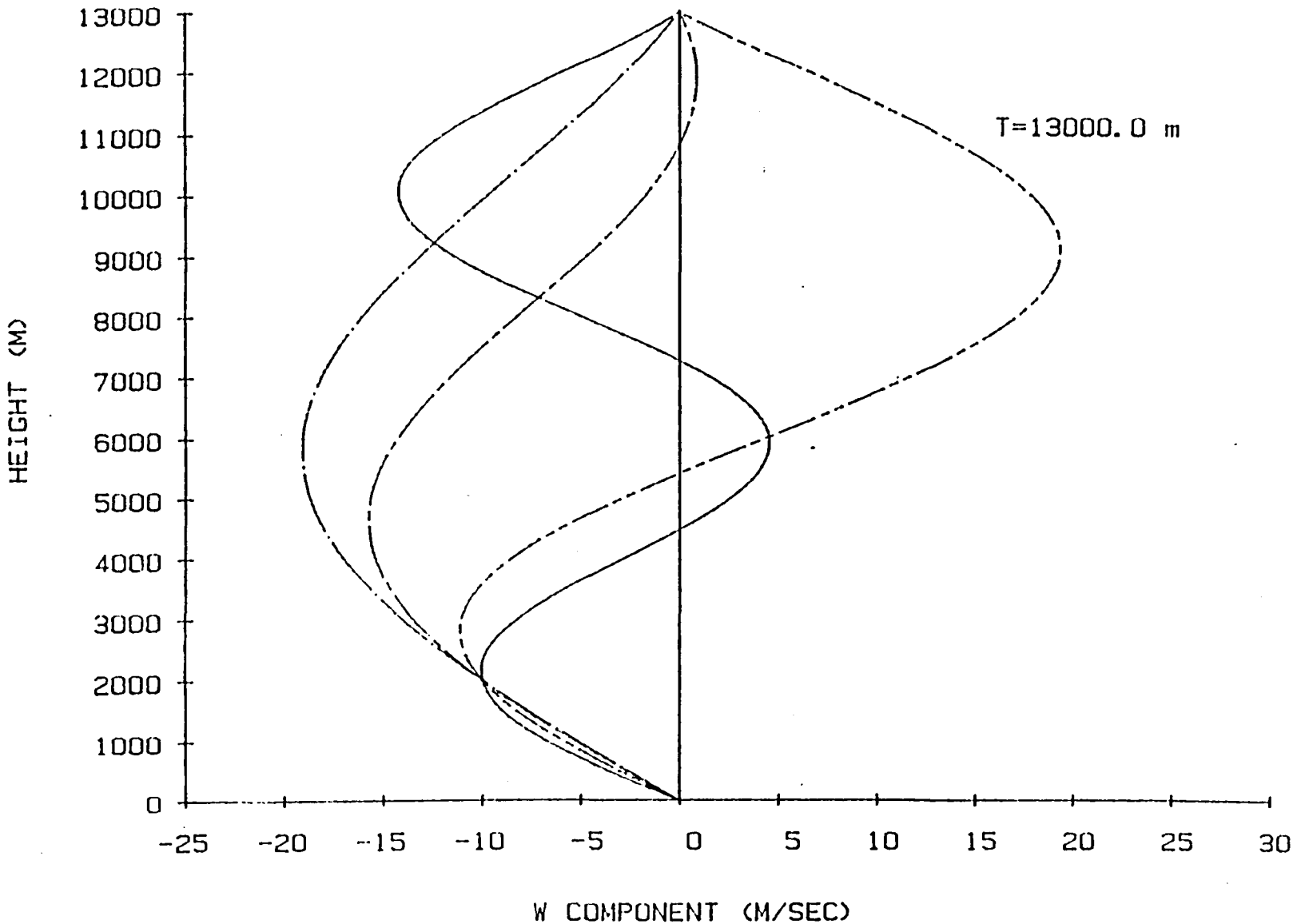
T=13000.0 m
HEIGHT (M)
13000
12000
11000
10000
9000
8000
7000
6000
5000
4000
3000
2000
1000
0
-25
-20
-15
-10
-5
0
5
10
15
20
25
30
W COMPONENT (M/SEC)

Figure 5.5(e).

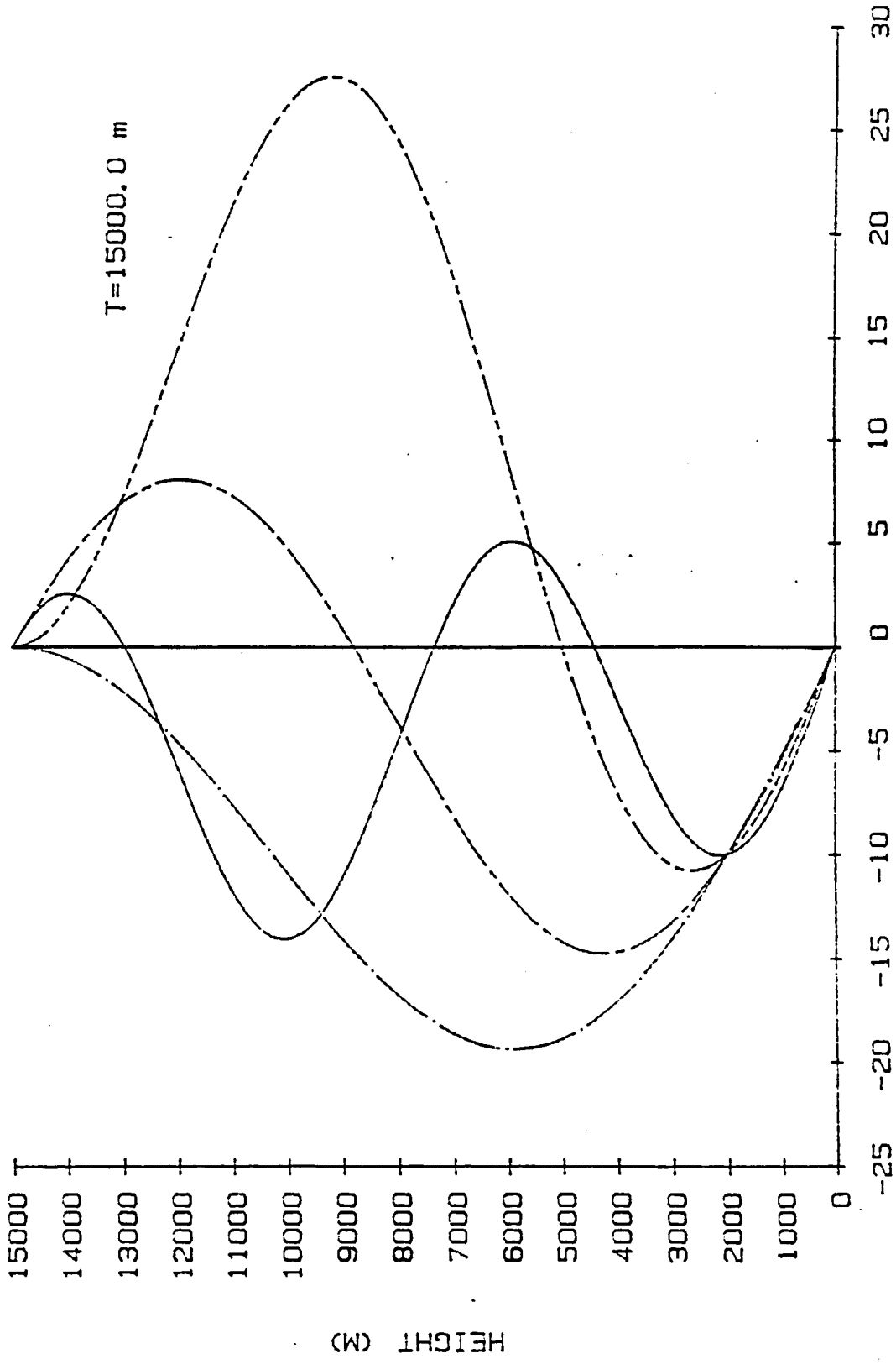
T=15000.0 m
HEIGHT (M)
15000
14000
13000
12000
11000
10000
9000
8000
7000
6000
5000
4000
3000
2000
1000
0
-25
-20
-15
-10
-5
0
5
10
15
20
25
30
W COMPONENT (M/SEC)

Figure 5.5(f).

Figure 5.6. A comparison of the flow within a mature storm as suggested by simple potential flow theory and other schematic flows suggested by observations. The four dashed solenoids represent the potential flow suggested by $\phi(r,z) = \chi(r,z) + \psi(r,z)$ in eq. (14).

The dotted streamlines are those suggested by Browning and Ludlam (1962) for the Wokingham storm. The solid streamlines represent the flow suggested by observations in Newton (1963). Moncrieff and Miller (1976) drew the flow in squall lines following a pattern similar to the dashed streamlines. The three observational schematic flows are consistent with the flow suggested by elementary potential flow.

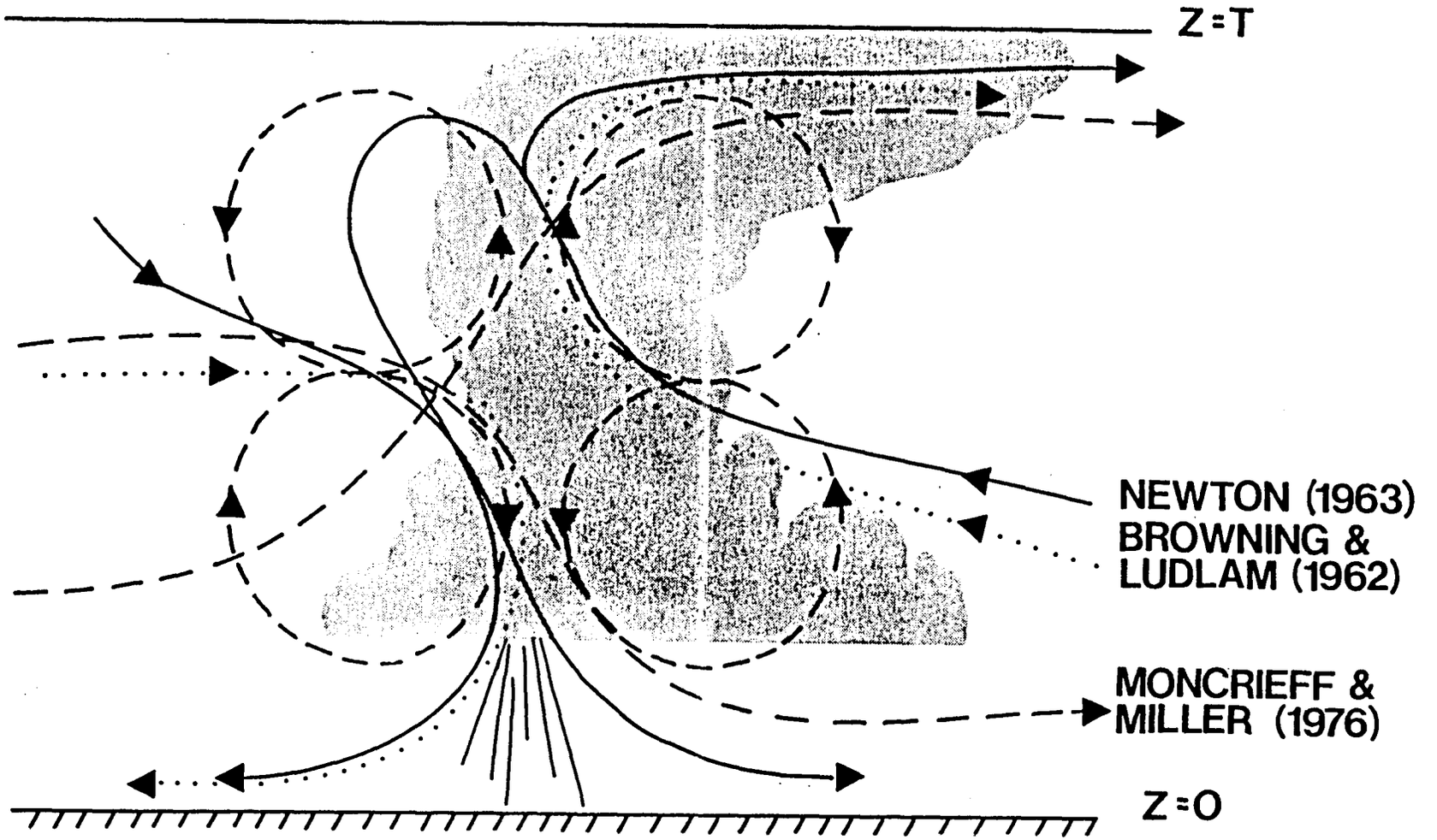
Z=T
NEWTON (1963)
BROWNING &
LUDLAM (1962)
MONCRIEFF &
MILLER (1976)
Z=O

Figure 5.6.

varies. Byers and Braham's (1949) description of the life cycle of thunderstorms, which is still accepted today, has 3 stages. They noted that in the earlier stages of a storm's lifetime the volume of the storm consisted of updrafts. Later in the cycle the lower part of the storm was occupied by downdrafts, while the upper parts were occupied by updrafts more powerful than the downdrafts beneath them. In the final stages, downdrafts occupied the entire storm volume.

These stages are reflected in the simulation. As the level of origin of the downdraft increases, the model storm goes through the mature and dissipating phases described by Byers and Braham.

If the downdraft originates too low in the troposphere, the nature of the flow is best described as a series of toroidal rolls, and in a sense, is disorganized. For example, the solid line plots in Figs. 5.5(c)-5.5(f). In Figs. 5.5(c,d) H was set at 4000 m, and T at 13 km. The resulting flow pattern is not similar to that of a mature storm. The level of H for which the flow becomes organized depends upon the depth of the troposphere. A similar, disorganized pattern results in Figs. 5.5(e) and 5.5(f), for T = 15,000.0, and H set at 4000 m. However, when the height of the tropopause is lowered to 10,000 m, the result of initiating a downdraft with H = 4000 m is an organized flow (Figs. 5.5(a,b), solid line).

In Figs. 5.5(a-f) the strength of the surface layer outflow is also seen to vary as the height of the top of the cylinder changes. Since the strength of the low level outflows from storms is important in the initiation of new, flanking convection, and in the convective scale feedback processes described in an earlier section of this report, it is instructive to investigate the change in strength of low level outflows with a variation in the levels of T and H.

In Fig. 5.7, the solid line is associated with a top height of 10 km, the dashed line with T = 13 km and the dash-dot line with T = 15 km. H (representative of the level of origin of the downdraft), is then allowed to vary from 3000 m to the top of the cylinder.

The plots show a series of maxima and minima in the resulting surface outflow speeds, which differ for each value of T, in the levels at which they occur and in their strength. Thus for a 'measured' downdraft speed of -10.0 m/sec at 2000 m, a cylinder radius of 2.5 km, and a given height for the level of origin of the downdraft and top, the strength of the outflows in the lower levels varies dramatically from minima of around 5 m/sec, to a maximum of greater than 20 m/sec.

In order to investigate further the effects of the relative variation of H and T, three top heights were selected. The three levels of T selected were 11.5 km (a typical summer high latitude height), 15.0 km (a height typical in the summertime for 30 degrees latitude) and 17.0 km (a typical tropical tropopause height).

The tropopause heights were then normalized to 1.0, and H was allowed to vary as before from the proportional level of 3000 m to the top of the troposphere where H = 1.0. The values for R and the downdraft speed at 3000 m (-10.0 m/sec) remained the same (Fig. 5.8).

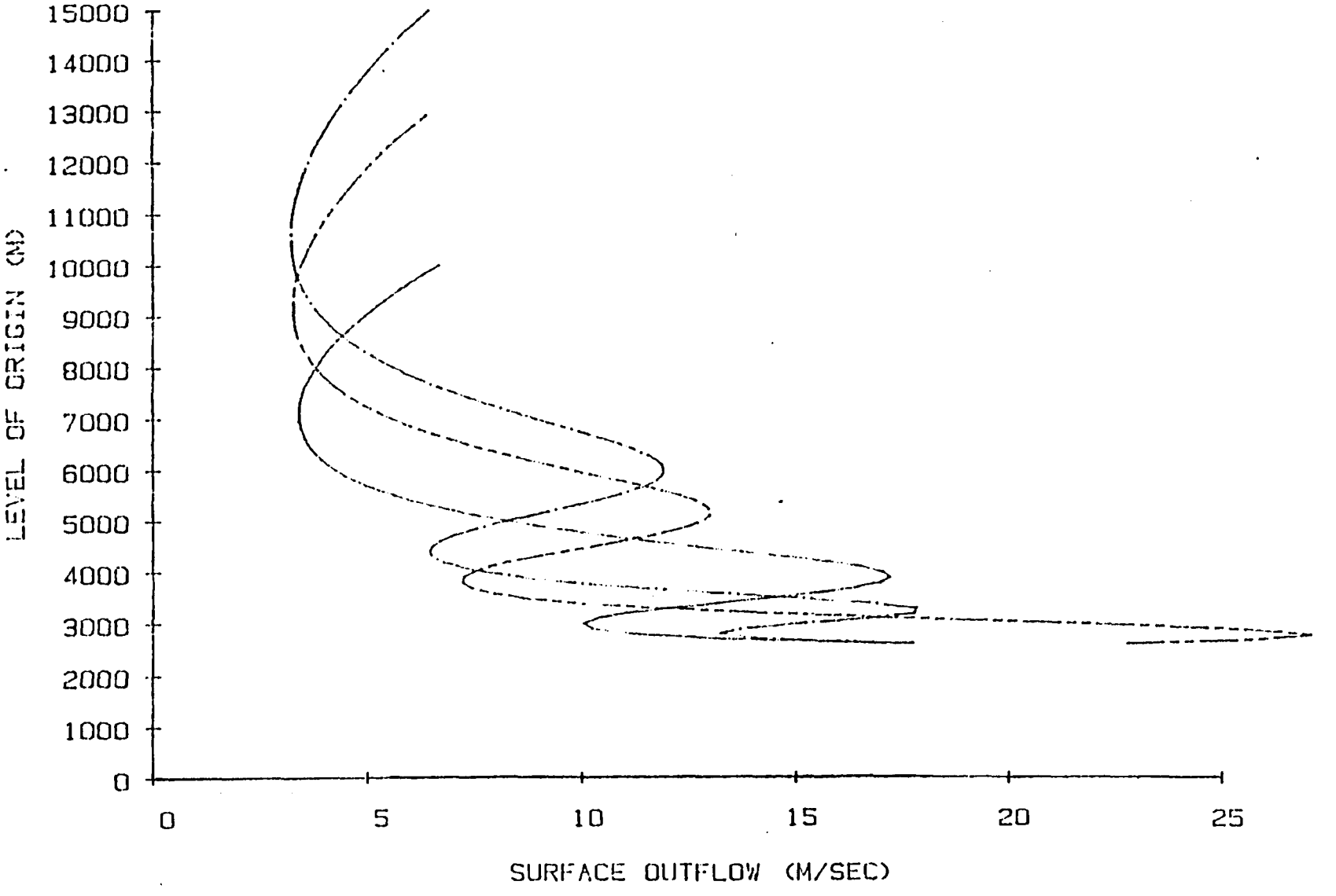

Figure 5.7. Changes in the strength of the surface outflows as the level of origin of the downdraft, H varies from 3000 m to T, for T = 10 km (solid line), T = 13 km (dashed line) and T = 15 km (dash-dot line).

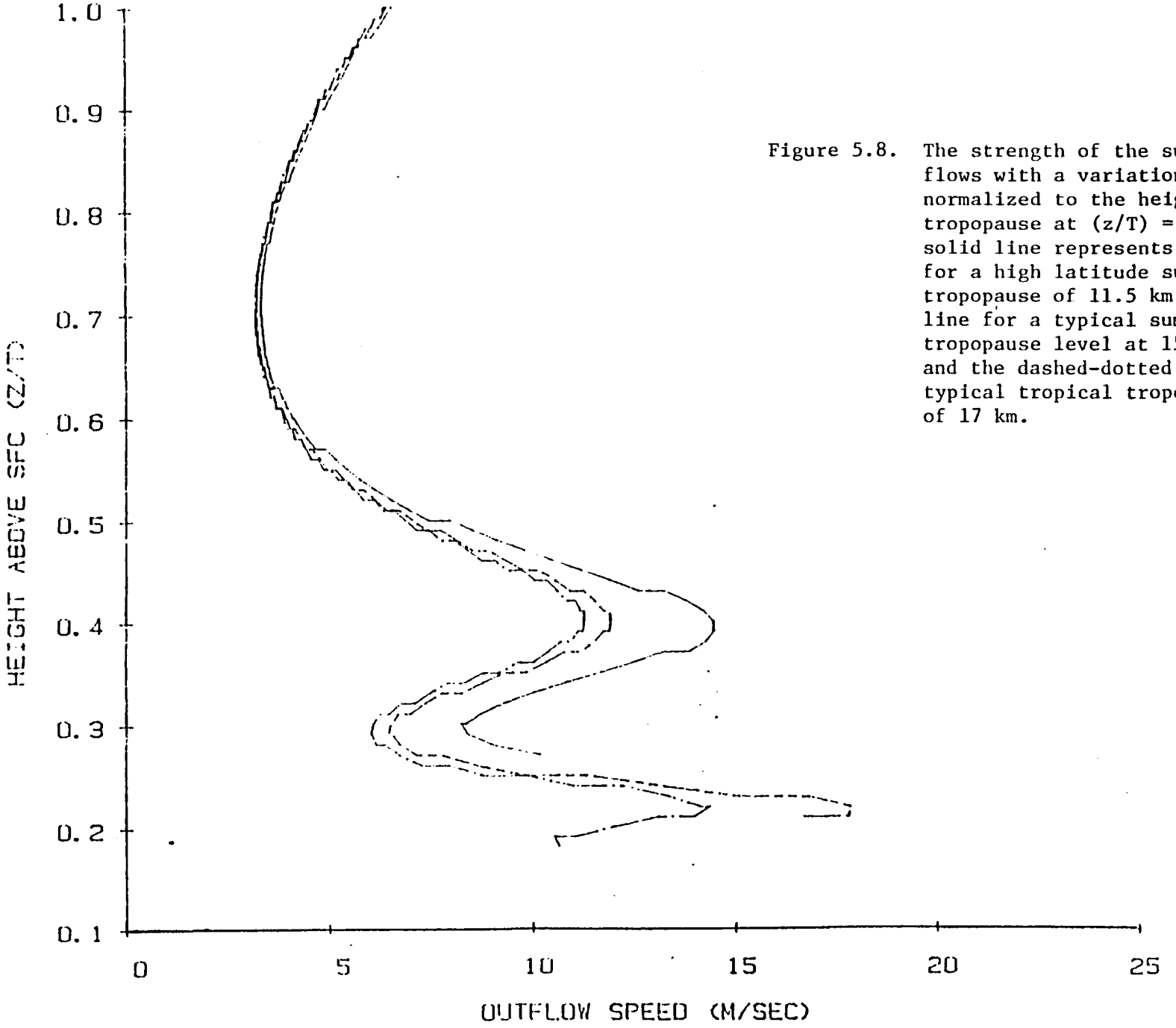

Figure 5.8. The strength of the surface outflows with a variation in H, normalized to the height of the tropopause at (z/T) = 1.0. The solid line represents the results for a high latitude summer tropopause of 11.5 km, the dashed line for a typical summertime tropopause level at 15 km at 30°N, and the dashed-dotted line is for typical tropical tropopause height of 17 km.

In Fig. 5.8 the solid line is the result of setting T = 11.5 km, the dashed line represents a T of 15.0 km (for 30°N), and the dashed-dot line is the tropical height of 17 km.

The graphs show two levels of origin which produce maximum outflows in the lower latitudes, and one level of maximum for the high latitude tropopause level. The two lower levels of maximum outflow available in the lower latitudes result in the type of 'disorganized' flow illustrated by the solid line in Figs. 5.5(c-f). The other, higher maximum at H = 0.40 x T, is available in all latitudes. The minima at H = 0.30 x T and around 0.70 x T are also present for all latitudes. The strength of the outflows produced by downdrafts originating at H = 0.40 x T is greater for the high latitude storms than for the lower latitude ones. Furthermore, this level of optimum production of outflows coincides with the level of minimum equivalent potential temperature in higher latitudes, where thermodynamically, the downdrafts produced would be most intense. The level of the trade wind inversion in the tropics, which is the level of minimum equivalent potential temperature there, is much lower, and the optimum level for downdraft production in Fig. 5.8 does not coincide.

Figures 5.9(a) and (b) show the horizontal and vertical speeds for the optimum levels of H for the three tropopause heights. Since the strongest outflows appear in the lower levels with the strongest upward and outward flows in the upper levels, a possible signal that the outflows in the low levels are at a maximum would be the initial appearance of cirroform anvils in the upper layers of the atmosphere.

This may be useful in selecting suitable candidate cells for analysis.

From this analysis, it would be expected that higher latitude storms are more likely to 'resonate' on the scale of the tropopause height, and so violent, long lived, and propagating convective storms would be more frequent in the higher latitudes than in the tropics.

5.3.2 Outside the Cylinder

The requirement that the space derivative of the radial speed at the edge of each cylinder be continuous leads to a radial speed of

$$u(r,z) = (c + 2)\, u(R,z)\, \frac{R^{c}}{r^{c}} - (c + 1)\, u(R,z)\, \frac{R^{c+1}}{r^{c+1}}$$

outside of each cylinder.

The constant c is determined from observations. During the FACE experiment, observations of surface wind fields from a 6.4 x 6.4 km station grid confirmed the findings of the Thunderstorm report that the divergence on the surface beneath moderate rainshafts was on the order of 10^{-3} sec^{-1}.

Figure 5.10 shows the frequency distribution of convergence of various magnitudes associated with maximum daily rainfall as recorded by 66 recording raingages in the FACE array during the summer of 1975. Figure 5.10 shows that > 90% of the time, during the maximum rainfall rate (i.e., when the storm was directly over the raingages and wind stations) convergence $\geq 10^{-3}$ sec^{-1} was generated in the wind station grid.

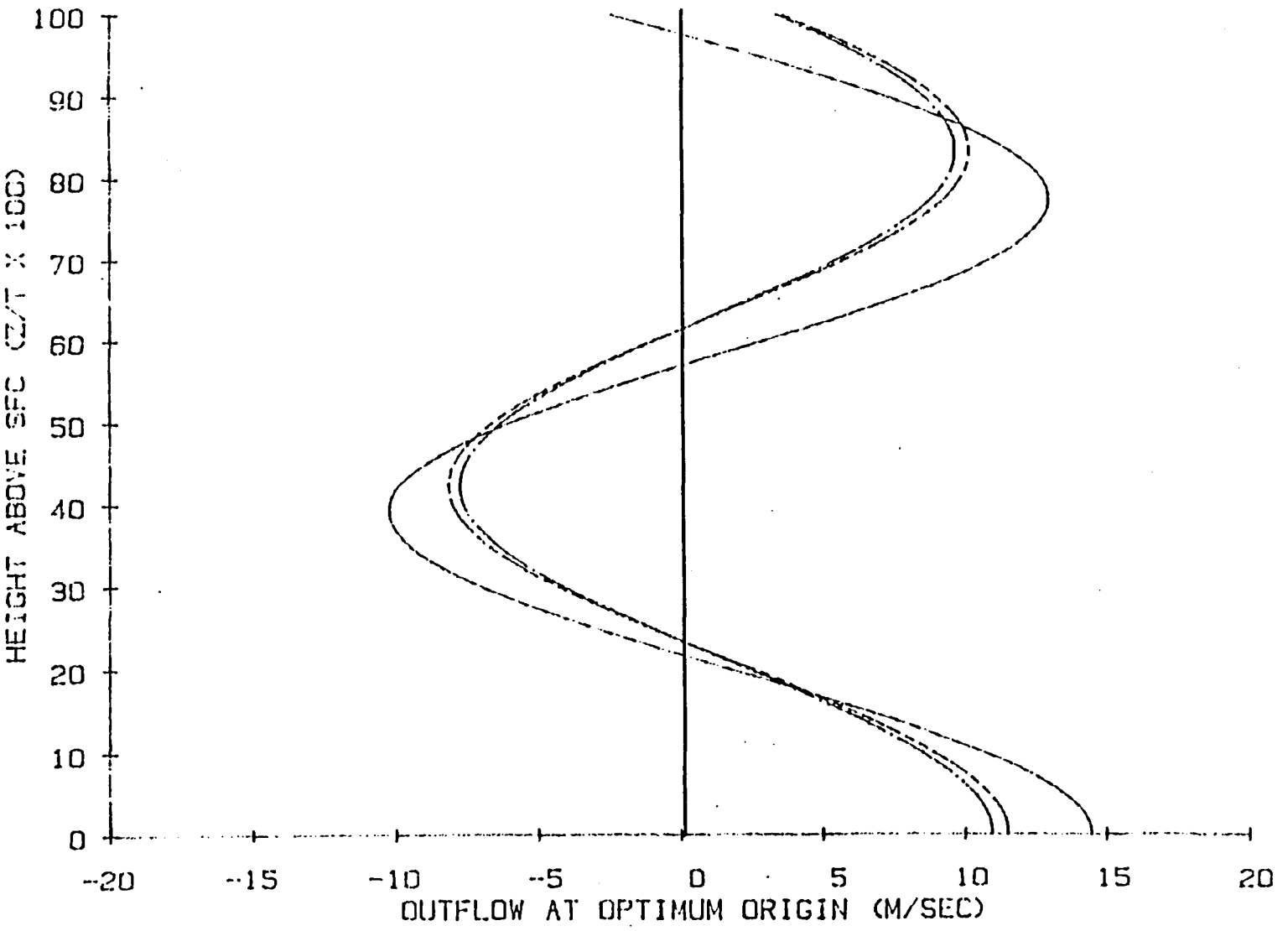

Figure 5.9(a). The horizontal component of wind as a function of height for the three tropopause heights of Fig. 5.8, but with H set at the optimum level to produce the strongest outflows in the lower layers. The height above ground is expressed as a percentage of the height of the tropopause.

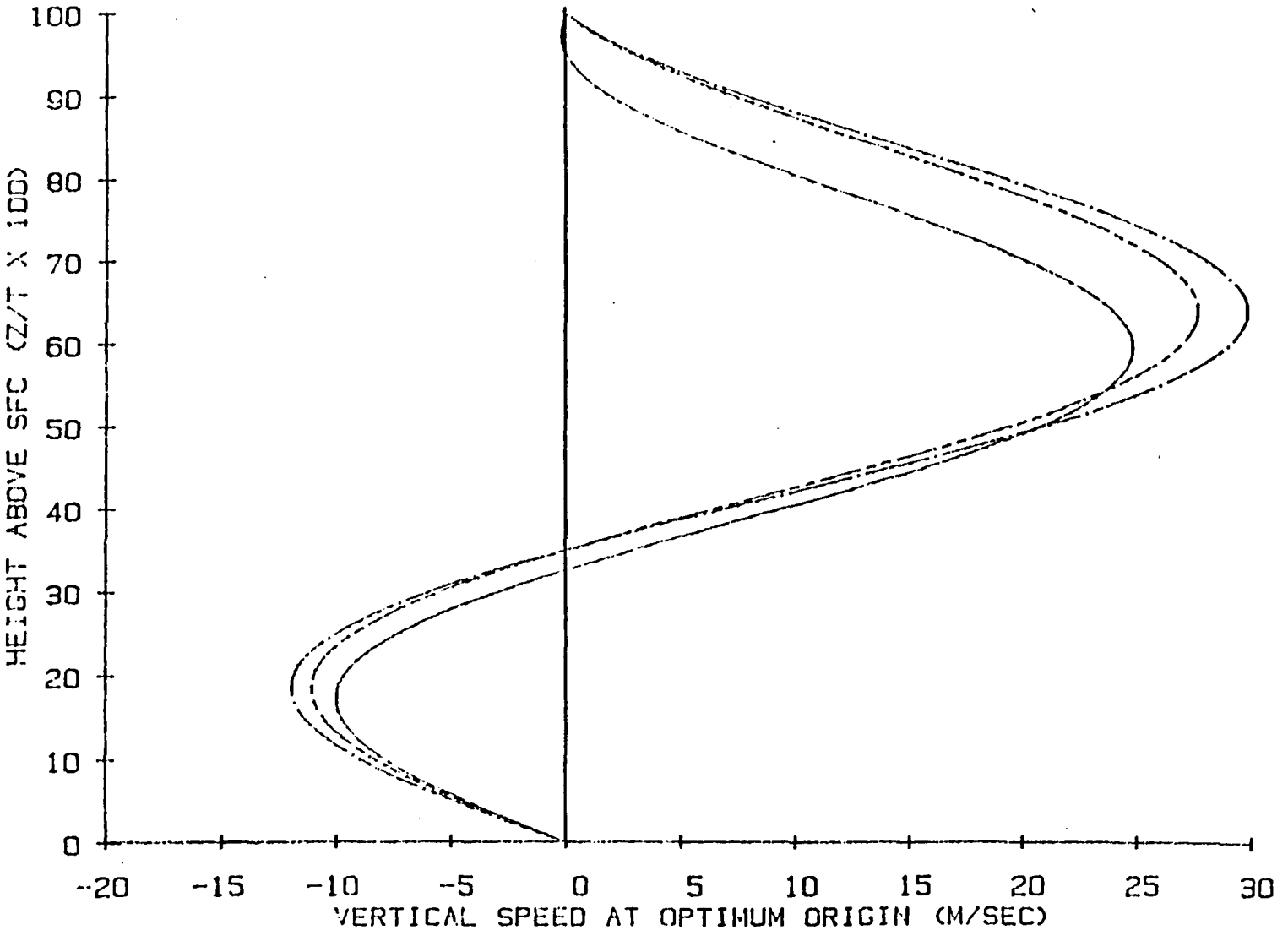

Figure 5.9(b). The same as Fig. 5.9(a) except for the vertical speed.

Figure 5.10. The frequencies of times of onset, before the time of maximum network rainfall, of continuous rainfall greater than 2.5 mm in 15 min at at least one station (thick solid line), and of continuous convergences within the network $\leq -4 \times 10^{-4}$ sec^{-1} (thin solid line), $\leq -6 \times 10^{-4}$ sec^{-1} (dashed) and $\leq -10^{-3}$ sec^{-1} (dash-dot). The rainfall and convergences are continuous within the network from the time of onset to the time of maximum network rainfall rate.

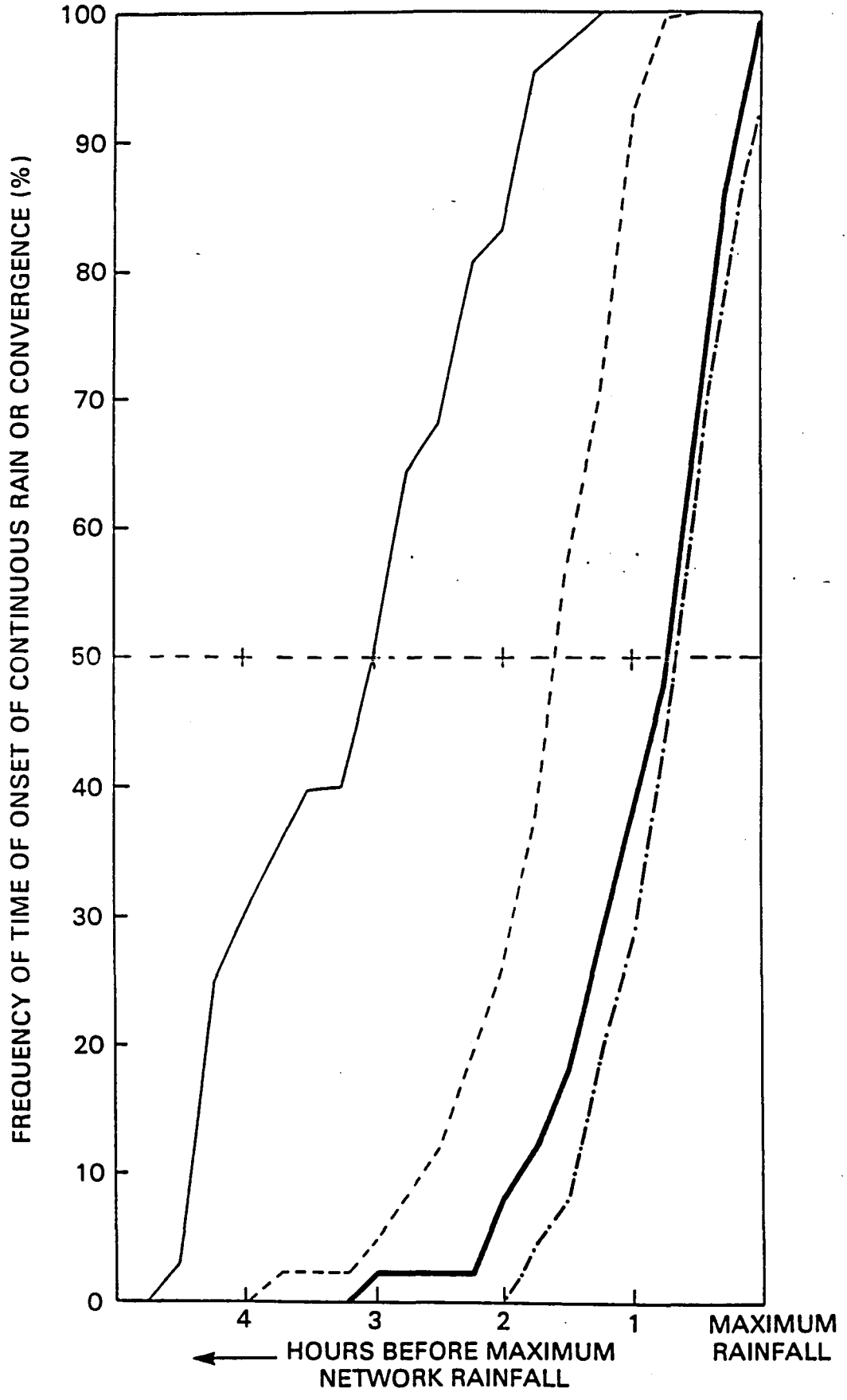
FREQUENCY OF TIME OF ONSET OF CONTINUOUS RAIN OR CONVERGENCE (%)
100
90
80
70
60
50
40
30
20
10
0
4
3
2
1
MAXIMUM RAINFALL
HOURS BEFORE MAXIMUM NETWORK RAINFALL

Figure 5.10.

The typical area of radar returns of 35 dBz in Florida was found by Gagin and Lopez (1985) to be about 30 km^2. This translates into a circular area of radius 3.09 km. To find the value of c, nine 2 x 2 km pixels with 35 dBz were placed at the center of a 6.4 x 6.4 km grid. The algorithm was set up with a vertical speed value at the top of the Florida boundary layer ($\sim$ 300 m) appropriate to divergence of 10^{-3} sec^{-1} at 4 meter height, which was the height of the anemometers during FACE.

The algorithm was then run with an all-top height of 6.8 km AGL (from Gagin and Lopez (1985)) in a zero-shear environment. The constant c was then numerically adjusted so that divergence of 10^{-3} sec^{-1} was generated in the 6.4 x 6.4 km square beneath the echo. The value of c was found to be 1.9165.

Values of dBz were divided into six categories as in the Table 5.1 below, and the divergence associated with each category of dBz weighted relative to 35 dBz and 10^{-3} sec^{-1}.

i.e., $$DIV(L) = 10^{-3}\left[\frac{DBZ(L)}{35}\right]^{1/1.5}$$

where the exponent 1/1.5 is taken from the Marshall-Palmer Z-R relationship.

Table 5.1.

DBZ(L)	L	DIV(L) * 10^{-3} sec^{-1}
37.5	1	1.047
42.5	2	1.138
47.5	3	1.226
52.5	4	1.311
57.5	5	1.393
$\geq$ 62.5	6	1.472

5.3.3 The Inclusion of Shear

Shear is included in two ways, first by assuming that the air being emitted through the sides of each cylinder carries with it the momentum of the middle layer air (this effect is assumed to decay radially at the same rate as does the radial component of the cylindrical flow), and second, by the advection of these effects in the direction of the appropriate shear vector for a period of five minutes (the approximate time between radar scans).

Relative to the moving cylinder, the horizontal velocity field of the environment is

$$\vec{V} = -\left[(ULO - ULZ)\hat{i} + (VLO - VLZ)\hat{j}\right]$$

where $$\vec{V}_o = ULO\hat{i} + VLO\hat{j}$$

is the motion vector of the cylinder, and

$$\vec{V}_L = ULZ\hat{i} + VLZ\hat{j}$$

is the motion vector of the larger-scale environmental flow at any level. We set $UM = \vec{V} \cdot \hat{i}$ and $VM = \vec{V} \cdot \hat{j}$.

Then the advection terms can be written as

$$u \frac{\partial u}{\partial x} = (u_x - um) \left[\frac{\partial u_x}{\partial x} - \frac{\partial um}{\partial x} \right]$$

where u_x is the component of the radial speed in the $\hat{i}$ direction. We will have similar terms in the j-direction.

We take the acceleration over a period of time Δt to be approximately

$$\Delta u = - \left[u \frac{\partial u}{\partial x} + v \frac{\partial u}{\partial y} \right] \frac{\Delta t}{2} \qquad (1)$$

Here we divide by 2 to get an "average" 5-minute wind speed.

In the advection terms,

$$\frac{\partial ux}{\partial x} = \frac{\partial}{\partial x} \left[u(r,z) \cos\theta \right]$$

$$= \frac{\partial}{\partial x} \left[u_o f(r) \frac{x}{r} \right] ,$$

where $f(r) = (c + 2) \frac{R^c}{r^c} - (c + 1) \frac{R^{c+1}}{r^{c+1}}$

Here $u_o = u(R,z)$, and θ is the angle $\vec{r}$ makes with the $\hat{i}$-direction.

Then

$$\frac{\partial ux}{\partial x} = u_o \left[\frac{f(r)}{r} + \cos^2\theta \left(\frac{\partial f}{\partial r} - \frac{f(r)}{r} \right) \right] .$$

Assuming the same radial decay rate for the momentum carried with the radial outflow

$$\frac{\partial um}{\partial x} = um \cos\theta \frac{\partial f}{\partial r}$$

also $$\frac{\partial ux}{\partial y} = u_o \left[\cos\theta \sin\theta \left(\frac{\partial f}{\partial r} - \frac{f(r)}{r} \right) \right]$$

and $$\frac{\partial um}{\partial y} = um \sin\theta \frac{\partial f}{\partial r} .$$

Similar calculations can be made for

$$\frac{\partial v_y}{\partial x}, \quad \frac{\partial v_y}{\partial y}, \quad \frac{\partial v_m}{\partial x} \quad \text{and} \quad \frac{\partial v_m}{\partial y},$$

and the accelerations at a point due to advection can be estimated by assuming the conditions to be steady over the period of one radar scan.

Table 5.2 below is a list of a series of tests using the average Florida 35 dBz cell mentioned above with varying advection times and varying shears and grid sizes.

Table 5.2.

Figure	GRID SIZE (km)	ULZ ($m\ s^{-1}$)	VLZ ($m\ s^{-1}$)	ULO ($m\ s^{-1}$)	VLO ($m\ s^{-1}$)	Δt (sec)
A.1	2x2	-5.0	0	10.0	0	300
A.2	5x5	-5.0	0	10.0	0	300
A.3	10x10	-5.0	0	10.0	0	300
A.4	2x2	-5.0	0	10.0	0	150
A.5	2x2	-5.0	0	10.0	0	60
B.1	2x2	-5.0	0	0	0	300
B.2	2x2	0	0	10.0	0	300
B.3	2x2	5.0	0	-10.0	0	300
B.4	2x2	3.53	3.53	-7.07	-7.07	300
B.5	2x2	-3.53	-3.53	7.07	7.07	300
B.6	10x10	0	0	10.0	0	300

In looking at Figures 5.A.1 through 5.B.6 one should be aware of the grid sizes. Figures A.1 and A.2 show that a 5x5 grid spacing retains the form of the low-level convergence fields generated by the algorithm. Even at 10x10 km resolution (Fig. 5.A.3) the general sense of the fields is retained, but at this resolution, we are likely to lose some of the important regions of convergence due to an unhappy relative positioning of radar pixels on grid points. The radar pixels are of course totally independent of the grid point spacing. Figures A.5, A.4 and A.1 show the effects of increasing the advection time from 1 min to 5 min. Air is 'piled up' on the downshear side of the cylinder as time progresses.

Figure 5.B.1 shows a stationary storm embedded in an easterly low-level flow of 5 m s^{-1}, with the weaker convergence on the eastern flank of the cylinder than in Fig. A.1. Figure 5.B.2 represents the dispersion of momentum from aloft by a storm moving to the east at 10 m s^{-1} through low-level air that is perfectly still. The distribution of westerly momentum from aloft around the storm that is shown is a result of the assumption

that this momentum is carried with the radial flow, and decays in intensity with distance at the same rate that the radial outflow speeds decay. Figure 5.B.6 shows that the amount of momentum re-distributed in this way dwindles rapidly to zero about 10 km from the center of the "storm".

Figures 5.B.3, B.4, and B.5 show how the strong convergence zones rotate around the flanks of the "storm" with varying middle-level and low-level flow.

Wind Field for 32/13/96 @ 2501 LST
Center: 0 0 km from radar

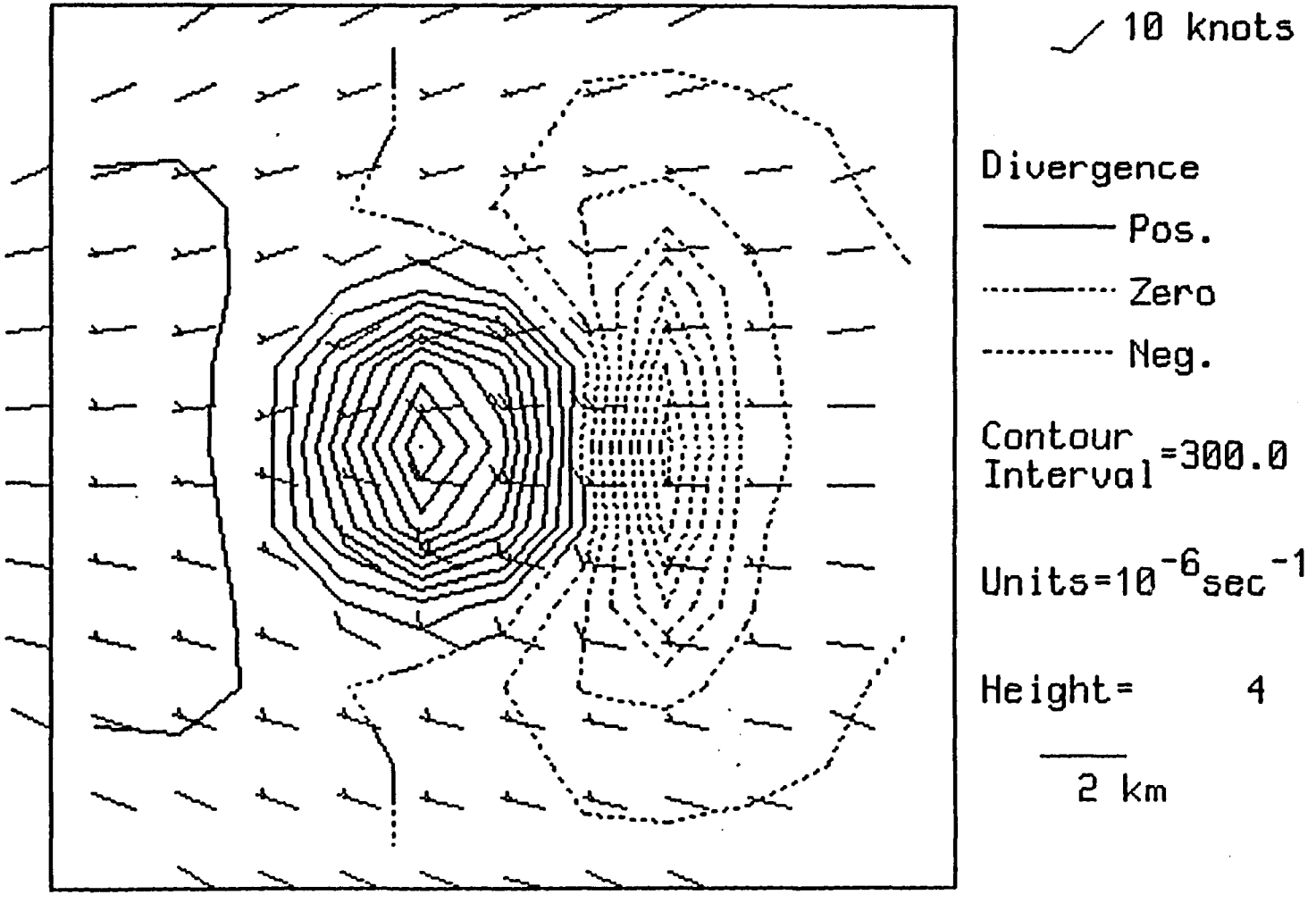

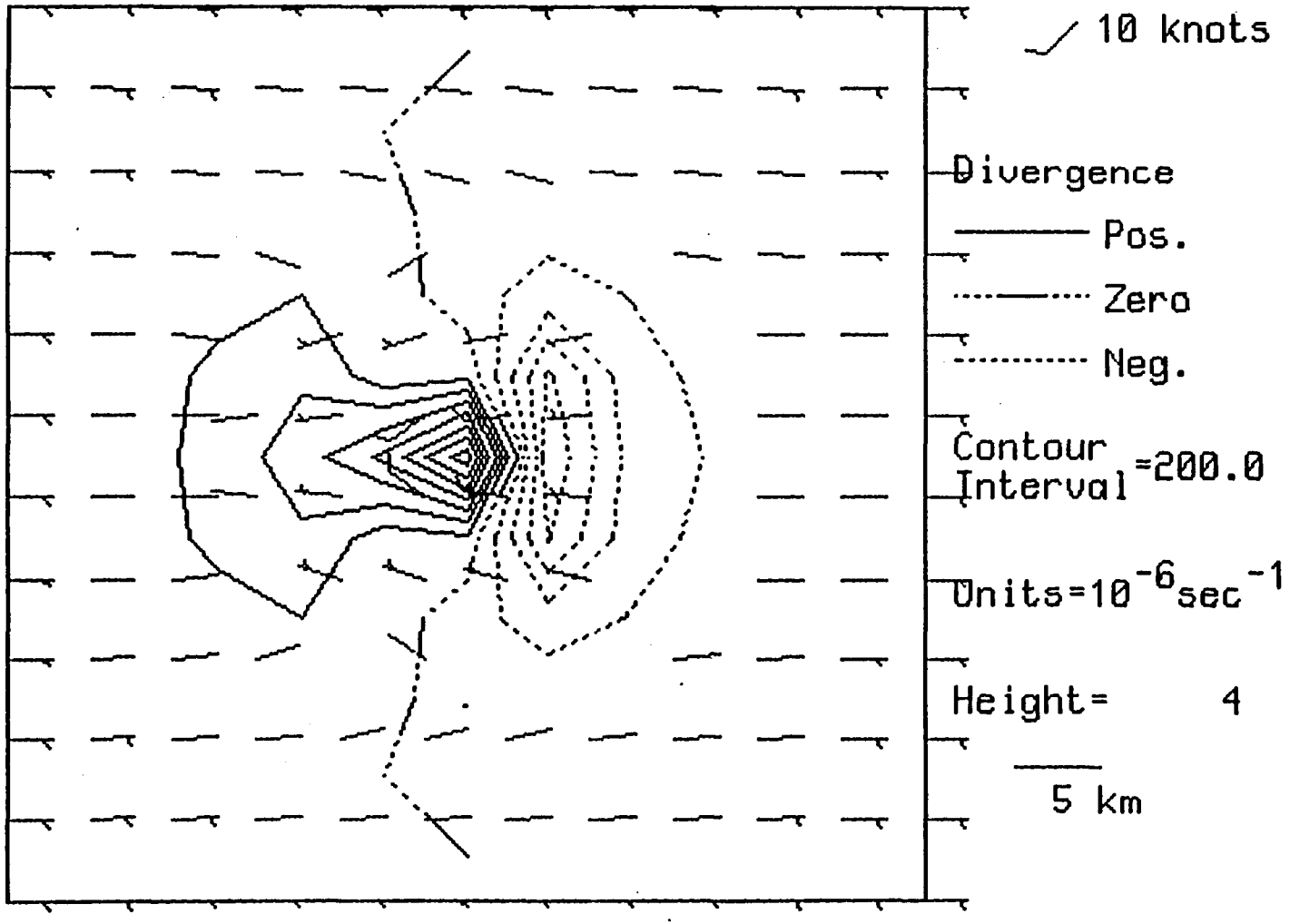
Wind Field for 32/13/96 @ 2501 LST
Center: 0 0 km from radar
10 knots
Divergence
Pos.
Zero
Neg.
Contour Interval=200.0
Units=10^-6 sec^-1
Height= 4
5 km

A.2

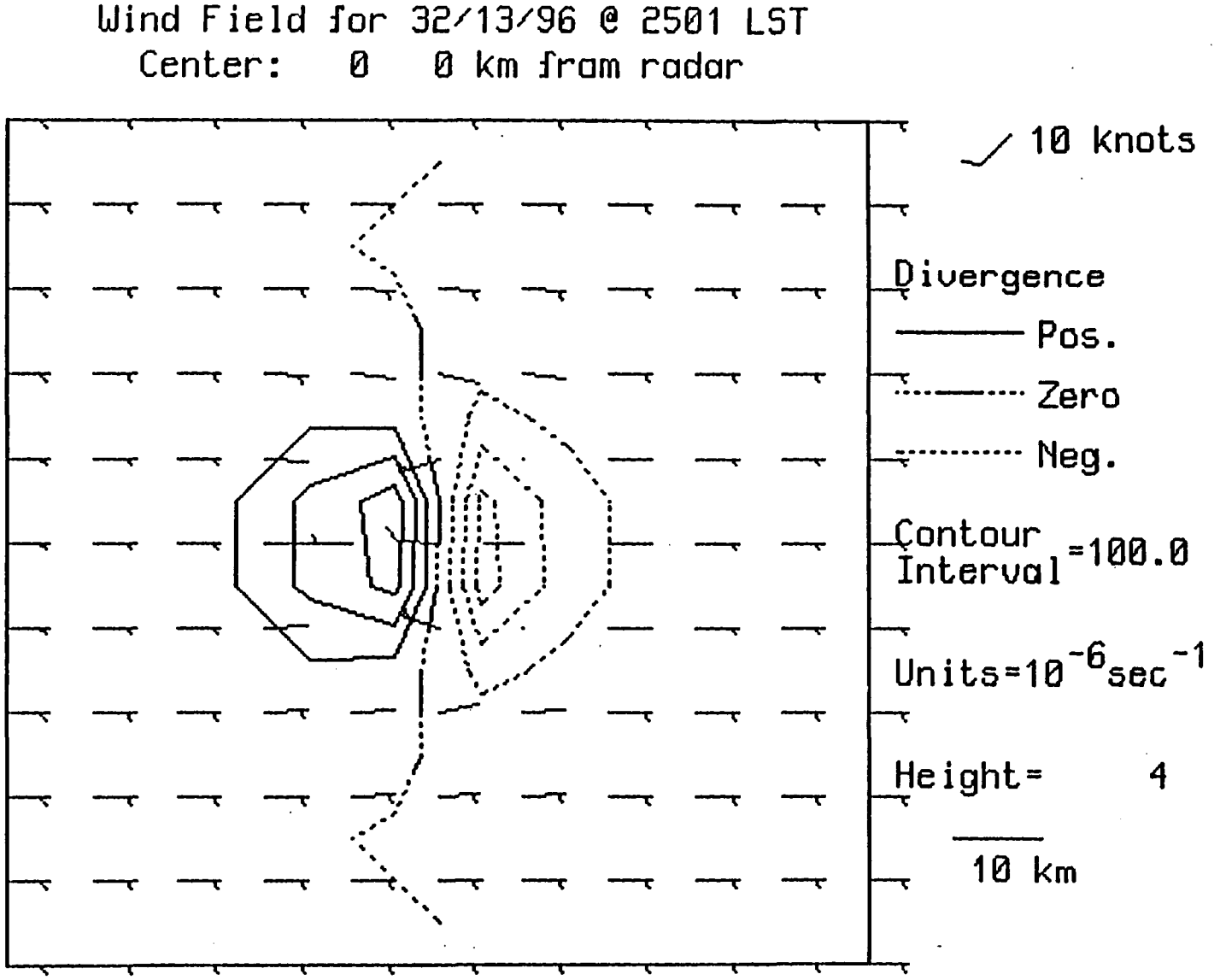
Wind Field for 32/13/96 @ 2501 LST
Center: 0 0 km from radar
10 knots
Divergence
Pos.
Zero
Neg.
Contour Interval =100.0
Units=10^-6 sec^-1
Height= 4
10 km

Wind Field for 32/13/96 @ 2501 LST
Center: 0 0 km from radar

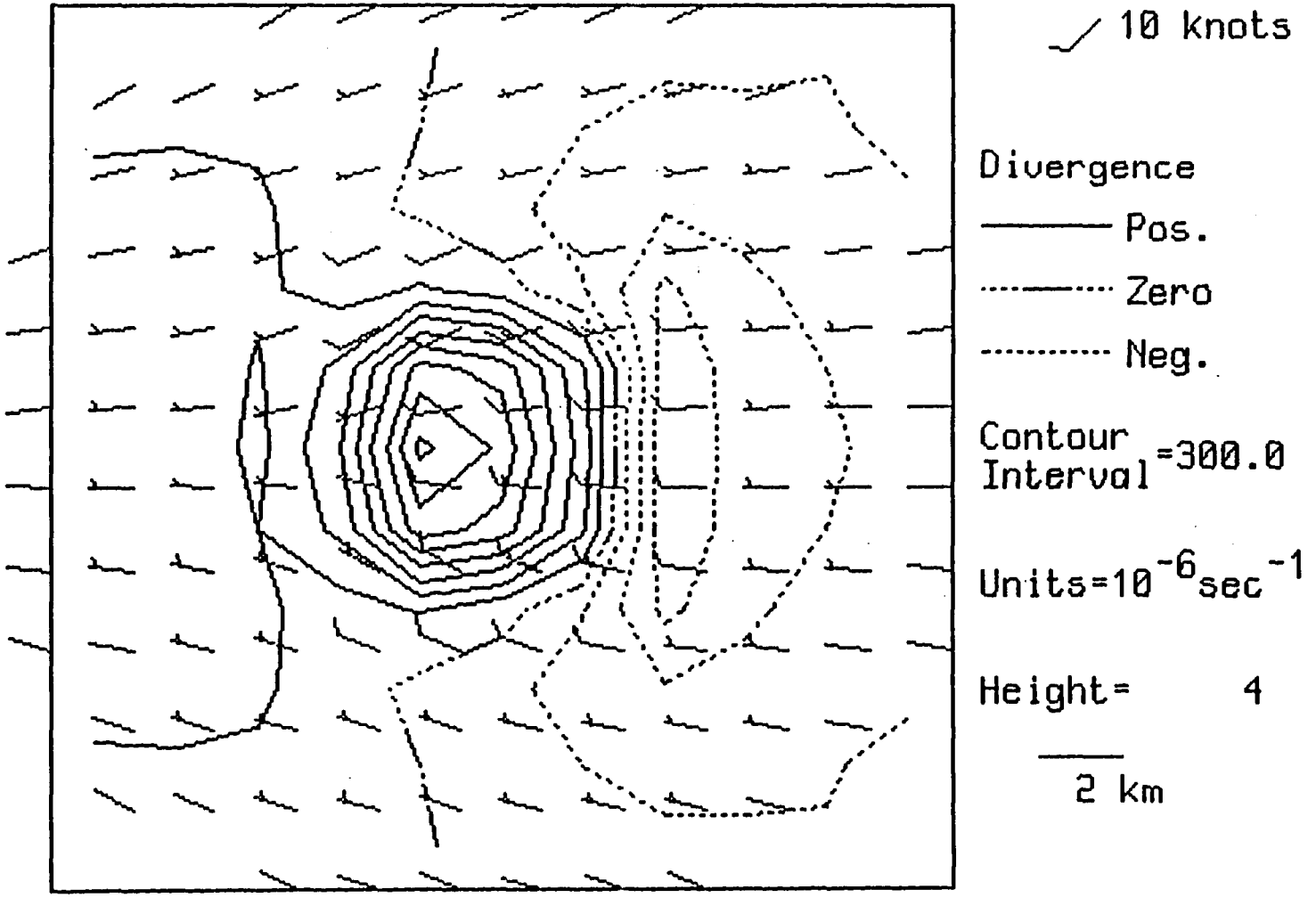

A.4

Wind Field for 32/13/96 @ 2501 LST
Center: 0 0 km from radar

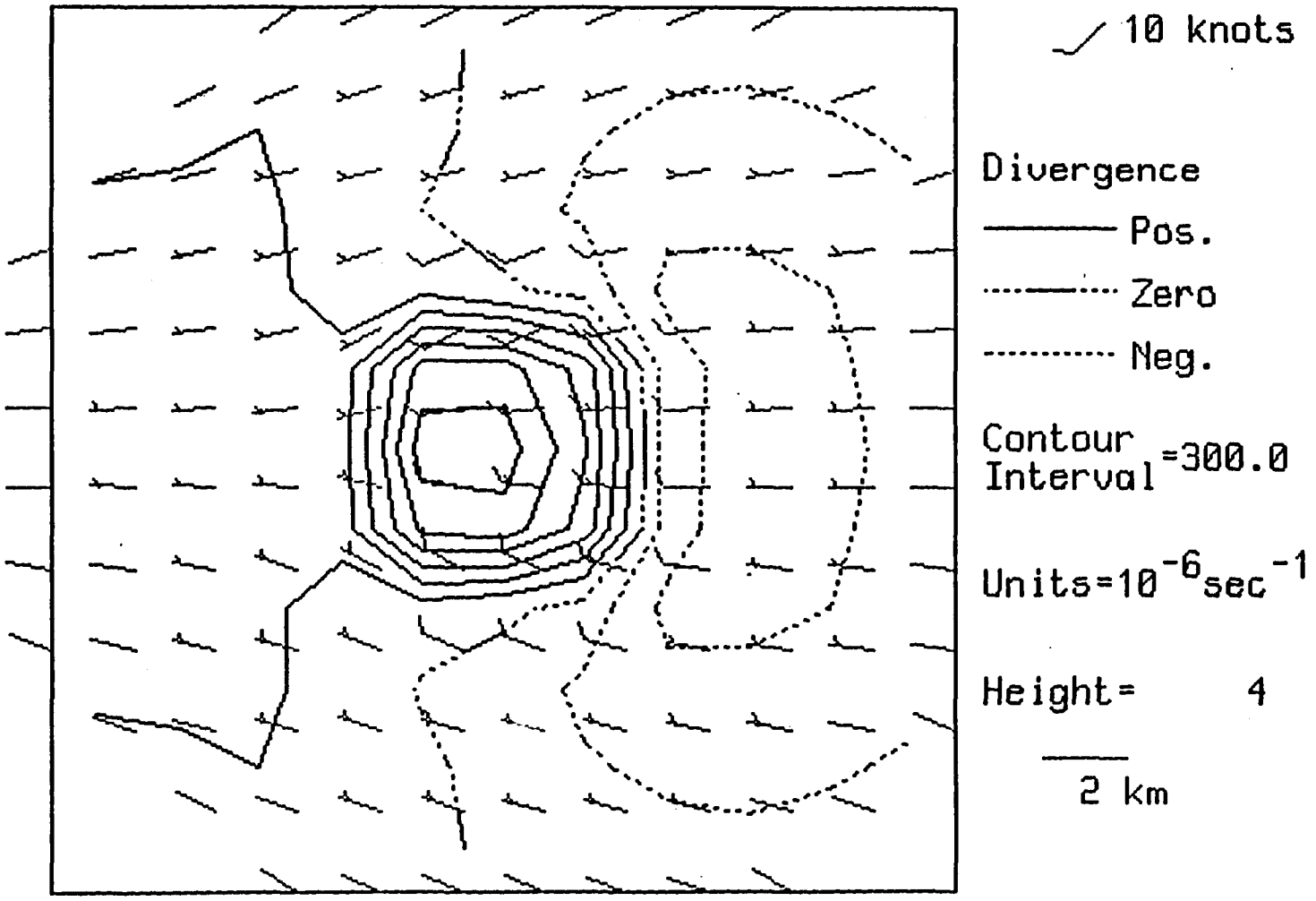

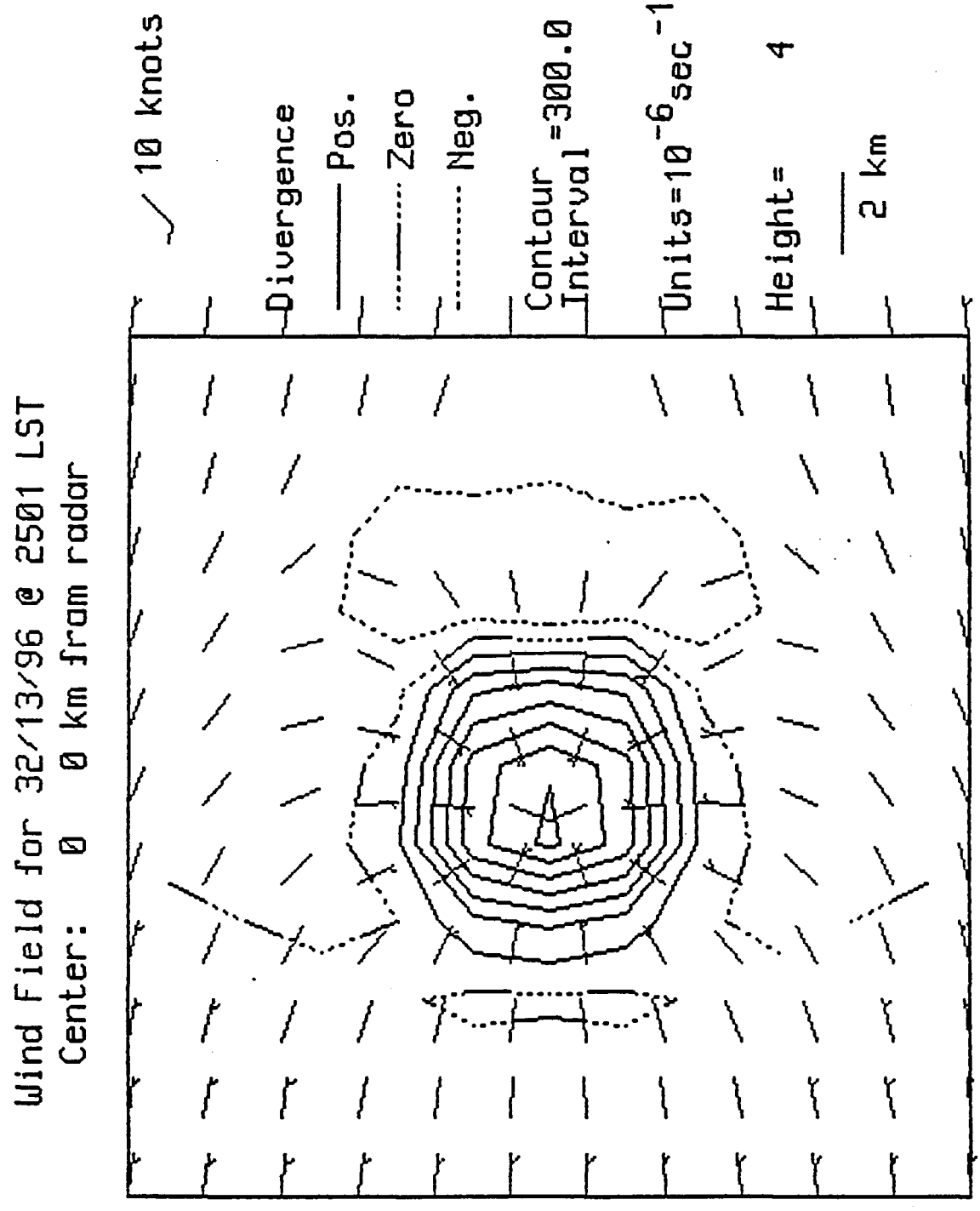
Wind Field for 32/13/96 @ 2501 LST
Center: 0 0 km from radar
10 knots
Divergence
Pos.
Zero
Neg.
Contour Interval =300.0
Units=10^-6 sec^-1
Height= 4
2 km

B.1

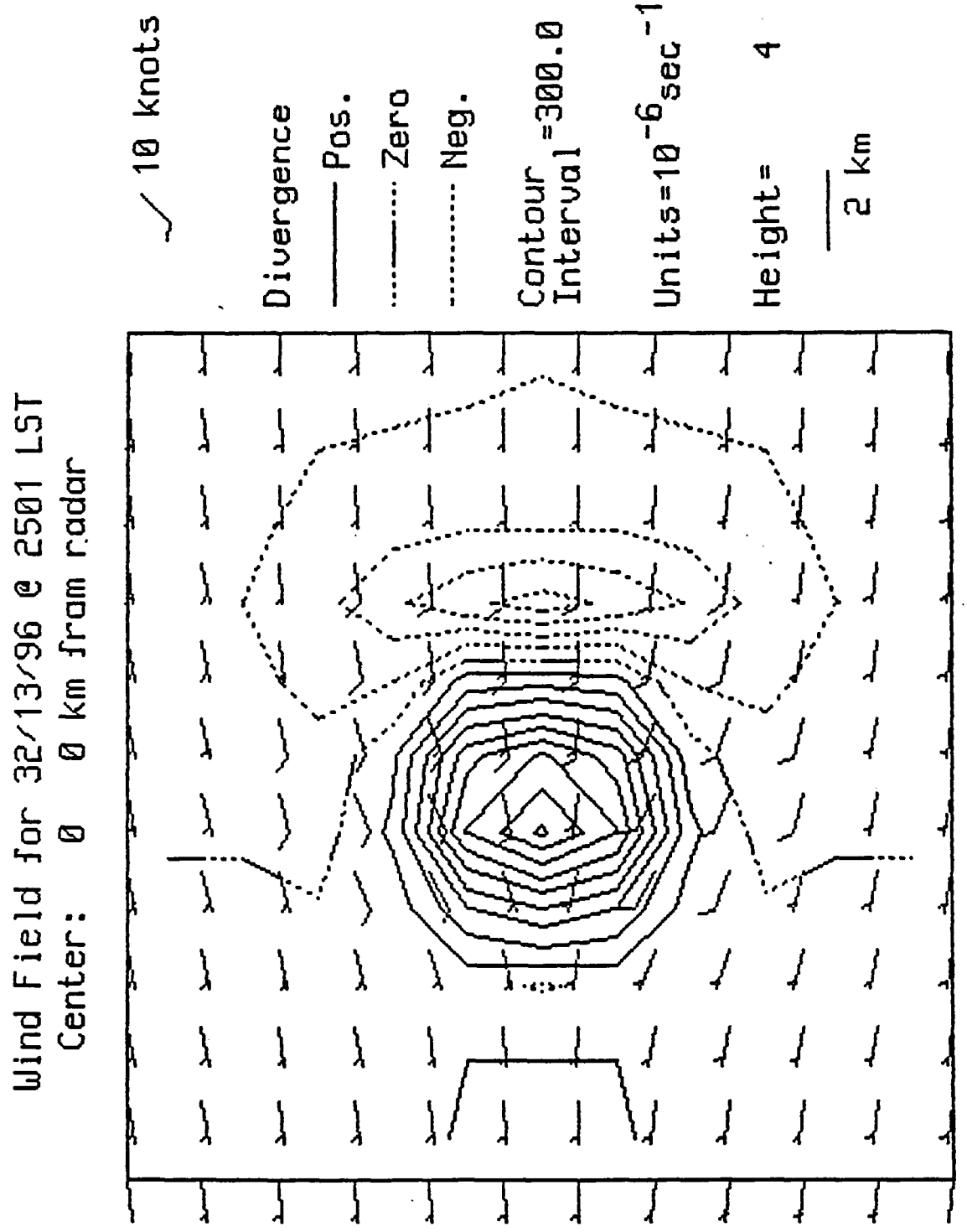
Wind Field for 32/13/96 @ 2501 LST
Center: 0 0 km from radar
10 knots
Divergence
Pos.
Zero
Neg.
Contour Interval=300.0
Units=10^-6 sec^-1
Height= 4
2 km

B.2

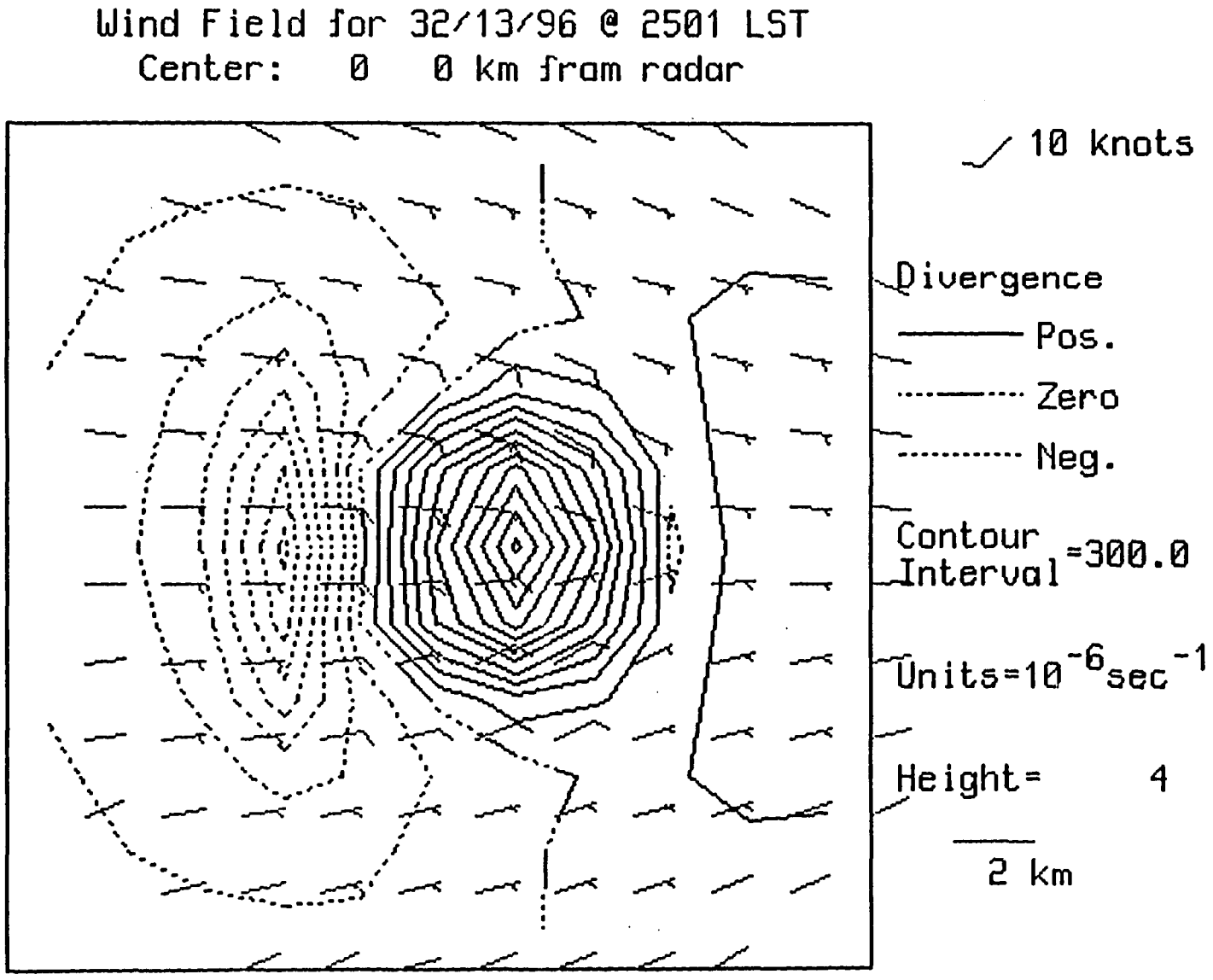
Wind Field for 32/13/96 @ 2501 LST
Center: 0 0 km from radar
10 knots
Divergence
Pos.
Zero
Neg.
Contour Interval =300.0
Units=10^-6 sec^-1
Height= 4
2 km

B.3

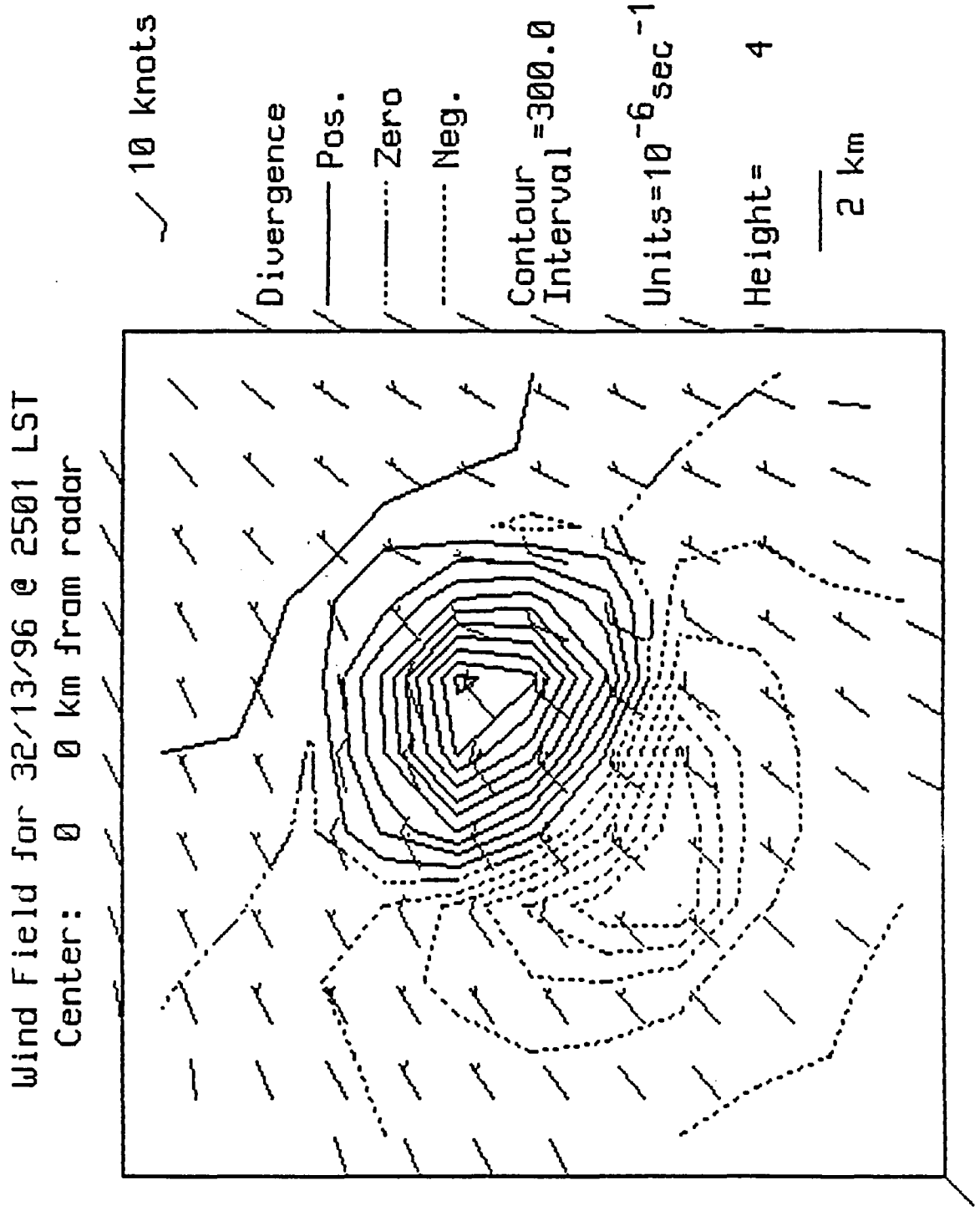
Wind Field for 32/13/96 @ 2501 LST
Center: 0 0 km from radar
10 knots
Divergence
Pos.
Zero
Neg.
Contour Interval=300.0
Units=10^-6 sec^-1
Height= 4
2 km

B.4

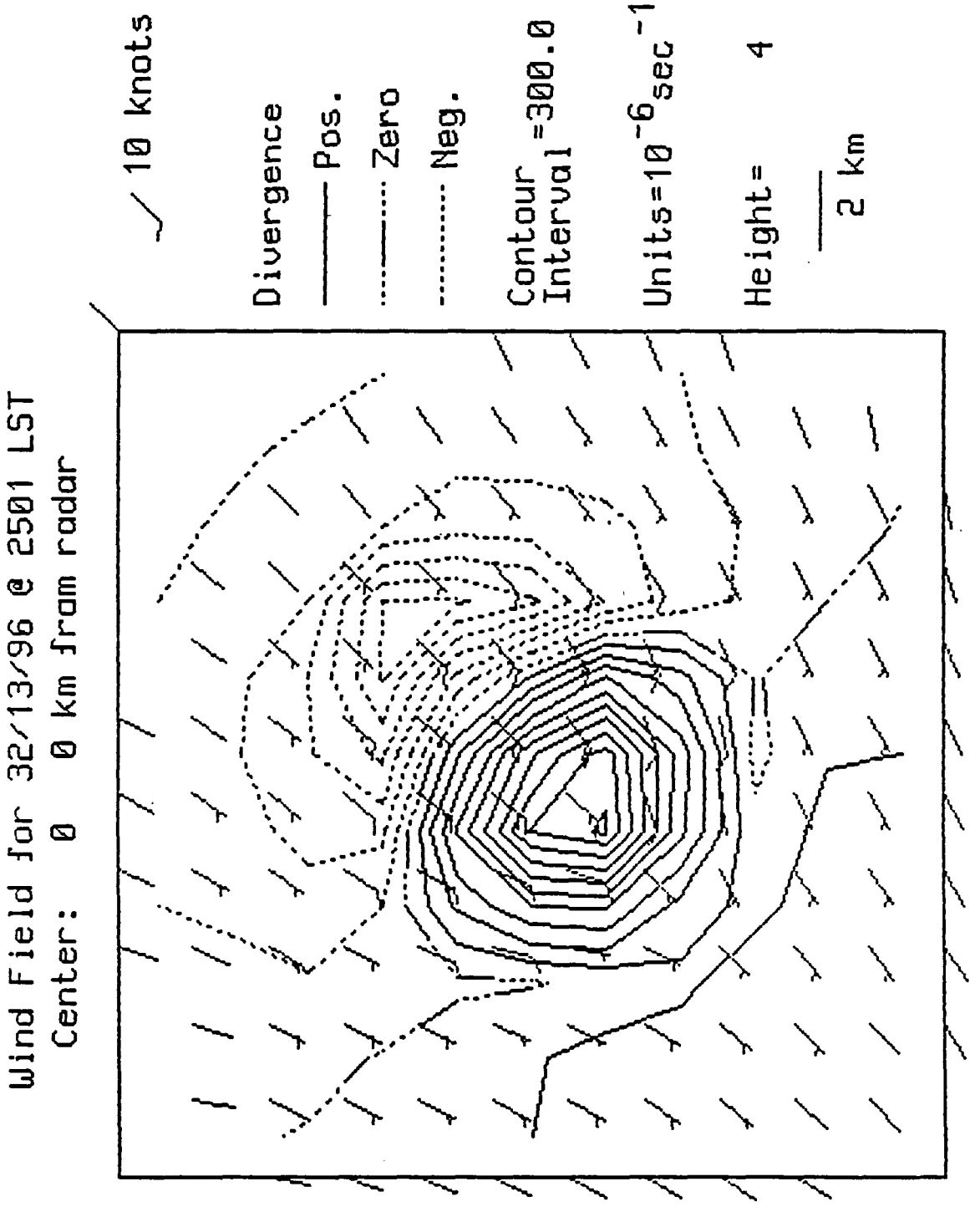
Wind Field for 32/13/96 @ 2501 LST
Center: 0 0 km from radar
10 knots
Divergence
Pos.
Zero
Neg.
Contour Interval =300.0
Units=10^-6 sec^-1
Height= 4
2 km

B.5

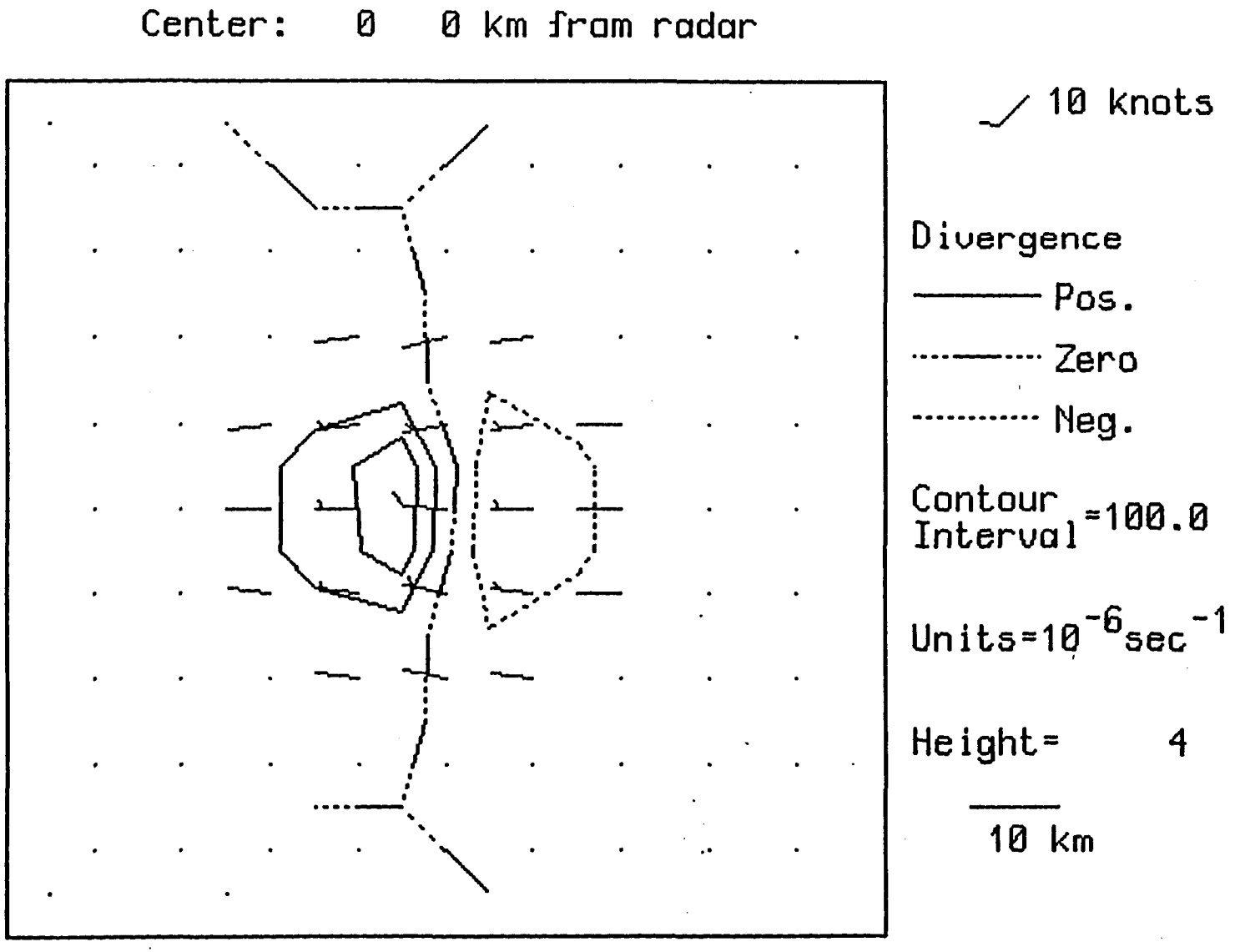
Center: 0 0 km from radar
10 knots
Divergence
Pos.
Zero
Neg.
Contour Interval=100.0
Units=10^-6 sec^-1
Height= 4
10 km

B.6

5.4 APPLICATIONS OF THE THUNDERSTORM OUTFLOW AND INTERACTION ALGORITHM USING PAWS DATA

5.4.A NOWCASTING

At present, there is no satisfactory way to observe the details of the kinematic fields within and around convection and convective complexes in the PAWS area. There is no other way to estimate the fine structure (say 5x5 km scale) of the vertical motions around storms except by inference from the conventional radar data which currently is used during operations.

The outflow algorithm outlined in this section has been specifically developed with this problem in mind. The algorithm puts together the radar echo return distribution, the observed vertical shear in the horizontal large scale winds and the conventional wisdom about how low level outflows from storms are likely to interact with one another. It is flexible enough to allow a local forecaster to introduce his/her knowledge of local conditions.

The simplest form of the algorithm has been run on the Nelspruit radar record for twenty days. The twenty days were selected for the variety of the conditions they represent and serve as case studies in the use of the algorithm. They comprise a total of about a thousand five-minute radar records. Six of the twenty days were selected at random for complete analysis.

5.4.1 Observations and Simulations

The rough terrain around Nelspruit was initially cause for concern, and undoubtedly affects the near surface flows from the storms. However, if we insist on using the algorithm in a diagnostic and relative sense, then it will be seen from what follows that useful information can be extracted from the radar record by its application.

First, we examine how the algorithm behaves over flat terrain. During 1979, 27 PAM (Portable Automated Mesonetwork) meteorological stations were deployed in Illinois for use during the VIN (Virginia/Illinois/NOAA) experiment. On 30 July of that year a large, well organized system passed over the network. Figure 5.11(a) shows the area-averaged divergence observed by the PAM system compared to the area-averaged divergence estimated by using the outflow algorithm. Two differences are evident:

1) The algorithm over estimates the area-averaged divergence (positive divergence) and under estimates the area-averaged convergence (negative divergence).

2) The signal produced by the algorithm is out of phase (precedes) with the signal observed.

The first difference in Fig. 5.11(a) can be explained by noting that the algorithm deals only with the convective scale response to the local convective scale rainfall-driven downdrafts, and is totally unaware of any other sources of motion. A reasonable large scale convergence of 10^{-4} s^{-1}

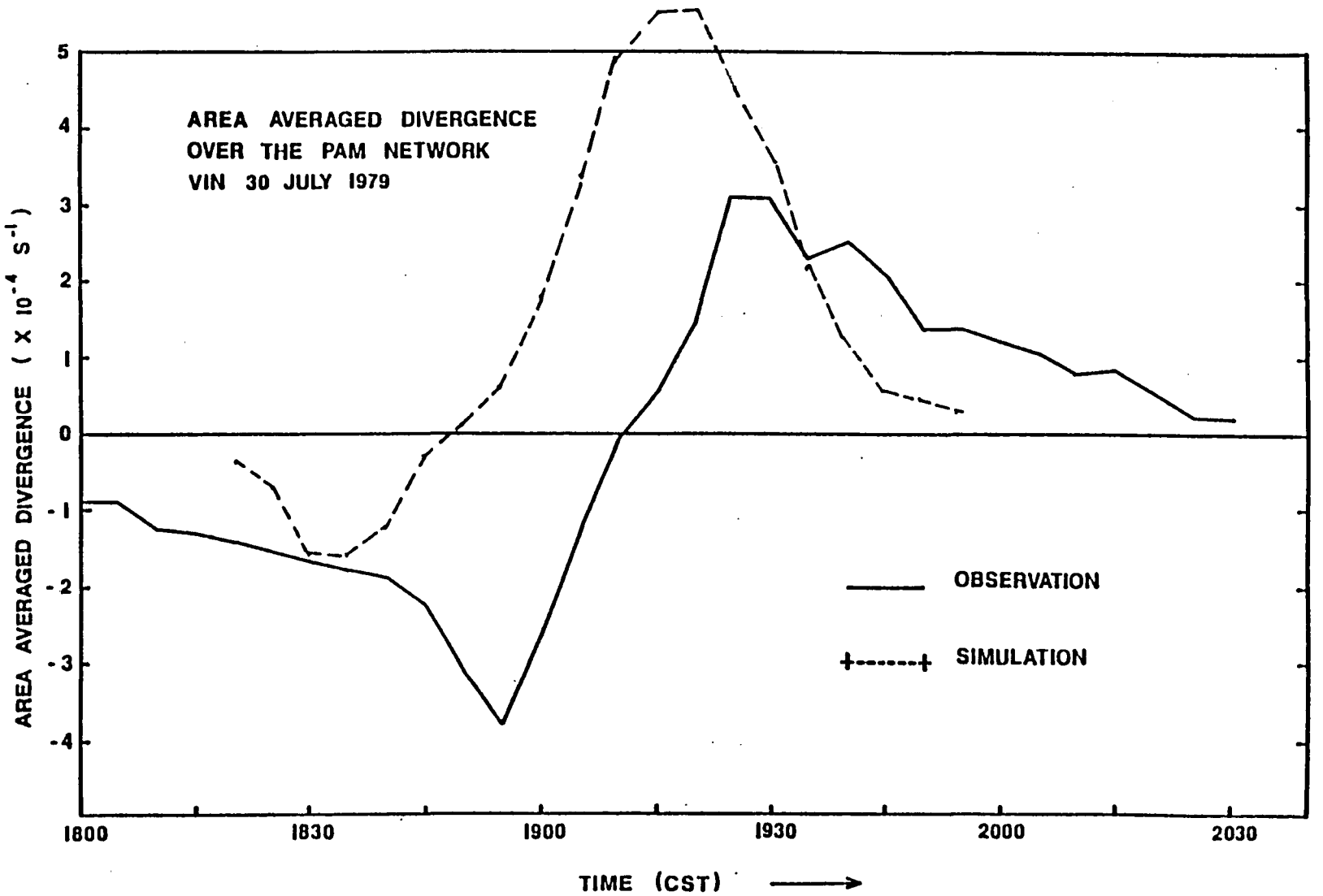
AREA AVERAGED DIVERGENCE
OVER THE PAM NETWORK
VIN 30 JULY 1979
AREA AVERAGED DIVERGENCE (X 10⁻⁴ S⁻¹)
5
4
3
2
1
0
-1
-2
-3
-4
1800
1830
1900
1930
2000
2030
TIME (CST)
OBSERVATION
SIMULATION

Figure 5.11(a).

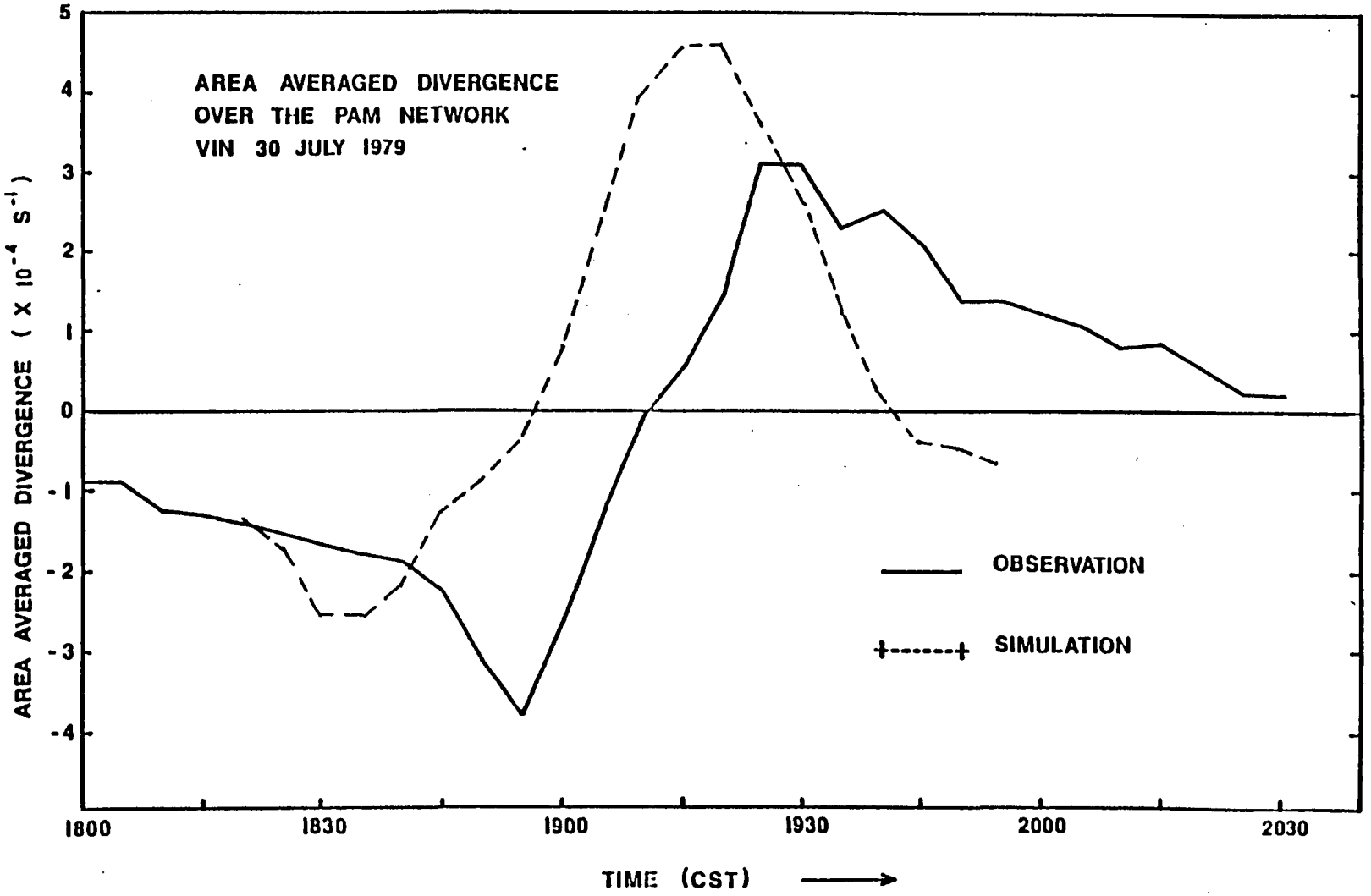
AREA AVERAGED DIVERGENCE
OVER THE PAM NETWORK
VIN 30 JULY 1979
AREA AVERAGED DIVERGENCE (X 10⁻⁴ S⁻¹)
5
4
3
2
1
0
-1
-2
-3
-4
1800
1830
1900
1930
2000
2030
TIME (CST)
OBSERVATION
SIMULATION

Figure 5.11(b).

added to the algorithm area-averaged divergence results in Fig. 5.11(b). Therefore, most of the differences in magnitude between the observed and simulated peaks in area-averaged divergence can be explained by introducing a reasonable background 'larger scale' convergence within which real systems are indeed observed to form.

If, in addition to the larger scale convergence, we assume that there will be a time lag of $\sim$ 10-15 min between the time that the rainfall was observed aloft by radar and the time that it produces outflow as it hits the ground, the phase differences between the observations and simulation disappear. A rain drop fall speed of 5 m s^{-1} from 4.5 km gives a time lag of 15 min. The result of these two adjustments is shown in Fig. 5.11(c). A comparison between the observed surface winds and simulated surface winds for this storm can be found in Figs. 5.4(a) and 5.4(b) in this volume.

The algorithm reproduces the main features (area-averaged convergence, approximate locations of regions of low level convergence and divergence) of the low level kinematic fields. In viewing the results of the calculations, we must bear in mind the phase adjustments and the fact that the algorithm will tend to over estimate divergence and under estimate convergence. We can assume that, given the correct inputs (which include timely upper-air observations), the algorithm will provide a good estimate of the larger scale convectively induced divergence and the general locations of regions of where we would expect to observe maxima and minima in local divergence induced by the interaction of cell outflows. At present, the configuration of the algorithm restricts these applications to the lower levels ($\leq$ 1000 m).

For the VIN case depicted in Fig. 5.11(a)-(c), the network consisted of 27 stations spaced approximately 10 km apart covering an area 50x50 km in length and breadth. The WRC surface wind network deployed around Nelspruit is a much coarser one and is in very rough, mountainous terrain. There were only 9 stations spaced 50 km apart, covering an area with a length scale of about 150 km. We cannot, therefore, expect the values of area-averaged network divergence estimated by the algorithm over this network to be as close to observed values as those obtained for the PAM network. Nevertheless, the algorithm was run for five days when the radar record was long enough to merit a comparison between the estimated divergence and the observed divergence. Figures 5.12(a)-(e) show the results. Again, if we adjust the "background" divergence level on each day, and allow for a 15 min time lag, the agreement is remarkably good. Figures 5.12(a)-(e) are unadjusted. On 7 DEC 85, 7 FEB 86 and 11 FEB 86, the time series in the area-averaged divergence over this coarse and mountainous network area is represented well by the algorithm, suggesting that on these days changes in the area-averaged divergence over the entire network could be attributed mostly to local convection acting within a background of escarpment-scale convergence.

On 3 JAN 86 and 12 FEB 86, the general agreement is not so good after the passage of the main storm system. On 3 JAN 86, both the observed and simulated area-averaged divergence become increasingly divergent until the storm passage, at which point the simulated area-averaged divergence becomes more convergent as the actual observations show a tendency towards greater divergence. Similarly, on 12 FEB 86 later in the day, the observations show an increase in network divergence while the

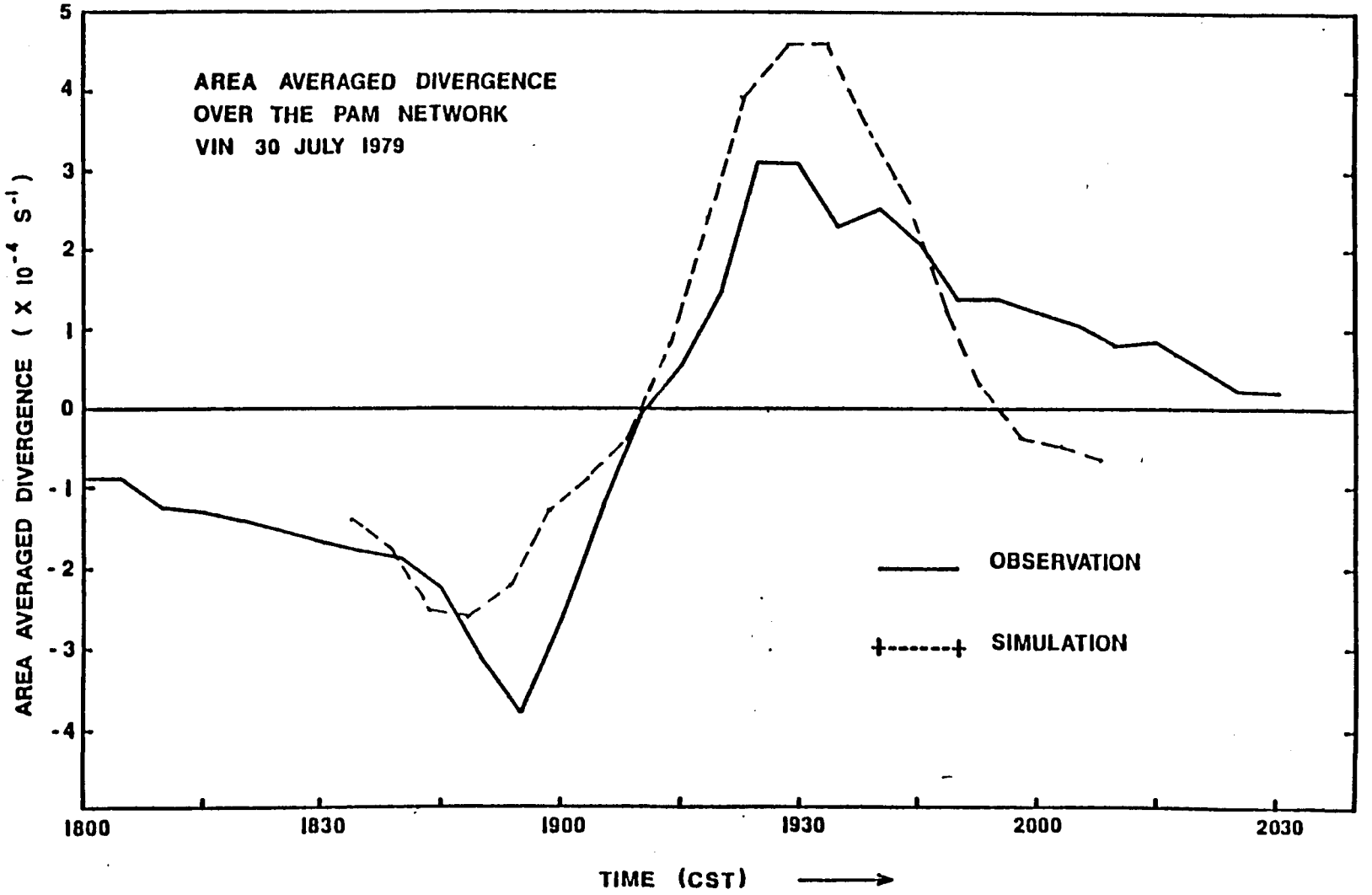
AREA AVERAGED DIVERGENCE
OVER THE PAM NETWORK
VIN 30 JULY 1979
AREA AVERAGED DIVERGENCE (X 10⁻⁴ S⁻¹)
5
4
3
2
1
0
-1
-2
-3
-4
1800
1830
1900
1930
2000
2030
TIME (CST)
OBSERVATION
SIMULATION

Figure 5.11(c).

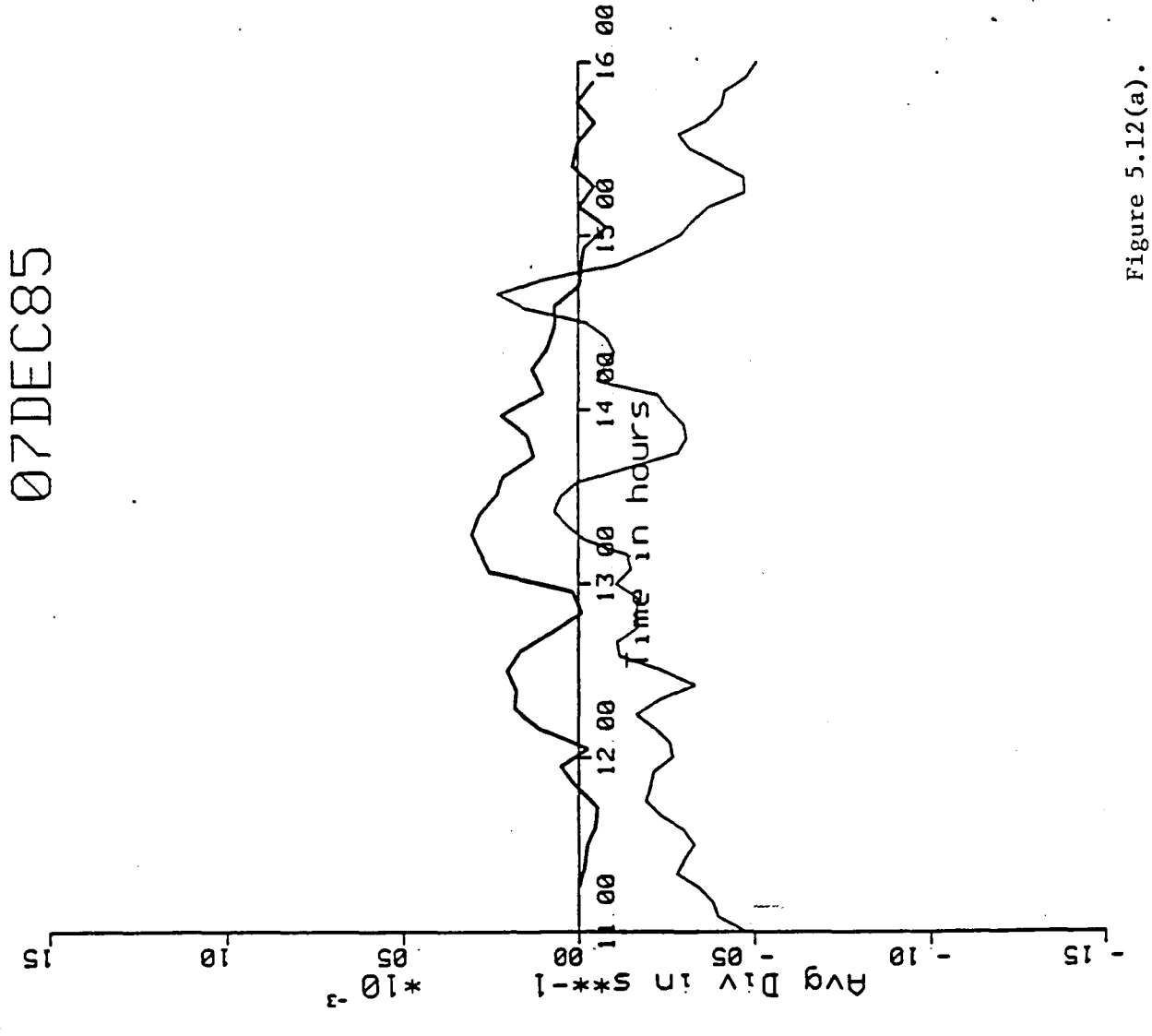
07DEC85
Avg Div in s**-1
*10 -3
-15
-10
-05
00
05
10
15
11 00
12 00
13 00
14 00
15 00
16 00
Time in hours

Figure 5.12(a).

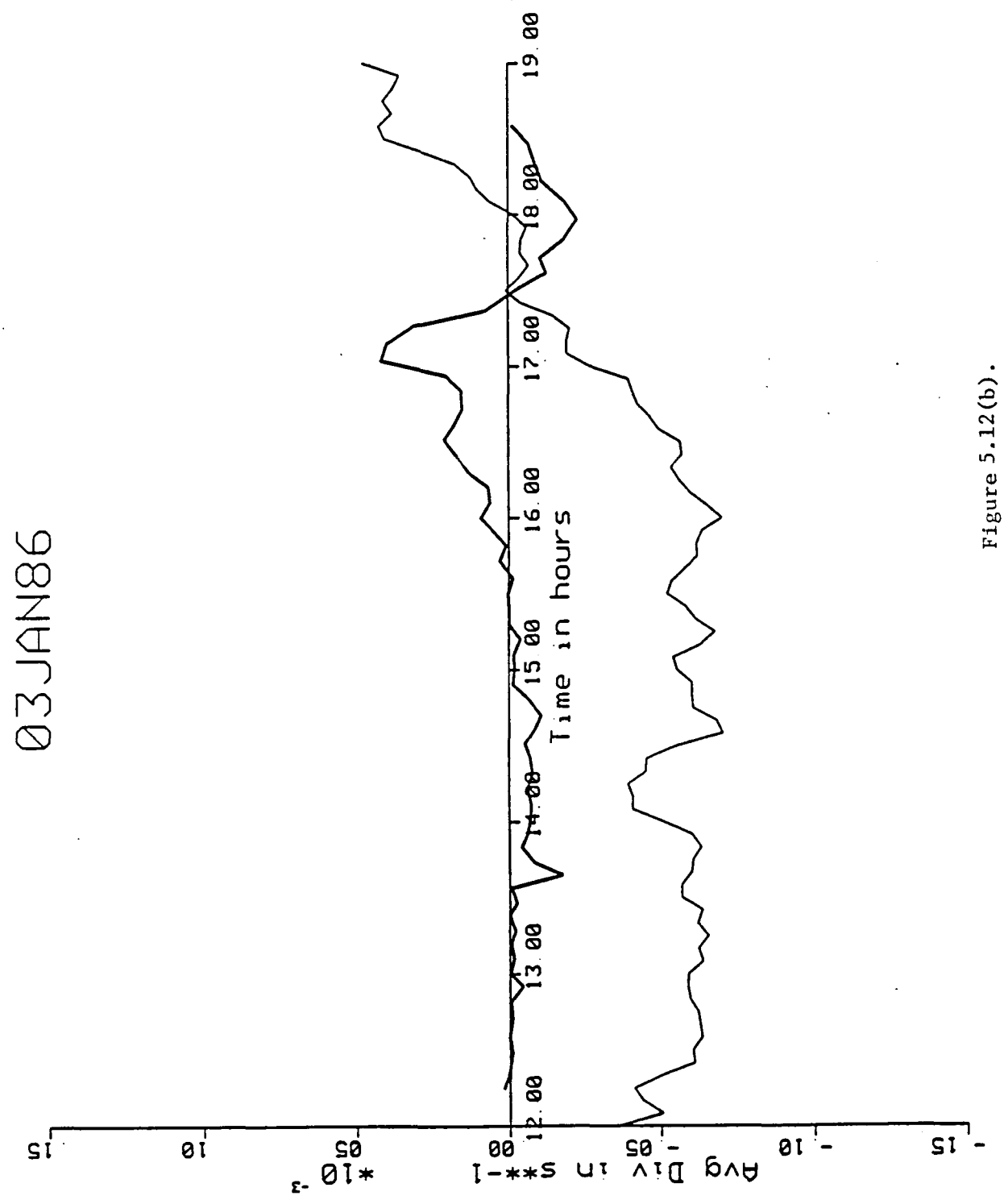
03JAN86
Avg Div in s**-1
*10 -3
15
10
05
00
- 05
- 10
- 15
12 00
13 00
14 00
15 00
16 00
17 00
18 00
19 00
Time in hours

Figure 5.12(b).

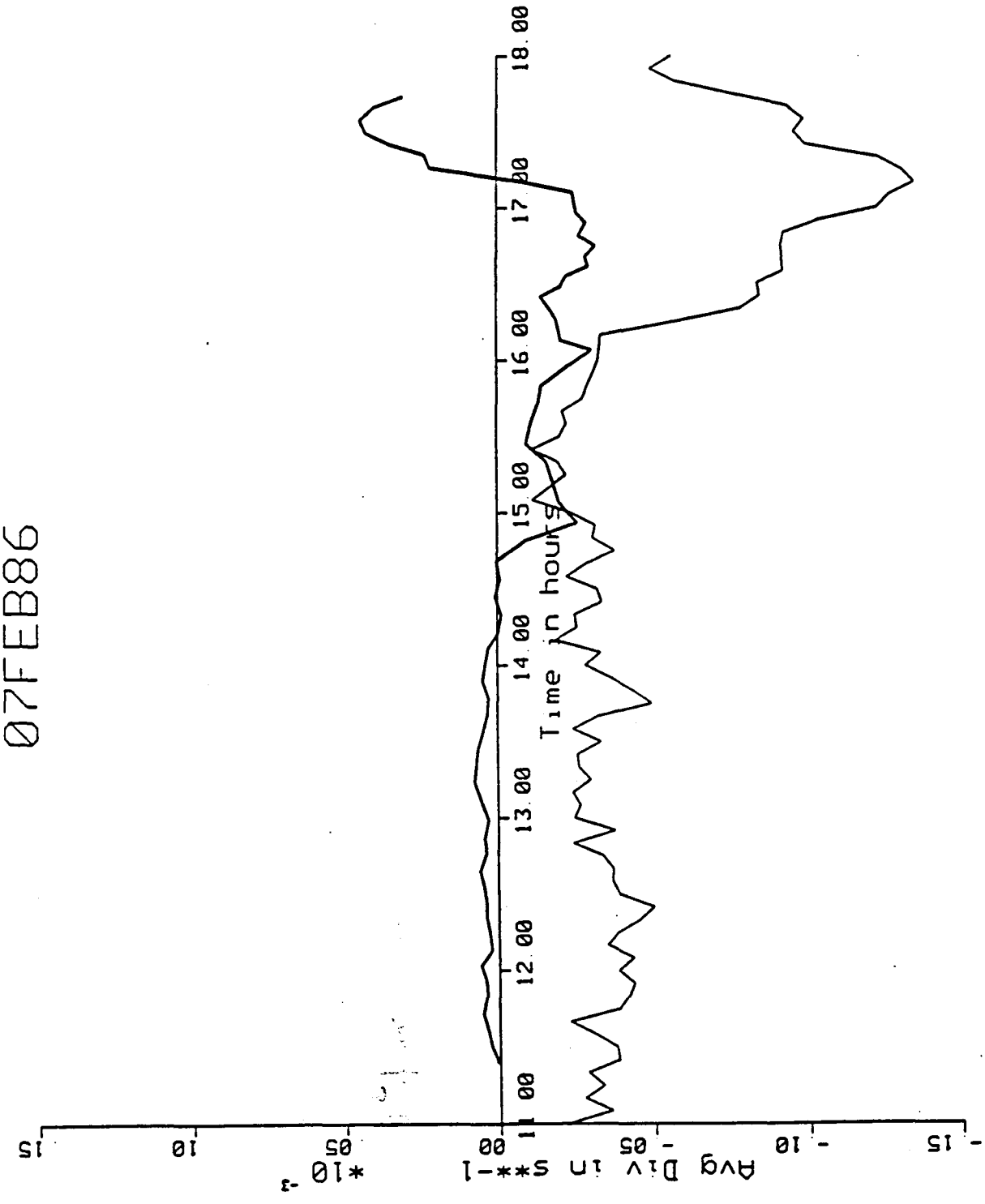
07FEB86
Avg Div in s**-1
*10 -3
15
10
05
00
- 05
- 10
- 15
11 00
12 00
13 00
14 00
15 00
16 00
17 00
18 00
Time in hours

Figure 5.12(c).

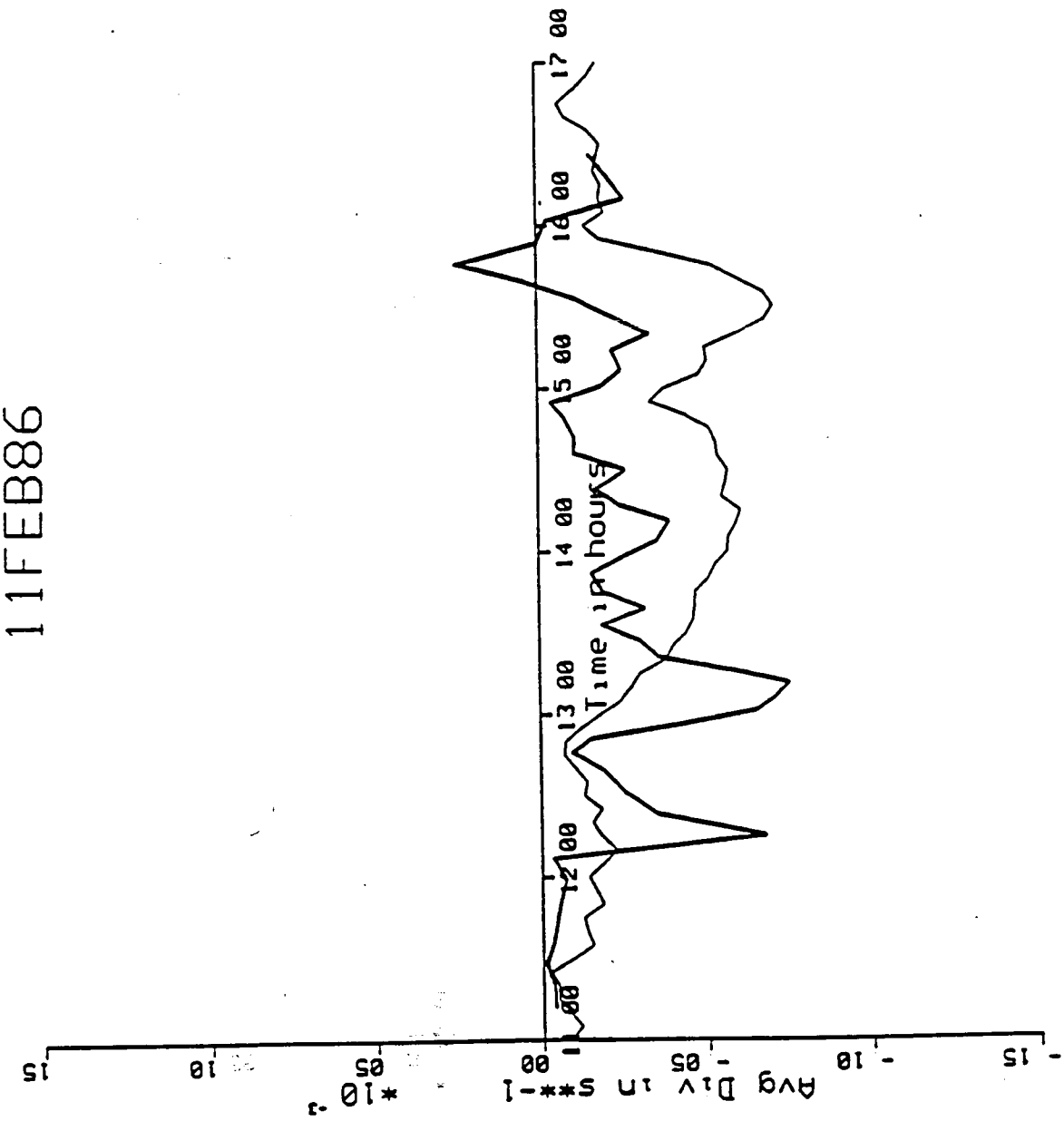
11FEB86
Avg Div in s**-1
*10 -3
15
10
05
00
- 05
- 10
- 15
12 00
13 00
14 00
15 00
16 00
17 00
Time in hours

Figure 5.12(d).

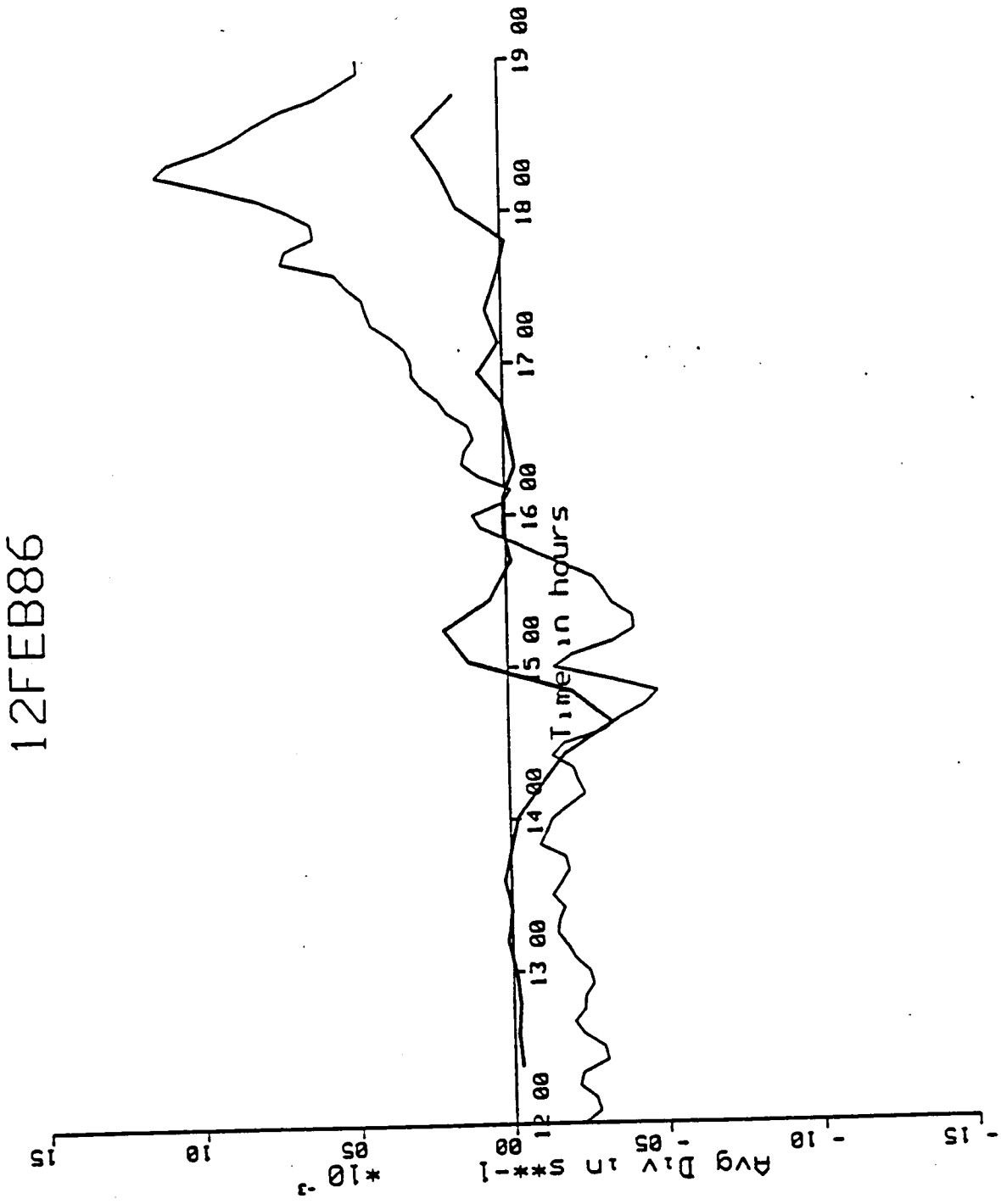
12FEB86
Time in hours
Avg Div in s**-1
*10 -3
12 00
13 00
14 00
15 00
16 00
17 00
18 00
19 00
15
10
05
00
-05
-10
-15

Figure 5.12(e).

simulation shows much less divergence. These periods of strong divergence in the network cannot be explained by the algorithm but it may be said that they are probably not due to the action of convective scale downdrafts.

5.4.2 Case Studies

Seven case studies were chosen at random from the 20 days under study to be presented here. They provide examples of the use of the algorithm as a diagnostic tool and as a short-term forecasting aid. The calculations can be performed rapidly enough to be displayed in real time, ideally overlayed on the radar screen. They hold out the possibility of contributing to the selection and classification of seeding targets.

The algorithm was run for each five minute radar record during which the cloud physics aircraft (the Lear) was in the air. A 5x5 km grid was then set up with the mean position of the aircraft for that radar record located at the center. Then the estimated winds for a 50x50 km area around the aircraft were calculated at each of the 121 grid points. Thus, a 50x50 km box with 5x5 km spacing followed the aircraft around.

Each figure which follows shows:

a) The radar echo return at the time indicated, with dBz between 35 and 40 represented as blue, dBz between 40 and 45 as yellow, between 45 and 50 dBz as red, 50-55 as green and above 55 dBz as purple.

b) The solid light green line is the line of zero divergence, the dashed green lines are lines of convergence (negative divergence) drawn every $2.0 * 10^{-4}$ s^{-1}. Positive divergence is not plotted.

c) The solid blue contours are the outlines of the 35 dBz radar return approximately 20 min later than the color-contoured return. The actual time is indicated.

d) The 30 km range rings from the Nelspruit radar are plotted to give a sense of position relative to Nelspruit.

e) The transponder track of the Lear jet is plotted as a red line joining red squares.

All runs were for 1000 m AGL, and all winds are storm-relative. The position of the center of the box relative to the Nelspruit radar is noted at the top of each frame.

The 'rear' of the storm is taken to be the divergent side, while the convergent side is referred to as the 'front' of the storm, regardless of absolute orientation.

5.4.2.1 Case 1: 27 NOV 84

The morning sounding shows strong westerly/southwesterly flow in the middle and upper layers and light northeasterlies below 5000 ft. The radar area increases from about 20 km^2 around 1245 LST to a peak of 170 km^2 around 1420, then declines to 27 km^2 by 1601. Figure 5.13 shows the estimated fields around the aircraft at 1235 LST. If there are no aircraft tracks plotted, then the aircraft was not in the air at the time.

The radar before 1235 LST showed little or no activity although the aircraft appeared to have spotted a suitable cell which has not yet reached 35 dBz in intensity. By 1235 LST a cell appears with echo greater than 35 dBz, and the algorithm puts in a downdraft at that location, integrates the shear from the sounding, and produces the convergence fields of Fig. 5.13.

The aircraft track during the 1235 LST radar scan arcs around the western edge of the storm, starting on the left flank, flying around the rear left flank towards the center, and then over the main convergence zone at the front. The new development occurred within the area outlined over the convergence zone in Fig. 5.13. All of the new development in the 30 min after 1235 LST occurs within that area.

This represents a case of isolated cells with little or no outflow interaction.

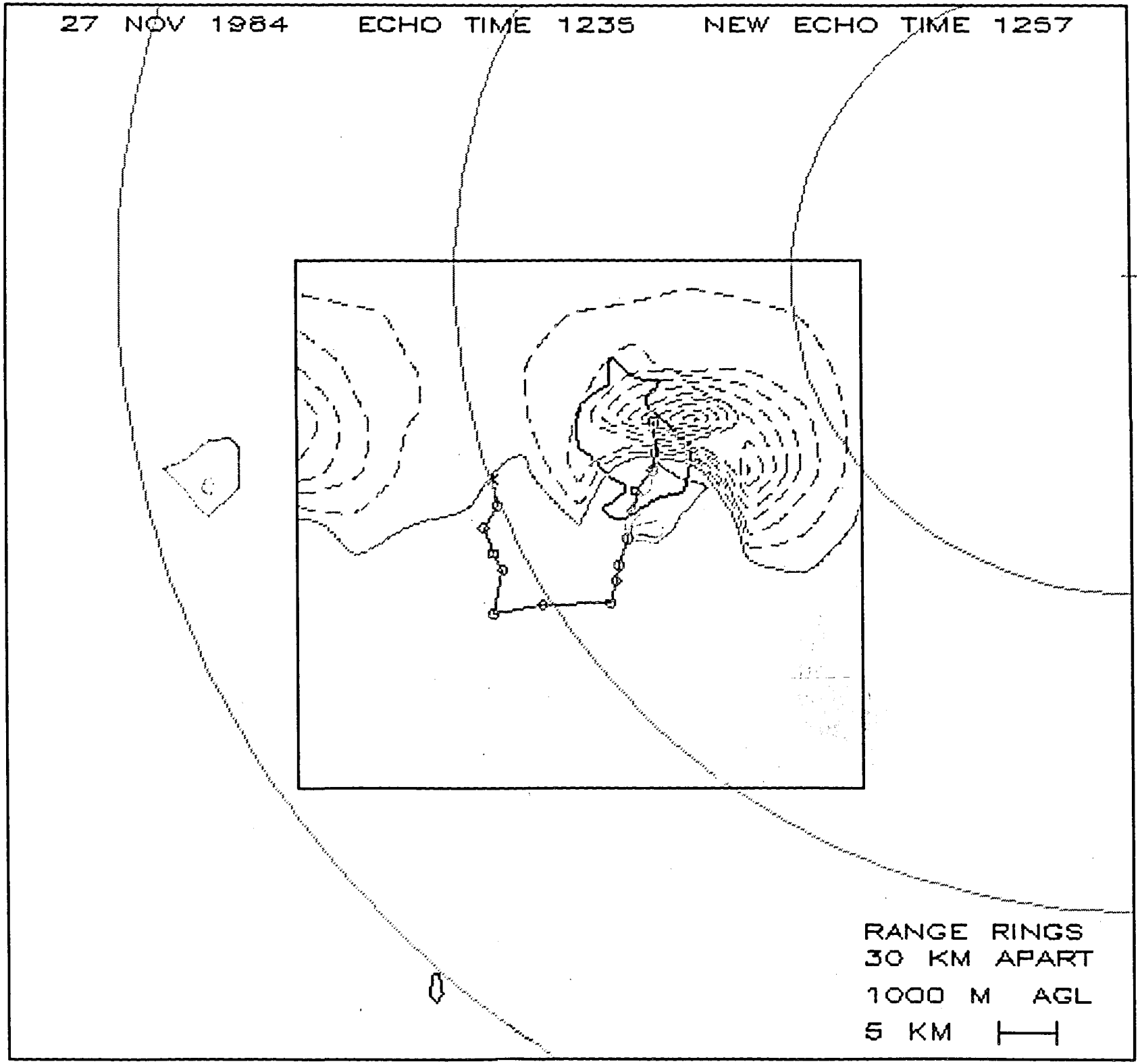
27 NOV 1984 ECHO TIME 1235 NEW ECHO TIME 1257
RANGE RINGS
30 KM APART
1000 M AGL
5 KM

Figure 5.13

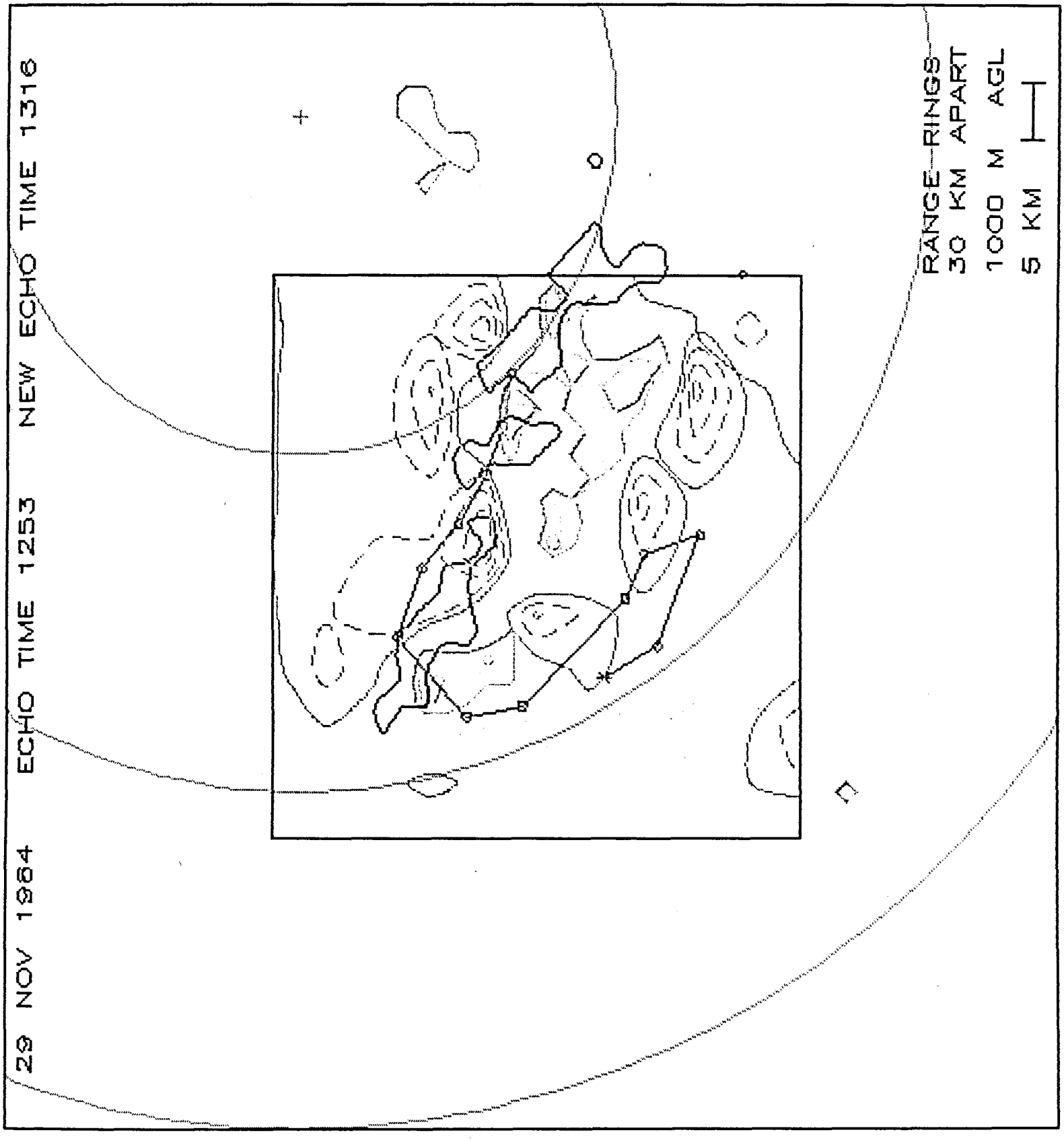
29 NOV 1984 ECHO TIME 1253 NEW ECHO TIME 1318
RANGE RINGS
30 KM APART
1000 M AGL
5 KM

Figure 5.14(a)

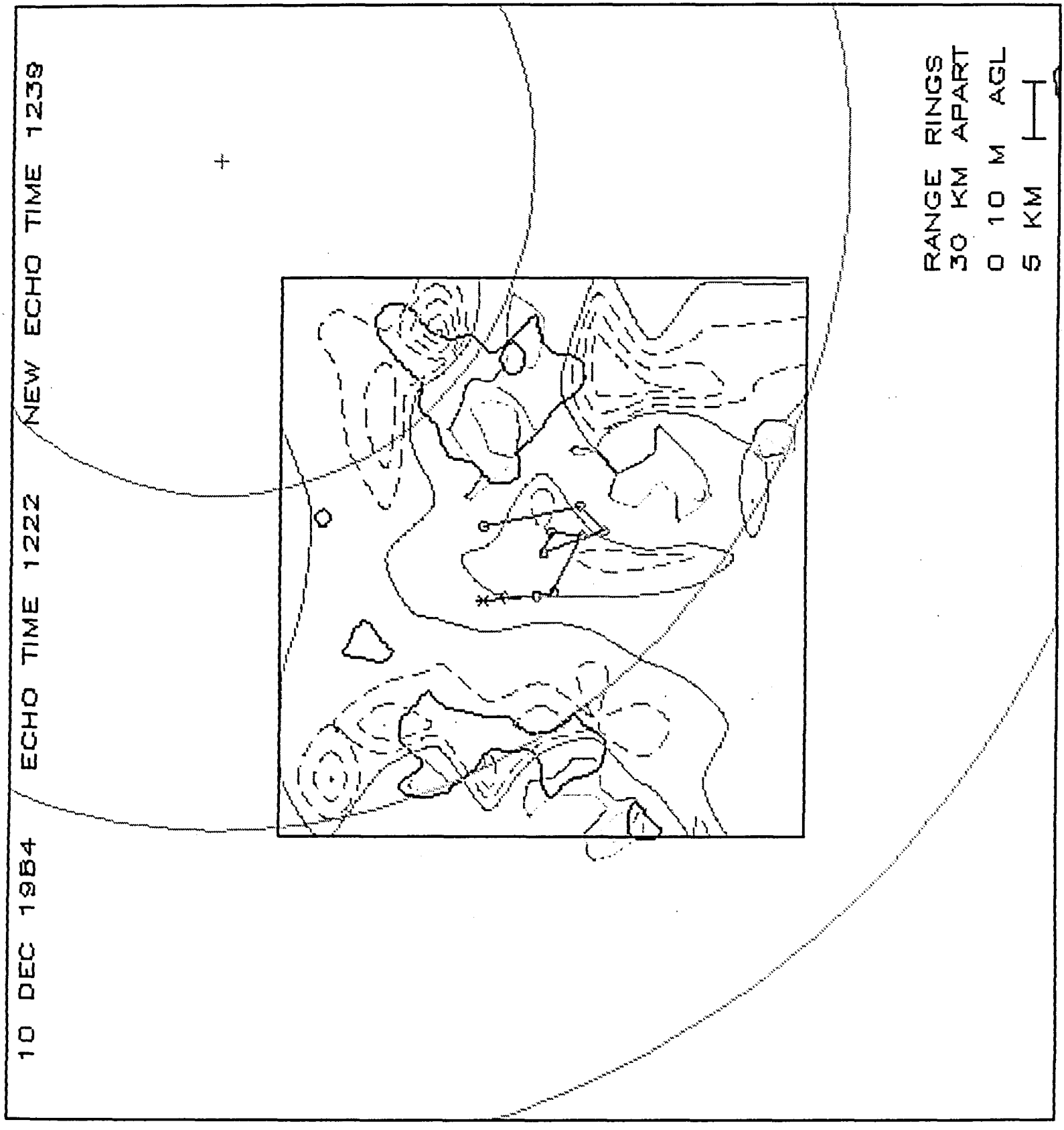
10 DEC 1984 ECHO TIME 1222 NEW ECHO TIME 1239
RANGE RINGS
30 KM APART
0 10 M AGL
5 KM

Figure 5.15(a)

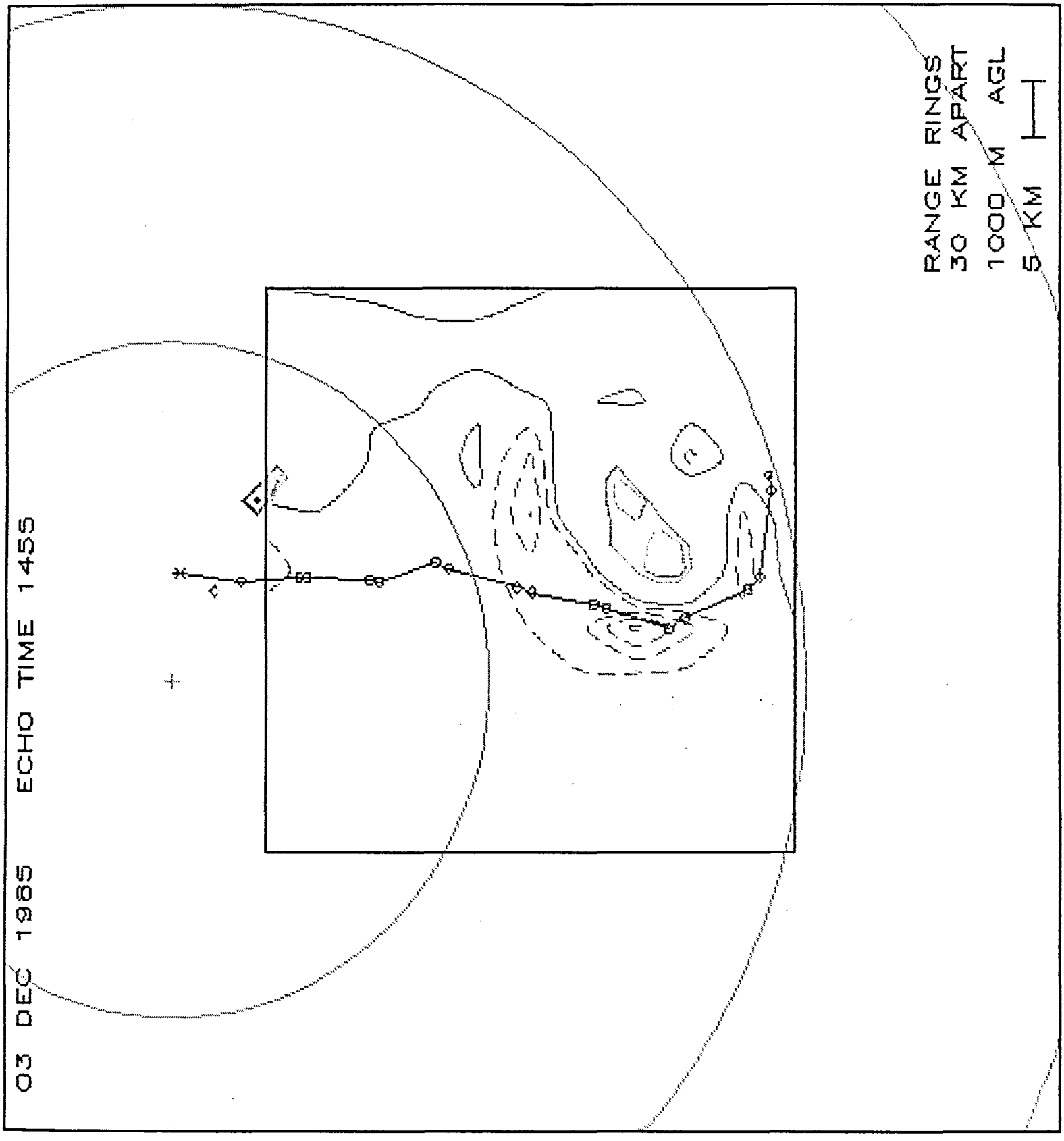
RANGE RINGS
30 KM APART
1000 M AGL
5 KM
03 DEC 1985 ECHO TIME 1455

Figure 5.16(a)

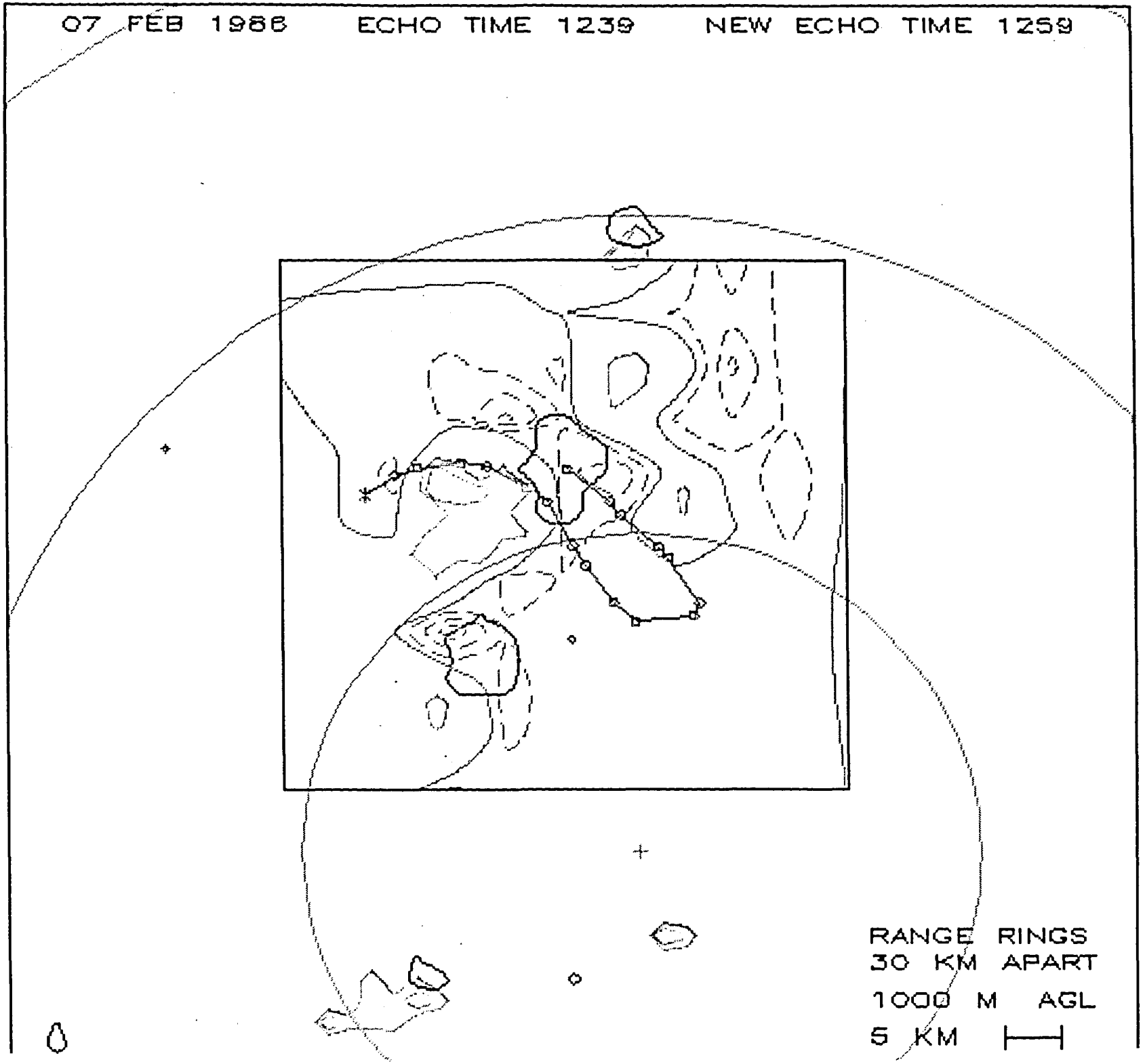
07 FEB 1986 ECHO TIME 1239 NEW ECHO TIME 1259
RANGE RINGS
30 KM APART
1000 M AGL
5 KM

Figure 5.17(a)

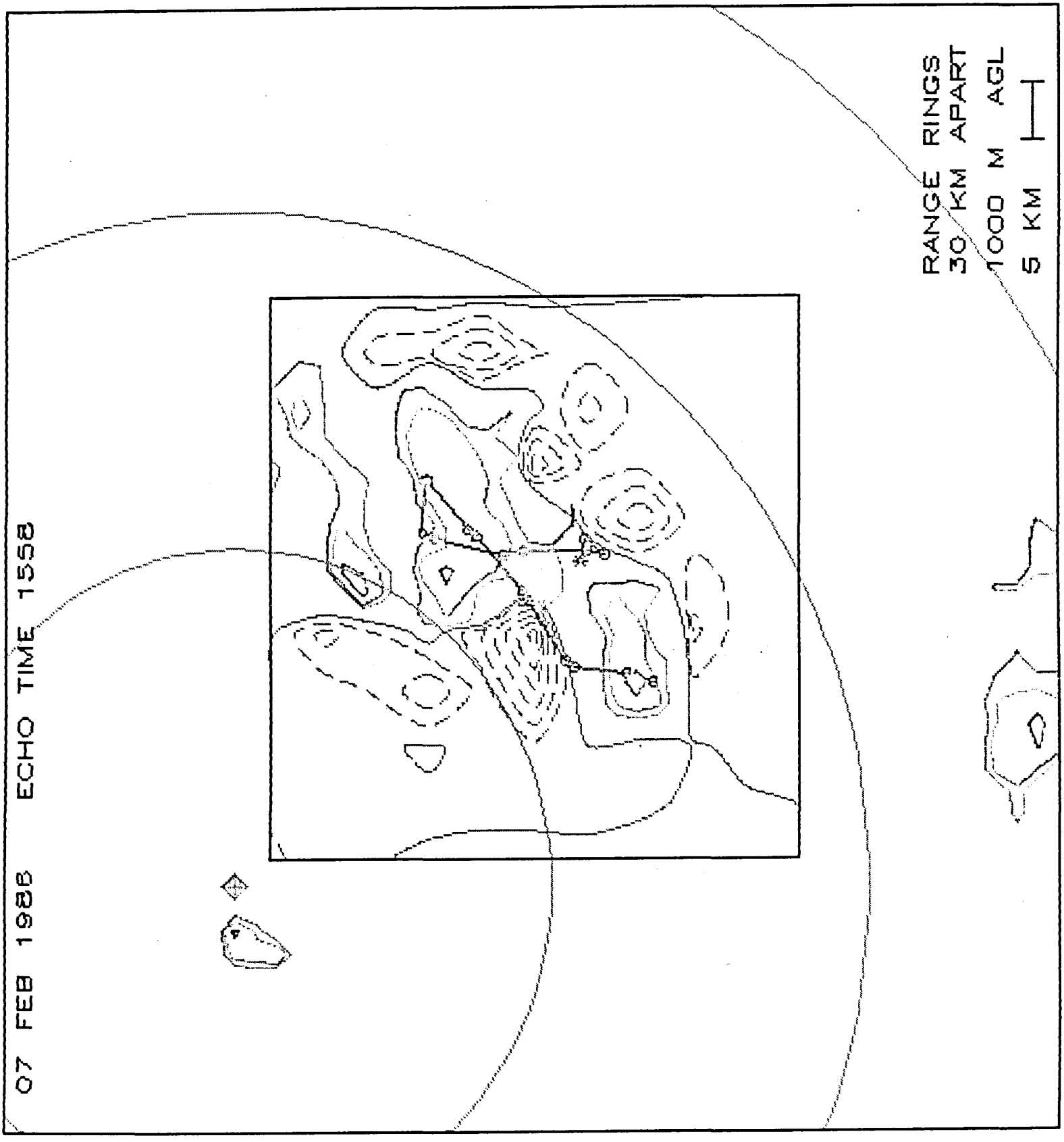
07 FEB 1988 ECHO TIME 1558
RANGE RINGS
30 KM APART
1000 M AGL
5 KM

Figure 5.18(a)

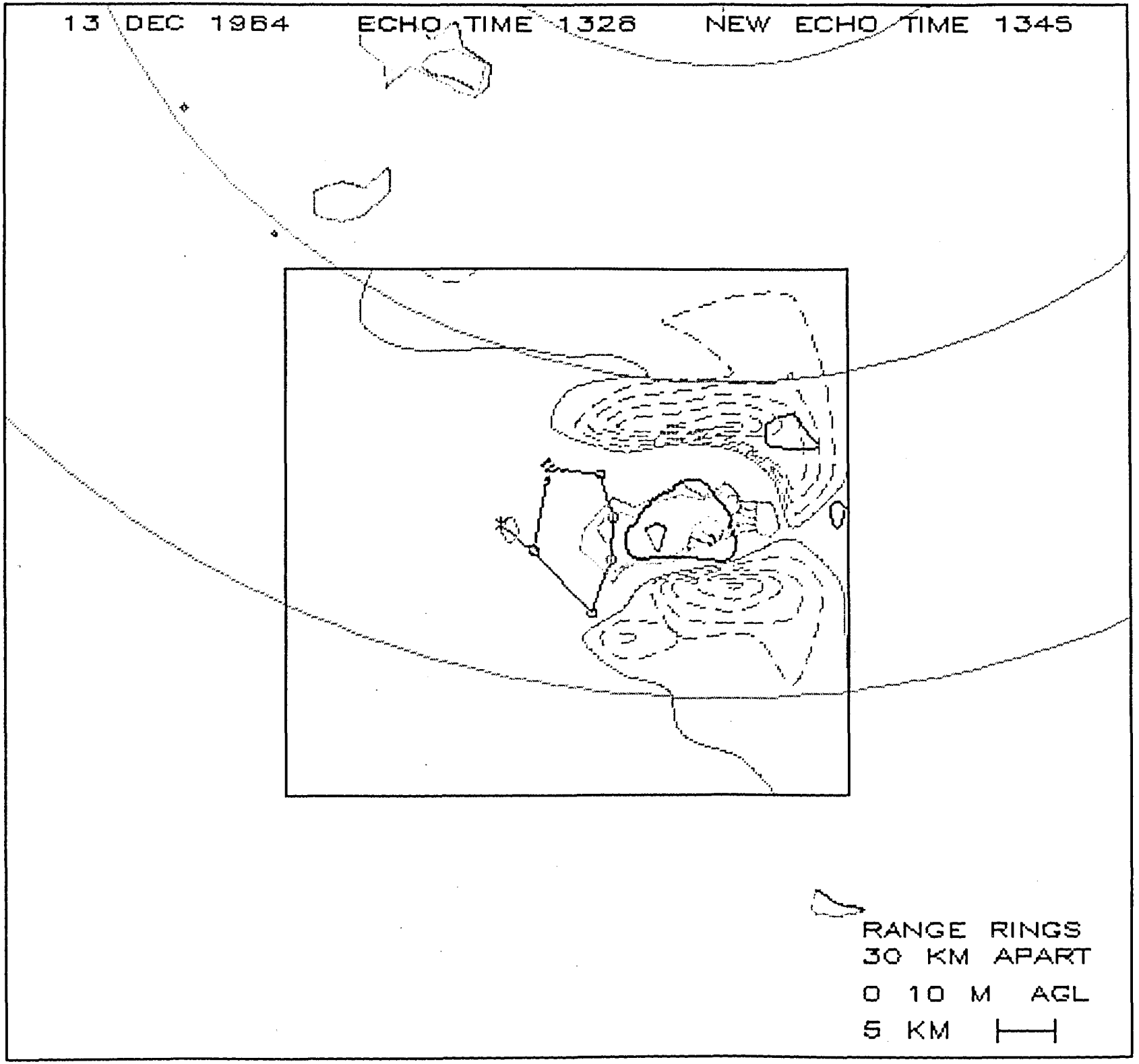
13 DEC 1964 ECHO TIME 1328 NEW ECHO TIME 1345
RANGE RINGS
30 KM APART
0 10 M AGL
5 KM

Figure 5.19(a)

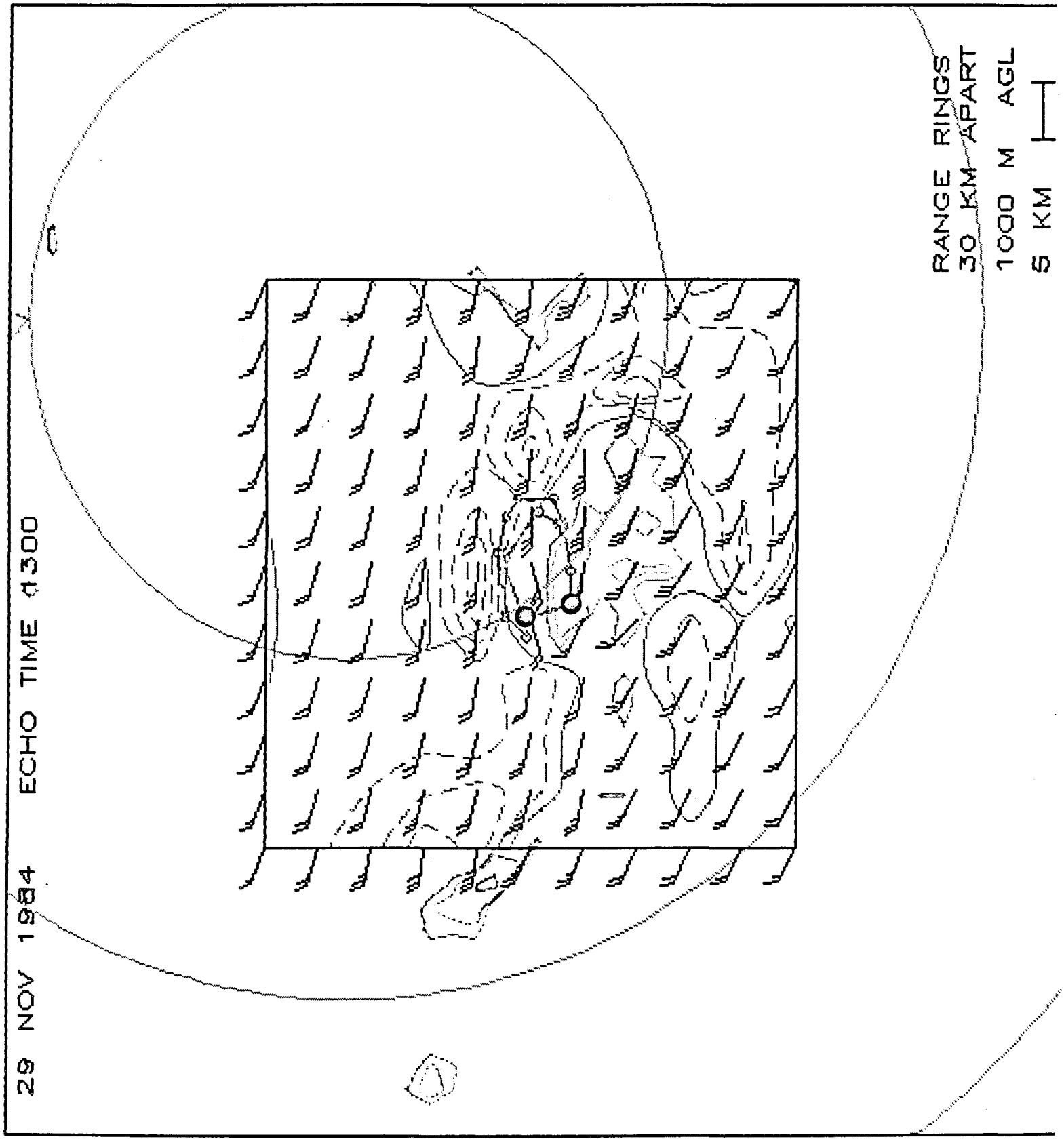
29 NOV 1984 ECHO TIME 1300
RANGE RINGS
30 KM APART
1000 M AGL
5 KM

Figure 5.21(a)

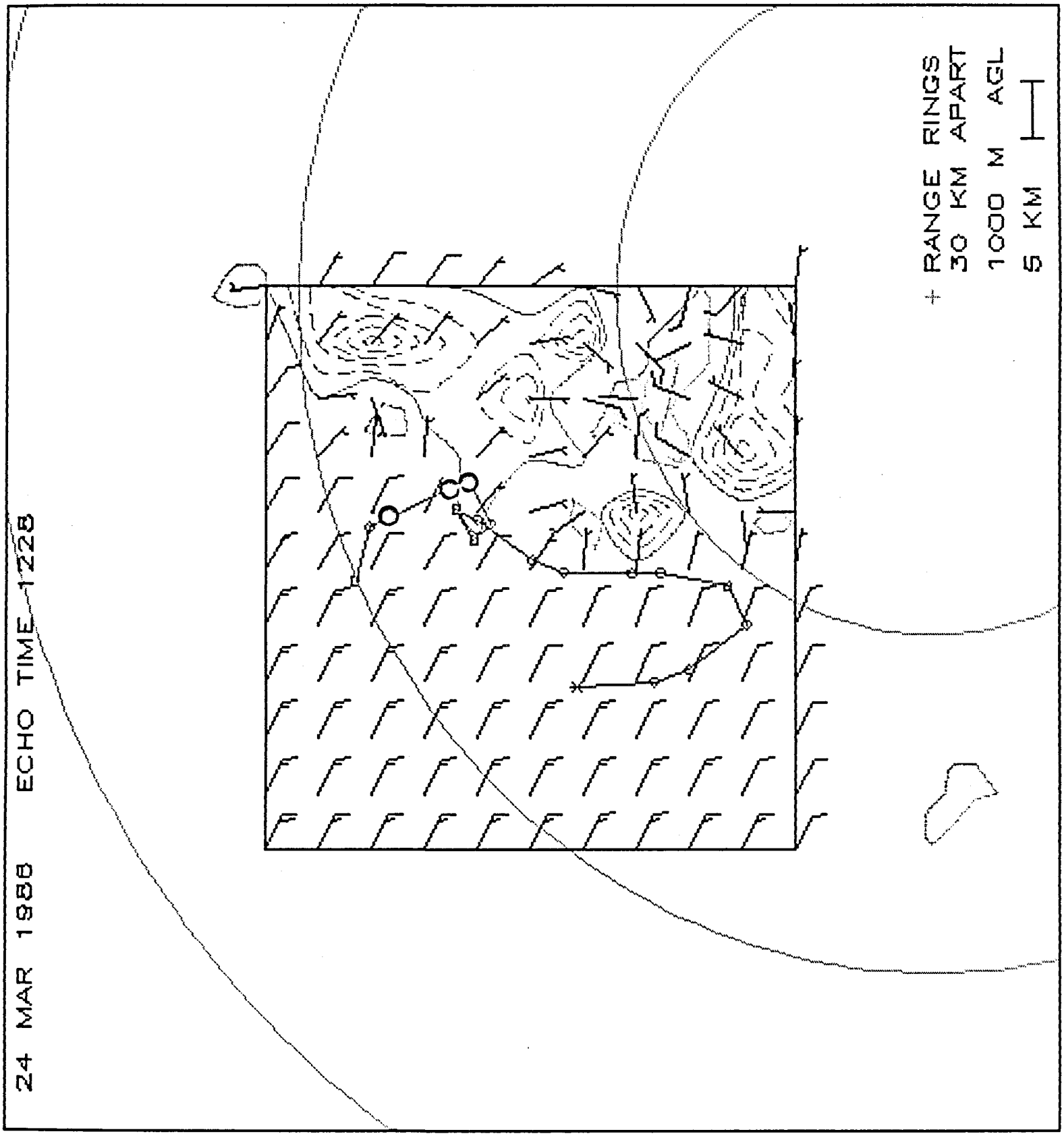
24 MAR 1988 ECHO TIME 1228
RANGE RINGS
30 KM APART
1000 M AGL
5 KM

Figure 5.21(d)

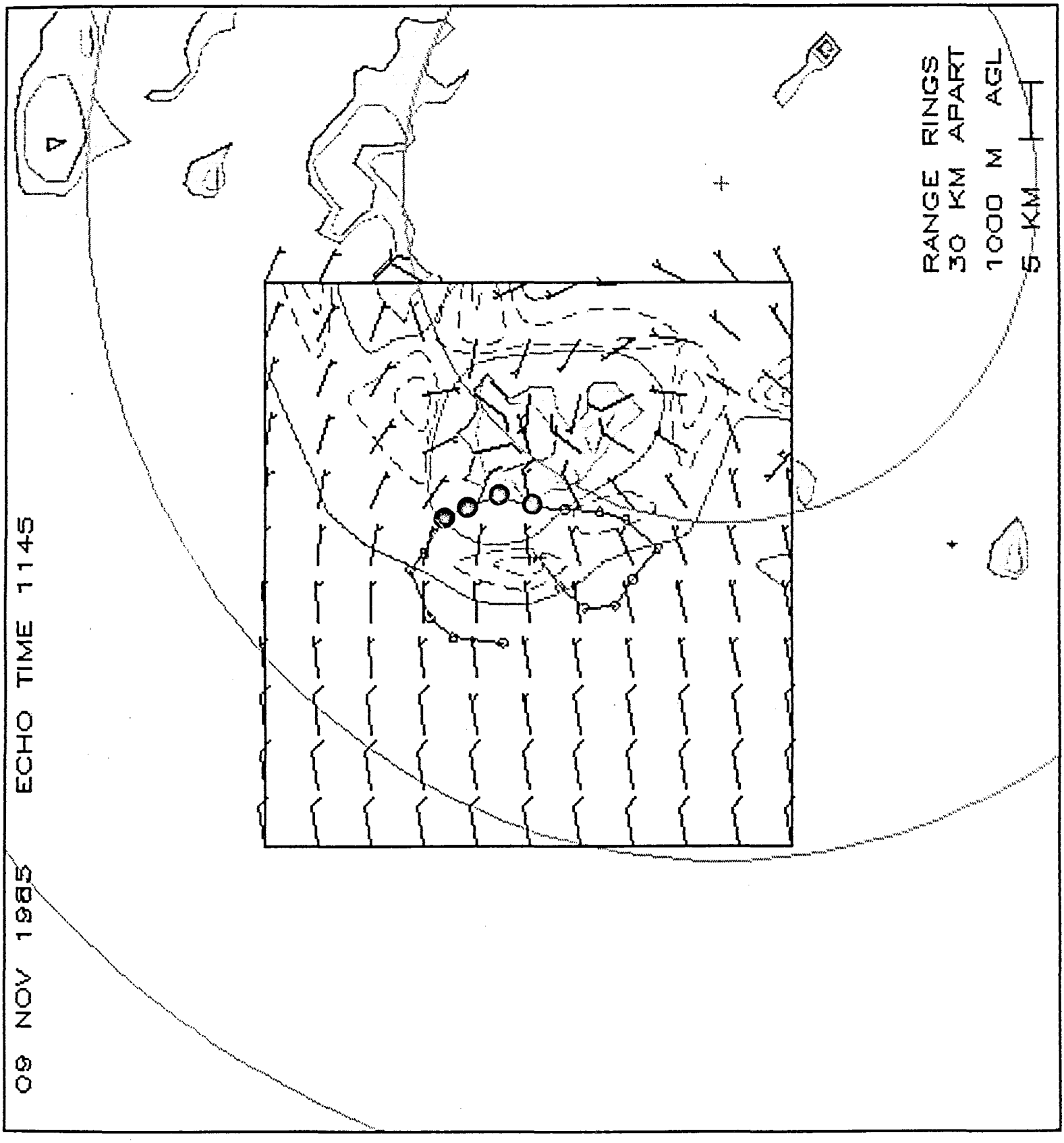
09 NOV 1985 ECHO TIME 1145
RANGE RINGS
30 KM APART
1000 M AGL
5 KM

Figure 5.21(g)

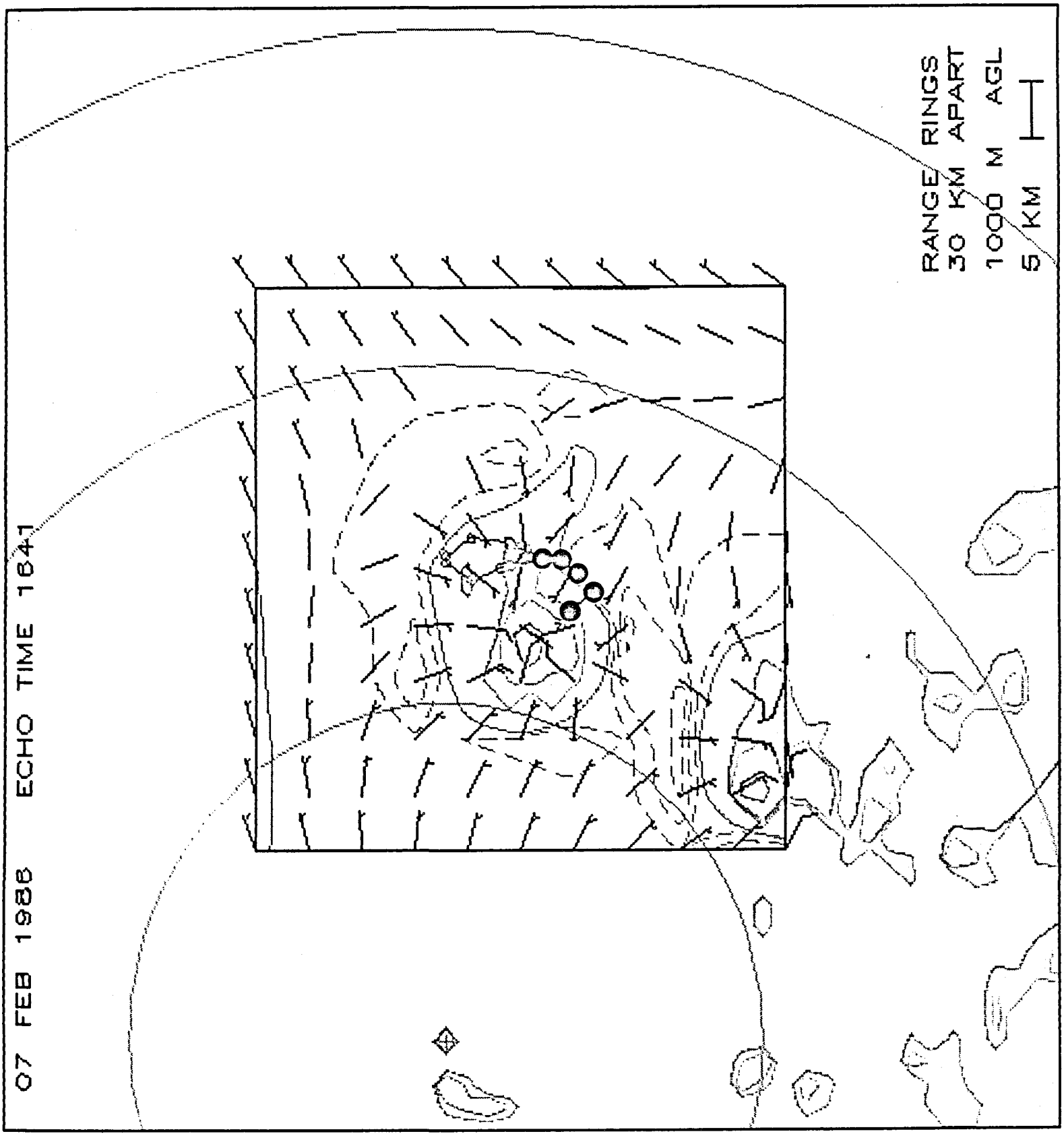
RANGE RINGS
30 KM APART
1000 M AGL
5 KM
07 FEB 1988 ECHO TIME 1641

Figure 5.21(J)

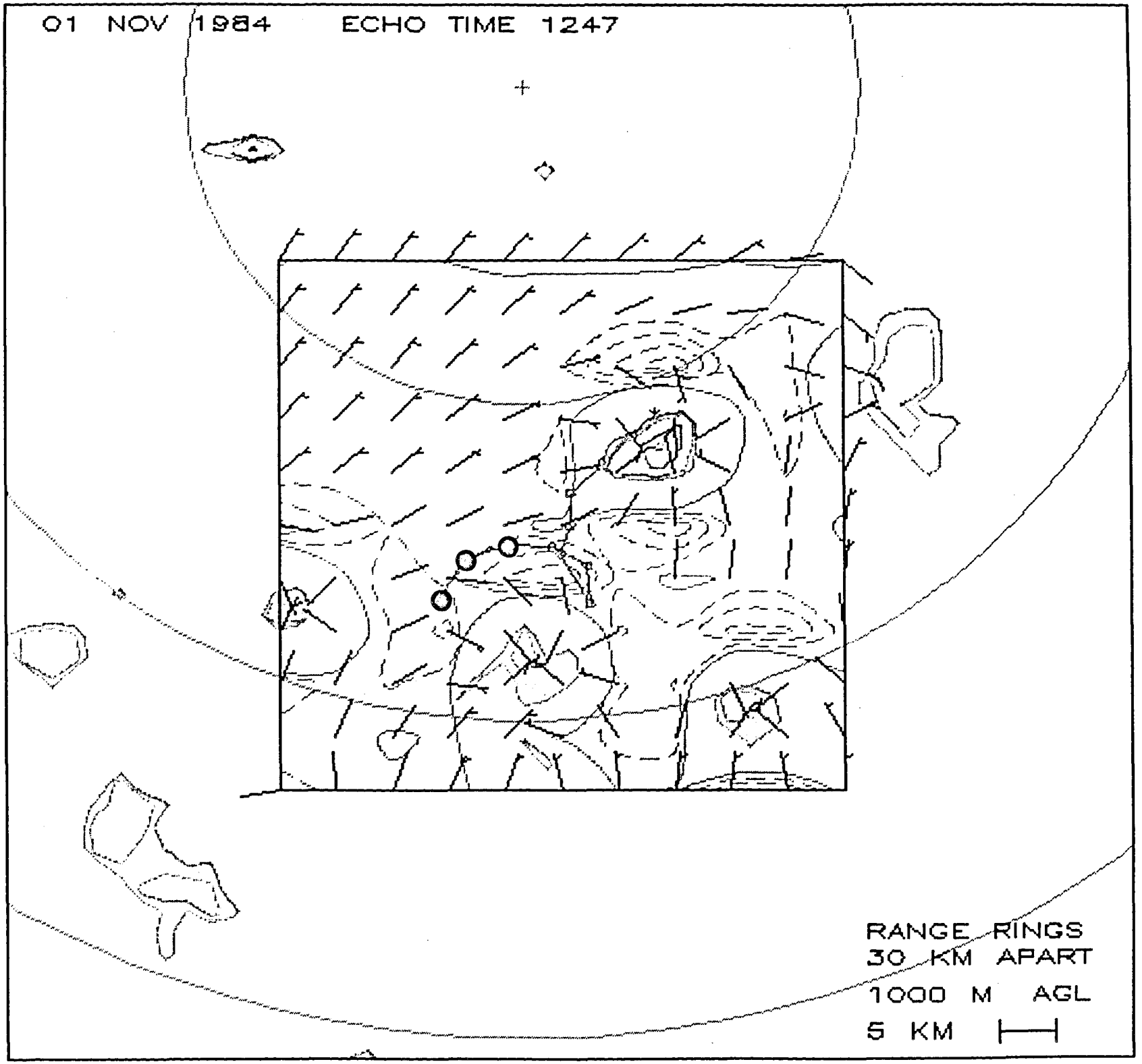
01 NOV 1984 ECHO TIME 1247
RANGE RINGS
30 KM APART
1000 M AGL
5 KM

Figure 5.21(m)

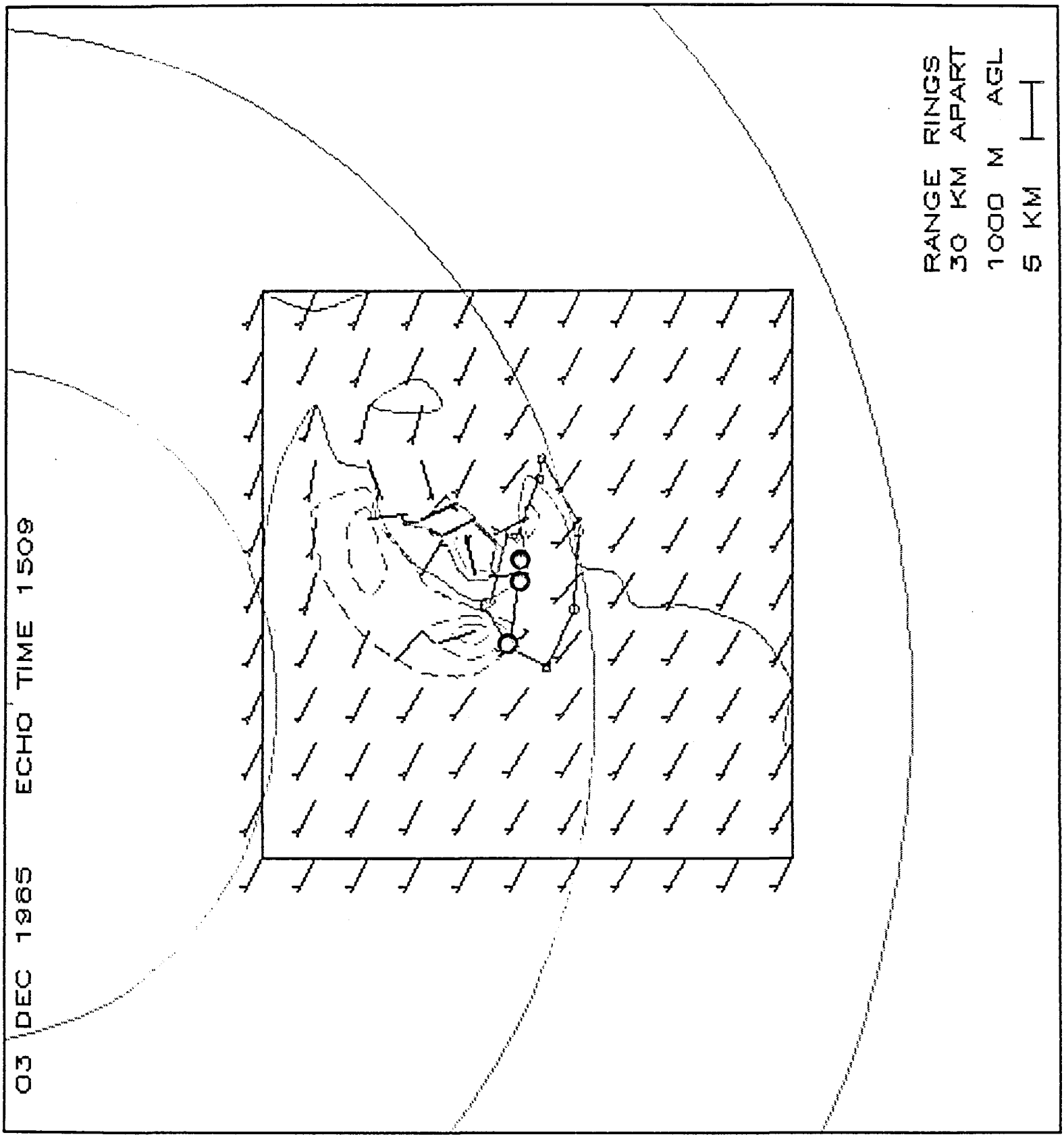
RANGE RINGS
30 KM APART
1000 M AGL
5 KM
03 DEC 1985 ECHO TIME 1509

Figure 5.21(q)

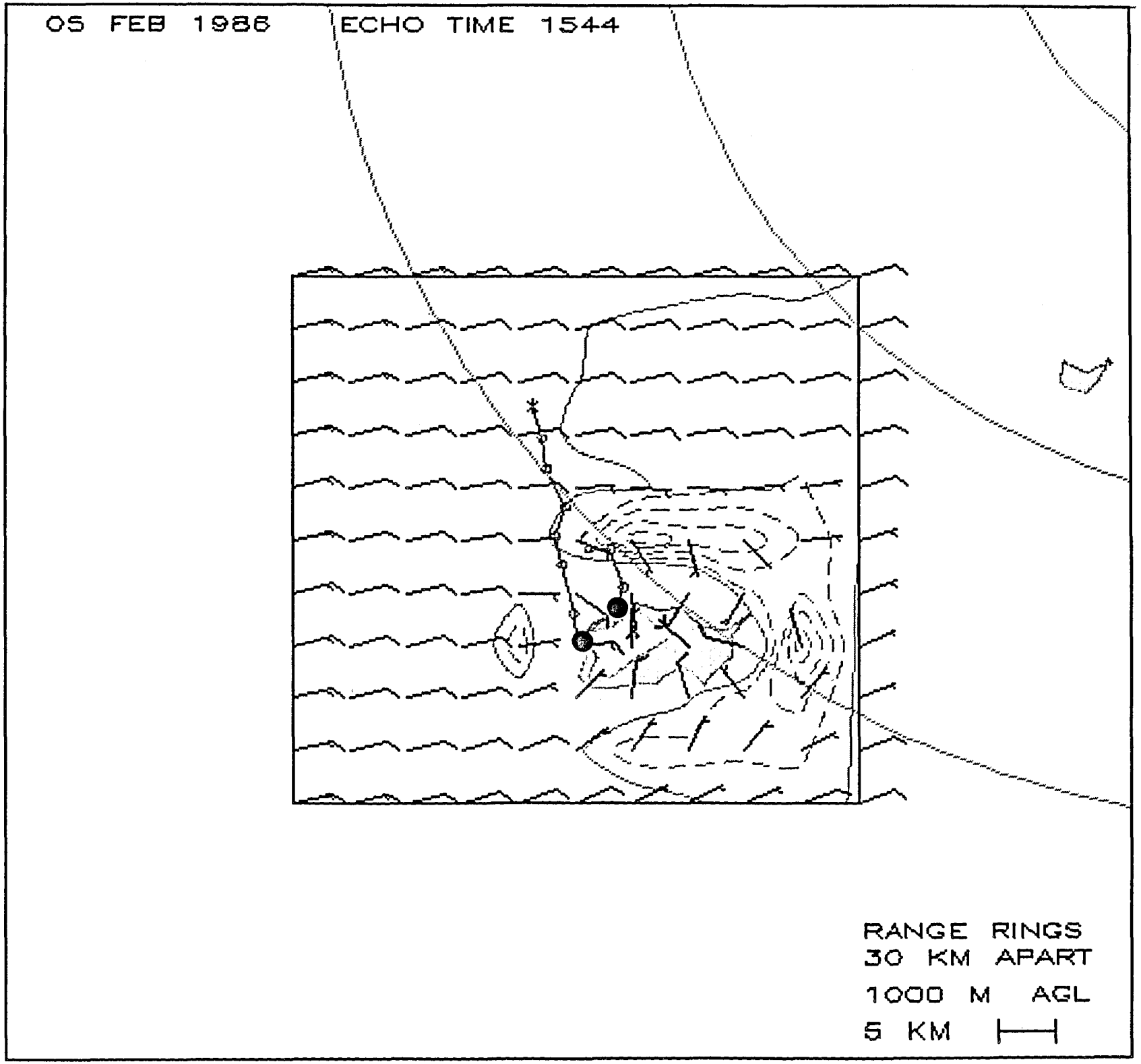
05 FEB 1986
ECHO TIME 1544
RANGE RINGS
30 KM APART
1000 M AGL
5 KM

Figure 5.21(v)

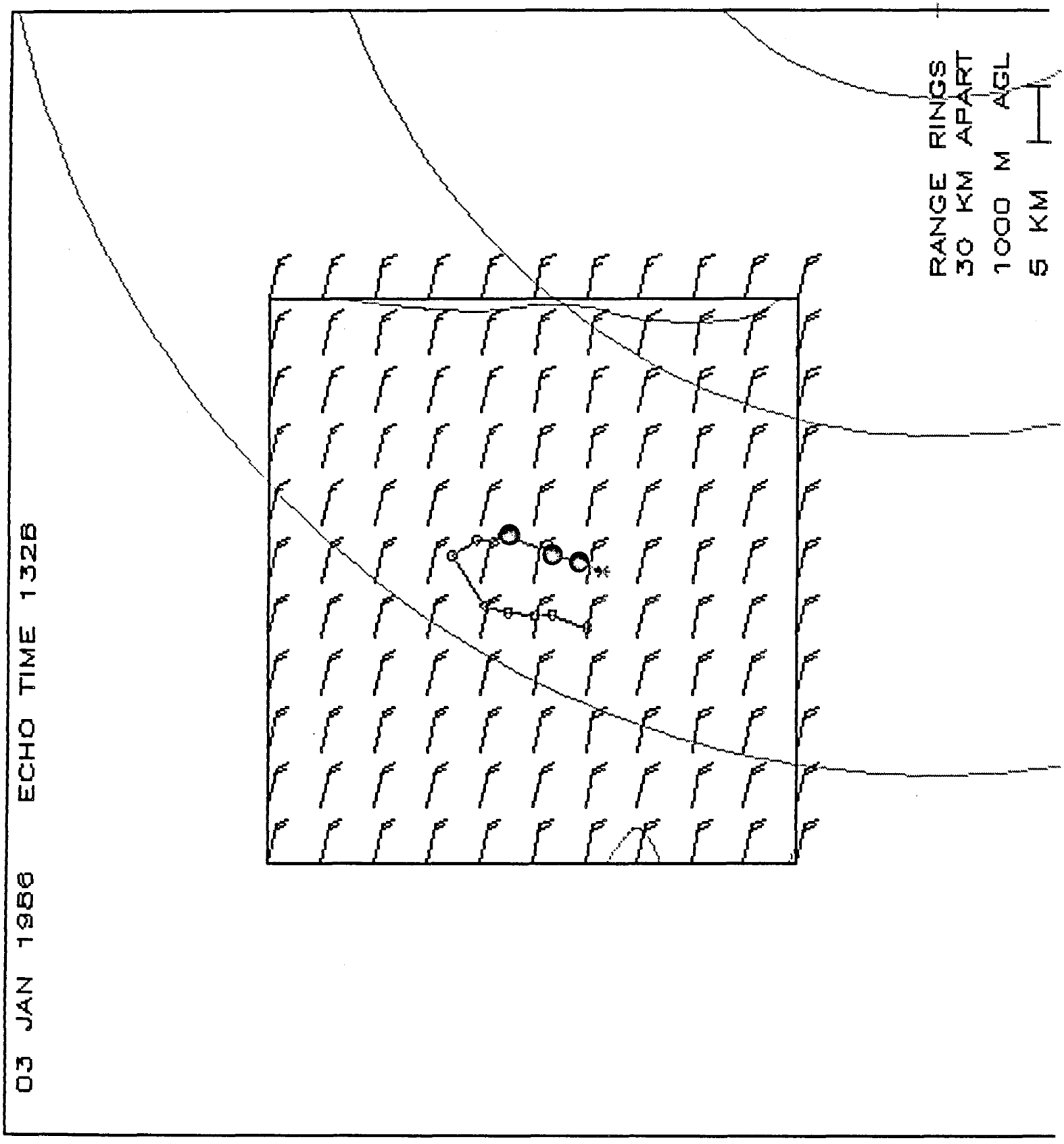

Figure 5.21(bb)

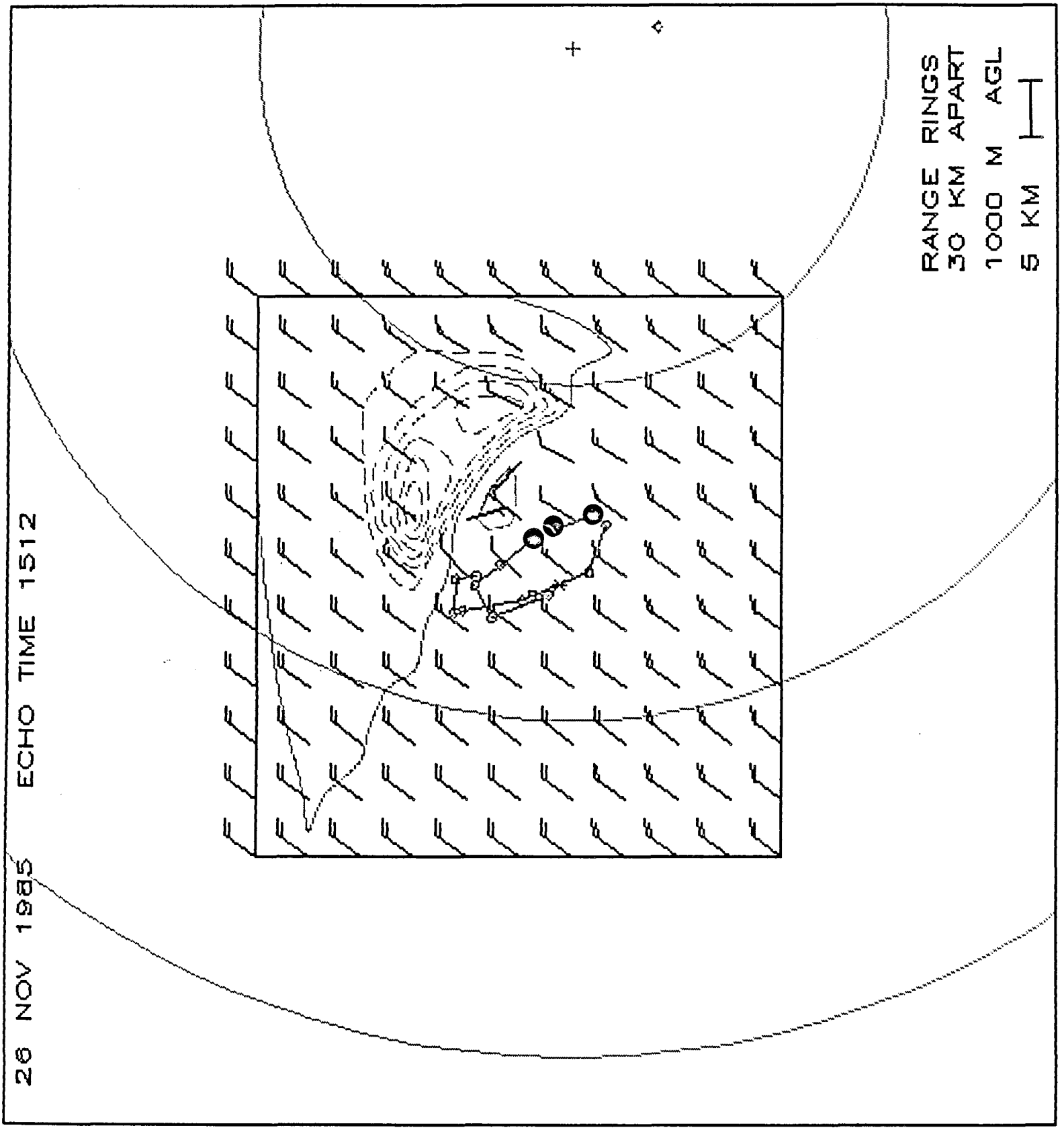

Figure 5.21(gg)

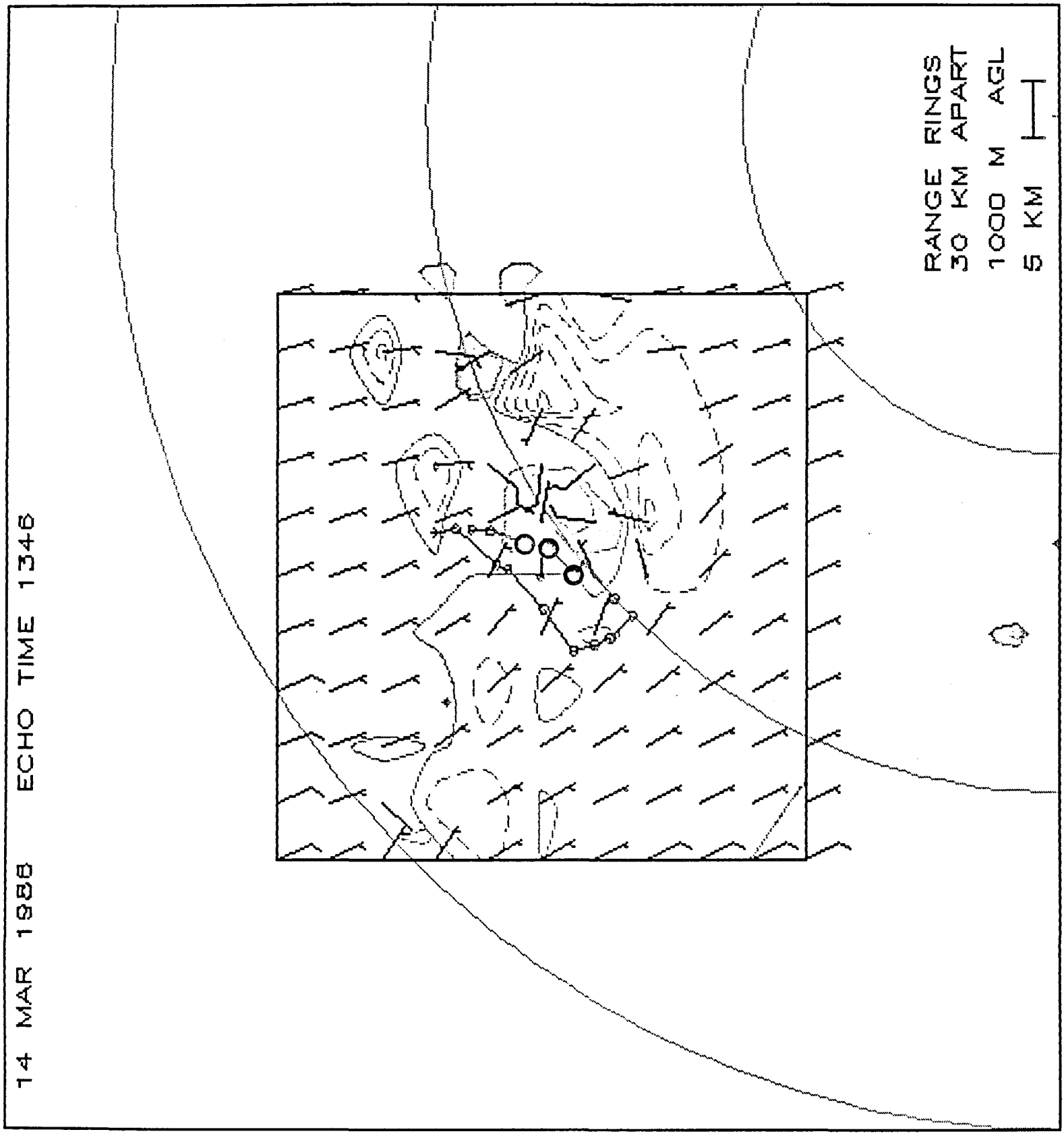

Figure 5.21(11)

6.5 The PAWS sounding database (Morrison and Morgan)

6.5.1 Introduction

The CIC-PAWS Sounding Database was generated at CIC in Nelspruit to provide rapid and simple access to processed aircraft and rawinsonde sounding data taken at Nelspruit. As many meaningful sounding parameters as possible have been computed in the database to eliminate the need for any intermediate processing of data between the database and statistical/graphical analysis programmes. The database was structured in a record-oriented ASCII format in order to take advantage of the SORT/MERGE utility available on the CIC MV4000 which permits high-speed, unlimited stratifications of disk files. Quality control has been very strict in assembling the database; any soundings with bad or questionable data have been excluded.

6.5.2. Physical structure of the database

As of 22 July 1986 the database is just over 1.25 MB in size. It consists of 921 records (715 Nelspruit rawinsonde, 176 Learjet, and 29 Aero-Commander soundings; and 1 terminator record) each of which is 1400 bytes long. The data begin with the 1982/83 summer season and currently run through the end of the 1985/86 season.

6.5.3. Logical structure of the database

Each record has a 200A7 FORTRAN format. The terminator record at the end of the database consists of all 9's. The contents of each data word is detailed in file ":UDD BRIAN:SOUNDING DB: SOUNDING DB PARAMS". The general categories of parameters in each record are listed below:

* identification parameters (date, time, ID code, etc)
* surface data parameters
* sounding vertical limits
* wind parameters (valid for rawinsonde soundings only)
* standard level temperature and mixing ratio data
* classical stability indices (K-index, etc)
* average boundary layer theta-e and mixing ratios
* cloud base and related parameters (e.g. LFC computed from cloud base, delta-T at 500 mb assuming moist adiabatic ascent from cloud base, etc)
* CCL and related parameters
* dry-bulb and wet-bulb freezing level parameters
* parcel ascent times from cloud base or CCL to -10°C
* experimental stability-related parameters (Theta-e max, etc)
* database management parameters
* spare (blank) words for future database expansion.

The file SOUNDING DB PARAMS mentioned above also contains the necessary information for decoding each data word, as well as the physical location of each data word and flag for including individual data words in statistical and graphical summaries.

6.5.4. Decoding database records

The data words in each record are either ASCII character strings, integer or real numbers encoded into an A7 word. Decoding is done according to the conversion equation assigned for each data word, described at the end of file SOUNDING DB PARAMS. The suggested sequence for decoding numerical data words is as follows: The subroutine READ SOUNDING DB PARAMS reads the file SOUNDING DB PARAMS, loads the parameter description and unites strings into string arrays, then loads the conversion equations and factors into integer arrays. These arrays are stored in COMMON blocks. Once this is done the subroutine CODE SOUND PARAMS can be called to decode any numerical parameter. Bad, missing or inapplicable data are represented by either a blank (" ") or flagged ("-999999") string prior to parameter decoding or by a value of -99 or -99.9 after decoding.

Only 2 of the data words in each record are non-numerical parameters. Parameter number 5 ("Sounding ID") identifies the sounding as from the Nelspruit rawinsonde ("Nst RAW"), CIC Learjet 24 ZS-LTK ("Lear 24"), or CIC Aero-Commander ZS-IZN ("Aer-Com"). All the rawinsonde soundings were taken at CIC, and all of the aircraft soundings were taken during ascent from or descent back into the Nelspruit airfield. Parameter number 6 ("Aircraft Mission") serves as a flag to identify operational days: "No Ops" for days on which no research aircraft missions were flown, "ERSE" for days on which the Exploratory Randomized Seeding Experiment was conducted, and "CldPhys" for all other days on which cloud physics research missions were flown.

6.5.5. Description of individual parameters

Most of the parameters are self-explanatory and will not be discussed here. Readers are referred to the subroutine SOUND DBASE COMPS for details on how most of the parameters were computed. Specific parameters requiring elaboration are briefly described below:

* params 24 to 27: Sounding top descriptors. Learjet upsoundings out of the Nelspruit airfield generally terminate at about 300 mb, although they may terminate as low as 350 mb. To permit computation of an equilibrium level from these soundings, the Nelspruit 06Z morning sounding data above the termination level is appended to the Lear soundings. If this has been done the minimum sounding pressure will be that of the morning rawinsonde sounding. Learjet downsoundings and Aero-Commander soundings are not modified in any way.

* Params 40 to 43: Low-level jet descriptors. We define the low level jet as the wind speed maximum 5 km AMSL.

* Params 45, 46, 48, 49: Wind shear vectors. These are the vectors constructed by the vectorial addition of the wind vectors for the specified levels.

* Params 69 to 72: Average boundary layer theta-e and mixing ratio. These quantities are averaged over either the lowest 60 mb or the lowest 100 mb for the given sounding.

* Params 73 to 92: Cloud base related parameters. We define cloud base as the point where the average theta-e and mixing ratio over the lowest 60 mb intersect. No LFC is computed if there is no conditionally unstable layer above the cloud base. No equilibrium level is computed if there is no LFC or if the sounding does not extend at least up to the top of the conditionally unstable layer. The adiabatic updraft for a parcel ascending from cloud base to the -10°C level is not computed if the parcel is not positively buoyant by the time it reaches the -10°C level. The delta-T's at 700, 500 and 300 mb are all computed assuming moist adiabatic ascent of a parcel from cloud base.

* Params 95 to 110: CCL related parameters. The CCL is found by following the temperature sounding downwards until the saturation mixing ratio intersects the average mixing ratio over the lowest 60 mb. Except for the absence of a separate LFC, all the computations in the paragraph above also apply here.

* Params 125 to 148: Experimental stability related parameters. Theta-e_{max} and Theta-es_{max} are found between the surface and 700 mb. Theta-e and theta-es_{min} are found above the theta-es_{max} level.

* Params 149 to 156: Special freezing level parameters. These parameters are computed at the intersection of the 0 degree isotherm and the specified line of constant theta-e.

6.5.6. Errors found in the database

One inconsistency has been found in the database. The CCL mixing ratio should be the mixing ratio of a parcel at the CCL which is equal to the average mixing ratio over the lowest 60 mb. Instead, the CCL mixing ratio computed in the database is computed from the CCL pressure and corresponding environmental dewpoint. The CCL mixing ratio should then be taken to be the same as that given in parameter 71 ("Avg Mix Ratio - 60 mb").

6.5.7. Support software

The Sounding Database software package contains four main programmes:

* GENERATE SOUND DBASE: This programme creates new database records. It reads in the raw data from rawinsonde or aircraft sounding disk files and computes all the derived parameters for

inclusion in the database. The SORT/MERGE utility is automatically run after each execution of this programme to merge new records into the proper database sequence.

* SOUND DBASE REPORTS: This programme prints out the contents of any selected database record.

* SOUND DBASE STATS: This programme computes simple statistics for each flagged numerical database parameter. It will also print out distributions of flagged parameters in histogram format. The SORT/MERGE utility is run prior to execution of this programme to select out the data desired for the statistical analysis.

* SOUND DBASE PLOT: In its current version, this programme does an X-Y plot on the Tektronix 4107 graphics terminal of any selected Nelspruit morning sounding parameter versus any selected Learjet upsounding parameter for the same days. Optional linear and polynomial regressions can be run and plotted for the given data. Once again, the SORT/MERGE utility can be run prior to programme execution to select the desired data.

* DATABASE XY PLOT: This programme plots any two parameters in the SAME database records against each other in an X-Y plot. The SORT/MERGE utility can be run prior to programme execution to extract the desired data. This programme is also shared with the Cloud Sample Database software (i.e. it works for BOTH databases).

6.6. Meteorological analyses related to thunderstorm forecasting at Nelspruit (Morgan and Morrison)

The radiosonde data collected over four seasons (82/83, 83/84, 84/85, 85/86) have been organized in a database format. With this fund of meteorological information we can begin to develop techniques for forecasting the stratification and stability of the atmosphere and the probable cloud type and characteristics.

What follows here is mainly intended to display the normal ranges of important parameters, their variations from month to month and over the four years (1982-1986). These are mere beginnings in the exploitation of the sounding data.

6.6.1. The mean trend of instability

Fig. 6.6.1(a) gives for the individual seasons, the monthly means of the low level maximum in Theta-e, Theta-e averaged over the lowest 60 mb (Theta-e 60) and the mid-level minimum of Theta-es. Also shown are monthly means of the difference Theta-e max minus Theta-es$_{min}$. The difference Theta-e$_{max}$ minus Theta-es$_{min}$ is an index of the mid-afternoon instability, as described in Section 6.3 of this Volume. The individual seasons exhibit variations, but a general behaviour is clear. The low level Theta-e max increases rapidly during the first months of the season, while the mid-level Theta-es increases more slowly. This

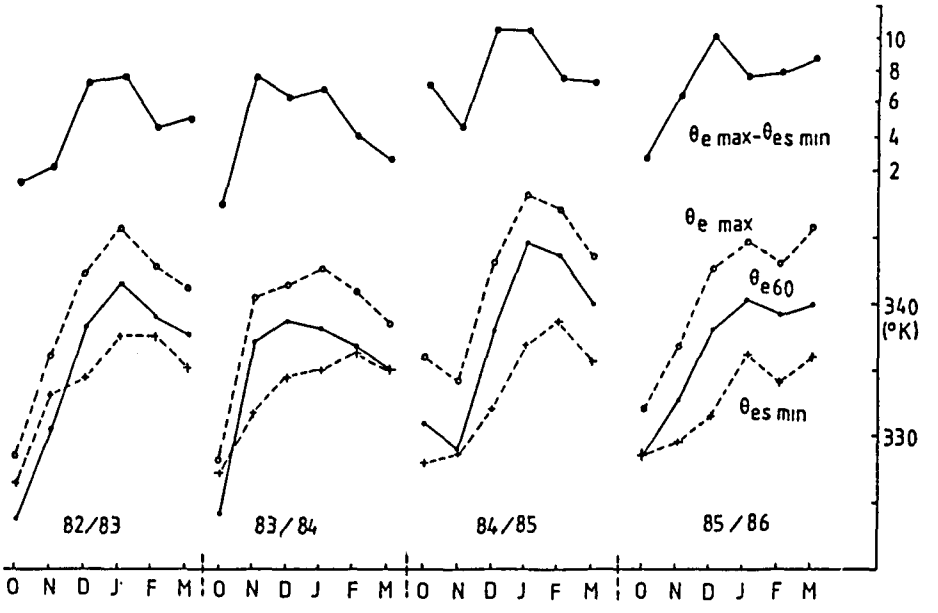

Fig. 6.6.1 (a). Seasonal monthly means of:
- Theta-e max minus Theta-e min
- low level Theta-e max
- Theta-e averaged over lowest 60 mb
- mid-level Theta-es min

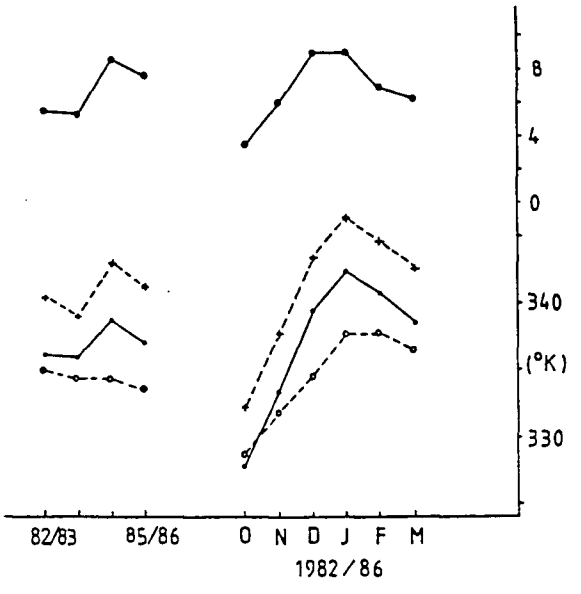

Fig. 6.6.1 (b) Four years means of the monthly means plotted in Fig. 6.6.1 (a).

is reasonable as the heating is applied to the atmosphere from the surface, and is diffused upward through mixing (turbulence and convective clouds). The result is an increase of the instability, seen as an increasing difference between the two quantities. The mean development of instability shown here is similar to that shown, for example, in northern Italy (Morgan 1973). The overall four year means of the monthly means are shown in Fig 6.6.1 (b). The means for the months, combining all four seasons, show steady warming near the ground and aloft through January, a strong reversal at the ground after that, and a lag in the reversal in the mid troposphere.

The instability peaks in December and January. The mean curve of instability does not correspond quite with our understanding of the month-to-month variations in storm activity. An examination of the standard deviations of instability and its components (Fig. 6.6.1 (c)) helps to explain why. The standard deviation can be taken as a measure of "storminess". This shows high values in November, a peak month of storm activity, and in March, offsetting the decreasing instability in that month.

Note the curves of the annual means (Fig. 6.6.1 (b)) which show a measurable cooling of the middle troposphere and a warming of the lowest layers, resulting in an average increase of instabilty over the four year period. This may be a sign of emergence from a dry period.

6.6.2. Wind speeds

Another environmental factor, to be combined with instability in seeking an explanation for the seasonal march of instability, is the strength of wind flow over the area. This is an index of cyclonic activity and mean proximity to the polar front. Figs. 6.6.2 and 6.6.3 show the mean wind speeds at 850, 700 and 500 mb for each month, by seasons and combined (82-86) and the seasonal (Oct-Mar) means for four years. The pattern which shows up in the four-year monthly means is quite strong and visible in each of the component years. November has the highest winds in the middle troposphere in each year, and November has been our peak month for storm activity.

The great instability of December-January is offset by weaker winds, while February, our second most stormy month, shows a secondary peak in 700 mb wind speed. October, the month of greatest instability, is nevertheless a month of high wind speeds and can be fairly stormy.

6.6.3. Depth of convection

Figure 6.6.4 shows some altitudes (in km amsl) of significant parameters on the sounding for the four seasons combined, month-by-month. The bottom curve is the mean altitude of the minimum of Theta-e, the hypothesized level of downdraft origin. It rises through the first half of the season and then levels off at around 4000m. The total variation is from just over

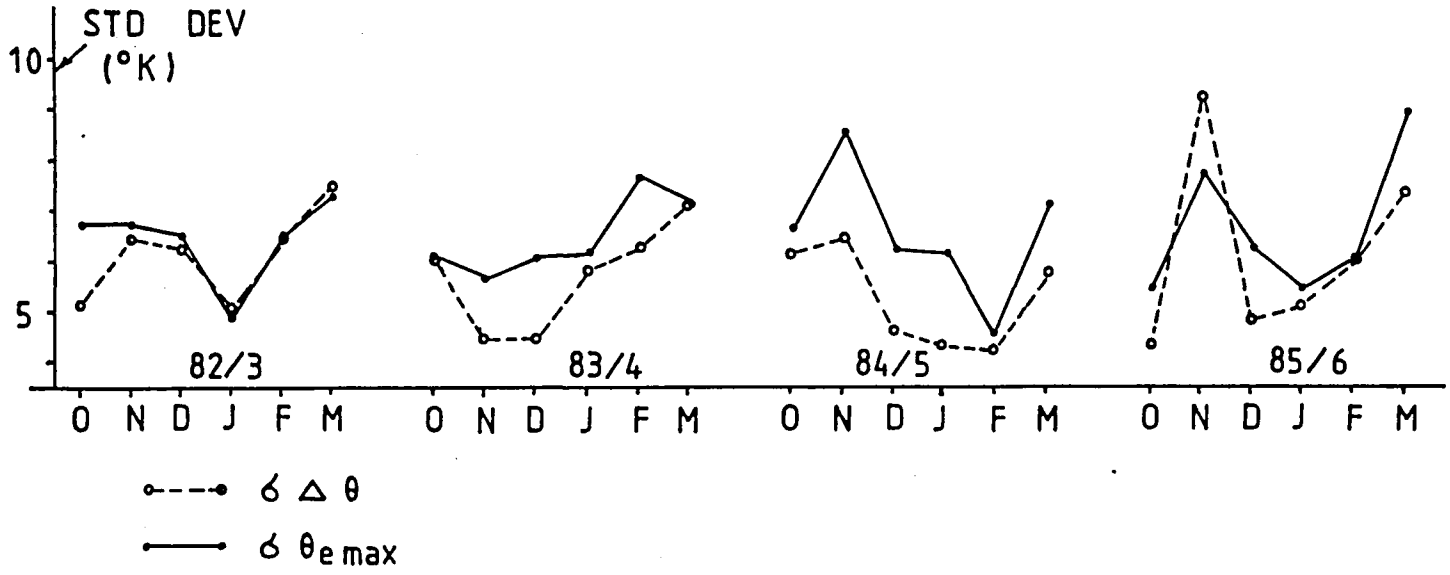

Fig. 6.6.1 (c). Standard deviations of Theta-e max and Theta-e max minus Theta-es min

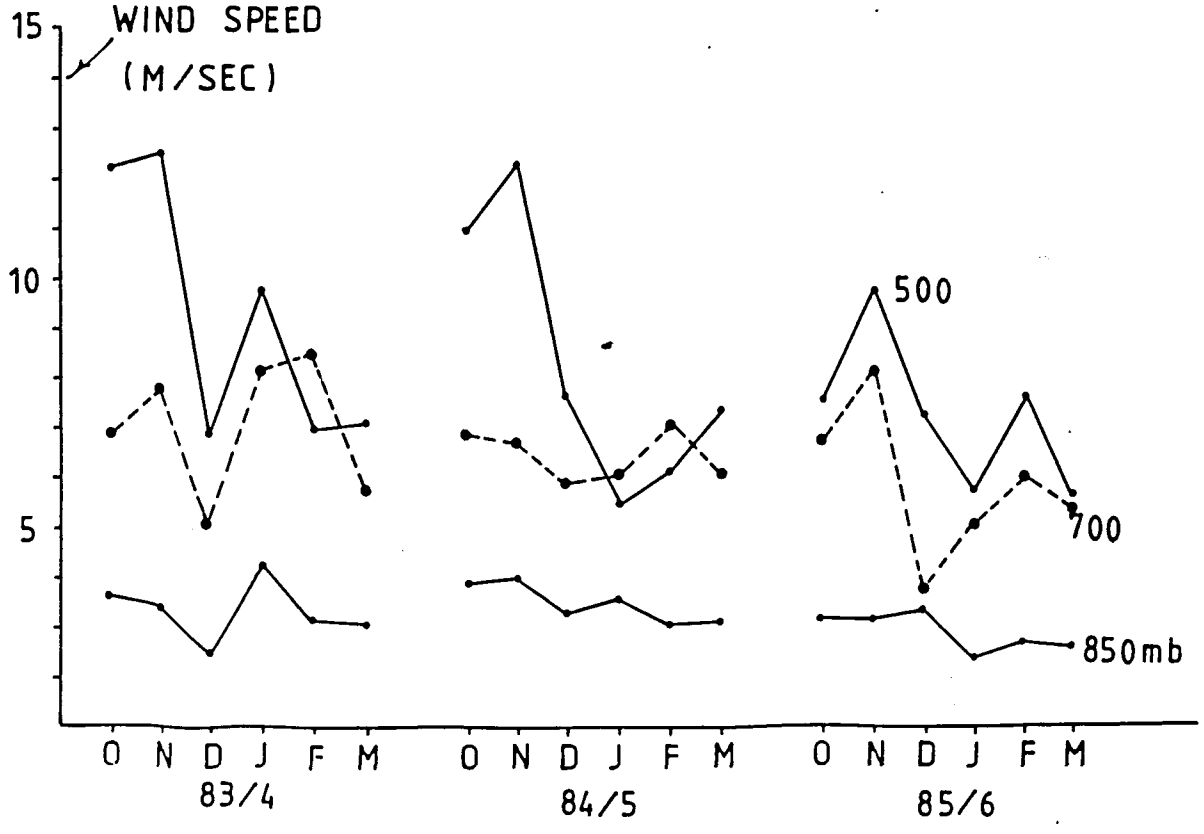

Fig. 6.6.2. Mean seasonal wind speeds: 500, 700 and 850 mb.

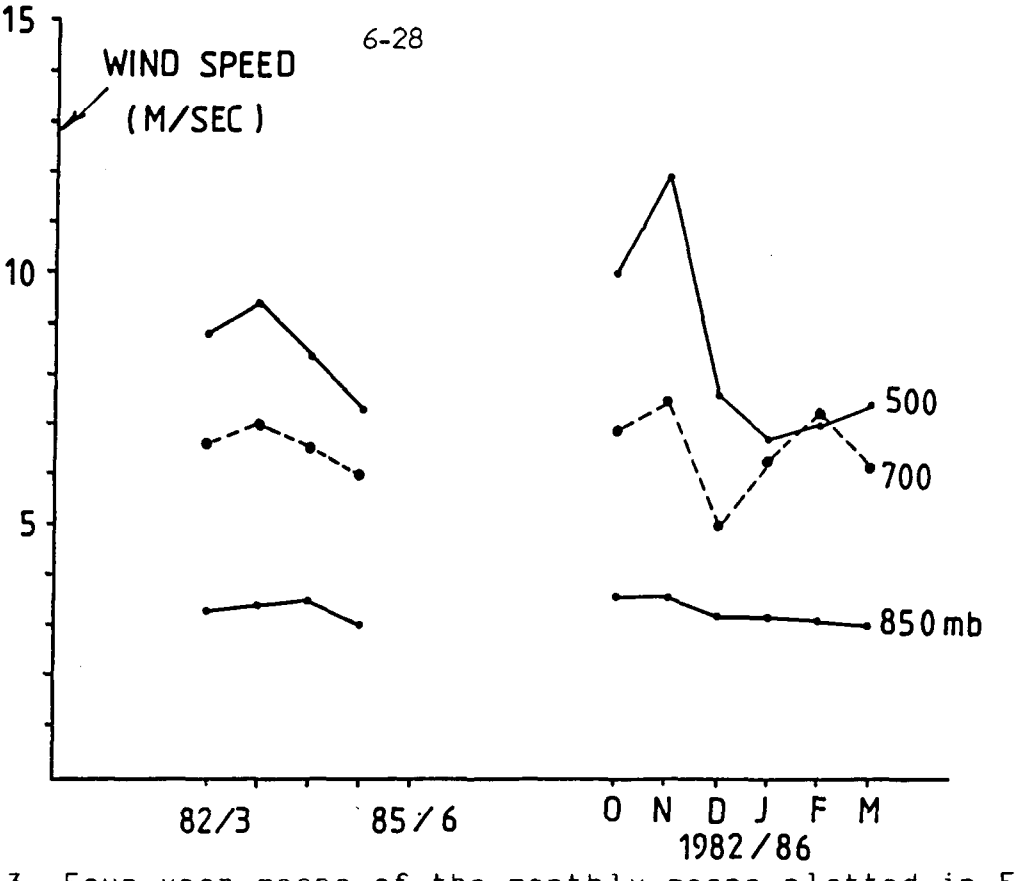

Fig. 6.6.3. Four year means of the monthly means plotted in Fig. 6.6.2.

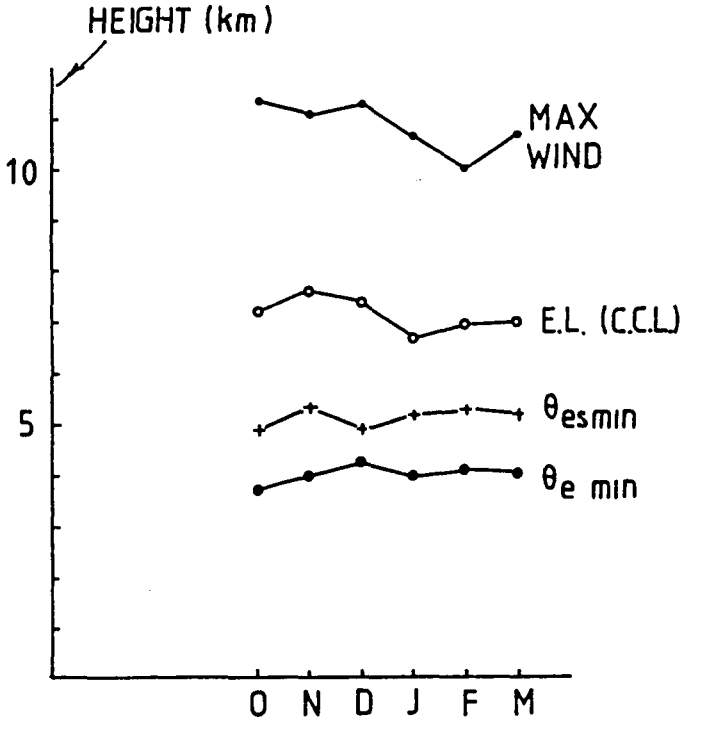

Fig. 6.6.4. Heights of seasonal means of:
- maximum wind
- convective equilibrium
- Theta-es min
- Theta-e min

3600 to just over 4200 m.

The next curve is the mean altitude of Theta-es minimum, the top of the conditionally unstable layer and the base of the layers of absolute stability. Here again, not a large variation, but November stands out, compared to its neighbour months.

The curve labelled E.L. (CCL) is the mean altitude of the equilibrium level (sometimes referred to as the "top of the positive area") for parcels rising from the CCL. This is the altitude where Theta-es of the environment equals Theta-es at the CCL. This shows a tendency for deeper convection in the early months of the season, again underlining the fact that, in the four year sample, November has been the most active month overall.

The top curve is the mean altitude of the maximum wind on the sounding. This has been shown here because the Nelspruit sounding seldom reaches the tropopause. The maximum wind is usually below the tropopause and follows it in its height variations. The tropopause is often a natural lid on convective storms, even when they are overshooting their equilibrium. Here, again, there is evidence for deeper convective storms in the early part of the season.

6.6.4. Freezing levels

The levels in the sounding at which certain temperatures equal $0^{o}C$ are important to the character and strength of convective storms, and their means are another useful way of displaying the character of a month or season.

Fig. 6.6.5 shows the behaviour of the mean heights of three types of freezing levels. The lowest curves are the wet-bulb-freezing-level or wet-bulb-zero (WBZ). This is the level at which the environmental wet-bulb temperature is $0^{o}C$. This is the lowest level to which hail or graupel can fall in the environment, without beginning to melt. It is an important hail forecasting parameter according to the USAF Severe Weather Warning Center (Miller, 1967). This has been questioned by Morgan (1970), based on observed correlations between WBZ and mean (over a layer) low level mixing ratio. This will be dealt with further on.

The middle (solid) curves are the environmental freezing level or freezing level, where the environmental temperature is $0^{o}C$.

The upper (dashed) curve is an estimate of the freezing level in the updraft. The updraft temperature profile is based on the constant Theta-e process (moist adiabatic) through Theta-e max.

There are other freezing levels in the sounding database, but they will not be dealt with here.

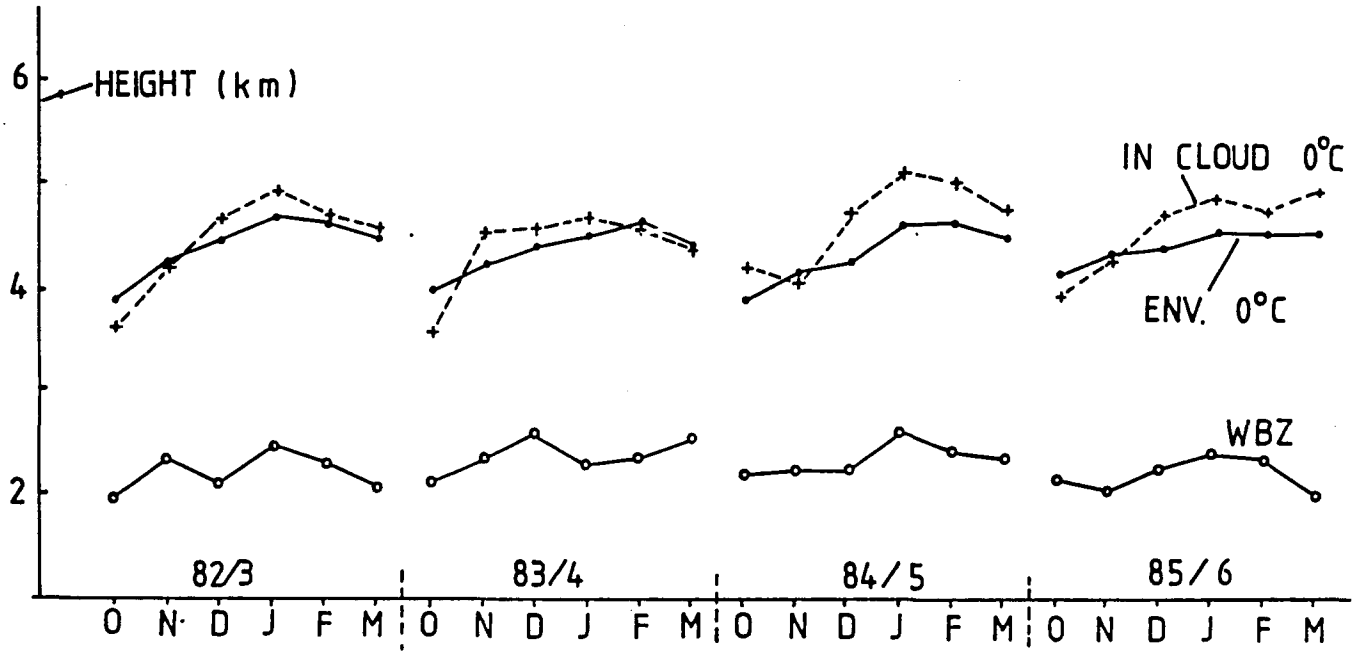

Fig. 6.6.5. Seasonal changes in mean heights of in-cloud, environmental and wet-bulb freezing levels.

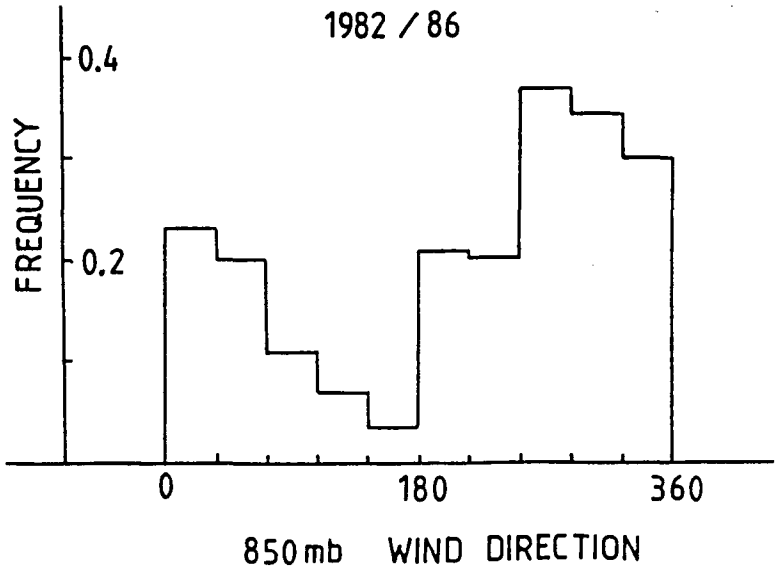

Fig. 6.6.6. Probability of operations versus morning (Nelspruit sounding) 850 mb wind direction.

850 mb Wind Direction (degrees)

ops Season	0	0-36	36-72	72-108	108-144	144-180	180-216	216-252	252-288	288-324	324-360	Total
all 82/83	11	18	16	11	21	15	13	13	24	15	18	175
all 83/84	11	19	9	13	32	27	11	12	9	20	18	181
all 84/85	5	16	10	12	20	25	8	14	15	22	23	170
all 85/86	9	17	10	17	27	20	15	5	13	15	21	169
all seasons	36	70	45	54	100	87	47	44	61	72	80	695
ops only	9	15	9	6	7	3	10	9	23	25	24	140
ratio	.25	.21	.2	.11	.07	.03	.21	.20	.37	.347	.30	.2

Table 6.6.1 Distribution of 850 mb wind direction - Nelspruit morning sounding.

Theta-es min

Season	321	321 323.5	323.5 326	326 328.5	328.5 331	331 333.5	333.5 336	336 338.5	338.5 341	341 343.5	343.5 346	346	Total
82/83	5	3	1	8	19	25	32	40	27	12	2	1	175
83/84	4	4	5	13	21	25	31	39	29	9	1	0	181
84/85	1	5	8	14	25	24	25	23	23	16	3	2	170
85/86	4	2	11	8	18	31	40	33	14	7	1	0	169
all seasons	14	14	25	43	83	105	129	135	93	44	7	3	695
ops days	0	0	3	7	18	24	25	32	20	7	2	2	140
ratio	0	0	.12	.163	.216	.23	.19	.24	.21	.16	.28	.67	.20

Instability

Theta-e max - Theta-es min

	-15	-15- -11	-11 - -7	-7 - -3	-3 - +1	1 - 5	5 - 9	9 - 13	13- 17	17- 21	21 - 25	Total
all seasons	2	5	13	31	78	146	169	139	79	28	5	695
ops days	0	0	0	1	4	15	35	31	37	15	2	140
ratio	0	0	0	.032	.051	.103	.206	.223	.468	.535	.40	.20

Table 6.6.2 Distribution of equivalent potential temperatures - Nelspruit morning sounding (see text for details).

Theta-e min (°K)

Season	≤ 310	310 - 312.5	312.5 - 315	315 - 317.5	317.5 - 320	320 - 322.5	322.5 - 325	325- 327.5	327.5- 330	330- 332.5	332.5- 335	> 335	Total
82/83	8	7	8	8	23	21	31	20	27	13	7	2	175
83/84	3	7	3	20	30	32	37	18	10	7	10	4	181
84/85	4	2	14	22	29	29	28	14	10	10	1	7	170
85/86	5	7	12	30	30	26	16	17	13	11	2	0	169
all seasons	20	23	37	80	112	108	112	69	60	41	20	13	695
ops days only	0	1	2	7	12	21	33	18	25	15	3	3	140
ratios	0	.04	.054	.087	.107	.185	.294	.246	.416	.366	.15	.23	.20

Theta-e max (°K)

Seasons	≤ 325	325- 329	329 - 333	333 - 337	337 - 341	341 - 345	345 - 349	349 - 353	353 - 357	357 - 361	361- 365	> 365	Total
82/83	7	13	17	20	33	29	31	19	4	2	0	0	175
83/84	10	10	23	24	35	34	27	12	4	1	0	1	181
84/85	5	7	17	10	23	33	30	32	6	5	2	0	170
85/86	6	10	17	16	28	31	34	20	4	3	0	0	169
all seasons	28	40	74	70	119	127	122	83	18	11	2	1	695
ops days	0	1	3	12	16	29	31	29	10	8	0	1	140
ratio	0	.025	.040	.171	.134	.23	.262	.35	.55	.72	0	1.00	.20

Table 6.6.2 Cont/.

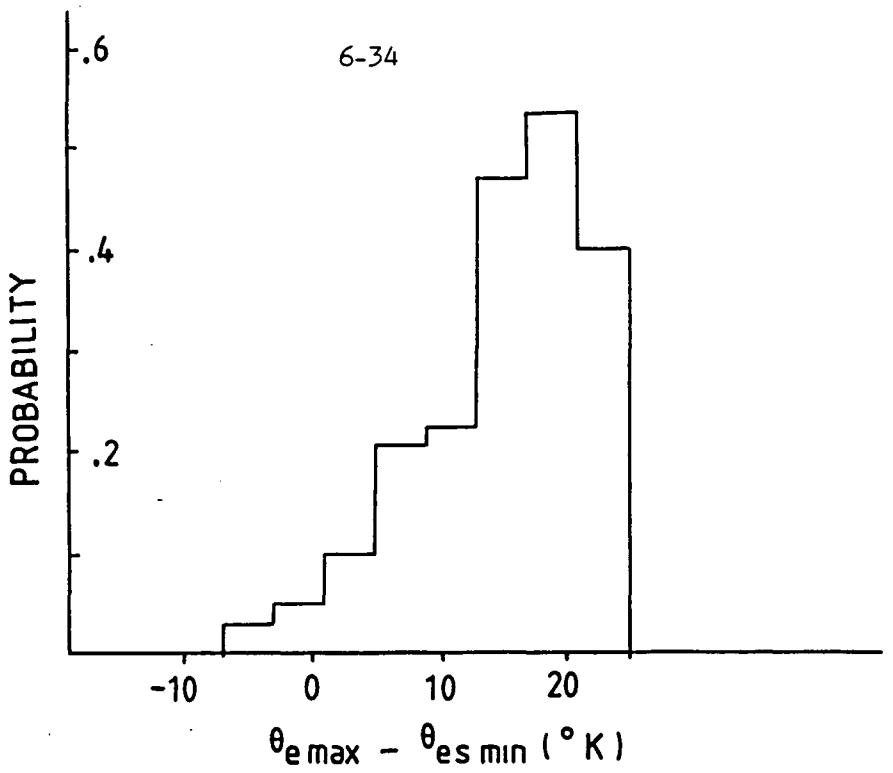

Fig. 6.6.7. Probability of operations versus Theta-e max minus Theta-es min from morning radiosonde.

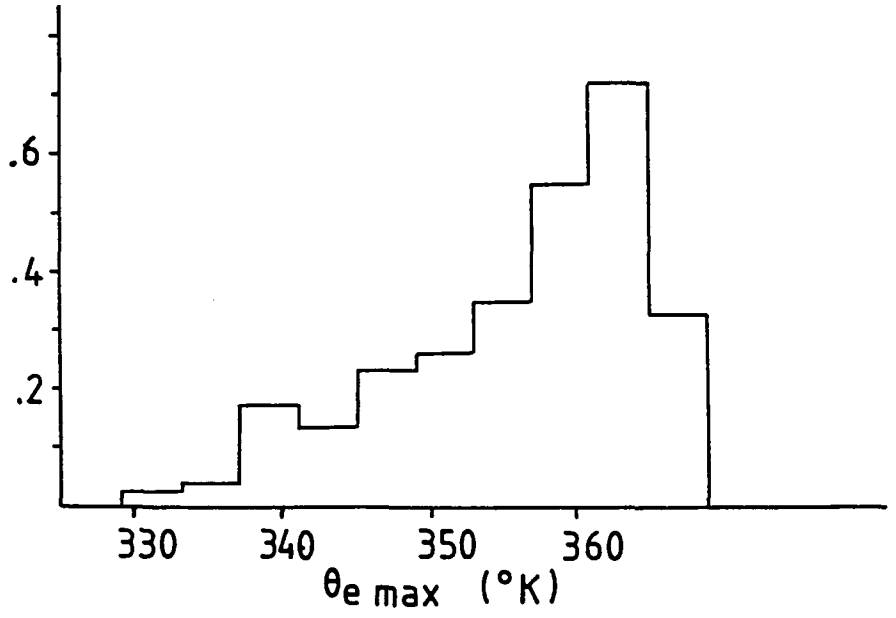

Fig. 6.6.8 (a). Same as Fig. 6.6.7 for Theta-e max.

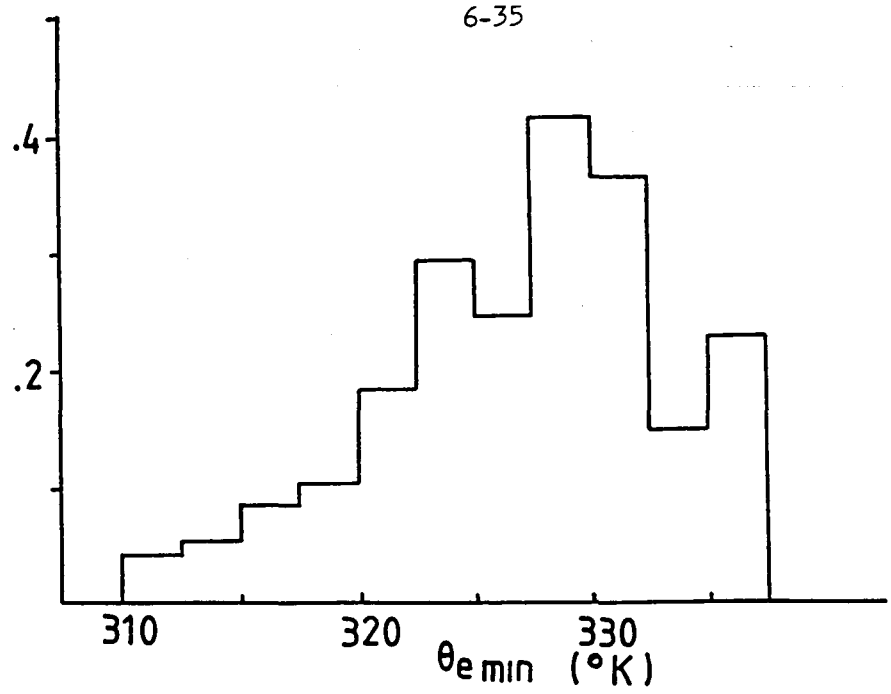

Fig. 6.6.8 (b). Same as Fig. 6.6.7 for Theta-e min.

6.6.5. Low-level wind direction

The winds in the lowest levels are an importnt element in any convective storm forecast scheme. Winds at and near the surface respond in characteristic ways to the approach and passage of synoptic systems and also are then highly correlated with the character of the advection of heat and moisture.

The importance of low level winds in favouring storms in Nelspruit is readily shown based on the wind direction at 850 mb, as measured by the morning sounding. Table 6.6.1 gives the distributions by 850 mb wind directions of all the morning soundings for each of four seasons and for all four combined. The last line gives the 850 mb morning winds for all operational days during the four seasons.

The following graph (Fig. 6.6.6) shows the ratio of operational days to all days for each 850 mb wind interval, and hence the probability of operations given only the morning 850 mb wind direction. The northwesterly wind direction preference is quite strong, a third of days being operational when the wind lies between 250 and 360 degrees. Even stronger is the probability minimum associated with southeastern wind direction.

The underlying cause for this is quite well known, the southeasterly winds being generally post-frontal (cool and moist). Though northwest winds (often pre-frontal) blow downslope, our experience with the metmaps (Section 6.4) has shown that such winds often bring higher mixing ratios into the area (and higher Theta-e, as well).

6.6.6. Equivalent potential temperatures and related measures.

The equivalent potential temperatures have been treated in the same manner as the 850 mb wind directions and the results are displayed in Tables 6.6.2 (a and b) and the graphs of Figs. 6.6.7 and 6.6.8. The probabilities of operations exceed 50 percent for certain classes of some of these variables. It should be noted that the overall probability of an ops day (number of ops days divided by total numbers of days) is 0.2 (20 percent) and so values above and below that show some effect of the variables. It should also be kept in mind that some of these variables are correlated with each other.

The uninteresting behavior of Theta-es min is somewhat surprising. Its combination with Theta-e max to form the difference (a stability index) however, seems a strong variable. The high probability in the last category of Theta-es min probably is the result of a few days with very tropical showers (low tops - strong coalescence).

6.6.7. Relationship between morning sounding parameters and Lear soundings later in the day

The parameters calculated from the morning sounding are really predictions of conditions during the afternoon, based on certain simplified assumptions about mixing of the lower layers. We can investigate the accuracy of these predictions by comparing them to values observed on soundings carried our later in the day. The largest number of such soundings are those made by the Learjet. This sample is, of course, biased by the fact that the Lear is launched only when storms of sufficient intensity break out. We have a very limited set of unbiased later soundings, from the Intensive Study Period of November 1984. Fig. 6.6.16 shows a sample regression plot based on these.

The regressions shown here have been determined using the Lear up-soundings only. It was felt that the down-soundings were too often contaminated by cloud and to use them would require too much screening effort.

The following plots (Fig. 6.6.9 to 6.6.16) show the scatter of the data, and regression equations relating the early to the later data. In many cases a curvilinear regression is also shown. The plots are presented, for the moment, without detailed comment. A few general comments follow:

1. The morning calculation of CCL tends to overestimate the variability of quantities later measured. For example, low morning CCL heights (high pressure) almost always are followed by higher cloud-bases.

2. Buoyancy (Delta-T 500) is generally overestimated by CCL.

3. Max Theta-e seems a better predictor of subsequent mean Theta-e than the early value of mean Theta-e. This seems quite natural given the heating that takes place.

These curves or linear regressions can be introduced into the morning sounding analysis package to give improved predictions of the afternoon cloud properties.

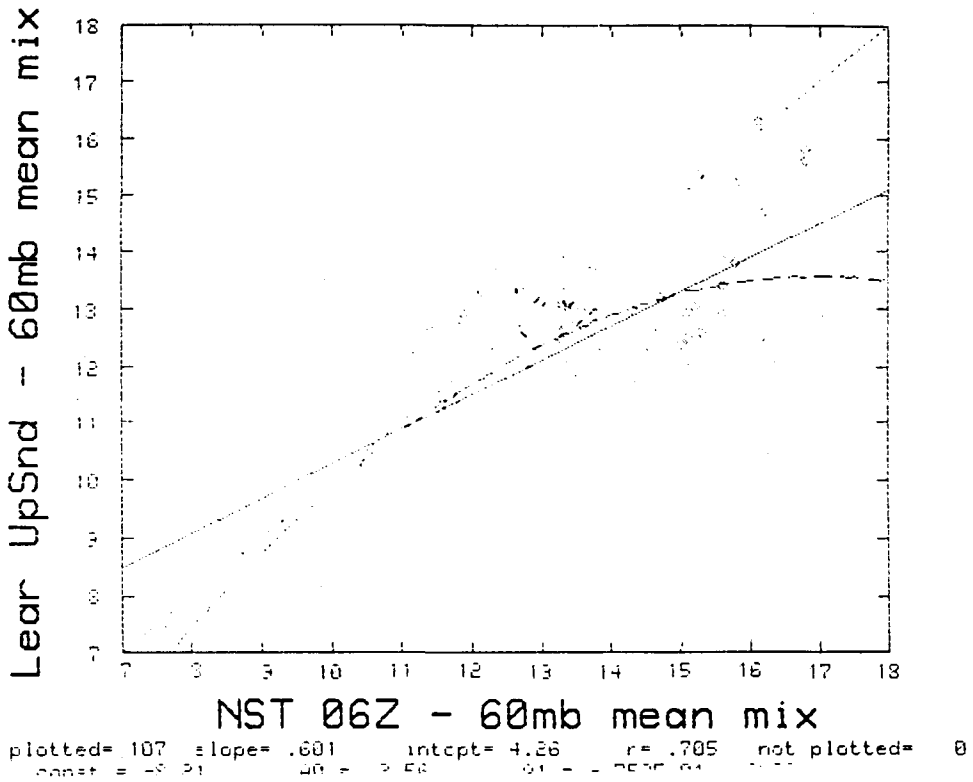

Fig. 6.6.9. Average mixing ratio in lowest 60 mb layer of the morning (0600Z) Nelspruit sounding versus the same mean mixing ratio for the subsequent Learjet climb out sounding.

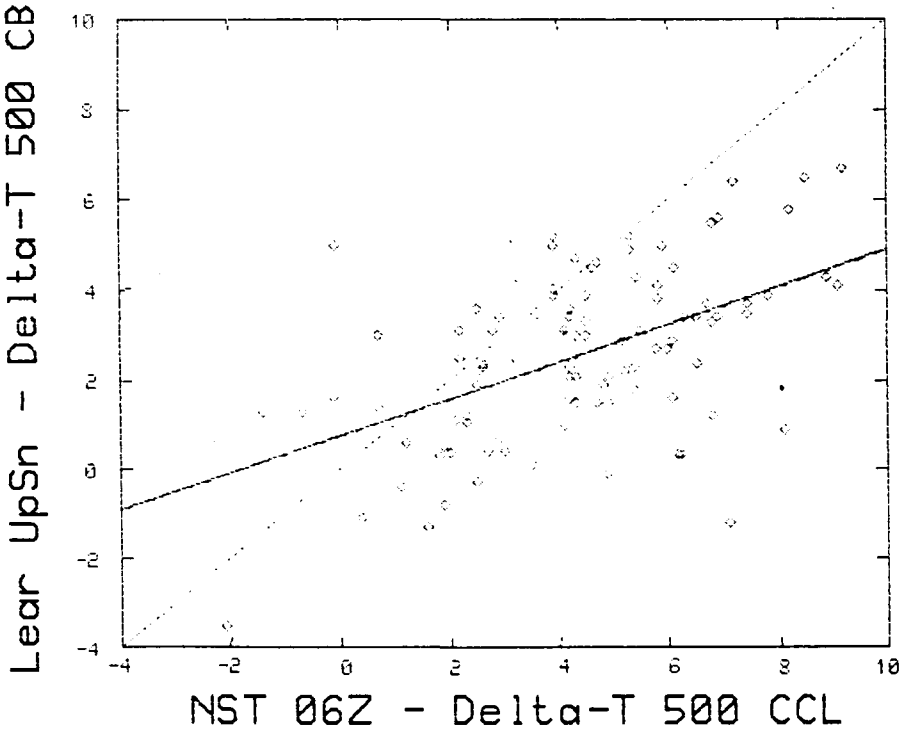

Fig. 6.6.10. As in 6.6.9, but for the 500 mb buoyancy estimated from the paired soundings.

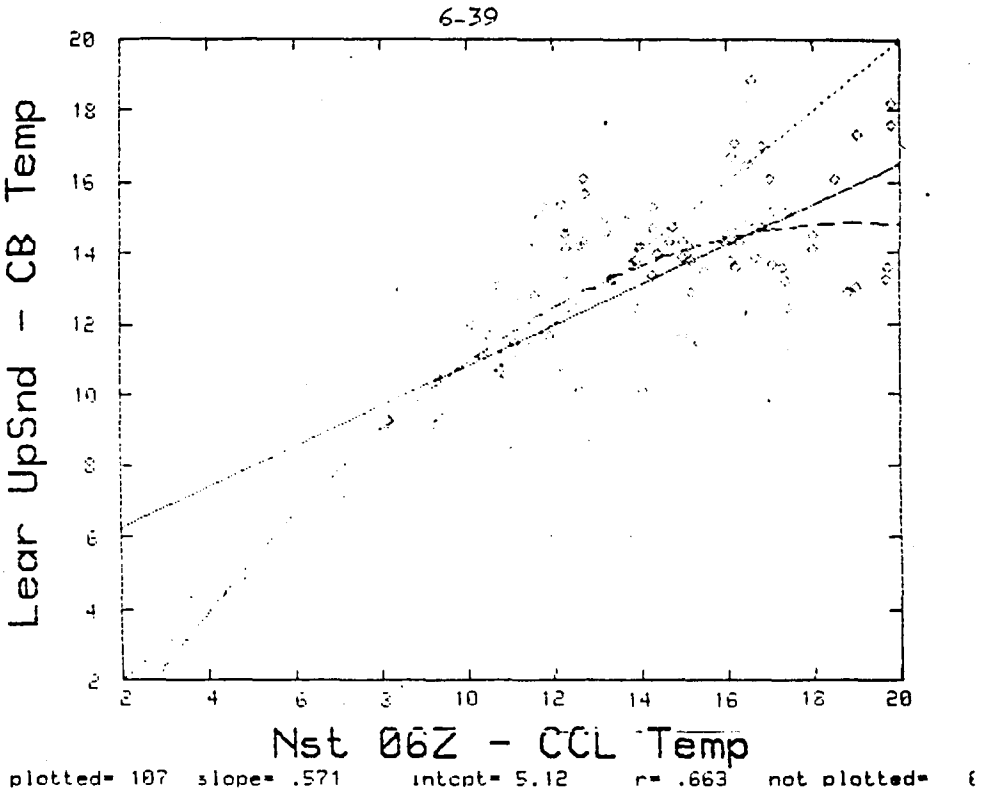

Fig. 6.6.11. As in 6.6.9, but showing the afternoon cloud base temperature against the morning CCL temperature.

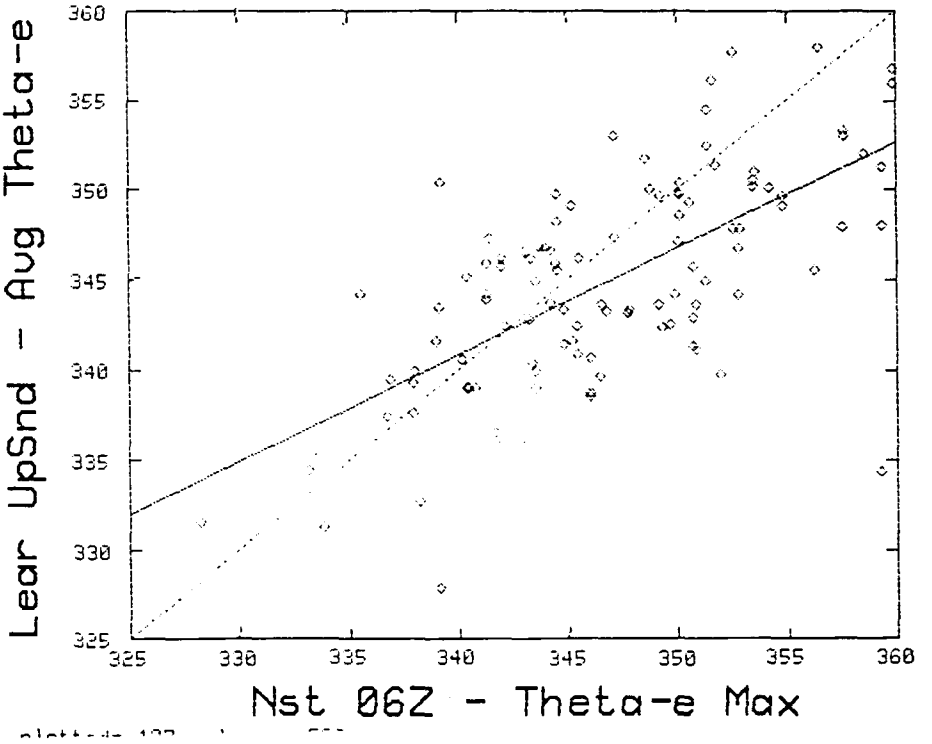

Fig. 6.6.12. As in 6.6.9, but showing the 60 mb average Theta-e in the afternoon versus the maximum Theta-e near the ground on the morning.

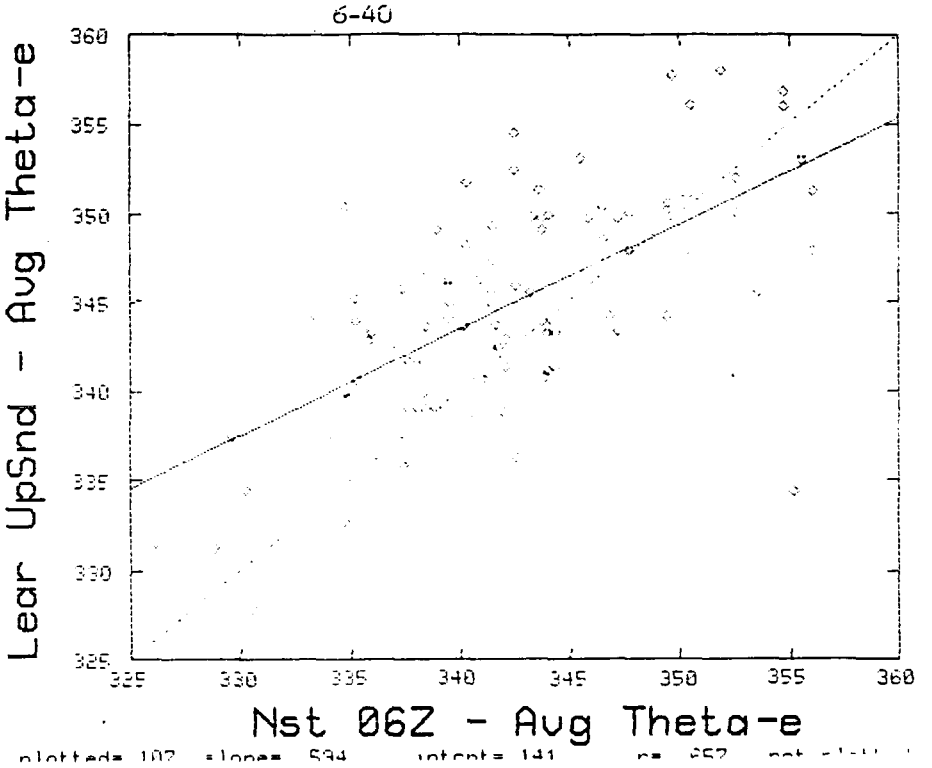

Fig. 6.6.13. As in 6.6.9, but showing the afternoon average 60 mb Theta-e versus the same quantity estimated from the morning sounding.

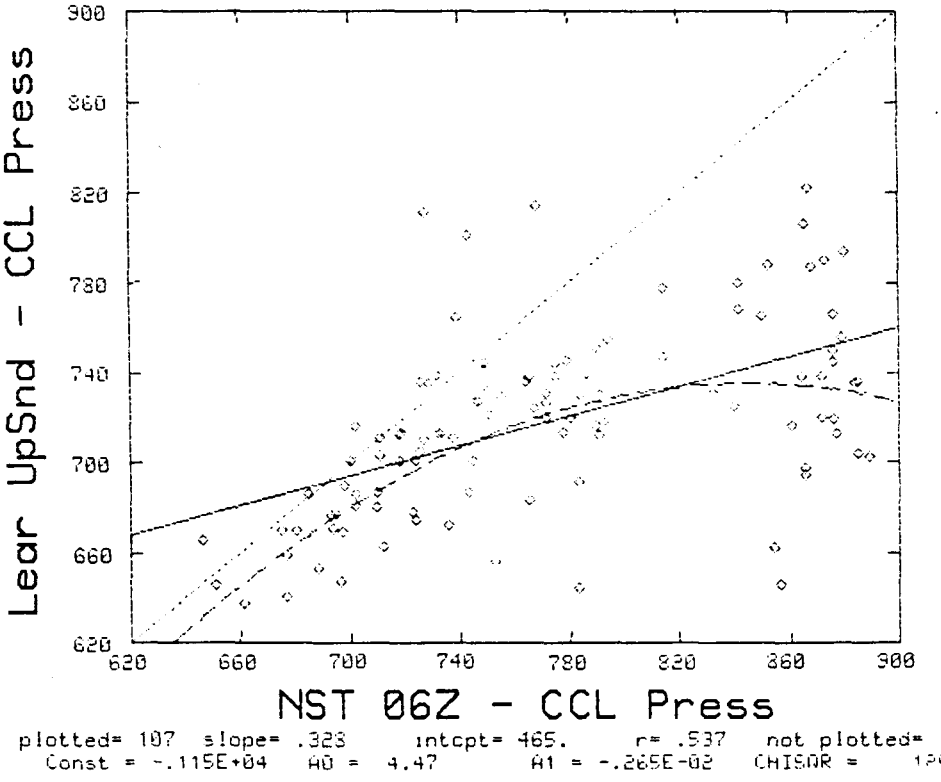

Fig. 6.6.14. As in 6.6.9, but comparing the CCL pressure estimated from the paired soundings.

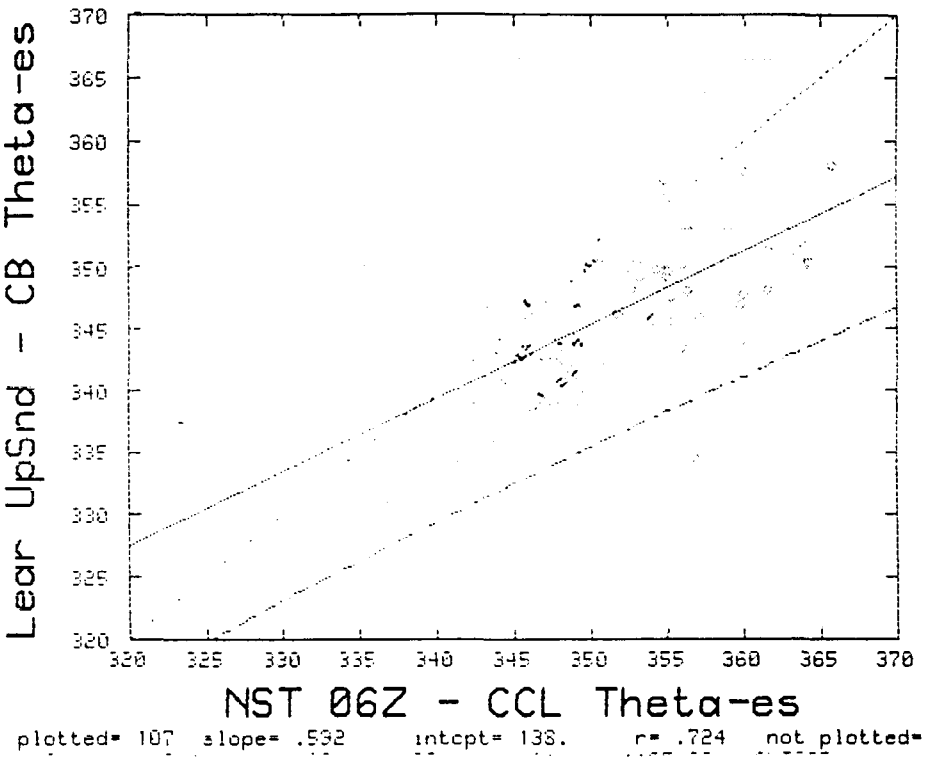

ig. 6.6.15. As in 6.6.9, but comparing the Theta-es at cloud base estimated from the afternoon (Learjet) sounding to the Theta-es at the CCL on the morning sounding.

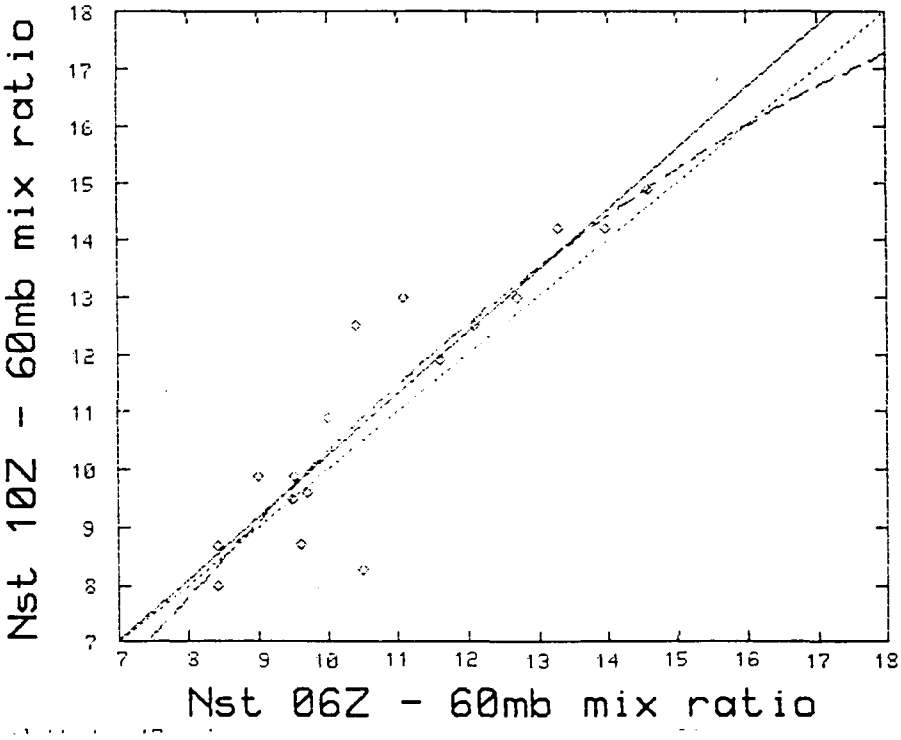

Fig. 6.6.16. A regression example from the small set of morning (0600Z) and local noon (1000Z) soundings performed during the Intensive Study Period of November 1984.

7.0 PROPERTIES OF DRY ICE AS A GLACIOGENIC SEEDING AGENT

For nearly forty years dry ice has been one of the most often used materials for glaciogenic seeding. The effectiveness of dry ice, i.e. how many detectable ice particles are generated per gram of dry ice sublimed, has been the focus of several field and laboratory experiments (Eadie and Mee, 1963; Fukuta, et al., 1971; Allee, et al., 1972; Holroyd, et al., 1978; Lozowski and Kochtubajda, 1980). More recent work by Morrison, et al. (1984), in the Colorado State University simulation laboratory has added evidence of not only a higher effectiveness than previously reported but also a temperature dependence for the ice production.

The laboratory work at CSU was a continuation of a series of experiments begun during the RAIN (Rain Augmentation in Nelspruit) project to examine, in detail, various aspects of dry ice pellet behavior in supercooled clouds. Some questions addressed during RAIN involved the size distribution of the pellets actually being delivered to the cloud, pellet lifetimes, variation of pellet fall velocities as pellet shape and size change, sublimation rates as a function of cloud liquid water content (LWC), and the significance of the ice "whiskers" that are shed from the falling pellets. A complete report of those experiments is contained in Emmitt, Roos and Morrison (1984).

7.1 LABORATORY ESTIMATES OF DRY ICE EFFECTIVENESS[1]

Despite the fact that dry ice has been widely utilized as a cloud seeding agent for several decades, there are misconceptions and deficiencies in the knowledge about dry ice nucleation that limit the scientific basis for its use. Laboratory experiments conducted at the Colorado State University (CSU) Cloud Simulation and Aerosol Laboratory used the 960 liter isothermal cloud chamber to address this problem. As part of the research an accurate effectiveness spectrum was established, rates of ice crystal production determined, and nucleation mechanism investigated. The laboratory effectiveness spectrum was also compared to values derived from a simple numerical model which estimates dry ice effectiveness using cloud physics data from aircraft observaations of dry ice seeding signatures.

7.1.1 Dry Ice Effectiveness

An electro-mechanical precision catapult apparatus was used to launch small spherical dry ice pellets vertically into the CSU cloud chamber at speeds up to 82% of terminal velocity. The pellets were exposed to the cloud over a 10.2 cm path length and then caught behind a motor-driven shutter in a trapping tube. A small fan was simultaneously operated for 4 seconds to minimize aggregation of ice embryos in the pellet plume and to mix them uniformly throughout the chamber. Ice crystal yields were measured by

---

[1]Material in this section (7.1) based solely upon conference paper by Morrison, Finnegan, Horn, and Grant. However, the research was funded by SWA and the Water Research Commission.

counting ice crystals under a microscope and the rates of ice crystal production were measured using a capillary type acoustic sensor system. The supercooled cloud was continuously replenished and monitored during the experiment.

The effectiveness spectrum for 5 mm diameter spherical pellets at a cloud liquid water content of 1.5 g m^{-3} is shown in Fig. 7.1. This result is substantially different from that of Fukuta et al. (1971) which shows no temperature dependence. Their effectiveness spectrum after correction for a computational error pointed out by Horn et al. (1982) is plotted as a dashed line in Fig. 7.1. The flat spectrum may be an artifact due to overseeding with subsequent sublimation loss of many ice embryos (Horn et al., 1982).

Model effectiveness values derived from RAIN field data are plotted in Fig. 7.1 as the circled numbers (Volume III, Section 2.0). They are generally within an order of magnitude of the laboratory-derived effectiveness spectrum and also imply a temperature dependence. This relative agreement is encouraging considering the simplicity of the model and the numerous assumptions involved.

7.1.2 Rates of Ice Crystal Production

Figure 7.2 illustrates the rates of ice crystal production in the form of kinetic plot. In this plot the total number of ice crystals counted by the acoustic sensor is taken to be the total number of viable ice embryos present after pellet transit at time t = 0. Then the depletion of these embryos with time as they grow to ice crystals and fall out is plotted from 100% on a natural log scale. For example, 90% of the ice crystals at $-2^{o}C$ are produced in 2.4 minutes and at $-15^{o}C$ in 1.3 minutes. The rate of ice crystal production is proportional to the slope of the resulting curve. These rates are generally faster than those observed for most aerosol type nucleants under the same conditions.

7.1.3 Nucleation Mechanism

A frequently held misconception is that dry ice functions primarily by the freezing of cloud droplets (Vonnegut, 1981). Our data confirms the preliminary experimental work by Horn et al. (1982) that this is not the case. If we assume a 100% droplet freezing efficiency at up to 4 times the pellet diameter from the axis of the path traversed by the 5 mm pellets, the number of cloud droplets that could be frozen amounts to only 2.5% of our total ice crystal yield at $-5^{o}C$ and 0.8% at $-15^{o}C$. In natural clouds, these percentages would be even less. Therefore, the predominant nucleation mechanism must be vapor dependent. This implies that the ice crystal yields in any cloud at a given temperature under the same seeding conditions should be similar regardless of droplet concentration and size distribution as long as the vapor supply is sufficient.

From these analyses we draw the following conclusions:

1) Dry ice effectiveness is temperature dependent and varies from 2.2×10^{11} ice crystal g^{-1} dry ice sublimed at $-2^{o}C$ to 8.9×10^{12} at $-20^{o}C$.

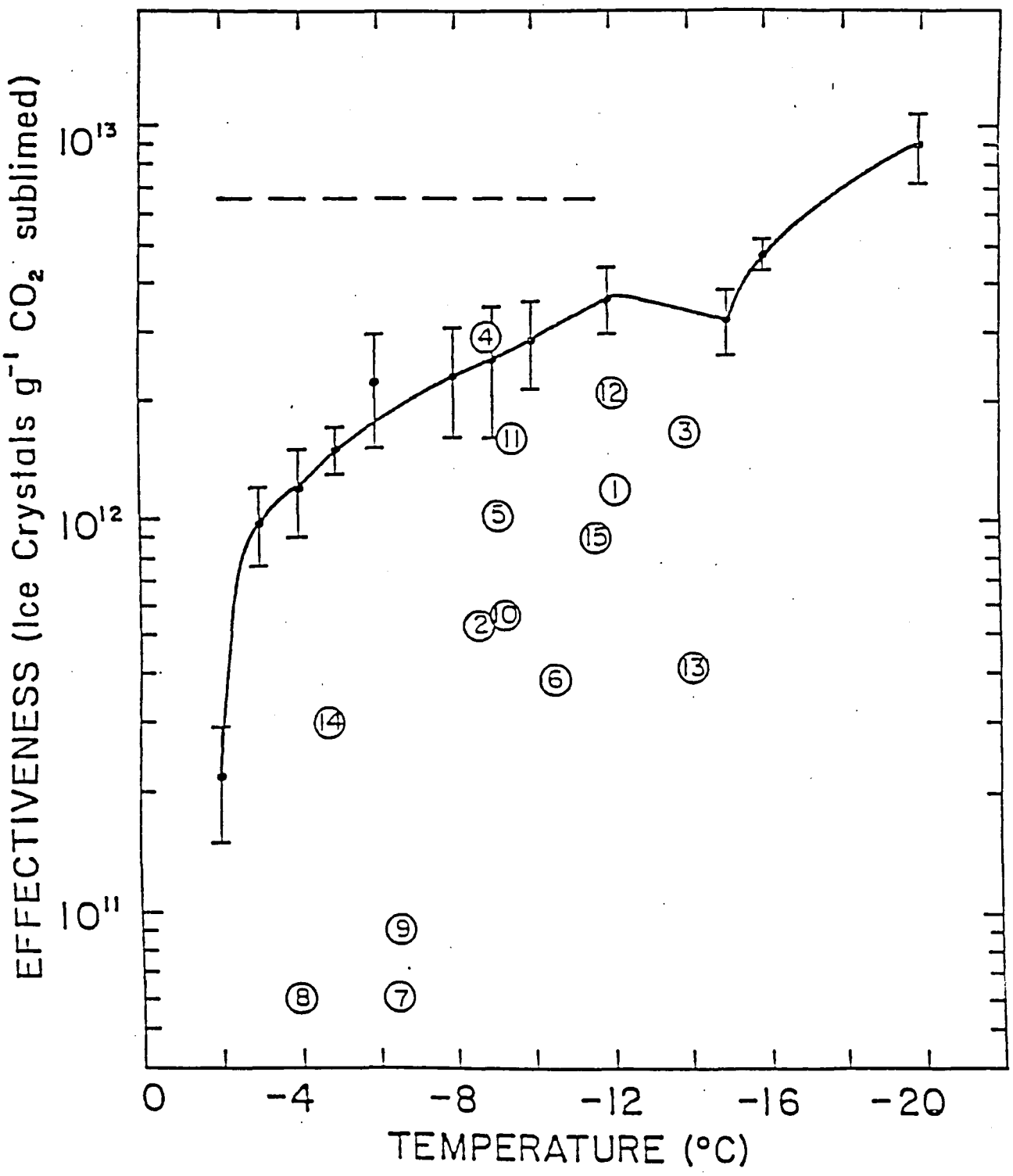

Figure 7.1. Laboratory derived effectiveness spectrum for 5 mm diameter dry ice pellets at 12.3 m s^{-1} and at a cloud liquid water content of 1.5 g m^{-3} (solid line). Simulation effectiveness values from field data of 15 clouds are plotted as the circled numbers. The Fukuta et al. (1971) spectrum after correction for a computational error (Horn et al., 1982) is shown as the dashed line.

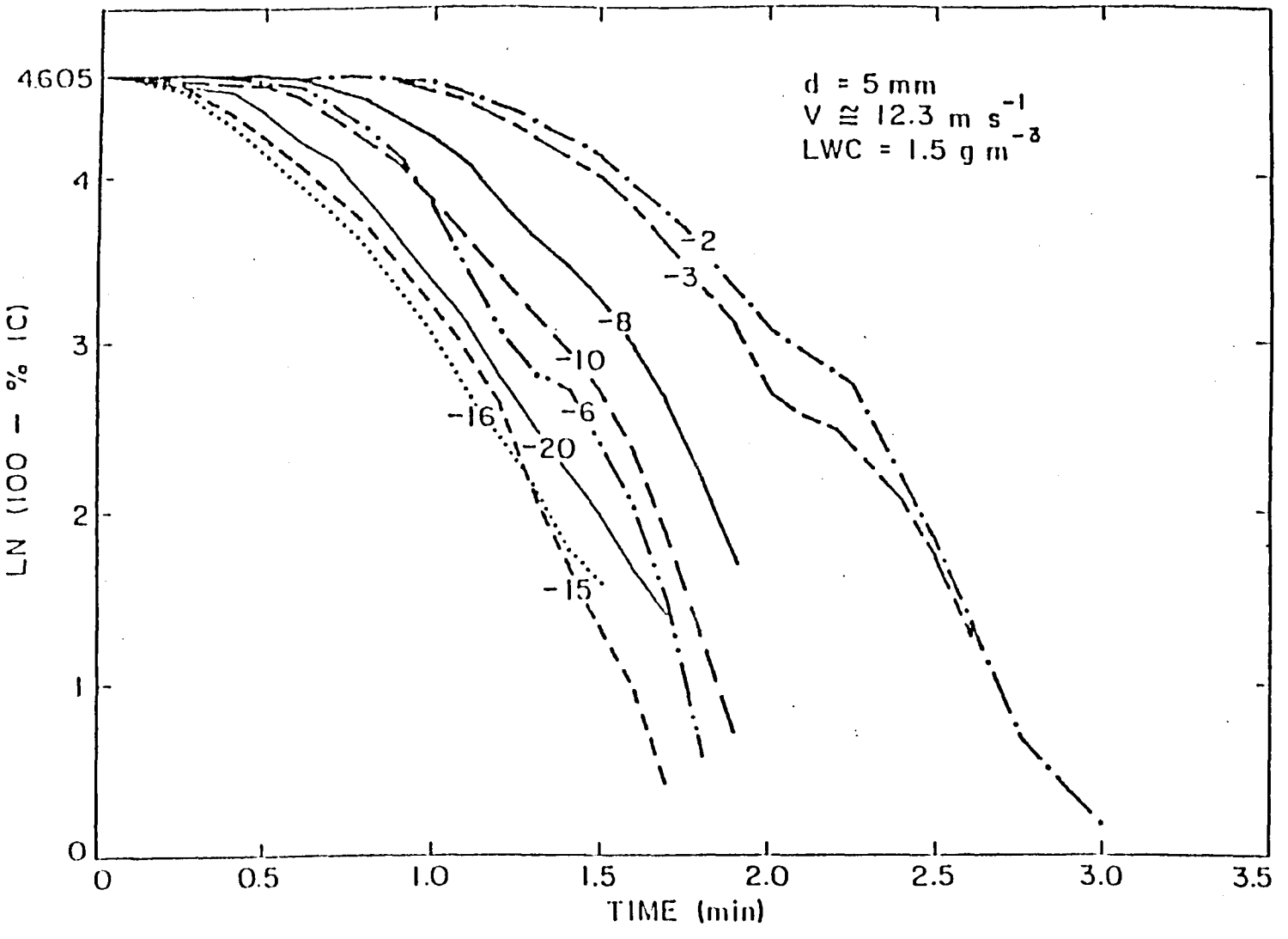

Figure 7.2. Composite kinetics plots for 15 mm dry ice pellets over a range of temperatures. The plots for -5, -9, and -12°C have not been included in order to reduce confusion in the figure.

2) Model derived effectiveness values using field data are generally within an order of magnitude of the laboratory values and also imply temperature dependence.

3) Rates of ice crystal production are much faster than most aerosol nucleants.

4) The predominant nucleation mechanism is vapor dependent.

7.2 FIELD EXPERIMENTS TO CHARACTERIZE PELLET BEHAVIOR

There were two phases of experimentation to empirically determine the terminal fall velocity and sublimation rate of the cylindrical dry ice pellets being used in the South African project. The first phase included dropping pellets from a slow (~80 kts) flying aircraft at heights ranging from 150 to 2100 meters above ground level (AGL). The second phase was carried out in the South African Council for Scientific and Industrial Research's (CSIR) cold room.

The pellets used in the field and laboratory were cylindrical in form with length to diameter ratios of ~ 1.0. These pellets are dispensed from the seeding aircraft at a controlled rate expressed in terms of kg/sec (.2 kg/sec for current equipment). To effectively describe the seeding treatment several key characteristics of the pellets were determined and are summarized in Table 7.1.

Table 7.1. Summary of dry ice pellet characteristics after dispensing through aircraft delivery system

	Small
Average pellet diameter (cm)	.89 (.02)*
Average pellet length (cm)	.87 (.62)
Average pellet density (g cm^{-3})	1.52 (.06)
Number density of pellets (#/kg)	~1300

*(Standard Deviations are Noted in ( ).)

The primary reasons for performing some of the field experiments in cloud free air were: 1) targeting the collection area with an aircraft would be nearly impossible from within clouds, and 2) the droplet free environment tests would provide baseline information for the laboratory experiments on

sublimation rates, terminal velocities and pellet survivability. The aircraft tests were the closest that we could get to examining the dynamical behavior of tumbling cylindrical dry ice pellets. The data thus obtained would then serve to assess our ability in the laboratory to simulate the evolution of the pellets in cloud free air. Once certain of the laboratory similarity in dry conditions, the effects of cloud droplets could then be examined.

The aircraft drops were conducted over a 150,000 m^2 sporting complex. The 3 to 5 cm high grass provided a cushion for the pellets (radius = .42 cm) and resulted in very little breakage upon impact. The fall time for the first pellet observed to contact the ground was recorded and used to compute terminal speeds. Pellet diameters and lengths were then measured within 2 minutes after the pellets reached the ground. The loss of mass during those two minutes was measured and found to be insignificant ($<5.0 \times 10^{-4}$ gm s^{-1}).

The 22 drops were carried out over a period of 4 days and repeated drops from reference heights showed little day-to-day variations. A complete discussion of these field tests is given in Emmitt, et al. (1984). However, as background for the laboratory tests, a summary of some of the field results is presented in Table 7.2.

Table 7.2. Summary of clear air dry ice pellet field experiments.

Summary of Clear Air Dry Ice Pellet Field Experiments

z	°K	P	r	dm/m	$\bar{V}$	dm/dz
(km)		(mb)	(cm)		(m s^{-1})	(gm cm^{-1})
2.0	284	720	.15	.87	12.6	3.6×10^{-6}
1.5	287	770	.23	.70	15.3	3.9×10^{-6}
1.0	290	820	.30	.49	17.2	4.1×10^{-6}
.5	293	870	.36	.26	17.8	4.4×10^{-6}
0	298	920	.42	-	-	-

z = drop height AGL; T_a = air temperature at drop height; P = pressure at drop height; r = radius of pellet after falling distance z; dm/m = fraction of mass loss over distance z; $\bar{V}$ = average fall speed over distance z; dm/dz = average mass sublimed per cm fall distance (per unit pellet length)

In general, the following two conclusions were drawn after completing the pellet experiments in cloud free air and developing models to determine pellet performance at seeding altitudes:

1) The cylindrical pellets fall at terminal velocities described in Fig. 7.3.

2) The average lifetime of pellets will be ~ 3-5 minutes depending upon the strength of the updrafts. Laboratory experiments show that the lifetime is also effected by the presence of supercooled water.

7.3 LABORATORY EXPERIMENTS TO DETERMINE EFFECTS OF SUPERCOOLED WATER

Study of the effects of supercooled water droplets on the sublimation rate of dry ice pellets and the production of ice "whiskers" necessitated the use of the sub-zero temperature vertical wind tunnel facility at CSIR in Pretoria. The wind tunnel was located in a 23 m^3 cold room with a -20°C capability. The spray nozzle, producing a controllable spectrum of supercooled droplets, was positioned on the tunnel axis, 1.2 m below the exit. The LWC of the induced cloud was determined from the measured air and water flow rates. For some of the experiments an additional LWC measurement was obtained with a Forward Scattering Spectrometer Probe (FSSP) positioned at the tunnel exit. A typical droplet size-distribution as measured by the FSSP at an airspeed of 15 m s^{-1} is shown in Figure 7.4. Comparison with spectra derived from gelatine coated slides shows a reasonable agreement except for the high counts in the smallest size bin.

The pellets used in the cold room experiments had radii of .55 cm and lengths ranging from 2-3 cm. Since we were looking for a % change in sublimation rates due to supercooled water droplets, the tunnel speed (15 m s^{-1}) and pellet exposure (rotation speed) were held constant throughout the experiments.

A complete set of runs was made at the three temperatures -5°C, -11°C and -16°C. More than 50 pellets were used to obtain sublimation values for LWC's of 0.0, 1.5, and 4.5 gm m^{-3}. The pellets were placed in the exit of the tunnel for 1 minute periods after which they were weighed to within $\pm$0.03 gm and then reexposed for additional one minute intervals until they could no longer survive for measurement. The results of these tests are summarized in Table 7.3. Figure 7.5 illustrates the pellet sublimation for T_{air} - -5°C. Since these experiments were made at a constant speed (15 m s^{-1}), only during the first minute or so should a comparison of the laboratory sublimation rates be made with values determined in the field (previous work by Emmitt et al., 1984).

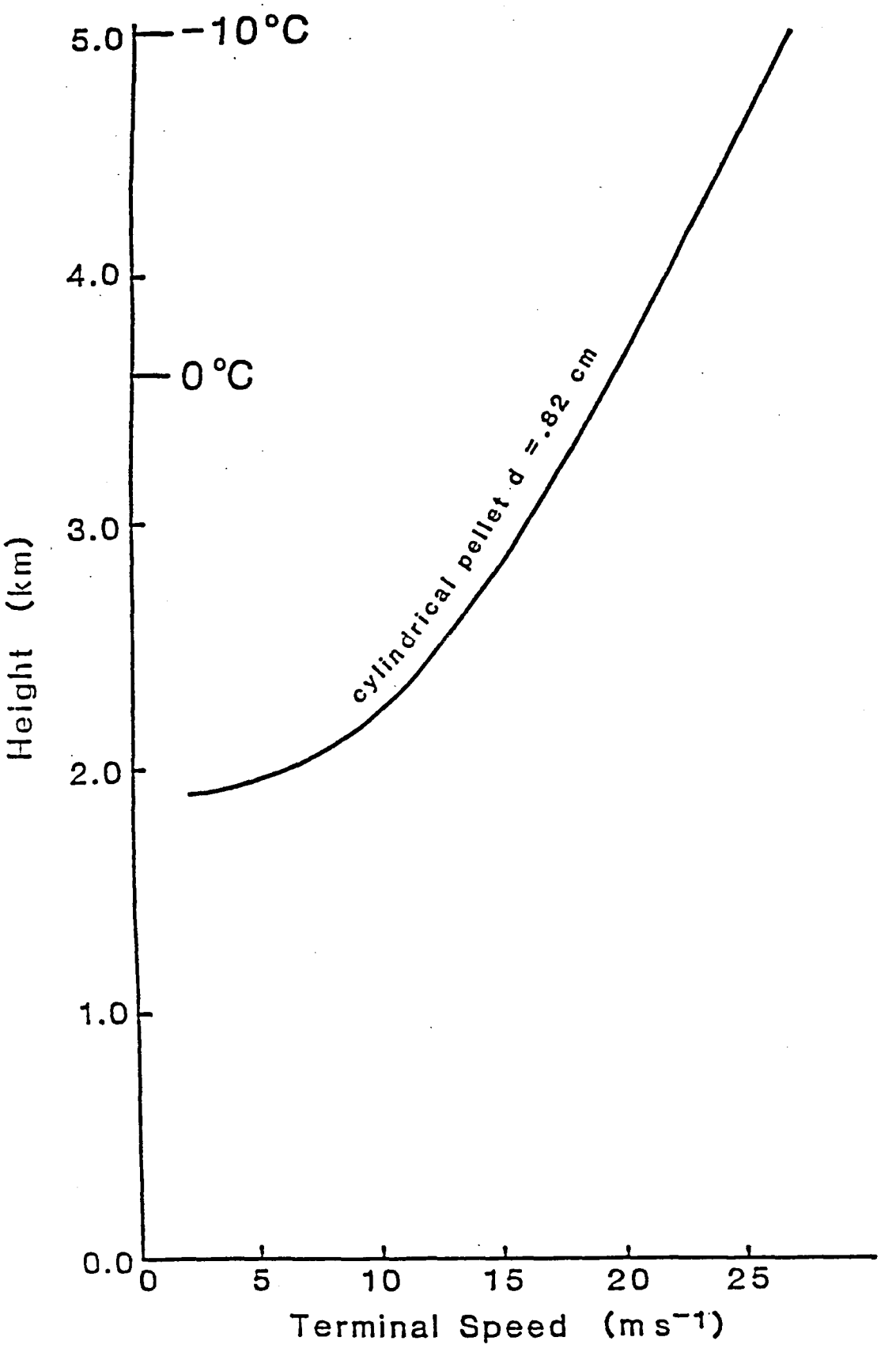

Figure 7.3. Model simulation of pellet speed as a function of height for a release at -10°C in cloud-free air.

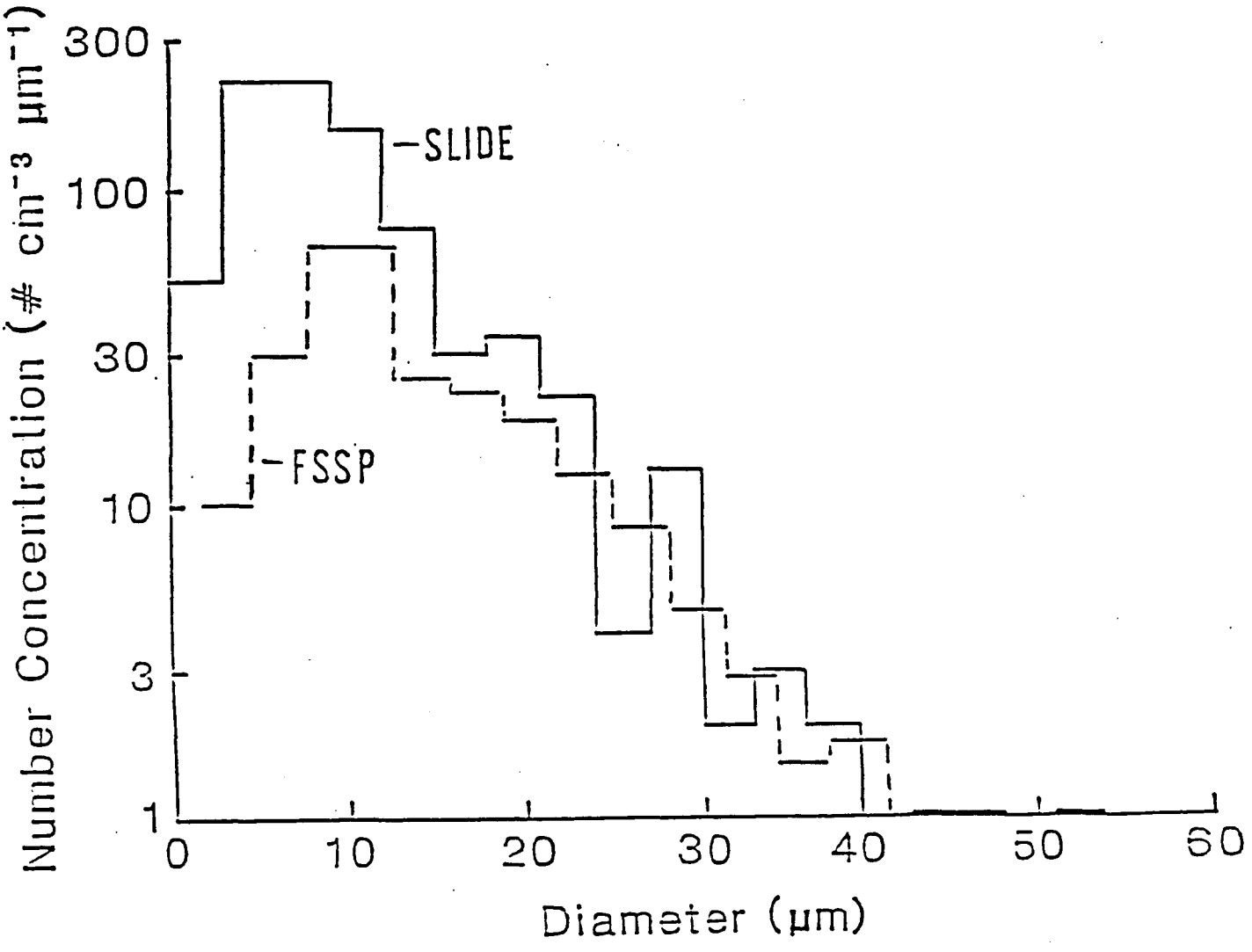

Figure 7.4. A supercooled water droplet spectra used in CSIR vertical wind tunnel. Solid line was obtained with FSSP; dashed line spectra was obtained with gelatine coated slides.

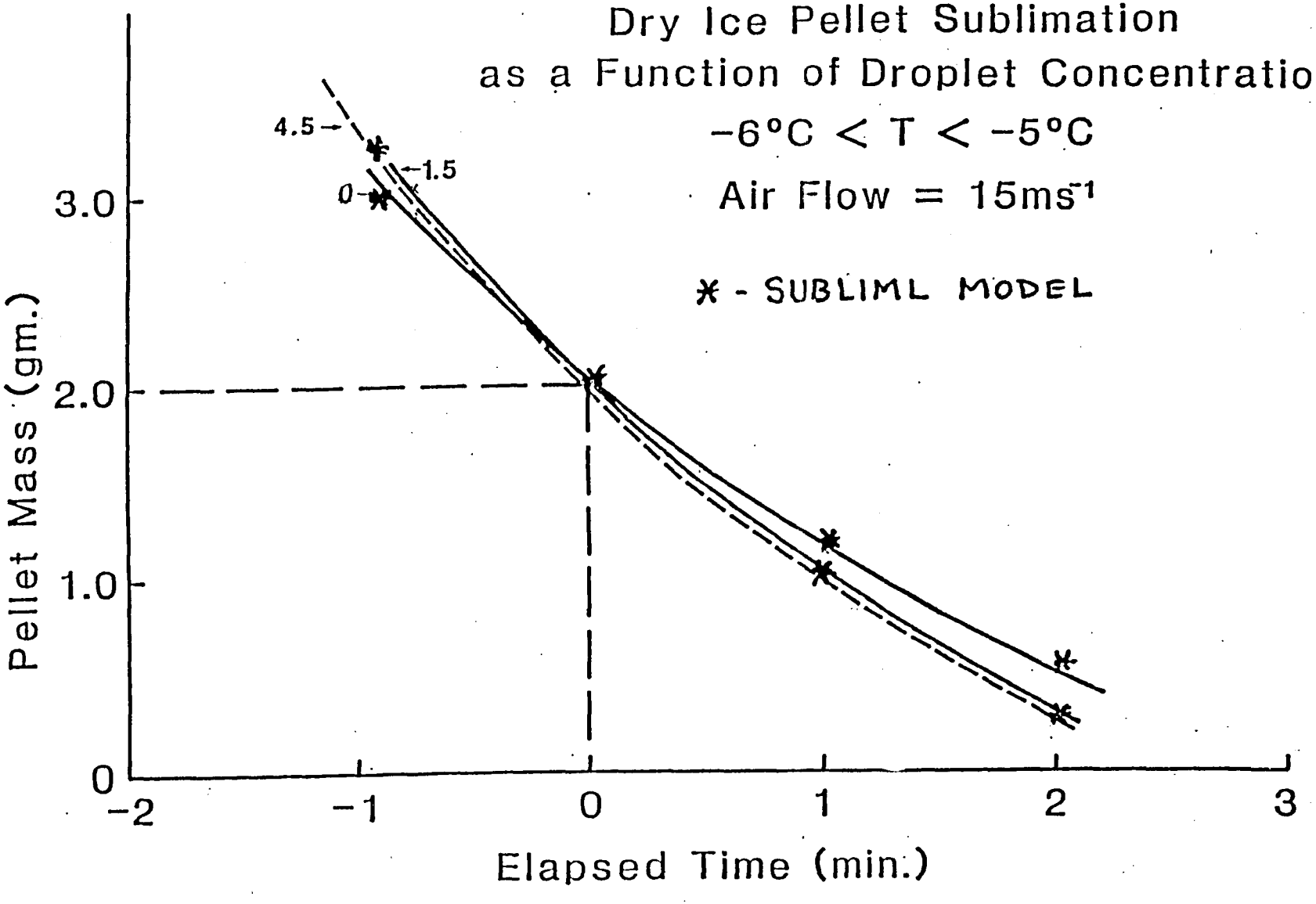

Figure 7.5. Laboratory measured and model predicted pellet sublimation at -5°C, airflow of 15 m s^{-1} and three liquid water contents (0, 1.5 and 4.5 gm m^{-1}).

Table 7.3. Pellet mass loss (%) after 1 minute time intervals.

Temp (°C)	LWC (gm m^{-3})	1 min	2 min	3 min
-5	0	37	66	90
	1.5	46	81	98
	4.5	44	76	97
-11	0	34	62	80
	1.5	40	69	92
	4.0	42	74	96
-16	0	38	67	85
	1.5	39	70	91
	4.5	41	76	96

An examination of Table 7.3 shows that the largest (24% increase) percentage change in rate of sublimation during the first minute occurred at -5°C and for 1.5 gm m^{-3} LWC; the smallest (3% increase) first minute change occurred at -16°C and 1.5 gm m^{-3}. This decrease in supercooled water effect with a decrease in temperature is consistent with the observation of a buildup of an ice layer on the pellet and its subsequent shedding. Riming was also noted by Lozowski and Kochtubajda (1980) and more recently Lozowski (personal communication) reported detecting a decrease in the effect of supercooled water with decreasing temperature. Although no attempt has been made to theoretically estimate the effect that riming may have on the sublimation rate, it is conceivable that the reduced heat conduction through the ice coating could actually reduce the cloudy air sublimation rate below the clear air rate, depending upon how often the ice was shed.

Although keeping the tunnel speed and pellet exposure constant gave us better control in the experiment, it did not allow for the tumbling action of the pellet which may affect the amount and pattern of riming which, in turn, could affect the aerodynamics of the pellet and therefore its tumbling behavior. However, in the judgement of the experimenters, the shedding of the ice coating seemed to be random and not particularly in phase with the pellet rotation. Whether the pellet was tumbling or not, the tendency to rime would be greater at the colder temperatures and thus the decreasing effect of the supercooled water on the dry ice sublimation rates would be in the same sense as was found in the laboratory.

In summary, these laboratory experiments have shown that:

1) in the presence of supercooled water droplets there is an increase in the sublimation rates of cylindrical dry ice pellets (range 3% - 25%),

2) the sublimation rate increase is largest at warm temperatures and while the pellets are large, and

3) in the seeding temperature range (-5°C to -15°C), the lifetimes of the pellets are reduced by 10-15%.

7.4 LABORATORY EVALUATION OF DRY ICE PELLET "WHISKERS"

Besides the riming of the dry ice pellets, there was visible evidence of frost particles being blown or knocked from the pellets' surface. A considerable effort went into examining the physical characteristics and quantifying number concentrations of these ice "whiskers" shed by the subliming dry ice pellets, both with and without supercooled water droplets.

The ability of dry ice to produce large and unnatural concentrations of ice particles in clouds has been demonstrated in laboratory and field experiments (Emmitt, 1984, Fukuta, et al., 1971), although the exact magnitude of the effectiveness (# ice particles/gm dry ice) may still be debated (Morrison, et al., 1984). It is generally accepted that the primary means of ice production by dry ice is homogeneous nucleation due to the low temperature (-79°C) of solid CO_2. Ice particles thus produced grow by vapor deposition for several minutes until they are large enough to grow by the accelerated process of riming. Contact freezing is considered a secondary process.

PAWS laboratory experiments have provided evidence of a way in which dry ice may produce instantly large ice particles of riming size. Because of their filament appearance under a microscope these particles are referred to as "whiskers."

7.4.1 Nature of Dry Ice Pellet "Whiskers"

Shortly after being made, a dry ice pellet exposed to the air will form a jacket of frost. Left undisturbed, the frost layer grows until an equilibrium between frost production and ice sublimation is achieved (Lozowski and Kochtubajda, 1980). When the pellet is subjected to an airflow of a few meters per second, a plume of frost "whiskers" can be seen being stripped off the pellet. Questions arise regarding the crystalline structure, maximum size (at terminal fall velocity of the pellet in clear and cloudy conditions) and the number concentrations of these particles. A primary question is, do the ice "whiskers" shed from a tumbling dry ice pellet provide a significant number of instantly large riming centers?

By re-orienting the CSIR wind tunnel into a horizontal position, the whisker plumes of dry ice pellets held at the tunnel outlet were sampled utilizing a PMS OAP-2D probe and formvar replicating slides. Typically, the 2-D probe was located at about 10 cm from the pellet and simultaneous formvar samples were taken just downstream of the 2D probe.

Whiskers in the plumes of dry ice pellets in dry airflows were clearly observed in the 2-D images (Figure 7.6). Concentrations of whiskers longer than 100 m derived from both formvar examination and computer processing of the 2-D images are in good agreement -- on the order of 40 to 50 per liter. Concentrations computed for these laboratory experiments should not be confused with concentrations that would be sensed with an aircraft two to three minutes after a seeding run. Further discussion of concentrations is presented in Section 7.4.2.

When small pieces of dry ice were observed under the laboratory microscope under a normal room environment with little air motion, dendrite or

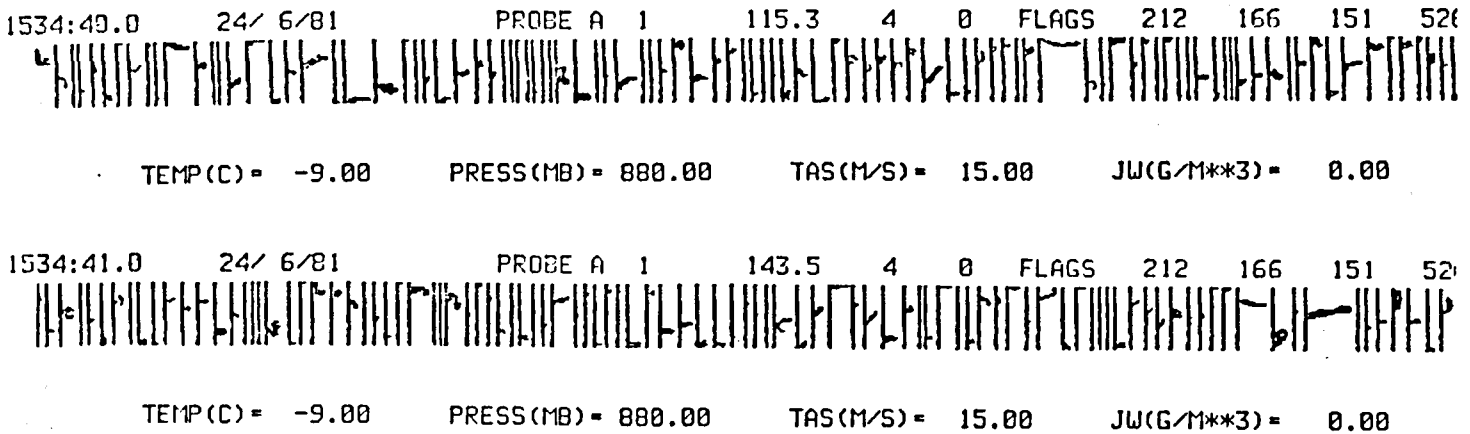

Figure 7.6. PMS-OAP-2D-C images of particles shed by dry ice pellet without any supercooled water droplets present.

fern-like structures Fig. 7.7 were readily seen growing as appendages outward from the frost jacket enveloping the sublimating dry ice pellet. These structures grow to tens of microns in length, sometimes becoming intertwined with neighboring structures and then breaking off from the jacket of frost due to turbulence caused by the strong temperature gradient near the dry ice surface.

In the cold room experiments with an airflow present these "whiskers" lost their crystalline appearance (Fig. 7.8) apparently due to mechanical stresses on the surface of the pellet. More recent experiments by SWA in Charlottesville have produced videos of "whisker" growth and shedding using a special mini-wind tunnel and a large laboratory microscope. Review of that video shows clearly why the "whiskers" lose their dendritic structure. The "whiskers" are actually an agglomeration of very small ice crystals that agglomerate by rolling along the surface of the pellet until enough ice is collected to be entrained into the strong airflow a few 10's of microns above the pellet surface. An attempt to estimate whisker number concentrations leads to numbers an order of magnitude larger than those obtained with the 2-D probe but showed similar sizes and shapes.

7.4.2 The Interaction of Whiskers with Supercooled Water Droplets

Formvar samples collected downwind of a pellet in cloudy air using the wind tunnel in the cold room showed large numbers of droplets in clusters, but no direct evidence of whiskers or fragments of whiskers. SEM examination of collected pellet products plus droplets revealed tiny objects, roughly rectangular in shape, on some of the drops.

Inspection of the FSSP droplet spectrum prior to the introduction of a dry ice pellet showed it agreed reasonably well with gelatine-derived spectra except for the very high counts in the first bin (see Figure 7.4). The mean total concentration of particles was 871 cm^{-3}, and mean particle diameter 10.6 microns with a dispersion of 0.64. When a dry ice pellet was added to the cloudy air of the wind tunnel, there was a slight increase of the FSSP particle count in the higher bins. The mean total concentration of particles in this case was 917 cm^{-3}; the mean particle diameter, 11.8 microns; and the dispersion, 0.66.

A typical 2-D spectrum of the supercooled droplets alone is shown in Fig. 7.9. The mean concentration of particles less than 105 microns was 400 per liter while the concentration of particles greater than 105 microns was 24 per liter. The addition of a dry ice pellet to the supercooled droplet environment caused an increase in the number of large particles imaged by the 2-D. Although the 2-D images still showed large numbers of zero images with a few large water droplets, some whiskers were also observed (2-D spectra in Fig. 7.10. The mean concentration of particles less than 105 microns decreased to 172 per liter, while those greater than 105 microns increased to 36 per liter.

The 2-D probe shows the apparent survival of a significant number of whiskers in the presence of supercooled water droplets. It is unclear as to why no evidence of whiskers was seen in formvar samples under the same conditions, unless their evidence was destroyed by the clustering of the droplets

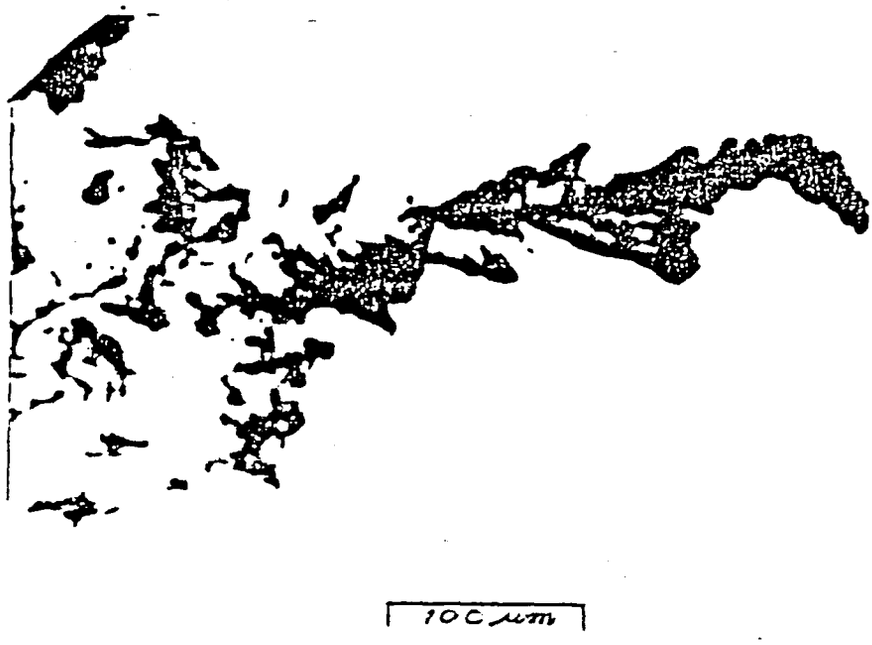

Figure 7.7. Replica of a whisker brushed off the dry ice showing a dendritic structure.

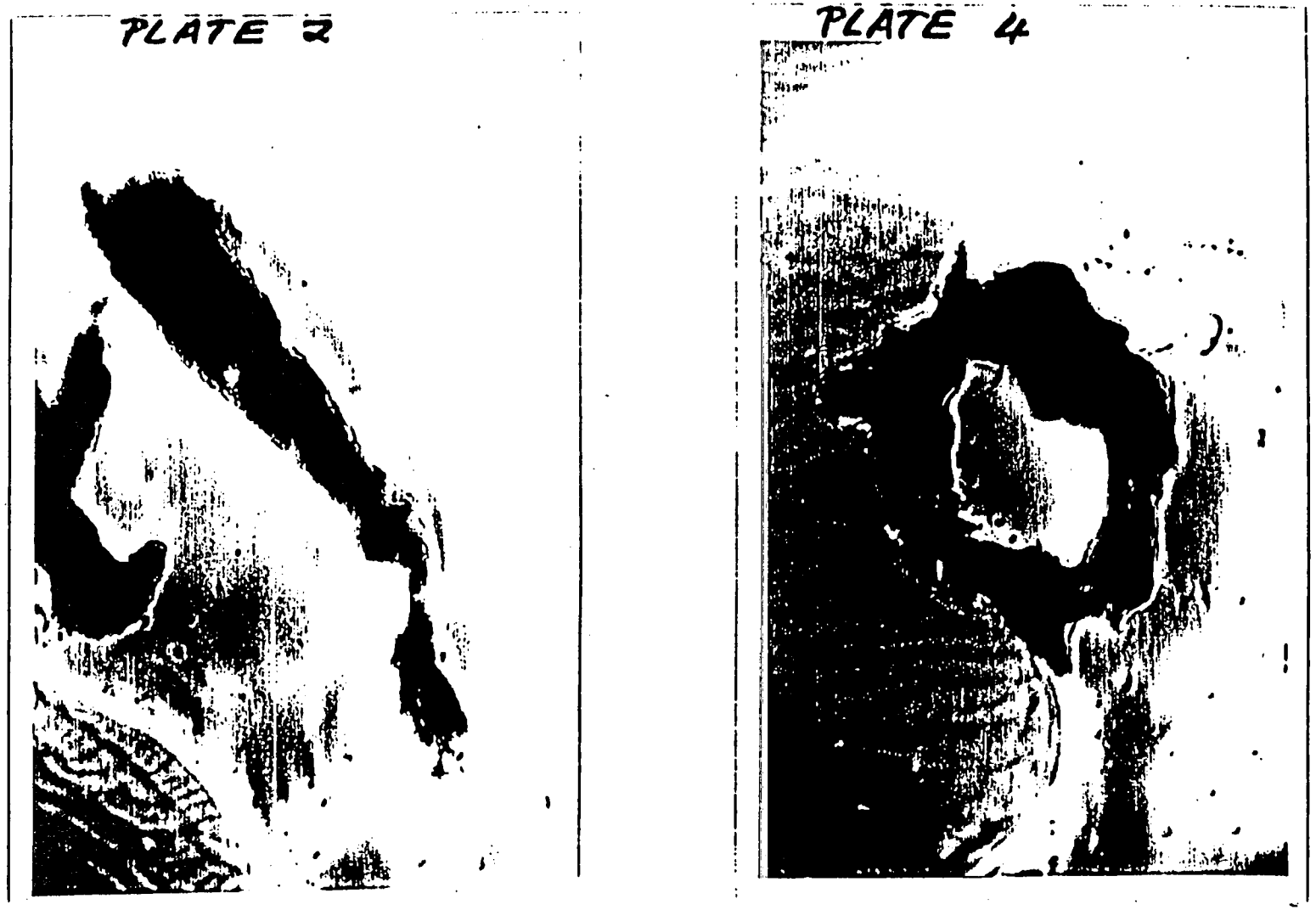

Figure 7.8. Formvar "whisker" replications as seen under a standard laboratory microscope.

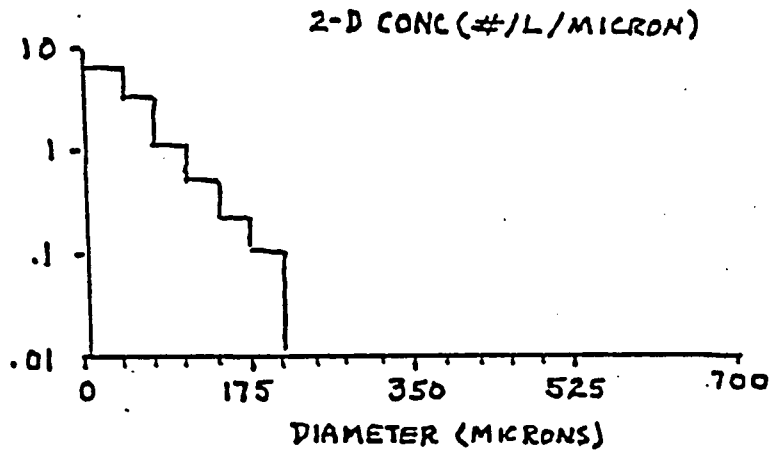

Figure 7.9. 2-D supercooled droplet only spectra.

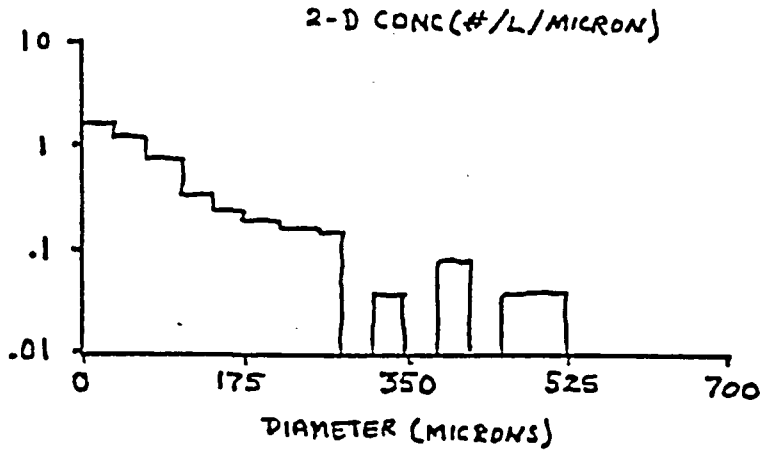

Figure 7.10. 2-D supercooled droplet with dry ice pellet spectra.

in the formvar film subsequent to sampling. As an alternative to formvar sampling, petri dishes filled with liquid hexane were subsequently used.

In one experiment, a dry ice pellet was held at the mouth of the tunnel and a dish of liquid hexane was quickly moved through the airflow at about 30 cm downstream. Large numbers of droplets, but only a few whiskers, were collected. Most of the droplets were still liquid when they entered the hexane. However, a few frozen droplets were observed. Nearly all the whiskers had frozen droplets attached to them; one such example is shown in Figure 7.11 where dendritic crystalline features can actually be seen inside the frozen drop, diverging from the point on the surface where the whisker had nucleated the supercooled bulk.

7.4.3 Significance of Whisker Products

The particle concentrations measured in the wind tunnel are not the same as those that would be measured by an aircraft flying through a dry ice seeding plume. To estimate the scale factor between the tunnel and aircraft measurements, the following arguments are made:

1. during seeding the pellets have a line density of ~1 m^{-1} along the aircraft track;

2. an average pellet sublimes at a rate of approximately .010 g s^{-1}, falls initially at ~25 ms^{-1} and thus sublimes ~4.0 x 10^{-4} gm/m;

3. the lateral turbulent diffusion spreads the ice pellet products out to a distance of .5 km on either side of the seeding track in 3 minutes after seeding.

After three minutes the particles generated in the first meter of pellet fall will be dispersed into nearly 10^3 m^3. With a fall speed of 25 m s^{-1} we need to divide any laboratory production rate (s^{-1}) by 2.5 x 10^4 m^3 s^{-1} to get a reasonable estimate of the particle concentration to be realized in a real seeding situation.

Next, the sampling efficiency of the formvar replicator and the 2D probe are estimated. The formvar slides have sample areas of .6 cm^2 while the 2D probe has a sample area of .7 cm^2. The area of the total ice plume of the pellets was visually estimated to be 10 cm^2 at the sampling distance of 10 cm. Therefore both the formvar slides and the 2D probe are intercepting ~6-7% of the ice products. Converting the formvar and 2D laboratory large (>100 m) particle concentrations of $\doteq 10^{-1}$ to number of particles per second of flow we get ~100 particles/second. Converting this number to its equivalent field concentration we get 4.0 x 10^{-3} m^3. Based upon the more recent visual counts using the micro-wind tunnel, a field concentration for the >100 μm whiskers may be $\doteq$ .1 m^{-3}. By comparison the generally accepted activity rate for dry ice (10^{12}/gm) yields 4.0 x 10^5 m^{-3} of the < 100 μm particles.

Review of initial cloud penetrations with an instrumented aircraft reveals frequent occasions when there is little ($<<10^3$ m^{-3}) or no 2-DP probe activity. The laboratory studies suggest that dry ice may deliver to these clouds the first large (>100 μm) ice particles at concentrations of 10^{-1} to 10^{-3} m^{-3}. In terms of growth by riming these particles have a several minute

Figure 7.11. Example of a supercooled droplet (diameter = 250 m) that had been nucleated by a "whisker" in mid-air. Dendritic arms, showing up at a result of air bubble contrasts in the ice, are seen diverging from the point of nucleation.

lead on the smaller dry ice produced particles which must first grow by vapor deposition. How important these particles are to the evolution of the cloud precipitation production process remains a question to be addressed by cloud models that can handle the broad range of number concentrations represented by these results.

8.0 RADAR ECHO CLIMATOLOGY STUDIES (Morgan, Parsons and Wightman)

8.1 The geographical patterns of radar echo frequency

The terrain over the area of coverage by the PAWS radar is such that one expects and observes a nonuniform geographical distribution of echo activity. The role of even small terrain features in triggering convective storms has been noted since the earliest days of radar meteorology and even before.

The geographical dependence of echo occurrence in the PAWS experimental area is readily shown utilizing the radar analysis software package developed by Dixon and described in Section 2.0 of this volume.

The radar coverage area (120 km radius from Nelspruit) has been divided into 10 km blocks and echo events occurring in those blocks are summed. The events are based on the entities which are tracked by the cell tracking software. The unit is the three-dimensional cell and an event consists of the presence of the centre of a cell in a block.

A simplified version of the terrain over the same area is shown in Fig. 8.1.1 based on a digitized terrain file provided to the Project by Prof. R E Schulze of the University of Natal. The height value in each block (the same blocks as used for the radar echo frequency patterns) is the average terrain elevation in each block.

The following geographical frequency distributions have been determined:

a. First Detection Distribution (FDD)

The First Detection Distribution is the frequency of occurrence of the beginnings of storm tracks. Each track appears only once on this frequency map, at its point of origin, thus the total of all the individual block frequencies is the total number of cells tracked by the software.

b. Limited Storm Frequency Distribution (LSFD)

This is the geographical distribution of the frequency of occurrence of storms over each block. A given storm (cell) can enter a given block total only once. So, if a storm passed over three blocks, spending three radar scan periods (about 7 min each) in each of them, it would enter each of the three block totals with a count of one.

c. Storm Frequency Distribution (SFD)

In this distribution a given storm contributes to the count in a given block a number equal to the number of scans on which it was centred somewhere over the block. The frequencies appearing in the blocks are thus a measure of the amount of time

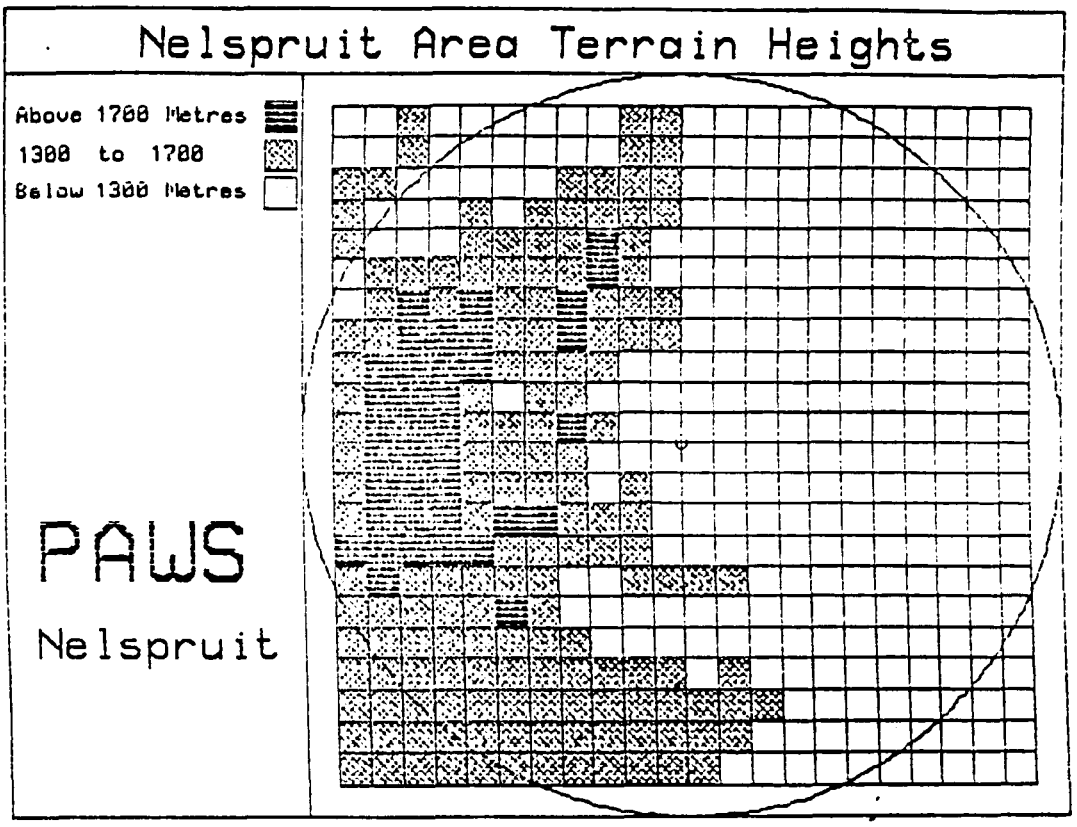

Fig. 8.1.1. Schematic relief map of terrain surrounding Nelspruit.

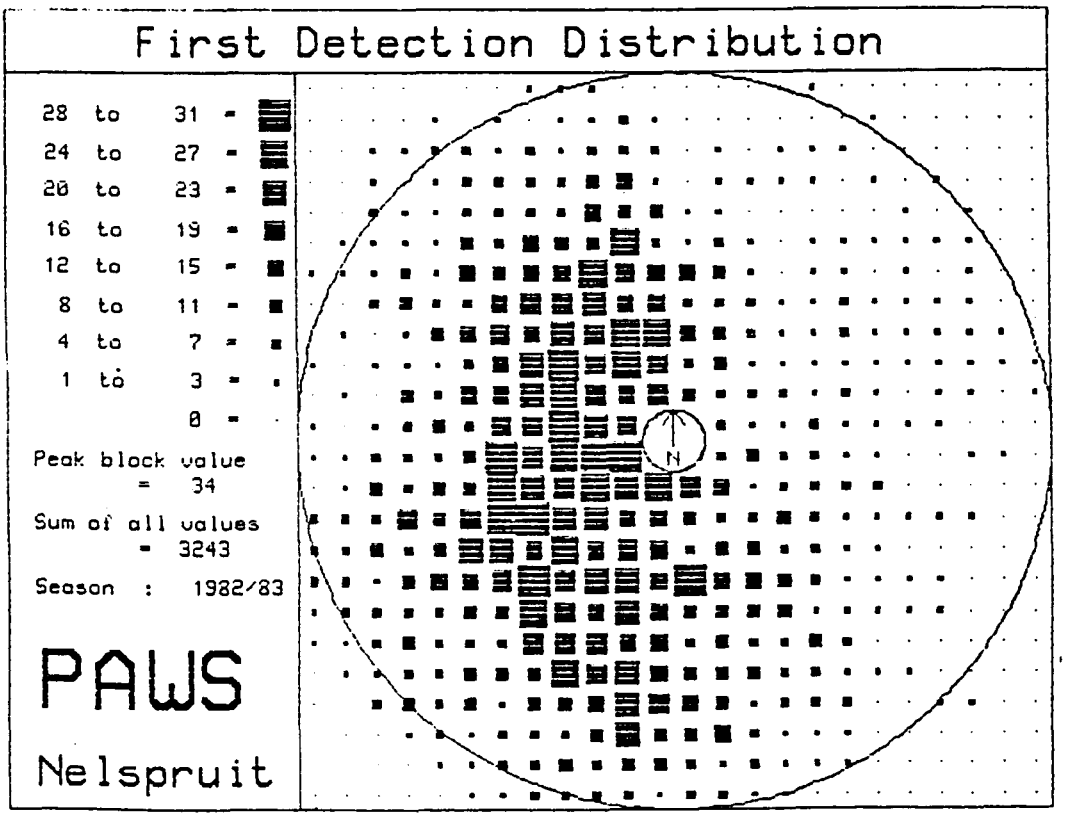

Fig. 8.1.2. Geographical distribution of first storm echo detection - 1982/83 season.

storms (centres) existed in the blocks.

d. Last Detection Distribution (LDD)

This is completely analogous to the First Detection Distribution except that each storm track enters the distribution only once, at the point of its demise.

8.1.1 Seasonal distributions

The most interesting seasonal maps, and the easiest to interpret, are the First Detection Distributions. Fig. 8.1.2 to 8.1.5 show the seasonal FDD's for 1982/83, 83/84, 84/85 and 85/86. There are differences between these, but they certainly have some common features. The most striking differences concern the varying relative strength of the activity to the southwest of the radar. It is quite pronounced in the 1982/83 sample, nearly absent in 1983/84, pronounced again in 1984/85, and very much attenuated in 1985/86. The high first detection frequencies to the northwest do not exhibit these dramatic variations. The differences that appear among these seasonal distributions are interesting and we shall seek explanation of them.

8.1.2 Combined distributions for the 1982 - 86 period

It is desirable to combine the four years to yield an "average" pattern. This has been done by dividing each seasonal field by the total number of storm initiations, then averaging. This produces an average pattern shape rather than a pattern of average frequencies, and accounts for the different modes of operation and incidental breaks in the data which affect the sample size. The 1982/83 season, for example, was not fully operational; software and operational volume scan procedures were being developed. This resulted in a low total number of storms being tracked, but the observations are well distributed through the season and can be considered an unbiased selection. In 1984/85, operations were carried out as needed, seven days per week, whereas during most of the rest of the time, Sundays were always considered non-operational. In 1983/84, most of the month of January was non-operational due to the loss of an engine on the Lear.

The average normalized pattern of First Detections for the 1982 - 1986 period is shown in Fig. 8.1.6 and confirms what had been learned over many years (since 1972) of radar operations in Nelspruit. The pattern of storm generation is closely tied to the major terrain features of the escarpment.

The Storm Frequency Distribution for the 1982 - 86 period is shown in Fig. 8.1.7.

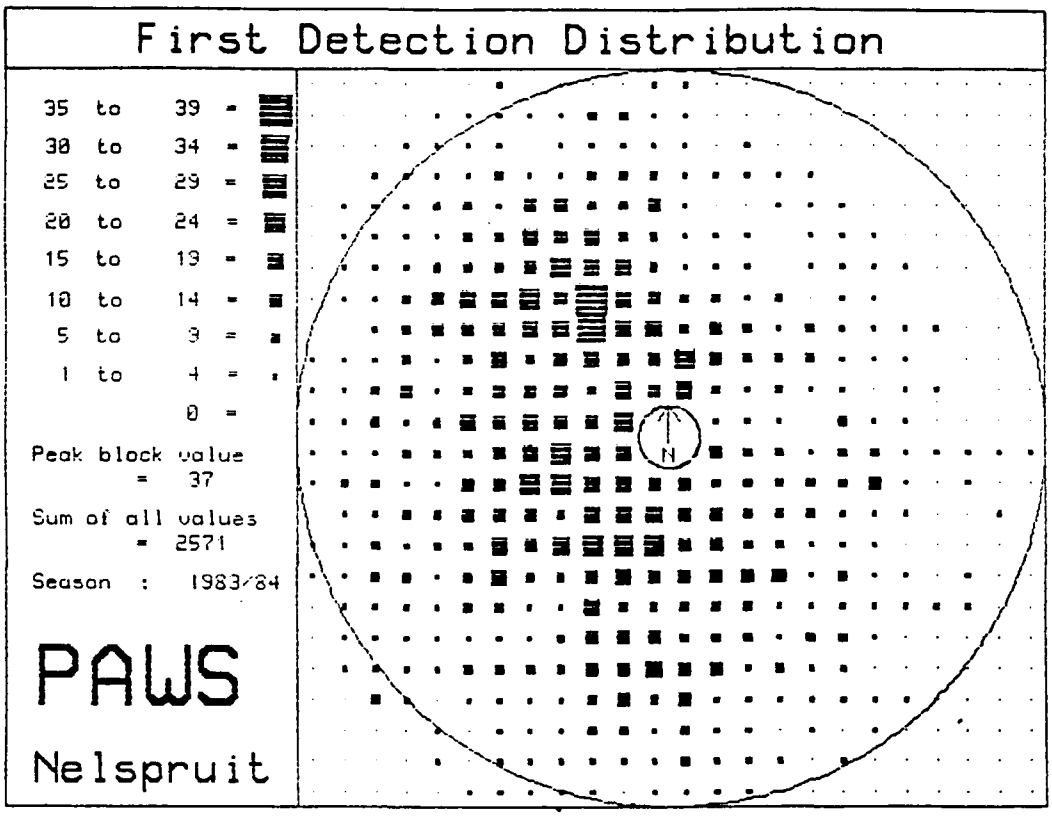

Fig. 8.1.3. As in Fig. 8.1.2 - 1983/84.

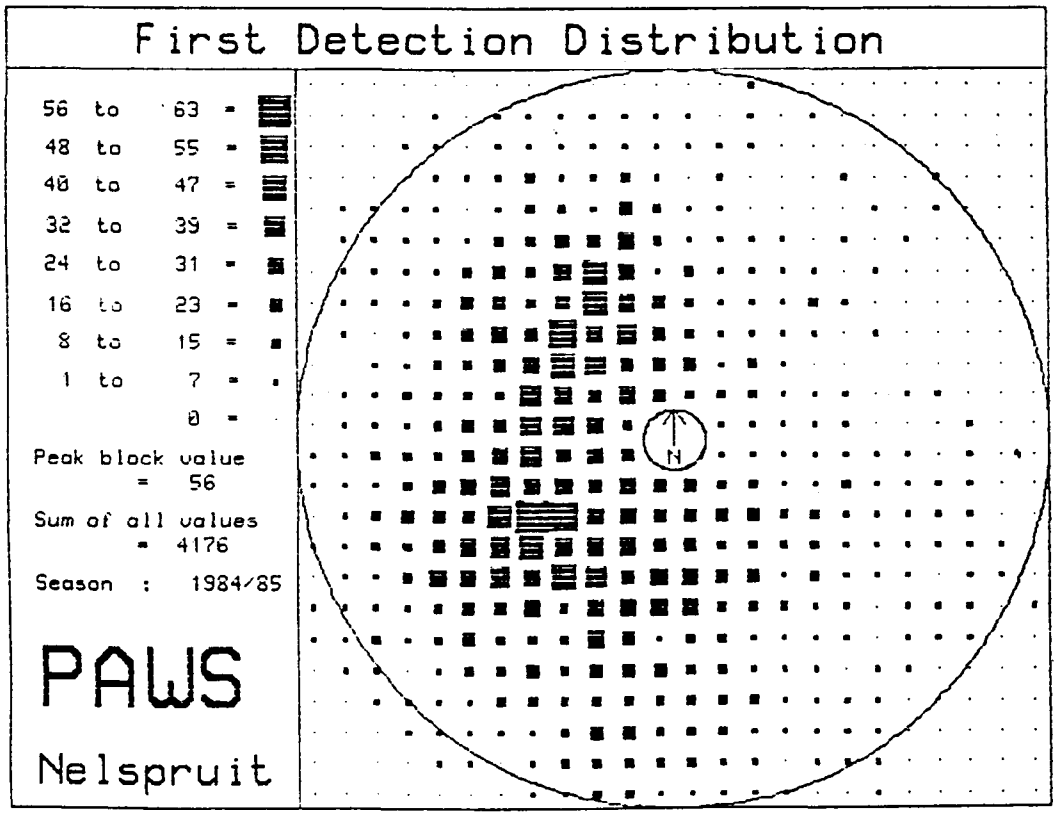

Fig. 8.1.4. As above - 1984/85.

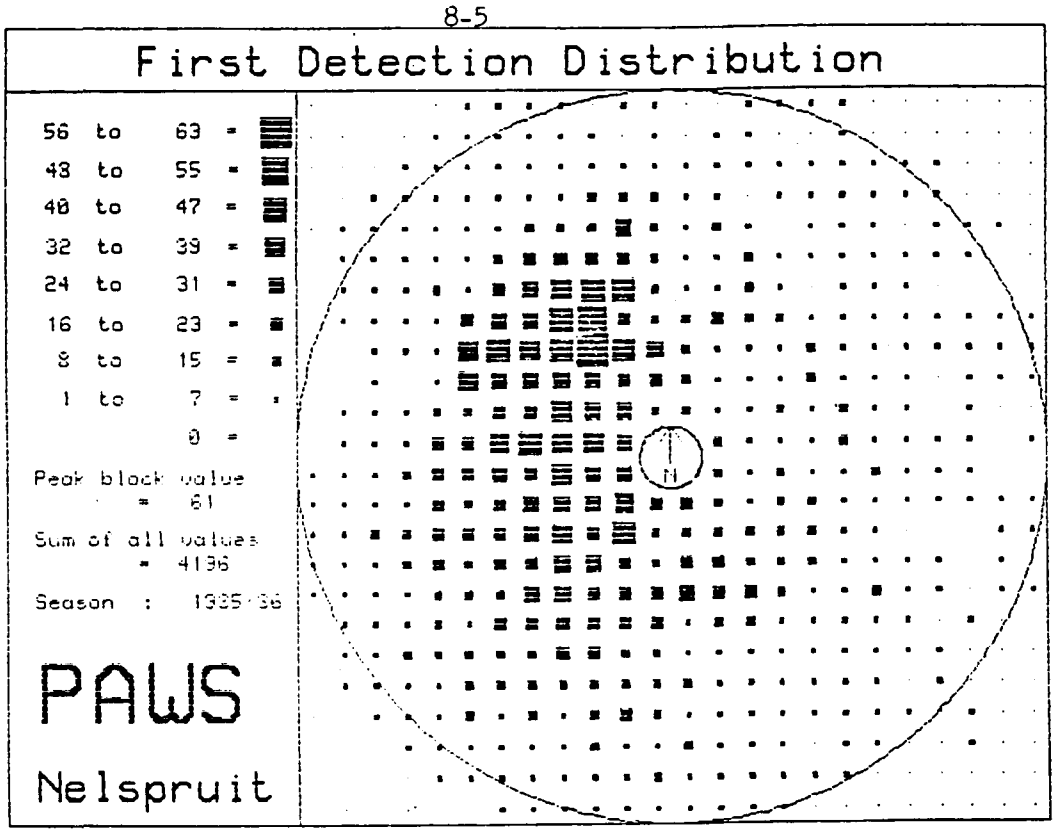

Fig. 8.1.5. As in Fig. 8.1.2 - 1985/86.

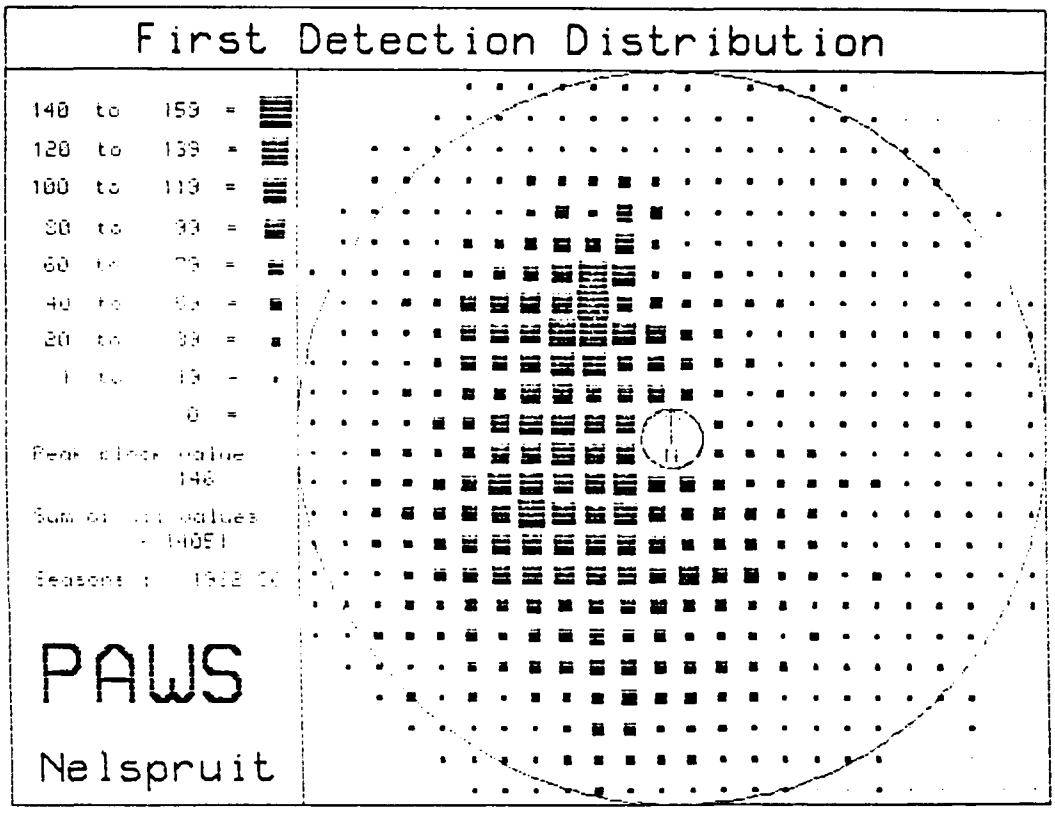

Fig. 8.1.6. Four season average of first storm echo detection.

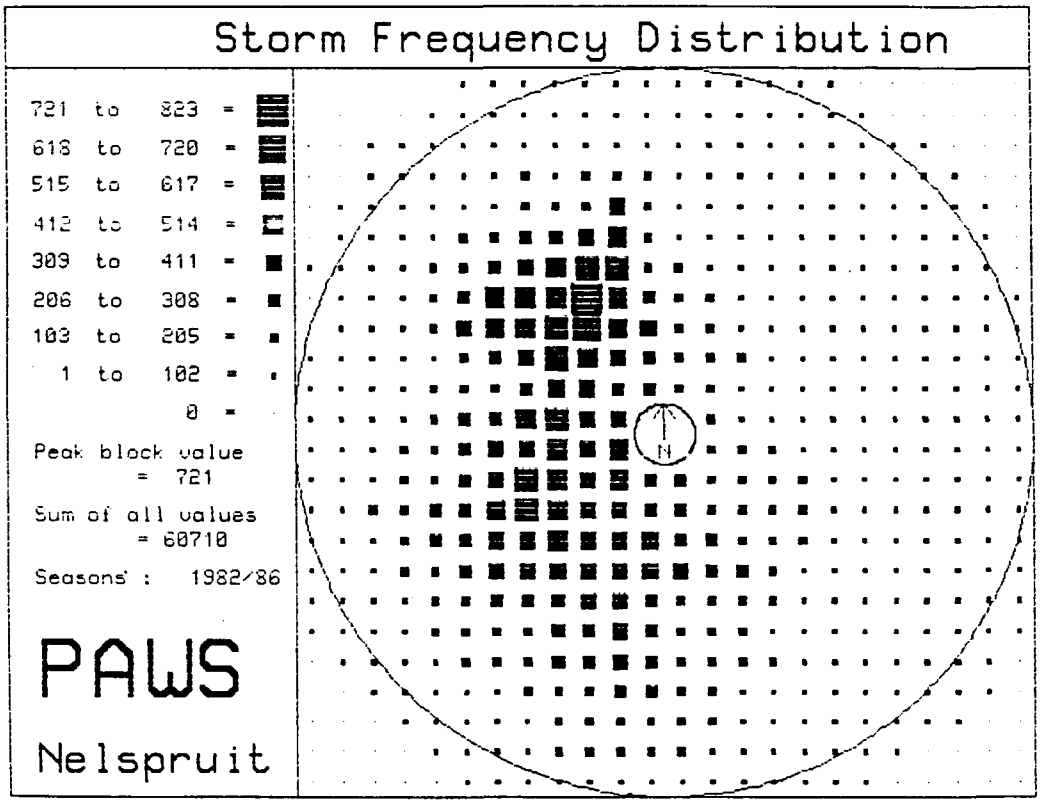

Fig. 8.1.7. Four season average of geographical distribution of storm frequency.

8.1.3 Storm speeds and lifetimes

We have four fields for each season. First Detection Distribution (FDD), Storm Frequency Distribution (SFD), Limited Storm Frequency Distribution (LSFD) and Last Detection Distribution (LDD). From these we may derive a few more fields.

The LSFD and SFD are related in such a way that if we divide, block-by-block, the SFD by the LSFD, the result is the field of average number of scans per storm per block. High values of this will indicate a tendency for storms to linger in the block, low values a tendency toward short lifetimes or rapid motion through the box.

The distributions resulting from the estimates of the ratios of SFD to LSFD are very ragged in the single seasons. When the four seasons were added together, the geographical distribution was of such astonishing uniformity, at a value of 2 scans per block per storm, that there is no point in presenting it graphically. This result is important and permits us to state that there is no localization of the combined effects of storm speed and lifetimes to be detected anywhere in the radar observational area.

8.1.4 Storm sources and sinks

The LSFD is interesting. It can be decomposed into distinct components which can be given letter names.

LSFD = A+B+C+D where
- A = number of storms which start and die within the block
- B = number of storms which start in the block and then leave the block
- C = number of storms which enter the box and then leave it
- D = number of storms which enter the block and die there

Using these behaviours, which are exclusive we see that

FDD = A + B, and
LDD = A + B

Further,

LSFD - FDD = C + D, the total number of storms which enter the block

LSFD - LDD = B + C, the total number of storms which leave the block and so on. Taking the difference between these yields the "divergence" of storms and this, since the storms which pass

right through the block (c) do not contribute, is just

$$(SFD-LDD)-(SFD-FDD) = FDD-LDD = B - D$$

Positive values of this mean that more storms leave the block than enter it, negative values mean that more storms enter and die in the block than start out there and leave it.

The terrain has been averaged in columns and rows in the same way as the various storm properties, to emphasize the relationship between the terrain and the storm behaviour.

The FDD - LDD distributions for single years are noisy. So, they are summed for all the four seasons (not shown). In this distribution, which we call the Storm Source-Sink Distribution (SSSD), a general area of predominant storm production is easily discernible to the West of Nelspruit, and a more distributed sink area can also be seen. To show this more dramatically, the columns and rows can be summed to give the E-W and N-S profiles of storm 'divergence'. The columns and row averages are calculated taking into account the length of the chord of the radar circle at each averaging position. The actual procedure consisted in applying fractional weights to the 10 x 10 km boxes on the border of the 120 km radius limit of radar observation. This results in the graphs of Figs. 8.1.8 and 8.1.9 The N-S profile (Fig. 8.1.8) has a noisy characteristic, no clear pattern. There is a tendency for more production of storms to the south, and more storm disappearance to the north. The E-W profile, however, shows a very strong and easily interpreted pattern. The peak to the W of Nelspruit is the storm generating effect of the escarpment. The deep trough immediately west of the Nelspruit axis is the effect of storms dying as they are moved off the higher ground by the prevailing westerlies. This supports the view that most storms in this area are generated and supported by the thermally direct circulation which develops over the higher ground. Storms do not often show rapid movement, but tend to drift away from their source area with the upper winds. They tend to die when they lose the support of the terrain and there may be a storm suppression mechanism (subsidence) east of the escarpment. This is, of course, not true for all storms; certainly not for the night-time storms which were not routinely recorded by our radar. The negative peak between 70 and 120 km is doubtless due to the faster moving storms. To some extent the character of the column averaged SSSD is a product of the shape of the FDD column averages and a tendency for storms to move from the west. If every storm just moved into the next box, a similar SSSD would result. The LDD, column averaged, would be just the FDD displaced one box to the right, and the SSSD would be determined mainly by the slope of the FDD. Storms, however, move a spectrum of distances and directions between birth and death, producing a more complex result.

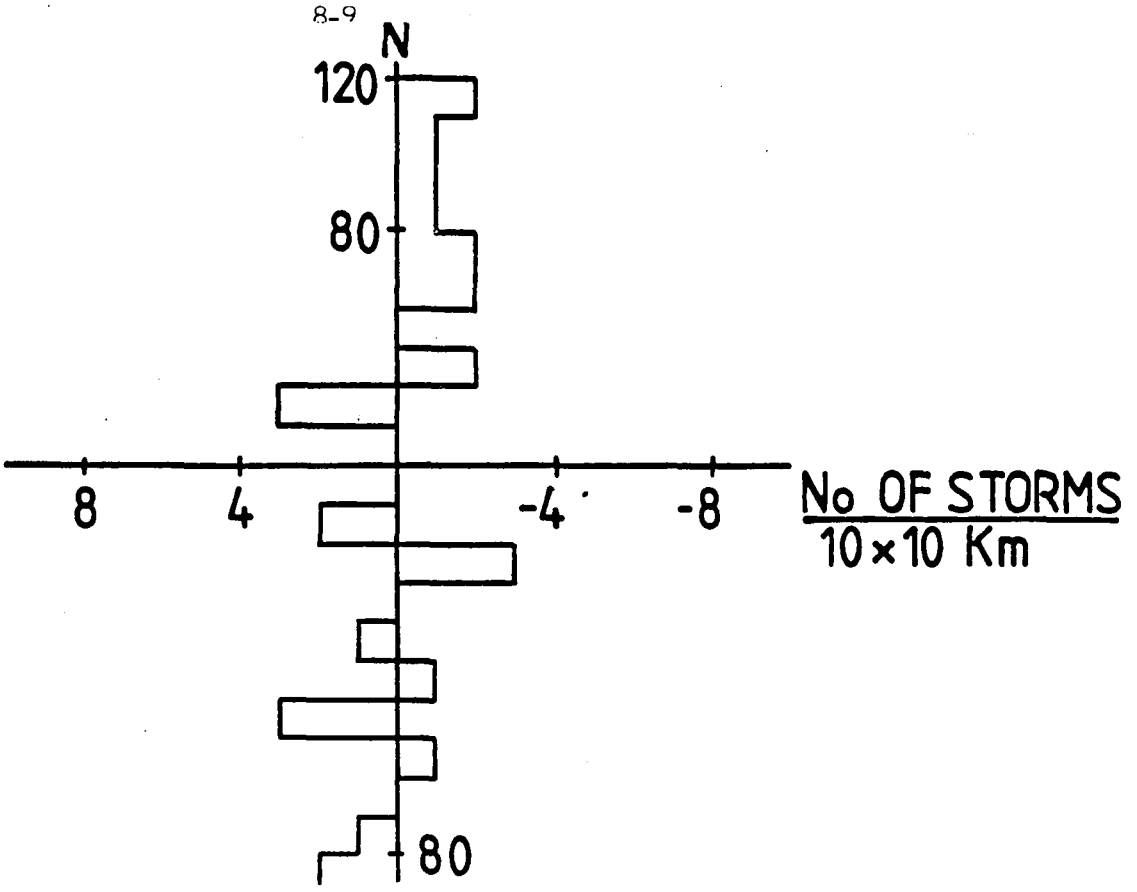

Fig. 8.1.8. North/south pattern of storm sources and sinks.

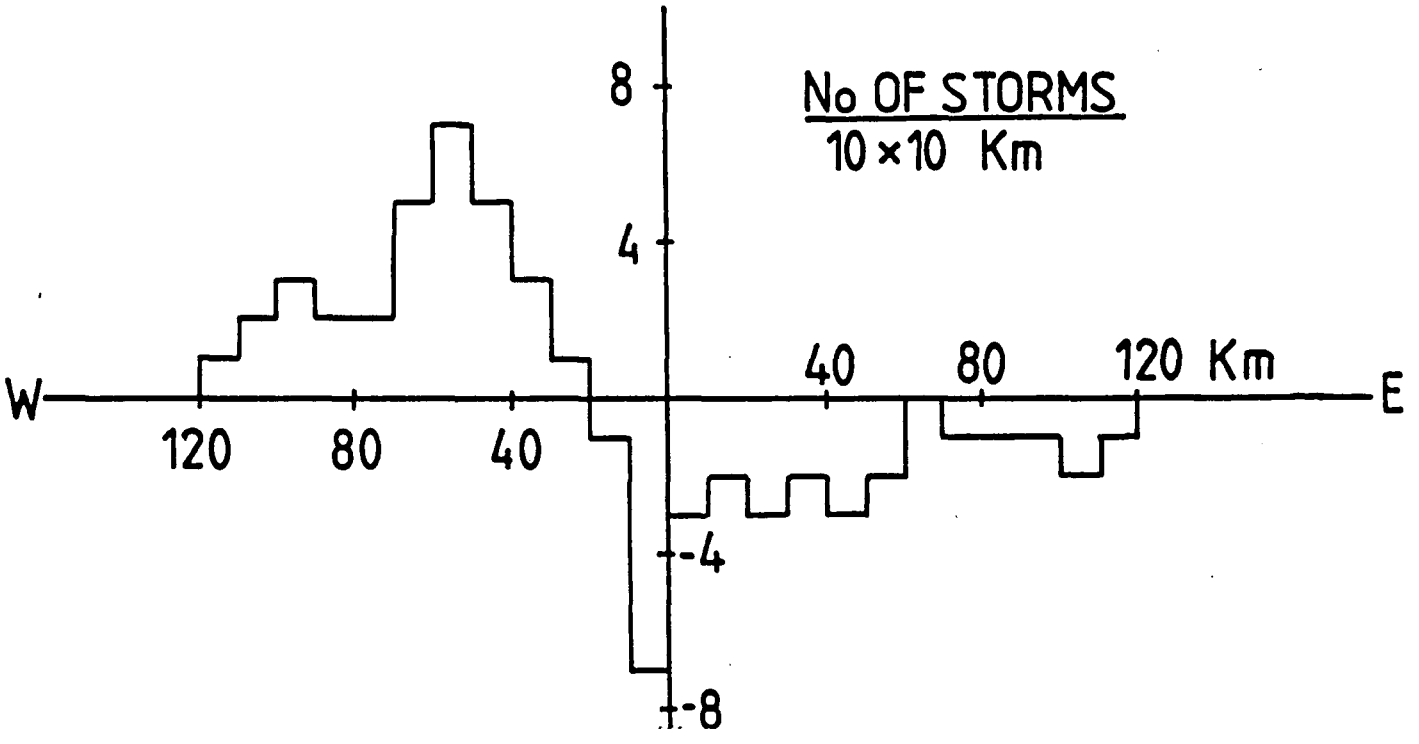

Fig. 8.1.9. West/east pattern of storm sources and sinks.

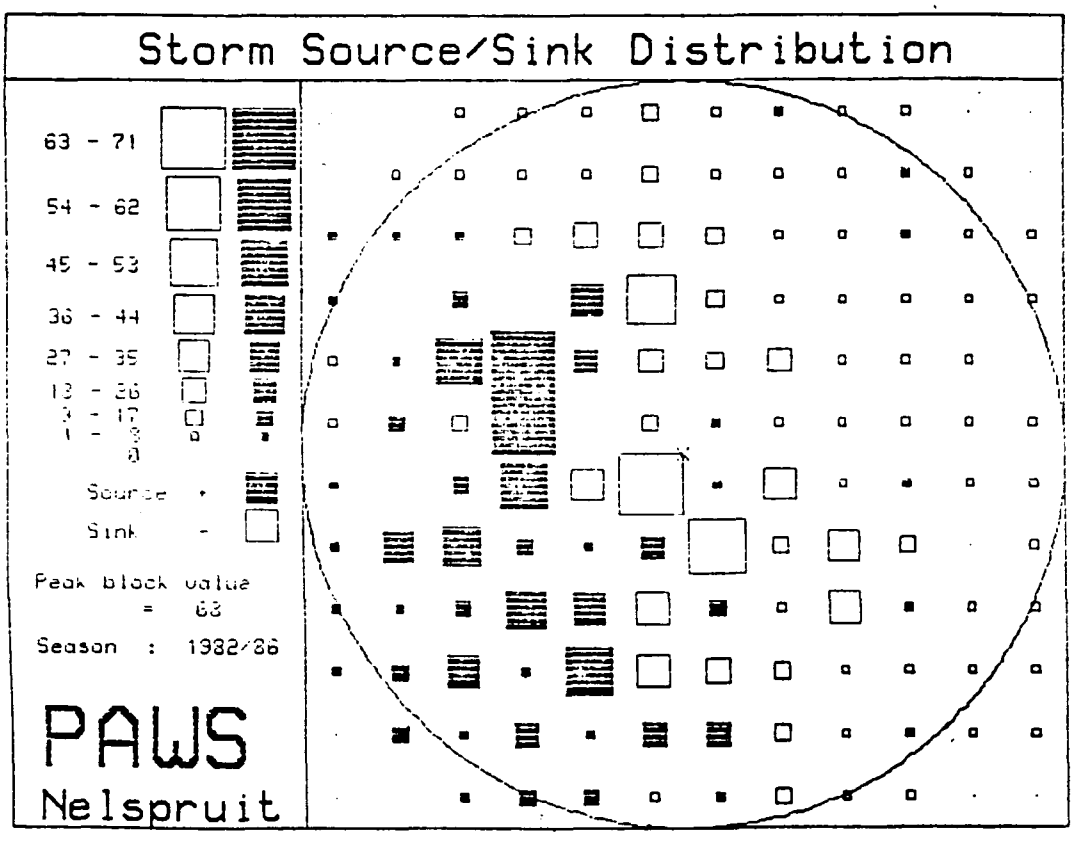

Fig. 8.1.10. Geographical distribution of storm sources and sinks - four season average.

The clarification resulting from summing the data in rows and columns suggests that some smoothing in the two-dimensional SSSD might be profitable. Fig. 8.1.10 results from changing the 10 x 10 km box size to 20 x 20 km (by summing four adjacent boxes). Here the pattern has been greatly clarified and seems highly significant.

The 20 x 20 km boxes adjacent to Nelspruit have had their values altered to account for the effect of the 10 km ring within which no radar data is analysed. Because of this ring, the 10 x 10 km boxes closest to Nelspruit do not contain valid data. The 20 x 20 boxes closest to the radar thus are composed of only three 10x10 km boxes each, and the numbers in them have been multiplied by 4/3.

8.1.5 Geographical effects on the direction of storm movement

It has been shown above that there are no significant variations in storm speed which are dependent on position. It remains to be shown whether there are or are not any significant connections between geographical position and preferred directions of storm movement. A straightforward computer analysis of the storm track data shows that in this case there are strong geographical effects.

In each 10 x 10 km block, as in previous analyses, as many estimates as possible of storm direction (vector) were made. These were assigned as frequencies to 30 degree sectors and these divided by the total number of estimates of direction in each block. This produces a relative frequency distribution, by 30 degree direction sectors, for each block. Maps were plotted of relative frequency for each 30^{o} sector and then adjacent sectors were combined in various ways to produce further maps. The accompanying two plots give a strong demonstration of directional preference in different areas. Values are plotted here, only for blocks in which the total number of direction estimates exceeded 100. The first (Fig. 8.1.11) shows the relative frequencies for the sector 330^{o} - 060^{o}, and one sees that in the northern portions of the area, and in a few other spots, over 40 percent of radar storms move with directions in that sector.

The second (Fig. 8.1.12) is an analogous plot for the sector 060 - 150^{o}. Here the pattern has virtually reversed itself, and in large areas of the southern part of the map, it is seen that over 50 percent of storms move with directions in the sector 060^{o} - 150^{o}.

These large shifts in direction are due to a combination of terrain and meteorology (winds). We shall attempt to separate the two effects as the research proceeds. The principal terrain effect on direction would appear to be the fact that the valleys to the north tend to run northeast-southwest, while those to the south are east-west. Storms tend to propogate along the terrain contours.

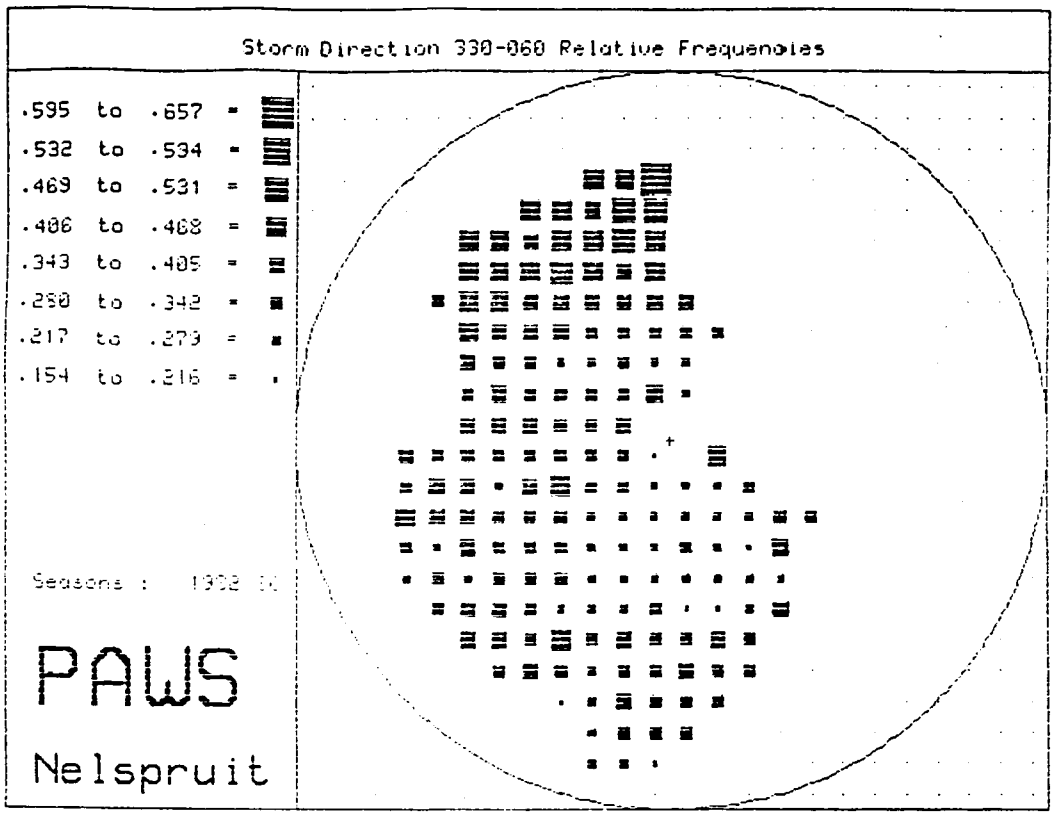

Fig. 8.1.11. Relative frequency of storm directions - northwest quadrant.

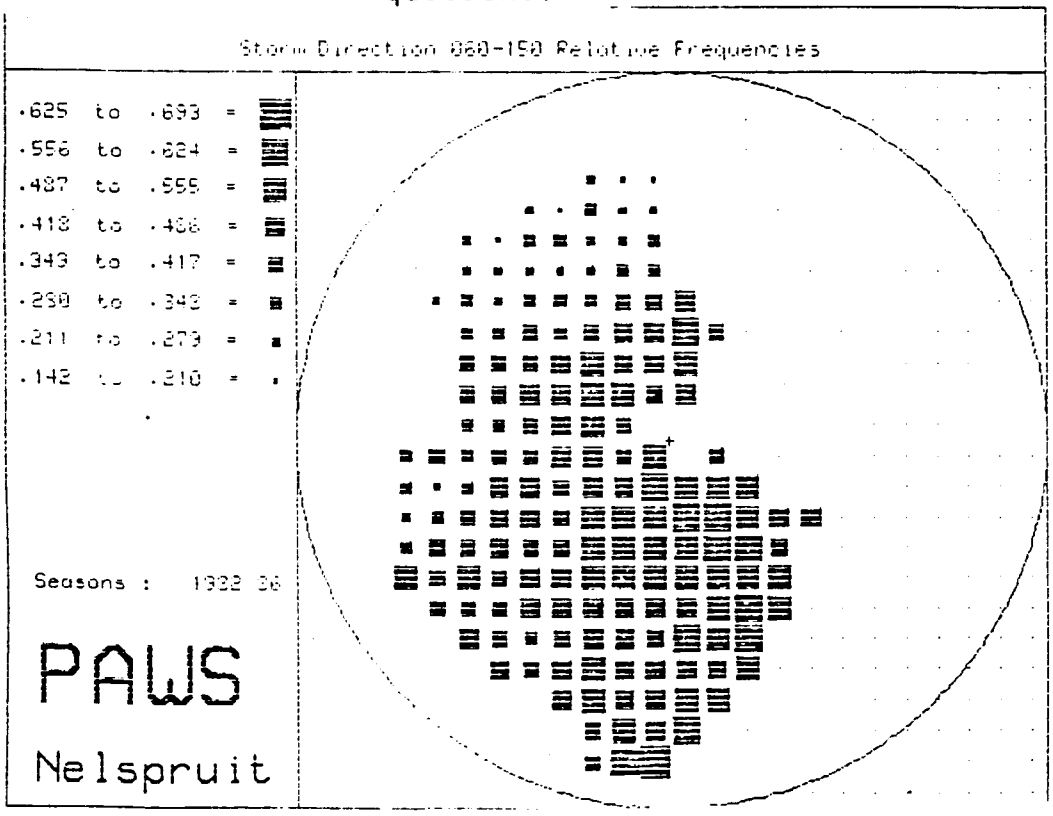

Fig. 8.1.12. As above - southwest quadrant.

8.2 A climatological Z-R relationship for the Nelspruit area (Mather and Parsons)

The rainfall analysis in this report uses the Marshall-Palmer relationship between radar reflectivity and rainfall:

$$Z = 200\ R^{1.6} \qquad (1)$$

where

Z = reflectivity in mm^6/m^3
R = rainfall rate in mm/hr

Efforts to develop a Z-R relationship for Nelspruit using individual rain gauge versus radar range bin comparisons have not been successful. This result echoes the efforts of many other studies of this sort.

A more promising approach, outlined in Smith et al. (1985), is to use non-simultaneous radar and rain gauge data to arrive at a "climatological" Z-R relationship for an area.

The 5 minute rain rates in excess of 15 mm per hour from the 16 automatic rain gauge network in the Badplaas valley are summed for the 1984/85 and 85/86 seasons. A threshold level of 15 mm per hour was used to eliminate most of the non-convective rainfall from the sample, resulting in a total of 3634 rainfall rate measurements. These data were used to construct the cumulative frequency distribution shown in Fig. 8.2.0.

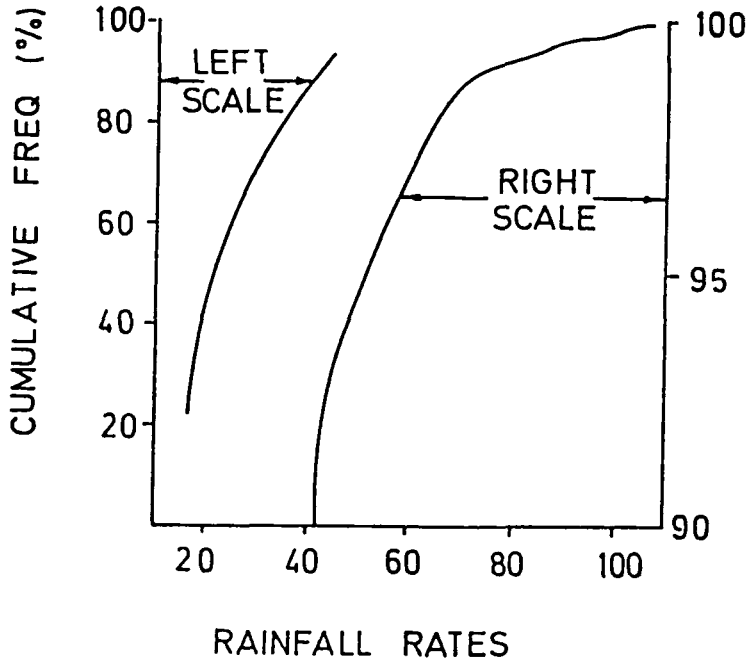

Fig. 8.2.0. Cumulative frequency distribution of rainfall rates from automatic rain gauge network - Badplaas valley.

Next, radar reflectivities in 2072 range bins (an area of 1098 km^2) over the gauge network for the same two seasons were summed and plotted as cumulative frequencies in Fig. 8.2.1. The curve in Fig. 8.2.2 was generated by pairs of Z and R values from Figs 8.2.0 and 8.2.1 chosen at corresponding cumulative frequency values resulting in a climatological Z-R relationship for the Nelspruit area of:

$$Z = 126\ R^{1.7} \qquad (2)$$

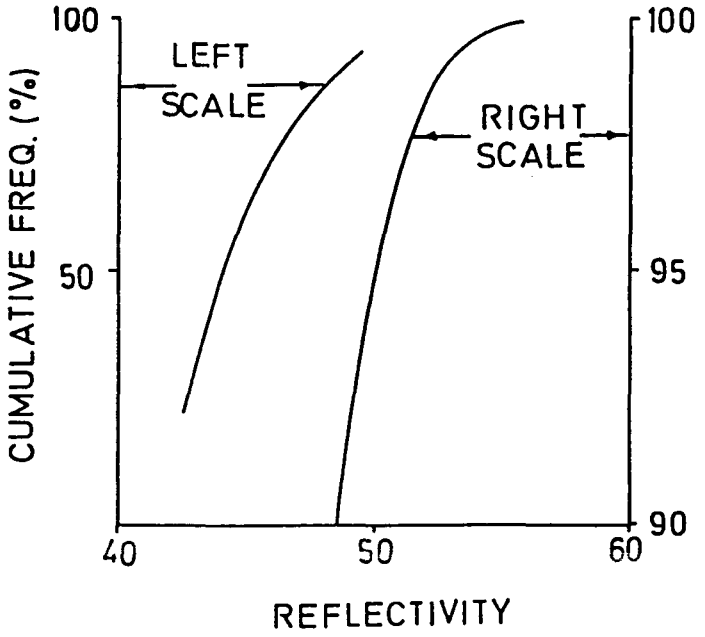

Fig. 8.2.1. Cumulative frequency distribution of reflectivities greater than 42 dBz from radar range bins over Badplaas valley.

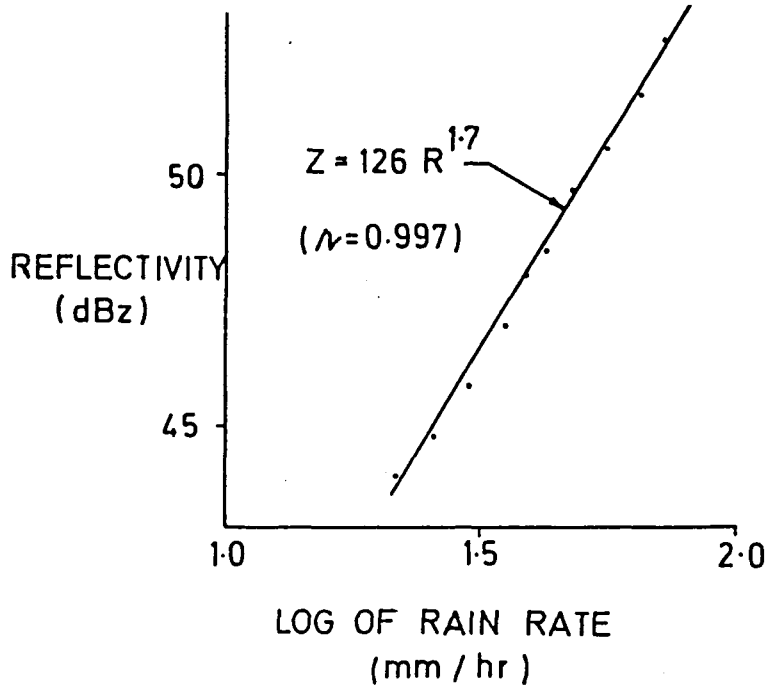

Fig. 8.2.2. Pairs of Z and R values from Figures 8.2.0 and 8.2.1.

The two Z-R relationships are compared in Fig. 8.2.3. This study indicates that the Marshall-Palmer Z-R relationship is entirely suitable for use in the current experiment.

In Section 5.0, Vol. III, the use of this Z-R relationship underestimates the actual rainfall as recorded by the recording rain gauge network in the Badplaas valley by about 70 percent (see Table 5.2, Vol. III). We believe that this is almost entirely explained by the poor siting of the radar at the Nelspruit airport.

a. The terrain rises to over 3^{o} in the sector where the radar is scanning over the rain gauge network (see Fig. 3.4, Section 3.4, this Volume), thus blocking the radar view in this direction.

b. The 3^{o} low level scan angle means that the radar is looking at about the 4 km level in clouds over the rain gauge network. This is more than 1 km above the usual cloud bases in the area.

Further meaningful comparisons of radar/rain gauge measurements of rainfall will have to await the re-siting of the rain gauge network and/or the radar.

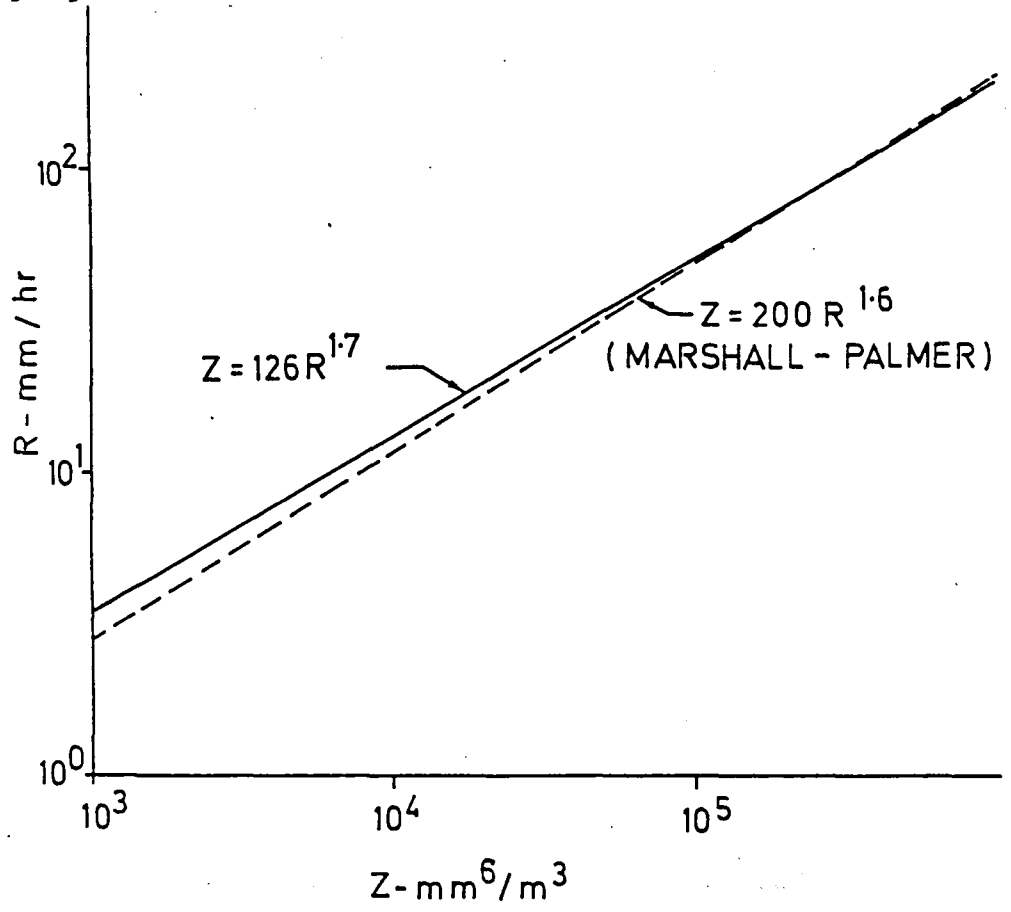

Fig. 8.2.3. Comparison of Nelspruit climatological and Marshall - Palmer Z-R relationships.

9.0 STUDIES AND DEVELOPMENTS IN CLOUD PHYSICS

9.1 Measurement of total and condensed water mixing ratios in warm based cumulus clouds (Morgan, Morrison and Mather)

One of the principal areas of the PAWS research concerns the description of natural precipitation processes and related environmental and cloud characteristics. Perhaps the most important specialized area of this has been the measurement and description of liquid water content.

Cloud exploration is carried out with a Learjet 24 aircraft equipped with a sophisticated instrumentation system. From the beginning of the research programme the aircraft carried the state-of-the-art equipment for measuring liquid water quantities:

a. Johnson-Williams hot wire (JW)

b. Particle Measurement Systems (PMS) Forward Scattering Spectrometer Probe (FSSP)

c. PMS 2D-C cloud particle image detector.

The JW is intended to measure the liquid water content contained in cloud droplets smaller than about 30 microns in diameter. The FSSP estimates the size-spectrum of cloud particles at diameters less than 47 microns and, by integration of their masses, the liquid water content contained in that range. The 2D-C, using a diode-shadowing principle, records the shadow images of particles out to diameters of 1.2 mm (and beyond). If shape and density are known one can determine water content from those images.

It became apparent early in the programme that this instrument set was not capable of describing the clouds we were interested in. The main problem seemed to be that the spectrum of particles in Transvaal clouds was one not dealt with in other cloud research projects. Transvaal clouds often develop precipitation through coalescence and contain large supercooled water drops (Mather et al., 1986). The three instruments listed above will not account for all the liquid water in such clouds for the following reasons:

a. When large (greater than 50 microns) drops are present in high concentrations the JW responds partially to them, giving uninterpretable readings (Morgan and Mather, 1984)

b. The 2D-C does not consistently detect liquid water particles smaller than some unknown size, which we suspect to lie in the 100-150 micron region, though it does detect ice particles below that size (Morgan and Mather, 1984)

c. When large rain drops are present their concentrations are poorly estimated by the 2D-C due to its small sample volume.

Thus, during important stages of the coalescence and rain development processes, liquid water is present which is either poorly sensed or totally invisible to the above instruments.

To fill this gap in our measurement capabilities, several developments were undertaken, two of which have succeeded in a very satisfactory manner. These have been reported in a series of papers (Morgan, Morrison and Mather, 1986 a; 1986 b; 1986 c).

9.1.1. The Engine-Vapour technique

9.1.1.1. Principles

The total water mixing ratio of a unit mass of cloud air is the sum of its vapour, its liquid (cloud and rain), and its ice contents. There are well known ways for estimating certain fractions of the above components of the total water mixing ratio, each with its problems and limitations. The small diameter (less than 30 microns) fraction of the liquid water content (LWC) is commonly sensed with the Johnson-Williams (J-W) hot wire sensor. The CSIRO-King hot wire sensor is used to sense LWC to somewhat larger sizes (about 100 microns). The Particle Measuring Systems (PMS) Forward Scattering Spectrometer Probe (FSSP) can estimate the size spectrum of cloud droplets up to 47 microns in diameter and this can be integrated to produce an estimate of the LWC in those sizes. The PMS 2D-C optical array probe images larger cloud particles and the spectrum of these can be integrated to yield an ice or water content if the proper assumptions are made concerning shape and density of the particle. Vapour content can be estimated in clear air with a dew point sensor and in clouds by measuring the air temperature and pressure and assuming saturation.

Early experience in using the J-W hot wire probe in the warm-based, wet cumulus congestus clouds of the Nelspruit area led to serious doubts about our ability to describe their character and evolution (Morgan and Mather, 1984). This was only natural since the J-W responds primarily to the LWC in the condensation peak below a diameter of about 30 microns and we strongly suspected the presence of much larger cloud droplets. For this reason the more promising King hot wire device was added to the aircraft in 1985; first a shielded version, which was later replaced by the unshielded probe.

It was hoped that the King device measures the liquid water up to diameters of 100 microns, although there is no information in the literature concerning the response of the instrument to drops around that size. Wind tunnel calibrations have not been performed with particles of that size and, in fact, such tests would be very difficult to perform. In a recent publication on

wind tunnel calibrations of the King instrument, King et al., (1985) stated "quantitative studies to examine the probe response to higher LWC (e.g. 4 - 5 g m^{-3}) at typical aircraft speeds and to drizzle and precipitation size drops are needed". Our experience in the field is that the King instrument shows a saturation effect at about 4.0 g m^{-3} for the unshielded sensor. We have concluded that, at least at the airspeeds at which the Learjet penetrates clouds (around 150 m s^{-1}), existing hot-wire devices are not capable of measuring liquid water contents in excess of that value.

An entirely different principle can be exploited which largely solves the liquid water measurement problem. This is the evaporation technique.

A turbojet engine has three main sections: a compressor at the front, a combustion section and, at the back, a turbine section. Air entering the inlet of the engine is compressed and heated in the compressor section, converting any water or ice in the air to vapour. The water vapour mixing ratio in the compressed air is then equal to the total water mixing ratio in the environmental air. Independent knowledge of the vapour mixing ratio of the outside (cloud) air permits the condensed water mixing ratio, w_c, to be calculated as a difference.

Evaporators have been applied in cloud investigations several times (Kyle, 1975; Gayet et al., 1977; Coulman and Parker, 1982; Ruskin and Scott, 1974). The instruments have all been limited by small inlet diameters and low volume flow rates. The inlets of the Learjet engines are large (0.1 m^2) and the air volume flow through the two engines on the aircraft is on the order of 30 m^3 s^{-1}. This huge sample volume assures that even the largest precipitation particles in the cloud are adequately sampled.

During the development of the system to be described here, the authors were apprised of an early, similar approach to total water content measurement (Roys, 1963; Roys and Kessler, 1966). An infrared sensor was used to measure water vapour from the 4th stage compressor bleed-air of the J-57 engine in an F100F aircraft. There were drawbacks to the infrared sensing equipment, such as very slow time response, and perhaps other problems, so that the investigation was never reported in the open literature. The approach, nevertheless, was essentially the same as taken here.

Engine compressor bleed-air is sampled from the line which feeds hot air to the external windscreen defoggers. This air sample flows through the measurement cell of a Lyman-alpha UV absorption humidiometer (Buck, 1976). Absorption at the Lyman-alpha line wavelength of 121.56 nm is proportional to the densities of water vapour and molecular oxygen. The molecular oxygen contribution is small and can be easily estimated. Given the water vapour density in the Lyman-alpha cell, the total and condensed water mixing ratios of outside cloud air can be

computed as follows.

The total water mixing ratio of the outside air, w_{ta}, is

$$w_{ta} = w_{va} + w_{la} + w_{ia} = w_{va} + w_{ca} \quad (1)$$

where the liquid and ice mixing ratios, w_{la} and w_{ia}, are combined into the condensed water mixing ratio, w_{ca}.

In the Lyman-alpha measurement cell, vapour density, ρ_{vc}, is the observed quantity. The dry air density in the cell, ρ_{ac}, may be computed from the ideal gas law. The pressure and temperature in the cell are measured by a pressure transducer and thermocouple, respectively.

The total water content mixing ratio for the outside air can then be computed as

$$w_{ta} = \frac{\rho_{vc}}{\rho_{ac}} \quad (2)$$

If the vapour content of the air is known, the condensed water mixing ratio can be directly calculated from equation (1) as

$$w_{ca} = w_{ta} - w_{va} \quad (3)$$

In cloud we assume that the water vapour mixing ratio, w_{va}, is equal to the saturation mixing ratio of the cloud air, $w_s(T_a,P_a)$, so that we can re-write equation 3 as

$$w_{ca} = w_{ta} - w_s\,(T_a,P_a) \quad (4)$$

The air temperature is measured by a Rosemount temperature probe.

The gap between UV source and detector in the Lyman-alpha test cell is a critical parameter which must be precisely known. It can be varied over a wide range, but we have not yet considered optimizing it for our particular types of measurements. It does offer a degree of freedom to the user and could be increased to give excellent resolution in clouds such as Great Plains cumulus clouds where condensed water contents are not expected to exceed 1 or 2 g m^{-3}. In our studies, the gap is set at between 4.0 - 4.5 mm.

9.1.1.2. Testing

Problems have been encountered and, we believe, solved during the testing of the Lyman-alpha humidiometer for the measurement of the bleed air vapour content. These derived mainly from our unique measurement environment. The instrument was not designed to operate over the wide range of pressures and temperatures encountered in jet engine bleed air lines.

Time was lost in the development of the instrument due to the presence of what appeared to be a slowly varying bias in the measurement. This appeared most clearly as a high value of the mixing ratio in the clear air; where the value would be expected to lie in the vicinity of 0.1 to 1.0 g kg^{-1} at -10°C the values fell repeatedly in the neighborhood of 3.0 g kg^{-1}. Suspicion first fell on the estimates of air density, based on the measurements of pressure and temperature in the Lyman-alpha measurement cell. However, after many checks it became clear that the bias could only be due to a contaminant in the bleed air sample. The contaminant is probably a hydrocarbon such as engine oil. This could enter the system via an oil seal at the front of the compressor or from the walls of the tubing of the bleed air system.

The bias due to the contaminant varies with parameters which determine the flow through the bleed air tubing. Most important of these are the engine power setting and outside air pressure (altitude). The sense of the variation is such that the higher the bleed air flow, the lower the bias. This is consistent with a fairly steady production of the contaminant by the tubing walls.

The Lyman-alpha system must therefore be baselined during a mission not only to determine the zero water vapour output (system gain) of the humidiometer, but also to calculate the bias added by the contaminant. In order to explicitly establish the system gain the instrumental setup includes a bottle of high purity nitrogen and appropriate plumbing to allow flushing of the Lyman-alpha measurement cell with the inert nitrogen. The contaminant term is found by baselining the system against the aircraft Cambridge EG&G dewpoint hygrometer. A drawback with this method is that, although the dewpoint hygrometer has good accuracy, its time response at relatively cold temperatures is poor. As a consequence, baselining in clear air at penetration altitudes is generally done before and after "working" a storm (after the dewpointer has stabilized) to provide good baselines for comparison against those values obtained in the unsaturated air prior to each individual cloud penetration. Any erroneous baseline values prior to cloud penetration can then be corrected.

Although not ideal, the above calibration technique has proved satisfactory. Any error introduced in the baselining operation with the dewpoint hygrometer, due to incorrect recovery from a previous cloud pass, would reduce the computed value of total water mixing ratio. The contaminant problem can probably be eliminated by installing dedicated, cleanable airlines to bring

the compressor air directly to the Lyman-alpha measurement cell.

9.1.1.3 Demonstration of Measurements

There are no standards of comparison for testing measurements of any internal cloud properties. We proceed here by inference, first by showing examples that illustrate the full spectrum of results obtained with this system over five months of routine operation and second, by showing that the cloud total water mixing ratios are bounded by the values to be expected for unmixed adiabatic ascents through the cores of clouds. We note here that a completely different method for measurement of cloud condensed water mixing ratio using one of the Lear turbojet engines has been developed and preliminary results support the validity of the engine vapour technique (Morgan et al. 1986(a)).

The examples that follow consist of four panels of strip chart plots of Learjet penetrations at the -10°C level through cumulus congestus turrets growing on the flanks of multicellular thunderstorms. The bottom panel shows the total water mixing ratio measured by the engine vapour system as a function of distance run (integration of aircraft true air speed). Also plotted in the bottom panel are the saturation mixing ratio (computed from the aircraft temperature and pressure sensors) and the cloud base mixing ratio computed from the routine Lear sounding during climb out from the Nelspruit airfield. For unmixed adiabatic ascent from cloud base in the absence of any significant accretional particle growth processes, the total water mixing ratios of the cloud air should equal the cloud base mixing ratio. The second panel is a plot of condensed water mixing ratio from the engine vapour system compared to the liquid water mixing ratio measured by the CSIRO-King hot wire. The third panel shows the cloud particle concentrations obtained from a PMS 2D-C optical array probe (35 micron resolution) using the particle weighting computational technique after standard artifact rejection. Finally, the top panel is a plot of reflectivity from the aircraft X-band radar. This measurement is obtained from a single range gate set approximately 1.5 km ahead of the aircraft. The signal is lagged in the plots to adjust for its displacement relative to the aircraft. Some of the plots appear incomplete because the recording was started when the range gate was already well inside the cloud.

The first example (Fig. 9.1) is from a cloud with relatively low liquid water content and almost no particles detectable by the 2D-C. The agreement between the engine vapour measurement and that of the King hot wire is excellent, except for a small tract at around 2.8 km where the mixing ratio exceeded 5 g kg^{-1}, the level at which we experienced saturation of the King instrument at this altitude. (The saturation of the King at this low value, equivalent to 3 g m^{-3}, was found later to be due to electronic saturation. This has been corrected, and for all flights subsequent to 15 December 1986 the saturation value occurs at about 4.0 g m^{-3}, or 6.0 g kg^{-1}). This cloud was sub-adiabatic throughout, as indicated by the total water mixing ratio being

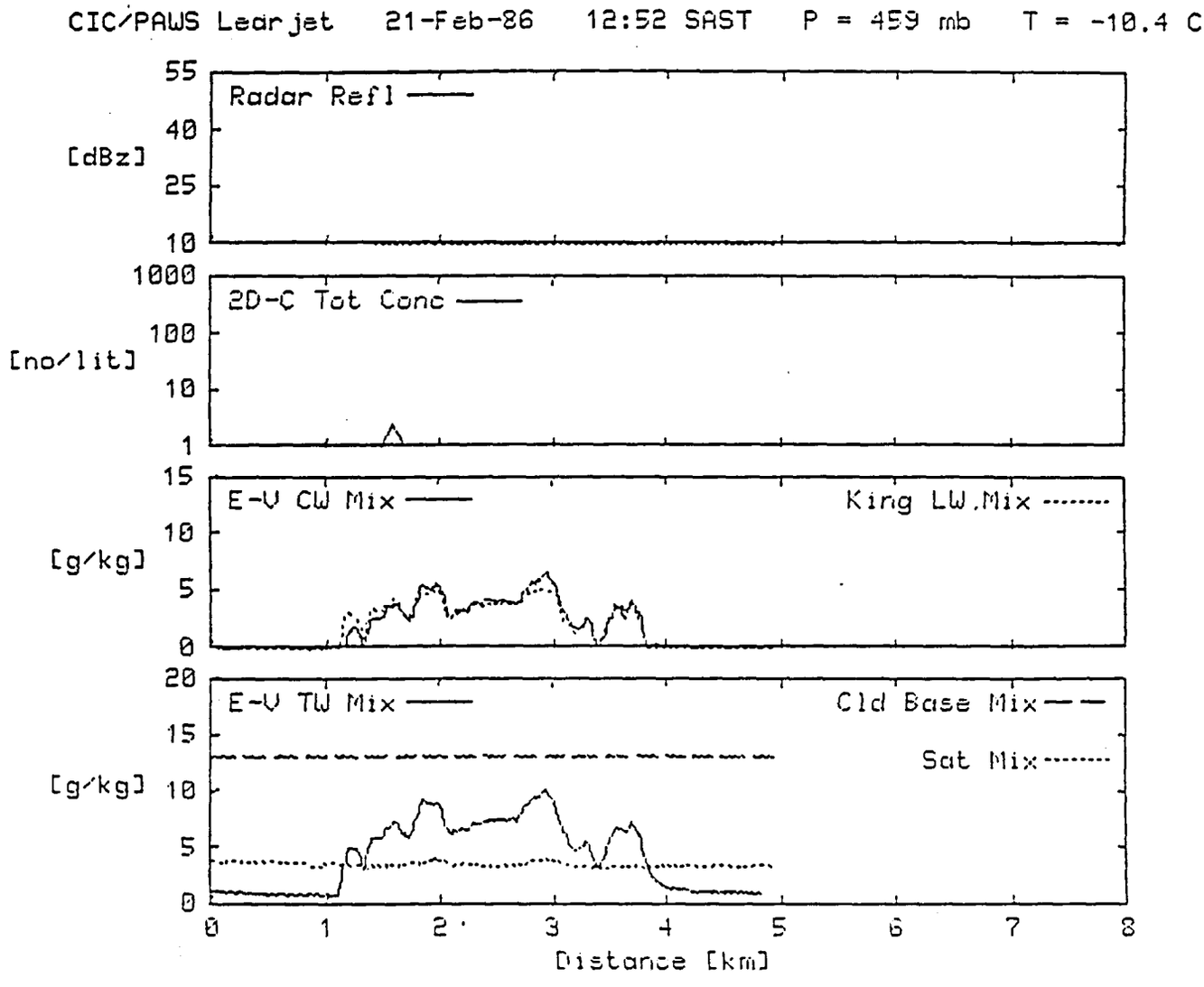

Figure 9.1. An example of agreement between the engine-vapor method and the CSIRO-King hot-wire probe, in a cloud with no large (liquid or ice) precipitation particles.

everywhere less than the cloud base mixing ratio.

Taken on the same mission the second example (Fig. 9.2) is from a well-iced cloud in which the 2D-C probe detected high concentrations of small, irregular particles showing only a weak proved satisfactory. Any error introduced in the baselining operation with the dewpoint hygrometer, due to incorrect recovery from a previous cloud pass, would reduce the computed value of total water mixing ratio. The contaminant problem can probably be eliminated by installing dedicated, cleanable airlines to bring the compressor air directly to the Lyman-alpha measurement cell.

The third example (Fig. 9.3) is taken from a cloud with a well developed graupel population. The King appears not to saturate here, probably because the graupel is consuming the cloud. A more substantial radar signal is evident for this penetration.

A fourth example (Fig. 9.4) shows a cloud with almost no 2D-C activity in which the King hot wire is saturated almost throughout. The lack of any significant radar return also implies an absence of cloud particles with large radar cross-sections. The liquid water mixing ratio exceeds the King saturation value by perhaps 50% almost everywhere. The total water mixing ratio hovers near the cloud base mixing ratio over much of the pass, implying a moist adiabatic unmixed cloud core.

The last example (Fig. 9.5) is a cloud in which liquid water accumulation appears is taking place (big drop zone). Between about 1.5 and 3.4 km the 2D-C images show predominantly large clearly defined liquid water drops. The response from the aircraft radar and examination of the videotape record of the cloud penetration also demonstrate the liquid phase of these large particles. These observations are not unusual in the turrets that occur in the experimental region (Mather et al., 1986). The King remains unsaturated throughout most of the record because the large drops are consuming the cloud water. It saturates in a small region near 3.5 km where the 2D-C concentration falls off. The total water mixing ratio indicates strongly super-adiabatic values where the 2D-C concentration is high, but is nearly moist adiabatic where the King reaches saturation and the cloud particle habit changes to mostly low concentrations of graupel. The aircraft data collected over the 1985/86 summer season contain even more spectacular examples of accumulation of supercooled water (Morgan et al. 1986(b)).

A check for internal consistency of data in this example is worthwhile. A cloud water budget is calculated in Table 9.1. If we subtract the King liquid water content from the E-V cloud water content, the remaining liquid water should be contained in the drops. This water content, calculated from the 2D-C images is 7.0 g/kg leaving just 0.7 g/kg unaccounted for. With such large drops present, the 2D-C has known sampling problems. A second budget calculations is carried out using measured radar reflectivity and the relationship (Brown and Braham, 1969),

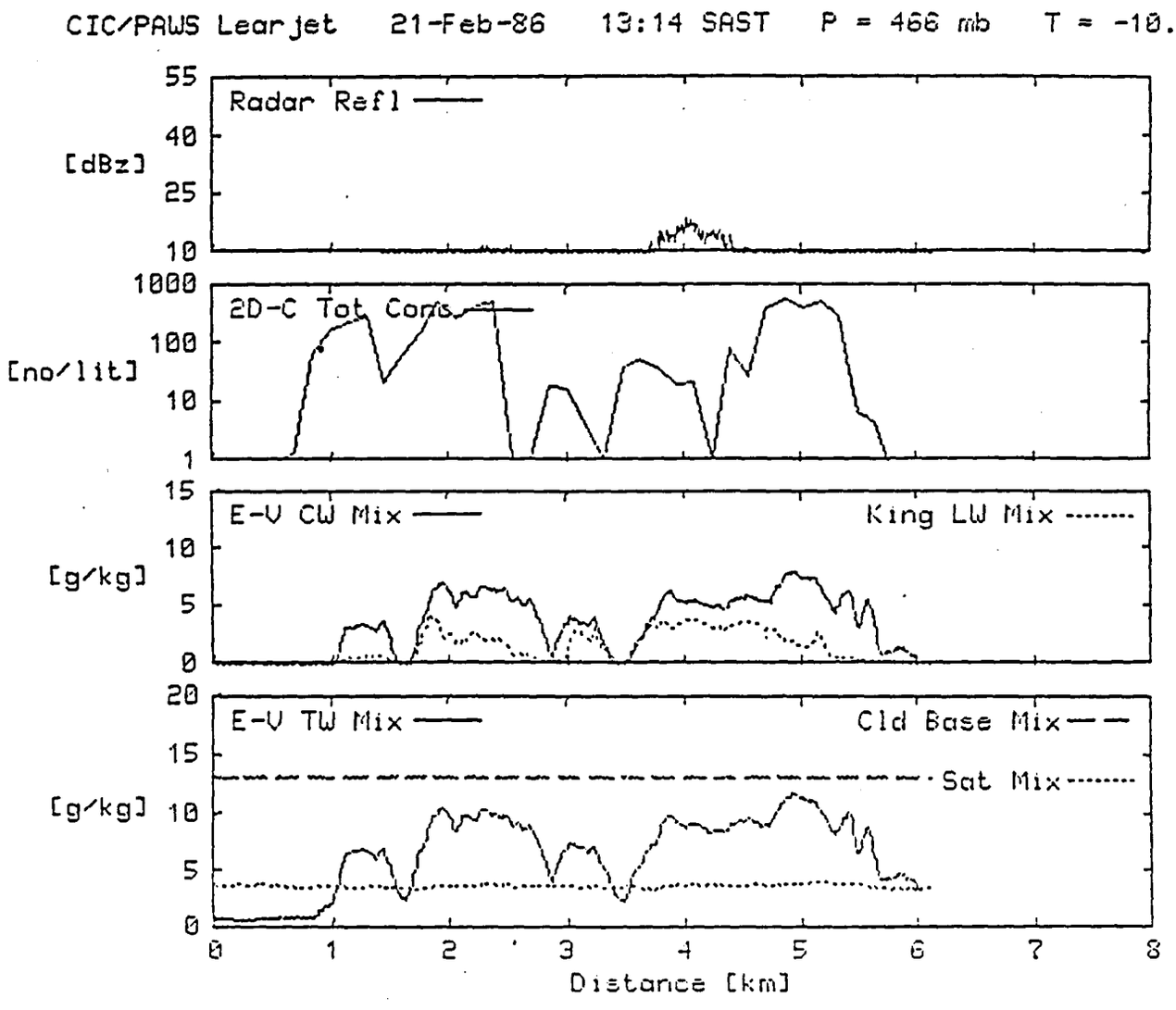

Figure 9.2. An example of the relative readings of the engine-vapor instrument and the CSIRO-King hot-wire probe in a glaciating cloud.

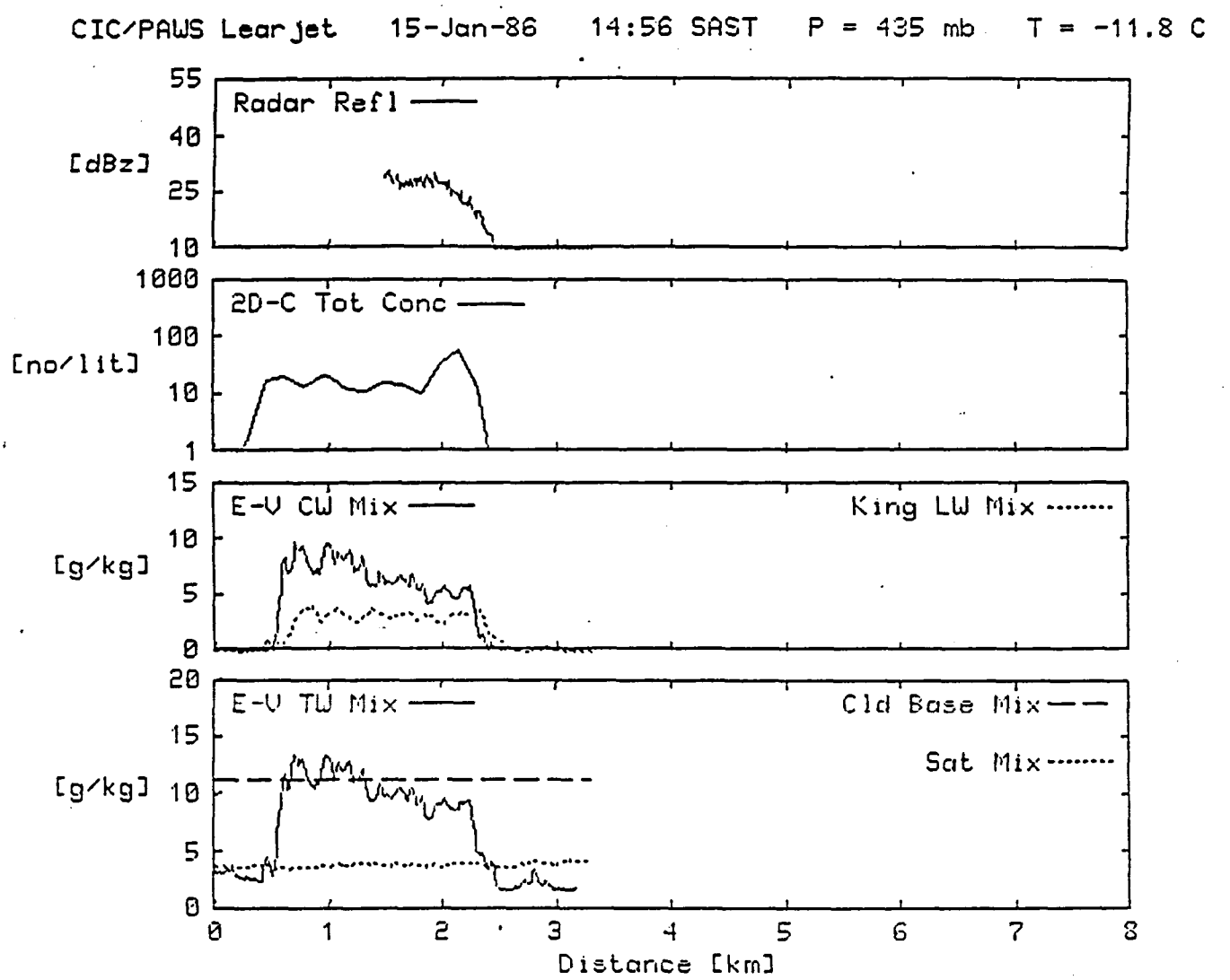

Figure 9.3. An example of engine-vapor and CSIRO-King hot-wire probe performance in a cloud with well-developed graupel.

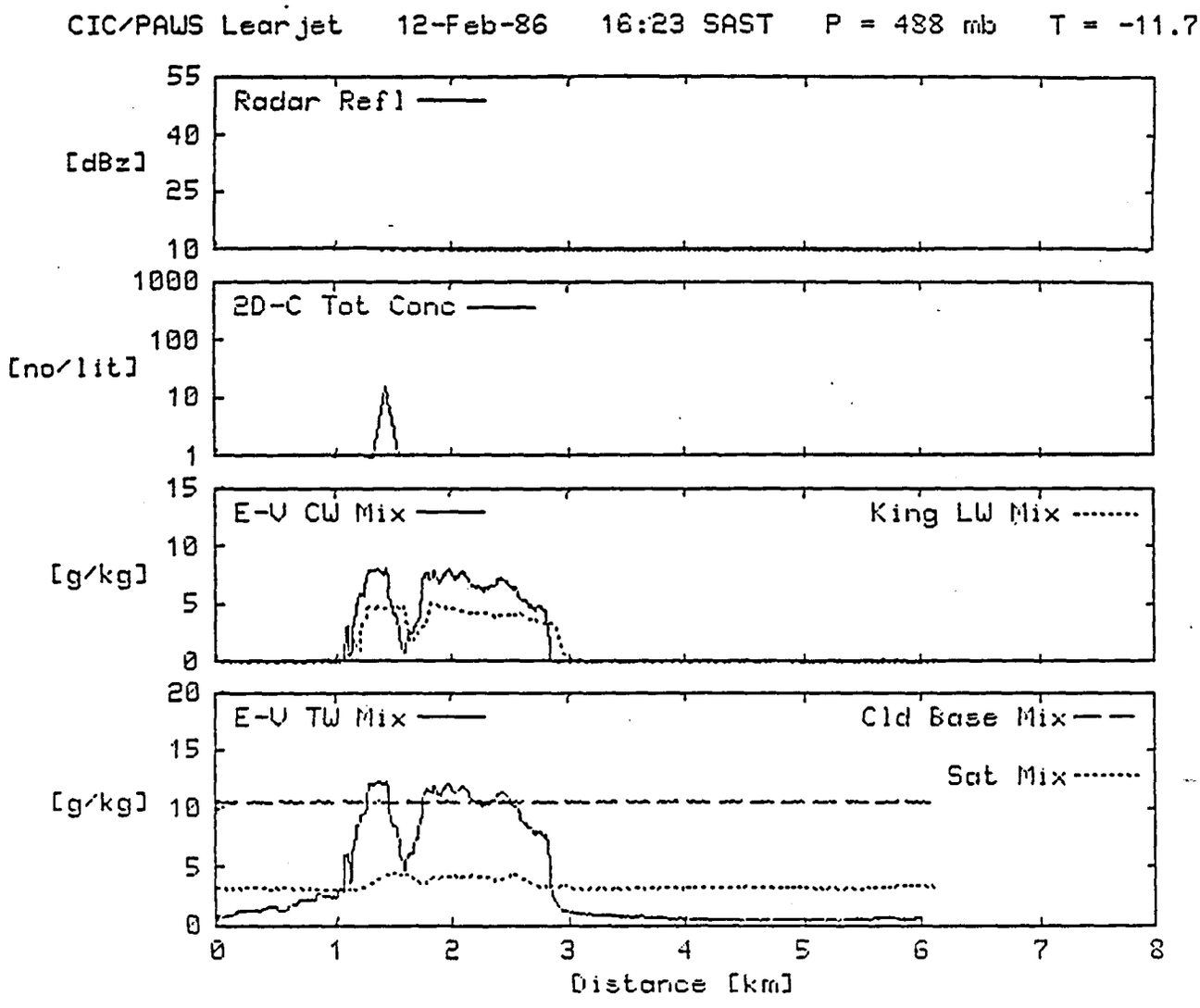

Figure 9.4. An example of a cloud with almost no significant 2D-C activity that exhibits saturation of the CSIRO-King hot-wire.

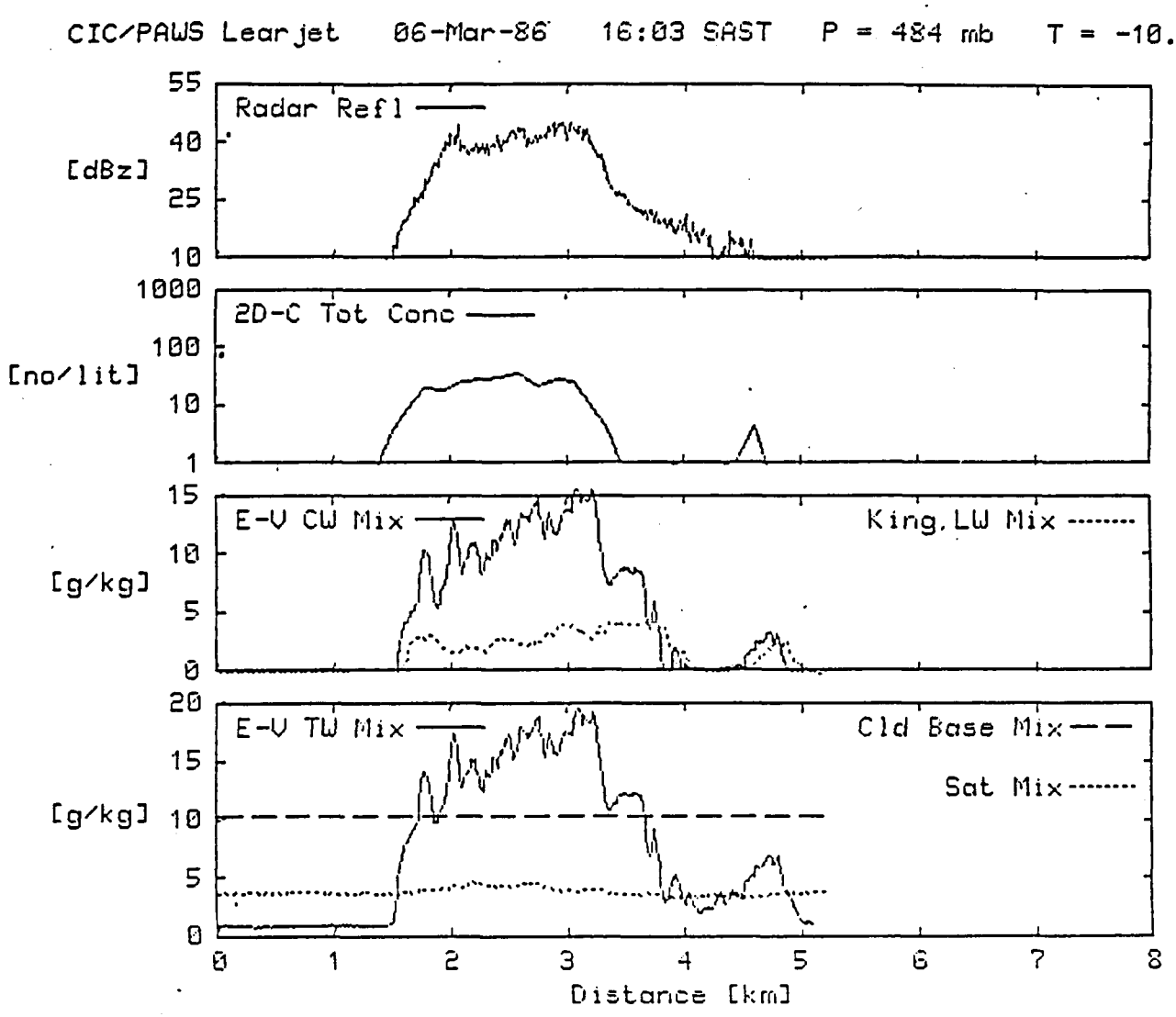

Figure 9.5. An example of engine-vapor and CSIRO-King hot-wire performance in a cloud with moderate accumulation of liquid water.

$$Z = 380\ M^{1.46}$$

where Z is the equivalent radar reflectivity factor (mm^6/m^3) and M is the liquid water content (g/m^3). Here, the budget using the radar estimate of liquid water to calculate the cloud water content and the E-V estimate are within 0.3 g/kg. Such internal consistency generates confidence in these measurements, measurements that have, in the past, been intractable. Both estimates confirm super-adiabatic values of total cloud water content in this example.

Table 9.1 Check on internal consistency of data (see Fig. 9.5). These results are averages over the event, defined as that period during which the 2D-C mean diameters exceed 100 microns (see Fig. 9.6).

E-V - cloud water content	10.54	g/kg
King-liquid water content	2.82	
	7.72	
2D-C water content	7.00	
	0.72	g/kg
RADAR: 36.1 dBz = 4074 Z; M = 5.08 g/m^3 = 8.05 g/kg		
RADAR - water content	8.05	
King	2.82	
	10.87	
E-V - cloud water content	10.54	
	0.33	

It is also instructive to briefly examine a larger ensemble of data from the 1985/86 season. Table 9.2 shows the ratio between peak measured total water mixing ratio and cloud base mixing ratio for 21 cloud penetrations during which the 2D-C probe was not triggered (zero concentration). Only one case showed a total water mixing ratio greater than 1.05 times the calculated cloud base value. Also shown in Table 9.2 is the same ratio for 61 cloud passes with low (less than 10 $litre^{-1}$) 2D-C total particle concentrations and for 41 cases with high (greater than 10 $litre^{-1}$) concentrations. As the 2D-C concentrations increase the distribution changes from one skewed toward sub-adiabatic values to one skewed toward super-adiabatic values. Taken together, the three distributions in Table 9.2, particularly the first, argue that the engine vapour system

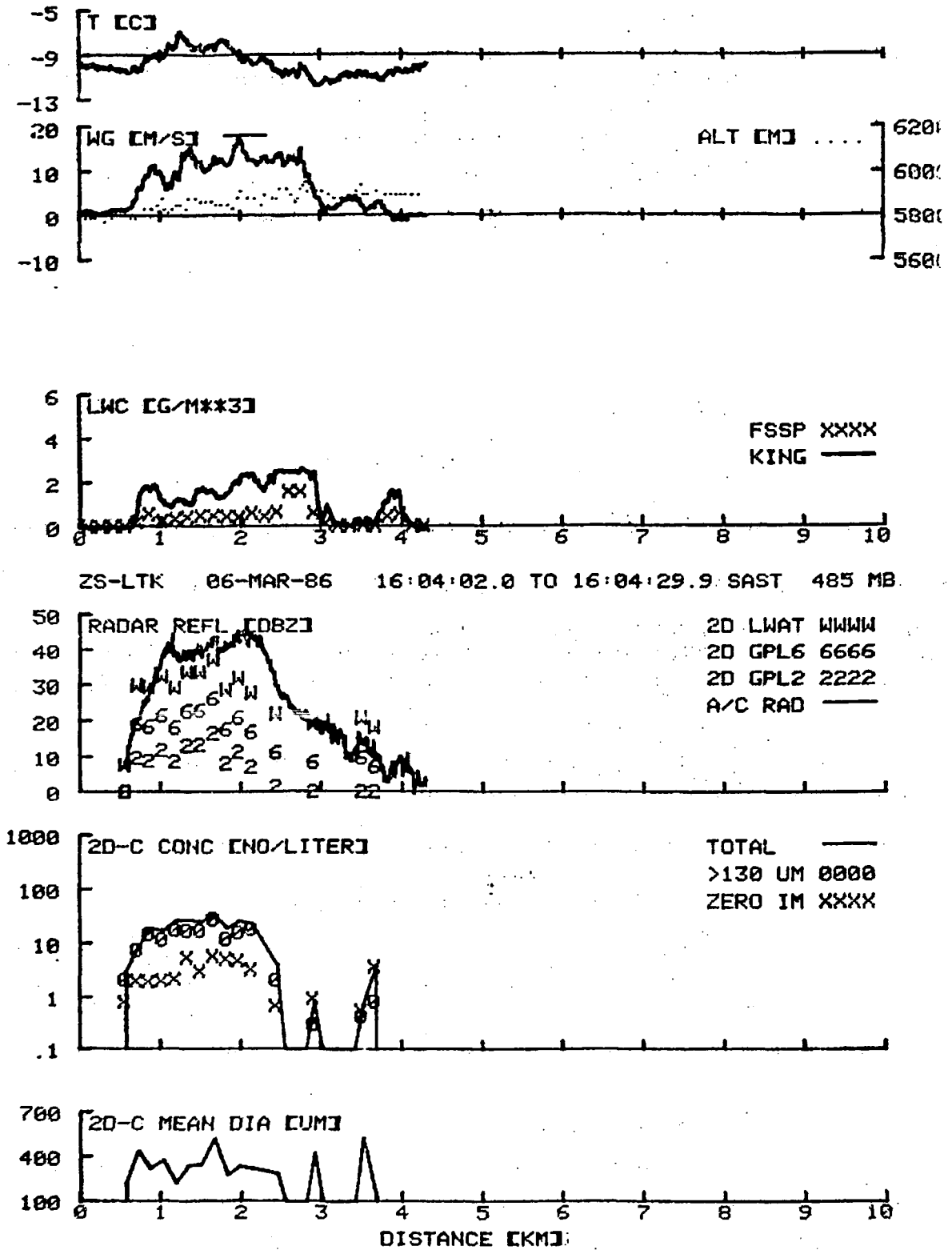

Fig. 9.6. Time histories of some of the measurements used in the cloud water budget in Table 9.1.

Max. Total Water Mixing Ratio/Cloud Base Mixing Ratio

2D-C Conc. (ℓ^{-1})	.3 to .45	.45 to .60	.60 to .75	.75 to .90	.90 to 1.05	1.05 to 1.20	1.20 to 1.35	1.35 to 1.50	1.50 to	N	Avg	σ
0	-	1	2	4	13	1	-	-	-	21	.88	.14
< 10	1	4	3	15	30	5	2	1	-	61	0.9	.18
> 10	-	1	1	4	8	16	5	2	4	41	1.13	.23

TABLE 9.2 : Peak Total Water mixing ratios, from engine-vapor instrument, divided by cloud base mixing ratio.

performs well and yields reasonable values of total water. Additionally, and these will be critically dealt with in a later paper, they suggest that Nelspruit cloud turrets have adiabatic cores, little affected by mixing and that as precipitation particles begin to develop in these clouds there is on some occasions a transient accumulation phenomenon.

Table 9.3 presents a comparison of simultaneous peak liquid water estimates from four different instruments available on the Learjet: the engine vapour system, CSIRO-King hot wire, Johnson-Williams (J-W) hot wire, and integration of the FSSP cloud droplet spectra from 2 to 47 microns. The data shown are for penetrations through 20 turrets between -9.5 and -14.0°C where the average total 2D-C particle concentrations are less than 10 litre^{-1} (no significant ice or large liquid water particles present). The engine vapour system shows an average peak liquid water content of 4.0 g m^{-3}.

9.1.1.4. Discussion

The jet engine vapour measurement of cloud total water mixing ratio is relatively inexpensive and easy to accomplish. The time response is excellent and its high volume sampling rate ensures adequate sampling of the entire spectrum of hydrometeors present in the air. No other system presently available is capable of measuring total and condensed water contents in the warm based wet eastern Transvaal clouds.

The Lyman-alpha humidiometer has proved to be a robust instrument, well adapted to routine day to day use. The system is considered fully operational and is being employed in a study of the feasibility of cloud seeding enhancement of rainfall from convective clouds in the eastern Transvaal. The measurements with the bleed air system have allowed us to demonstrate the existence of liquid water contents beyond the reach of other state-of-the-art instrumentation.

The rapid development of graupel particles following dry ice seeding of eastern Transvaal clouds has been often noted in past years. This rapid graupel growth can now be understood in terms of the results of the engine vapour measurements. The large particles, often water drops, once frozen, can grow rapidly in the high liquid water contents we now know to exist in the Nelspruit clouds.

The ability to apply the engine vapour technique for measurement of water quantities is further justification for the employment of high performance jet aircraft for research in cumulus clouds. The airborne instrumentation system described here is capable of assessing the liquid water in warm based cumulus congestus. The use of hot wire liquid water meters in clouds outside of semi-arid regions is likely to produce misleading assessments of their liquid water contents.

TABLE 9.3

A) LIQUID WATER CONTENT [g m^{-3}]

	0-1	1-2	2-3	3-4	4-5	5-6	6-7	Avg	σ
Engine-vapor system	0	1	4	2	11	1	1	4.02	1.10
CSIRO-King hot-wire	0	4	14	2	0	0	0	2.47	0.46
J-W hot-wire	1	13	6	0	0	0	0	1.71	0.42
FSSP	0	14	6	0	0	0	0	1.91	0.44

B) LIQUID WATER MIXING RATIO [g kg^{-1}]

	0-1	1-2	2-3	3-4	4-5	5-6	6-7	7-8	8-9	9-10	Avg	σ
Engine-vapor system	0	0	1	3	1	1	5	6	1	2	6.48	1.86
CSIRO-King hot-wire	0	1	1	6	12	0	0	0	0	0	3.96	0.80
J-W hot wire	0	3	8	9	0	0	0	0	0	0	2.75	0.70
FSSP	0	1	11	6	2	0	0	0	0	0	3.06	0.69

9.1.2 The Engine Theta technique

9.1.2.1 Principles

A completely different physical principle may be employed to measure the condensed water mixing ratio alone, again using the engine compressor. This new approach is calorimetric in character, making use of the cooling of the compressed air due to evaporation of the cloud condensate. Test trials have been carried out using this technique in parallel with the engine vapour method, and it is now possible to demonstrate the soundness of the principle. Since employment of the technique by others will require adaptation to the particular engines involved, it is considered useful to report on the technique at this stage of development.

Dry air entering the engine compressor at outside pressure P_a and temperature T_a (hence potential temperature Theta-a) undergoes compression and heating. The heating is mostly adiabatic but also in part due to frictional work as the air is driven through the eight stages of the compressor. The air that is bled out of the compressor expands to some intermediate pressure in the utility lines of the aircraft. At a suitable point in the engine bleed-air line the potential temperature in the measurement cell, should be

$$\theta_c = \theta_a + \Delta\theta_f \qquad (1)$$

where $\Delta\theta_f$ is the increase in θ_c due to the frictional heating. $\Delta\theta_f$ is a function of engine performance and the air viscosity. It can be evaluated by flying at different altitudes and power settings.

In fact, during research flights it can be evaluated at the beginning of each run, after the aircraft has been stabilized for cloud penetration. In cloud air, there will be an additional change in θ_c due to the evaporation of the condensate, $\Delta\theta_{cond}$, such that

$$\theta_c = \theta_a + \Delta\theta_f - \Delta\theta_{cond} \qquad (2)$$

can be specified as a function of the mixing ratios of ice and liquid water in the air. We compute this term as follows:

An amount dw_l of liquid water is evaporated into a kilogram of air at temperature T. This results in a temperature change

$$dT = \frac{L_e(T)\ dw_l}{c_p} \tag{3}$$

and, consequently, a potential temperature change

$$d\theta = \left(\frac{1000}{P}\right)^{\gamma} dt = \left(\frac{1000}{\bar{P}}\right)^{\gamma} \frac{L_e(T)\ dw_l}{c_p} \tag{4}$$

where $\gamma = 0.286$, P is pressure, $L_e(T)$ is the latent heat of evaporation of water, and c_p is the specific heat of dry air at constant pressure.

Similar equations hold for the sublimation of ice, with the latent heat of sublimation, $L_s(T)$, and the ice mixing ratio, w_i, taking the place of the latent heat of evaporation and the liquid water mixing ratio. For a mixture of liquid and ice the net change in will be

$$d\theta = \left(\frac{1000}{P}\right)^{\gamma} \frac{L_e(T)\ dw_l + L_s(T)\ dw_i}{c_p} \tag{5}$$

Since,

$$L_s(T) = L_e(T) + L_f \tag{6}$$

then we can rewrite equation 5 as

$$d\theta = \left(\frac{1000}{P}\right)^{\gamma} \frac{L_e(T)\ (dw_l + dw_i) + L_f\ dw_i}{c_p} \qquad (7)$$

The condensed water mixing ratio, w_c, is the sum of the liquid and ice water mixing ratios and therefore

$$d\theta = \left(\frac{1000}{P}\right)^{\gamma} \frac{L_e(T)\ dw_c + L_f\ dw_i}{c_p} \qquad (8)$$

A difficulty arises due to the temperature dependence of L_e. This can be taken care of empirically by flying in all-water clouds and determining an effective value of L_e or, equivalently, an effective evaporation temperature. Substituting equation 8 into equation 2 we get

$$\theta_c = \theta_a + \Delta\theta_f - \left(\frac{1000}{P}\right)^{\gamma} \frac{L_e(T)\ w_c}{c_p} - \left(\frac{1000}{P}\right)^{\gamma} \frac{L_f\ w_i}{c_p} \qquad (9)$$

The condensed water mixing ratio can be independently determined using the engine vapour technique. Then, knowing all the terms in equation 9 but the last, we can solve for the ice water mixing ratio as

$$w_i = \frac{c_p}{L_f} \left(\frac{P}{1000}\right)^{\gamma} \left[\theta_a + \theta_c + \Delta\theta_f - \left(\frac{1000}{P}\right)^{\gamma} \frac{L_e(T)\ w_c}{c_p}\right] \qquad (10)$$

The temperature change due to the presence of ice is not large, about $0.33^{\circ}C\ g^{-1}\ kg^{-1}$. Ability to make estimates of w_i will depend on the stability of the engine behaviour.

At this stage of development of the engine theta technique we set aside the refinement of distinguishing between ice and liquid, and show only the ability to make reasonable estimates of total condensed water content. For this we can use equation 9 solved for the condensed water mixing ratio, neglecting the ice

water term. The latent heat of evaporation will be fixed at its $0^{o}C$ value of 2.500×10^{6} J kg^{-1} as a first approximation.

Sensors of pressure and temperature have been mounted directly on the port engine of the Learjet and their signals recorded. The pressure and temperature sensors employed in these trials were chosen primarily on the basis of ready availability at limited cost and they are not optimum. They are nevertheless adequate for demonstrating the feasibility of the engine theta technique.

Measurements were made in the tops of growing cloud turrets on the flanks of multi-cellular thunderstorms in the vicinity of the $-10^{o}C$ level (near 6.0 km ASL altitude).

9.1.2.2 Results

Fig. 9.6 shows the result of a cloud penetration at 1155 SAST on 10 March 1986, at 468 mb and $-11.2^{o}C$. The drop in temperature due to the evaporation of condensate is clear in the records of both engine temperature and engine potential temperature. Note that just prior to cloud entry the potential temperature in the engine (right scale) is approximately 30 ^{o}K higher than that of the environment (left scale). That is typical of the frictional heating which occurs in the compressor (the compressor consists of eight stages rotating at 12000-15000 rpm). Pressure in the engine is about 2.6 atmospheres and the temperature in the neighbourhood of $190^{o}C$. The condensed water mixing ratio, derived from application of equation 9 (neglecting the ice water term) shows excellent similarity to that derived from the engine-vapour system. The general shape of the two curves and the overall values are in quite good agreement, but the engine theta measurements obviously respond sluggishly. This is due to the engine temperature measurement, which is the most important element of the technique. This should be solved by a combination of a higher response sensor and perhaps more careful placement of the sensor in the engine bleed air outlet.

9.1.2.3 Summary

The principle of measuring changes of potential temperature in jet engine compressor bleed air as an estimate of condensed water mixing ratio in clouds has been tested and shown to be quite sound. Problems remain to be solved in order to realize the full potential and accuracy of the technique. The reasonable agreement shown to occur between the engine theta measurements and the engine vapour technique indicates that the condensed water estimates from the engine vapour method are indeed due to water evaporated in the engine compressor and not some quirk of the Lyman-alpha device and its associated electronics and plumbing.

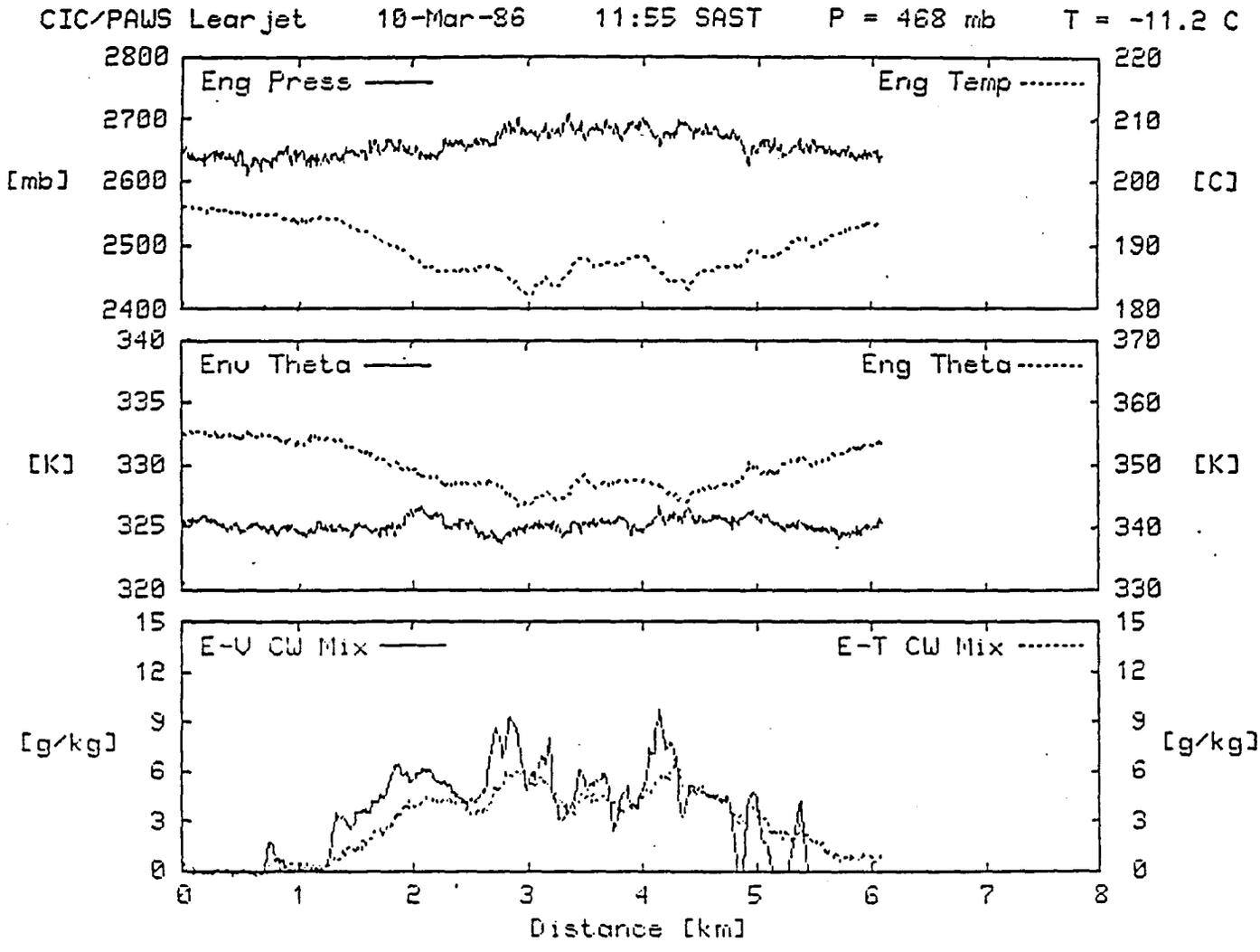

Figure 9.6. Engine-theta and engine-vapor measurements from the cloud pass at 1155 SAST, 10 March 1986. Three panels are shown displaying analog traces as a function of distance run (integration of aircraft true air speed and time). The top panel shows the pressure (solid line; left scale) and temperature (dotted line; right scale) in the port Learjet engine through the run. The middle panel displays the potential temperature computed for the ambient environment (solid line; left scale) and in the engine (dotted line; right scale). The condensed water mixing ratios using the engine-vapor technique (solid line) and the engine-theta technique (dotted line) are given in the bottom panel.

The time response of the thermocouple mounted in the engine is undesireably slow. This may be due not only to the thermocouple itself but also to its positioning in the engine bleed air outlet. Much also remains to be done in precisely determining the frictional heating by the compressor as a function of engine power setting and environmental parameters, and in specifying the effective evaporation temperature of the water.

Given the successful resolution of these engineering problems, the engine theta technique combined with the engine vapour method will provide a unique system for obtaining accurate water content measurements in convective clouds, a goal currently beyond the capabilities of standard airborne cloud physics measurement systems.

9.2 Evidence for the accummulation of very high concentrations of supercooled water in thunderstorms

9.2.1 Background

During the 1960's western scientists became aware of claims by Soviet researchers of great success in reducing hail damage to crops through ice phase cloud seeding. The Soviet method of hail prevention was based on a largely conceptual model of natural hail formation and growth, at whose core lay the concept of an "accumulation zone" (sometimes called the "Big Drop Zone" or BDZ). The accumulation zone (AZ) occurred above the updraft speed maximum where the vertical air velocity was in the range of the fall speeds of the smallest and largest rain drops. In such a region the numbers of drops and the liquid water content increase rapidly (a more complete explanation of this phenomenon is given in Morgan, 1972) and, according to the Soviets, could reach values in excess of 40 $g\,m^{-3}$. The accumulation zone was small, of the order of a few km^3, and was identified with a rapidly developing elevated peak in the radar reflectivity profile. In the AZ, it was claimed, hail could grow very rapidly, and its prevention could be affected by shooting a nucleant into the AZ with a rocket. Haman (1967) and later Morgan (1972), pointed out problems with this concept and attempted to show alternative ways in which the accumulation could be brought about.

The Soviet claims to great success in hail suppression led to American interest in hail suppression and eventually to the undertaking known as the National Hail Research Experiment (NHRE) in northeast Colorado. The history of NHRE is recounted by Morgan and Squires (1982) and by Morgan and Crow (1982). The NHRE, established in a semi-arid region, failed to produce evidence for the AZ.

An announcement by Kyle and Sands (1973) of having measured very high (40 g m^{-3}) liquid water contents in a Colorado storm was later criticized by Smith (1976) and the observation shown to be due to the low volume sampling rate of Kyle's evaporator.

Attempts were made during Grossversuch IV, the three nation hail suppression experiment in Switzerland, to detect evidence for the accumulation zone phenomenon (Musil et. al. 1984; Musil and Smith, 1985) using the T-28 armoured aircraft. After 14 cloud penetrations on three hailstorms it was reported that no evidence even for the presence of large water drops was found.

In the eastern Transvaal, the average cloud base temperature is 14°C (Mather et al., 1986) and at times values as high as 20°C are observed. By comparison, NHRE was carried out in a region where average cloud base temperature was 4.4 °C (Faukhauser and Wade, 1982) with maximum values of less than 12 °C. Ackerman et al., 1979 , using a Ruskin evaporator in clouds with average base temperatures of 19.5°C (range 15.3 to 21.8°C), found the total water content to exceed the adiabatic value on two thirds of cloud passes near the 0°C level. On several occasions the total water reached 20 g m^{-3}. They concluded that accumulation was occurring.

On two occasions the new instruments described here have detected condensed water contents in warm based Transvaal clouds which suggest the existence of accumulation zones.

9.2.2 The observations

March 12, 1986 was one of the first operational days on which both engine vapour and engine theta instruments were on board the aircraft. During a cloud penetration at -10°C at 1537 SAST, the engine vapour method produced a peak estimate of condensed (liquid and ice phase) water mixing ratio of 39.6 g kg^{-1} (23.7 g m^{-3}) as shown in the third panel of figure 9.7. This was a mixture of large raindrops and round graupel. There had been a previous occurrence of very high water content, as will be shown below, which had been set aside for study because of the suspicion that something had malfunctioned in the Lyman-alpha humidiometer. In the present case, however, we were able to analyze the engine-theta records, resulting in the dotted curve in the bottom panel of Fig. 9.8. The pressure, temperature and theta curves of Fig. 9.8 should be compared to similar curves shown in section 9.3 above, to fully appreciate how extraordinary this case was.

The pilots and observer on the flight described the experience as similar to driving through a downpour; the high water content was very apparent to all three. A video tape record furnished dramatic documentation of enormous water drops striking and streaming across the copilot's windscreen. An additional data record from the Learjet lends further support to the measurement. Radar Z_e values, shifted by 1.5 km to correspond, point for point, with the rest of the data set, are shown in the

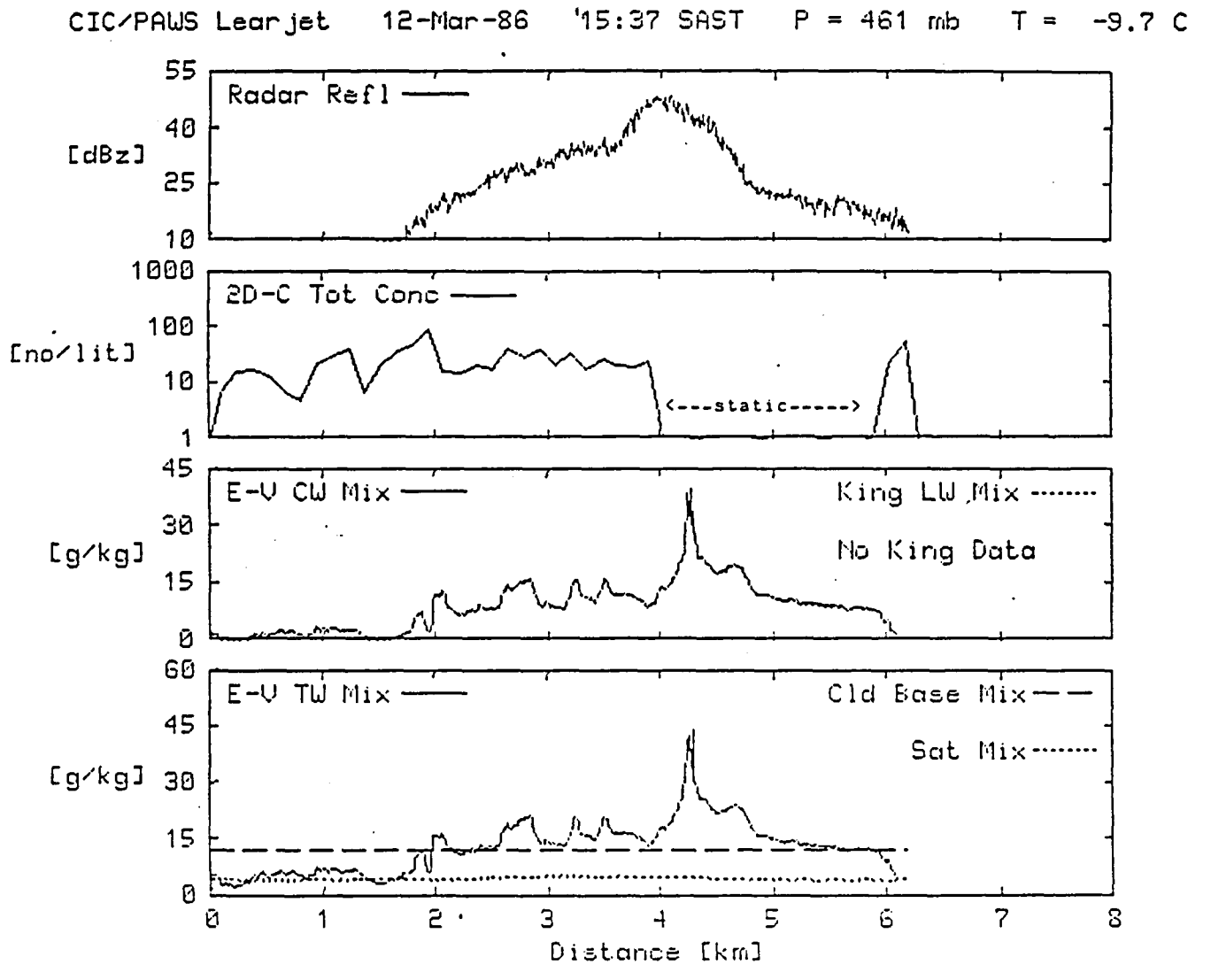

Figure 9.7. The 12 March 1986 accumulation zone observations. Analog traces are shown as a function of distance run. The bottom panel shows the total water mixing ratio by the engine-vapor system (solid line), saturation mixing ratio (dotted line) and cloud base mixing ratio (dashed line). The second panel displays the engine-vapor system condensed water mixing ratio (solid line) and King liquid water mixing ratio (dotted line if data is present). 2D-C probe total particle concentration is shown in the third panel and aircraft 3 cm radar reflectivity (adjusted for horizontal displacement ahead of the aircraft) is shown in the top panel.

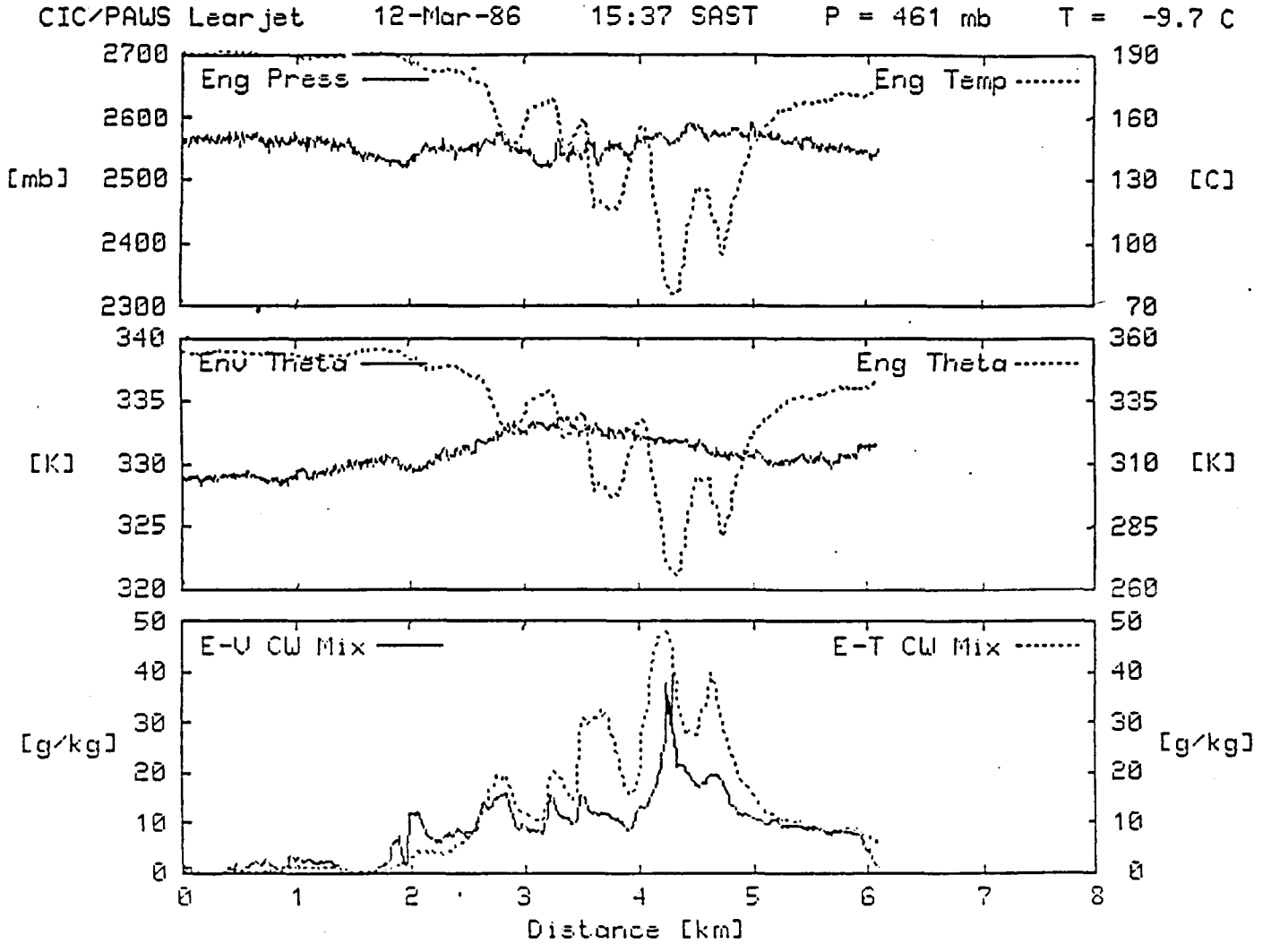

Figure 9.8. A comparison of the condensed water mixing ratio computed using the engine-vapor method for the 12 March 1986 observation is shown in the bottom panel as the solid line, and using the engine-theta technique as the dotted line. The other two panels show data relevant to the engine-theta technique: potential temperature for the environment (solid line) and computed in the engine (dotted line) are shown in the second panel; and the pressure (solid line) and temperature (dotted line) in the engine are displayed in the top panel.

top panel of Fig. 9.7. The radar indicates a much broader feature than is apparent in the condensed water profile. This is due to the resolution of the radar; the half pulse length is about 350 m. Had the radar been able to measure at the same scale as the engine instruments, a much higher value of Z_e would clearly have resulted. A peak reflectivity of 48.8 dBz coincides well in position with the peak in water content. The updraft speed was close to 9.10 m s^{-1} in the vicinity of the high Z_e and high water contents. Such a value would be consistent with accumulation of millimetre sized drops.

Recorded volume scan data from the project's ground based C-band radar showed reflectivities up to 47 dBz along the aircraft's flight track on this penetration. The adjacent parent storm contained a peak reflectivity of 56 dBz.

Since the above case apparently ruled out instrument malfunction as an explanation for the exceptionally high condensed water measurements, an earlier and even more spectacular flight was re-examined. Fig. 9.9 shows the observations from a cloud penetration made at -10°C at 1504 SAST on 15 January 1986. This cloud, too, consisted of large drops, and graupel. The engine theta instruments were not installed at that time.

The peak engine vapour condensed water mixing ratio recorded on this pass was 80 g kg^{-1}, corresponding to 46 g m^{-3}. The crew's sensations of driving through a rainstorm on this pass were similar to those on the penetration just described above. Unfortunately, the video recorder ran out of tape just prior to this run. However, there was a video recording which fully justified a report of very heavy rain at around -10°C on a previous run, where no cloud physical data were recorded. On leaving this cloud the Lear was forced to pass through a neighbouring tower in which it encountered hail causing minor damage to the airframe and exposed instruments.

The full value of 80 g kg^{-1} shown is not a real measure of the cloud content. What had happened in this case is that condensation had taken place in the measurement cell. The pressure and temperature in the cell were 750 mb and 35°C. The corresponding saturation mixing ratio is 50.5 g kg^{-1}. When the mixing ratio rose to that value, condensation must have occurred in the cell and the narrow copper pipe leading to it. The apparent mixing ratio remained at about 80 g kg^{-1} for a long period as the condensate re-evaporated. So, what we do know is that for an indeterminate period the total water mixing ratio exceeded 50.5 g kg^{-1} (29 g m^{-3}) by an indeterminate amount. Once the mixing ratio exceeded that amount, the instrument saturated. It is very likely that something similar to this occurred to produce the exceptional value of 44 g m^{-3} reported by Roys (1963).

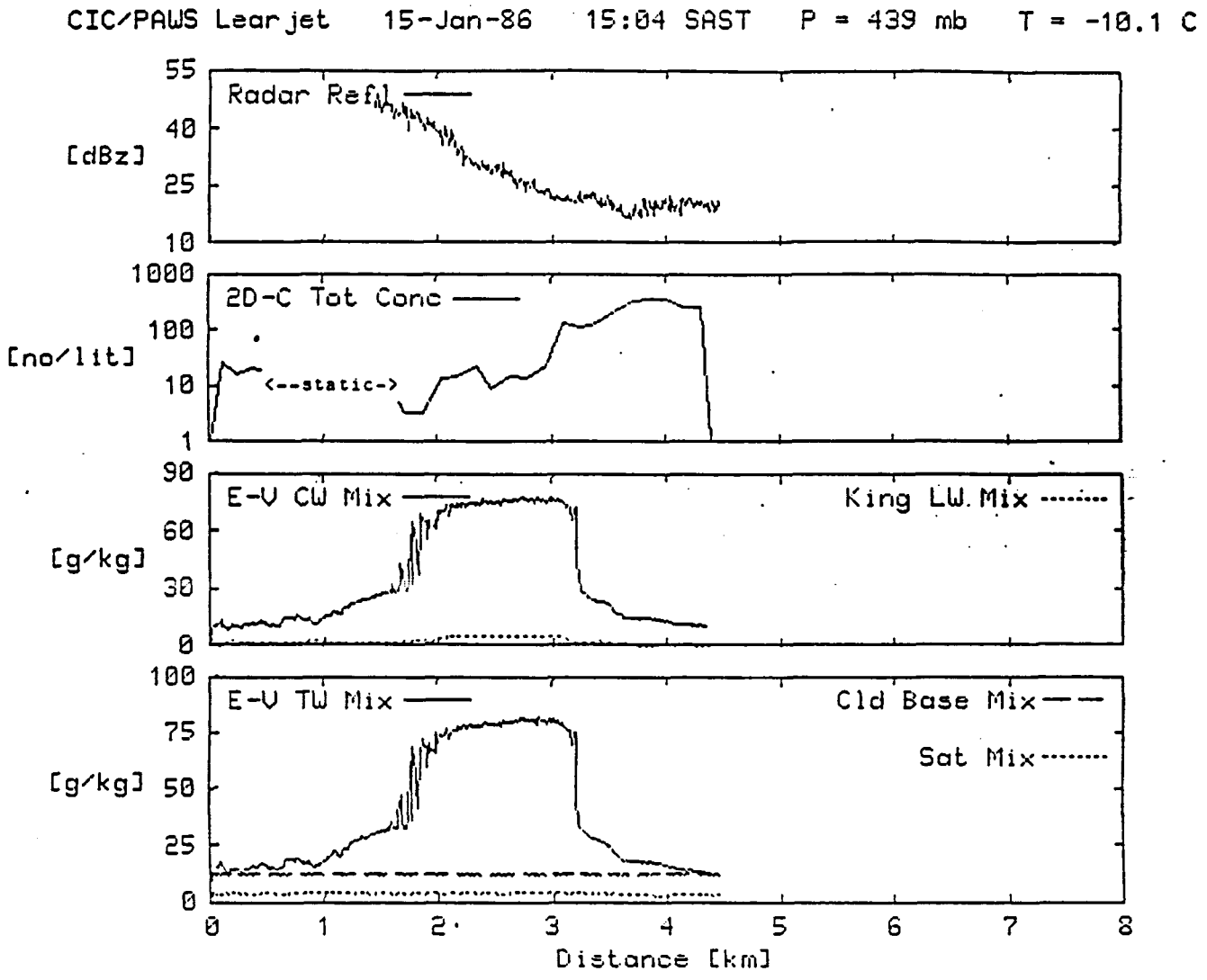

Figure 9.9. The 15 January 1986 accumulation zone observations. Figure shown is the same format as Fig. 8.9 except that the scales in the bottom two panels have been expanded.

In the absence of the engine theta measurement, the main support for the reality of the exceptional water content value must come from the on board radar recording. Unfortunately, on this pass, the tape recorder was turned on late, at the time when the flying range gate was just passing the region of high water content. Nevertheless, as the radar recording was begun the Z_e value was around 50 dBz.

The ground based radar at Nelspruit recorded radar reflectivities as high as 49 dBz along the aircraft's track on this cloud penetration and the adjacent parent storm contained reflectivities as high as 54 dBz.

9.2.3 Comments

How often does this accumulation phenomenon occur? That would be a difficult question to answer at this point, but the following observations are relevant.

A total of 30 flight days have occurred on which the engine vapour instrument was operational on the aircraft; the phenomenon has been observed on two of them. The flight programme is not designed to look for the AZ. Flights are performed so as to sample, and, when dictated by a randomization procedure, to seed clouds at about the -10°C level. Only a fraction of the cloud turrets which occur are sampled. In fact, one possible outcome of the randomization procedure dictates that the turrets on a selected storm be neither seeded nor sampled.

In the years from 1973 to 1981, the Learjet was employed in an operational hail suppression project (without its present sophisticated instrument complement) penetrating cloud turrets over a wide range of temperatures. During those years the experience of "driving through a downpour" while flying at sub-zero temperatures, was not uncommon. Heavy clear icing on unheated surfaces was common in clouds at -20°C and -25°C.

The observations reported here which could not have been made with conventional instrumentation are interpreted as indicating that the accumulation phenomenon exists. Its significance in the clouds in question is unknown; there are no reliable records of hail occurrence or non-occurrence in the region of study.

Though it is suggested above that accumulation occurs only in clouds with high cloud base temperatures, that is not a proven fact since adequate measurements in Colorado and Switzerland have not been made. Certainly, if the AZ phenomenon exists, as these observations suggest, any attempt to numerically model thunderstorms must deal with that fact. Model results should display the AZ phenomenon at times. A major factor in the occurrence or absence of the liquid water AZ must be the ice nucleation behaviour of the cloud. Underlying the AZ phenomenon is a major mechanism for precipitation development, coalescence. Mather et al. (1986), have shown the importance of coalescence

in Transvaal clouds and determined the conditions under which it clearly predominates. They also pointed out that ice nucleation can interfere with that process, producing a graupel population at the sampling level (-10°C) rather than drops.

The AZ of Sulakvelidze et al. (1967), which has been so poorly esteemed in Western scientific circles must be seriously reconsidered. So, too, must be the report by Roys (1963) of a liquid water content of 44 g m^{-3} in an Oklahoma thunderstorm. At the same time, the conceptual model of hail formation and hail suppression advanced by Sulakvelidze must be re-examined.

9.3 Studies on the state of mixing in Nelspruit clouds (Morgan and Morrison)

Cumulus clouds are the visible elements of a very complex spectrum of mixing processes in the atmosphere. The spectrum of mixing processes is a continuous one with much interaction and movement of energy through the spectrum. The rising masses of warm air which make up the cumulus clouds are not like corks, bobbing to the surface of a pail of water, but are constantly mingling with their surroundings, taking in environmental air and shedding some of their mass into the environment. This has a profound effect on the lifetimes of clouds and on their internal precipitation forming processes.

Theory concerning mixing is a very complex problem and not at a satisfactory stage of development. It would be completely beyond the scope and means of the PAWS project to attempt theoretical studies or the development of models to deal with this important problem which most certainly has impact on the weather modification problem. It is also not likely that significant theoretical advancement for our purposes is forthcoming from any quarter. We can, however, attempt to describe the impact of the mixing in an empirical way and present an overall view of the clouds, seen as being composed of zones of varying degrees of mixing.

In Section 9.1 it was shown, using measurements of total water mixing ratio, that clouds in which no precipitation has formed at about the -10°C level have adiabatic cores. We can now take this small sample of such clouds and examine the question of the importance of these cores.

The approach is based on fluxes. The calculations of the fluxes are discussed in Section 10. We pose the question, what portion of the upward flux of air in the cloud is adiabatic or nearly adiabatic? It is important to discuss this in terms of flux because there is a correlation between the upward air velocities and the total water content, the quasi-adiabatic regions tending to be in the faster moving interior of the cloud.

We can form, for each traverse the relative frequency and cumulative frequency distributions of upward flux (percent of total) versus total water mixing ratio expressed as a fraction of the adiabatic value (we actually assume that the peak value in the cloud is the adiabatic value, small departures from adiabatic being due to local values of low level mixing ratios being slightly different from those estimated on the aircraft sounding at Nelspruit). An example of this is the pass made at 1348 SAST on 29 October 1985, shown in Fig. 9.3.1. Examination of this plot shows that in this cloud, at the penetration level, 50 percent of the upward flux of air contained total water mixing ratios within 10 percent of the adiabatic value.

Fig. 9.3.2 is a combined result for 14 cloud passes in which there were no 2D-C images and the total water mixing ratio was greater than 0.9 times the adiabatic value. This shows that for this ensemble, over thirty percent of the upward flux was within 10 percent of adiabatic and 60 percent of the upward flux was within 20 percent of adiabatic. These were clouds averaging 2.0 km in diameter and almost 4.0 km^2 in cross-sectional area. The mean flux of air was 14.65 Kton sec^{-1}. Separating the up and down portions of the vertical speed record resulted in an average up flux of air of 16.37 Kton sec^{-1} and an average down flux of 1.72 Kton sec^{-1}. At least one of the clouds contained no downdraft and in one the updraft occupied only about 8 percent of the traverse; the average of the set of clouds was 70 percent updraft and 30 percent downdraft.

We next enlarge our sample by including cases in which there was a very small amount of precipitation in the cloud (2D-C average concentration less than 10 l^{-1}). Here we look at cases with a peak total water mixing ratio from 0.9 to 1.05 times the adiabatic value. The result is Fig. 9.3.3 for 25 cases, and is almost identical to the previous figure.

The percent of each traverse which is updraft is an interesting parameter which is related to mixing and is recorded in the cloud sample database. It varies from zero to 100 percent. In an attempt to determine relations between this and other cloud parameters, a number of scatter plots similar to Fig. 9.3.4 have been examined. Here, the percent of each traverse which is updraft is plotted against the maximum vertical velocity measured on the traverse, for traverses performed between -5 and -10°C. There is a very clear tendency for clouds with weak updrafts to contain large percentages of downdraft, and for clouds with strong updrafts to contain large amounts of updraft. Similar plots for other temperature intervals look the same. One conclusion from this is that the mixing and development of downdrafts in the cloud cause it to arrive at the penetration level with a weak updraft.

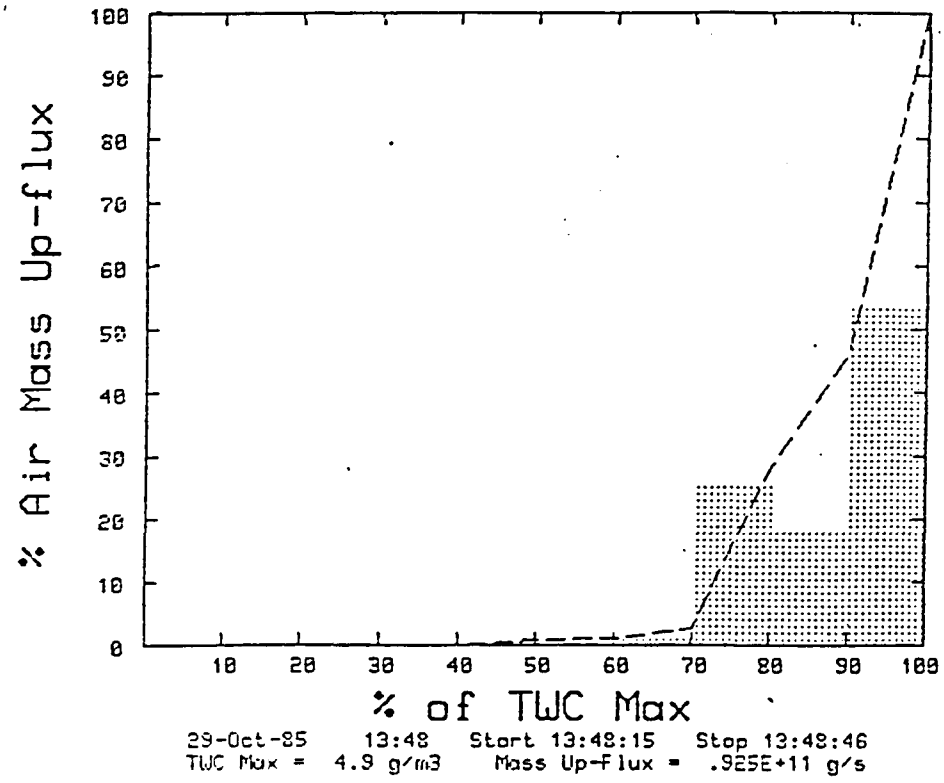

Fig. 9.3.1. Cumulative frequency distribution of upward air flux versus the total water mixing ratio expressed as a percent of the adiabatic value.

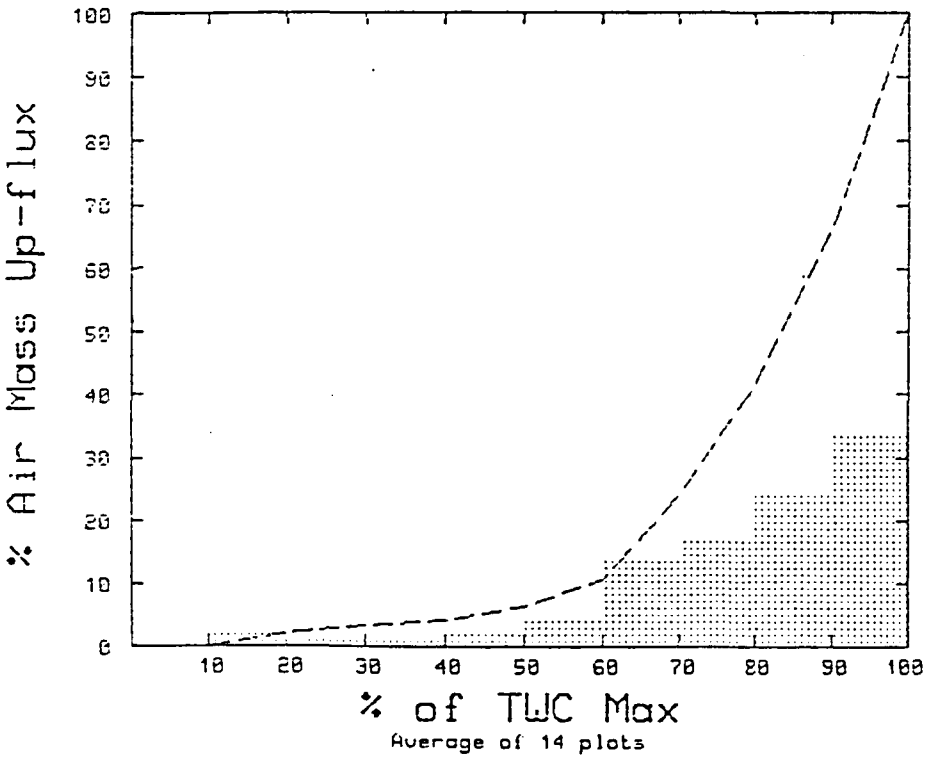

Fig. 9.3.2. As above, for 14 passes containing no 2D-C images and total water mixing ratios greater than 90 percent of the adiabatic value.

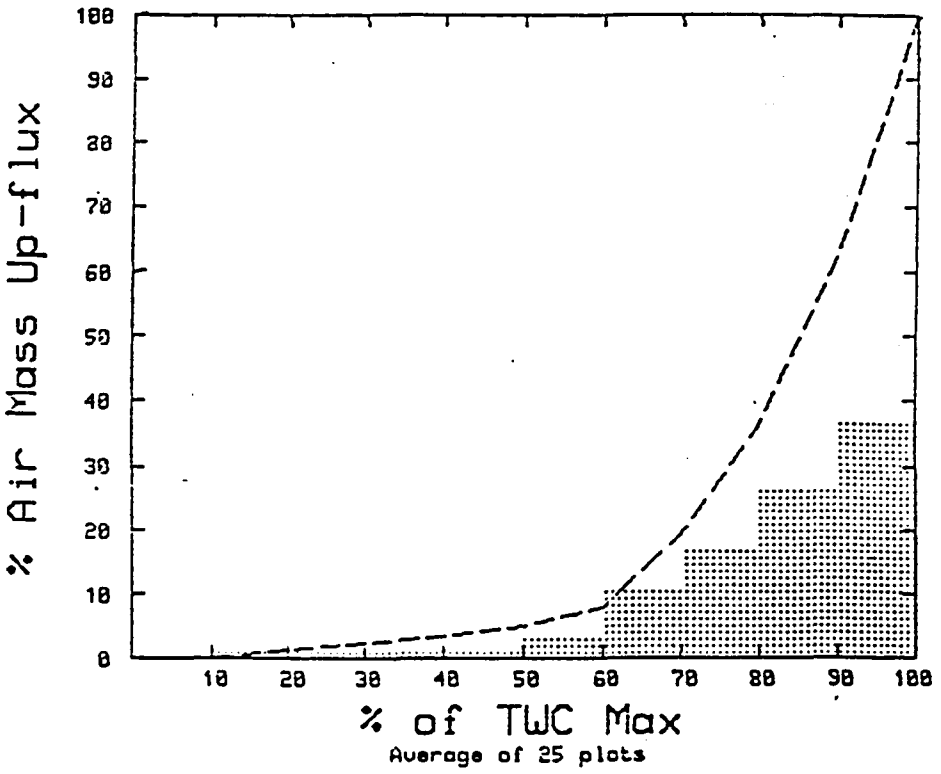

Fig. 9.3.3. As in Fig. 9.3.1, with average 2D-C concentrations less than 10 l^{-1} and total water mixing ratios 90 to 105 percent of the adiabatic value.

10 < Env T < -5

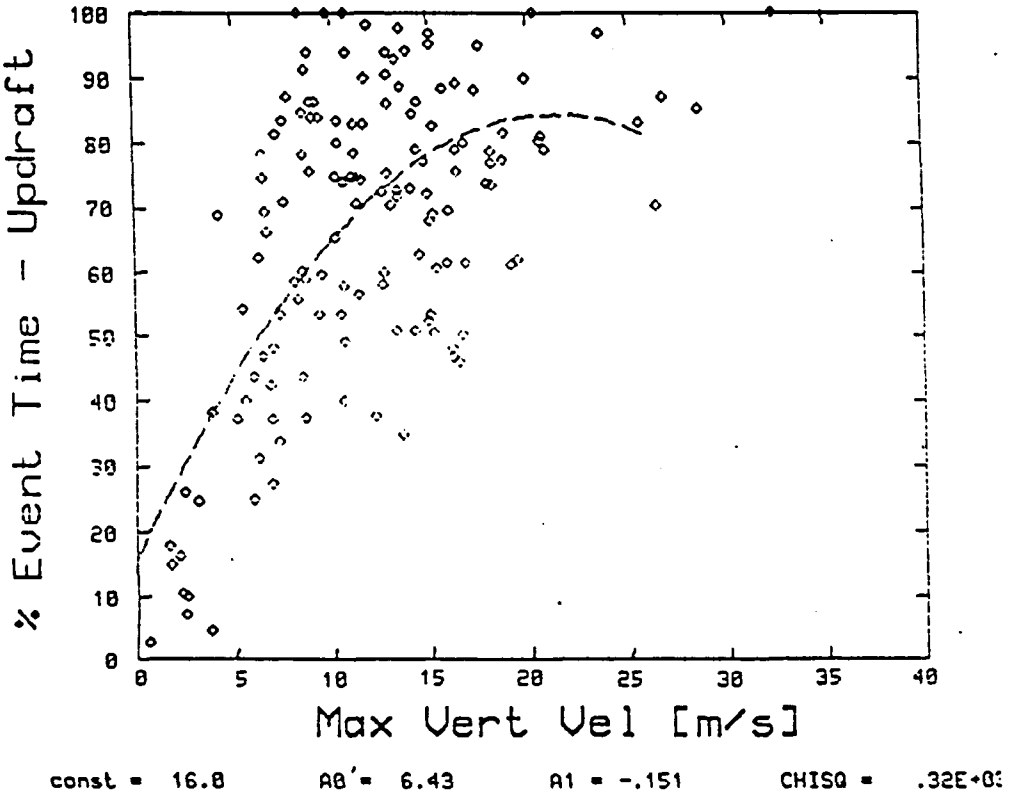

Fig. 9.3.4. The percent of a cloud traverse that is updraft versus maximum vertical velocity.

9.4 The dependence of the frequency of occurrence of certain cloud properties in the -15 to -5°C layer, on terrain height (Morgan and Morrison)

The terrain over the experimental area varies from near 200 m asl in the East to around 2200 m to the northwest of Nelspruit. This should have influences on the internal properties of clouds as they are viewed in a fixed altitude or temperature interval. Two main effects expected to play a role in determining cloud characteristics are:

a. The higher the terrain, the shallower the moist layer, hence the higher and cooler the bases of the clouds

b. The lower the terrain the greater the distance between the surface and any fixed altitude or temperature level, and, following a), the greater the distance from cloud base to that level. The importance of this to the development of precipitation through coalescence is documented in Section 5.2 of Vol. III and in Mather et al., (1986).

A very simple test of the existence of these influences has been performed using the cloud sample database. All data from Learjet missions between October 1982 and April 1986 have been sorted to select first passes occurring between - 15 and -5°C (environmental temperature) with valid 2D-C data, then sorted into sets according to the terrain elevation below each sampled cloud.

The terrain intervals in Tables 9.4.1 and 9.4.2 are unequal and chosen for convenience, with due respect for sample sizes. The lowest interval includes all terrain lying below the base of the Nelspruit sounding. Clouds over that region have beneath them a layer of moisture which is not sensed by our soundings and which can extend as much as 700 m below it. The other intervals were set by examining the overall histogram of underlying terrain heights and attempting to split the sample up meaningfully. Table 9.4.1 shows the probability (percent) of encountering large liquid drops in clouds for four categories of terrain height. This probability goes from 11 percent over the highest terrain to 67 percent over the lowest terrain east of Nelspruit.

The average peak radar reflectivity factor for clouds in the same terrain height intervals (Table 9.4.2) also varies in a way which is consistent with the above. The general decrease of Z with height can be expected, due to a greater percentage of clouds with large particles over the lower ground, and a greater role being played by coalescence generated large drops there.

No other cloud parameters in the database showed consistent or marked tendencies under this stratification.

Table 9.4.1 The dependence of the relative frequency of occurrence (percent of 1st cloud passes) of drops in the 2D-C images on terrain height. Data from 1982 to 1986, first passes only in the environmetal temperature range -15 to -5°C.

Terrain ht interval (m)	Number of clouds	Number with drops	Percent with drops	Number with no 2D	Percent with no 2D
900	37	24	65	2	5
900-1500	89	27	30	19	21
1500-1700	128	30	23	24	19
1700	46	5	11	9	20

Table 9.4.2 The Mean peak radar reflectivity factor Z (dBz), in turret clouds sampled over four categories of terrain height.

Terrain height interval (m)	Max radar reflectivities (dBz)	No of cases
900	23.7	24
900 - 1500	18.1	67
1500 - 1700	16.3	109
1700	13.3	41

9.5 The efficiency of precipitation formation (Morgan and Morrison)

Precipitation efficiency is a term often discussed in the weather modification context. It is often used in a loose way or without clear reference to its definition. Perhaps the most common definition is that the precipitation efficiency is the total amount of precipitation falling to the ground during the life of a cloud divided by the total amount of water vapour which enters the base of the cloud during its life. Difficulties with this are obvious. It is extremely difficult to monitor either the

rainfall or the inflow. Nevertheless, such concepts allow one to discuss the major limits to precipitation efficiency, even if it cannot be practically measured. Efficiency is limited by factors such as mixing and by evaporation below cloud base, and by exhaustion of water through anvils, to name a few.

Efficiency as defined above is an important concept to PAWS, but we will try and approach it from a point of view most suited to the types of data we have. We will attempt to discuss efficiency from a "local" point of view, as we can estimate it from data collected in clouds.

This will be done by estimating the sizes of terms in a simple precipitation formation equation and pointing out their relative values. By taking this local point of view we do not want to imply that it presents the whole picture. Local conditions may be completely offset by conditions at other places or times.

9.5.1 Analysis of first passes

Precipitation growth rate is computed for each 2D-C data record assuming precipitation particle densities of 0.2, 0.4, 0.6, 0.8, or 1.0 g cm^{-3}. For use in the calculations described below, a bulk particle density was assumed for each cloud penetration according to the 2D-C image classification parameter stored in the Cloud Sample Database using the following scheme: Penetrations consisting predominantly of water drops were given a bulk density of 1.0. Runs that were predominantly graupel were assigned a density of 0.6. All-ice runs were assigned a density of 0.2. Mixtures of graupel and drops were assumed to have a density of 0.8. Images that were too small to discriminate phase (ice versus small water drops) were assigned a value of 0.8. Zero images were assumed to be ice and were given a density of 0.2.

Three terms described above have been computed across the updraft of turrets penetrated by the Learjet and are combined into two parameters which were stored in the Cloud Sample Database. These parameters are the "conversion efficiency", CE, and the "reservoir effect", RE, and are defined as follows.

The conversion efficiency is defined as :

$$CE = \frac{AC + PGR}{CR}$$

where AC = autoconversion rate [g m^{-3} s^{-1}]
PGR = precipitation growth rate [g m^{-3} s^{-1}]
CR = condensation rate [g m^{-3} s^{-1}]

This dimensionless parameter is the ratio of the rate of precipitation production (AC + PGR) to the rate of cloud water production (CR). Small values (less than 1.0) imply that little of the cloud liquid water being produced is being converted to precipitation suggesting a locally inefficient precipitation mechanism. A value of 1.0 implies that precipitation is being produced at the same rate as that of cloud liquid water. If we assumed a steady state supply of cloud liquid water and precipitation embryos (which is not realistic for convective clouds), this would be optimal. However, this does not take into account the substantial reservoir of supercooled liquid water, frequently in excess of 3 g m^{-3}, which already exists when precipitation production begins. Values of the conversion efficiency somewhat greater than 1.0 would therefore be more ideal. Excessively high values much greater than 1.0 could exhaust both the production of liquid water and the existing supply resulting in a decline in efficiency.

The reservoir effect parameter, RE, directly addresses the question of the exhaustion of the supply of liquid water. It is defined as :

$$RE = \frac{AC + PGR}{LWC}$$

where LWC = cloud liquid water content from J-W or FSSP [g m^{-3}]

It has units of s^{-1}. The cloud liquid water content is taken from the J-W hot wire data or, if the J-W data is missing or bad, from the integrated FSSP liquid water spectrum. This parameter is inversely proportional to the rate at which precipitation scavenges the cloud liquid water. Very small values imply a slow rate of cloud water uptake and, therefore, inefficient utilization of cloud water. Very large rates, however, could lead to depletion of the local liquid water supply required for continued precipitation development and growth.

Recognizing the assumptions and limitations inherent in these parameters, and emphasizing that they address only LOCAL precipitation efficiency and not that of the overall cloud or cloud system, we can make some general statements concerning the natural clouds in the study area.

Figure 9.5.1 shows the cumulative curves for the updraft conversion efficiency over four temperature ranges in untreated (first pass) turrets. In the -4 to -8°C range precipitation efficiency is the lowest. Only 10% of the penetrations show precipitation developing at a rate equal to or faster than the condensation rate. This figure increases to 38% in the -8 to -12°C range, then decreases slightly to 28% in the -12 to -16°C range, then increases to about 42% in the -16 to -20°C range. This implies that there is a significant population of inefficient and therefore potentially seedable turrets.

Cumulative curves for the reservoir effect in natural turrets over the same temperature ranges are shown in Fig. 9.5.2. We can assume that the time to deplete the cloud liquid water supply is about 1.0/RE. Therefore, at the 50th percentile this time would be 1515 seconds in the -4 to -8°C temperature range, 625 seconds in the -8 to -12°C range, and 588 seconds in both the -12 to -16°C and -16 to -20°C ranges. Even at the colder temperatures, this time scale of about 10 minutes (588 secs) implies locally inefficient utilization of the available cloud liquid water supply.

9.5.2 Analysis of seeding effects

Given that there is opportunity for static mode glaciogenic seeding to enhance precipitation efficiency, how does seeding with dry ice pellets affect natural efficiency? To answer this question we must examine changes in the efficiency parameters defined above in unseeded and seeded turrets.

Figures 9.5.3 and 9.5.4 show the cumulative frequencies of CE and RE, respectively, for all first Learjet passes (natural cloud state), and subsequent repenetrations into seeded and unseeded turrets in the temperature range -10 to -20°C. The data on repenetrations was insufficient to allow examination of narrower temperature ranges. In both the seeded and unseeded turrets there is a positive shift towards higher values of CE and RE from first passes to repenetrations. The shift is greater in the seeded cases.

These results must be interpreted with caution because of the limited sample size. The values of CE and RE from the first passes on the seeded and unseeded turrets are plotted against all first passes available in the data set in the temperature range from -10 to -20°C in Figures 9.5.5 and 9.5.6. These figures show that, while the turrets selected for the unseeded cases are reasonably representative of the entire population of natural turrets (especially in the CE parameter), the turrets in the seeded cases show initially higher values of CE and RE than are found in the natural population. Definitive statements about the effects of dry ice seeding, as revealed by this analysis, will have to await the acquisition of further measurements from seeded turrets.

9.6 The dependence of cloud droplet concentration on precipitation development (Morgan and Morrison)

As a parcel of air rises through the cloud base, a cloud forms in it. This cloud is composed of droplets with diameters less than 30 - 35 microns. The FSSP mounted on the port tip-tank of the Lear is capable of counting and sizing the droplets in this size range.

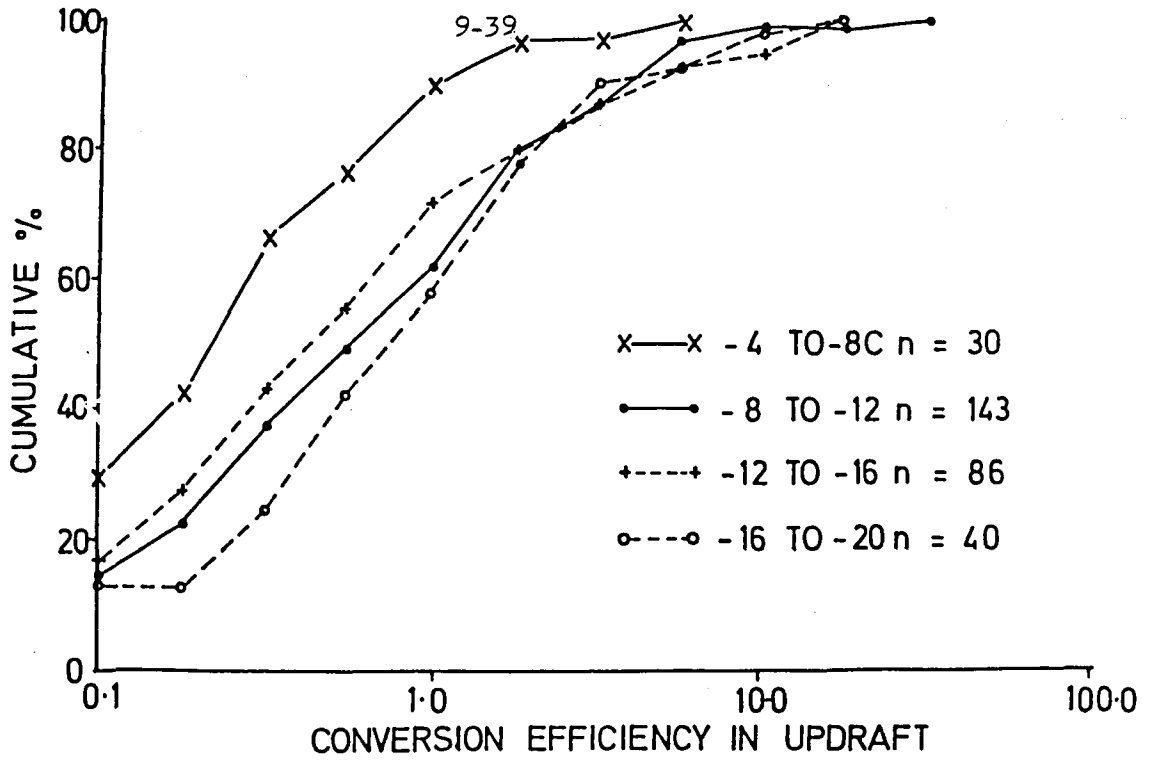

Fig. 9.5.1. Updraft conversion efficiency (CE) over 4 temperature ranges in untreated clouds.

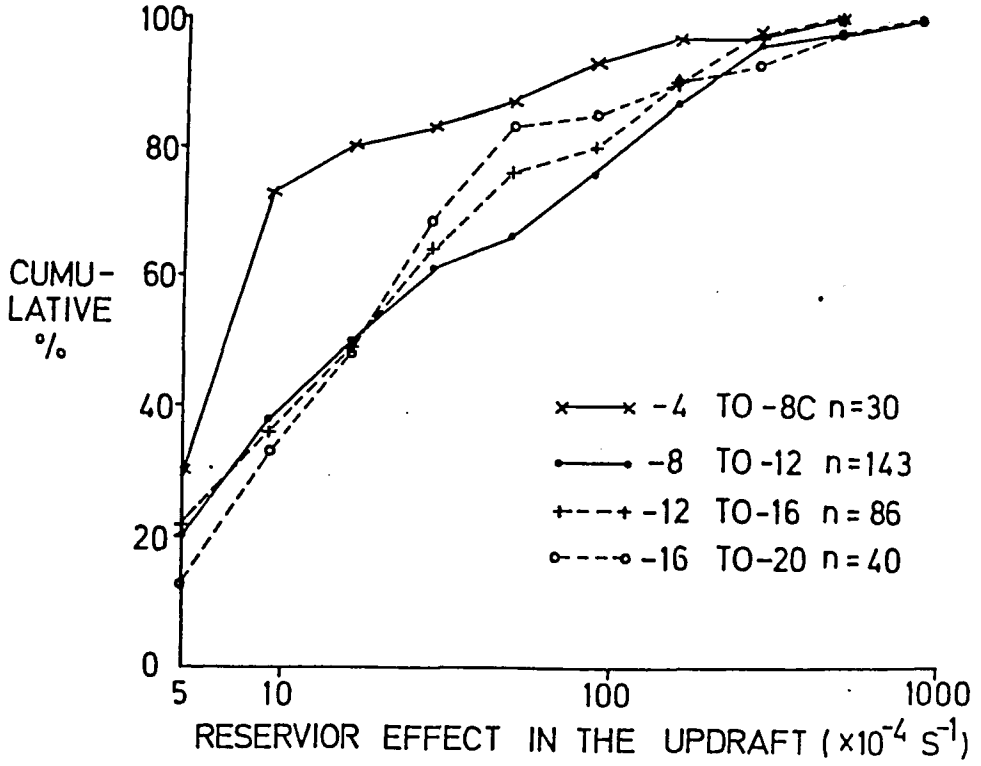

Fig. 9.5.2. Reservoir effect (RE) for above samples.

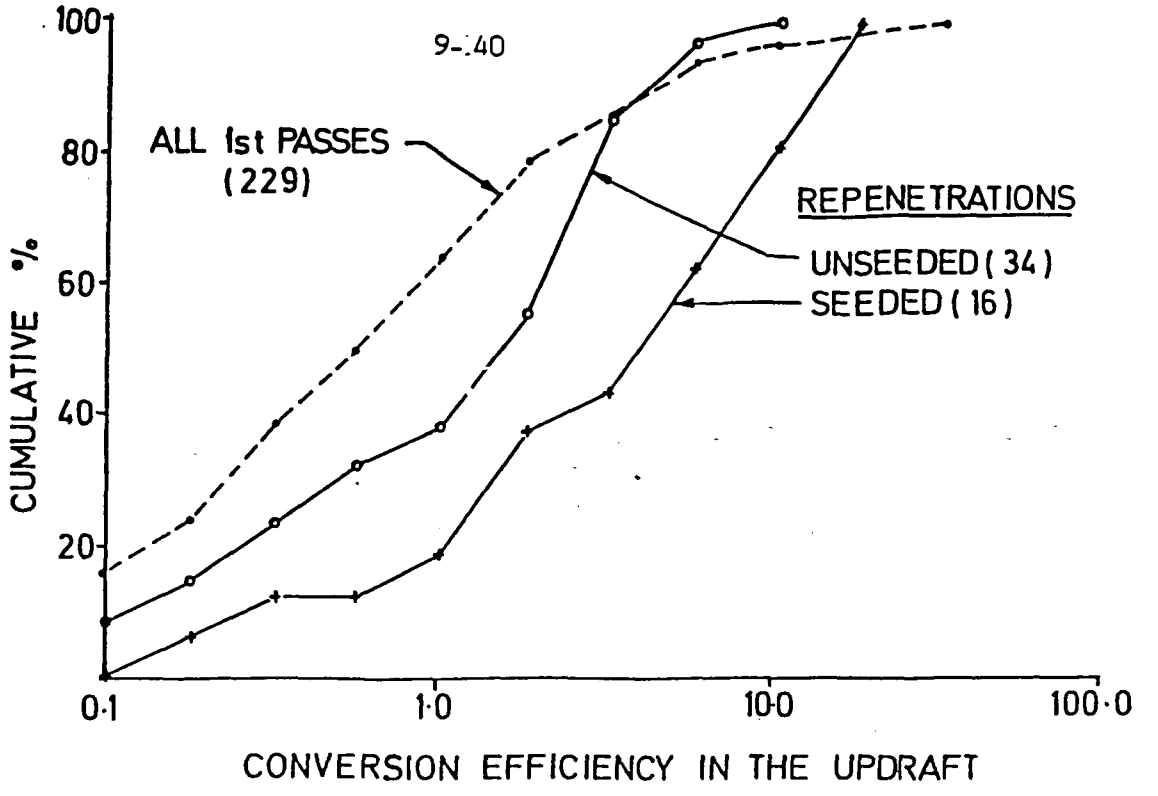

Fig. 9.5.3. CE for all first passes and subsequent repenetrations between -10 and -20°C.

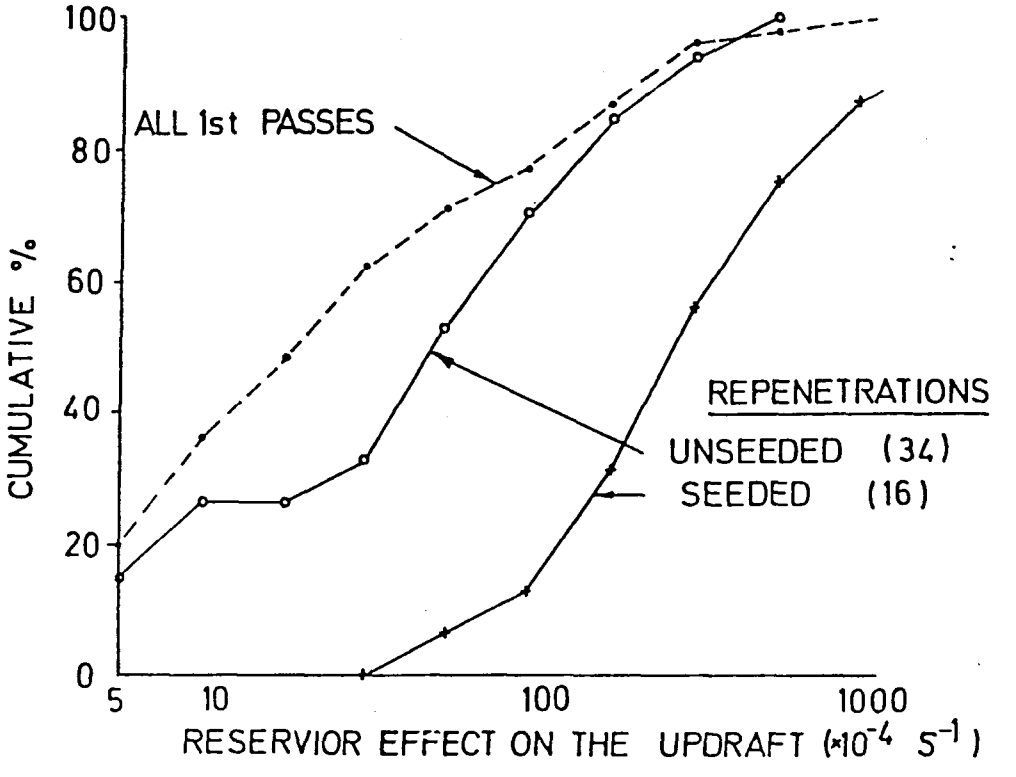

Fig. 9.5.4. RE for above samples.

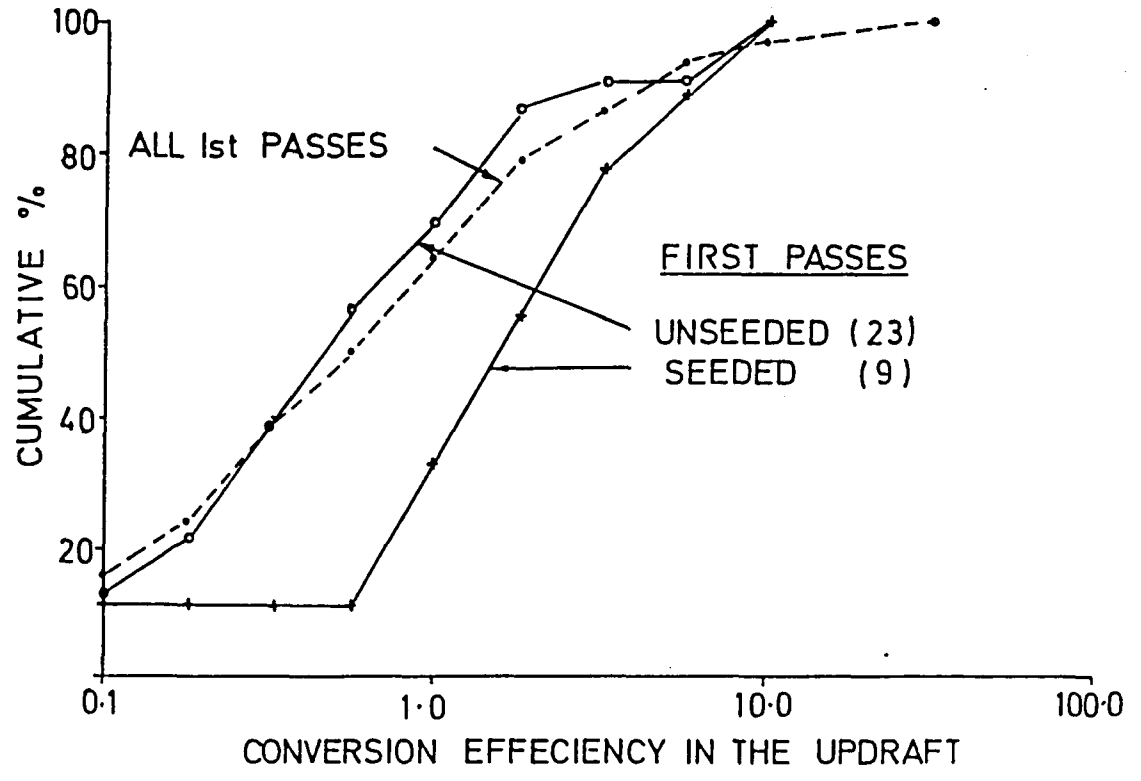

Fig. 9.5.5. CE for first passes through seeded and unseeded clouds.

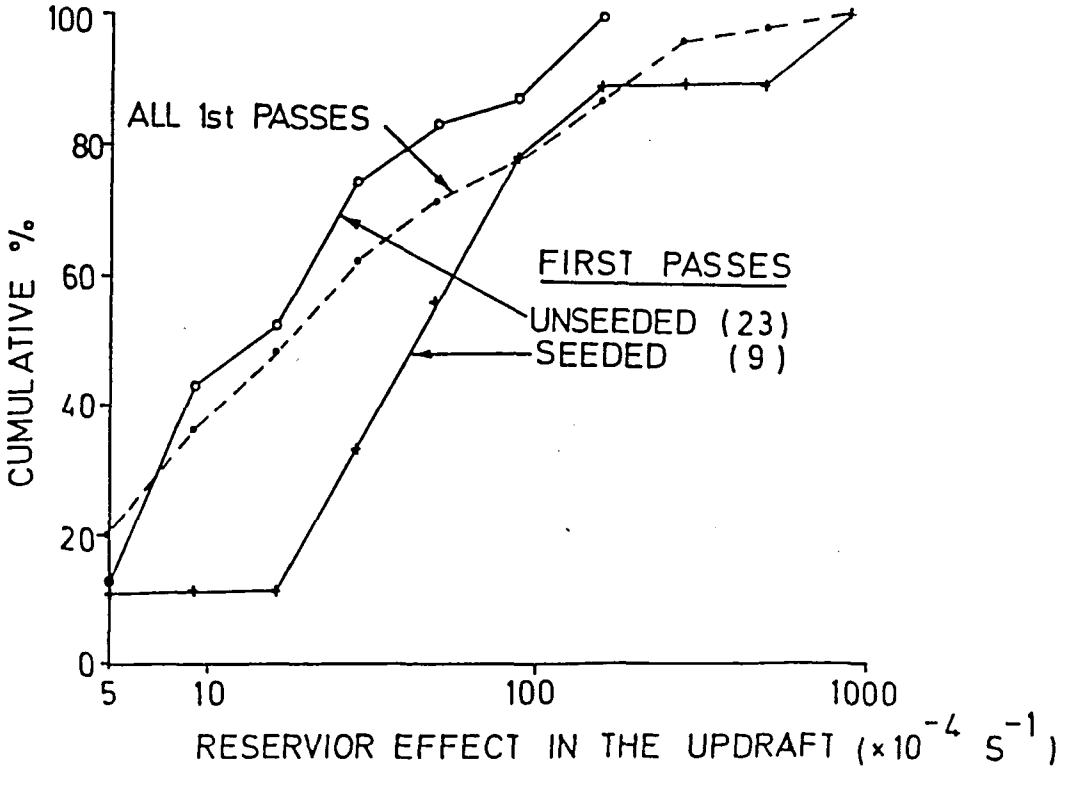

Fig. 9.5.6. RE for above samples.

With further rise in the atmosphere, more and more water condenses onto these particles, the mass of the cloud water increases, and , if sufficient time elapses, coalescence will begin to take place. When sufficient coalescence has taken place, droplets will have been formed which are too large to appear in the 0 - 47 micron window of the FSSP. At this point, the early stages of coalescence precipitation formation, the development of the cloud and precipitation are governed by: a. the condensation rate since virtually all of the water condensed out can be considered as going to increase the volume of cloud water, because the total surface area of the cloud drops is orders of magnitude greater than that of the larger coalescence products; b. the rate at which new coalescence products are being created, and c. the rate at which the coalescence products are sweeping out the cloud water.

We deal in a separate section with the relative values of the terms of the precipitation equation just described.

Here, we describe a simple attempt at detecting an effect which should exist as a consequence of the above interacting and competing phenomena. Detecting the effect would provide evidence that we do indeed know the important factors of the problem and that our measurements are of sufficient quality to promise fruitful investigations in this problem area.

During the early stage of precipitation development, water flows from the vapour to the cloud and then to the nascent precipitation. The cloud water content at any time may be increasing or decreasing, depending on the condensation rate and the amount of precipitation present. However, the number of cloud droplets (given no resupply of droplets) must be decreasing steadily.

To show this effect, we look for an inverse relationship between the condensed water content, estimated with the Engine Vapour (E-V) instrumentation described in Section 9 of this volume, and the FSSP concentration. To assure that we restrict ourselves to the earliest stages of precipitation formation we consider only cloud passes on which the average 2D-C total concentration was less than 10 l^{-1}, and we consider only cloud passes occurring between -8 and -12^{o}C.

The result is displayed in Fig. 9.6.1. The negative relationship is clear, apart from two wild points, and in spite of day to day variability.

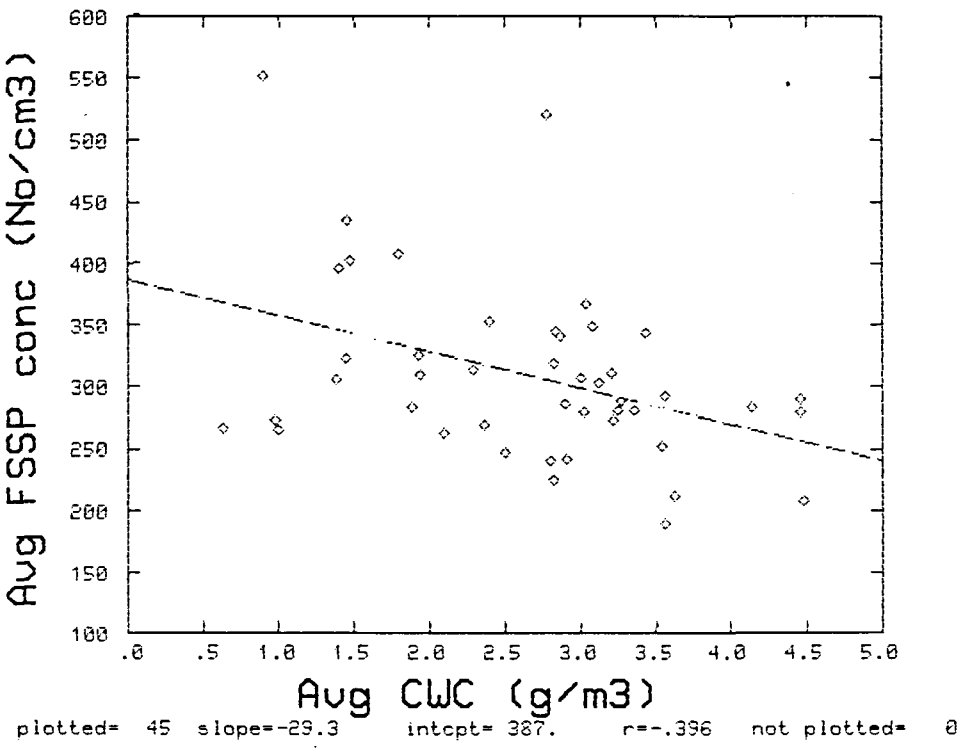

Fig. 9.6.1. The dependence of FSSP cloud particle concentrations on the condensed water content in clouds with little or no precipitation. Temperature range -8 to -12°C.

9.7 The variation of in-cloud equivalent potential temperature with time and location (Morgan and Morrison)

The temperature (or equivalent potential temperature) in the storm is one of the elements which we attempt to forecast in arriving at our various estimates of stability or cloud updraft strength. The measurements of quantities such as in-cloud Theta-es, and updraft speeds by the instrumented Learjet are our most direct physical measure of the strengths of convection, at least during its early (cloud turret) stages. These same measures also constitute the most direct means of detecting small scale (cloud scale) terrain influences on convection.

An intensive search for terrain effects on clouds has been carried out using the cloud sample database and the digitized terrain file. Theta-es measured during cloud penetrations has been plotted against terrain height; Theta-es has been normalized by subtracting out Theta-e_{max} from the morning sounding; daily and mission averages have been subtracted. None of these manipulations has led to the detection of any coherent effect of terrain heights on cloud properties . This is true for in-cloud Theta-es, updraft speeds, water quantities of various kinds and FSSP and 2D concentrations. The only terrain height effect which has been seen is the large drop frequency effect described in Section 9.4 above.

In pursuing this attempt to see a terrain effect, a concerted effort was made to detect a consistent time effect on Theta-es in cloud. This appears to be weakly present, but so immersed in noise that it is not worth presenting.

This finding is preliminary, and further attempts will be made in future to discover meaningful influences of terrain height and configuration on cloud properties.

9.8 Variability of ice concentration in Nelspruit clouds (Morgan and Morrison)

The ice content of Nelspruit cumulus turrets is quite variable. This bears importantly on the question of seedability of these clouds and so it is important to display the variations that are observed.

Four temperature intervals, centred on -5, -10, -15 and -20°C, were selected and the Cloud Sample Database was searched for clouds (first passes only) with average vertical velocities greater than 2.5 m sec^{-1} (to ensure they are growing turrets). This produced a sample of 201 cloud passes.

Setting aside ambiguous cases, the remaining cases can be classed as containing ice or no ice, drops or no drops, ice only or drops only. Table 9.8.1 summarizes the results. One sees that some water drops are found even at -20°C, and that ice is found even at -5°C.

The cloud passes which contained only images which were unmistakably ice (image classes: large graupel, small graupel, ice) were then re-analysed to display the concentrations and variabilities. An examination of the data showed that the sample size was inadequate at -5°C (1 case) and at -20°C (5 cases) and that there was no strong trend with height (for example, the average total 2D concentration at -10° C was 20.5 l^{-1}, and at -15°C, 25.5.) so the results for the -8 to -17°C layer were combined in Table 9.8.2.

Table 9.8.1 The occurrence of 2D-C image categories as a function of temperature for growing cloud turrets (average vertical velocity 2.5 m sec^{-1}) sampled from 1981 to 1986. Total number of cloud penetrations, 201. Figures in () are percent

Degrees C	-3 to -7	-8 to -12	-13to -17	-18 to -22
no 2D-C images	3	27	10	1
graupel or ice	0	28	15	5
mixed ice and water	2	45	14	4
water drops	5	17	1	0
unclassified, zero images, streakers)	1	16	5	2
TOTAL	11	133	45	12
containing ice	2 (20)	73 (62)	29 (72)	9 (90)
containing no ice	8 (80)	44 (38)	11 (28)	1 (10)
TOTAL	10	117	40	10
containing drops	7 (70)	62 (52)	15 (37)	4 (40)
containing no drops	3 (30)	55 (48)	25 (63)	6 (60)
TOTAL	10	117	40	10
% no precipitation	(30)	(23)	(25)	(10)
% ice only	(0)	(24)	(37)	(50)
% water only	(50)	(15)	(2.5)	(0)

Table 9.8.2 The variability of ice concentration in clouds with average updraft speeds 2.5 m sec^{-1}, with 2D-C image classifications graupel and ice

	avg	max	std.dev	N
Average over cloud	20.3	137.1	29.3	52
Maximum over cloud	78.4	684.5	140.9	52
Average 0 images	6.1	50.3	10.8	52
Maximum 0 images	21.7	196.7	38.3	52
Average < 128 microns	10.4	79.0	17.2	52
Maximum < 128 microns	41.3	438.6	80.2	52
Average > 128 microns	10.5	61.7	12.9	52
Maximum > 128 microns	44.2	455.0	79.8	52
Average > 1067 microns	0.2	1.1	0.3	38
Maximum > 1067 microns	1.8	16.9	3.6	38

9.9 Empirical estimation of coalescence rate (Morgan and Morrison)

Coalescence is an important part of the precipitation formation process in all rain producing clouds in Nelspruit, and the dominant one in a large percentage of them. In Vol.II Section 5.6, and in Mather et al., (1986) it has been shown that the probability of encountering larger drops in cumulus turrets at the $-10^{o}C$ level can be predicted by a parameter based on the time of rise of a cloud parcel from cloud base to that level.

Here we wish to explore the possibility of expressing the degree of development of coalescence in a more quantitative way.

The detailed physics of coalescence is a complex one, and in fact the theoretical field cannot be considered settled. A good introduction to its state is given in an important study by Leighton and Rogers (1974).

We will examine the possibility of employing a very simple bulk parameterization of the coalescence process and of determining the coefficients of the parameterization empirically, using observations of cloud water content, updraft speed, and condensed water content (CWC).

9.9.1 A simple parameterization

The observations on which this study are based are those cloud passes in the neighbourhood of $-10^{o}C$ in which there were few or no 2D-C images and the total water content indicated moist adiabatic ascent from cloud base.

The parameterization we will test is based on a simple equation for the rate of change of cloud liquid water content, m, under the competing influences of condensation and coalescence. Coalescence is described in terms of two effects:

1. Cloud coalescence, described in the manner of Kessler (1969)

$$\left(\frac{dm}{dt}\right)_{cloud} = 0 \quad \text{for } m \leq 1.0 \text{ gm m}^{-3}$$
$$= B(m - 1.0) \quad \text{for } m > 1.0 \text{ gm m}^{-3} \qquad (1)$$

and

2. An interaction between the cloud (droplets less than 35 microns diameter) and the nascent precipitation (the coalescence products).

$$\left(\frac{dm}{dt}\right)_{coal.} = A(cwc-m)m \qquad (2)$$

The rate of change is

$$\frac{dm}{dt} = \text{cond.} - A(cwc-m)m - B(m - 1.0) \qquad (3)$$

where cond. is the condensation rate (Section 10.3). The problem now is the estimation of the constants

$A(g^{-1}\ kg\ sec^{-1})$ and $B\ (sec^{-1})$

This can be integrated over time, from cloud base to penetration level (subscript p denotes penetration level, b is base level)

$$m_p = \int_{t_b}^{t_p} \text{cond. } dt - A \int_{t_b}^{t_p} (cwc - m)m\ dt - B \int_{t_b}^{t_p} (m - 1.0)\, dt \qquad (4)$$

$$w_1 = w_s(T_1) \approx \varepsilon \frac{e_s(T_1)}{P} \tag{1}$$

The one gram of water is frozen, releasing 79.7 calories of heat, resulting in a new temperature, T_2, given by

$$T_2 = T_1 + \frac{79.7}{C_p d} = T_1 + 0.33°C \tag{2}$$

C_p is the specific heat of air at constant pressure

This first step temperature rise is not a function of P and T.

The parcel at this stage has a temperature T_2 and a mixing ratio w_s (T_1). It now undergoes a wet bulb process (see Rogers, 1979) which cools it to T_3 and restores saturation with respect to water.

The wet bulb process is described by

$$\frac{T - T_w}{w_s(T_w) - w} = \frac{L}{C_p} \tag{3}$$

which results in a temperature change, ΔT_2, given by

$$\Delta T_2 = \frac{e_{s_o} \varepsilon L}{C_p P} \left[\exp \frac{L}{R_v} \left(\frac{1}{T_o} - \frac{1}{T_3} \right) - \exp \frac{L}{R_v} \left(\frac{1}{T_o} - \frac{1}{T_1} \right) \right] \tag{4}$$

(2)

The net change in temperature then, is

$$\Delta T = \Delta T_1 - \Delta T_2 \tag{5}$$

For an arbitrary amount, m of water frozen, this becomes

$$\Delta T(m) = 0.33\ m - (2) \tag{6}$$

This is not linear in m because of the non-linearity of the wet bulb process.

The first term integrates to the condensed water content. We change time integration to integration over height by introducing

dt = dz/W, where W is the updraft speed

$$m_p = CWC_p - A\int_{z_b}^{z_p} \frac{(cwc - m)m}{W}\, dz - B\int_{z_b}^{z_p} \frac{(m - 0.5)}{W}\, dz \qquad (5)$$

We assume a linear updraft profile, with 1.0 m sec^{-1} at the cloud base.

$$W_{(z)} = W_b + \frac{(Wp - Wb)\,(Z - Z_b)}{(Z_p - Z_b)} \qquad (6)$$

w_b = 1.0 m sec^{-1}

$$T_z = T_p + \int_{z_p}^{z} \frac{dT}{dz}\, dz \qquad (7)$$

Calculation of dT/dz is described in Section 10.5

cond. = C.M. (P,T) W(Z) (8)

where C.M. is the condensation multiplier described in Section 10.3.

$$P(z) = P_p + \int_{z_p}^{z} \rho g\, dz = P_p + g\int_{z_p}^{z} \frac{P(z)}{R_d T(z)}\, dz \qquad (9)$$

$$CWC(z) = \rho_a\,(w_{sb} - w_s(z))$$

w_{sb} = (TWCMIX)$_p$; TWCMIX is the Total Water Mixing Ratio at penetration level (See Section 9.1) (10)

$$w_s(z) = W_{sp} - \int_{z_p}^{z} C.M.\, dz \qquad (11)$$

$$m(z) = \int_{z_b}^{z} C.M.\, dz - A\int_{z_b}^{z} \frac{(cwc - m)m}{W}\, dz - B\int_{z_b}^{z} \frac{(m - c)}{W}\, dz \qquad (12)$$

The cloud base is where

$$W_{sp} + \int_{z_p}^{z} C.M.\ dz = TWCMIX_p \qquad (13)$$

The constants are determined by running the integrations for a matrix of values for A and B.

We have tested this approach on a set of 24 cloud passes for which the 2D-C average total concentration was less than 5.0 l^{-1}. The result, not entirely satisfying, was that, though the average error in predicting m, the cloud liquid water content, could be reduced to just over 0.6 g m^{-3}, this occurred when the coefficient of the autoconversion term was 6.5 x 10^{-3} (compared with Kessler's value of 1.0 x 10^{-3}), and the interaction term was zero.

This would mean that the (invisible) droplets in the coalescence portion of the spectrum have not grown to such sizes as to collectively capture a significant amount of the cloud water.

The results were best for clouds with TWMR less than about 12.0 g kg^{-1}, suggesting that perhaps the role of the interaction is more important in warmer clouds with more water at play, but requires a more complex form than we have given it.

We will continue to pursue this approach to the study of coalescence, as it will be important to be able to predict the coalescence development as it can be described by our measured quantities.

9.10 Aircraft observations of target turrets on multi-cellular storms showing radar response to dry ice seeding (Morrison, Mather and Morgan)

9.10.1 Introduction

Microphysical and radar studies of natural and experimentally seeded storms and an Exploratory Randomized Seeding Experiment (ERSE) began in October 1984. To date (early March, 1986) 98 convective complexes developing within 100 km of the project C-band radar near Nelspruit have been selected by the objective criteria of the ERSE randomization procedures; of these 48 have been seeded with dry ice pellets and 50 have not been seeded. Of the unseeded cases 23 have been sampled by the aircraft and 27 have not been touched.

Preliminary analyses using re-randomization techniques indicate an overall net positive radar response to seeding.

The objective of the ERSE was to generate a sample of randomly selected seeded and unseeded storms upon which to perform analyses which would lead to the definition of hypotheses and procedures for a subsequent confirmatory experiment. This exploratory study is a first attempt to compare aircraft observations of target cloud turrets on seeded storms that show an apparent positive radar seeding response to those storms that show no or negative responses.

9.10.2 General characteristics of target clouds

Newly developed cumulus congestus turrets rising vigorously through the -10°C level are targetted for seeding and/or sampling by the project Learjet aircraft. The turrets on the selected storms must show no signs of glaciation, have firm and well defined bases, and must not be excessively sheared.

Studies conducted prior to the ERSE by CIC and SWA showed that the target turrets contain large amounts of supercooled water, frequently in excess of 1.5 g m^{-3} at -10°C. The concentrations of natural ice in these turrets is relatively low with average 2D-C concentrations of particles greater than 105 microns of about 7 per litre. The predominant ice particle habit is well rimed graupel. Pristine ice crystals are rarely observed. Cloud base temperature is highly variable between about 7 to 16 °C, generally averaging around 14°C at an altitude of 2 km AMSL with an average mixing ratio of 13 g kg^{-1}. Vertical air velocities average 3.5 m s^{-1} with updraft around 12 m s^{-1}.

9.10.3 Radar response to seeding

The radar analysis technique and results are detailed in Dixon (1986). The storm track property selected for this study is a relative echo height change parameter (EHC) defined as :

$$EHC = \frac{EHEIGHT\ 1 - EHEIGHT\ 0}{MAX\ (EHEIGHT\ 0,\ EHEIGHT\ 1)}$$

where EHEIGHT 0 = Height of the 30 dBz echo at storm selection time

EHEIGHT 1 = The maximum height of the 30 dBz echo from 5 to 30 minutes after storm selection time

This is simply the difference between the maximum 30 dBz echo top height measured from 5 to 30 minutes after "decision time" and the 30 dBz echo height at decision time divided by the maximum value of the two parameters. If the echo top height does not change within the given time "window", the statistic has a value of 0, if the 30 dBz echo top height increases it is positive, if it decreases it is negative.

The distributions of EHC for 41 NO-SEED case tracks and 35 SEED (as of February 1986) case tracks is shown in Figure 9.10.1. Of the SEED cases, 79% have values greater than or equal to 0.05 compared to 41% of the NO-SEED cases. Values of 1.00 can occur if the maximum echo reflectivity did not exceed 30 dBz at decision time. Similarly, values of -1.00 can occur if the maximum echo reflectivity dropped below 30 dBz in the 5 to 30 minute window after decision time. For all valid case tracks up to 17 January 1986 the difference in EHC between the seeded and unseeded storms is significant at a p-value of 93%, the difference being tested by re-randomization.

NO-SEED cases (n=41)					SEED cases (n=35)		
60%	30	0		0	30	60%	
n							n
2	.	**	1.00	*****	.	.	5
1	.	*	0.30 to 0.35		.	.	
3	.	***	0.25 to 0.30	.	.	.	
2	.	**	0.20 to 0.25	**	.	.	2
4	.	****	0.15 to 0.20	**********	.	.	9
5	.	*****	0.10 to 0.15	***	.	.	3
	.		0.05 to 0.10	*****	.	.	5
7	.	*******	0.00 to 0.05	****	.	.	4
2	.	**	-0.05 to 0.00	**	.	.	2
5	.	*****	-0.10 to -0.05	**	.	.	2
3	.	***	-0.15 to -0.10	**	.	.	2
3	.	***	-0.20 to -0.15		.	.	
1	.	*	-0.25 to -0.20		.	.	
1	.	*	-0.30 to -0.25	*	.	.	1
1	.	*	-0.35 to -0.30		.	.	
1	.	*	-1.00		.	.	

Fig. 9.10.1. Distribution of EHC for no seed and seed cases.

For the analysis presented in this paper, the EHC parameter was chosen as a means of testing for possible dynamic seeding effects. The values of EHC for all the SEED cases were ranked from highest to lowest. The five values of 1.00 were rejected leaving 30 values from 0.248 to -.285. The ranked values were divided into thirds so that the top ten cases were selected as the "best" seed cases possibly due to a dynamic seeding response and the bottom ten cases selected as the "worst" seed cases exhibiting an apparent nil or negative response. The range of EHC for the "best" cases is 0.248 to 0.150 and for the "worst" cases range from -0.285 to 0.016. The aircraft data for the "best" cases were then compared to the "worst" cases to search for any significant differences between the two data sets that might provide some support for the presence or absence of a dynamic seeding response.

9.10.4 Aircraft measurements

Summary data and derived parameters for each cloud penetration are stored in a Cloud Sample Database (Section 10.2 of this volume) on disk in the project MV4000 computer. Currently, over 170 parameters are stored in the database for each penetration. A partial list of the major categories of

parameters is shown in Table 9.10.1.

Table 9.10.1 Major Categories of Cloud Sample Database Parameters

1. Identification
2. Seed/No-seed parameters
3. Aircraft position
4. Terrain beneath a/c position
5. Cloud dimensions
6. Environmental state parameters
7. Cloud state parameters
8. Liquid water contents
9. Total and condensed water contents
10. Vertical air velocity parameters
11. Turbulence
12. FSSP particle concentrations and sizes
13. Aircraft radar parameters
14. 2D-C particle concentrations and sizes
15. Vertical fluxes of various thermodynamic and particle parameters
16. Data management parameters.

9.10.5 Data analysis

After a storm has been selected as a SEED/SAMPLE case the Learjet commences seeding runs through the growing turrets at around the $-10^{o}C$ level. Usually the aircraft simultaneously samples the cloud during these penetrations to document the untreated cloud state. The turrets are seeded only once although they may be re-penetrated by the Lear for "post-seed" samples. In the present analysis, the database parameters for the first runs on each sampled turret in the 10 "best" and 10 "worst" seed cases are compared. This amounts to 40 turrets in the "best" cases and 43 in the "worst" cases.

Some of the database parameters show no significant differences between the two data sets. These include cloud length (approx. 3 km), adiabatic water mixing ratio (approx. 12.6 g kg^{-1}), average downdraft speed (approx. 2.5 m s^{-1}), and average turbulance dissipation (approx. 830 cm^{2} s^{-3}).

A large number of parameters however, did show some important differences. A list of some of the more interesting parameters in this category is given in Table 9.10.2.

One important difference is the apparent presence of higher supercooled liquid water in the "best" cases. JW measurements of liquid water between the two data sets show little difference, but, as already pointed out, the JW probe has proved to be inadequate in the high liquid water environments encountered in these clouds. The King-CSIRO probe, however, shows a clear tendency for the "best" cases to have greater liquid water contents.

Further support for the creation of conditions conducive to higher water contents can be implied from some of the other parameters. On average, vertical air velocities in the "best" cases are lower permitting more time for particle growth. This is further borne out by the lower cloudy air buoyancy computed for the "best" cases (difference between environmental virtual temperature and cloud virtual temperature). Additionally, the average cloud saturated equivalent potential temperature is nearly 2.5 degrees higher in the "best" cases which can imply a warmer cloud base neglecting any ice formation. There is also some evidence that the "best" suffer less entrainment than the "worst" cases. The difference between the maximum cloud saturated equivalent potential temperature and cloud base equivalent potential temperature computed from the Learjet upsounding at the start of a mission is less in the "best" cases which can imply turret cores closer to adiabatic conditions.

Table 9.10.2 Selected parameters showing significant differences between the "best" and "worst" cases.

Parameter (units)	"Worst" Cases n	avg value	"Best" Cases n	avg value
Avg cloud θ_{es} (K)	43	341.0	40	343.4
Max cloud θ_{es} - cloud base θ_e (K)	43	- 2.3	40	0.4
Excess Tv (C)	43	0.6	40	0.1
Max CSIRO- King LWC (g m^{-3})	20	2.14	28	2.55
Avg vertical air velocity (m s^{-1})	42	5.0	38	2.8
Max vertical air velocity (m s^{-1})	42	14.0	38	11.0
Avg FSSP particle conc (cm^{-3})	43	305	40	265
Avg. FSSP conc in 32-47μm range (cm^{-3})	43	0.929	40	1.499
Avg FSSP mass-weighted mean dia (μm)	43	21.5	40	23.1
Max aircraft radar reflectivity(dBz)	43	10.3	40	23.9
Avg 2D-C total particle conc (litre^{-1})	36	13.2	39	33.2
Max 2D-C total particle conc (litre^{-1})	36	37.2	39	131.2

Given that the liquid water content is higher in the "best" cases, how does this extra water manifest itself? We can first examine the liquid water in the small cloud droplet range as measured by the FSSP from 2 to 47 microns. The liquid water content integrated over the range of the FSSP does not show much change between data sets (averaging about 1.1 g m^{-3}) despite the fact that the average total concentration is somewhat less in the "best" cases. The increase in FSSP mass weighted mean diameter and the increase in particle concentrations at the high end of the FSSP spectrum from 32 to 47 microns (Table 9.10.2) suggests a shift in the size distribution of liquid water drops away from the small cloud droplet range.

The 2D-C array imaging probe data show a nearly three-fold increase in average total particle concentration in the "best" cases. Interestingly enough, much of this increase in concentration occurs in the lower range of the probe below particle diameters of about 130 microns. Unfortunately, for these

small sizes, it is very difficult to distinguish between graupel and water drops by visual inspection of the 2D-C images. However, clear images of some water drops greater than about 300 microns are observed in 35% of the turrets in the "best" cases compared to 15% of the turrets in the "worst" cases. It is therefore possible that some of the extra supercooled water observed in the "best" cases is in the higher end of the cloud droplet spectrum.

Further evidence arguing for the presence of liquid water in the form of large cloud droplets is seen when examining the difference in maximum aircraft radar returns for the "best" versus the "worst" cases. The maximum reflectivity observed in penetrations in the "best" cases is better than double that of the "worst" cases. The implication is that the observed higher reflectivities may be due to higher concentrations of large cloud droplets in the "best" cases.

The presence of higher concentrations of large supercooled cloud droplets in the "best" cases would be consistent with a dynamic seeding response. Lamb, Hallet and Sax (1981) have shown that maximum latent heat release available for dynamic invigoration of deep convective clouds can be crucially dependent on the presence of large supercooled water droplets.

9.10.6 Conclusions

In an exploratory investigation a radar measured storm track property which may help to identify possible dynamic seeding effects was used to group aircraft observations of cloud turrets prior to seeding into cases showing an apparent dynamic response and cases showing a nil or negative apparent response. Comparison of the two sets of aircraft observations strongly suggests that the cases with an apparent positive response had lower vertical air velocities, warmer cloud bases, and higher concentrations of supercooled liquid water possibly in the form of relatively large cloud droplets.

Further analyses will be made along these lines using other radar storm track properties and also to test the NO-SEED/SAMPLE data set as a control. The environmental characteristics on days with "good" and "bad" cases will also be examined.

9.11 Heating of cloud air by the freezing of the large diameter fraction of the condensed water content. (Morgan and Morrison).

The calculation of the maximum possible temperature increase due to the freezing of supercooled water is described in Section 10.6. The equation shown there has been used to calculate this quantity for each applicable cloud pass and the results have been entered into the cloud sample database.

We are not at present able to deal with problems related to the rate at which drops freeze, so the following estimates of temperature increase must be considered upper estimates. The calculations were done on the assumption that the water which can be most quickly frozen is the particles with diameters larger than those sensed by the FSSP or the JW. This is estimated as the difference between the CWC mixing ratio minus FSSP liquid water mixing ratio. If this difference is assumed to be all liquid then it is the amount entered into the temperature change equation. The 2D-C image classes: No data, Rain and Water Drops correspond to this case. For other classes, fractions of the difference were assumed to be freezable. For Mixed BD, 75% was frozen and for Graupel BD, 50% was frozen. Figure 9.11.0 shows the distribution of temperature changes for those passes in the 1985/86 season for which the calculations could be made. Sixty additional cloud passes gave a value of zero due to the 2D-C image class indicating graupel or mixed water and ice. We did not venture to assign a freezable fraction value to this class of image.

These estimates of temperature change are based on CWC and FSSP LWC which are averaged over each cloud pass. They nevertheless yield values which would be significant. These changes should be viewed against the background of the observed buoyancies (Vol. II, Section 5; the values of buoyancy shown are also averages over each pass) which tend to be quite low.

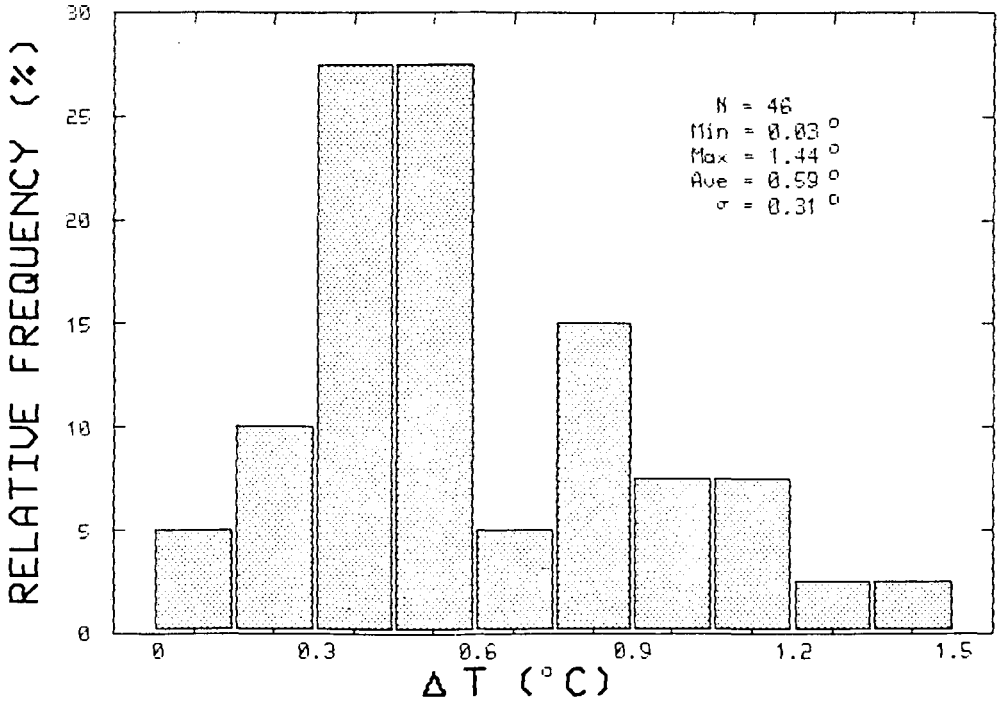

Fig. 9.11.0. Calculated temperature rise due to freezing the large diameter of the liquid water.

10.0 DETAILS OF CALCULATIONS

10.1 Calculations of the condensation rate (Morgan and Morrison)

The condensation rate (g kg^{-1} sec^{-1}) for a moist adiabatic ascent is given by

$$\frac{dm_c}{dT} = -\frac{dw_s}{dT} = -W\frac{dw_s}{dZ} \qquad (1)$$

where W is the updraft speed (m sec^{-1}) and m_c is the cloud water mixing ratio. dw/dz, which we call the condensation multiplier, can be computed assuming that for moist adiabatic ascent, the static energy per unit mass, σ is constant, and

$$\sigma = \text{const.} = CpT + LW_s + gz$$

$$d\sigma = 0 = CpdT + Ldw_s + gdz \qquad (2)$$

With the aid of the definition of W_s ($W_s = \epsilon \sigma s/p$), the hydrostatic equation and the Clausius-Clapeyron equation, this results in

$$\frac{dw_s}{\partial z} = \frac{g\varepsilon}{PR_d}\frac{(611)\exp\left[\frac{L}{R_v}\left(\frac{1}{273}-\frac{1}{T}\right)\right]\left(CpR_vT - R_dL\right)}{\left(CpR_vT^2 - \frac{L^2\varepsilon}{P}(611)\exp\left[\frac{L}{R_v}\left(\frac{1}{273}-\frac{1}{T}\right)\right]\right.} \qquad (3)$$

This is just a function of temperature and pressure. To display this, we have put isolines of the condensation multiplier on Thetaplot, in place of saturation mixing ratio lines. This appears in Fig. 10.1.1.

The condensation rate is an important quantity in the microphysics of cumulus clouds. The amount of water condensed in moist adiabatic ascent is, of course, strictly a function of vertical displacement. The rate of displacement plays an important role in precipitation development since it is proportional to the rate at which cloud water is made available for precipitation growth. The sweep up of cloud by larger particles, however, is at any instant independent of the rate of vertical displacement.

Rapid precipitation growth can lead to exhausting the cloud water if the condensation rate is not such as to replenish it at a pace as great as its depletion.

Figure 10.1.2 shows the range of values of condensation rate estimated from flight level temperature, pressure and vertical velocity over the entire 1984-85 cloud sample of the season. Values fall over a wide range, from -.022 to + .047 g kg^{-1} sec^{-1}.

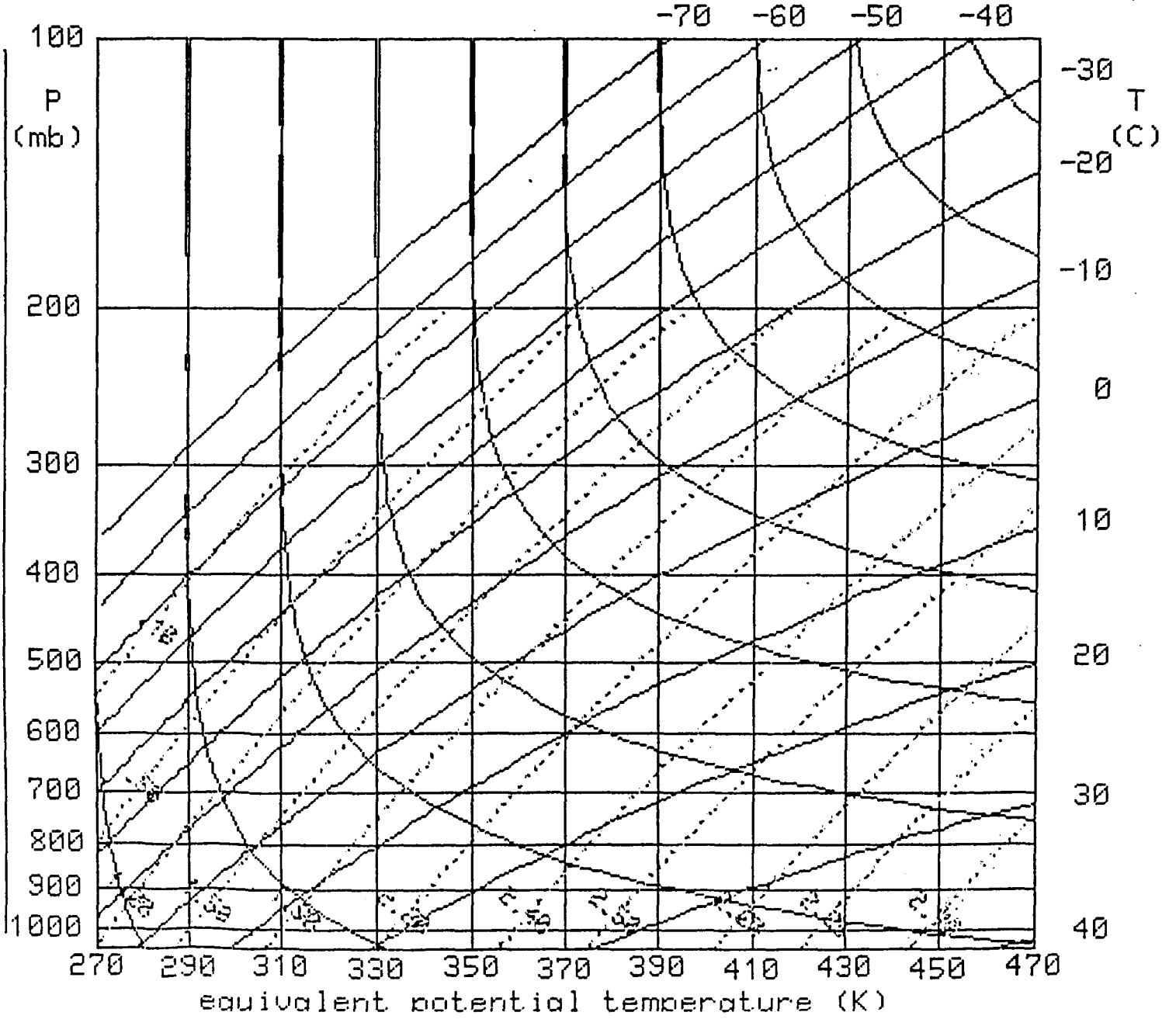

Fig. 10.1.1. The condensation multiplier plotted on Thetaplot, in place of the saturation mixing ratio. Values are multiples of 10^{-3} g kg^{-1} sec^{-1}.

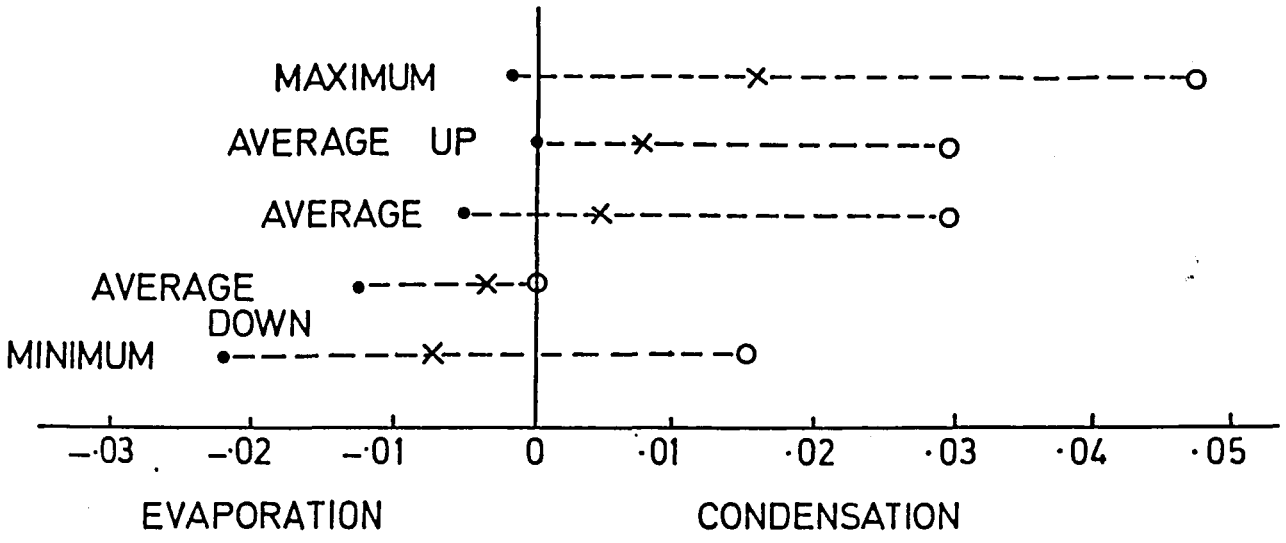

Fig. 10.1.2. Estimates of condensation rates (g kg^{-1} sec^{-1}).

On a very few passes, the average condensation rate was actually negative (evaporation).

Condensation rates in the updrafts were generally stronger than were the evaporation rates in the downdrafts, reflecting the relative strength of updraft and downdraft observed at our penetration altitudes.

10.2 Calculations of vertical fluxes (Morgan and Morrison)

Vertical fluxes of several quantities measured in cloud by the aircraft have been calculated and some of these require assumptions which cannot be rigorously defended.

Point flux values are straightforward and are all of the form:

$$F_p = P \rho_a W \qquad (1)$$

where F_p is the flux property P which can be in the form of a mixing ratio or a density.

We have also calculated total fluxes based on the assumption that the measured profiles of the vertical velocity and the property are representative random samples of a cloud which is not radially symmetric. The total flux of property P is then

$$F_p = P \rho_a W \cdot \frac{\pi}{4} D^2 \qquad (2)$$

where D is the diameter of the cloud, assumed circular. D is determined from the true air speed (TAS) and the time in cloud. Single estimates of F determined in this way can be greatly in error, but a large number of such estimates will allow us to gain a "feel" for the typical magnitude of these fluxes and their variations in the vertical.

The histograms of Fig. 10.2.1. show the distributions of the fluxes of water vapour (tons per sec) and of air (in kilotons per sec). The analysis also presents the important fractions of the various fluxes, the up flux, and the down flux.

10.3 Calculations of the variations of temperature with pressure on a moist adiabat (Morgan and Morrison)

The aircraft experiences vertical displacements as it traverses a cumulus cloud. These result in difficulties in trying to estimate the buoyancy from the temperature profile as plotted in time-history format. It is convenient, then, to correct for these height displacements and graph out a profile of the temperature which is corrected to the pressure at the beginning

tons/s		0 25 50 75 100 %			
(=	-100.00	I*	1	N	205
-100.00 to	-50.00	I*	3		
-50.00 to	.00	I********	31	Minimum	-113.87
.00 to	50.00	I**********	95		
50.00 to	100.00	I**********	40	Maximum	551.63
100.00 to	150.00	I***	15		
150.00 to	200.00	I*	5	Average	55.31
200.00 to	250.00	I**	7		
250.00 to	300.00	I*	2	Std Dev	86.43
300.00 to	350.00	I*	3		
350.00 to	400.00	I*	1	Skewness	2.294
)	400.00	I*	2		

170 Vapor flux

ktons/s		0 25 50 75 100 %			
(=	-30.00	I			
-30.00 to	-20.00	I*	3	N	205
-20.00 to	-10.00	I**	7		
-10.00 to	.00	I******	27	Minimum	-29.67
.00 to	10.00	I**************	76		
10.00 to	20.00	I*******	34	Maximum	141.24
20.00 to	30.00	I******	29		
30.00 to	40.00	I***	13	Average	14.71
40.00 to	50.00	I*	2		
50.00 to	60.00	I*	4	Std Dev	23.16
60.00 to	70.00	I*	2		
)	70.00	I**	8	Skewness	2.340

171 Air mass flux

Fig. 10.2.1. Frequency distributions of the fluxes of water vapour (tons per sec) and of air (kilotons per sec).

of the traverse. For this we require the temperature as a function of pressure along any moist adiabat. This is easily derived by using the static energy as the characteristic value of the moist adiabat (see equation 2, Section 10.1). Making use of the Clausius-Clapeyron equation, the equation of state, and the hydrostatic equation:

$$\frac{\partial T}{\partial P} = \frac{1}{P}\left(\frac{LW_s + RT}{Cp + \frac{W_s L^2}{R_v T^2}}\right) \qquad (1)$$

This is used at every point of the traverse to correct the temperature to the pressure at the beginning of the record.

10.4 Aircraft sounding frost points and dew points (Morgan and Morrison)

The Cambridge dew point sensor on the Lear measures dewpoint (T_d) in the lower part of the atmosphere but measures frost point (T_f) when the dew point is below 0 degrees C.

T_f is a higher temperature than T_d and will yield for example, higher mixing ratios if it is treated as dewpoint in the sounding programme. This can be allowed for in several ways, but we have chosen to calculate T_d given T_f.

A first order correction factor for converting frost point values to dew points has been added to the aircraft sounding software.

The correction is as follows:

$$\frac{T_d}{T_f} = \frac{L_{cond}}{T_f\left(\frac{L_{cond} - L_{sub}}{273}\right) + L_{sub}} \qquad (1)$$

The correction is not exact due to our use of Clapeyron's equation and constant values of Lc and Ls. We have introduced values valid at $-10^{o}C$, taken from a standard text.

The introduction of frost points into the calculations only extends the usefulness of the Cambridge dewpointer down to about $T_d = -10^{o}C$.

10.5 Engine vapour signal processing (Morrison)

Lyman-alpha hygrometry is based upon the absorption of monochromatic radiation in the absence of scattering as described by Beer's law (Buck, 1976). This can be expressed as

$$I = I_o \exp(-k\rho x/\rho_o) \qquad (1)$$

where I = received intensity of radiation at wavelength

I_o = transmitted intensity

k = absorption coefficient of the gaseous medium at wavelength i

ρ = density of the gaseous medium

X = length of the absorbing path

ρ_o = density of the gaseous medium at standard temperature and pressure (0°C, 1013 mb)

At the Lyman-alpha line wavelength of 121.56 nm the only significant absorbing gases in the troposphere are water vapour and molecular oxygen. In the current application of sampling bleed air from the 8th compressor stage of the turbojet engines a hydrocarbon contaminant is apparently also acting as an obsorber. After replacing I and I_o by their sensed voltage equivalents, we may rewrite equation (1) as :

$$V = V_o \exp[-(k_{H_2O} \rho_{H_2O} x/\rho_{oH_2O}) - (k_{O_2} \rho_{O_2} x/\rho_{oO_2}) - (k_{cont} \rho_{cont} x/\rho_{ocont}) \qquad (2)$$

where V_o is system gain proportional to I_o, window transmission, and detector quantum efficiency, and V is the sensed voltage analogue output from the Lyman-alpha. The subscripts H_2O, O_2, and cont refer to water vapour, molecular oxygen, and bleed air contaminant, respectively. Solving (3) for water vapour density we get:

$$\rho_{H_2O} = \left[\frac{\rho_{oH_2O}}{k_{oH_2O}x}\right]_A \ln V_o - \ln V - \left(\frac{k_{O_2}\rho_{O_2}^x}{\rho_{oO_2}}\right)_B - \left(\frac{k_{cont}\rho_{cont}^x}{\rho_{ocont}}\right)_C \qquad (3)$$

The three unknowns in equation (3) (c) are system gain (term A), oxygen absorption (term B), and contaminent absorption (term C). The system gain term can easily be determined by flushing the Lyman-alpha with nitrogen so that the density of each absorbing gas is zero and $\ln V_o = \ln V$

The oxygen absorption term can be well estimated by computing the density of molecular oxygen, using the ideal gas law.

In the well mixed troposphere the partial pressure of oxygen can be taken to be the molar fraction of oxygen in air or 21% of total ambient pressure.

The contaminant absorption term, however, is an unknown which cannot currently be computed in a straightforward fashion. It appears to be a function of bleed air flow through the Lyman-alpha and the temperature in the bleed air system which are controlled by engine power setting, pressure altitude and the control settings for wing heat, nacelle heat, and air flow. Lacking explicit definition of this term, we are forced to calculate it implicitly through baselining of the Lyman-alpha against the EG & G dewpoint hygrometer. The main drawback of this method is that, although the EG & G dewpoint hygrometer has a reasonable accuracy, its time response at relatively cold temperatures is poor, particularly after large altitude changes or cloud penetrations. However, if sufficient time has passed to obtain a reliable dewpoint measurement at penetration altitude and if the aircraft is operated in cloud penetration configuration, then the contaminant term can be computed in the sub-saturated air just prior to penetration in the following manner.

The ambient air mixing ratio, is computed from pressure and dew point. Then, since the mixing ratio of water vapour in the Lyman-alpha cell is the same as that in the free air, the vapour density in the cell is given by:

$$\rho_{H_2O} = W\rho_d \qquad (4)$$

where ρ_d = density of dry air in Lyman-alpha cell

The dry air density in the Lyman-alpha cell is simply computed using the ideal gas law.

The temperature and pressure in the Lyman-alpha cell are measured using a thermocouple and pressure transducer. Then, the contaminant term can be obtained from equation 2.

The programme LYAL-BASELINE computes terms A, B, and C using the first two seconds of clear air data prior to a cloud penetration or using data from a straight and level baselining file. The system gain (term A) and the contaminant (term C) are then combined into a single offset term which can then be used in the data processing subroutine LYMAN-ALPHA in programme ULTRADAS using the formula derived from equation (3).

$$\rho_{H_2O} = \frac{\rho_{oH_2O}}{k_{oH_2O}{}^{x}} \left[\text{OFFSET} - \ln V - \left(\frac{k_{O_2} \rho_{O_2}{}^{x}}{\rho_{oO_2}} \right) \right] \qquad (5)$$

where OFFSET = term A - term C

Once the vapour density in the cell is computed the mixing ratio is calculated to give the total water content of the environmental air. The results from this approach seem satisfactory. However, it is desirable to control or quantify the bleed air contamination to eliminate the need for baselining against the EG & G dewpoint hygrometer.

10.6 Calculations of the heating of air by the freezing of supercooled water in it (Morgan)

The release of the latent heat of fusion by the freezing of supercooled water is the primary concept underlying the dynamic hypothesis for ice phase rainfall stimulation. It is well known that the temperature of water rises as it freezes due to the release of about 80 calories for each gram of water frozen.

The heating of the air by the freezing of supercooled water contained in it is slightly more complex than just the liberation of a certain amount of heat. The heat must be diffused into the air and a certain amount of water must be evaporated to restore the air to saturation.

The process can be broken down into two steps. First, the heat released by the freezing is thoroughly mixed with the air (ignoring the temperature dependence of the latent heat and the heat content of the condensed phases) producing a warmed and unsaturated air parcel. Then water is evaporated into the air to bring it to saturation, according to a wet bulb process. This results in less heating of the air than would result from the first step alone, due to the latent heat absorbed in evaporating the water. Our calculations will assume that enough cloud water remains at all times to maintain saturation with respect to water (the calculation can easily be done assuming saturation over ice).

Consider a water-saturated cloud parcel containing one kilogram of dry air, m grams of cloud water and one gram of water which is to be frozen. The initial temperature and pressure of the parcel are P and T_1. Its mixing ratio is

10.7 Calculations of cloud virtual temperature; the effect of condensed water content on density and buoyancy (Morgan)

Condensed water in cloudy air consists of particles falling at their terminal velocities. Terminal velocity is that fall speed at which the particles exert a drag on the air equal to their weight. Thus they contribute their weight to the weight of the whole and contribute to the total density of the air. We can take account of this in displaying temperature profiles in clouds by calculating a cloud virtual temperature, analogous to the way the effect of water vapour is accounted for by means of the conventional virtual temperature.

Cloud virtual temperature is defined as :

$$T_{cv} \equiv \frac{P}{R_d \varrho} \qquad (1)$$

where T_{cv} = cloud virtual temperature

P = pressure

ϱ = density (air plus condensate)

R_d = gas constant for dry air

using the ideal gas law and

$$T_v = T(1 + 0.61\ w) \qquad (2)$$

where

w = mixing ratio

T_v = virtual temperature

we can derive:

$$T_{cv} = T\left[\frac{1}{w_c + (1 + 0.61w)}\right] \qquad (3)$$

(w_c = cloud water mixing ratio)

10.8 Cloud measurement and tracking with the video camera aboard the Lear 24

The Lear 24 has been equipped with an experimental video camera and recorder which is being evaluated for several tasks:

1. Measurement of cloud dimensions (heights, widths, etc) and locations

2. Recording the character of objects (drops, graupel) striking the windscreen during cloud penetrations

3. Recording the character of ice build up on parts of the aircraft

4. Assembling case studies.

Perhaps the most important of these will be (1) and this section covers the overall procedures for carrying out the cloud measurements.

The following photogrammetric techniques are first approximations and are not intended to be high precision. An evaluation of the errors is under way.

The following calculations ignore the drift of the aircraft and the movements of the clouds over short time intervals. Aircraft drift and cloud movement are not wholly independent and there should be some compensation between them.

We are using these techniques to track and monitor development of entities which are characteristically 5 km in diameter and separated from each other by that distance and more, most of the time. These techniques are adequate to maintain separate and distinct records of these entities, give a reasonable record of their developments and movements, and assure that, on returning to a cloud tower a short time after first penetration, the aircraft is operating on the same tower.

10.8.1 Video equipment

The camera and recorder set up which we have mounted on the Lear has a zoom system and automatic focus feature. It also incorporates a small keyboard for titling and an elapsed time feature which gives the time from recorder turn-on in hours, minutes, seconds and tenths of seconds.

A video monitor is used for viewing the recorder tapes after flight missions. The camera is mounted close to the windscreen on the copilot's side of the aircraft, pointing forward and close to level. The recorder is mounted on the bulkhead just behind the pilot.

The DAS system records clock time and is sychronized to the radar computer clock. At take off the DAS recorder is turned on for the climb out sounding just prior to starting to roll, and the video recorder is turned on at the same instant. In this way, the elapsed time can be converted to clock time simply by adding the time of start of the sounding file on the DAS tape.

10.8.2 Measurement of height of cloud tower about to be penetrated

Fig. 10.8.1 shows the geometry of the measurement of cloud top height for this simplest case. The measurement time is chosen by the tape analyst and the times are taken from the sound channel of the video tape. A histogram of these measurements is shown in Fig. 10.8.2.

10.8.3 Measurements on clouds off the line of flight

Fig. 10.8.3 shows the geometry for making height measurements on clouds off the line of flight (and not penetrated).

10.8.4 Determination of cloud positions

The Lear is tracked by the ground radar by means of a transponder system. Position estimates are updated each time the radar beam sweeps the aircraft, and are recorded on the same tape as the radar data. With the position and heading of the aircraft known, and knowing the bearing and distance of the storm from the aircraft as described in Fig. 10.8.3, the ground position of the cloud can be determined. This is shown in Fig. 10.8.4. The heading of the aircraft is not at the moment directly recorded (this is planned) and must be read onto the video sound track by the pilot.

A computer programme has been prepared which allows entering measurements of bearing angles (vertical and horizontal), elapsed times, headings, altitudes and airspeeds into a file which then computes the various calculated aircraft heights and positions.

10.8.5 The screen overlay for measuring angles

The angle measurements necessary for the above calculations are made with the aid of a ruled transparent overlay on the TV screen. This overlay was prepared by recording a scene on the tape and measuring the bearing angles of points in the scene with a theodolite colocated with the camera. Then, with the scene on the screen the values of the angles are plotted on the screen and the grid interpolated from the plotted points. Further corrections are added by video taping a regular grid and measuring the resulting distortions on the screen during playback. It is planned to carry out the same process with the camera in place on its fixed mount in the Lear, so as to allow for correcting for all the optical and video distortions, including those introduced by the windscreen of the Lear.

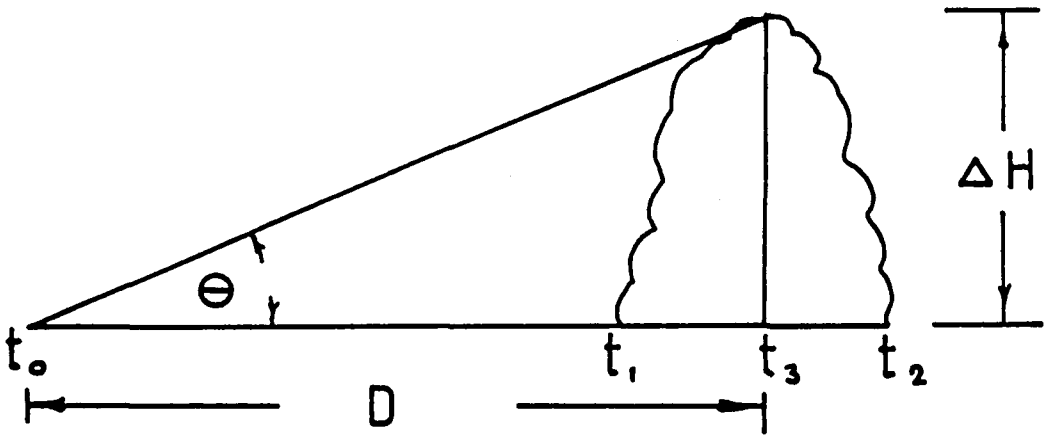

Θ = elevation angle of cloud top at t_o

t_o = time of angle measurement

t_1 = time of cloud entry

t_2 = time of cloud exit

t_3 = centre time of pass = $\frac{t_1 + t_2}{2}$

D = distance from point of angle measurement to centre of cloud
= TAS x $(t_3 - t_o)$

Δ H = height of cloud top above flight level
= D tan Θ

H = cloud top height
= ALT + Δ H

Fig. 10.8.1. Geometry of the measurement of cloud top height from the Learjet.

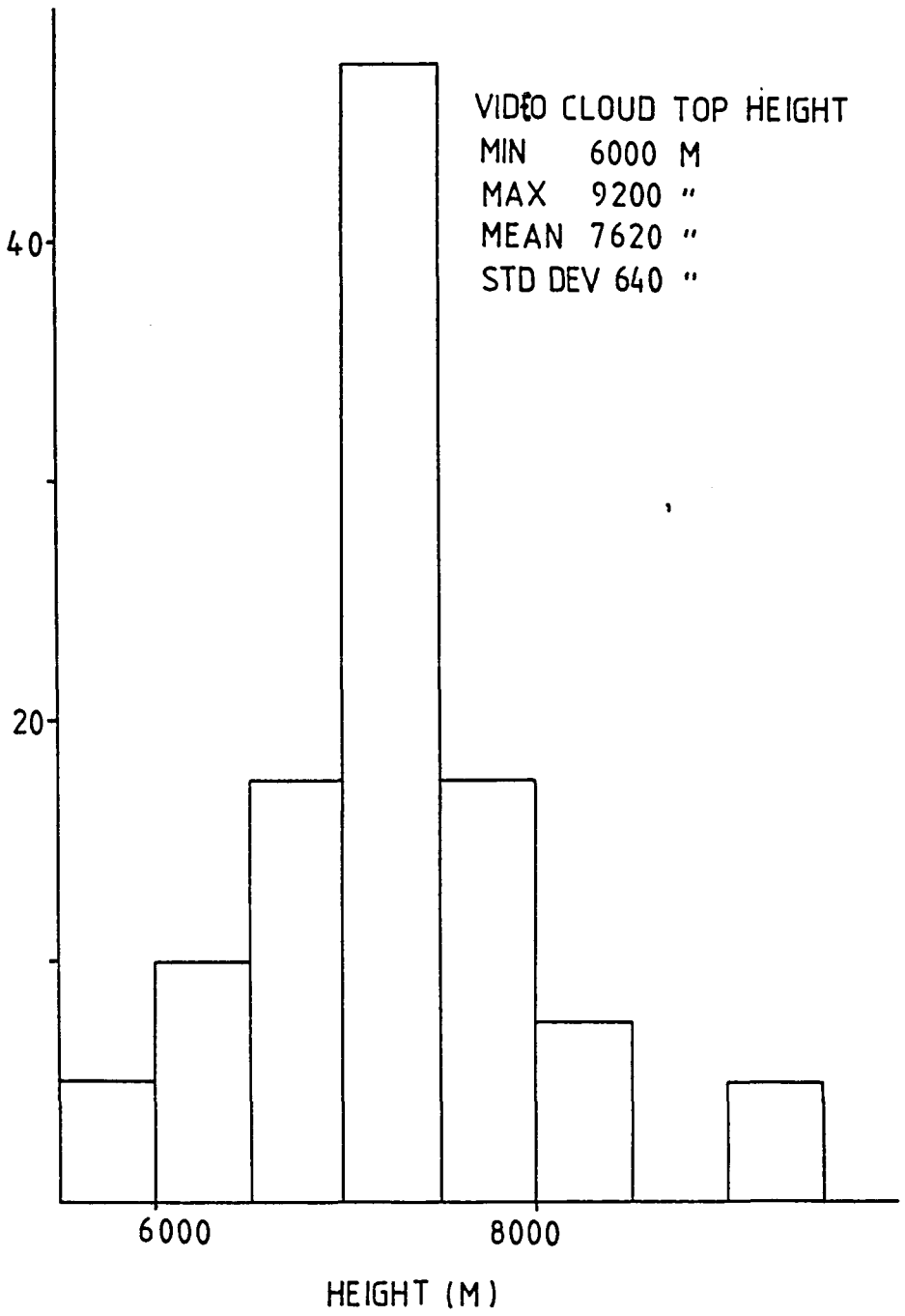

Fig. 10.8.2. A summary of measurements of cloud top heights determined from the cockpit video.

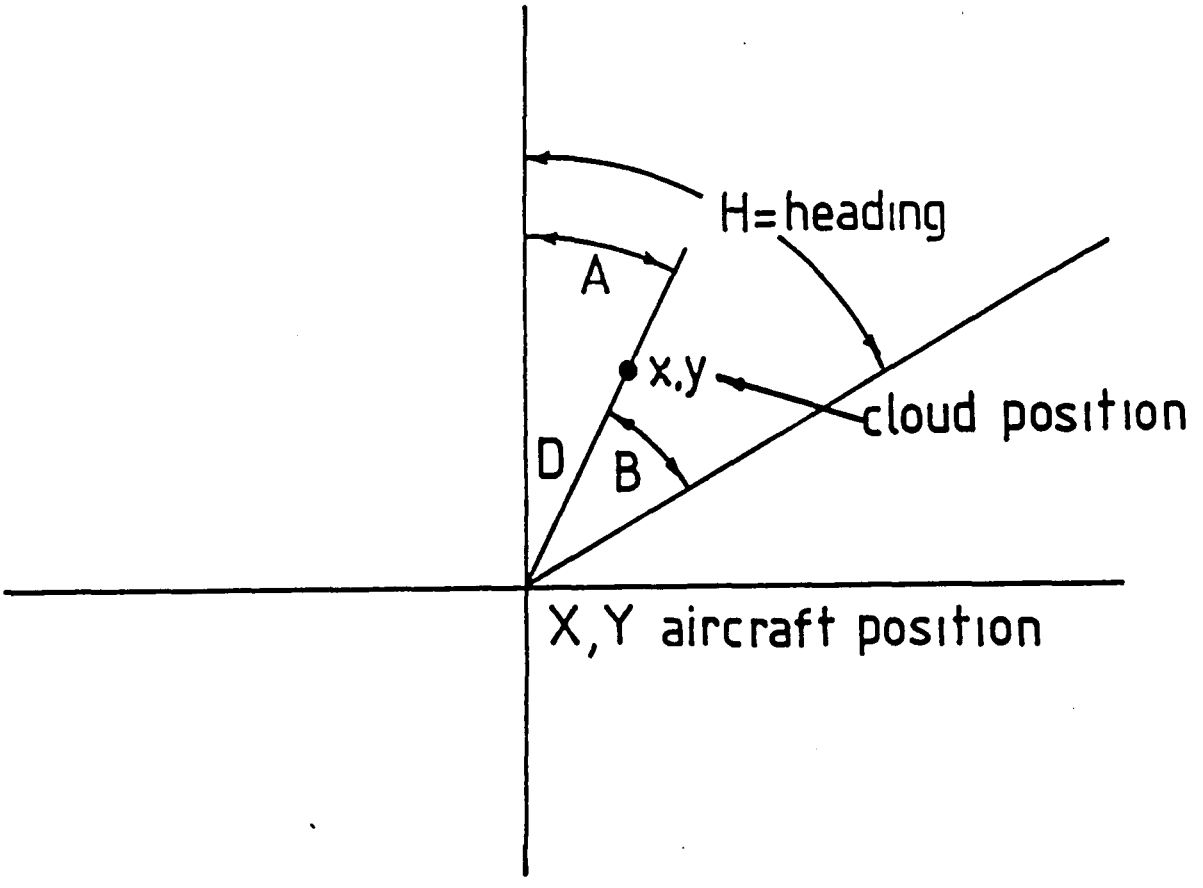

x, y	= cloud position
X,Y	= aircraft position
A	= H + B (B negative left, positive right) = true azimuth of cloud from aircraft, X,Y
x	= X + D sin A
y	= Y + D cos A
D	= distance from aircraft to cloud

Fig. 10.8.3. Geometry of making estimates of cloud top heights off the line of the aircraft flight path.

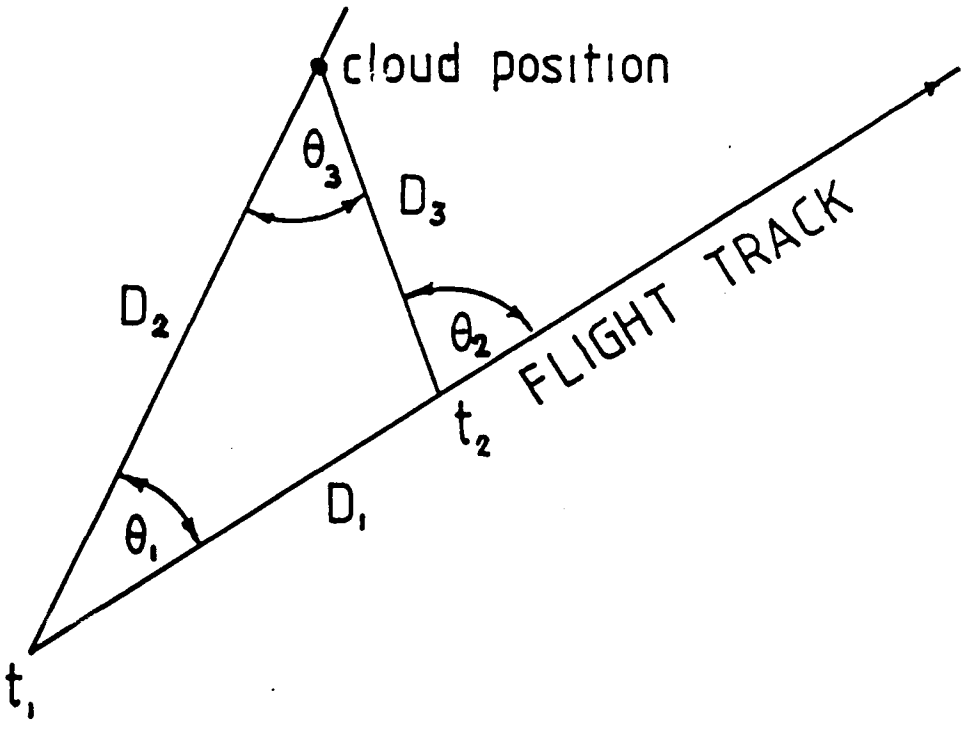

$$\frac{D_1}{\sin\Phi_3} = \frac{D_3}{\sin\Phi_1} = \frac{D_2}{\sin(\pi-\Phi_2)}$$

$$\Phi_3 = \Phi_2 - \Phi_1$$

Φ_1 = azimuth angle to cloud at t_1

Φ_2 = azimuth angle to cloud at t_2

D_1 = distance flown between measurements

$= TAS \times (t_2 - t_1)$, or

$$= \int_{t_1}^{t_2} TAS\ dt$$

Fig. 10.8.4. Geometry of making estimates of the geographical (ground) position of the cloud.

In practice, the overlay is aligned as follows: the aircraft is flown level with a visible horizon and the centre line of the overlay lined up over the horizon of the resulting image. When the horizon is visible during measurements this can always be done, even if the aircraft is not perfectly level. When the horizon is not visible the aircraft must be levelled for the measurements, and the overlay lined up with the predetermined horizon.

10.9 Calculations of precipitation growth rates from 2D-C data (Morrison and Morgan)

In the initial processing of Learjet cloud penetration data using programme ULTRADAS, accretional growth rates are computed from the 2D-C imaging probe data in subroutine TWOD-CALCULATIONS according to a scheme given by Pflaum and Pruppacher (1979). In their approach they compute a collection kernel as an empirical function of particle momentum. The mass growth rate is then taken as the product of the collection kernel and the liquid water content of the air. The growth rates for valid particles are summed over each image frame and then divided by the sample volume to yield a bulk growth rate for the 2D-C image frame. Particle densities are computed as being 0.2, 0.4, 0.6, 0.8 or 1.0 g cm^{-3} resulting in five different estimates of growth rate.

In Pflaum and Pruppacher (1979), collection kernels were determined experimentally using the relation

$$K = \frac{dM/dt}{W} \qquad (1)$$

where K = collection kernel ($cm^{-3}\ s^{-1}$)
dM/dt = average particle growth rate from some initial mass to a final mass (g s^{-1})
W = average liquid water content of the air (g m^{-3})

Solving for dM/dt we get

$$dM/dt = K \times W \qquad (2)$$

Expressing the collection kernel for graupel as a function of the momentum of the individual graupel particles, the visual best-fit line to their experimental results for collection of 10 micron radius water drops is:

$$K = 10.77\ (M \times V)^{0.753} \qquad (3)$$

where M = equivalent water mass (g)
V = particle terminal velocity (cm s^{-1})

They found this scheme reasonable for graupel up to several millimetres in diameter as long as the droplets collected are small (r-collected/ r-graupel 0.1). In the special case where the collectors are large water drops rather than graupel they refer to the theoretical collection kernel by Beard and Grover (1974):

$$K = 9.13\ (M \times V)^{0.738}$$

where, once again, the water droplets that are collected are assumed to be about 10 microns in radius.

The terminal velocities for the particles in the 2D-C images are estimated in subroutines WATER-DROPLET-TERM-VELOCITY for density assumption of 1.0, and in subroutine GRAUPEL-TERMINAL-VELOCITY for density assumptions 0.2, 0.4, 0.6 and 0.8. The first subroutine computes water droplet terminal velocities over three size ranges that run from 0.5 microns in diameter to 7.0 mm as given by Beard (1976). The second subroutine estimates the terminal velocities for graupel particles for any specified density using the relationships given in Locatelli and Hobbs (1974). If the particle size is outside the range of their measurements the results are extrapolated. The terminal velocity is corrected for altitude using the method given in Pruppacher and Klett (1978).

After computation of the particle terminal velocity and its water-equivalent mass (particle volume assuming a sphere, multiplied by the assumed density) we compute the collection kernel using either equation (3) or (4) as appropriate for the density assumption. Taking the cloud liquid water content as measured from the King hot wire device (or from the J-W hot wire or FSSP if the King is not available) we then compute the mass growth rate from equation (2).

11.0 ICE NUCLEATION STUDIES (Morgan)

Elsewhere in this report (Vol. II Section 5.6, Vol. IV Section 9.9) it has been shown that the icing behavior of Nelspruit clouds is quite variable. Many clouds are ice-free at flight altitudes and others contain ice in widely varying concentrations. The degree of development of ice in clouds is important to the natural precipitation processes and to the question of seedability of the clouds. Accurate prediction of ice concentrations in clouds would be an important covariate in an evaluation of the effect of seeding clouds, and would enhance understanding of the natural rain characteristics.

The key to this problem lies in the difficult study area of ice nucleation. During the hail suppression period a few measurements of ice nuclei were made at Nelspruit (CIC 1978). These few measurements showed concentrations of the order of .04 l^{-1} (40 m^{-3}) at -18°C. The method of processing the sampling filters was one which would only detect the sorption mode of nucleation.

The collaboration of Dr Jan Rosinski of NCAR was obtained to explore the possibility that nuclei might be active by another mode, condensation-freezing. In concert with Dr. Rosinski, an exploratory programme of ice nucleus sampling was run during February and March 1986.

Air was sampled with Millipore filters. Two filters were run simultaneously and approximately 100 l of air was sampled on each filter. The dates, times and sample volumes as well as brief weather notes are given in Table 11.1.

The filters were sent to NCAR in Boulder, Colorado, for processing. Fig. 11.1 shows the ice forming nuclei (IFN) concentrations at -15°C and 2 percent supersaturation with respect to a water surface. These show variations over several orders of magnitude (from near zero to 4000 m^{-3}). Sorption IFN (zero supersaturation over water) were in very low concentration (peak, 150 m^{-3} on 12 March, otherwise well below 100 m^{-3}). Note that the concentrations show trends over consecutive days.

A paper examining these IFN concentrations and their relationship to meteorological and other conditions is in preparation.

Table 11.1 Brief weather notes - at filter times

Filter No	Date	Times (SAST)	Time Interval (min)	Volume (l)	Comments
1,2	17-2-86	1358-1413	15	105	S E flow; fine, partly cloudy day
3,4	18-2-86	1350-1409	19	147	shower in progress, light E flow
5,6	19-2-86	1443-1458	15	105	clear to scattered, fine day
7,8	20-2-86	1418-1433	15	105	clear day with isolated storms on Escarpment
9,10	21-2-86	1408-1423	15	105	gentle E wind, high moisture, storms strongly developed on escarpment
11,12	22-2-86	1488-1510	22	178	very high surface T with humidity, well developed storms on escarpment
13,14	23-2-86	1221-1238	17	119	large storms on escarpment, 29° C at 1221 TW 24.5° C
15,16	24-2-86	1357-1452	55		post frontal, but warm surface air, E flow
17,18	25-2-86	1411-1426	15	105	cool, post frontal, middle overcast
19,20	26-2-86	1357-1415	18	140	overcast, cool
21,22	27-2-86	1615-1630	15	105	cool, scattered clouds, light winds
23,24	28-2-86	1414-1429	15	105	almost clear, light haze, warm, wind E
25,26	01-3-86	1327-1342	15	105	warm, almost clear, no wind
27,28	02-3-86	1509-1531	22	178	warm, calm, storms on escarpment to N-W and S
29,30	03-3-86	1435-1450	15	105	scattered, very warm, few storms on escarpment

31,32	04-3-86	1350-1409	19	147	broken Cu, deep E flow, warmish
33,34	05-3-86	1410-1425	15	105	scattered and warm, still E flow
35,36	06-3-86	1439-1455	16	112	scattered, warm (front?)
37,38	07-3-86	1405-1426	21	171	scattered and quite warm, some sort of front yesterday
39,40	08-3-86	1507-1523	16	112	warm, scattered, isolated TsTms SW
41,42	09-3-86	1101-1117	16	112	warm, almost clear, storms developed later
43,44	10-3-86	1516-1531	15	105	post squall, after heavy rain, cool
45,46	11-3-86	1344-1441	57	399	1st scattered, hot, wind W. 2nd. isolated
47,48	11-3-86	1444-1459	15	105	thunderstorm S
49,50	12-3-86	1406-1426	20	154	cool here, hot on Highveld, line forming on escarpment
51,52	13-3-86	1418-1434	16	112	calm, cool to warm ($26^{o}C$) broken clouds
53,54	14-3-86	1422-1438	16	112	scattered to broken, storms all day, escarpment and Swaziland.
55,56	22-3-86	1453-1558	65	455	hot and clear

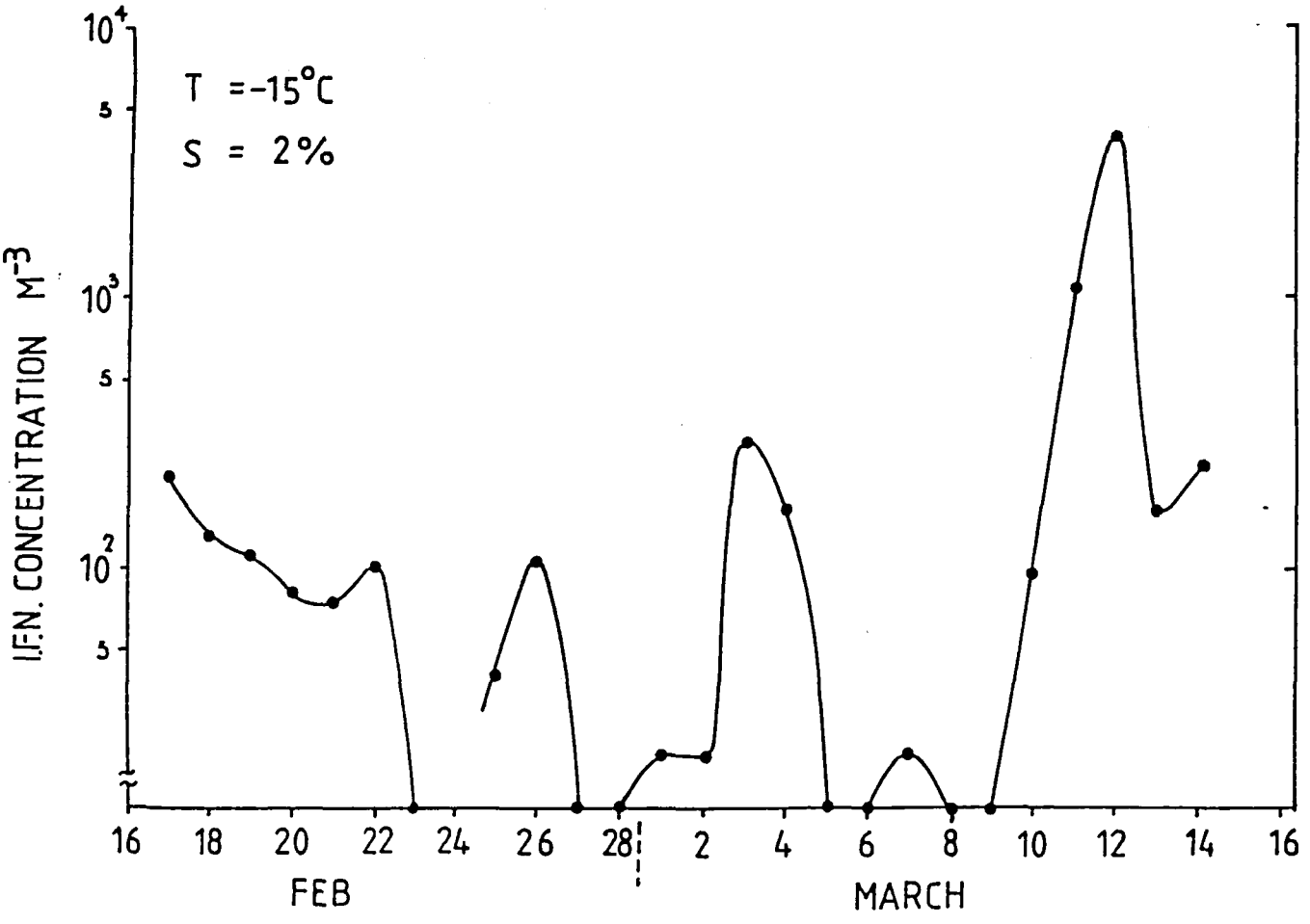

Fig. 11.1. Ice forming nulcei (IFN) concentrations at Nelspruit; February and March 1987.

12.0 PAWS DATA ARCHIVING

A data archive and software package for future data storage has been established in Nelspruit. The data base, located either on disk on the MV4000 computer or on magnetic tape at Cansas International Corporation, is copied onto magnetic tape and taken to the Subtropical Fruit and Citrus Research Institute (Nelspruit) for safe keeping. Notes and log books are also photocopied and archived. A selected portion of the data base is sent to Simpson Weather Associates in Charlottesville, Virginia, for data analyses as well as for additional storage.

This data base covers almost every aspect of the PAWS project. Table 1 shows the types of data which have been archived and the periods of record that they cover. A documentation file accompanies the magnetic tapes at the Institute. This file contains information necessary for dumping the data from tape to disk and explains what the numbers in each data set represent. In the file, each tape has an information sheet (Sample 2), a list of the files contained on the tape, a sample of the data format, and printouts of the programs used to write the data to tape or to dump it to disk.

TABLE 1

Archived Data

Data Type	Format	Period of Record
Nelspruit soundings	mag. tape	82/83, 83/84, 84/85
Rainfall network (16 stations)	mag. tape	82/83, 83/84
Rainfall network (25 stations)	mag. tape	84/85
Radar, blue sky suppressed*	mag. tape	82/83, 83/84, 84/85
WRC surface mesonetwork (9 stations - winds and temperatures)	mag. tape	84/85
Radiation	mag. tape	84/85
Aircraft	mag. tape	80/81, 81/82, 82/83, 83/84, 84/85
Radar log book	paper	82/83. 83/84, 84/85
Pilot's and observer's notes	paper	82/83, 83/84, 84/85
G. Mather's daily log book	paper	82/83, 83/84, 84/85
Principle component analysis	paper	82/83, 83/84, 84/85
Nelspruit 24-hour rainfall	paper	82/83, 83/84, 84/85
Barograph strip charts (Nelspruit)	paper	82/83, 83/84, 84/85
Hygrothermograph strip charts (Nelspruit)	paper	82/83, 83/84, 84/85

*Archiving will be completed before the start of the 85/86 season

Sample 2

SECTION : RAINFALL

TAPE NO : 2

TAPE TITLE : "Rainfall Data, 82/83, 83/84, + 84/85 seasons"

DATE OF TAPE CREATION : 29 MAR 1985

DATA TYPE (ASCII binary, EBCDIC, etc): ASCII

TAPE DENSITY: 1600 bpi

TAPE LENGTH : 600 ft.

WHO WROTE THE DATA TO TAPE: Wendy London

NAME OF THE TAPE WRITING PROGRAM : RAINTAPE.F77

WHO WORKS WITH AND ANALYSES THIS DATA : Parsons, London, Emmitt

NUMBER OF FILES ON THE TAPE : 57

NUMBER OF BLOCKS PER FILE : Variable

NUMBER OF RECORDS PER BLOCK : 100

NUMBER OF WORDS PER BLOCK : 2000

DESCRIPTION OF THE DATA : Header record of file name such as STATION01.83, where 01 is station # and 83 is the 83/84 season, then one record per each 5 minute interval of the season that had rain. Data is: year, Julian date, time and the number of tips, where 1 tip = 0.25 mm.

OTHER COPIES OF THIS DATA ARE LOCATED AT : CIC (Nelsprint), SWA (Virginia)

IS THERE A PROGRAM TO TAKE THE DATA OFF OF THE TAPE? yes

PROGRAM NAME: RAINOFFTAPE.F77

13.0 REFERENCES

Ackerman, B., R.C. Grosh and R.Y. Sun, 1979: Assessing midwest cloud characteristics for weather modification. Final Report ENV 77-11527, National Science Foundation, Illinois Water Survey, Irbana, Illinois.

Adler, R.F., and R.A. Mack, 1984: Thunderstorm cloud height-rainfall relations for use with satellite rainfall estimation techniques. J. Climate Appl. Meteor., 23, 280-296.

Ahlberg, J.H., E.N. Nilson and J.L. Walsh, 1967: The Theory of Splines and their Applications. New York, Academic Press.

Allee, P.A., B.T. Patten and E.W. Barrett, 1972: The dynamic calibration of an airborne ice nuclei generator. J. Rech. Atmos., 6, 29-40.

Batchelor, G.K., 1970: An introduction to fluid dynamics. Cambridge University Press, 615 pp.

Barnes, Stanley L., 1973: Mesoscale objective map analysis using weighted time-series observations. NOAA Technical Memorandum, ERL NSSL 62, March 1973.

------, and S.W. Grover, 1974: Numerical collision efficiencies for small raindrops colliding with micron sized particles. J. Atmos. Sci., 31, 543-550.

Beard, K.V., 1976: Terminal velocity and shape of cloud precipitation drops aloft. J. Atmos. Sci., 33, 851-864.

Berry, F.A., and E. Bolay, 1973: Handbook of meteorology. McGraw Hill Publication.

Bolton, D. 1980: The computation of equivalent potential temperature. Mon. Wea. Rev., 108, 1046-1053.

Browning, K.A., and F.H. Ludlain, 1962: Airflow in convective storms. Quart. J. Roy. Meteor. Soc., 89, 75-84.

Buck, A., 1976: The variable-path Lyman-alpha hygrometer and its operating characteristics. Bull. Amer. Met. Soc., 57, 1113-1118.

Byers, H.R., and R.R. Braham, 1949: The thunderstorms. Wash. D.C., U.S. Govt. Printing Office.

CIC, 1978: Annual report weather modification season 1976/77. Submitted to Laeveldse Tabak Kooperasie Beperk. Cansas International Corporation.

Cooper, H., M. Garstang and J. Simpson, 1982: The diurnal interaction between convection and peninsular-scale forcing over south Florida. Mon. Wea. Rev. 110, 488-503.

Coulman, C.E., and M.A. Parker, 1982: On the calibration and performance of an instrument for measuring total water mixing ratio in cloud. J. Appl. Meteor., 21, 695-702.

Cressman, G.P., 1959: An operational objective analysis scheme. Mon. Wea. Rev., 108, 1046-1053.

Dixon, M., and G.K. Mather, 1986: Radar evaluation of a randomized rain-augmentation experiment: Some preliminary results. Tenth AMS Conf. on Planned and Inadvert. Wea. Modif., Arlington, Virginia.

Eadie, W.J., and T.R. Mee, 1963: The effect of dry ice pellet velocity on the generation of ice crystals. J. Appl. Meteor. 2, 260-265.

Emmitt, G.D., D.S. Roos and B.J. Morrison, 1984: Dry ice pellet experiments (DIPEX) - field and laboratory. Report to Water Research Commission Republic of South Africa.

Frankhauser, J.C., and C. Wade, 1982: The environment of the storms; Chapter 2 of hailstorms of the central high plains, Vol. 1, The National Hail Research Experiment. Colorado Associated University Press, Boulder, Colorado, 5-33.

Frank, N., P.L. Moore and G.E. Fisher, 1967: Summer shower distribution over the Florida peninsula as deduced from digitized radar. J. Appl. Meteor., 6, 309-316.

Fukuta, N., W.A. Schmeling and L.F. Evans, 1971: Experimental determination of ice nucleation by falling dry ice pellets. J. Appl. Meteor., 10, 1174-1179.

Gagin, A., D. Rosenfeld and R.E. Lopez, 1985: The relationship between height and precipitation characteristics of summertime convective cells in south Florida. J. Atmos. Sci., 42, 84-94.

Gayet, J.F., M. Friedlander and J.P. Pinty, 1977: Sur la mesur de la teneur en eau totale des nuages. Sci. Rep. No 22, Lab. Assoc. Meteor. Phys, Aubiere, France.

Haman, K., 1967: On the accumulation of liquid water in a buoyant jet and its relation to hail phenomena. Acta Geophys. Pol., 15, 9-27.

Hobbs, P.V., R.J. Farber and R.G. Joppa, 1973: Collection of ice particles from aircraft using decelerators. J. Appl, Meteor., 12, 522-528.

Holroyd, E.W., A.B. Super and B.A. Silverman, 1978: The practicability of dry ice for on top seeding of convective clouds. J. Appl. Meteor. 17, 49-63.

Horn, R.D., W.G. Finnegan, and P.J. DeMott, 1982: Experimental studies of nucleation by dry ice. J. Appl. Meteor., 21, 1567-1570.

Kessler, E., 1969: On the distribution and continuity of water substance in atmospheric circulations. Met. Monographs, 10, No 32, AMS. Boston.

King, W.D., J.E. Dye, J.W. Strapp, D. Baumgardner and D. Huffman, 1985: Icing wind tunnel tests on the CSIRO liquid water probe. J. Atmos. Ocean Tech., 2, 340-352.

Knight, C.A., W.A. Cooper, D.W. Breed, I.R. Paluch, P.L. Smith and G. Vali, 1982: Microphysics, Chapter 7 of hailstorms of the central high plains, Vol. 1, The National Hail Research Experiment. Knight and Squires, Eds. Colorado Associated University Press. Boulder, Colorado.

Kyle, T.G., and W.R. Sands, 1973: Water content in convective storm clouds. Science, 180, 1274-1275.

-----, 1975: The measurement of water content by an evaporator, J. Appl. Meteor., 14, 327-332.

Lamb, D., J. Hallet and R. Sax 1981: Mechanistic limitations to the release of latent heat during the natural and artificial glaciation of deep convective clouds. Quart. J.R. Met. Soc. 107, 935-954.

Leighton, H.G., and R.R. Rogers, 1974: Droplet growth by condensation and coalescence in a strong updraft. Jour. Atmos. Sci., 31, No 1, 271-279.

Lilly, D.K., 1979: The dynamical structure and evolution of thunderstorms and squall lines. Ann. Rev. Earth Planet Sci., 7, 117-161.

Locatelli, J. D., and P.V. Hobbs, 1974: Fall speeds and masses of solid precipitation particles. J. Geophys. Res., 79, 2185-2197.

Lozowski, E.P., and B. Kochtubajda, 1980: Theory and measurements of dry ice sublimation in clear air and simulated cloud. Proc. WMO Third Scientific Conf. on Weather Modification, Clermont-Ferrand, France, 409-416.

Mader, G.N., 1979: Numerical study of storms in the Transvaal. S. African Geo. J. 61, No 2.

Mandrioli, P., M.G. Negrini, G. Cesari and G. Morgan, 1983: Evidence for long range transport of biological and anthropogenic aerosol particles in the atmosphere. Grana, 23, No 1, 43-53.

Mather, G.K., B.J. Morrison and G.M. Morgan, 1986: A preliminary assessment of the importance of coalescence in convective clouds of the eastern Transvaal. Submitted to J. Clim. Appl. Meteor.

-----, 1986: The Nelspruit program - history and current status. Tenth AMS Conf. on Planned and Inadvert. Wea. Modif. Arlington, Virginia.

Miller, R.C., 1967: Semi-objective evaluation of the relative importance of parameters favouring production of severe storms. Preprints 5th Conf. Severe Local Storms, St. Louis, Amer. Meteor. Soc., 2-9.

Moncrieff, M.W., and J.J. Miller, 1976: The dynamics and simulations of tropical squall lines. Quart. J. Roy. Meteor. Soc., 102, 373-394.

Morgan, G.M., 1970: An examination of the wet-bulb zero as a hail forecasting parameter in the Po Valley, Italy. J. Appl. Meteor., 9, 537-540.

-----, and R.C. Beebe, 1971: Analysis of the time-space behaviour of the field of equivalent temperature during a severe weather situation. Preprints, 7th Conference on Severe Local Storms, A.M.S., Kansas City, Missouri, 54-59.

-----, 1972: On the growth of large hail. Mon. Wea. rev., 100, 196-205.

-----,and E.A. Mueller, 1972: The total liquid water mass of large convective storms. Preprints, 15th Radar Meteor. Conf., AMS, Boston, 4 pp.

-----, 1973: A general description of the hail problem in the Po Valley of Northern Italy. J. Appl. Meteor., 12, 338-353.

-----, and P. Squires, 1972: Introduction to Chapter 1 of hailstorms of the central high plains, Vol. 1, The National Hail Research Experiment. Colorado Associated University Press, Boulder, Colorado, 1-4.

-----, and E.L. Crow, 1982: Statistical testing of hail suppression hypothesis; Chapter 11 of hailstorms of the central high plains, Vol. 1, The National Hail Research Experiment. Colorado Associated University Press, Boulder, Colorado, 249-261.

-----, and J. Tuttle, 1982: Some experimental techniques for the study of the evolution of atmospheric thermodynamic instability. Proceedings of the Second International Conference on Hailstorms and Hail Prevention, Sofia, Bulgaria, Printing Office of the Bulgarian Hydrometeorological Service, Sofia, 192-196.

-----, and G.K. Mather, 1984: Problems in the measurement of liquid water content in Transvaal clouds. Paper presented at the Ninth Conf. on Wea. Mod., Park City, Utah, American Meteorological Society.

-----, and B.J. Morrison, 1985: Jet engine bleed air measurements of water quantities in convective clouds. Second Annual Conf., S.A. Soc. for Atmos. Sci., Pretoria.

-----, B.J. Morrison, and G.K. Mather, 1986a: Total and condensed water contents in warm based thunderstorm turrets: their estimation with a jet engine bleed air measurement technique. Submitted to J. Clim. Appl. Meteor.

-----, -----, and -----, 1986b: Sensing of cloud condensed water mixing ratio in jet engine compressor bleed air by the potential temperature method. Submitted to J. Atmos. Ocean. Tech.

-----, -----, and -----, 1986c: Evidence for the accumulation of very high concentrations of supercooled liquid water in thunderstorms. Submitted to J. Clim. Appl. Meteor.

Morrison, B.J., G.K. Mather, and G.M. Morgan, 1986: Aircraft observations of target turrets on multicellular storms showing radar response to dry ice seeding. Tenth Conf. Wea. Modif. Arlington, Virginia. American Meteorological Society.

-----, B.J., W.G. Finnegan, R.D. Horn and L.O. Grant, 1984: A laboratory characterization of dry ice as a glaciogenic seeding agent. Ninth Conference on Planned and Inadvert. Wea. Modif. 21-23 May 1984, Park City, Utah.

Musil, D.J., P.L. Smith and A. Waldvogen, 1984: Evaluation of the applicability of the accumulation zone hypothesis to Swiss hailstorms. Extended Abstracts. Ninth Conf. Wea. Mod. Park City, Utah, A.M.S. Boston, 29-30.

-----, and -----, 1985: Aircraft penetrations of Swiss hailstorms: An update. Abstracts, First European Conf. of the Wea. Mod. Assoc., Clermont-Ferrand, Toulouse, France.

Newton, C.W., 1963: Dynamics of severe convective storms. Meteorol. Monogr. 5, 33-55.

Pflaum, J.C., and H.R. Pruppacher, 1979: A wind tunnel investigation of the growth of graupel initiated from frozen drops. J. Atmos. Sci, 34, 680-689.

Plate, E.J., 1971: Aerodynamic characteristics of the atmospheric boundary layer. U.S. Dept. of Energy, Rept. prepared for the U.S. Atomic Energy Commission, 190 pp.

Pruppacher, H.R., and J.D. Klett, 1978: Microphysics of clouds and precipitation. D. Reidel, Dordrecht, Holland.

Reinsch, C.H., 1967: Smoothing by spline functions. Numerische Mathematik, 10, 177-183.

Rogers, R.R., 1979: A short course in cloud physics. 2nd Edition. Pergamon International Library, Oxford.

Roys, G.P., 1963: Airborne instrumentation system for measuring meteorological phenomena inside thunderstorms. Tech. Doc. Rept. No. ASD-TDR-63-231, Directorate of Flight Test, Aeron. Systems Div., AF Systems Command, Wright-Patterson AB, Ohio.

-----, and E. Kessler, 1966: Measurement by aircraft of condensed water in Great Plains thunderstorms. Tech. Note 49-NSSP-19. U.S. Dept. of Commerce, ESSA, Wash. D.C.

Ruskin, R.E., and W.D. Scott, 1974: Weather and climate modification. W.N. Hess, Ed., Chap. 4, Wiley.

Schlesinger, R., 1975: A three-dimensional numerical model of a violated deep convective cloud: preliminary results. J. Atmos. Sci., 32, 934-957.

Smith, P.L., Jr., 1976: Comments on the measurement of water content by an evaporator. J. Appl. Meteor., 15, 189-191.

-----, P.L., J.R. Miller, A.A. Doneand, J.H. Hursch, D.L. Pregnitz, P.E. Price, K.J. Tyler and H.D. Orville, 1985: Research to develop evaluation techniques for operational convective cloud modification projects. report SDSMT/IAS/R - 85/02, Institute of Atmospheric Sciences, South Dakota School of Mines and Technology, Rapid City S.D. 93 pp.

Sulakvelidze, G.K., N.S. Bibilashvili and V.F. Lapcheva, 1967: Formation of precipitation and modification of hail processes. Israel Program for Scientific Translations, Jerulsalem.

Tsonis, A.A., G.L. Austin and S. Lovejoy, 1984: A proposal for a new statistic and technique development for the design and evaluation of cloud seeding experiments. Atmos-Ocean 22, 67-82.

Ulanski, S.L., and M. Garstang, 1978: The role of surface divergence and vorticity in the life cycle of convective rainfall. Part 1: Observations and analysis. J. Atmos. Sci., 35, 1047-1062.

Vonnegut, B., 1981. Misconceptions about cloud seeding with dry ice. J. Wea. Modif., 13, 9-10.